THERMAL PROPERTIES OF THE GAS IN EARLY-TYPE GALAXIES AND GALAXY CLUSTERS

By

Rachel L.S. Frisbie

A DISSERTATION

Submitted to
Michigan State University
in partial fulfillment of the requirements
for the degree of

Astrophysics – Doctor of Philosophy

2020

ABSTRACT

THERMAL PROPERTIES OF THE GAS IN EARLY-TYPE GALAXIES AND GALAXY CLUSTERS

By

Rachel L.S. Frisbie

Most of the baryons, or “normal" matter, found in galaxies and galaxy clusters are found in the hot, X-ray emitting gas known as the circumgalactic medium (CGM) or intracluster medium (ICM). The hot gas traces the gravitational potential well and is affected by both thermal and gravitational processes, so we use observations of the hot gas to explore changes across the galaxy or cluster's radius. Heating and cooling in the central regions of galaxies and clusters is primarily driven by feedback processes, including Active Galactic Nuclei (AGNs) and Type Ia supernovae. We can use X-ray observations of the hot gas to understand its thermal history and how the various feedback mechanisms affect the gas at small and large radii. Furthermore, we use X-ray gas properties (temperature, density, entropy, concentration, centroid shift, and power ratios) to characterize galaxies and clusters, understand their evolution, and classify them in meaningful ways. The combination of observations along with theoretical models and simulations explored in this thesis provides key insight into understanding how feedback processes affect the hot gas.

I begin by presenting thermal property results for a uniformly reduced sample of 348 galaxy clusters and show how those results can be used to characterize the sample and for further galaxy cluster science. I will then turn my focus to early-type galaxies for the remainder of this work. I examine a sample of 12 nearby early-type galaxies with powerful radio sources and find that IC 4296 exhibits unusually low central entropy as previously observed in NGC 4261. We also find some evidence that the minimum of the ratio between the cooling time and free-fall time, if it occurs at the galaxy center, may indicate the presence of a powerful radio source. Finally, I examine the galactic atmospheres of a sample of 49 early-type galaxies. I will show that the equilibrium pressure and density radial profiles for single- and multiphase galaxies agree with the Voit et al. (2020) theoretical model. I also find evidence for a correlation between the central

velocity dispersion and entropy profile slope of the galaxies in the sample that agrees with the theoretical model.

For Dustin and Torrey

ACKNOWLEDGEMENTS

Defending my dissertation virtually and amidst a pandemic is not exactly how I envisioned closing this chapter of my life, but here we are. I would not be presenting this work if not for the wonderful people I have in my life, both personally and professionally.

First, I want to thank my advisor, Megan Donahue, and my committee, Mark Voit, Brian O'Shea, Wolfgang Kerzendorf, and Tyce DeYoung for their scientific guidance and support throughout my PhD. My collaborators, Thomas Connor, Yuan Li, Kiran Lakhchaura, Ming Sun, Norbert Werner, Romana Grossova, and Lorenzo Lovisari were also instrumental in developing the work in this thesis.

I want to thank the teachers and mentors who inspired me to become a scientist and educator and encouraged me every step of the way. My middle and high school science teachers, Susan Thackara, George Croll, and Suzanne Croll introduced me to science and taught me to ask questions about the world around me. My undergraduate research advisor, mentor, and professor, Jeremy Sepinsky, introduced me to astronomy research and supported my development as a scientist. I would also like to thank the ISEE Professional Development Program, especially Devin Silvia, Austin Barnes, Lisa Hunter, Rafael Palomino, and Philipp Grete for giving me the opportunity to grow as an educator and providing me with a community when I needed it most.

I want to thank my family and friends. From our early days in undergraduate physics to now, my husband Dustin has been my biggest supporter, best friend, and the best rubber duck. I also want to thank our dog Freya for being the sweetest puppy and giving me all the snuggles I needed during graduate school. To my wonderful nephew Tristan, for letting your Aunt Rachie read you endless stories on video chat, thank you for being a wonderfully bright spot during the last several months of my PhD. My older sister Torrey paved the way for me to become a scientist and has mentored and supported me from the beginning. I also want to thank my parents for supporting me in all of my endeavours. I am endlessly thankful to my fellow grad students, Dana Koeppe, Jennifer Ranta, Austin Edmister, Carl Fields, Forrest Glines, Jessica Maldonado, and Kathryn Bowen for bringing much needed joy to graduate school. I also especially want to thank Kim Crosslan for her endless patience and support throughout my time in graduate school. There are many more people who have been part of my community for the past 27 years, and nowhere near enough space to list them. Thank you all for being a part of my life and helping to shape me into the person I am today.

TABLE OF CONTENTS

LIST OF TABLES

LIST OF FIGURES

CHAPTER 1

INTRODUCTION

1.1 Galaxy Clusters and Early-Type Galaxies

The Hubble Deep Field image (Figure 1.1, Williams et al. (1996)) revealed that there were 3,000 galaxies in just one twenty-four-millionth of the sky, indicating that the universe is full of galaxies. The masses, stellar populations, and shapes of galaxies vary widely, and astronomers still often use the early Hubble classifications of galaxies to group them by their defining characteristics. Broadly, there are elliptical, spiral, and irregular galaxies. The Hubble "tuning fork" (see Figure 1.2) was developed because Hubble believed that elliptical galaxies would eventually evolve into spiral galaxies. The belief that ellipticals evolved into spirals turned out to be incorrect, but the naming convention of referring to generally elliptical shaped galaxies as "early-type" and spiral shaped galaxies as "late-type" has prevailed and will appear in this thesis. While the tuning fork does not sort galaxies by evolutionary stage, it does sort them by their angular momentum with spiral galaxies generally rotating faster than elliptical galaxies. Elliptical galaxies are generally red in color, contain mostly older, low mass stars, have little active star formation, and are the most massive galaxies. Spiral galaxies, like our own Milky Way, are generally blue in color, have all types of stars, and are actively forming stars. Irregular galaxies have no specific shape, contain all types of stars, are usually actively forming stars, and are the least massive of the three types. Particularly low mass galaxies are known as dwarf galaxies, but they are beyond the scope of this thesis.

More recently, sky surveys of galaxies (the 2dF Galaxy survey (Colless et al., 2001) and the Sloan Digital Digital Sky Survey (Stoughton et al., 2002)) revealed that galaxies are clumped together along large scale filaments around large voids with diameters of ~150 million light years (see Figure 1.3) . The large scale filaments trace the distribution of dark matter in the universe. Dark matter and dark energy are so named because we cannot directly observe them, we can only

Figure 1.1 The *Hubble* Deep Field image shows the 3,000 galaxies found in one twenty-four-millionth of the sky. The image was composed of data from the *Hubble Space Telescope* taken over ten days in 1995 and published in 1996 (Williams et al., 1996).

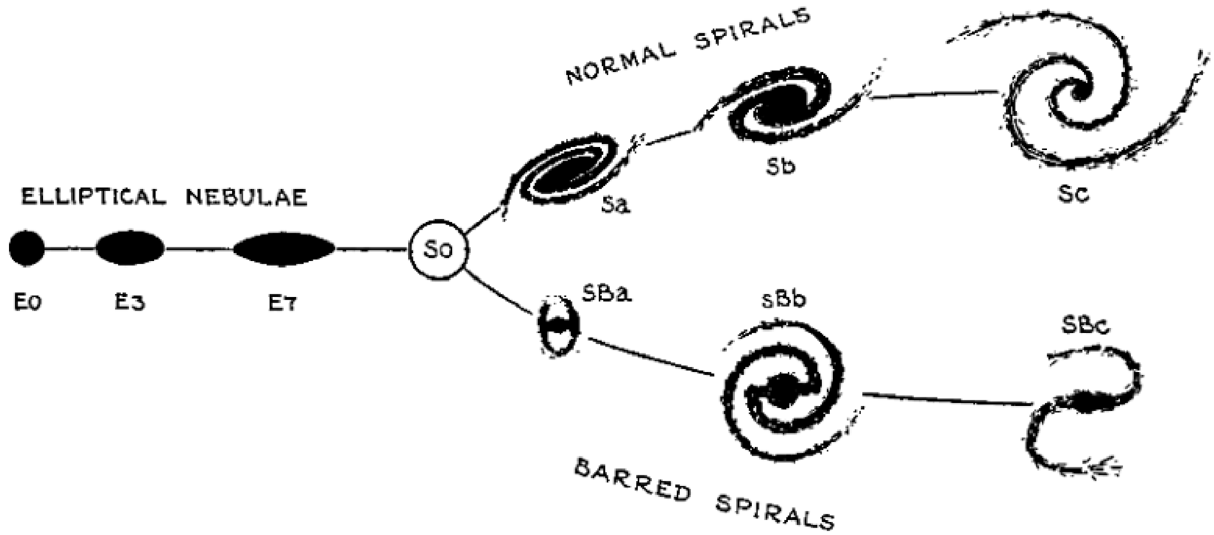

Figure 1.2 The original tuning fork diagram from Hubble's 1936 book, *The Realm of the Nebulae* (Hubble, 1936). Hubble developed the tuning fork to classify galaxies by their "family traits" and thought that galaxies evolved along the tuning fork from ellipticals to spirals. While we now know that the classifications are not evolutionary, but rather by angular momentum, astronomers still classify galaxies in this way.

observe their gravitational influence on the universe. Dark matter and dark energy represent most of the content of the universe, with dark energy comprising $\sim 70\%$ and dark matter comprising $\sim 25\%$ (Planck Collaboration et al., 2016). However, the focus of this thesis is on the normal, or "baryonic", matter in the universe. Baryons make up the remaining $\sim 5\%$ of the matter in the universe. However, there are some baryons that can be difficult to detect, leading to the "missing baryon problem" in Cosmology.

The "missing baryon problem" refers to the disparity between the baryonic mass density inferred from primordial nucleosynthesis via Cosmic Microwave Background (CMB) measurements and the baryonic mass density of galaxies, where the baryonic mass from galaxies falls far short of the baryonic mass from the CMB. The "Warm-Hot-Intergalactic-Medium" (WHIM) model was proposed to account for the missing baryons (see Cen & Ostriker 1999; Bregman 2007). The WHIM is characterized by a low-density, hot (10^6 K) plasma which produces a weak signal and would be challenging to detect. Bregman et al. (2018) showed that baryon density estimates could

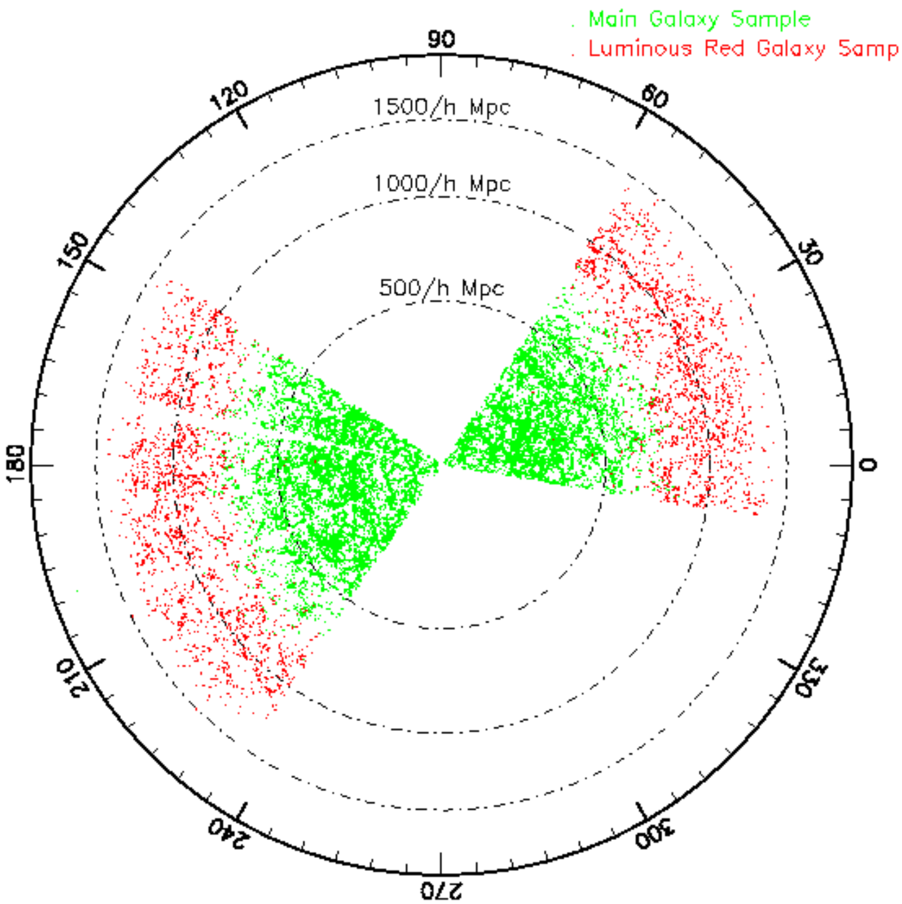

Figure 1.3 The distribution of galaxies from the first Sloan Digital Sky Survey (SDSS) data release (Stoughton et al., 2002). The green galaxies are from the main SDSS galaxy sample, and the red galaxies are from the luminous red galaxy sample (LRG).

be made, even with a weak signal, by stacking X-ray observations of many early-type galaxies, scaled by their radii (R_{200}). The stacked observations revealed that most, if not all, of the "missing baryons" are hot and located beyond R_{200}. While the source of missing baryons for early-type galaxies can be accounted for with the stacked X-ray observations, Bregman et al. (2018) also showed that the observed signal from early-type galaxies would be too high for spiral galaxies. Therefore, the hot halos of spiral galaxies may be different, and further constraints on the hot gas content of early-type galaxies are needed from next generation X-ray observatories.

The large scale structure of the universe likely formed in a "bottom-up" fashion, meaning that

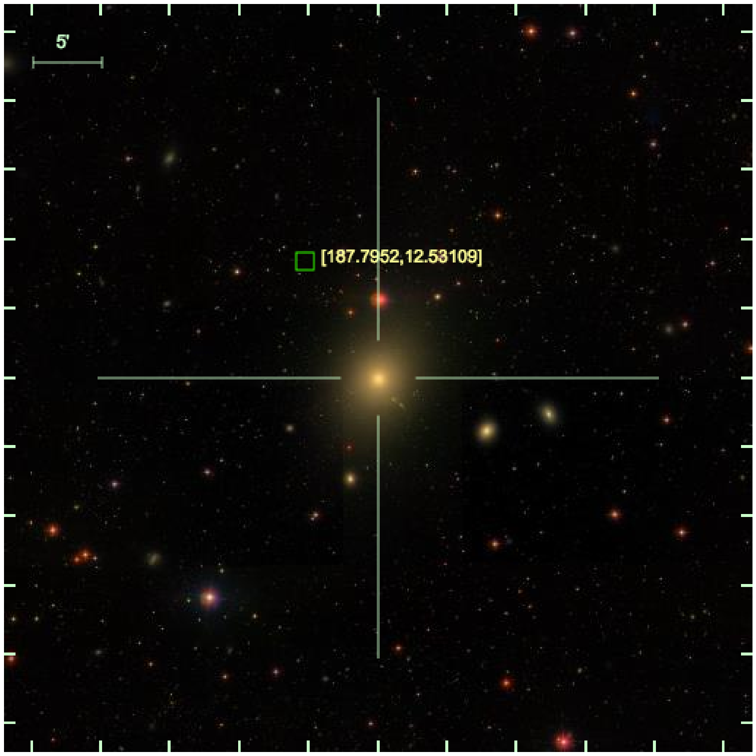

Figure 1.4 Image of the Virgo Cluster assembled from SDSS DR15 optical data (Aguado et al., 2019). The Brightest Cluster Galaxy (BCG) is M87 (NGC 4486) and is marked by the cross-hairs.

smaller scale structures merge and join together to create larger structures, along the distribution of dark matter. The largest gravitationally bound structures in the universe are galaxy clusters, composed of 100s-1000s of galaxies, all within a large clump of dark matter known as a dark matter potential well (see Figure 1.4). Galaxy clusters can contain all types of galaxies, but the majority of galaxy clusters are dominated by one galaxy called the Brightest Cluster Galaxy (BCG). BCGs are usually the brightest, most massive galaxies in a cluster, are centrally located in the cluster, and are usually elliptical galaxies. The BCG and the cluster evolve together, and understanding how BCGs (and massive elliptical galaxies) work is crucial for understanding how galaxy clusters evolve.

1.2 Cosmology Primer

Hubble (1929) observed a sample of galaxies and found that all galaxies are moving away from our own, and their recessional velocities are proportional to their distance from our galaxies

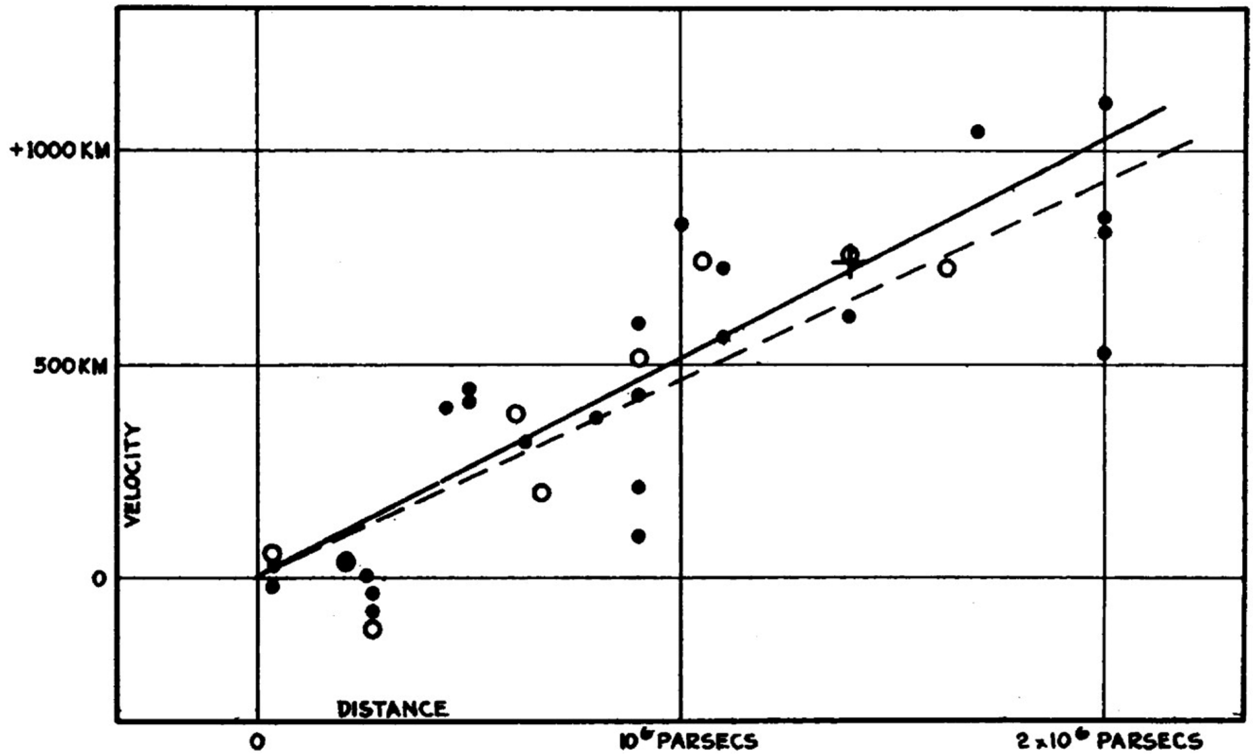

Figure 1.5 Figure 1 from Hubble (1929) shows the distances and velocities to the sample of galaxies Hubble used to show that the universe is expanding. The y-axis are the radial velocities, corrected for solar motion, and the x-axis are the distances estimated from stars and mean luminosities in the galaxies. The slope of this distance-velocity relationship is the Hubble parameter, H_0.

(see Figure 1.5). The velocity-distance relation, $v = H_0\, r$ (*Hubble's Law*), where H_0 is referred to as *Hubble's constant*, shows that the universe is expanding uniformly. *Hubble's constant* characterizes the expansion of the universe and remains an active area of research. Type Ia supernovae measurements give $H_0 = 73.8 \pm 2.4$ km s^{-1} Mpc^{-1} (Riess et al., 2011), while Cosmic Microwave Background measurements give $H_0 = 67.4 \pm 0.5$ km s^{-1} Mpc^{-1} (Planck Collaboration et al., 2018). In this thesis, we will use the widely accepted value for a cold-dark matter cosmology of $H_0 = 70$ km s^{-1} Mpc^{-1}. The effect of choosing the Type Ia supernovae value or Cosmic Microwave background value much smaller than the statistical uncertainty for our relevant measurements, so our choice to use single digit precision for H_0 is negligible for this work. Furthermore, for the work in Chapters 3 and 4, the galaxies are nearby enough to have distance measurements independent of H_0. In modern astronomy, when it became possible to obtain spectra of galaxies, the distances to galaxies could be described more precisely with a quantity known as redshift, z. Redshift is measured by the shift of the galaxy's spectrum due to its motion away from us in the the expanding universe. The shifting of a receding galaxy's optical spectrum is similar to how an ambulance's siren appears to drop in pitch as it drives away. In the case of the ambulance, the frequency of the receding siren is lowered and can be measured by the Doppler effect for a receding source. For a receding galaxy, the shift is observed in the optical (rather than sound) spectrum, but the effect is the similar. The spectrum shifts to longer (redder) wavelengths the farther the galaxy is from us because we know from Hubble's Law that the farther a galaxy is from us, the faster it is moving. The redshift, z of the galaxy's spectrum therefore

$$z = \frac{\lambda_{\rm obs} - \lambda_{\rm rest}}{\lambda_{\rm rest}} \tag{1.1}$$

where $\lambda_{\rm obs}$ is the observed wavelength, and $\lambda_{\rm rest}$ is the emitted wavelength. A small redshift indicates that the galaxy is in the local universe, and a larger redshift indicates that the galaxy is far away. Because higher redshifts correspond to larger distances, which in turn correspond to longer light travel times, redshift also provides us with an idea of how the universe looked at earlier times. For context, our furthest observations of lensed quasars[1] are around $z \sim 6.5$ (Fan et al., 2019). The furthest spectroscopic redshift obtained from a galaxy (GN-z11) is at $z = 11.1$ (Oesch et al., 2016). However, the nearby galaxies in this thesis range from $z = 0.001 - 0.02$, and the galaxy clusters extend to $z \sim 1.5$.

The expansion of the universe provides insight into what sort of universe we live in, and key cosmological parameters describe fundamental characteristics of that universe. As the quality of observations has increased along with our theoretical understanding, our ability to describe the universe with cosmological parameters has improved. Cosmic Microwave Background (CMB) measurements showed that, in general, the universe is homogeneous and isotropic, and thus, H_0 should be constant in all directions. However, because the expansion of the universe is accelerating

[1]"Quasi-stellar objects," are extremely luminous Active Galactic Nuclei found in the centers of early galaxies.

due to the presence of dark energy, H_0 is dependent on redshift by:

$$H(z) = H_0\, E(z), \tag{1.2}$$

where $E(z) = \sqrt{\Omega_M(1+z)^3 + \Omega_\Lambda}$, and the cosmological parameters $\Omega_M \simeq 0.3$ and $\Omega_\Lambda \simeq 0.7$ refer to the matter and dark energy content of the universe, respectively. For this thesis, we will assume the stated values for Ω_M and Ω_Λ when determining distances and spatial properties of galaxy clusters and early-type galaxies, except when redshift-independent distance measures are available in the case of nearby galaxies (see Chapter 3). The effect of using lower precision values for Ω_M and Ω_Λ affect $E(z)$ by $\sim 2\%$ which is much lower than our statistical uncertainty, so we are safe to make this assumption for this thesis.

1.3 X-ray Observations

1.3.1 A Brief History of X-ray Astronomy

Much of the work in this thesis builds on a long history of discoveries in the X-ray universe. We can trace the historical context and motivation for my study of early-type galaxies and galaxy clusters from the early days of X-ray astronomy to now. In contrast to many other fields of observational astronomy that date back hundreds to even thousands of years, the ~ 70 history of X-ray astronomy is comparatively short. Because X-rays are almost entirely blocked by the Earth's atmosphere, the only way to observe the X-ray universe is from space. As a result, observations of the X-ray universe were out of reach until detectors could be launched sufficiently high in the atmosphere. Giacconi et al. (1962) launched a rocket that detected Sco X-1, the first X-ray source besides the Sun (first observed in the late 1940s (Burnight, 1949)), and detected an isotropic X-ray background. The discovery of the first X-ray source was monumental and inspired further exploration of the X-ray universe.

The first observations of extra-galactic X-ray sources were made with the *Uhuru* X-ray satellite (Giacconi et al., 1971), launched in 1970. In a series of 4 letters, (Giacconi et al. 1971; Tananbaum et al. 1971; Gursky et al. 1971; Kellogg et al. 1971), presented observations from *Uhuru* that confirmed the existence of extra-galactic X-ray sources. Furthermore, they provided observations of the spectral features and the variability of X-ray sources and the structure of X-ray emitting regions at a resolution of $30'$. The observations also led to the first observations of extended emission from galaxy clusters from the Perseus cluster (Forman et al., 1972). The results from the *Uhuru* satellite planted the first seeds for a great X-ray observatory that would eventually lead to the launch of *Chandra* in 1999.

One major question X-ray astronomers sought to address when developing the successors to *Uhuru* was whether the extended emission from extra-galactic X-ray sources was due to the integrated contributions of several discrete X-ray point sources or from diffuse processes, particularly in galaxies. To address the question of the nature of the extended emission, the *Einstein* X-ray telescope (Giacconi et al., 1979b), was developed and launched in 1978 with significantly increased spatial resolution and sensitivity ($\sim 10^6$ more sensitive than the early X-ray detectors). *Einstein* showed that many clusters of galaxies were "young" in dynamical age and involved in mergers rather than "old" and dynamically relaxed (Jones et al. 1979; Jones & Forman 1984). Forman et al. (1985) showed that early-type galaxies have hot gaseous coronae, a discovery that still influences our exploration of the hot gas in early-type galaxies today. *Einstein* confirmed the presence of extended X-ray emission in galaxy clusters, but nearby, early-type galaxies remained an area of debate (see Sarazin (1986) for a review). While observations of the emission from early-type galaxies from *Einstein* did contribute to understanding the extended emission from nearby early-type galaxies (Giacconi et al., 1979a), the debate over its origin continued and would continue until *Chandra* began collecting data and showed clear evidence for diffuse, extended, X-ray gas from the Intracluster Medium (ICM) and Circumgalactic Medium (CGM).

In between the *Einstein* and the launch of finer spatial resolution X-ray telescopes, the *Roentgen Satellite* (*ROSAT*, (Pfeffermann et al., 1987)) provided the first spatially resolved X-ray all-sky survey. *ROSAT* was launched in 1990 and completed its all-sky survey in the first 6 months and continued to take pointed observations for the next nine years. The satellite was sensitive to the "soft" X-rays between 0.1–2 keV, and contributed to mapping the diffuse galactic X-ray background

(Snowden et al., 1995) among many other discoveries. *ROSAT* remains the best X-ray all-sky survey to this day.

1.3.1.1 *Chandra* X-ray Observatory

NASA's *Chandra* X-ray Observatory (Weisskopf et al., 2002) is a telescope specially designed to detect X-ray emission from very hot regions of the universe such as exploded stars, clusters of galaxies, and matter around black holes. The telescope orbits above the Earth's atmosphere, up to an altitude of 139,000 km, to capture the X-rays normally blocked by the atmosphere. The telescope was launched on July 23, 1999 and has been providing unparalleled X-ray observations for almost 20 years.

Chandra carries four precisely-constructed mirrors nested inside each other. Using data acquired with X-ray CCD detectors, detailed spectroscopic images of the cosmic source can be made and analyzed. *Chandra* has unparalleled spatial resolution and has provided countless insights for the X-ray universe. One of the richest contributions of *Chandra* is the publicly available *Chandra* Data Archive of observations, and the analysis software developed to reduce the data (Fruscione et al., 2006). The *Chandra* X-ray observations used in this thesis are entirely from the archive, and this work would not be possible without the available data.

1.3.2 X-ray Observables

In this thesis, we are primarily concerned with the radial properties of galaxies and galaxy clusters. X-ray telescopes, like *Chandra* and *XMM*, obtain time, spatial, and energy information about X-ray photons emitted from the hot gas in galaxy clusters and early-type galaxies. The X-ray emission from the hot gas is primarily in the form of thermal bremmstrahlung radiation, due to interactions between ions and electrons. While the temperature of the hot gas in galaxy clusters is hotter than groups or individual galaxies, they all exhibit extended X-ray emission, meaning that the X-ray emission is coming from diffuse, hot gas, rather than point sources (see Sarazin (1986) for a review). In galaxies, the extended X-ray gas is called the circumgalactic medium (CGM), and in galaxy clusters, it is called the intracluster medium (ICM). The hot gas traces the gravitational potential well and is affected by both thermal and gravitational processes, so we use observations of the hot gas to explore changes across the galaxy or cluster's radius.

The temperature of the hot gas can be directly measured from X-ray observations, and the density can be measured by modeling the hot gas properties (e.g. cooling, emissivity, metallicity) and accounting for the hydrogen column density (N_H). Because clusters and nearby early-type galaxies are large enough to be resolved by *Chandra* and *XMM*, we can break up the images of extended sources into annuli, centered on the peak of the X-ray emission, to obtain independent X-ray spectra. Then we use the spectra to derive radial profiles of temperature and density. The width of the annuli is usually set by a signal-to-noise threshold based on the science goals for a particular analysis but must be larger than the observatory's point-spread-function (PSF) to avoid significant corrections for light scatter outside the annuli. Profiles constructed from two-dimensional annuli are known as "projected" radial profiles because the emission is assumed to be two-dimensional, and the annuli are independent of each other. Projected profiles can be useful, particularly because of their low computational cost, but they are limited in their ability to capture the three-dimensional nature of the hot gas. Therefore, we rely on deprojection techniques to extract radial properties.

1.3.3 Deprojection as a Tool for X-ray Spectroscopy

If we can assume that the emissivity of the gas is constant and optically thin within a spherical shell, we can use deprojection to obtain three-dimensional source properties from a two-dimensional image. Figure 1.6 shows a geometric view of how deprojection works. The ICM/CGM are approximately spherical, the gas is optically thin, and variations in the gas properties are small across annuli, so deprojection is well suited for obtaining radial profiles. Like projected profiles, the image is broken up into annuli, centered approximately on the peak of the X-ray emission, based on a signal-to-noise threshold for the annuli. However, rather than each annulus being independent, the spectra of the annuli are fit from the outermost annulus inwards, with each bin accounting for the properties of the previous bins. The technique is often referred to as "onion-peeling" because it

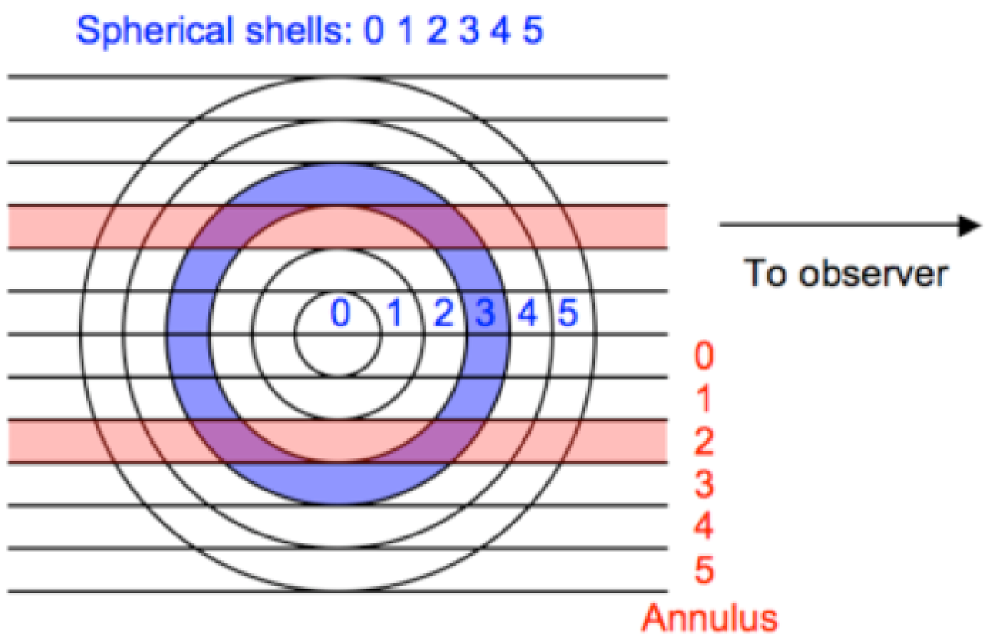

Figure 1.6 Geometric view of how deprojection works. The two-dimensional annuli are converted to spherical shells to obtain two-dimensional source properties of a three-dimensional object, in this case, a galaxy or galaxy cluster. Image courtesy of `deproject` documentation (https://deproject-test.readthedocs.io).

treats the source as an onion where each annulus is representative of a spherical shell of emission, so the emission in an annulus includes contributions from all external annuli.

Deprojection requires more computational time because of the iterative spectral fitting process and does not work as well for non-spherical emission or radii where the emission is close to the contribution from the background. However, it does provide more accurate measurements for temperature and density in the centers of galaxy clusters and early-type galaxies where we are most interested in the radial gas properties. This thesis contains multiple uses of deprojected profiles to better understand the ICM and CGM at smaller radii.

1.3.4 Using Entropy to Understand X-ray Gas

For a monoatomic gas, the gas pressure is proportional to entropy and density by $P \propto K\ n^{5/3}$, where K is the entropy and n is the number density. Recasting that equation in terms of the X-ray observables temperature and electron density, we get the quantity we call entropy:

$$K = kT_{\mathrm{keV}}\, n_e^{-2/3}, \tag{1.3}$$

where kT_{keV} is the temperature of the gas in keV, and n_e is the electron density. It is the preferred physical quantity for capturing feedback in galaxies because the density and temperature of the gas can change independently. Feedback processes such as thermal cooling, supernovae, or AGN outbursts do not necessarily heat the gas, but they can change the rate at which it radiates energy away which can change the time it takes the gas to cool. Entropy tracks gains and losses of energy in the X-ray gas. The galaxy potential well serves as an entropy sorting device, with higher entropy gas at outer radii and lower entropy gas at small radii. The lowest entropy gas is the densest and brightest in the X-ray.

1.3.5 Morphology

In addition to determining the gas properties from X-ray observations, we can also quantify what the galaxies and clusters "look" like, or their morphology. For a discussion of how to calculate morphological properties, see Section 2.2.2.1, but here I will introduce the ways in which we quantify the X-ray emission distribution qualitatively. We can describe how "peaked" the emission is with a parameter referred to as concentration. Concentration is a ratio between the luminosity interior to some inner radius to the total luminosity inside a larger radius. The value of the ratio is between 0 and 1, where 1 indicates that all of the emission is within the inner radius and 0 indicates that all of the emission would be outside the inner radius. X-ray luminosity is an observationally easy measurement to make for most clusters, so determining how it relates to other properties of the X-ray gas could allow us to make predictions for measurements that ordinarily require much longer observation time.

We can also determine how spherically symmetric, or "relaxed" the hot gas is by calculating the centroid shift and power ratios. Full details of these calculations are provided in Section 2.2.2. Centroid shift is measured by calculating the distance between the peak and centroid of the X-ray emission. Small centroid shift indicates that the gas is more compact, and large centroid shift indicates that it is more diffuse. For measurements of power ratio, any number of moments can be calculated for the hot gas, but the most relevant are the 0th and 3rd moments because their ratio provides an indication of asymmetries in the gas. If the 3rd moment is large in comparison to the 0th moment, there is more substructure in the gas, meaning it is less symmetric and less relaxed.

1.4 The Gas in Clusters and Early-Type Galaxies

In the center of (almost) every galaxy, there is a supermassive black hole that is tightly coupled to the evolution of the galaxy (e.g. Kormendy & Richstone 1995; Haehnelt et al. 1998; Magorrian et al. 1998; Ferrarese & Merritt 2000; Gebhardt et al. 2000; Kormendy & Ho 2013; Reines & Volonteri 2015; Saglia et al. 2016; Ricarte et al. 2019). Many galaxies also have an Active Galactic Nucleus (AGN) powered by accretion onto the black hole (Brandt & Hasinger, 2005). AGNs are very small spatially in comparison to their host galaxy yet they are able to affect the hot gas on much larger scales (see Figure 1.7). How exactly the accretion fueling of the black hole is coupled to the surrounding medium is still an unanswered question, but it may be through precipitation driven feedback (e.g. Pizzolato & Soker 2005; McCourt et al. 2012; Voit et al. 2015b; Sharma et al. 2012; Voit et al. 2017). Feedback from the central black hole holds the CGM in a state marginally unstable to condensation, so with the right conditions gas can precipitate out. As gas cools and falls into the black-hole, the AGN will turn on, heating the gas, thus lengthening its cooling time and diminishing precipitation. In this thesis, I will explore how AGNs couple to the galactic atmosphere and affect the gas entropy (see Chapters 3 and 4).

1.4.1 Multiphase Gas

Up to this point, I have focused on the hot X-ray emitting gas in galaxies and clusters, but I also explored some of the other gas found in the ICM/CGM. At smaller radii in the ICM/CGM, we find multiphase gas: gas at different temperatures and ionization states found in proximity to each other. The hot X-ray emitting gas is the volume-filling “ambient” phase of the atmosphere, while

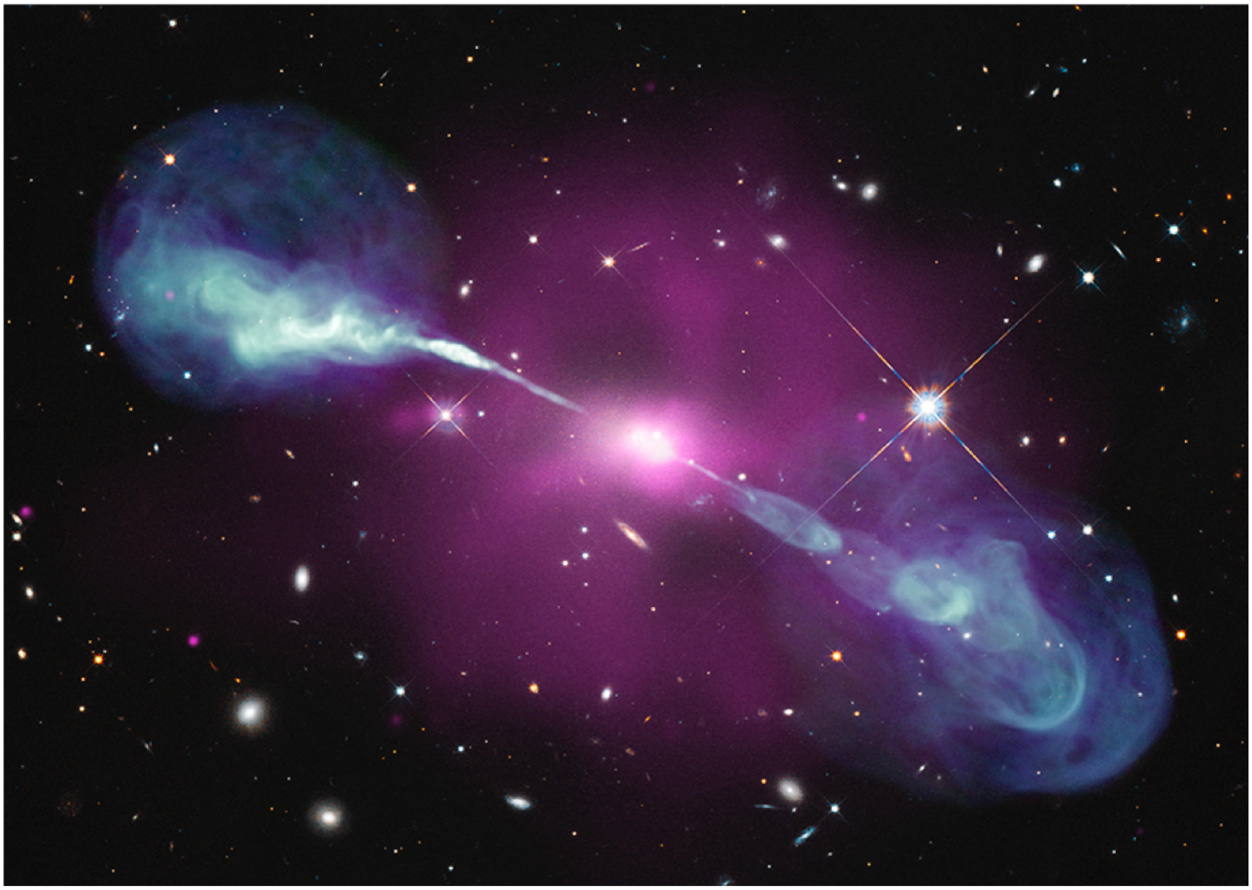

Figure 1.7 A composite image (X-ray (pink), optical, and radio emission (blue)) for the nearby early-type galaxy Hercules A. The composite image illustrates the importance of a multi-wavelength approach to studying the phenomena in galaxies and galaxy clusters. *NASA/CXC/SAO*

the molecular gas is generally found towards the cluster/galaxy center. The presence of $H\alpha$ (often observed as CO) emission usually indicates abundant molecular gas (Edge, 2001) and the potential for active star formation. Some galaxies, particularly early-type or elliptical galaxies, have little to no active star formation and thus have no extended multiphase gas, so we call these "single phase" galaxies. Chapters 3 and 4 examine how the multiphase gas extent relates to other galaxy properties. We also expect clusters to have multiphase gas if their gas entropy is low in the center.

1.4.2 SNIa Feedback in Clusters vs. Galaxies

In addition to feedback from AGN, this thesis is also concerned with feedback from Type Ia supernovae (SNIa), particularly with respect to its affect on the hot atmospheres of early-type galaxies (Voit et al., 2015b, 2020). Despite their generally older, low mass stellar populations, SNIa are found in early-type galaxies because SNIa progenitors are long-lived white dwarf stars in binary systems. Unlike core-collapse supernovae, SNIa result from systems where a white dwarf accretes matter from a low-mass companion star until oxygen fusion begins and the white dwarf explodes, rather than collapsing. Because SNIa are found in older stellar populations, they can also be used as standard candles to measure the expansion of the universe (see Section 1.2 and Riess et al. (2011)).

In galaxy clusters, the contributions to the sweeping of gas via SNIa can usually be neglected because the effect is small in comparison to the other feedback processes, and clusters are much more massive than galaxies. However, contributions from SNIa via stellar winds can be sufficient to remove gas from the inner radii of an early-type galaxy. Chapter 4 discusses how stellar winds from SNIa contribute to the balance of feedback and cooling in early-type galaxies.

1.5 Structure of this Thesis

The structure of this thesis is as follows. In Chapter 2, I will discuss the ACCEPT 2.0 entropy profile and morphology measurements and present an early science application of the ACCEPT 2.0 database. In Chapter 3, I will present the results of Frisbie et al. (2020) exploring the thermal properties of the gas in a small sample of early-type galaxies with powerful radio sources and compare them to simulations. In Chapter 4, I will present an observational test of the black-hole feedback valve model for galactic atmospheres using early-type galaxies. Chapter 5 contains a summary of this thesis as well as potential future projects.

CHAPTER 2

ACCEPT 2.0 AND XMM HERITAGE

2.1 Introduction

Most of the baryonic mass in a galaxy clusters is actually not in the galaxies but in the hot ($10^7 - 10^8$ K) Intracluster Medium (ICM). The X-ray emission we observe comes from the radiation of the ICM gas, and the baryons track the dark matter halo. In a galaxy cluster, the cooling of gas, winds, and the heating of gas due to feedback from Active Galactic Nuclei (AGN) drive the cluster cores away from hydrostatic equilibrium. To study the non-gravitational processes of the X-ray gas, we primarily use the gas entropy (K) (see Section 1.3.4). Convection in the hot ICM, bound by the gravitational potential of a cluster, causes high entropy gas to rise and low entropy gas to sink, creating a positive entropy gradient across the cluster radius ($dK/dr > 0$). If the physics of the hot ICM is dominated only by gravitational processes and gas accretion, the entropy should be a single power law, so departures from power law entropy allow us to measure the effect of feedback and radiative cooling in the X-ray gas.

Cavagnolo et al. (2009) presented the ACCEPT (Archive of Chandra Cluster Entropy Profile Tables) project and showed that generally, every galaxy cluster has an entropy excess near its center. To quantify the entropy excess, they fit a mathematical model of a power law with a core excess:

$$K(r) = K_0 + K_{100}\left(\frac{r}{100\text{ kpc}}\right)^{\alpha}, \tag{2.1}$$

where K_0 is a characteristic central entropy, K_{100} is the best fit entropy at a radius of 100 kpc, and α is the best fit power law slope. They measured K_0 for a sample of 239 clusters and found that, while the model to fit the entropy profiles was a purely mathematical model, the distribution of K_0 values in the sample was bimodal with peaks at 15 keV cm^2 and 150 keV cm^2 and a threshold entropy of 30 keV cm^2. Furthermore, they found that clusters with "low" central entropy ($K_0 < 30$ keV cm^2) generally also had multiphase gas present while clusters with "high" central entropy ($K_0 > 30$ keV cm^2) never have multiphase gas. Therefore, central entropy serves as a convenient way to sort galaxy clusters into those with BCGs that might have multi-phase gas and those with BCGs that never have it.

The sorting of clusters by central entropy also fairly neatly separates clusters into cool core (CC) and non-cool core (NCC). The division between cool-core and non-cool core arises from the radial temperature profiles of clusters. Cool-core clusters have a drop in temperature towards the center that aligns with a sharper peak in surface brightness and an increase in density. In non-cool core clusters, however, the surface brightness peaks less dramatically, and their temperature profiles are flatter.

While the *Chandra* telescope remains the same, computational power and the number of clusters observed have greatly increased since 2009. Therefore, the ACCEPT 2.0 project was established in 2015. The X-ray data reduction was completed by Alessandro Baldi and full details of the reduction pipeline can be found Section A.1. The morphological measurements were completed with a pipeline written and run by Megan Donahue in 2018 (see section 2.2.2.1). The main improvements from ACCEPT to ACCEPT 2.0 are summarized in Table 2.1, but I will highlight the most significant for my thesis work here.

Table 2.1 Comparison between the data products of ACCEPT and ACCEPT 2.0

	ACCEPT	**ACCEPT 2.0**
# of Clusters	239	606
# of Profiles	239	348
Deprojected Density	Yes	Yes
Deprojected Temperature	No	Yes
Global T, L, Z	No	Yes
Morphology	No	Yes

ACCEPT 2.0 contains entropy (and the associated temperature and density) profiles for 348 clusters and global measurements for up to 606 clusters. Deprojection is computationally intensive because of the iterative fitting process required, and in 2009, sufficient computational resources were not available, so Cavagnolo et al. (2009) used projected temperature profiles instead. ACCEPT 2.0

uses deprojected profiles which provide a more accurate measure of the temperature and density than projected temperatures. Rather than determining the temperature from two-dimensional annulus, deprojected profiles use three-dimensional spherical annuli (see Section 1.3.3 for a full description), accounting for the three-dimensional nature of galaxy clusters and providing more accurate profile measurements. In addition to more robust profile measurements, ACCEPT 2.0 includes morphology (here referring to the shape and distribution of the X-ray gas) measurements while ACCEPT did not. Finally, ACCEPT 2.0 contains global property measurements for the sample while ACCEPT did not.

2.2 Entropy Profile Fitting

The X-ray gas in clusters tends to be relatively spherically symmetric and centrally peaked (usually on the BCG), so deprojection generally works well. However, deprojection does have its limitations. The primary limitation that is relevant in this work is that when the difference between the background and source emission is small, specifically in the outer edges of the cluster, the contents of the deprojected bins can be over- or under- subtracted, resulting in a jagged profile. The jagged profile results because one bin compensates for the estimated contents of an outer bin. For that reason, direct deprojection is far more stable when the inner bins are far brighter than the outer bins as in extended but centrally-peaked source distributions. Deprojection generally assumes spherical or ellipsoidal symmetry, so clusters that have mergers, shocks, or other significant asymmetries in the X-ray gas will have more uncertain profiles. Finally, there is covariance in the radial profile that would not be present in a projected profile, but it generally does not need to be considered for my analysis.

Because entropy traces gains and losses of energy in the gas, we can use an entropy profile to gain an understanding of the thermal history of the cluster. The goal of fitting entropy profiles is to characterize the core excess of entropy because it provides a simple way of examining sub-populations of galaxy clusters with similar characteristics. Specifically, Cavagnolo et al. (2009) showed that there is some correlation between the presence of multiphase gas and cool-core clusters and the absence of multiphase gas in non cool-core clusters. Furthermore, galaxy clusters with low central entropy may have more peaked surface brightness profiles and may be more relaxed. Therefore, central entropy measurements can provide additional ways to examine the morphological properties of galaxy clusters, particularly with a sample as large as ACCEPT 2.0.

The entropy profiles are fit with the functional form in Equation 2.1. While the functional form describes the shape of the entropy profile well, it is not a physically motivated model. Because the data are not always smooth and not uniform across clusters, we elected to fit the entropy profiles Markov-Chain Monte Carlo fitting, rather than simpler, less computationally expensive methods. The best fit parameters were determined using the `emcee` Python package. Because the best fit parameters for K_0, K_{100}, and α are not expected to have a particular a priori distribution, we chose to initially limit parameter space broadly in log space for K_0 and K_{100} ($-10^2 < K_0 < 10^3$, $0 < K_{100} < 10^3$) and linear space for α ($0 < \alpha < 2$). To manage the computational time required, we utilized 1000 parallel random walkers, each taking 1500 steps to obtain a statistical distribution for the best fit parameters. See Figure 2.1 shows the results for one galaxy cluster (Abell 209). Errors were determined from 1 σ contours in two dimensions (16th and 84th percentile). The complete results of these fits are available in a table in Appendix B and radial entropy profiles are in Appendix C.

For the purposes of classifying the clusters of ACCEPT 2.0 by central entropy, our priority was to characterize the shape of the entropy profiles in the innermost regions of the galaxy clusters. In 80 of the clusters, to obtain a reasonable fit in the central region, we restricted the radial range of the fit to the central radial bins (see Appendix C for radial ranges), rather than requiring a good fit to points at radii greater than $\sim$ 100 kpc. If restricting the radial range of the fit did not improve the statistical significance of the fit, or if there were insufficient radial bins (less than 4) to fit inside the region of interest, we removed the profile from the sample. Of the 606 galaxy clusters in ACCEPT 2.0, 348 had sufficient counts to fit an entropy profile. Of those 348 profiles, 39 were removed from the sample because of insufficient data resolution in the region of interest or the lack of a statistically significant fit (reduced $\chi^2 > 1.1$) in the region of interest.

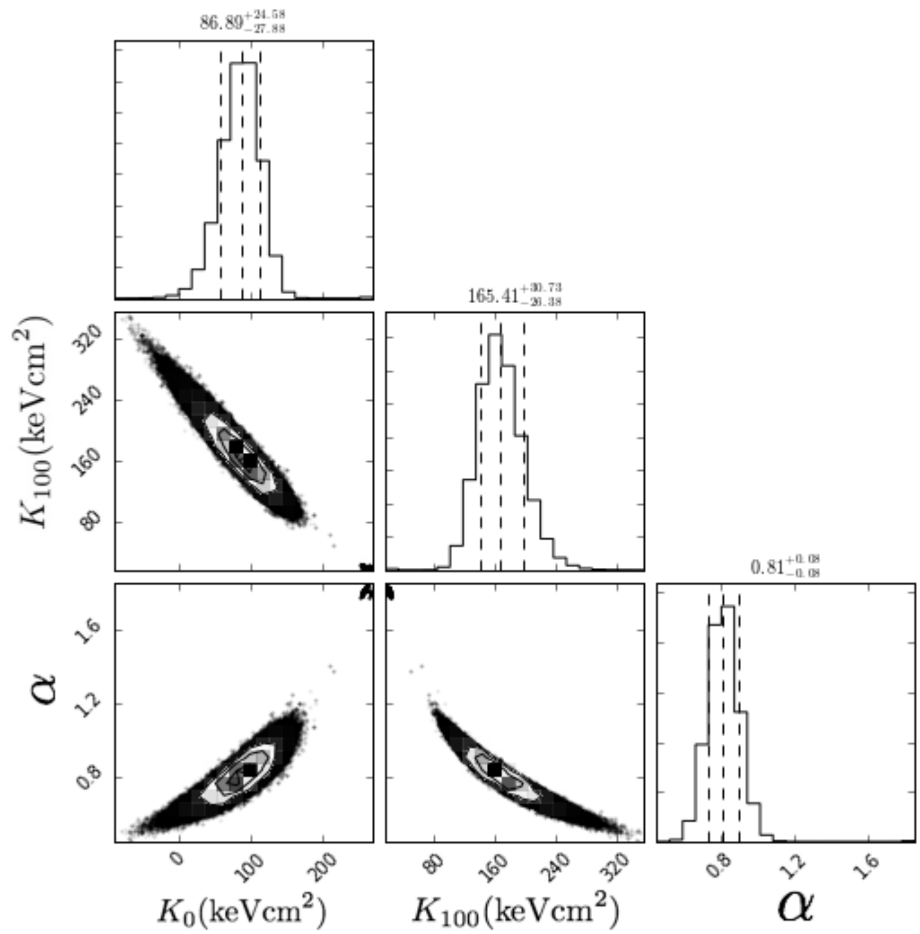

Figure 2.1 Results of MCMC fitting for the entropy profiles using `emcee` for Abell 209 (used here as a representative of the fitting process). Two dimensional distributions of K_0, K_{100}, and α are given with respect to each other as well as the distribution of each parameter independently with 1σ errors.

2.2.1 Comparison to ACCEPT

As a first validation of the ACCEPT 2.0 data reduction pipeline and central entropy fitting and a test of the conclusions from Cavagnolo et al. (2009), we compared the K_0 results for clusters present in both ACCEPT and ACCEPT 2.0 and the K_0 results for all clusters in ACCEPT 2.0. While in general, the best fit central entropies are slightly lower in ACCEPT 2.0 than in ACCEPT, there is strong agreement between the clusters present in both samples, providing convincing validation of both the entropy profile fitting procedure and the data reduction pipeline (see Figures 2.2 and

2.3). In Figure 2.4, we compare the best fit K_0 for all ACCEPT clusters with the best fit K_0 for all ACCEPT 2.0 clusters. Cavagnolo et al. (2009) showed that the distribution of K_0 was bimodal with peaks at 15 keV cm^2 and 150 keV cm^2. They also showed that the characteristic central entropy, K_0 = 30 keV cm^2, divides clusters into cool core and non-cool core clusters, and we recover that same threshold entropy in the ACCEPT 2.0 cluster sample. Furthermore, ACCEPT showed that K_0 = 30 keV cm^2 divides clusters into those with central radio sources and evidence for multiphase gas (K_0 < 30 keV cm^2) and those without (K_0 > 30 keV cm^2), and we would expect the same behavior from ACCEPT 2.0 clusters.

While it does not strongly affect the agreement between ACCEPT and ACCEPT 2.0, there is a small offset between the results of ACCEPT and ACCEPT 2.0. Deprojected inner temperatures (as we used in ACCEPT 2.0) are generally lower than projected temperatures (as we used in ACCEPT) because deprojected temperatures are obtained by subtracting off the contribution of a spherical shell rather than a two-dimensional annulus (as discussed in Section 2.2). Therefore, the slightly lower characteristic central entropies in ACCEPT 2.0 are reasonable, and in fact, expected. In my comparison of ACCEPT to ACCEPT 2.0 profiles, I found that 21 (see Table 2.2 ACCEPT profiles were systematically offset from ACCEPT 2.0 as a result of an extraneous correction factor of $\sim$ 1.2 applied to the electron density computation in the ACCEPT profiles. However, the systematic offset in density was small relative to the uncertainty in temperature and the statistical uncertainty in determining K_0, so clusters with the offset in ACCEPT remained in the comparison.

2.2.2 Morphology Calculations and K_0

Morphological measurements of galaxy clusters give us a way to characterize the shape and distribution of the X-ray gas. The different morphology measurements provide insight into the history of galaxy clusters, including significant mergers, star formation, and feedback processes. We look at morphology measurements in relation to K_0 for two primary reasons. First, because K_0 is a convenient way to divide a sample of galaxy clusters into groups with respect to the presence of multiphase gas, we want to understand what correlations, if any, exist with respect to

Table 2.2 The clusters with a systematic offset of ∼ 1.2 in density in ACCEPT (listed by ACCEPT 2.0 name).

ACCEPT 2.0 Name
MFGC_06756
Abell_223
ABELL_0402
ABELL_0611
ABELL_0963
ABELL_2069
ABELL_2813
ABELL_3088
ABELL_3444
ABELL_S0592
MACS_J2214-1359
MCXC_J0220.9-3829
MCXC_J0439.0+0520
MCXC_J0454.1-0300
MCXC_J0547.0-3904
MCXC_J1000.5+4409
MCXC_J1010.5-1239
MCXC_J1022.0+3830
MCXC_J1130.0+3637
ZwCl_0857.9+2107
ZwCl_0949.6+5207

the morphological properties (power ratio, P_3/P_0, centroid shift, w, and concentration, c). Second, K_0 is an observationally expensive measurement to make because it requires sufficient counts to construct a robust deprojected entropy profile, and concentration requires far fewer counts, so we want to determine if concentration could be used to sort cluster populations instead of K_0.

2.2.2.1 Calculating Centroid Shift, Concentration, and Power Ratios

The morphological calculations were completed by Alessandro Baldi in 2015 (concentration) and Megan Donahue in 2018 (centroid shift and power ratio) but the details are included here because of their relevance to my thesis work. The full table of morphological properties can be found in Appendix D.

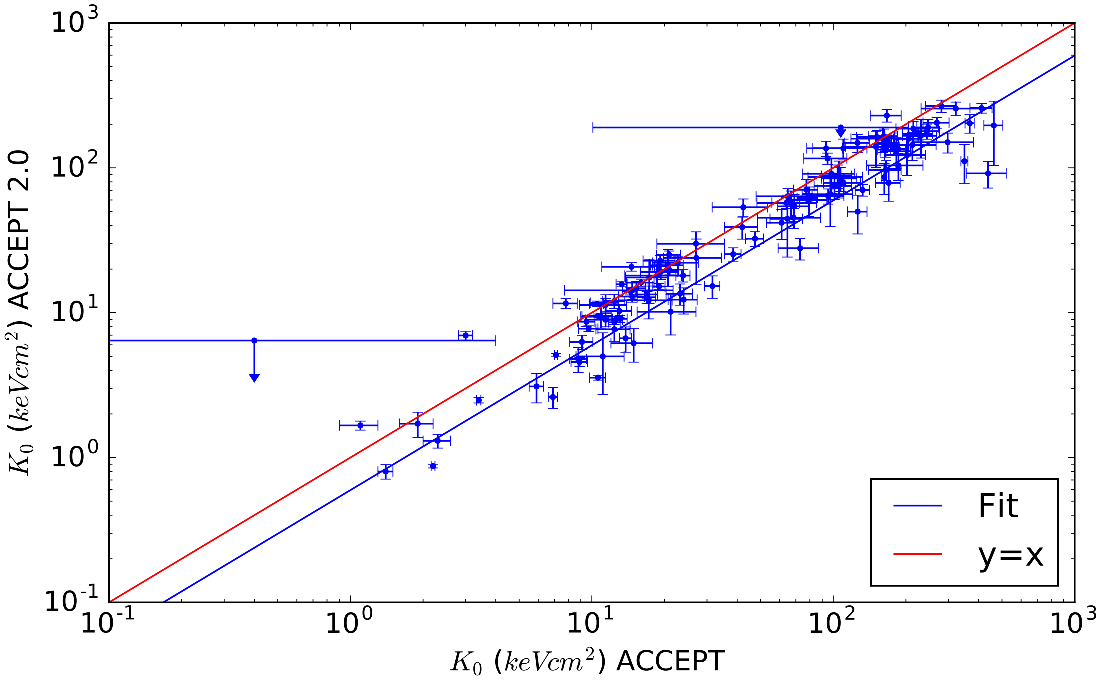

Figure 2.2 K_0 for ACCEPT vs. K_0 for ACCEPT 2.0 to visualize consistency between the best fit K_0 values that overlap between the two samples. Errors are 1-sigma. The blue line is a linear fit to the data where the slope is the average of the ratio between K_0 for ACCEPT and K_0 for ACCEPT 2.0, weighted by their statistical errors, and the red line plots $y = x$ (the results if the K_0 values were perfectly consistent), for comparison.

2.2.2.1.1 Centroid Shift

The dimensionless centroid shift, w, used in this work is based on the definition from Cassano et al. (2010):

$$w = \left[\frac{1}{N-1}\Sigma(\Delta_i - <\Delta>)^2\right]^{1/2}\frac{1}{R_{max}}, \tag{2.2}$$

where the index i is for each sub-aperture (i runs from 1 to N, and in this case, $N = 20$), Δ_i is the distance between the X-ray peak within R_{max} and the centroid of the i-th aperture, and $< \Delta >$ is the average of this separation for all the apertures. For this morphology analysis, $R_{max} = R_{2500}$ from the ACCEPT 2.0 core-excised global temperatures.

The centroid derived from the largest aperture was used for the power ratio estimations. The first moment, P_0, is not particularly interesting but verifies that the centroid is reasonable. The

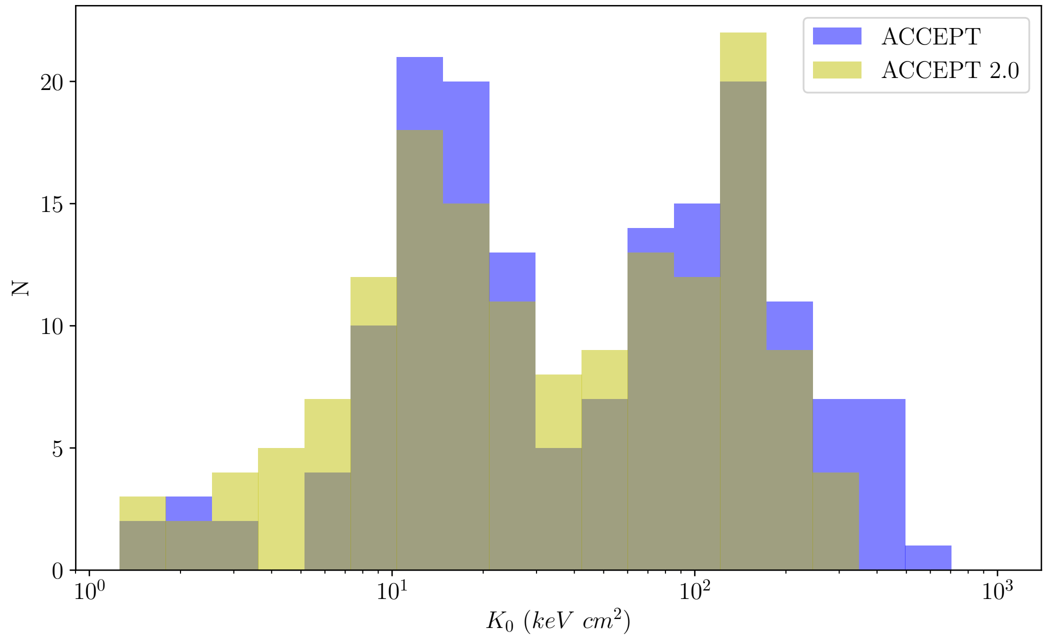

Figure 2.3 Distribution of K_0 for 164 clusters present in both ACCEPT and ACCEPT 2.0, with statistically significant fits in ACCEPT 2.0. The ACCEPT clusters are in blue, and the ACCEPT 2.0 clusters are in yellow.

second moment, P_2, gives the ellipticity and position angle, and the third moment, P_3, indicates asymmetries in the surface brightness. Following the treatment in Buote & Tsai (1995), and noting that the surface brightness maps are in units of counts per image pixel (where an image pixel for these maps was a double-binned physical pixel), $S_x(x, y)$, is given as

$$S_{int} = \sum S_x(x^2 + y^2 < R_{max}^2), \tag{2.3}$$

$$P_{1x} = \frac{\sum S_x(x, y)x}{S_{int}}, \tag{2.4}$$

$$P_{1y} = \frac{\sum S_x(x, y)y}{S_{int}}, \tag{2.5}$$

where x, y are defined to be the horizontal and vertical offset from the nominal centroid position.

If the centroid is correct, $P_{1x} \sim P_{1y} \sim 0$. We used this as an internal verification for the computation of centroids. The second moments lead to the computation of the ellipticity and position angle inside 500 kpc or R_{max} as allowed by the field of view, similar to the procedure in

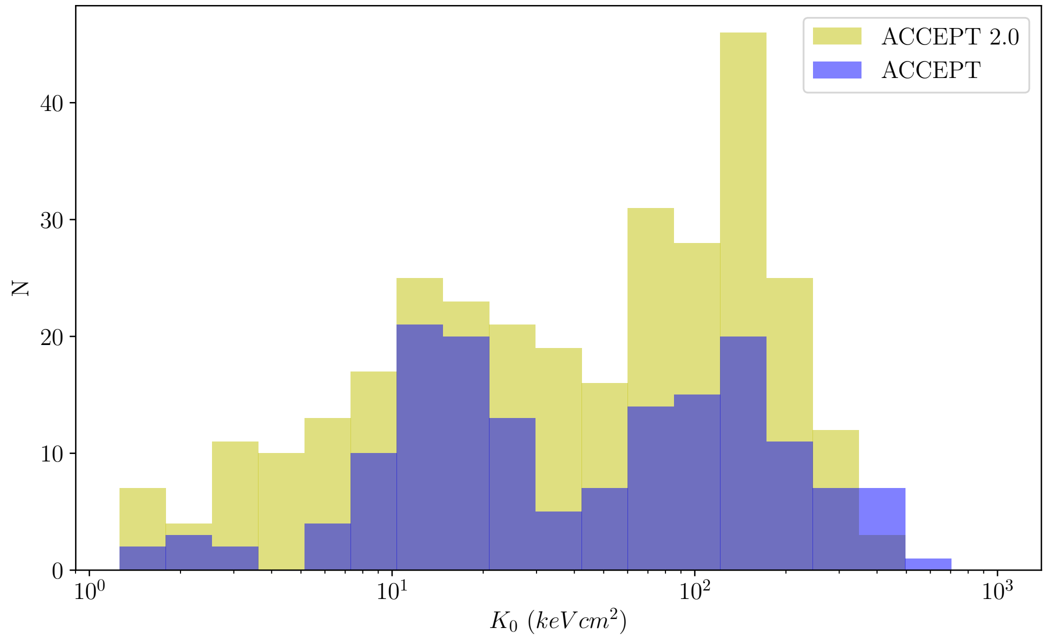

Figure 2.4 Distribution of K_0 for 164 clusters in ACCEPT with 348 clusters with a measured K_0 in ACCEPT 2.0. The ACCEPT clusters are in blue, and the ACCEPT 2.0 clusters are in yellow.

Donahue et al. (2014). We computed 3 terms,

$$A_{xx,yy,xy} = \frac{\sum S_x(x, y) \times (xx, yy, xy)}{S_{int}}, \tag{2.6}$$

and then diagonalized the matrix,

$$\begin{bmatrix} A_{xx} & A_{xy} \\ A_{xy} & A_{yy} \end{bmatrix} \tag{2.7}$$

2.2.2.1.2 Concentration

Two surface brightness concentration parameters, $c_{500\ \mathrm{kpc}}$ and c_{R500}, are computed to measure the concentration of the X-ray-emission in the ACCEPT 2.0 clusters. Concentration has been defined in various ways in the literature. In this work, we adopt a common convention, that concentration is a ratio, ranging from 0.0 to 1.0, between the total X-ray luminosity interior to an inner radius, r_{inner}, to the total luminosity inside a larger radius, r_{outer}. If all the detected flux is inside both radii, then the concentration is close to 1.0, and if the source were somehow shaped like a donut, with an empty center, the concentration would be zero. We have defined two interpretation of concentration: $c_{500\ \mathrm{kpc}}$, where r_{inner} = 100 kpc and r_{outer} = 500 kpc (eg, Cassano et al. (2010)), and c_{R500}, where $r_{inner} = 0.1 r_{500}$ and $r_{outer} = 0.5 r_{500}$ (as in Rasia et al. (2012)).

2.2.2.1.3 Power Ratios

Power ratios (Buote & Tsai, 1995), mimic a multiple decomposition of the 2-D projected mass distribution inside a certain aperture, R_{ap} (R_{2500} for this analysis), but it is much simpler to apply this decomposition to the X-ray surface brightness images S, instead of the mass. The m-th order power ratio ($m > 0$) is defined as P_m/P_0 with

$$P_m = \frac{1}{2m^2 R_{ap}^{2m}}(a_m^2 + b_m^2); P_0 = a_0 ln(R_{ap}), \tag{2.8}$$

where a_0 is the total intensity within the aperture radius, and a_m and b_m are expressed in polar coordinates (R and ϕ) and given by

$$a_m(r) = \int_{R' \leq R_{ap}} S(x')(R')^m cos(m\phi')d^2x', \tag{2.9}$$

and

$$b_m(r) = \int_{R' \leq R_{ap}} S(x')(R')^m sin(m\phi')d^2x'. \tag{2.10}$$

The power ratio P_2/P_0 gives information about the cluster ellipticity and P_3/P_0 is an indicator of bimodal distribution in the surface brightness and therefore is the most sensitive to detect asymmetries or substructures. P_4/P_0 is similar to P_2/P_0 but more sensitive to smaller scales. The ACCEPT 2.0 pipeline computes all power ratios P_m/P_0 with $1 \leq m \leq 6$, but we will focus on P_3/P_0 in this work because of its sensitivity to substructure.

2.3 Science with ACCEPT 2.0

The primary goal of ACCEPT 2.0 was to provide a uniformly reduced database of galaxy clusters with as many X-ray observable properties as possible, given data reduction constraints.

While there are multiphase gas measurements for the clusters of ACCEPT, the sample in ACCEPT 2.0 can be used to further examine the presence or absence of multiphase gas and its correlation with central entropy. The selection function of ACCEPT 2.0 is quite complicated because it is a purely archival sample and therefore not only holds potential bias in mass, luminosity, and other observables, but also in the selection of targets themselves. Future work could attempt to characterize the selection function to answer scientific questions such as how common certain types of clusters are and cosmological questions about the cluster mass function using the largest possible sample. However, because ACCEPT 2.0 is a large, uniformly reduced sample, it is currently well suited for drawing well-defined sub-samples. As an example of this type of work, I have used ACCEPT 2.0 data for an initial exploration of the sample of galaxy clusters observed through the XMM Heritage project. The science uses for ACCEPT 2.0 discussed in this thesis represent just a few of the countless projects that could use ACCEPT 2.0 to address key questions in cosmology and cluster and galaxy evolution.

2.3.1 Morphological Properties and K_0 for Sample Comparisons

Broadly, morphological properties describe what the galaxy clusters "look" like, including how the X-ray gas is distributed (see Section 2.2.2.1 for details). Cassano et al. (2010) showed that, for a small (32 clusters) sample, the power ratio P_3/P_0 is correlated with the centroid shift, w, and the concentration, c; and concentration is correlated with centroid shift. Here, we will examine the morphological properties for the ACCEPT 2.0 sample and two sub-samples; ROSAT-ESO Flux-Limited X-ray (REFLEX) Galaxy Cluster Survey (Böhringer et al., 2004) and XMM Heritage.

In Figure 2.5, we show the results for correlation between P_3/P_0, w, and c_{500} for the entire ACCEPT 2.0 sample. As in Cassano et al. (2010), we see correlation between P_3/P_0 and w, but the correlation between P_3/P_0 and c_{500} is less clear. Overall, the clusters exhibit a correlation between centroid shift and power ratio, and there are fewer clusters in the less relaxed, less symmetric parameter space.

In Figure 2.6, we plot the central entropy fit values and the concentration parameter. The hope

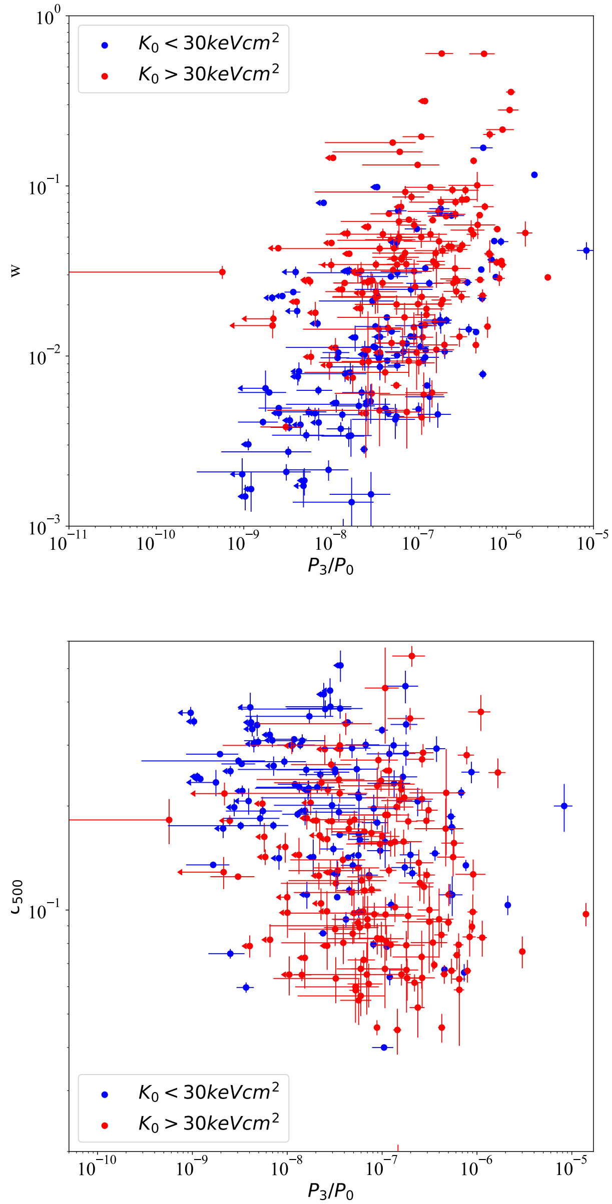

Figure 2.5 Power ratios compared to centroid shift, w, and concentration, c_{500}, colored by central entropy. Red points are clusters with $K_0 > 30\text{keVcm}^2$ and blue points are clusters with $K_0 < 30\text{keVcm}^2$ for all of ACCEPT 2.0.

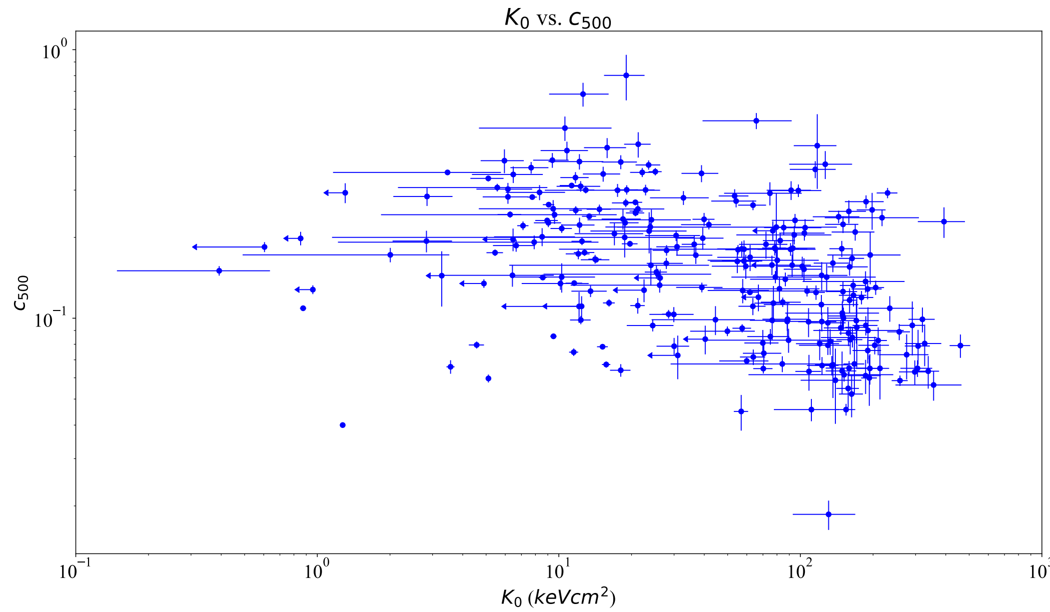

Figure 2.6 Central entropy, K_0, is plotted with c_{500} for clusters in ACCEPT 2.0 to illustrate the potential for concentration to serve as a low-signal proxy for K_0.

is that concentration could serve as a low-signal proxy for central entropy because we expect low entropy clusters to be highly concentrated and high entropy clusters to not be as concentrated. That is, if we know the concentration for a galaxy cluster with data quality insufficient to get a deprojected entropy profile, we could make a prediction about the central entropy. While there is weak correlation between c_{500} and K_0, it is not strong enough to provide strong predictions for a K_0 measurement based on measured concentration. One weakness of c_{500} is that it is based on r_{500} which may be too large a radius to be captured in the *Chandra* field of view.

2.3.2 ACCEPT 2.0 Comparison with REFLEX and XMM Heritage

The XMM Heritage project seeks to create a signal to noise limited sample of deep observations from XMM of 118 clusters from the Planck PSZ2 cosmological catalog. The targets include a local sample at $z < 0.2$ with a mass range of $10^{14}\ M_\odot < M_{500} < 9 \times 10^9 M_\odot$ and the most massive ($M_{500} > 10^{14}\ M_\odot$) clusters at $z < 0.6$. The Archive of Chandra Cluster Entropy Profile Tables

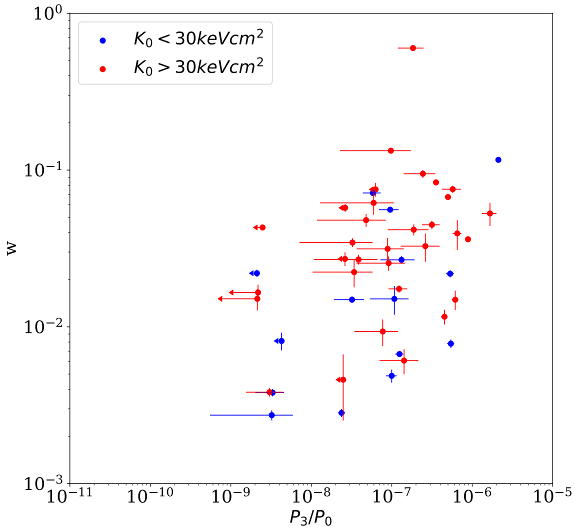

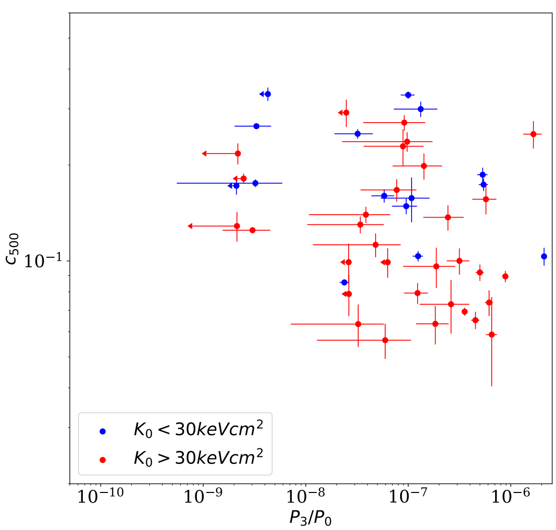

Figure 2.7 Power ratios compared to centroid shift, w, and concentration, c_{500}, colored by central entropy. Red points are clusters with $K_0 > 30\text{keVcm}^2$ and blue points are clusters with $K_0 < 30\text{keVcm}^2$ for the REFLEX sub-sample of ACCEPT 2.0.

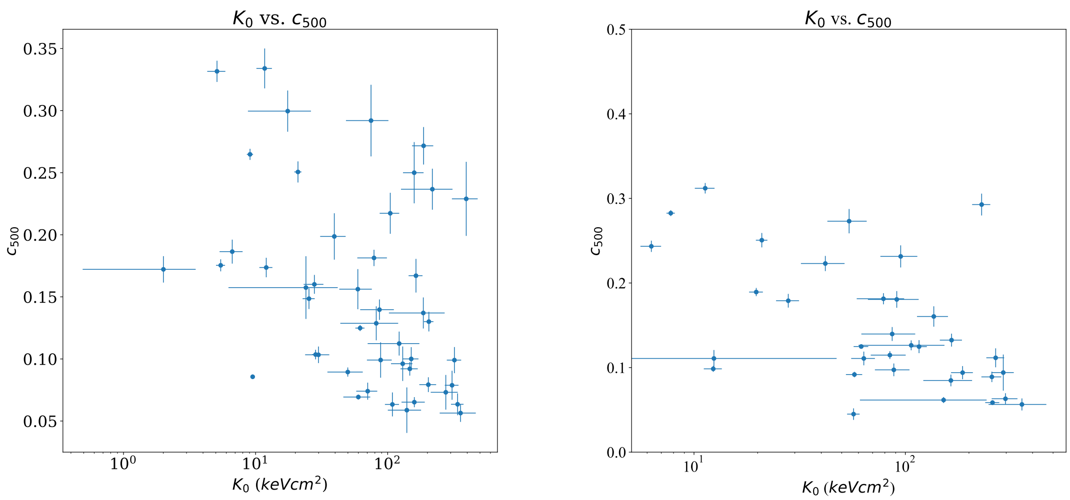

Figure 2.8 Central entropy, K_0, is plotted with c_{500} for clusters in ACCEPT 2.0 and REFLEX (left) and ACCEPT 2.0 and XMM Heritage (right).

(ACCEPT) 2.0 is an archival sample of galaxy clusters observed by Chandra and is an expansion and analysis improvement of the ACCEPT project (Cavagnolo et al., 2009). Here we combine our data products for clusters present in both samples to gain insight into the properties of the X-ray gas in the XMM Heritage sample.

Bringing together the morphological properties and central entropies with the common clusters between the two samples, we see that they exhibit a correlation between centroid shift and power ratio, and the lower entropy clusters are not present at the less relaxed, less symmetric parameter space (Figure 2.9). Shown in a different way, we also find that as in Bauer et al. (2005), cool core clusters are more likely to be compact and symmetric.

Figure 2.7 shows the same plots as in Figure 2.9 but made for the common clusters between ACCEPT 2.0 and the REFLEX sample (Böhringer et al., 2004). Between the two sub-samples of ACCEPT 2.0, we see small differences in the plots for selection between X-ray flux selected (REFLEX) and high X-ray pressure selected (XMM Heritage/SZ) clusters. The pressure selected sample that overlaps with ACCEPT 2.0 contains fewer cool core clusters and fewer symmetric, relaxed clusters than the flux selected sample overlapping with ACCEPT 2.0.

This work represents one of the early tests of the broad applications of the ACCEPT 2.0 project.

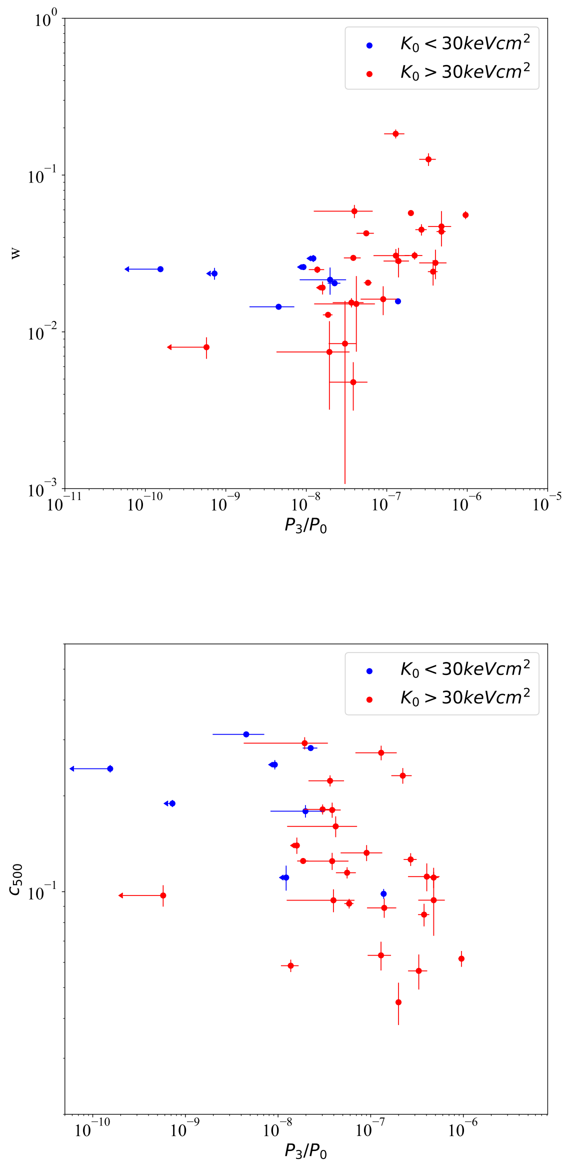

Figure 2.9 Power ratios compared to centroid shift, w, and concentration, c_{500}, colored by central entropy. Red points are clusters with $K_0 > 30\mathrm{keVcm}^2$ and blue points are clusters with $K_0 < 30\mathrm{keVcm}^2$ for the XMM Heritage sub-sample of ACCEPT 2.0.

As more data for the XMM Heritage project are taken, we will be able to use the insights learned from ACCEPT 2.0 to learn more about the thermal properties of the X-ray gas in these clusters. We are also able to identify and confirm Brightest Cluster Galaxy (BCG) coordinates for the overlapping targets. Through our comparison of the XMM Heritage-ACCEPT 2.0 and REFLEX-ACCEPT 2.0 samples, we can begin to see the X-ray selection effects for samples of galaxy clusters as well as the value of archival data. The scientific applications for both ACCEPT 2.0 and the XMM Heritage projects are widespread and extensive.

2.4 Summary

ACCEPT 2.0 expands and improves upon the work done by Cavagnolo et al. (2009). In this chapter, I have presented the initial pipeline verification via comparison to ACCEPT and a few early science applications of the ACCEPT 2.0 data. Initial verification was accomplished by comparing the deprojected temperature, density, and entropy profiles for the common clusters between ACCEPT and ACCEPT 2.0 as well as comparing the overall sample characteristics of the profiles and central entropy between ACCEPT and all ACCEPT 2.0 clusters. As in Cavagnolo et al. (2009), I found that the distribution of central entropy was bimodal, with a break at 30 keV cm^2 and peaks at $\sim$ 15keV cm^2 and $\sim$ 150keV cm^2. The distribution of central entropy suggests that almost all galaxy clusters have a core excess of entropy, and that central entropy can approximately divide galaxy clusters into cool core and non-cool core clusters, a classification scheme that proves to be useful when examining cluster properties for large samples.

We applied the classification via central entropy to the XMM Heritage and comparison samples to understand some of the selection characteristics, and we found that XMM Heritage has more non-cool core clusters in the less relaxed, less symmetric parameters space compared to cool core clusters. The distribution of clusters in the XMM Heritage sample by central entropy and morphology may be the result of the sample being selected by X-ray pressure rather than X-ray luminosity. Pressure selected samples are selected based on measurements of the Sunyaev-Zeldovich effect which is more significant for less-relaxed clusters, like those that have undergone recent mergers. We do find that in the ACCEPT 2.0 sample, and more strongly in the XMM Heritage sample, the power ratio and centroid shift do exhibit some correlation, supporting the work of Cassano et al. (2010) on a smaller sample.

The ACCEPT 2.0 pipeline provides a large, uniformly reduced sample of galaxy cluster properties, and the measurements largely support claims about the distribution of galaxy cluster parameters from previous works. Furthermore, ACCEPT 2.0 is an invaluable resource for comparisons to other X-ray samples, particularly for understanding sample selection characteristics. We expect that ACCEPT 2.0 will provide a springboard for galaxy cluster studies for years to come.

CHAPTER 3

PROPERTIES OF THE CGM IN EARLY-TYPE GALAXIES WITH POWERFUL RADIO SOURCES

This paper was published by the Astrophysical Journal Volume 899, number 2, in August 2020 (see Frisbie et al. (2020)).

3.1 Abstract

We present an archival analysis of *Chandra* X-ray observations for 12 nearby early-type galaxies hosting radio sources with radio power $> 10^{23}$ W Hz^{-1} at 1.4 GHz, similar to the radio power of the radio source in NGC 4261. Previously, in a similar analysis of eight nearby X-ray and optically bright elliptical galaxies, Werner et al. (2012), found that NGC 4261 exhibited unusually low central gas entropy compared to the full sample. In the central 0.3 kpc of NGC 4261, the ratio of cooling time to freefall time ($t_{\rm cool}/t_{\rm ff}$) is less than 10, indicating that cold clouds may be precipitating out of the hot ambient medium and providing fuel for accretion in the central region. NGC 4261 also hosts the most powerful radio source in the original sample. Because NGC 4261 may represent an important phase during which powerful feedback from a central active galactic nucleus (AGN) is fueled by multiphase condensation in the central kiloparsec, we searched the *Chandra* archive for analogs to NGC 4261. We present entropy profiles of those galaxies as well as profiles of $t_{\rm cool}/t_{\rm ff}$. We find that one of them, IC 4296, exhibits properties similar to NGC 4261, including the presence of only single-phase gas outside of $r \sim 2$ kpc and a similar central velocity dispersion. We compare the properties of NGC 4261 and IC 4296 to hydrodynamic simulations of AGN feedback fueled by precipitation. Over the course of those simulations, the single-phase galaxy has an entropy gradient that remains similar to the entropy profiles inferred from our observations.

3.2 Introduction

Over the past two decades, *Chandra* has been used to observe the ambient medium of early-type galaxies because of its high sensitivity in the soft X-ray band (0.5-2.0 keV) and its spatial resolution, resulting in 2D spectroscopy of unprecedented quality (e.g. Kim et al. 2018; Diehl & Statler 2007, 2008a,b; Lakhchaura et al. 2018; Sun 2009). The hot atmospheres of those early-type galaxies have provided key clues about the energetic processes known as "feedback" (McNamara & Nulsen, 2012; Soker, 2016; Fabian, 2012). X-ray signatures of feedback processes observed in the hot atmospheres of nearby, early-type galaxies are also commonly and prominently observed in the hot atmospheres of Brightest Cluster Galaxies (BCG), the brightest and most massive galaxies in galaxy clusters. The supermassive black holes at the center of BCGs in clusters interact with the surrounding medium, inflating bubbles of relativistic plasma (e.g. Boehringer et al. 1993; Churazov et al. 2000; Fabian et al. 2003, 2006; Bîrzan et al. 2004; Dunn & Fabian 2006, 2008; Dunn et al. 2005; Forman et al. 2005, 2007; Rafferty et al. 2006; McNamara & Nulsen 2007). One insight from studying feedback processes in galaxy clusters is that the activity state of the central Active Galactic Nucleus (AGN) in a BCG is closely coupled to the thermodynamic state of the Intracluster Medium (ICM) (e.g. Cavagnolo et al., 2008; Rafferty et al., 2008; Voit & Donahue, 2015; Voit et al., 2015a). However, in individual early-type galaxies in groups, like those we discuss in this work, the relationship may be a little more complex (Sun, 2009; Connor et al., 2014). Because the gravitational potential depths are shallower for galaxies in groups than galaxies in clusters, supernova explosions and galactic winds are energetically more important for galaxies than for galaxy clusters. Furthermore, while nearly any reasonable amount of kinetic AGN output can be contained in a cluster atmosphere, the question of whether or not a powerful AGN jet thermalizes its energy output near or far from the AGN depends on the external gas pressure. In turn, the external gas pressure may depend on the large-scale structure the galaxy inhabits.

McNamara & Nulsen (2007, 2012) have summarized the evidence suggesting that black holes suppress the star formation in massive galaxies, but how the accretion onto the black hole is affected by the surrounding hot gas is less clear. Precipitation-regulated feedback models hypothesize that feedback suspends the ambient medium in a state that is marginally stable to multiphase condensation. Feedback input affects the thermodynamic state and susceptibility of the ambient gas to condensation. Feedback output depends sensitively on the rate at which cold clouds precipitate out of the hot medium (Pizzolato & Soker, 2005; Sharma et al., 2012; Gaspari et al., 2012, 2013, 2015, 2017; Voit et al., 2015b, 2017; Wang et al., 2019). Such a system is self-regulated, and finds a balance at the marginally stable point.

Spatially resolved X-ray spectroscopy of the hot ambient medium provides insight into its thermal evolution. The normalization and shape of an X-ray spectrum yields gas electron density (n_e), temperature (T_X), and metallicity (Z). Broadly, for early-type galaxies, the temperature of the hot gas is $\sim$1 keV with a nearly isothermal radial profile, and the radial profile of the electron density approximately follows a power law. The temperature and density of the X-ray gas, considered independently, do not reveal the thermal history because heating and cooling of gravitationally confined gas can cause it to expand or contract without much change in temperature. However, combining these two X-ray observables to make the quantity $K = kT_X n_e^{-2/3}$ provides us with more direct information about thermal history, because changes in $kT_X n_e^{-2/3}$ correspond directly to changes in the specific entropy of the gas. Only gains and losses of heat energy in the gas can change the entropy, so we can trace the thermal history of the ambient gas of a galaxy cluster by observing the profile $K(r)$, which we will call an entropy profile.

In addition to what we have learned from X-ray observations, numerical simulations show that cool clouds can precipitate out of a galaxy's hot gas atmosphere via thermal instability even if the galaxy is in a state of global thermal balance, with heating approximately equal to cooling (Gaspari et al., 2012; McCourt et al., 2012; Sharma et al., 2012). The critical criterion for precipitation is the ratio between the cooling and freefall times of the gas. Here, the cooling time ($t_{\rm cool}$) is defined to be the time needed for a gas at temperature T to radiate an energy $3kT/2$ per particle, and the free fall time from a galactocentric radius r at the local gravitational acceleration g is defined to be $t_{\rm ff} = (2r/g)^{1/2}$. We note that these models do not presume to claim that the gas must be freely falling. The parameter $t_{\rm ff}$ merely specifies a useful dynamical timescale that characterizes gravitationally driven motions. The freefall time does not assume anything about the turbulence, viscosity, or other fluid properties and is based on galaxy properties that can be inferred from observations of the stellar light.

In both observations and in simulations (McCourt et al., 2012; Sharma et al., 2012; Gaspari et al., 2012; Li & Bryan, 2014a), cooling appears to be fast enough for a fraction of the hot gas to condense into cold clouds and precipitate out of the hot medium if $t_{\rm cool}/t_{\rm ff} \sim 10$. Precipitation may therefore play an essential role in maintaining the required state of global thermal balance if gas cooled from the hot phase boosts the fuel supply for accretion (Pizzolato & Soker, 2010; Gaspari et al., 2013, 2015; Li & Bryan, 2014a,b). In numerical simulations, accretion of precipitating clouds can produce a black hole fueling rate two orders of magnitude greater than the Bondi accretion rate of ambient gas. Such strong accretion then produces a feedback response that heats the gas, bringing the system into approximate balance near $t_{\rm cool}/t_{\rm ff} \approx 10$. Voit et al. (2015b) showed that early-type galaxies do indeed have $\min(t_{\rm cool}/t_{\rm ff}) \approx 10$.

The hot atmosphere of an early-type galaxy can be broadly categorized as single-phase gas or multiphase gas, depending on the extent of the Hα and [N 2] emission. Observationally, galaxies with multiphase atmospheres have extended Hα and [N 2] emission present outside their centers (central ~1 kpc), whereas galaxies with single-phase atmospheres have no evidence for extended Hα emission outside of $\sim$ 2 kpc. X-ray observations of giant ellipticals from Werner et al. (2012, 2014) showed that single- and multiphase galaxies are distinctly bimodal from 1–10 kpc. The entropy profiles of single-phase galaxies scale as $K \propto r$, while in multiphase galaxies the entropy scales as $K \propto r^{2/3}$. However, both types exhibit excess entropy in the innermost kiloparsec equivalent to $\sim$ 2 keV cm^2.

While Werner et al. (2012, 2014) showed that both single- and multiphase galaxies tend to have entropy excesses relative to a power law in the central kiloparsec, one galaxy differed from the rest. X-ray observations of NGC 4261 from Werner et al. (2012) revealed that the entropy profile of NGC 4261 follows a single power law ($K \propto r$), but instead of exhibiting an excess within the central kpc, the power law continues into the central ~0.5 kpc (~4″). The unusually low entropy in the center ($K \approx 0.8$ keV cm^2) results in $t_{\rm cool}/t_{\rm ff} < 10$, putting it slightly below the limit at which precipitation appears inevitable. NGC 4261's radio luminosity is 2 orders of magnitude greater than the rest of the Werner et al. (2012) sample, and the central jet power is 10^{44} erg s^{-1}. Adopting a central black hole mass of $M_{\rm BH} = 5 \times 10^8 M_\odot$ (Gaspari et al., 2013) would require an implausible 30% mass energy to jet power conversion efficiency for the radio source to be powered by Bondi accretion alone (Voit et al., 2015b). Simulations from Gaspari et al. (2013, 2015) showed that a transition to chaotic cold accretion could boost the jet power by up to 100 times over what Bondi accretion of hot ambient gas could achieve and occurs when $t_{\rm cool}/t_{\rm ff} \approx 10$.

Because this transitional regime has not been extensively investigated, we decided to explore it by looking for other galaxies like NGC 4261. To that end, we analyzed an archival sample of *Chandra* observations of 12 additional early-type galaxies with powerful radio sources. In this paper, we present a summary of our findings for this archival study, which yielded at least one additional nearby analog, IC 4296, that similarly has both a steep entropy profile with $t_{\rm cool}/t_{\rm ff} < 10$ at small radii and a powerful radio source.

The structure of our paper is as follows. Section 3.3 describes our sample selection, data analysis, and our measurements of the thermodynamic properties. Section 3.4 presents a comparison of $t_{\rm cool}/t_{\rm ff}$ profiles to previous works, a comparison with simulations, and an analysis of the effects of metallicity assumptions on our measurements. Section 3.5 concludes by discussing how our sample adds to the paradigm of precipitation-regulated feedback in massive galaxies. We assume a ΛCDM cosmology with $H_0 = 70$ km s^{-1} Mpc^{-1} and $\Omega_M = 0.3$ ($\Omega_\Lambda = 0.7$) throughout.

3.3 Sample Selection and Data Analysis

3.3.1 Sample Selection and Distances

NGC 4261 exhibits an unusually low central entropy, as well as $t_{\rm cool}/t_{\rm ff} < 10$ at $r < 0.3$ kpc (Voit et al., 2015b). It also has a powerful radio source emitting 2.3×10^{24} W Hz^{-1} in the 1.4 GHz band, which may be powered by chaotic cold accretion onto the central supermassive black hole (Gaspari et al., 2012, 2013, 2015) fed by precipitation of cold clouds out of the hot atmosphere (Voit et al.,

Table 3.1 Column (1): galaxy name; Column (2): redshift obtained from NED;[a] Column (3): distance calculated from $z_{\rm spec}$ with the exception of NGC 4374 and NGC 7626, for which we use redshift-independent distances from Tonry et al. (2001) and Cantiello et al. (2007), respectively. Column (4): galactic neutral hydrogen column densities from Kalberla et al. (2005) and HI4PI Collaboration et al. (2016); Column (5): radio fluxes from VLA or NVSS (Condon et al., 1998) except for NGC 4261 (PKS, Brown et al. 2011); Column (9) whether there were sufficient counts to make deprojected temperature and density profiles for a galaxy. Column (10): power-law entropy slope α determined by fitting the relation $K \propto r^{\alpha}$ in the 1–10 kpc interval; Column (11): central velocity dispersion from Makarov et al. (2014); Column (12): Hα+[N 2] morphology reported by Lakhchaura et al. (2018) from Connor (in preparation) and Sun (in preparation), classified as follows: N: no cool gas emission; NE: Hα+[N 2] extent < 2 kpc; E: $H\alpha$+[N 2] extent ≥ 2 kpc; U: galaxies for which the presence/absence of Hα+[N 2] could not be confirmed with current observations.

Galaxy	$z_{\rm spec}$	D (Mpc)	$N_{\rm H,HI}$ (10^{20}cm^{-2})	**1.4 GHz** (10^{24} W Hz^{-1})	**ObsID**	**Exp** (ks)	**Net Counts** per Bin	**Profile** (Y/N)	α (1-10 kpc)	σ_v (km s^{-1})	**Hα+[N 2]** Morph[d]
(1)	(2)	(3)	(4)	(5)	(6)	(7)	(8)	(9)	(10)	(11)	(12)
NGC 193	0.015	63.08	2.46	0.468	11389	93.13	300	N	−−	197.6	E
NGC 193	0.015	63.08	2.46	0.468	11389	93.13	300	N	-	197.6±4.8	E
NGC 315	0.016	67.20	5.88	0.973	4156	53.84	930	N	-	293.6±10.1	U
NGC 741	0.018	75.42	4.24	0.327	17198	91.02	1500	Y	-	287.4±9.3	N
NGC 1316	0.006	25.51	1.99	9.75	2022	29.86	450	Y	0.80±0.08	223.1±3.3	E
IC 1459	0.006	25.51	0.94	0.1	2196	58.00	300	Y	-	296.1±6.4	E
NGC 3801	0.011	46.48	1.99	0.296	6843	59.20	330	N	-	191.8±16.6	-
NGC 3894	0.011	46.48	1.83	0.125	10389	38.54	300	N	-	252.8±11.3	-
NGC 4261	0.007	31.32	1.61	2.58	9569	100.34	1600	Y	1.09±0.07	296.7±4.3	NE
IC 4296	0.012	50.64	3.95	5.52	3394	24.84	800	Y	1.12±0.12	327.4±5.4	NE[b]
NGC 4374	0.003	18.37	2.90	0.125	803	28.46	650	Y	0.75±0.05	277.6±2.4	NE
NGC 4782	0.015	63.08	3.10	3.33	3220	49.33	320	Y	-	310.0±11.3	NE
NGC 5419	0.014	58.94	5.40	0.146	5000	14.81	320	Y	-	344.3±5.4	N
NGC 7626	0.011	58.34	4.59	0.222	2074	26.54	370	Y	-	266.6±3.7	E

[a] The NASA/IPAC Extragalactic Database (NED) is funded by the National Aeronautics and Space Administration and operated by the California Institute of Technology.

[b] IC 4296 was identified as E in Lakhchaura et al. (2018). Since its multiphase gas is at < 2 kpc, we classify it here as NE.

[c] Based on observations obtained at the Southern Astrophysical Research (SOAR) telescope, which is a joint project of the Ministério da Ciência, Tecnologia, Inovações e Comunicações (MCTIC) do Brasil, the U.S. National Optical Astronomy Observatory (NOAO), the University of North Carolina at Chapel Hill (UNC), and Michigan State University (MSU)

[d] Based on observations obtained with the Apache Point Observatory 3.5-meter telescope, which is owned and operated by the Astrophysical Research Consortium.

2015b).

In search of other systems similar to NGC 4261, we compiled a *Chandra* archival sample of nearby ($z < 0.02$) massive early-type galaxies hosting radio sources with a power output $> 10^{23}$ W Hz^{-1} at 1.4 GHz (Condon et al., 1998, see Table 3.1). Other recent studies of *Chandra* observations of early-type galaxies (e.g. Lakhchaura et al., 2018; Grossová et al., 2019; Juráňová et al., 2019) include some of the same galaxies, but our sample emphasizes powerful radio sources in order to identify galaxies similar to NGC 4261.

In our analysis, we used distances derived from the redshifts of the galaxies when calculating the electron density, because the effect of small uncertainties in distance on the inferred density, entropy, and cooling time is small. However, for NGC 4374 and NGC 7626 we used the redshift-independent measurements because the differences between the best redshift-independent distance measurements and the redshift-dependent distances are large ($20 - 30\%$; see Table 3.1).

In this work, we pay particular attention to NGC 4374 (M84), NGC 1316 (Fornax A), and IC 4296 because *Chandra* observations of the central 10 kpc of those galaxies have the best signal-to-noise ratios among those in our sample, and we are most interested in atmospheric properties closest to the center. Each galaxy represents a different manifestation of a powerful radio source. M84 hosts an FR I radio jet[1](Harris et al., 2002). Fornax A has a weak core in the radio (250 mJy), but its radio lobes are some of the brightest radio sources in the sky (125,000 mJy, Ekers et al., 1983). IC 4296 is the Brightest Group Galaxy (BGG) in a nearby galaxy group (Abell 3565), and *Hubble Space Telescope* (*HST*) spectroscopy indicates a central black hole mass of $\sim 10^9 M_\odot$ (Dalla Bontà et al., 2009). Recent *Very Large Array* (*VLA*) D-configuration observations show improved mapping of the 160 kpc diameter radio lobes, first discovered by Killeen et al. (1986), located over 230 kpc from the AGN host galaxy, as well as *X-ray Multi-Mirror Mission* (*XMM*) observations that reveal a corresponding X-ray cavity (Grossová et al., 2019).

[1]Defined as a radio source in which the low-brightness regions of the jet are farther from the galaxy than the high-brightness regions (Fanaroff & Riley, 1974)

3.3.2 *Chandra* data reduction

All of the data used in this work are archival *Chandra* data taken between 2000 May and 2015 December. All observations were taken with the ACIS-S detector, except for NGC 5419 and NGC 7626, which were obtained with the ACIS-I detector. We reprocessed the archival *Chandra* data listed in Table 3.1 using CIAO 4.9 and CALDB version 4.7.4. For simplicity, in the case of targets with multiple observations, we chose to analyze the one with the longest net exposure time.

The time intervals containing data with anomalously high background were identified and removed using the `deflare` script in CIAO. Bright point sources were identified and removed using the `wavdetect` script (Freeman et al., 2002). We opted to account for the effect of central point sources in our spatially resolved spectral analysis. Background images and spectra were derived from the blank-sky fields available from the *Chandra* X-ray Center. The background files contain both particle and photon backgrounds and were filtered and reprojected to match the target observations. We rescaled the reprojected background rates to match the particle count rates, gauged from the event rate between 10.0 and 12.0 keV (Hickox & Markevitch, 2006). Because our analyses are based on regions of the galaxy where the signal is much higher than the background, our results are insensitive to the details of the background scaling.

3.3.3 Spectral Analysis

We derived deprojected radial profiles of the X-ray gas properties: temperature, density, and gas entropy. To prepare the spectra, we defined radial annuli each containing at least 300 counts after background subtraction (at temperatures around $0.7 - 1$ keV, a minimum of $\sim$300 counts between 0.5 and 7 keV are required for a robust X-ray temperature estimate). We used the definitions of these radial bins to extract radially binned X-ray event spectra for each galaxy and background spectrum from the scaled and reprojected deep background data.

For each galaxy, we fit all radial bins simultaneously with `XSPEC` v.12.9 (Arnaud, 1996) using the `projct` model together with the X-ray thermal emission model `apec` and Galactic absorption column model `phabs`. Because the spectral band above 2 keV is more likely to be dominated by emission from X-ray background and unresolved point sources in typical X-ray spectra of early-type galaxies, we restricted the energy range for the spectral fits to 0.6 – 2.0 keV.

For each galaxy, the Galactic column density and redshift were fixed to the values in Table 1, and the gas metallicity was fixed at a solar abundance. We will discuss the impact of this abundance assumption in Section 3.4.4. Because the X-ray temperature gradient across the radial range we are interested in is small, we can produce better statistical fits with deprojection by fitting a single temperature across multiple (two to five) adjacent annuli while allowing the spectral normalization to be free in each annulus. The full tabulated results of these fits including uncertainties are provided in Table 3.2.

NGC 193, NGC 3801, and NGC 3894 were removed from our sample because there were not enough counts to obtain a deprojected temperature profile with three or more radial bins. NGC 4782 had sufficient counts to extract a profile but had a bright central point source resulting in large uncertainties in the central bins. For NGC 1316 and IC 4296, we do not attempt to fit the central point sources because our primary goal is to assess the shape of the entropy profile and the data quality for future work. Therefore, the central 2″ from IC 4296 and NGC 1316, 0.25 and 0.12 kpc, respectively, were excluded from our deprojection analyses of these two galaxies.

3.3.4 Thermodynamic Properties

3.3.4.1 Electron Density Profiles

To estimate the electron density within a given concentric shell i, we use the best-fit spectral normalization from the deprojection model in `XSPEC`,

$$\eta_i = \frac{10^{-14}}{4\pi D^2(1+z)^2} \int n_{e,i} n_{p,i} dV_i \quad . \tag{3.1}$$

The `projct` model performs the projection from 3D to 2D and the total emission measure within the extraction volume as shown in Equation 3.1, in which D is the angular diameter distance to the galaxy in centimeters (Table 1), n_e and n_p are the electron and proton number densities, respectively, in cm^{-3}, and V_i is the volume of the concentric shell in cm^3. With this definition of

Table 3.2 A portion of this table is printed here for form and content, Additional profiles can be found in Appendix E. Errors given for radius represent bin widths; all other errors are 1σ. Column (1): galaxy name. Column (2): radial bin center. Column (3): half-width of the radial bin. Column (4): grouping of temperature bins. Columns (5)-(6): best-fit temperatures and their errors. Column (7): electron density bin number. Columns (8)-(9): best-fit densities and their errors. in units of 10^{-2} cm^{-3} for compactness. Columns (10)-(11): calculated entropies and their errors.

Galaxy	radius	Δr	kT bin	kT	σ_{kT}	n_e bin	n_e	σ_{n_e}	K	σ_K
	(kpc)	(kpc)	ID	(keV)	(keV)	ID	(10^{-2} cm^{-3})	(10^{-2} cm^{-3})	(keV cm^2)	(keV cm^2)
IC 4296	0.48	0.24	1	0.75	0.02	1	16.50	0.57	2.48	0.09
IC 4296	0.72	0.12	1	0.75	0.02	2	10.10	0.53	3.44	0.16
IC 4296	0.97	0.12	2	0.78	0.03	3	5.62	0.39	5.29	0.33
IC 4296	1.45	0.24	2	0.78	0.03	4	3.52	0.20	7.23	0.41
IC 4296	1.93	0.24	3	0.84	0.03	5	2.50	0.18	9.82	0.63
IC 4296	2.66	0.36	3	0.84	0.03	6	1.19	0.06	16.08	0.86
IC 4296	3.87	0.60	4	0.89	0.05	7	0.49	0.03	30.82	1.98
IC 4296	6.28	1.21	4	0.89	0.05	8	0.38	0.03	36.60	2.73
IC 4296	9.42	1.57	5	2.10	1.07	9	0.24	0.03	116.60	59.92
IC 4296	12.56	1.57	5	2.10	1.07	10	0.16	0.03	152.23	79.11
IC 4296	15.46	1.45	6	1.29	0.21	11	0.17	0.03	91.31	18.74
IC 4296	17.88	1.21	6	1.29	0.21	12	0.17	0.05	91.62	22.83
			...		...		...		...	

normalization, the expression

$$n_e(shell) = \sqrt{\frac{4\pi\eta(shell)D^2(1+z)^2}{10^{-14}(n_e/n_p)V(shell)}} \tag{3.2}$$

gives us the deprojected radial electron density profile for each galaxy.

3.3.4.2 Entropy and $t_{\rm cool}/t_{\rm ff}$ Profiles

We plot the entropy profiles of the galaxies in our sample in Figure 3.1. Radial profiles of the $t_{\rm cool}/t_{\rm ff}$ ratio are shown in Figure 3.2, with $t_{\rm cool}$ defined by

$$t_{\rm cool} = \frac{3}{2}\frac{nkT}{n_e n_H \Lambda(T,Z)} \tag{3.3}$$

where n is the total number density of particles, n_e is the electron density, n_p is the hydrogen density (where we assume $n_p = n_e/1.2$), and $\Lambda(T,Z)$ is the temperature-dependent cooling function for plasma of metallicity Z. Our fiducial cooling function, from Schure et al. (2009), assumes a solar-metallicity ($Z_\odot$) plasma. The freefall time is calculated assuming a singular isothermal sphere with

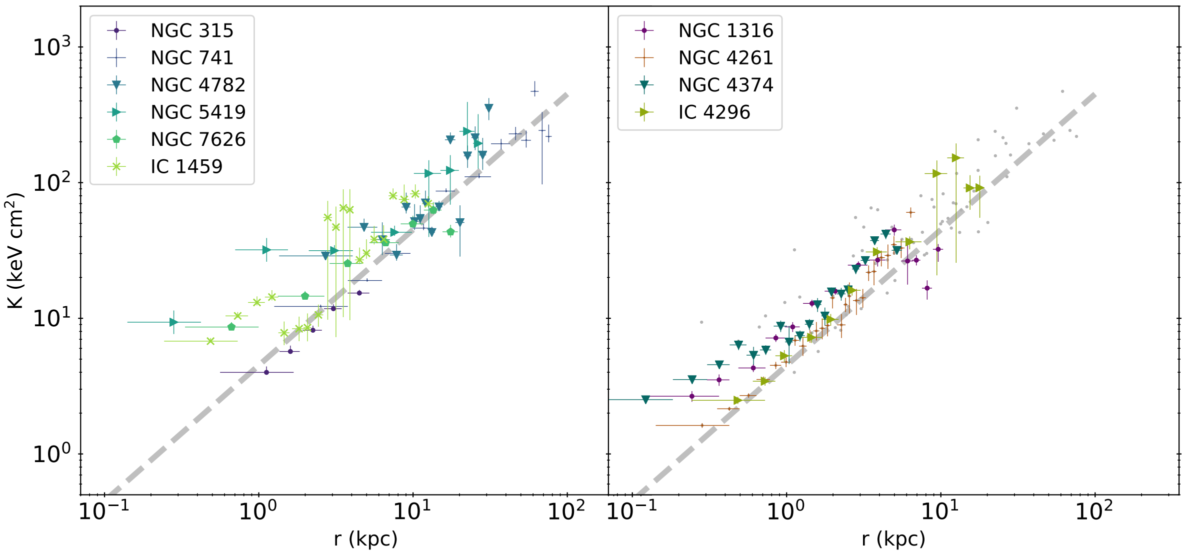

Figure 3.1 Left panel: entropy profiles for the galaxies in our sample with sufficient data counts to extract a deprojected radial profile but insufficient data to isolate the central ~0.5 kpc. Right panel: deprojected entropy profiles of the four galaxies with the best data quality (NGC 4261, IC 4296, NGC 1316, NGC 4374). For comparison, the gray dots are the data points from the galaxies in the left panel. Gray dashed lines on both plots show power-law profiles with $K \propto r$ to illustrate that NGC 4261 and IC 4296 differ from the other galaxies with comparable data quality (NGC 1316 and NGC 4374) by approximately following a similar power law into the central kiloparsec, rather than exhibiting a small excess like the other single-phase galaxies.

velocity dispersions found in Table 3.1. We calculated $t_{\rm cool}/t_{\rm ff}$ for NGC 4261 and three additional galaxies with the best data quality (NGC 1316, NGC 4374, and IC 4296).

3.4 Discussion

3.4.1 $t_{\rm cool}/t_{\rm ff}$ Profiles and Multiphase Gas

Figure 3.2 shows the $t_{\rm cool}/t_{\rm ff}$ profiles for the four galaxies with entropy profiles that come closest to probing the inner ~0.5 kpc of the galaxy. The profiles of IC 4296 and NGC 4374 are of particular interest. While the data are not of the resolution of NGC 4261, they still allow us to see the shape of the $t_{\rm cool}/t_{\rm ff}$ and entropy profiles near the central ~ 0.5 kpc of the galaxy. We also note that while the X-ray structure of NGC 315 is not resolved inside ~1 kpc, its gas entropy profile appears to follow a single power law like IC 4296 and NGC 4261. Furthermore, from the spectra reported in

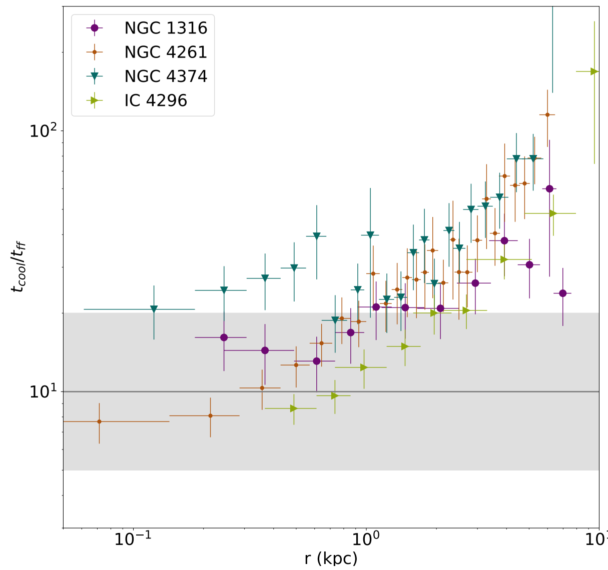

Figure 3.2 Radial profiles of $t_{\rm cool}/t_{\rm ff}$ for the four galaxies with the best S/N. The shaded region ($t_{\rm cool}/t_{\rm ff}$ = 5−20) represents the precipitation zone where multiphase gas is found for r = 1−10 kpc. We find that, like NGC 4261, IC 4296 reaches $t_{\rm cool}/t_{\rm ff} < 10$ in the central ~1 kpc while the other galaxies do not.

Ho et al. (1997, 1993), its multiphase gas appears to be confined to the nucleus, making it another promising candidate for a system in this powerful but possibly short-lived state.

Voit et al. (2015b) showed that $t_{\rm cool}/t_{\rm ff}$ in the central ∼ 1 kpc of both single- and multiphase galaxies usually remains above the apparent precipitation limit at $t_{\rm cool}/t_{\rm ff} \sim 10$. Farther out from the center (1–10 kpc), galaxies with multiphase gas have $t_{\rm cool}/t_{\rm ff}$ profiles that approximately track this precipitation limit, whereas galaxies with single-phase gas generally lie above the precipitation zone at $t_{\rm cool}/t_{\rm ff} \sim 5-20$ (blue shaded region in Figure 3.2). Voit et al. (2015b) found that, in a sample of morphologically relaxed, X-ray-bright galaxies (Werner et al., 2012), only the radial profile for NGC 4261 dipped below $t_{\rm cool}/t_{\rm ff} \sim 10$ in the center.

In our sample, the $t_{\rm cool}/t_{\rm ff}$ profile for NGC 4374 remains above the precipitation zone, and NGC 1316 is consistent with the multiphase galaxy pattern from Voit et al. (2015b). However, IC 4296 goes down to $t_{\rm cool}/t_{\rm ff} \sim 10$ near the center, as in NGC 4261, suggesting that the AGN feedback occurring in IC 4296 has interesting similarities to that of NGC 4261. The data were sufficient to probe the inner ∼ 0.5 kpc of NGC 4261, but in general the profiles more closely follow a single power law than a power law with an excess inside the central kiloparsec.

The Hα emission in NGC 4261 is nuclear rather than extended (Ferrarese et al., 1996; Lakhchaura et al., 2018), consistent with the picture of giant galaxies with single-phase gas having entropy profiles that scale as $K(r) \propto r$. Of our studied galaxies, IC 4296 most closely resembles NGC 4261, and Grossová et al. (2019) reported that in narrowband images from the *Hubble* and Southern Astrophysical Research (SOAR) telescopes, IC 4296 also has no Hα emission beyond $r \sim 2$ kpc.

3.4.1.1 Comparison with Previous X-ray Analysis

In an independent analysis, Lakhchaura et al. (2018) report entropy profiles for a sample of 49 elliptical galaxies, including eight of the galaxies analyzed in this paper: NGC 315, NGC 741, NGC 1316, NGC 4261, NGC 4374, NGC 4782, IC 4296, and NGC 5419. While there are small variations among bin sizes and radial ranges, we verified that our results are nevertheless mutually consistent within the measurement uncertainties. However, the work of Lakhchaura et al. (2018) treated gas metallicity differently, which we address in Section 3.4.4. In Section 3.4.2, we include some of the results of Lakhchaura et al. (2018) in our discussion. Additionally, in Table 3.1, we report the multiphase gas classifications from Lakhchaura et al. (2018) as well as additional results from Connor (in preparation) and Sun (in preparation) that use observations carried out using the SOAR optical Imager (SOI) and Goodman High Throughput Spectrograph of the 4.1m SOAR telescope and the Apache Point Observatory (APO) Astrophysics Research Consortium (ARC) 3.5m telescope.

3.4.2 Radio Luminosity and $t_{\rm cool}/t_{\rm ff}$

Figure 3.3 shows the minimum values of $t_{\rm cool}/t_{\rm ff}$ for NGC 4261, IC 4296, NGC 1316, and NGC 4374, along with the giant ellipticals from Lakhchaura et al. (2018), plotted as a function of the radius at which $t_{\rm cool}/t_{\rm ff}$ reaches its minimum value. We have adjusted the min($t_{\rm cool}/t_{\rm ff}$) values reported by Lakhchaura et al. (2018) for uniform comparison with our work, using the correction factor estimated in Section 3.4.4. The typical amplitude and direction of that correction are plotted in Figure 3.3 in the form of a purple arrow. This adjustment typically decreased the $t_c/t_{\rm ff}$ estimates from Lakhchaura et al. (2018) by a factor of 1.6. Points vary in size according to radio power in the 1.4 GHz band.

Notice that NGC 4261, IC 4296, and NGC 1316 have a lower min($t_{\rm cool}/t_{\rm ff}$) at a smaller radius than most of the other giant elliptical galaxies in the Lakhchaura et al. (2018) sample. Furthermore, the $t_{\rm cool}/t_{\rm ff}$ profiles in NGC 4261 and IC 4296, reach their minimum values in the central radial bin, raising the possibility that min($t_{\rm cool}/t_{\rm ff}$) is overestimated in these galaxies because of limited spatial resolution. However, it is also possible for those min($t_{\rm cool}/t_{\rm ff}$) values to be slight underestimates. In well-resolved galaxies that reach min($t_{\rm cool}/t_{\rm ff}$) outside the central radial bin, statistical fluctuations tend to cause the measurement of min($t_{\rm cool}/t_{\rm ff}$) to be biased low. Figure 3.2 shows why the magnitude of that bias in the galaxies we are focusing on is likely to be small. In all four galaxies, the second-lowest value of $t_{\rm cool}/t_{\rm ff}$ is nearly identical to the minimum value, well within the 1-sigma statistical uncertainties. Also, the $t_{\rm cool}/t_{\rm ff}$ profiles of those four galaxies are not constant in the 1–10 kpc range but only within the central $\sim$ 1 kpc, where there are only a few radial bins, reducing the likelihood of an unrepresentative statistical fluctuation. Consequently, the fact that NGC 4261 and IC 4296 have unusually low min($t_{\rm cool}/t_{\rm ff}$) and greater radio power than most other galaxies in the sample suggests that there may be a correlation between high radio power and $t_{\rm cool}/t_{\rm ff} < 10$ at small radii. In particular, the combination of low min($t_{\rm cool}/t_{\rm ff}$) and a power-law entropy slope that does not significantly flatten within the central kiloparsec is a unique feature of NGC 4261 and IC 4296. The other galaxies, in which the central entropy profile is flatter and min($t_{\rm cool}/t_{\rm ff}$) occurs at a larger radius, could be systems in which AGN feedback has recently elevated the entropy in the central kiloparsec.

3.4.3 Comparison to Simulations

Voit et al. (2015b) showed that the presence of multiphase gas outside the central kiloparsec of an early-type galaxy correlates with the slope of the entropy profile. Galaxies with an entropy slope of

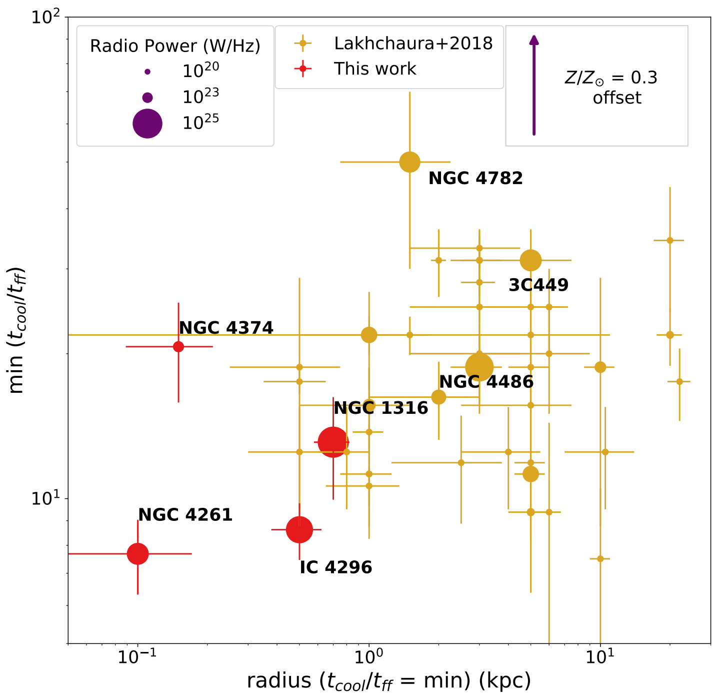

Figure 3.3 Radius where we measured the minimum value of the $t_{\rm cool}/t_{\rm ff}$ profile is plotted against the minimum $t_{\rm cool}/t_{\rm ff}$ for the sample of Lakhchaura et al. (2018, gold) offset to solar metallicity (see 3.4.4), with our four galaxies of best data quality (red). The purple arrow represents the offset between the adjusted values and the 0.3 $Z_\odot$ values from Lakhchaura et al. (2018). The relative size of the points represents their radio power (in W Hz^{-1}) in the 1.4 GHz band. NGC 4261, IC 4296, and NGC 1316 have a small min($t_{\rm cool}/t_{\rm ff}$) radius, a low min($t_{\rm cool}/t_{\rm ff}$), and a greater radio power than most galaxies in the sample.

$K \propto r^{2/3}$ have multiphase gas present at $r > 1$ kpc, while galaxies with an entropy slope of $K \propto r$ have only single-phase gas beyond $r \sim 1$ kpc. In order to better understand this relationship, we have compared our observed entropy profiles with the profiles of simulated galaxies from Wang et al. (2019). Figure 3.4 shows a comparison between our data for NGC 4261 and IC 4296 and simulated elliptical galaxies with both single- and multiphase gas as well as the entropy profiles for galaxies classified as having extended multiphase gas and no extended multiphase gas from Lakhchaura et al. (2018). The initial conditions for the simulations are chosen to mimic X-ray observations of NGC 5044 (multiphase) and NGC 4472 (single-phase), but the simulations were designed to represent generic single- and multiphase galaxies. The simulations do not resolve the gas profiles at < 1 kpc, meaning that our data have greater effective physical resolution than the

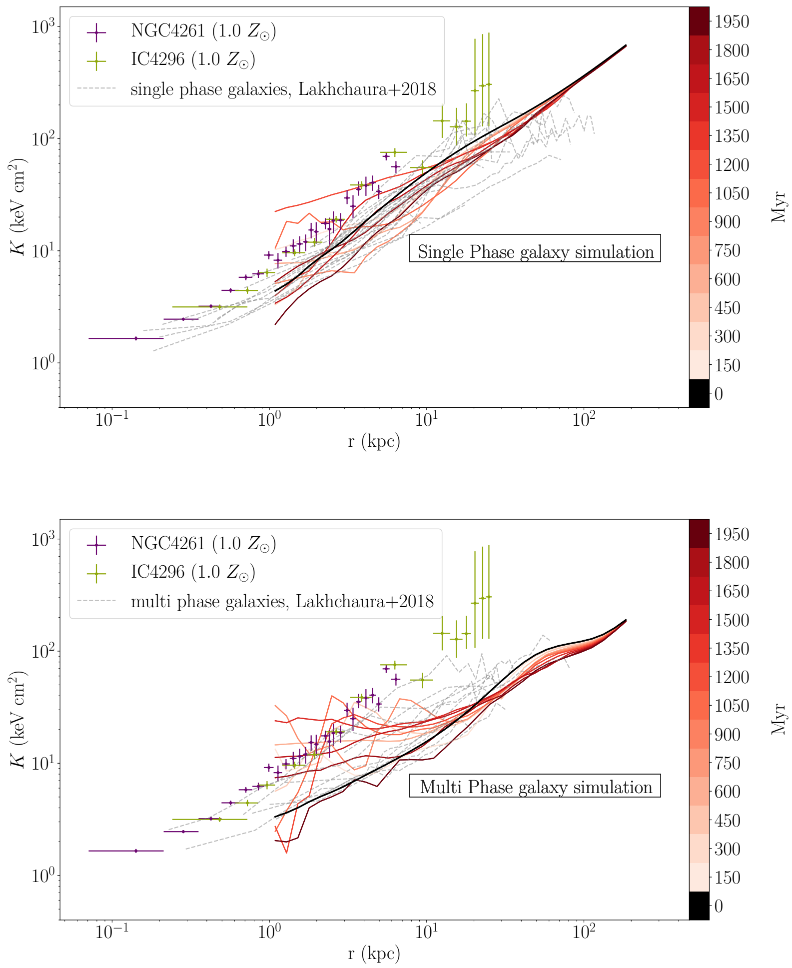

Figure 3.4 Entropy profiles of NGC 4261 and IC 4296 compared to simulations of somewhat lower mass giant elliptical galaxies with single-phase gas (top) and multiphase gas (bottom) from Wang et al. (2019) along with the single-phase (top) and extended multiphase (bottom) galaxies from Lakhchaura et al. (2018). Simulated profiles are shown at intervals 150 Myr, with earlier snapshots being shown in lighter red. The initial conditions are given by the black line and represent typical entropy profiles for single-phase and multiphase galaxies, based on NGC 4472 and NGC 5044, respectively. Galaxies classified as “N” (no extended multiphase gas) and “E” (extended multiphase gas) from Lakhchaura et al. (2018) are included in gray with errors bars removed for clarity. The simulated galaxies have lower velocity dispersions than the observed galaxies, but the simulations were designed to represent the behavior over time of generic single- and multiphase galaxies, rather than simulating a specific galaxy. The galaxies are referred to as MPG (multi phase galaxy) and SPG (single-phase galaxy) instead of their names throughout Wang et al. (2019). Note that the simulations do not resolve the gas profiles inside 1 kpc, and the flattening of the profiles in the center is likely a numerical effect because the resolution limit of the simulations can result in the simulated AGN affecting a larger region of the galaxy than real jets (Wang et al., 2019). Therefore, we expect the entropy slopes of the single-phase simulations to be the same as our observations, though the normalization can differ. The measured entropy gradients are consistent with those seen in single-phase gas simulations of radio sources in early-type galaxies.

simulations. However, we can still make comparisons in the $1 - 10$ kpc range.

We begin by considering whether the simulated galaxies are appropriate comparisons for our sample. From Makarov et al. (2014), the velocity dispersions of NGC 5044 and NGC 4472 are 224.9 ± 9.1 km s^{-1} and 282 ± 2.9 km s^{-1}, respectively, while the velocity dispersions for IC 4296 and NGC 4261 are 327.4 ± 5.4 km s^{-1} and 296.7 ± 4.3 km s^{-1}, respectively. Voit et al. (2015b) introduced the idea that there may be a correlation between the presence of multiphase gas, the velocity dispersion, and entropy profile slope in early-type galaxies. In contrast, Lakhchaura et al. (2018) found little correlation in entropy profile slope and the presence of multiphase gas when examining a larger sample. However, this is still an area of open study in both theory and observations of early-type galaxies. We do not expect the simulated profiles to match our data exactly because the velocity dispersions of the simulated galaxies are smaller than those of NGC 4261 and IC 4296. However, we can still make useful comparisons between the overall behavior of the simulations and observations that account for how the entropy profile slope correlates with velocity dispersion and the presence or absence of multiphase gas (Voit et al., 2015b).

For the single- and multiphase initial conditions simulated by Wang et al. (2019), the entropy profiles agree with the expectations of the simple physical models shown in Voit et al. (2015b). The multiphase gas simulation has an entropy profile of $K(r) = 3.5\ r_{\rm kpc}^{2/3}$keV cm^2, which corresponds to the hypothesized precipitation limit at $t_c/t_{\rm ff} \approx 10$. The steeper entropy profile characteristic of single-phase galaxies, $K(r) = 5\ r_{\rm kpc}$keVcm^2, is consistent with models in which heating by Type Ia supernovae drives an outflow. The implication is that self-regulated AGN feedback can maintain the observed properties of both the single- and multiphase galaxies, consistent with both idealized analytical models (Voit et al., 2015b) and simulations (Wang et al., 2019).

When we compare the single-phase simulation to NGC 4261 and IC 4296, the simulated galaxy does appear to maintain approximately the same entropy slope as our data. Furthermore, the comparison shows that the slopes of the single-phase entropy profiles from Lakhchaura et al. (2018) are different from the slopes of the multiphase entropy profiles, and the multiphase data have similar slopes to the multiphase simulations. The comparison between NGC 4261 and IC 4296,

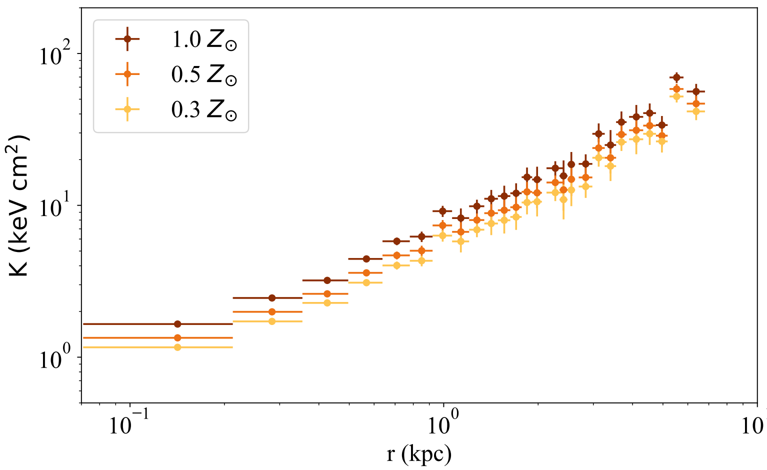

Figure 3.5 Comparison of the inferred entropy profiles for NGC 4261 for different assumed values of abundance. The points represent 1.0 $Z_\odot$ (red), 0.5 $Z_\odot$ (orange), and 0.3 $Z_\odot$ (yellow). For increasing values of metallicity, the amplitude of the entropy profile increases. Therefore, if a galaxy has a different metallicity than we have assumed, and if we no longer assume that each galaxy has uniform metallicity, the slope of the entropy profile could change as well. However, we would still expect the profile to fall within the metallicity range illustrated in the figure.

the multiphase galaxy simulations, and the extended multiphase gas data show that our galaxies are better represented by single-phase galaxies. The observed entropy profile slopes between 1 and 10 kpc are consistent with the entropy profile of a single-phase galaxy, which has a steeper slope ($\alpha \sim 1$). For some time steps, the central entropy profile of the simulated single-phase galaxy flattens out, which could represent epochs when the black hole in the simulations is particularly active. However, it could also be a numerical effect because the resolution limit of the simulations can result in the simulated AGN affecting a larger region of the galaxy than real jets (Wang et al., 2019).

3.4.4 Metallicity Analysis

When fitting entropy profiles, we assumed that each galaxy had a constant metallicity of 1.0 $Z_\odot$ across the profile. The hot gas abundances of early-type galaxies are difficult to obtain from low-resolution X-ray data, so we fixed the gas metallicities while fitting our observations. Here we quantify the sensitivity of our estimates of the X-ray densities and temperatures to the assumed metallicities. In Figure 3.5, we show an example result of the impact of three different metallicity assumptions on the entropy profiles for NGC 4261: 0.3, 0.5, and 1.0 $Z_{\odot}$. This range of abundances spans those from various treatments of early-type galaxies in observations and simulations found in the literature (Werner et al., 2012; Li & Bryan, 2014b; Wang et al., 2019). The amplitude of the inferred entropy increases as assumed abundance increases, but the slope of the entropy profile shows little change. Therefore, abundance changes over the full range of expected gas abundances from 0.3 to 1.0 solar would result in a change in amplitude of the inferred entropy profile on the order of 10 – 20% (see Figure 3.5).

In comparing our results with entropy profiles from previous work, we find that different abundance assumptions indeed result in small differences in the inferred entropy profiles. However, when the identical assumptions for abundances are used, the entropy profile results for different authors are the same within the uncertainties. For example, for the giant ellipticals examined by Werner et al. (2012), the assumed abundances in the central kiloparsec were $Z \sim 0.5\ Z_{\odot}$ and match our entropy profile results for NGC 4261 for a metallicity of $Z \sim 0.5\ Z_{\odot}$.

The relation between abundance and electron density for an `apec` model for a narrow range of gas temperatures (0.5 – 1.2 keV) can be quantified approximately by

$$\log\left[\frac{n_e(Z)}{n_e(Z_{\odot})}\right] = -m \log\left(Z/Z_{\odot}\right) \tag{3.4}$$

where Z is metallicity assumed in the determination of n_e and m is the power-law slope. We would expect $m \sim 0.4$ based on the dependence of $\Lambda(T)$ on Z in this temperature range (approximately $\Lambda \propto Z^{0.8}$) and form of the emission integral. To verify this estimate, we found the best-fit n_e and $T_{\rm X}$ for the four galaxies with the best data quality, sampling a range of assumed metallicities. We determined that the best-fit temperature was insensitive to the metallicity assumption, while density and assumed metallicity were related as in Equation 3.4 with $m = 0.43 \pm 0.04$ (NGC 1316), $m = 0.43 \pm 0.04$ (NGC 4261), $m = 0.39 \pm 0.11$ (NGC 4374), and $m = 0.29 \pm 0.18$ (IC 4296), where uncertainties on m are 1σ. These results are consistent with the expectations from X-ray plasma emission model for $kT \sim 0.6 - 1$ keV. The inferred electron density is therefore inversely related to the assumed abundance.

Furthermore, if the abundance is actually lower in the center than we assume, we have underestimated the central density and overestimated the central entropy. So if a galaxy's gas is less metal-rich in the center than we have assumed, its central entropy profile could be slightly steeper than shown (e.g. Lakhchaura et al., 2019). However, even if the central metallicity is lower than we assumed, the minima of the $t_{\rm cool}/t_{\rm ff}$ profiles are less than $t_{\rm cool}/t_{\rm ff} = 20$ for NGC 4261 and IC 4296.

3.5 Conclusions

Our analysis of the entropy profiles for a sample of nearby early-type galaxies with powerful radio sources shows that at least one other galaxy (IC 4296) is like NGC 4261 in having a powerful AGN and $t_{\rm cool}/t_{\rm ff} \sim 10$ at < 1 kpc. While the spatial resolution of the X-ray data for IC 4296 is not as good as for NGC 4261, both of their entropy profiles appear to be single power laws, and neither has extended multiphase gas greater than 2 kpc from their nuclei. To be certain of their similarity, we will need additional *Chandra* observations of IC 4296 to match the data quality of NGC 4261.

We produced deprojected temperature and density profiles for the hot gas surrounding seven additional early-type galaxies with powerful radio sources, but these observations lacked sufficient data quality to quantify the slope in the central ~ 0.5 kpc. Unfortunately, these galaxies are likely not good candidates for further study at this time because the additional *Chandra ACIS* observations needed to achieve comparable data quality to NGC 4261 are prohibitively long, given the degradation of *Chandra's* sensitivity to soft X-rays. We found that, in comparing independent analyses of entropy profiles in early-type galaxies, the treatment of abundance affects the amplitude of the entropy profile. Additionally, if the gas is not well mixed, it may have a metallicity gradient, meaning that the slope of the profile could be affected as well. Finally, we compared IC 4296 and NGC 4261 to recent simulations (Wang et al., 2019) and found that they are consistent with a single-phase gas model galaxy. The simulations agree well with our observational results, providing positive evidence for their ability to robustly model the hot ambient medium in early-type galaxies. In this work we were able to show excellent agreement between our observations, the theory of

Voit et al. (2015b), and the simulations of Wang et al. (2019).

CHAPTER 4

RELATIONSHIPS BETWEEN CENTRAL VELOCITY DISPERSIONS AND ATMOSPHERES OF EARLY-TYPE GALAXIES

4.1 Abstract

The Voit et al. (2020) black-hole feedback valve analytic model predicts relationships between stellar velocity dispersion and atmospheric structure for massive galaxies. In this work, we test the analytic model using the Chandra archival sample of 49 early-type galaxies from Lakhchaura et al. (2018). We consider the relationships between stellar velocity dispersion and entropy profile slope, multiphase gas extent, and ratio between cooling time and free-fall time simultaneously. We classify sub-samples limited to observations of high data quality and by entropy profile properties to explore the potential relationships between parameters and test the analytic model predictions. We find evidence for agreement with the equilibrium radial profiles from the Voit et al. (2020) model as well as agreement with the analytic model for the sample with low central entropy and limited velocity dispersion.

4.2 Introduction

Early-type galaxies, encompassing both elliptical and lenticular galaxies, are characterized by their elliptical shapes, older stellar populations, and lack of significant active star formation. Star formation in galaxies occurs when there is sufficient molecular gas to form stars and proceeds until the molecular gas supply runs out, either through stars forming more rapidly than the molecular gas can accumulate or the galaxy preventing further accumulation of molecular gas. It follows then, because little star formation is observed in early-type galaxies, that the galaxy must be preventing the molecular gas from accumulating. Molecular gas can accumulate in galaxies via cold streams (e.g. Kereš et al. 2005, 2009; Dekel et al. 2009), cooling flows (e.g. White & Frenk 1991; Fabian 1994; McNamara & Nulsen 2007, 2012; Werner et al. 2019), or stellar mass loss (e.g. Mathews &

Brighenti 2003; Leitner & Kravtsov 2011; Voit & Donahue 2011). Therefore, feedback processes in early-type galaxies must act to prevent each of these sources.

Observationally, the effect of feedback processes on the galactic atmosphere can be captured via observations of the hot X-ray gas. Entropy, in terms of X-ray observables, $K \equiv kTn_e^{2/3}$, where kT is the X-ray temperature and n_e is the electron density, is the preferred quantity for investigating feedback processes in galaxies. Feedback can change the rate at which the gas radiates energy away, affecting the cooling time of the gas. If the heating due to feedback is gradual compared to the time it takes for the heated gas to expand within the gravitational potential, the temperature of the gas may not change while the gas density lowers, lengthening the cooling time. We turn to entropy to capture gains and losses of energy in the gas. The gas entropy across the radius of a galaxy provides insight into the thermal history of the galactic atmosphere. In general, the galaxy potential well serves as an entropy sorting device, where lower entropy gas sinks to small radii, and higher entropy gas rises to larger radii. The lowest entropy gas is the densest and brightest gas in the galaxy, as observed in the X-ray. Voit et al. (2015b) examined the properties of a sample of 14 massive elliptical galaxies previously studied by Werner et al. (2012, 2014) and showed that the entropy profile slopes of early-type galaxies and the presence of multiphase gas are correlated. In the Werner et al. (2012) sample, inside ~ 2 kpc, the gas entropy levels of the galaxies are similar, but outside ~ 2 kpc, the slopes of the entropy profiles can differ from galaxy to galaxy depending on what thermal processes dominate. Galaxies with extended multiphase gas exhibit entropy profiles with $K \propto r^{2/3}$ from ∼1–10 kpc while galaxies with no extended multiphase gas (hereafter referred to as single phase galaxies) exhibit steeper entropy profiles, with $K \propto r$ from ∼1–10 kpc. The difference in the entropy profile slopes for galaxies with or without extended multiphase gas could be due to SNIa heating and sweeping gas ejected by the old stellar population out of single phase galaxies into an extended gaseous halo (Voit et al., 2015b). Voit et al. (2015b) also found that the velocity dispersions of the galaxies with extended multiphase gas were $\sigma \leq 255$ km s^{-1} while galaxies with no extended multiphase gas had velocity dispersions of $\sigma \geq 263$ km s^{-1}, indicating that entropy profile slope, velocity dispersion, and multiphase gas extent may be correlated and related to how the black hole interacts with the galactic atmosphere.

Lakhchaura et al. (2018) explored the relationship between entropy profile slope and multiphase gas extent for a larger archival sample (~50 galaxies) and did not report evidence for a relationship. However, Lakhchaura et al. (2018) did find evidence that the average behavior of entropy profiles and the ratio of the cooling time and free-fall time of the gas are related. Babyk et al. (2018) explored the relationship between entropy profile slope and velocity dispersion for an archival sample of 40 early-type galaxies (and 110 clusters). They also reported no evidence for a relationship between entropy profile slope and velocity dispersion, but they did find some evidence for a relationship between entropy profile slope and temperature.

Voit et al. (2020) investigated the coupling between supernova sweeping of stellar ejecta, the confining circumgalactic medium (CGM) pressure, and bipolar kinetic feedback fueled by accretion of cooling gas onto the central black hole, forming what they called a black hole feedback valve. They proposed an analytic model, investigating this idea, that predicts a relationship between the velocity dispersion and the entropy profile slope, that determines the effect of feedback on the galactic atmosphere, and whether multiphase gas can form. The model is informed by both numerical simulations and observations and analytically models feedback processes in massive galaxies. The model predicts that the entropy profile slope over the radial range where supernova heating exceeds radiative cooling ($\sim$ 1–10 kpc) is determined by the ratio of the specific thermal energy of the ejected stellar gas to the depth of the galactic potential well, as long as the velocity field is subsonic.

The structure of this paper is as follows: Section 4.3 describes our sample selection and data analysis processes, Section 4.4 discusses the connection between observations and theory, and Section 4.5 concludes by discussing how this work adds to the current understanding of precipitation-driven feedback in massive galaxies.

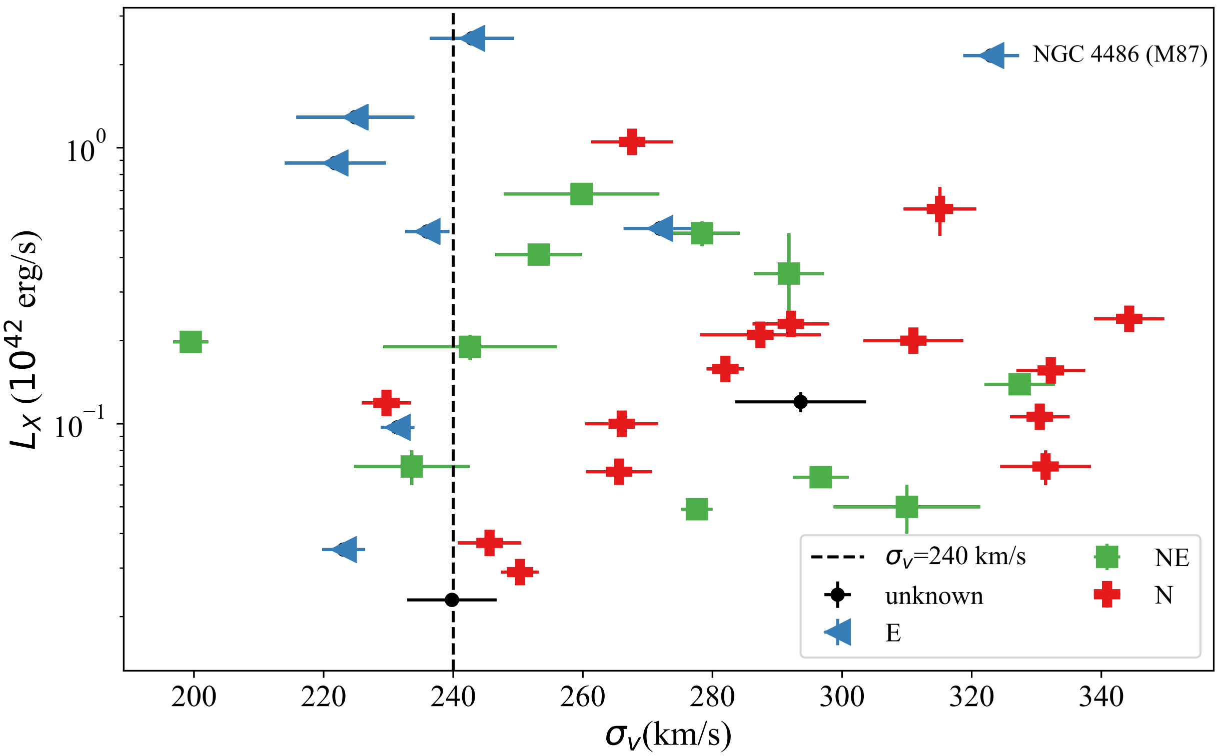

Figure 4.1 Stellar velocity dispersion, σ_v, is plotted with the X-ray luminosity within 10 kpc for the subsample of galaxies from Lakhchaura et al. (2018) with sufficient data to measure an accurate entropy profile slope at 1-10 kpc. The points are also classified by their multiphase gas extent from Lakhchaura et al. (2018). Blue triangles are galaxies with extended multiphase gas, red crosses are galaxies with no extended multiphase gas, green squares are galaxies with multiphase gas contained within 2 kpc, and black dots are galaxies without a gas extent classification. The vertical dashed line indicates the velocity dispersion (240 km s^{-1}) that corresponds to the critical entropy profile slope of $\alpha_K = 2/3$ (Voit et al., 2020).

4.3 Methods

4.3.1 Sample Description

Our primary goal in this woris to determine whether the relationship between the velocity dispersion and entropy profile slope is consistent with the analytic model predictions from Voit et al. (2020). Making such a comparison requires sufficient resolution to measure an entropy profile slope, so we need to use a sample of early-type galaxies with accurate entropy profiles and velocity dispersion measurements to test the analytic model's predictions.

The main sample explored in this work is the sample of 49 nearby, X-ray and optically bright, elliptical galaxies with archival *Chandra* data from Lakhchaura et al. (2018). We use the derived radial profile measurements of electron density, n_e, X-ray temperature, kT, entropy, K, and ratio of cooling time to free-fall time, t_c/t_{ff}, as well as their multiphase gas classification scheme[1] and X-ray luminosities. Full details of the galaxy parameters are found in Table 4.1.

Figure 4.1 shows the relationships between X-ray luminosity, stellar velocity dispersion, and multiphase gas characteristics for galaxies with sufficiently resolved entropy profiles (see Section 4.3.3 for details). Voit et al. (2020) showed that $\sigma_v = 240\text{km s}^{-1}$ corresponds to $\alpha_K = 2/3$ and represents a critical number for the analytic model. Extended multiphase gas appears to be more common among galaxies with $\sigma_v < 240\text{km s}^{-1}$ than among those with $\sigma_v > 240\text{km s}^{-1}$ (Voit et al., 2015b). The most notable exception is M87 (upper right of Figure 4.1) which resides in one of the most massive halos in the sample and has one of the highest X-ray luminosities. The massive halo and high luminosity indicate that the galaxy likely has high external gas pressure, and that its atmospheric characteristics are representative of the entire massive halo rather than only this single galaxy. Apart from M87, the upper envelope of the sample exhibits a decline in X-ray luminosity with increasing velocity dispersion. Voit et al. 2015b, 2020 also predicted that galaxies with higher velocity dispersion will have steeper entropy profile slopes. A steeper entropy profile slope means that the electron density of the gas is lower at 10 kpc (the aperture for measuring L_X) than it would be for shallower entropy profiles slopes.

The sample from Lakhchaura et al. (2018), after initial data quality limits are applied, is well-suited to test the analytic model predictions from Voit et al. (2020). In Section 4.3.4, we will discuss further the ways in which we subdivide the sample in our test of the analytic model.

[1]Except for IC 4296 which is correctly identified as NE, rather than E, in Frisbie et al. (2020)

Table 4.1: (1) Name; (2) redshift obtained from NED; (3) redshift independent distance; (4) σ_v and error; (5) 0.5–7.0 keV intrinsic X-ray luminosities and their errors estimated from a 10 kpc radius circular region around the X-ray peak (Lakhchaura et al., 2018); (6) Hα+[N 2] morphology classified as follows: N: no cool gas emission, NE: Hα+[N 2] extent < 2 kpc, E: $H\alpha$+[N 2] extent ≥ 2 kpc and U: galaxies for which the presence/absence of Hα+[N 2] could not be confirmed (Lakhchaura et al., 2018); (7) α_K and error; (8) minimum ratio of cooling time to free-fall time and error; (9) Fit central entropy and error.

Galaxy	z	D Mpc	σ_v km/s	L_X 10^{42}erg/s	gas extent	α_K	min (t_{cool}/t_{ff})	K_0 keV/cm^2
(1)	(2)	(3)	(4)	(5)	(6)	(7)	(8)	(9)
IC1860	0.0229	95.75	259.8 ± 12.0	0.68 ± 0.050	NE	0.66 ± 0.24	18.42 ± 2.40	5.92 ± 0.97
IC4296	0.0124	47.31	327.4 ± 5.4	0.14 ± 0.003	NE	1.23 ± 0.11	11.63 ± 0.78	0.69 ± 0.20
IC4765	0.0150	59.52	278.4 ± 5.8	0.49 ± 0.050	NE	0.88 ± 0.22	11.01 ± 1.20	1.82 ± 0.72
NGC315	0.0164	56.01	293.6 ± 10.1	0.12 ± 0.010	U	0.83 ± 0.24	20.02 ± 4.65	0.91 ± 0.96
NGC410	0.0176	66.00	291.8 ± 5.4	0.35 ± 0.140	NE	0.76 ± 0.35	27.30 ± 5.22	4.93 ± 1.36
NGC499	0.0147	60.74	253.2 ± 6.7	0.41 ± 0.030	NE	0.74 ± 0.24	34.18 ± 3.19	6.90 ± 4.16
NGC507	0.0164	59.83	292.1 ± 5.9	0.23 ± 0.020	N	0.80 ± 0.34	30.15 ± 5.61	7.14 ± 3.38
NGC533	0.0184	61.58	271.9 ± 5.6	0.51 ± 0.030	E	0.88 ± 0.14	12.28 ± 3.75	1.74 ± 0.36
NGC708	0.0162	64.19	221.8 ± 7.8	0.88 ± 0.020	E	0.64 ± 0.06	12.04 ± 0.29	5.38 ± 0.15
NGC741	0.0186	64.39	287.4 ± 9.3	0.21 ± 0.010	N	0.93 ± 0.09	19.16 ± 0.73	2.57 ± 0.39
NGC777	0.0167	58.08	315.1 ± 5.6	0.60 ± 0.120	N	0.59 ± 0.24	24.11 ± 3.01	5.22 ± 1.01
NGC1316	0.0059	19.25	223.1 ± 3.3	0.04 ± 0.002	E	0.72 ± 0.25	32.57 ± 6.72	0.58 ± 0.61
NGC1399	0.0048	17.75	332.2 ± 5.3	0.16 ± 0.004	N	0.94 ± 0.03	26.05 ± 0.40	0.89 ± 0.11
NGC1404	0.0065	19.18	229.7 ± 3.8	0.12 ± 0.001	N	0.80 ± 0.03	20.23 ± 0.51	0.70 ± 0.04
NGC1407	0.0060	23.27	265.6 ± 5.1	0.07 ± 0.003	N	0.83 ± 0.06	41.92 ± 1.67	4.13 ± 0.25
NGC1521	0.0140	50.93	233.6 ± 8.9	0.07 ± 0.010	NE	0.38 ± 0.39	20.90 ± 5.21	0.96 ± 0.83
NGC1600	0.0158	45.77	331.4 ± 7.0	0.07 ± 0.010	N	0.72 ± 0.18	42.60 ± 7.16	5.07 ± 0.39
NGC2300	0.0064	41.45	266.0 ± 5.6	0.10 ± 0.010	N	0.91 ± 0.13	26.09 ± 1.27	4.18 ± 0.43
NGC2305	0.0113	47.88	242.6 ± 13.4	0.19 ± 0.020	NE	0.70 ± 0.25	20.22 ± 3.36	1.54 ± 0.58
NGC3091	0.0122	48.32	311.0 ± 7.7	0.20 ± 0.020	N	0.40 ± 0.10	30.74 ± 4.16	3.48 ± 2.54

Galaxy	z	D	σ_v	L_X	gas	α_K	min	K_0
		Mpc	km/s	10^{42}erg/s	extent		$(t_{\rm cool}/t_{\rm ff})$	keV/cm^2
(1)	(2)	(3)	(4)	(5)	(6)	(7)	(8)	(9)
NGC3923	0.0058	20.97	245.6 ± 4.9	0.04 ± 0.001	N	0.92 ± 0.12	21.98 ± 1.41	1.34 ± 0.12
NGC4073	0.0197	60.08	267.6 ± 6.3	1.05 ± 0.050	N	0.61 ± 0.20	32.22 ± 2.92	8.30 ± 1.18
NGC4125	0.0045	21.41	239.8 ± 6.9	0.02 ± 0.001	U	0.13 ± 0.45	28.22 ± 12.35	1.43 ± 1.40
NGC4261	0.0073	29.58	296.7 ± 4.3	0.06 ± 0.003	NE	1.16 ± 0.06	14.17 ± 1.47	0.52 ± 0.08
NGC4374	0.0033	16.68	277.6 ± 2.4	0.05 ± 0.002	NE	1.18 ± 0.14	25.04 ± 6.58	1.86 ± 0.19
NGC4406	0.0006	16.08	231.4 ± 2.6	0.10 ± 0.004	E	0.54 ± 0.14	26.28 ± 1.60	5.21 ± 3.26
NGC4472	0.0032	15.82	282.0 ± 2.9	0.16 ± 0.001	N	0.96 ± 0.02	26.80 ± 0.23	1.17 ± 0.05
NGC4486	0.0042	16.56	323.0 ± 4.3	2.16 ± 0.004	E	0.61 ± 0.01	22.73 ± 0.27	3.00 ± 0.10
NGC4552	0.0009	15.97	250.3 ± 2.9	0.03 ± 0.001	N	0.95 ± 0.09	11.35 ± 0.63	2.23 ± 0.11
NGC4636	0.0031	15.96	199.5 ± 2.7	0.20 ± 0.002	NE	1.00 ± 0.03	10.79 ± 0.36	1.89 ± 0.08
NGC4649	0.0034	16.55	330.5 ± 4.6	0.11 ± 0.002	N	1.00 ± 0.02	22.63 ± 0.35	1.49 ± 0.02
NGC4696	0.0098	37.48	242.9 ± 6.5	2.49 ± 0.010	E	0.69 ± 0.01	4.73 ± 0.03	2.24 ± 0.07
NGC4782	0.0133	48.63	310.0 ± 11.3	0.05 ± 0.010	NE	0.59 ± 0.26	18.94 ± 9.92	4.30 ± 2.62
NGC5044	0.0090	35.75	224.9 ± 9.1	1.29 ± 0.010	E	0.56 ± 0.03	5.75 ± 0.14	0.08 ± 0.12
NGC5419	0.0139	50.87	344.3 ± 5.4	0.24 ± 0.020	N	1.19 ± 0.28	17.30 ± 2.21	1.38 ± 0.70
NGC5813	0.0064	29.23	236.0 ± 3.4	0.50 ± 0.003	E	0.51 ± 0.02	12.20 ± 0.26	3.44 ± 0.13

4.3.2 Theoretical Model

Voit et al. (2020) presents a basic model for the relationship between the entropy profile slope, α_K and the stellar velocity dispersion, σ_v. The basic model assumes that the stellar mass distribution can be approximated by a singular isothermal sphere with one-dimensional velocity dispersion, $\sigma_v = v_c/\sqrt{2}$. The outflow driving by supernova heating is assumed to be subsonic and therefore close to hydrostatic equilibrium. Combining the contributions to the entropy profile from supernova energy, orbital energy, and gravitational potential energy then gives the following relation between

α_K and σ_v:

$$\alpha_K \approx \frac{5}{3}\left(\frac{\epsilon_*}{v_c^2} - \frac{1}{4}\right)^{-1}, \tag{4.1}$$

where ϵ_* is the mean specific energy of the gas coming from stars. Therefore, the structure of the galaxy's atmosphere at $1 - 10$ kpc depends strongly on the ratio of ϵ_*/v_c^2. Given this relationship between the entropy profile slope and the stellar velocity dispersion, we will use the velocity dispersions and entropy profile slopes from observations to test the model.

Voit et al. (2020) also generalized the basic model by instead assuming that the galaxy's halo has an NFW density profile and the stellar mass density follows a modified Einasto profile. Numerical integration of the more complex model shows that the basic model over-predicts the entropy profile slope for $\sigma_v > 300$ km s^{-1}, and we will compare that modification of the model with data in Section 4.4.1.2.

4.3.3 Entropy Profiles

Equation 4.1 is based on a pressure-bounded, subsonic outflow solution, heated only by SNIa, and predicts a constant radial slope for the entropy profile. Because we want to test that model's prediction for the relationship between the power-law slope of the entropy profile and stellar velocity dispersion, we limit the range over which we fit the power-law slope to the radial range that is affected as little as possible by other heating processes. The AGN, if as powerful as NGC 4261 and IC4296 (see Frisbie et al. (2020)), typically deposits its energy (drilling through the hot gas via jet) rather far from the center ($r > 10$ kpc). In some systems, some fraction of the AGN energy output might couple to gas closer to the AGN, resulting in flattening or even inversion of the entropy profile near 1 kpc. Therefore, we limit our gas slope measurements to 1-10 kpc to get a "clean" measure of the gas slope where stellar processes are most likely to dominate.

While a few of the galaxies in our sample have entropy profiles that resemble a single power law (Frisbie et al., 2020), most have an excess of entropy over a single power law in the central ~kpc. Therefore, we have adapted the functional form from Donahue et al. 2005, 2006; Voit &

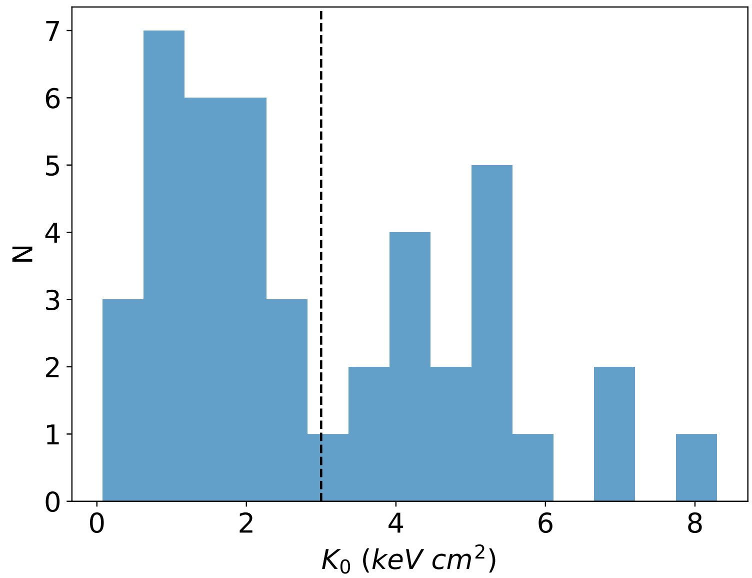

Figure 4.2 Histogram of K_0 values for the sample where K_0 is fit using Equation 4.2. The black dashed vertical line is at $K_0 = 3$ keV cm^2 and represents the limit we applied to remove galaxies with elevated central entropy outside of 1 kpc.

Donahue 2005; Cavagnolo et al. 2009 to the radial range for galaxies instead of clusters,

$$K(r) = K_0 + K_{10}\left(\frac{r}{10\ \mathrm{kpc}}\right)^{\alpha_K}, \tag{4.2}$$

where K_0 is the best fit central entropy, K_{10} is the best fit entropy at a radius of 10 kpc, and α_K is the best fit power law slope. We fit over 1-10 kpc because as discussed in Section 4.3.4, that radial range is where the potential effect of SNIa on the entropy profile is best measured. We calculate the best fit parameters using the python package `emcee`. We establish an initial broad expected range for the parameters in log space with $0 < K_0 < 10^2$, $0 < K_{10} < 10^2$, and $0 < \alpha_K < 2$. Errors were determined from 1 σ contours in two dimensions.

4.3.3.1 Distribution of Central Entropy

Our entropy profile fits suggest that approximately half of the overall sample is clustered near $K_0 \sim 1 - 2$keV cm^2, while the rest have $K_0 \gtrsim 3$ keV cm^2 (see Figure 4.2). In the group with low K_0, the entropy profile at 1–10 kpc is close to a pure power law. This sub-sample is therefore more suitable for testing the prediction represented in Equation 4.1. The subsample with greater K_0, on the other hand, clearly deviates from the pure power-law entropy profile predicted by the basic model for an outflow heated by only SNIa. In those galaxies, central heating by the AGN may be producing an entropy floor at small radii, causing a break in the power-law profile. The best-fitting values of α_K in the high-K_0 sample may still be representative of SNIa heating, but the measurements of α_K are not as clean because of greater degeneracy between K_0 and α_K in the fitting procedure.

4.3.4 Sub-Sample Selection

During our analysis, we subdivided the full sample so as to test the prediction in Equation 4.1 as accurately as possible. Our smallest sub-sample with the most restrictive criteria represents the cleanest case to test the model predictions, and the full sample with the least restrictive criteria provides a more general lower limit on the value of α_K associated with a given σ_v. Our analysis requires a statistically significant measurement of the slope parameter α_K, so we only include those galaxies from the sample with sufficient resolution (at least 4 radial bins) from 1–10 kpc. There are 36 galaxies from the sample that fit this criterion, hereafter referred to as the high quality (HQ) sample.

We implement two further limits on our sample for the analysis: central entropy, K_0, and velocity dispersion, σ_v. Of the 36 galaxy profiles with sufficient data quality, we define a sample of 22 profiles with low central gas entropy (hereafter referred to as the low K_0 sub-sample). We describe the rationale for that selection in Section 4.3.3.1. From that sample, we filter galaxies with velocity dispersions of 210–310 km s^{-1} (hereafter referred to as the restricted σ_v sample), leaving us with a sample of 16 galaxies. We discuss the rationale for that selection in Section 4.4.1.2.

Table 4.2 Each sample is a subset of the previously listed samples. Descriptions of the sample are in Section 4.3.4. The fit is an ordinary least-squares fit to a linear model ($\alpha_K = A\sigma_{240} + B$) with intrinsic scatter (Akritas & Bershady, 1996), and errors on the slope are 1σ. Column 1: Sample selection criteria; Column 2: Slope of ordinary least squares fit to the data; Column 3: Reduced chi squared for the fit; Column 3: Intrinsic scatter and error; Column 5: Number of galaxies included in the fit.

Sample	**Slope**	**Reduced χ^2**	**Intrinsic Scatter**	**Number**
High Quality (HQ)	0.52 ± 0.24	1.03	0.18 ± 0.02	36
Low K_0	0.80 ± 0.33	1.05	0.22 ± 0.03	22
restricted σ_v	1.80 ± 0.51	1.08	0.16 ± 0.02	16

4.4 Discussion

4.4.1 Low Central Entropy, restricted σ_v and the Analytical Prediction

4.4.1.1 The Black-hole Feedback Valve Prediction

The Voit et al. (2020) analytic model predicts a relationship for stellar velocity dispersion and entropy profile slope (Equation 4.1) in the radial range where SNIa heating is significant (1–10 kpc). Elevated central entropy, K_0, beyond 1 kpc, suggests that the central AGN is more strongly coupled to the surrounding medium. Therefore, SNIa heating is not the dominant heating process, and the model is not expected to apply. Because the model applies best to galaxies without elevated central entropy, we will investigate the relationship between velocity dispersion and entropy profile slope for that particular sub-sample.

4.4.1.2 Comparison to the Analytic Prediction

With the criteria explained in Section 4.3, we examine the relationship between the stellar velocity dispersion, σ_v, and the entropy profile slope, α_K. Table 4.2 summarizes the results for our exploration of the relationship between velocity dispersion and entropy profile slope for the three samples. To quantify the potential relationship between α_K and σ_v, we assume that the relationship is approximately linear, $\alpha_K = A\sigma_{240} + B$, with intrinsic scatter and determine the strength of the relationship by fitting a linear model with intrinsic scatter to the entropy profile slope, α_K, versus the scaled velocity dispersion, σ_{240}, with ordinary least squares (Akritas & Bershady, 1996). We use the same process for each sub-sample of galaxies, limited via criteria discussed in 4.3.4.

We first show that, with the requirement for radial resolution and fitting entropy profile slope between 1-10 kpc (see Section 4.3.3 for the entropy profile fitting procedure), some relationship emerges (see Figure 4.3). The slope of the relation is 0.53 ± 0.27, so while the slope is only about 2σ away from from 0, there is some evidence for relationship between σ_v and α_K before any additional limits were placed on the sample. Limiting the radial range of the entropy profile fit and requiring sufficient data resolution over that radial range clearly reduces some of the ambiguity found in previous work (e.g. Babyk et al. 2018; Lakhchaura et al. 2018).

The main sample generally contains massive elliptical galaxies, but there are some that are not necessarily representative of the galaxies the Voit et al. (2020) model sets out to describe. Figure 4.4 shows the fit for the the low K_0 sub-sample determined by the criteria discussed in Section 4.3.3. The slope is 0.80 ± 0.33, so we see mildly stronger evidence for a relationship when the sample is limited to those galaxies without elevated central entropy.

We determined our final sub-sample, the restricted σ_v sample, shown in Figure 4.4 using the σ_v limiting stated in Section 4.3.4. Galaxies with $\sigma_v < 210$ km s^{-1} may not yet have a well-developed and sufficiently hot circumgalactic medium, so there is no reason to believe that the analytic model would apply. We limit $\sigma_v < 310$ km s^{-1} on the upper end for two reasons. (1) The Voit et al. (2020) model assumes a singular isothermal sphere which simplifies the mass profile (see Section 4.3.2), resulting in the analytic model to overpredicting the entropy profile slope for galaxies with high σ_v. (2) Some galaxies in the sample, like M87, are in galaxy groups, and thus are in a potential well with a stellar velocity dispersion significantly greater than that of the central galaxy, resulting in a shallower entropy profile slope than predicted for an isolated galaxy. Limiting the velocity dispersion in this way limits the sample to galaxies most representative of the restricted σ_v the analytic model describes.

For the restricted σ_v sample, we find a slope of 1.80 ± 0.51, or $\sim 3\sigma$ away from a flat line.

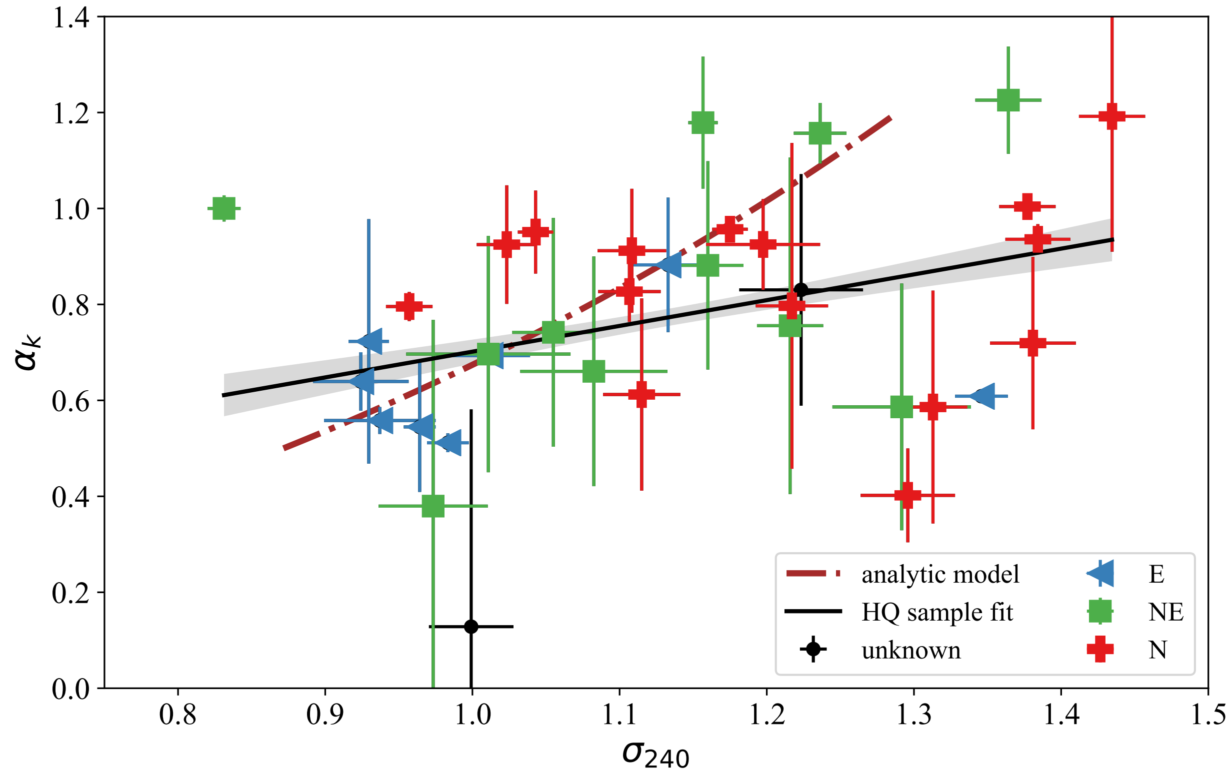

Figure 4.3 Stellar velocity dispersion, σ_v, is plotted with the entropy profile slope, α_K for the subsample of galaxies from Lakhchaura et al. (2018) with sufficient data between 1-10 kpc. The points are also classified by their multiphase gas extent from Lakhchaura et al. (2018). Blue triangles are galaxies with extended multiphase gas, red crosses are galaxies with no extended multiphase gas, green squares are galaxies with multiphase gas contained within 2 kpc, and black dots are galaxies without a gas extent classification. The black line is the ordinary least squares fit to the data, and the grey band is the 1σ error.

The criteria we have applied limit the main sample to those galaxies that are most likely to follow the analytic model, so it is not surprising that the evidence for a relationship is stronger when the sample is limited to the galaxies to which the model is expected to apply: velocity dispersion-limited galaxies with limited direct central coupling ($r < 10$ kpc) by the central AGN, as shown by lack of central entropy elevations or inversions in the entropy profile. However, the relationship between entropy profile slope and velocity dispersion may be stronger than indicated by previous works.

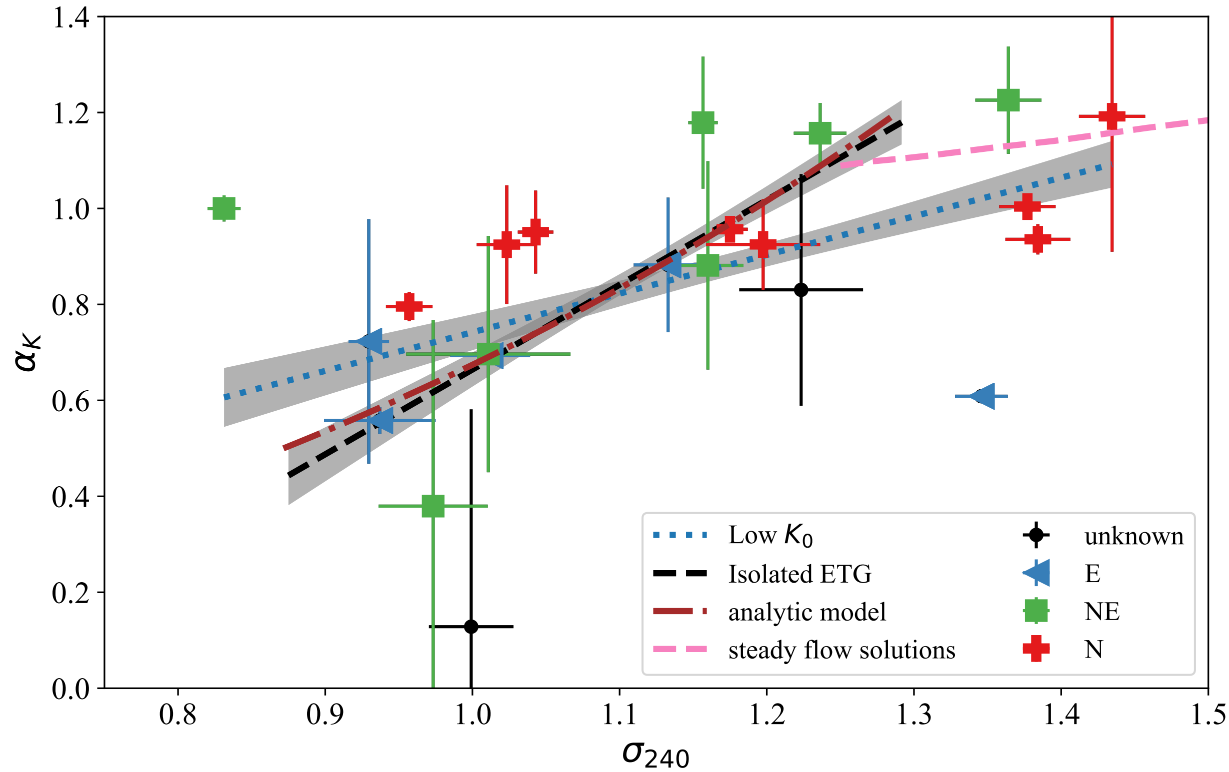

Figure 4.4 Stellar velocity dispersion, σ_v, is plotted with the entropy profile slope, α_K, for the subsample of galaxies with $K_0 < 3$ keV cm^2, and ordinary least squares fits are given for both the for low K_0 subsample ($K_0 < 3$ keV cm^2) and the restricted σ_v subsample (210 km s^{-1} $< \sigma_v <$ 310 km s^{-1}, $K_0 < 3$ keV cm^2). The blue dotted line is the fit to the low K_0 sample, and the black dashed line is the fit to the σ_v limited sample. The maroon dash-dotted line is the analytic solution from Voit et al. (2020). The pink dashed lines represents the steady flow solutions for $\sigma_v \gtrsim 300$ km s^{-1}. The grey bands are 1σ errors.

4.4.2 Comparison to the Analytic Model and Numerical Integration Results

Figure 4.4 also includes the analytic model plotted with the fit to the K_0 and σ_v limited sample. We find very good agreement over the range of the "best case" fit. Furthermore, as discussed in Section 4.3.2, the analytic model over-predicts the entropy profile slopes for galaxies with higher σ_v, so the numerical integration results may actually better represent the data for $\sigma_v > 310$ km s^{-1} than the analytic model.

The analytic prediction for the relation between σ_v and α_K from Equation 6 of Voit et al. (2020) is a good fit when the data are restricted to the 210 km s^{-1} $< \sigma_v <$ 310 km s^{-1} interval. However, the 9 points at $\sigma_v > 310$ km s^{-1} all fall below the model prediction and the 1 point at

$\sigma_v < 210$ km s^{-1} (NGC 4636) is above it. A closer look at the modeling shows that Equation 6 overpredicts α_K at $\sigma_v < 300$ km s^{-1}, compared to the numerical steady flow solutions, shown by the pink dashed line in Figure 4.6.

4.4.3 Best fit Entropy Profile Slope, Multiphase gas extent, and min($t_{\rm cool}/t_{\rm ff}$)

The free-fall time, $t_{\rm ff} = (2r/g)^{1/2}$, where r is the galactocentric radius and g is the local gravitational acceleration, provides a dynamical timescale to characterize the gravitationally-driven motions of the gas and is based on observations of the stellar light from the galaxy. For our purposes, we will use the form $t_{\rm ff} = r/\sigma_v$. The cooling time is defined as:

$$t_{\rm cool} = \frac{3}{2}\frac{nkT}{n_e n_H \Lambda(T,Z)}, \tag{4.3}$$

where n is the total number density of particles, n_e is the electron density, n_p is the hydrogen density (where we assume $n_H = n_e/1.2$), and $\Lambda(T,Z)$ is the temperature dependent cooling function for plasma of metallicity Z. The ratio of the cooling time to the free-fall time $t_{\rm cool}/t_{\rm ff}$ indicates if precipitation occurs in the ambient gas. For $t_{\rm cool}/t_{\rm ff} = 5 - 20$, the galaxy is said to be in the precipitation zone, where multiphase gas is found (Voit et al., 2015b). Voit et al. (2015b) also showed that from 1–10 kpc, galaxies with extended multiphase gas generally track the precipitation zone whereas galaxies without extended multiphase gas generally remain above the precipitation zone. The minimum value of $t_{\rm cool}/t_{\rm ff}$ is anti-correlated with the presence of multiphase gas (Voit & Donahue, 2015), so we expect galaxies with greater min($t_{\rm cool}/t_{\rm ff}$) to have little to no multiphase gas in their centers.

The expectation from theoretical models is that the entropy profile slope should correlate with multiphase gas extent, with galaxies with no extended multiphase gas having entropy profile slopes of $K \sim r$ and galaxies with extended multiphase gas having $K \sim r^{2/3}$. Furthermore, $t_{\rm cool}/t_{\rm ff}$ is coupled with the entropy profile, meaning that profiles with higher min($t_{\rm cool}/t_{\rm ff}$) have higher entropy gas with longer cooling times.

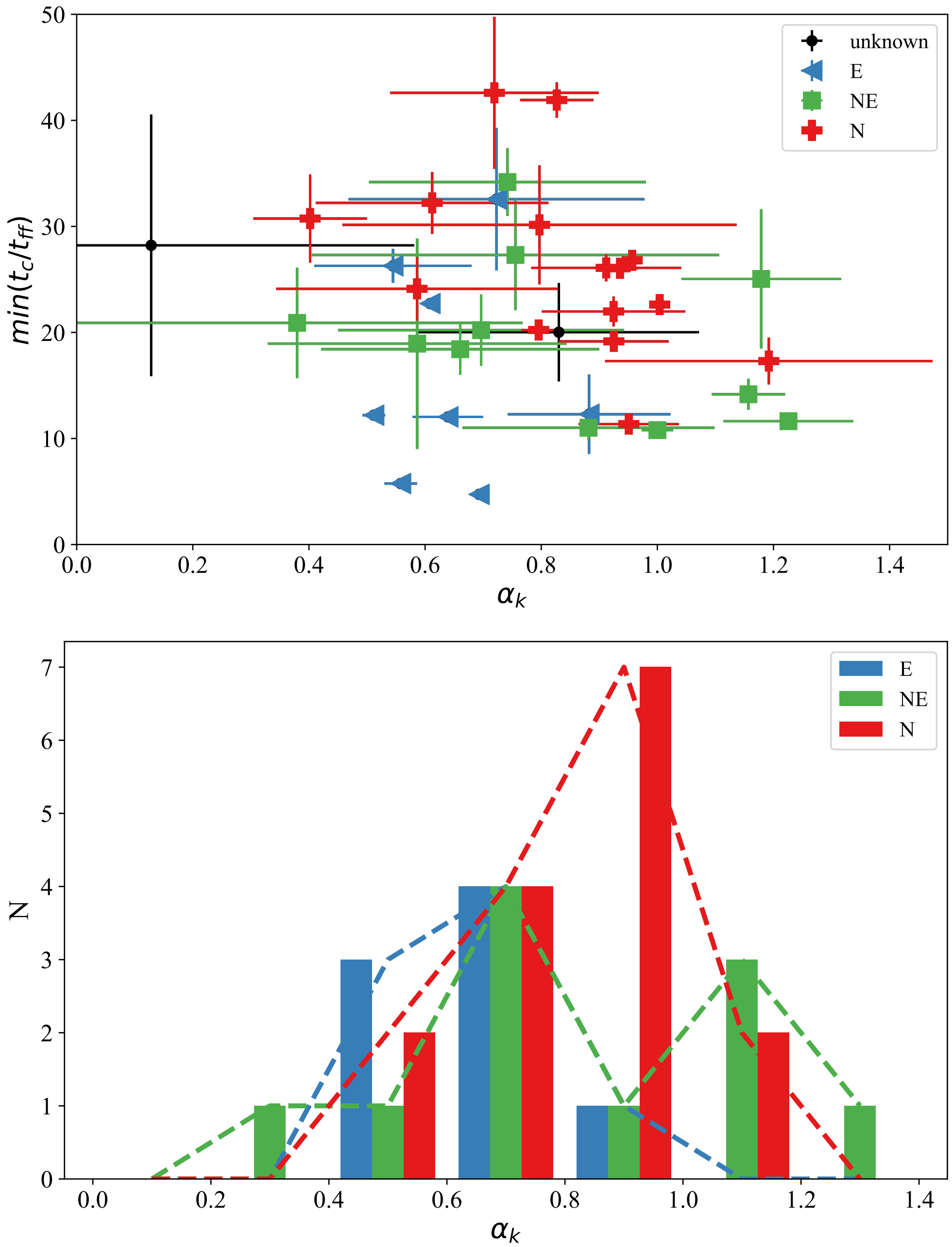

Figure 4.5 Top: α_K vs. $\min(t_{\rm cool}/t_{\rm ff})$ for the main sample Bottom: Histogram of α_K by gas extent for the High Quality sample. Multiphase gas classifications are from Lakhchaura et al. (2018). Blue triangles are galaxies with extended multiphase gas, green squares are galaxies with extended multiphase gas that does not extended past 2 kpc, red crosses are galaxies with no extended multiphase gas, and black dots are galaxies with no multiphase gas extent classification. The colors indicated each category of multiphase gas extent are the same in the bottom histogram.

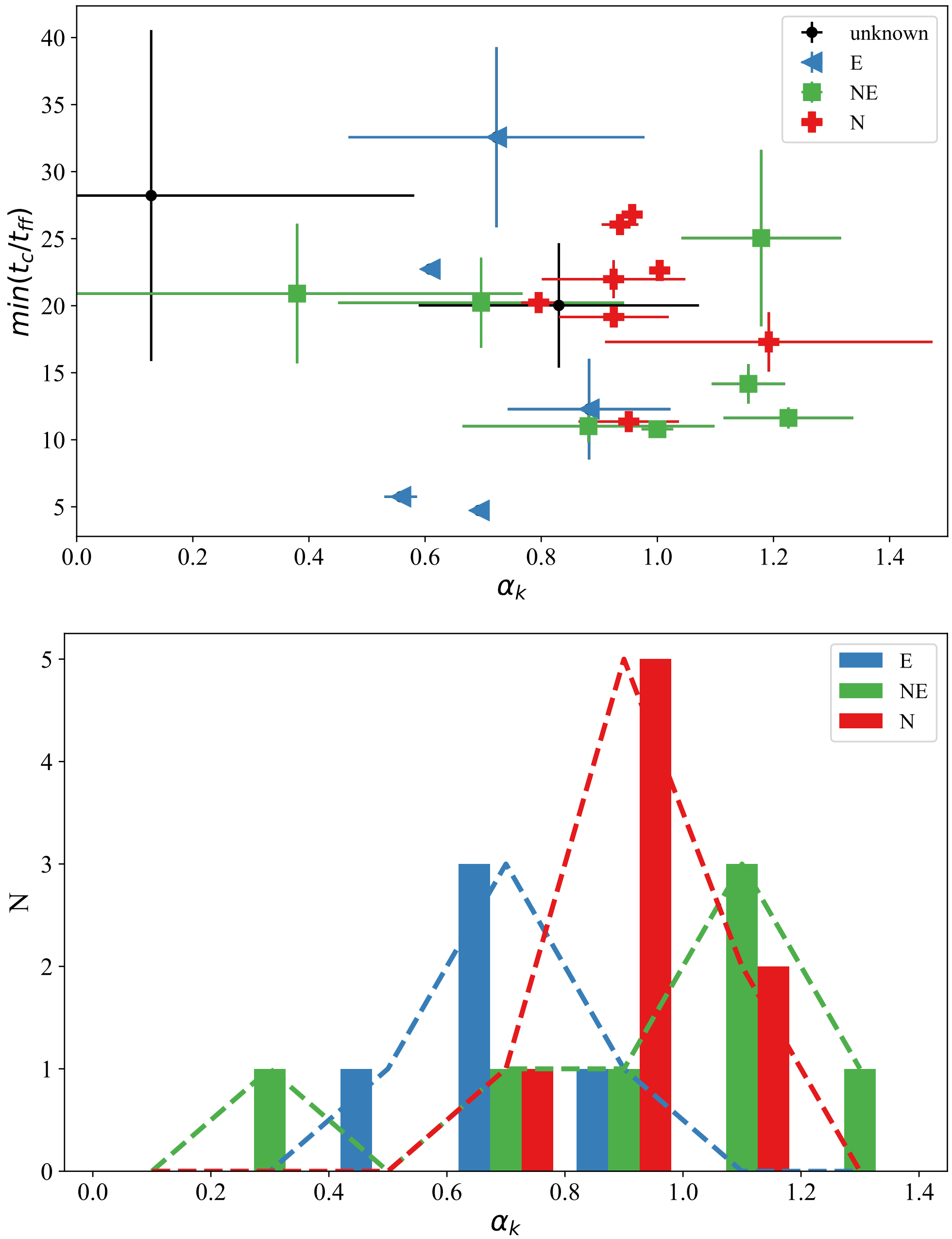

Figure 4.6 Top: α_K vs. $\min(t_{\mathrm{cool}}/t_{\mathrm{ff}})$ Bottom: Histogram of α_K by gas extent for the low K_0 sample. Blue triangles are galaxies with extended multiphase gas, green squares are galaxies with extended multiphase gas that does not extended past 2 kpc, red crosses are galaxies with no extended multiphase gas, and black dots are galaxies with no multiphase gas extent classification. The colors indicated each category of multiphase gas extent are the same in the bottom histogram.

We can expand our understanding of the relationships between galaxy parameters by exploring $\min(t_{\rm cool}/t_{\rm ff})$ for both the high quality sample and the sample limited to galaxies with $K_0 < 3$ keV cm^2, along with the multiphase gas extent and entropy profile slope, α_K. Figure 4.5 and Figure 4.6 summarize this relationship for the high quality sample and the low K_0 sample, respectively. In Figure 4.5, we consider the high quality sample, and we find that galaxies with extended multiphase gas (categorized as "E") have entropy profile slopes close to $r^{2/3}$, but the galaxies with no extended multiphase gas (categorized as "N"), that we would expect to have entropy profiles slopes around r, extend down to lower entropy profile slopes. However, when we examine the low K_0 sample in Figure 4.6, we find that removing galaxies with elevated central entropy outside 1 kpc effectively removes the galaxies with no multiphase gas and lower entropy profile slopes. Furthermore, we see that removing galaxies with elevated central entropy also removes many of the galaxies with greater $\min(t_{\rm cool}/t_{\rm ff})$, likely because the feedback increases the cooling time.

If we consider the high quality sample, we find that the galaxies with high σ_v and no extended multiphase gas extend down to lower entropy profile slopes, Taken together, the two samples show that elevated K_0 outside 1 kpc and higher $\min(t_{\rm c}/t_{\rm ff})$ can serve as flags for galaxies that are not representative of SN-heated outflows, but rather have been flattened by feedback, allowing us to better test the analytical model.

4.4.4 Comments on Individual Galaxies

In Figure 4.3, some galaxies stand out as not conforming to the model. NGC 533 conforms to the analytical prediction by entropy profile slope and velocity dispersion, but its multiphase gas extent does not. Other galaxies (M87, NGC 4636, NGC 1521, NGC 1404, and NGC 4125) do not conform to the analytical prediction. Here, we present possible explanations for these notable exceptions to the model.

4.4.4.1 M87

M87 has high σ_v, but an entropy profile near $\alpha_K = 2/3$. However, we do not expect M87 to conform to the model because it is in a potential well with a velocity dispersion significantly greater than the stellar velocity dispersion of the central galaxy, though α_K is consistent with a galaxy near the precipitation limit.

4.4.4.2 NGC 4636

NGC 4636, has $\alpha_K \sim 1$ but is classified as having multiphase gas present inside 2 kpc. The entropy profile is consistent with the precipitation limit from 0.5–8 kpc, but is also consistent with a pure cooling flow from 0–2 kpc (Voit et al., 2020). Voit et al. (2020) also states that at smaller radii, the entropy profile flattens, relative to the the $K \propto r^{2/3}$ precipitation-limited profile, but reaches ~ 1 keV cm^2 inside of 100 pc, considerably below the level expected from $\sim 10^{42}$erg s^{-1} of intermittent kinetic feedback power. There are several possible explanations for this low central entropy level: (1) time-averaged kinetic AGN power has been $\sim 10^{41}$erg s^{-1} for the last ~ 100 Myr, (2) the AGN power has been highly collimated, as in NGC 4261, and has penetrated to $\gg 1$ kpc without dissipating much power, (3) AGN power has been too weak to balance cooling for the last ~ 100 Myr. In this last case, a cooling catastrophe is imminent, as suggested by the entropy profile between 0.5 and 2 kpc, and will soon trigger a strong feedback episode.

4.4.4.3 NGC 1521

NGC 1521 does not conform to the model, most likely because of low spatial resolution. The entropy profile only has four radial bins between 1–10 kpc, and only one additional radial bin, interior to 1 kpc. The best fit entropy profile slope has a large uncertainty, and the uncertainty does overlap the analytic prediction. Therefore, improved spatial resolution is necessary to determine if the galaxy conforms to the model.

4.4.4.4 NGC 4125

NGC 4125 does not conform to the analytic model, but like NGC 1521, may not conform due to spatial resolution. However, the shape of the entropy profile and the galaxy parameters are a bit more interesting. The X-ray luminosity (measured inside 10 kpc) is the lowest in the HQ sample ($0.023 \pm 0.001 \times 10^{42}$ erg s^{-1}). Between 1–10 kpc, the entropy profile is almost flat and based on six radial bins, resulting in a low best fit entropy profile slope (and larger uncertainty). However, interior to 1 kpc, the entropy profile slope is much steeper, and Lakhchaura et al. (2018) find a power law component of the spectrum, indicating the presence of an AGN with luminosity $0.006 \pm 0.001 \times 10^{41}$erg/s. Wiklind et al. (1995) detected an upper limit for the molecular gas content, but the measurement is uncertain due to high systematic errors. The combination of the presence of an AGN, $\sigma_v < 240$ km s^{-1}, and the flattened entropy profile at larger radii may indicate that this is a galaxy where the steady flow is cooling dominated at larger radii and prone to developing entropy inversions (Voit et al., 2020).

4.4.4.5 NGC 1404

NGC 1404 is not far from the analytic prediction, but it has low σ_v for its α_K because it has an entropy profile with a sharp increase in slope beyond 7 kpc. It is a satellite of NGC 1399, so the sharp increase in the entropy profile could potentially be a result of ram-pressure stripping by the IGM around NGC 1399.

4.4.4.6 NGC 533

NGC 533 has $\sigma_v = 272$ km s^{-1} and $\alpha_K = 0.9$. The velocity dispersion of the surrounding galaxies is ~464 km s^{-1}, according to Zabludoff & Mulchaey (1998), so we would not expect the basic model to apply.

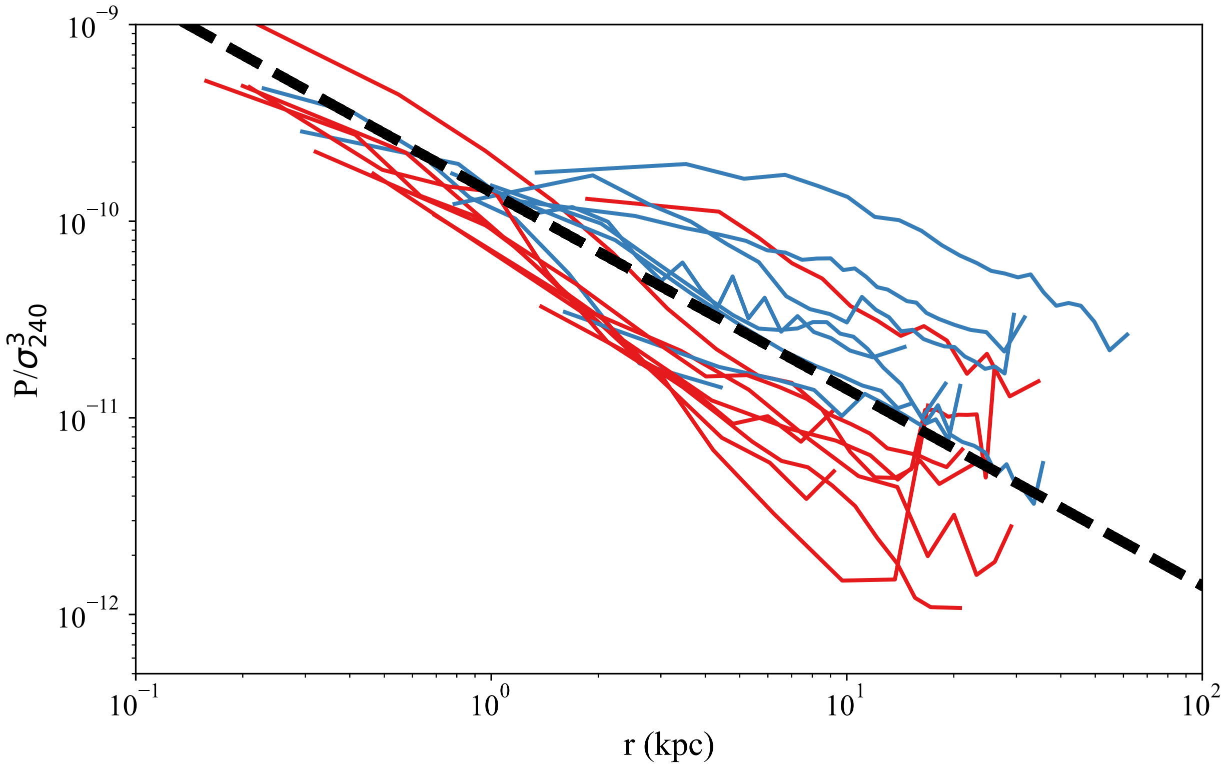

Figure 4.7 The equilibrium pressure at temperature T, for radius r (black dashed line), is plotted with the extended multiphase (E, blue lines) and single-phase (N, red lines) galaxies in the HQ sample. Errors bars are removed from the profiles for clarity.

4.4.5 Predictions for Equilibrium Pressure and Density Profiles

The analytic model of Voit et al. (2020) explores the behavior of the heating/cooling equality based on the Black-hole feedback valve model. Here, we present an observational test of the derived equilibrium profiles with the pressure and density profiles from Lakhchaura et al. (2018). An entropy profile slope of $\alpha_K \approx 2/3$ is a critical slope for the analytic model, meaning that the behavior of the galactic outflows should be fundamentally different above and below $\alpha_K \approx 2/3$. Voit et al. (2020) shows that the ratio of stellar heating to radiative cooling decreases with radius for galaxies with an entropy profile slope below $\alpha_K \approx 2/3$ and rises with radius for galaxies with an entropy profile slope above $\alpha_K \approx 2/3$. Following from Equation 4.1, the velocity dispersion corresponding to this critical entropy profile slope is ≈ 240 km s^{-1}.

When radiative cooling per unit volume equals stellar heating per unit volume, for a given

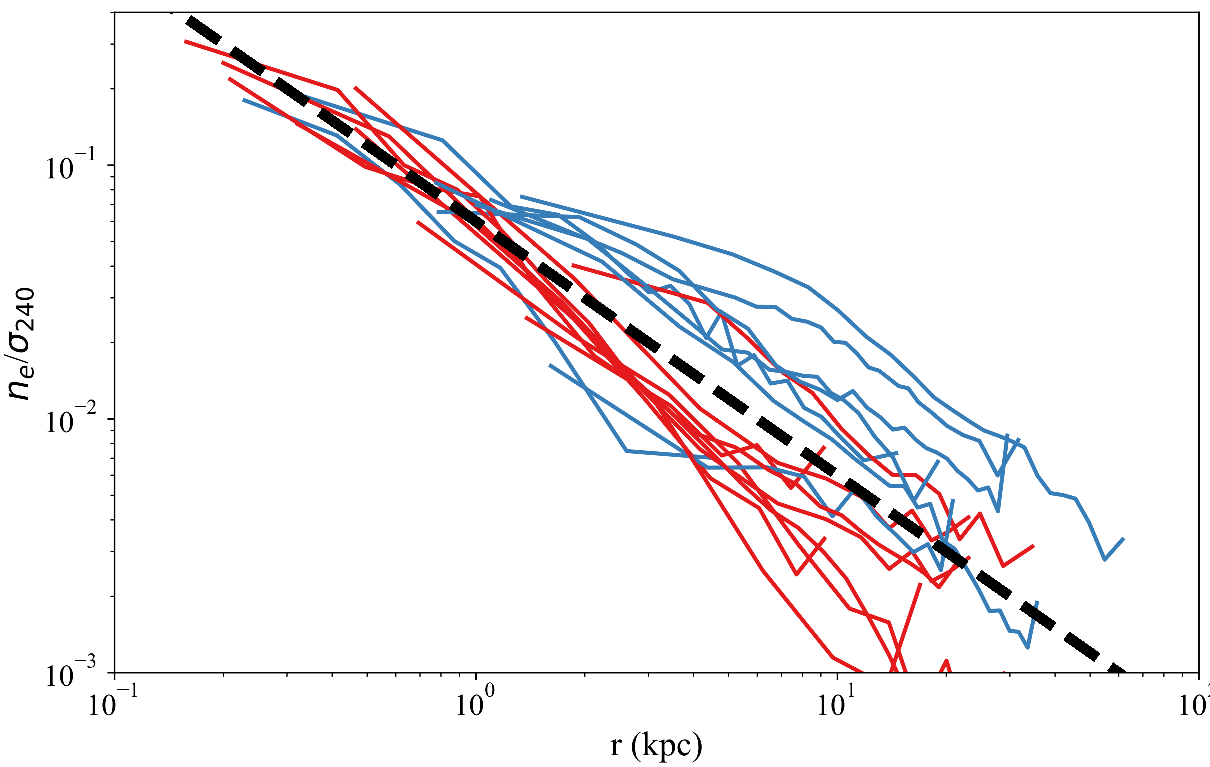

Figure 4.8 The equilibrium electron density at temperature T, for radius r (black dashed line), is plotted with the extended multiphase (E, blue lines) and single-phase (N, red lines) galaxies in the HQ sample. Errors bars are removed from the profiles for clarity.

radius, they find an equilibrium pressure profile along which supernova heating equals radiative cooling for a temperature, T (Equation 11 in Voit et al. (2020)):

$$P_{\rm eq}(r) \equiv \left[\left(\epsilon_* + \frac{3}{2}\sigma_v^2\right)\left(\frac{n^2}{n_e n_p}\right)\frac{\rho_*}{t_* \Lambda(T)}\right]^{1/2} kT, \tag{4.4}$$

where n_p is the proton density, ρ_* is the stellar mass density, t_*^{-1} is the specific stellar mass-loss rate, and $\Lambda(T)$ is the radiative cooling function. For the velocity dispersion and temperature corresponding to the critical entropy profile slope ($\sigma_v \approx 240$ km s^{-1}, $kT \approx 0.75$ keV, $\alpha_K \approx 2/3$), the critical profiles are as follows (Equations 12 and 13 in Voit et al. (2020)):

$$P_{\rm eq}(r) \approx (1.4 \times 10^{-10} \text{erg cm}^{-3})\ \sigma_{240}^3 r_{\rm kpc}^{-1} \tag{4.5}$$

$$n_{e,\rm eq} \approx (0.06\ \text{cm}^{-3})\ \sigma_{240} r_{\rm kpc}^{-1}, \tag{4.6}$$

where $r_{\rm kpc} \equiv r/1$ kpc, $\sigma_{240} \equiv \sigma_v/240$ km s^{-1}, $\rho_* = \sigma_v/2\pi G r^2$, the isothermal stellar mass distribution, and the fiducial values $\mu m_p \epsilon_* \approx 2$ keV and $t_* \approx 200$ Gyr, if the weak dependence of $\Lambda(T)$ on σ_v is ignored.

Figures 4.7 and 4.8 show the comparison of the extended multiphase (E) and single-phase (N) galaxies in our sample to the equilibrium pressure and density profiles. The galaxies with multiphase gas confined to the central 2 kpc have been removed for clarity. The model predicts that the equilibrium profiles should divide the profiles of galaxies with extended multiphase gas ($\alpha_K \lesssim 2/3$) from the galaxies with no extended multiphase gas (generally higher $\alpha_K \gtrsim 2/3$). We find that overall, the equilibrium profiles for both $P_{\rm eq}$ and $n_{e,\rm eq}$ do indeed divide our sample as predicted. However, there are a two notable exceptions; one each from the multiphase and single-phase galaxies. The multiphase galaxy, NGC 1316, does conform to the analytic model within uncertainty, but the entropy profile exhibits an inversion at $r \sim 2.5$ kpc, an entropy profile characteristic of massive elliptical galaxies with $\sigma_v \lesssim 240$ km s^{-1} predicted by Voit et al. (2020). NGC 1316 is also one of the lowest luminosity galaxies in the sample. The single-phase galaxy, NGC 4073, has one of the highest luminosities and one of the highest temperatures in the sample. It is classified as a single-phase galaxy but has $\alpha_K \approx 0.6$ and $\sigma_v \approx 268$ km s^{-1} and does not conform to the analytic model within uncertainty.

4.5 Conclusions

In this work, we were able to show that not only is there evidence for a relationship between the stellar velocity dispersion, σ_v, and the entropy profile slope, α_K, the relationship agrees with the analytic model proposed in Voit et al. (2020). In contrast to previous analyses of this relation, we applied limits to data quality of the archival observations as well as limits on the parameters explored as informed by the data and the analytic model. While the results from the sample limited by both K_0 and σ_v are a more promising comparison to the analytic model, we still see evidence for a relationship between α_K and σ_v for the samples with fewer limits applied. Furthermore, results from the numerical integration of the analytic model suggest that the data may agree with the model for higher σ_v as well. For galaxies in groups with much lower entropy profile slopes than predicted for their velocity dispersion, Voit et al. (2020) proposes that the entropy profile may have a slope of $\alpha_K = 2/3$ that is more representative of a cool-core cluster with extended multiphase gas or galaxies with 200 km s^{-1} < σ_v < 240 km s^{-1}.

When we set out to characterize the sample by central entropy K_0, we found that there were two populations of galaxies that we could separate by applying a limit of $K_0 < 3$ keV cm^2. Those galaxies with $K_0 > 3$ keV cm^2 that were removed from the sample are likely galaxies that have experienced recent feedback, elevating their entropy out to larger radii. When we explored the min($t_{\rm cool}/t_{\rm ff}$), multiphase gas extent, and entropy profiles slopes of those galaxies as well, we found that galaxies with no extended multiphase gas and lower entropy profile slopes than expected also typically had higher min($t_{\rm cool}/t_{\rm ff}$), providing further evidence for recent feedback causing lower α_K. However, we also note that the galaxies with multiphase gas present but inside 2 kpc remain spread across the range of α_K, though more with lower α_K were removed than with higher α_K, indicating that some entropy profiles may be flattened due to feedback, but the effect is less clear. The analytic model requires the galaxies to be in equilibrium, so it is not surprising that galaxies out of equilibrium do not follow it, but model does agree with galaxies close to equilibrium.

Our work shows that while the Voit et al. (2020) analytic model may be relatively simple, it describes the relationship between key galaxy parameters well and can be used to further our understanding of how feedback in massive galaxies works. The comparison of the model to the data supports the notion that SNIa supernova feedback plays an important role in the thermal evolution of massive galaxies. Furthermore, the relationship between entropy profile slope and velocity dispersion is highly dependent on the external gas pressure at larger radii. Current X-ray observations are not able to resolve pressure measurements at large radii, but *Athena* and *LYNX* may be able to. Taking the model predictions and existing observations, one could predict what the gas pressure at large radii and then test that prediction with the next generation of X-ray telescopes.

CHAPTER 5

SUMMARY

5.1 Summary

This thesis sought to add to our understanding of the thermal properties of galaxy clusters and early-type galaxies. Chapter 2 introduced the ACCEPT 2.0 database, presented my analysis of the entropy profiles for clusters with deprojected radial temperature and density profiles, and provided an example of the science applications of the ACCEPT 2.0 data products including central entropy and morphology measurements. I showed that ACCEPT 2.0 provides robust, uniformly reduced, deprojected entropy profiles and central entropy classifications as well as morphology measurements with great potential for scientific impact. The central entropy measurements I obtained show that ACCEPT 2.0 reproduces the distribution of central entropy, K_0 from ACCEPT and that distribution holds when all of the new clusters with central entropy measurements in ACCEPT 2.0 are introduced. Finally, ACCEPT 2.0 reproduces some of the early morphology work from Cassano et al. (2010) and provides meaningful insights about sample selection for the *XMM* Heritage sample.

In Chapter 3, I explored the properties of early-type galaxies with powerful radio sources. I found that there are other galaxies, like NGC 4261, with powerful radio sources and single power law entropy profiles, namely IC 4296 and potentially NGC 315. Furthermore, if the ratio of the cooling time to the free-fall time is lowest in the central radial bin, it may indicate the presence of a powerful radio source. Finally, when I compared the radial entropy profiles for NGC 4261 and IC 4296, along with the radial entropy profiles from Lakhchaura et al. (2018), to the simulations of Wang et al. (2019), I found good agreement in the general entropy profile slope behavior between observations and simulations for both single phase and multiphase galaxies.

In Chapter 4, I presented an observational test of the black-hole feedback valve model for galactic atmospheres from Voit et al. (2020) using the sample of early-type galaxies from Lakhchaura et al.

(2018). I found that equilibrium pressure and density profiles support the model prediction that galaxies above and below the critical values, $\alpha \sim 2/3$ and $\sigma_v \sim 240$ km s^{-1} behave differently. I also found that, when we select a sub-sample of galaxies from the original sample that the analytic model would be expected to apply to, based on velocity dispersion and central entropy measurements, there is a correlation between the entropy profile slope and velocity dispersion. The slope of the relation between velocity dispersion and entropy profile slope for this sub-sample is at the 3σ level and matches the analytic prediction well. When we broaden our analysis to include all galaxies in the sample with sufficient data resolution to obtain an entropy profile slope, including those that may not be expected to follow the analytic model, we still find some evidence for correlation, although at closer to 2σ significance.

5.2 Future Work

There are many possible avenues to explore from the work completed in this thesis, both in the realm of galaxies and galaxy clusters. With the release of ACCEPT 2.0 data products, it w be the largest uniformly reduced, publicly available database of cluster properties and thus can be used to gain insight into the systematics of other X-ray samples. As shown in Chapter 3, X-ray systematics are significant enough to affect conclusions made from data, so the uniform reduction of ACCEPT 2.0 is helpful for exploring the characteristics of large samples of galaxy clusters.

With respect to early-type galaxies, we have obtained additional X-ray data for IC 4296 from both *Chandra* and *XMM* that will hopefully allow us to better probe the inner ~ kpc of the galaxy. In the more distant future, improved spatial resolution from an X-ray observatory like *LYNX* would allow us to examine the central kpc of the galaxies in our sample that would require prohibitively long observations to achieve the resolution of NGC 4261 with current telescopes. Looking ahead to *Athena* or *LYNX*, we could make predictions about the external gas pressure in early-type galaxies, based on the black-hole feedback valve model for galactic atmospheres, that could be tested with more sensitive X-ray telescopes.

APPENDIX

APPENDIX

APPENDIX A

ACCEPT 2.0 PIPELINE DESCIPTION

A.1 ACCEPT 2.0 Pipeline Details

A.1.1 Sample Selection and Data Processing and Analysis

This Appendix is provided to document choices made within the ACCEPT 2.0 pipeline. This text is heavily drawing on the text that the author team of the ACCEPT 2.0 data release paper, in draft, will be publishing in an Astrophysical Journal Supplement Series.

The ACCEPT 2.0 cluster sample was selected from all Chandra archival observations available as of July 2014. The automated pipeline (integrated with visual inspection of the products, when necessary) was developed to select the sample and perform the data processing and analysis. Using CIAO v4.7, CALDB 4.5, and SHERPA they ran an automated quick spectral analysis of all clusters available in the archive in order to have a rough estimate of the temperature of each cluster. The temperature estimate was used to set a count threshold to decide whether to include a cluster in the sample. To establish a 20% error threshhold on the cluster temperature measurement from at least three spatial bins, they determined from simulations that the minimum number of counts required in the 0.5–7 keV band is given by $n_{min,res} = 1377 \cdot kT - 537$, where kT is the cluster temperature in keV. For a 20% error on the temperature in a single spatial bin, the number of counts required in the 0.5–7 keV band is given by $n_{min,glb} = (1377 \cdot kT - 537)/3$. They set $n_{min,glb}$ and $n_{min,res}$ as the minimum counts necessary to include a cluster in our total sample and in the spatially resolved sample, respectively. The total ACCEPT 2.0 sample consists of 606 clusters of which 402 are suitable for a spatially resolved analysis in at least three spatial bins. Of the clusters with spatially resolved analysis, 348 had sufficient counts for deprojection. Chandra data reprocessing was performed in an automated fashion using CIAO task *chandra_repro*, which applies the appropriate ACIS gain maps, the time-dependent ACIS gain correction, and the ACIS charge transfer inefficiency correction. The background light curve during each observation was used to detect and remove periods of anomalously high background following the recommendations of Markevitch et al. (2003). The automated procedure to remove background flares was followed by a manual visual inspection of the light curves to check for undetected flares or excessive flare cleaning.

A.1.1.1 Initial Pipeline Spatial Analysis

Once clean event files for each ObsID of a cluster are obtained, they used the CIAO tool *merge_obs* to produce fluxed images and exposure maps for each ObsID and for the sum of all ObsIDs. Images and exposure maps are created with a binning factor of 2, corresponding to a pixel size in the image of 0.984 arcsec. At this stage, point sources are detected in the merged image using CIAO tool *wavdetect* in order to create a list of point sources that will be excluded from the spatial and spectral analysis of the cluster and to create an image of the diffuse emission using CIAO tool *dmfilth*. The point source list is also visually inspected using *DS9* in order to prevent false detections or excess exclusion of undetected point sources.

As a default, the X-ray emission peak was used as the center of the radial profiles, however the pipeline allowed manual inspection of the validity of this choice and to use the X-ray emission centroid if necessary. They initially considered concentric annuli with a thickness of 5 arcsec. If the cluster had at least 1500 counts in the 0.5-7 keV band, they grouped the annuli in the radial profile to have at least 300 counts per spatial bin prior to background subtraction. If the cluster had less than 1500 total counts, the minimum number of counts required for each spatial bin was lowered to one-fifth of the total counts in the cluster. The radial profiles extend out until the number of source counts in a given annulus reach 30% of the background counts in that annulus (or when an annulus reaches the chip boundary, in very bright and extended clusters).

The pipeline then performs a fit of the image from a 2-D Lorentz model with a varying power law (also known as a 2-D β model) using *Sherpa*. The function fitted to the image is:

$$f(x,y) = f(r) = A(1 + [r/r_0]^2)^{-\alpha} \tag{A.1}$$

where $r(x,y) = \sqrt{[x_{new}^2(1-\epsilon)^2 + y_{new}^2]/(1-\epsilon)}$, $x_{new} = (x - x_o)cos(\theta) + (y - y_o)sin(\theta)$, and $y_{new} = (y - y_o)cos(\theta) - (x - x_o)sin(\theta)$. The most important parameters of this model are the core radius r_0, the power-law index α, the ellipticity ϵ, and the angle of ellipticity θ. The last two parameters are used for a morphological analysis of the clusters in relation with other cluster properties (see Section 2.2.2.1). This spatial analysis procedure was repeated for every single cluster in the sample.

A.1.1.2 Global Spectral Extraction and Analysis

To analyze the global properties of each cluster, the pipeline performs a spectral extraction in three different spatial regions: the whole cluster ($r < r_{cluster}$), the cluster core ($r < r_{core}$), and the cluster with the core excised ($r_{core} < r < r_{cluster}$). They used the CIAO tool *specextract* to generate the spectra, appropriate redistribution matrix files (RMFs), and ancillary response files (ARFs). The maximum cluster extension $r_{cluster}$ has been set to 500 h^{-1} kpc. If the maximum radius cannot fit in the S2 chip, the cluster was observed only with ACIS-S, or was observed in all four chips of ACIS-I, if at least one of the observations was performed with ACIS-I, the largest radius that can fit in the ACIS field of view is used. The core radius was set by default to 70 h^{-1} kpc, but if this radius is larger than $0.3r_{cluster}$, the core radius is set to $r_{core} = 0.3r_{cluster}$. Detected point sources are excised from the spectra of the diffuse emission from the cluster. At this stage background spectra and radial profiles are also built.

A.1.1.2.1 Background Subtraction

The pipeline used the blank-field observations, processed identically to the cluster observations, and reprojected onto the sky using the aspect information from the cluster pointings. The synthetic backgrounds correspond to far longer exposure times ($\sim$ 0.5 Msec) than the majority of the cluster observations, giving a good estimate of the background. For clusters observed on ACIS-I, the blank-field background correction is renormalized to the background of the observation, using the ACIS-S2 chip, in a region of the ACIS field of view practically free from cluster emission. For clusters observed with ACIS-S, the chip used for the renormalization is ACIS-S1. The energy band from 9.5 to 12 keV (mostly dominated by charged particles) is used to perform the normalization. Using the renormalized and reprojected background event files, the pipeline produces radial profiles of background counts and surface brightness for use in the analysis of the cluster surface brightness profiles.

A.1.1.2.2 Spectral Analysis

The spectra of the whole cluster, the cluster core, and the cluster with the core excised were analyzed in an automatic fashion by the pipeline using the Python tools within *Sherpa*. The spectra were analyzed in the 0.5-8 keV spectral band, and the source and background are fitted simultaneously. The source model used is a *mekal* model Kaastra et al. 1996; Liedahl et al. 1995 in which the ratio between the elements is fixed to the solar value as in Anders & Grevesse (1989). They considered line of sight absorption fixed at the Galactic value n_H (Stark et al., 1992), and an additional internal absorption component left free to vary (consistent with zero in the large majority of clusters). The free parameters in the *mekal* model are temperature, kT, metal abundance, Z, and normalization, η. The redshift, z, was fixed at the literature value for the cluster. The background model used was composed of two power-law models, several gaussian emission lines, and an *apec* thermal model at low temperature ($kT = 0.17$ keV, to account for the soft, diffuse X-ray background). The power-law slopes and the quantity, position, and strength of the emission lines depends on the specific ACIS chip used and are adjusted accordingly. The shape of the spectrum is held fixed.

A.1.1.3 Spatially Resolved Spectral Extraction and Analysis

For clusters with a sufficient number of counts and at least three spatial bins, a spatially-resolved spectral analysis was performed. The cluster was divided into concentric annuli that are required to contain at least $n_{min,res}/3$ counts per annulus for the projected spectral analysis and $n_{min,res}$ counts per annulus for the deprojected spectral analysis. In both analyses, the annuli have a minimum thickness of 5 arcsec and extend out until the source counts reach 50% of the background counts.

CIAO tool *specextract* was then used to generate the spectra of each annular region and their relative RMFs and ARFs.

The projected spectral analysis fits each annular region spectrum independently from the others. The X-ray band considered is 0.5-8 keV. Similarly to the global spectral analysis, source and background spectra are fitted simultaneously using the same models described in Section A.1.1.2.2. If at least three spatial annuli exist, the pipeline uses the `deproject` module in *Sherpa* to extract the deprojected temperature and density profiles (see Section 1.3.3 for a discussion of deprojection).

APPENDIX B

ACCEPT 2.0 CENTRAL ENTROPY FITTING RESULTS

Table B.1: Best fit K_0, K_{100}, and α for ACCEPT 2.0 clusters. Column 1: Cluster Name; Column 2-4: Best fit K_0 and associated 1σ errors; Column 5-7: Best fit K_{100} and associated 1σ errors; Column 2-4: Best fit α and associated 1σ errors.

Cluster Name	K_0	$\sigma_{K_0}-$	$\sigma_{K_0}+$	K_{100}	$\sigma_{K_{100}}-$	$\sigma_{K_{100}}+$	α	$\sigma_\alpha-$	$\sigma_\alpha+$
		(keV cm^2)			(keV cm^2)				
Ophiuchus_CLUSTER	-22.281	1.747	1.747	259.384	2.600	2.600	0.513	0.013	0.013
ABELL_0141	158.783	28.161	28.161	61.340	34.694	34.694	1.396	0.285	0.285
ABELL_3017	36.916	7.731	7.731	109.848	14.716	14.716	1.258	0.086	0.086
RBS_0653	27.862	4.749	4.749	164.154	10.315	10.315	0.941	0.043	0.043
ABELL_0401	154.597	14.171	14.171	115.707	17.379	17.379	0.940	0.098	0.098
ABELL_2146	85.695	4.204	4.204	66.396	6.028	6.028	1.891	0.078	0.078
ABELL_S0579	129.966	24.011	24.011	68.501	26.967	26.967	1.134	0.185	0.185
NGC_5044	1.305	0.143	0.143	47.729	1.766	1.766	0.722	0.022	0.022
WHL_J102339.9+490838	128.079	20.582	20.582	65.204	22.416	22.416	1.253	0.177	0.177
ABELL_0980	150.124	21.661	21.661	62.493	23.780	23.780	1.465	0.227	0.227
ABELL_3581	8.670	0.667	0.667	183.191	51.951	51.951	1.380	0.150	0.150
ClG_2153.8+3746	55.189	6.284	6.284	325.021	34.317	34.317	1.708	0.178	0.178
ABELL_3128	12.128	60.726	60.726	200.471	72.740	72.740	0.341	0.215	0.215
MACS_J0308.9+2645	144.011	31.449	31.449	106.556	32.825	32.825	1.111	0.141	0.141
MCXC_J2014.8-2430	5.104	0.800	0.800	116.626	3.757	3.757	1.208	0.035	0.035
NGC_5171	41.304	17.842	17.842	103.650	84.833	84.833	0.987	0.735	0.735
ABELL_2443	164.262	42.641	42.641	113.150	83.701	83.701	0.799	0.365	0.365
ABELL_1835	11.299	1.211	1.211	105.985	4.227	4.227	1.323	0.034	0.034
ABELL_2813	136.338	22.780	22.780	65.152	32.801	32.801	1.403	0.287	0.287
ABELL_1300	65.709	26.357	26.357	203.526	36.791	36.791	0.929	0.083	0.083
MCXC_J0547.0-3904	10.804	2.398	2.398	124.928	8.182	8.182	1.179	0.072	0.072
ABELL_3880	0.853	0.950	0.950	139.151	4.029	4.029	0.890	0.032	0.032

Cluster Name	K_0	σ_{K_0-}	σ_{K_0+}	K_{100}	$\sigma_{K_{100}-}$	$\sigma_{K_{100}+}$	α	$\sigma_{\alpha-}$	$\sigma_{\alpha+}$
		(keV cm^2)			(keV cm^2)				
ABELL_0586	116.110	10.286	10.286	67.379	10.676	10.676	1.443	0.092	0.092
NGC_3402_GROUP	1.666	0.119	0.119	93.942	2.839	2.839	0.955	0.020	0.020
ABELL_S0780	20.933	1.311	1.311	114.084	10.975	10.975	1.817	0.128	0.128
MCXC_J1524.2-3154	5.444	0.428	0.428	104.851	2.303	2.303	1.195	0.022	0.022
ABELL_0562	122.537	34.177	34.177	82.469	77.220	77.220	0.761	0.498	0.498
ABELL_2256	111.092	33.408	33.408	159.118	57.048	57.048	0.764	0.272	0.272
SDSS-C4_3072	19.703	1.477	1.477	104.101	4.069	4.069	1.308	0.030	0.030
SDSS_CE_J198.070190+00.996231	26.415	75.970	75.970	144.383	81.807	81.807	0.393	0.231	0.231
G139.59+24.18	32.801	8.952	8.952	150.993	18.544	18.544	1.244	0.247	0.247
NGC_3551	-21.019	22.510	22.510	218.204	37.104	37.104	0.491	0.317	0.317
MCXC_J0303.7-7752	187.074	34.239	34.239	85.939	47.786	47.786	1.420	0.316	0.316
NSCS_J144726+082824	11.220	1.701	1.701	195.746	8.898	8.898	1.556	0.061	0.061
ABELL_2415	2.830	0.781	0.781	142.155	6.585	6.585	1.027	0.046	0.046
Hercules_A	0.604	2.871	2.871	211.799	20.461	20.461	1.072	0.127	0.127
ABELL_1775	56.894	3.877	3.877	256.554	19.789	19.789	1.860	0.099	0.099
ABELL_2219	258.490	19.763	19.763	49.427	17.930	17.930	1.458	0.189	0.189
ABELL_0550	120.247	24.385	24.385	102.004	32.615	32.615	1.014	0.181	0.181
MCXC_J2311.5+0338	85.303	14.556	14.556	121.671	17.017	17.017	1.189	0.071	0.071
Fornax_Cluster	0.346	0.066	0.066	274.257	7.900	7.900	0.918	0.011	0.011
CIZA_J0616.3-2156	234.527	60.544	60.544	117.417	92.762	92.762	0.854	0.290	0.290
CIZA_J1804.4+1002	26.268	48.513	48.513	220.224	70.702	70.702	0.494	0.134	0.134
MCXC_J1215.4-3900	275.446	63.700	63.700	71.648	105.128	105.128	1.131	0.466	0.466
PLCKESZ_G286.58-31.25	149.127	62.571	62.571	146.327	86.892	86.892	0.782	0.226	0.226
MCXC_J2218.6-3853	132.838	15.498	15.498	47.640	17.748	17.748	1.423	0.219	0.219
ABELL_1576	103.880	22.109	22.109	127.184	31.722	31.722	1.026	0.135	0.135
ABELL_2550	-0.845	2.976	2.976	114.201	5.202	5.202	0.714	0.060	0.060
MACS_J1311.0-0311	32.423	3.781	3.781	83.827	8.127	8.127	1.357	0.085	0.085
MACS_J1720.2+3536	12.312	2.523	2.523	131.324	7.489	7.489	1.122	0.048	0.048
Hydra_A	15.711	0.627	0.627	142.639	19.031	19.031	1.462	0.111	0.111
MCXC_J0439.0+0520	6.155	1.597	1.597	118.345	5.101	5.101	1.067	0.044	0.044

Cluster Name	K_0	$\sigma_{K_0}-$	$\sigma_{K_0}+$	K_{100}	$\sigma_{K_{100}}-$	$\sigma_{K_{100}}+$	α	$\sigma_{\alpha}-$	$\sigma_{\alpha}+$
		(keV cm^2)			(keV cm^2)				
ABELL_2457	24.049	17.816	17.816	181.200	33.329	33.329	0.700	0.120	0.120
2MFGC_06756	12.469	1.187	1.187	95.625	3.373	3.373	1.177	0.034	0.034
HCG_037	2.267	1.280	1.280	503.351	339.928	339.928	1.180	0.198	0.198
ABELL_0970	102.112	18.122	18.122	122.251	26.244	26.244	1.014	0.145	0.145
ZwCl_1006.1+1201	122.660	18.258	18.258	86.035	23.767	23.767	1.187	0.175	0.175
SPT-CLJ2043-5035	15.848	3.138	3.138	82.653	8.551	8.551	1.242	0.089	0.089
ABELL_3921	75.119	14.847	14.847	162.521	20.746	20.746	0.787	0.073	0.073
ABELL_3571	59.964	13.817	13.817	210.881	14.705	14.705	0.699	0.151	0.151
MESSIER_089	1.274	0.032	0.032	928.754	52.840	52.840	1.230	0.016	0.016
NSCS_J122648+215157	57.719	16.388	16.388	120.674	26.521	26.521	0.911	0.164	0.164
MCXC_J2003.5-2323	217.888	91.725	91.725	134.248	149.277	149.277	0.877	0.468	0.468
ABELL_0611	63.673	8.437	8.437	112.999	14.631	14.631	1.241	0.111	0.111
ABELL_2125	171.248	17.883	17.883	25.368	19.667	19.667	1.588	0.272	0.272
NSCS_J135021+094042	-6.289	1.541	1.541	172.190	5.844	5.844	0.831	0.040	0.040
MCXC_J1022.0+3830	38.803	9.494	9.494	177.395	16.646	16.646	1.018	0.255	0.255
ABELL_1190	213.612	19.437	19.437	25.935	18.426	18.426	1.686	0.227	0.227
3C_444	0.958	1.150	1.150	151.868	3.525	3.525	1.019	0.039	0.039
ABELL_3399	59.435	16.441	16.441	164.359	25.195	25.195	0.867	0.078	0.078
ABELL_1914	84.494	15.900	15.900	139.103	22.462	22.462	0.853	0.081	0.081
WHL_J114224.8+583205	459.851	44.958	44.958	14.713	25.032	25.032	1.732	0.197	0.197
ABELL_3444	20.762	1.805	1.805	94.190	4.675	4.675	1.340	0.045	0.045
ABELL_S1101	11.526	0.499	0.499	77.480	1.226	1.226	1.127	0.018	0.018
PLCKESZ_G167.65+17.64	209.979	18.217	18.217	21.819	7.294	7.294	1.886	0.086	0.086
ABELL_0370	256.699	27.693	27.693	42.280	25.614	25.614	1.614	0.236	0.236
ABELL_2009	18.811	2.582	2.582	133.365	7.018	7.018	1.105	0.044	0.044
ABELL_2104	159.142	31.845	31.845	127.169	43.602	43.602	0.820	0.178	0.178
ABELL_3562	70.592	12.786	12.786	144.224	18.709	18.709	0.942	0.101	0.101
ABELL_2294	58.446	48.431	48.431	216.653	77.184	77.184	0.724	0.174	0.174
ZwCl_0949.6+5207	4.895	8.399	8.399	129.424	12.195	12.195	1.070	0.097	0.097
ABELL_0963	39.105	8.506	8.506	149.621	13.215	13.215	0.826	0.057	0.057

Cluster Name	K_0	σ_{K_0-}	σ_{K_0+}	K_{100}	$\sigma_{K_{100}-}$	$\sigma_{K_{100}+}$	α	$\sigma_{\alpha-}$	$\sigma_{\alpha+}$
		(keV cm^2)			(keV cm^2)				
WHL_J131505.2+514902	159.895	30.277	30.277	100.569	32.233	32.233	1.161	0.150	0.150
ARP_318	5.359	0.210	0.210	157.740	311.625	311.625	1.810	0.141	0.141
ABELL_3364	205.019	17.037	17.037	42.820	17.143	17.143	1.635	0.206	0.206
3C_089	30.855	5.532	5.532	214.297	11.182	11.182	1.347	0.077	0.077
MACS_J1829.0+6913	36.357	4.091	4.091	99.984	8.250	8.250	1.328	0.094	0.094
ABELL_3653	174.821	44.382	44.382	172.274	103.031	103.031	1.184	0.517	0.517
Abell_222	148.849	21.545	21.545	48.218	37.967	37.967	1.362	0.395	0.395
ABELL_0598	8.320	2.293	2.293	144.903	7.307	7.307	1.134	0.082	0.082
ABELL_0576	63.842	7.638	7.638	204.151	14.401	14.401	1.295	0.200	0.200
ABELL_2345	286.760	114.145	114.145	143.127	175.850	175.850	0.694	0.381	0.381
ABELL_1553	180.396	25.875	25.875	57.808	22.365	22.365	1.443	0.192	0.192
SDSS-C4_3062	46.651	12.194	12.194	160.145	27.816	27.816	1.264	0.264	0.264
UGCl_120	-2.576	2.074	2.074	238.187	25.844	25.844	0.979	0.094	0.094
2MASSi_J0913454+405628	23.534	2.754	2.754	96.232	5.776	5.776	1.162	0.046	0.046
Centaurus_Cluster	0.873	0.026	0.026	324.906	3.843	3.843	1.198	0.005	0.005
WARP_J1415.1+3612	-10.568	40.951	40.951	162.648	57.392	57.392	0.456	0.217	0.217
MCXC_J0532.9-3701	98.106	24.012	24.012	128.772	35.406	35.406	1.020	0.151	0.151
ABELL_0548A	23.658	10.142	10.142	170.653	20.112	20.112	0.920	0.173	0.173
IC_1880_GROUP	4.003	1.229	1.229	342.980	75.624	75.624	1.588	0.154	0.154
ABELL_1423	36.915	6.299	6.299	359.425	31.006	31.006	1.209	0.143	0.143
ABELL_0578	16.576	48.228	48.228	216.253	74.410	74.410	0.644	0.369	0.369
ABELL_0402	115.241	24.785	24.785	87.153	30.745	30.745	1.202	0.192	0.192
ABELL_3809	10.277	3.844	3.844	132.956	8.319	8.319	0.867	0.059	0.059
MACS_J1621.3+3810	-2.413	5.626	5.626	168.760	12.893	12.893	0.917	0.058	0.058
IC_1365	160.833	19.732	19.732	71.379	38.386	38.386	1.338	0.371	0.371
MACS_J2229.8-2756	7.679	1.376	1.376	93.191	5.100	5.100	1.285	0.054	0.054
ABELL_0098N	10.598	5.928	5.928	179.603	13.006	13.006	0.982	0.097	0.097
SSGC_081	44.512	20.290	20.290	165.343	31.988	31.988	0.614	0.122	0.122
FBQS_J074417.4+375317	-18.950	10.380	10.380	163.806	19.684	19.684	0.802	0.094	0.094
ABELL_1668	6.156	1.317	1.317	167.323	7.882	7.882	1.033	0.053	0.053

Cluster Name	K_0	$\sigma_{K_0}-$	$\sigma_{K_0}+$	K_{100}	$\sigma_{K_{100}}-$	$\sigma_{K_{100}}+$	α	$\sigma_{\alpha}-$	$\sigma_{\alpha}+$
		(keV cm^2)			(keV cm^2)				
PLCKESZ_G337.09-25.97	78.316	8.850	8.850	64.347	13.718	13.718	1.663	0.191	0.191
MCXC_J1852.1+5711	9.598	7.763	7.763	168.070	13.197	13.197	0.843	0.097	0.097
NGC4936-offset2	-0.354	3.076	3.076	102.788	11.701	11.701	0.593	0.131	0.131
ABELL_S0295	165.939	21.589	21.589	36.248	26.526	26.526	1.560	0.279	0.279
MCXC_J1558.3-1410	28.469	1.712	1.712	115.116	4.612	4.612	1.496	0.102	0.102
NGC_4636	0.801	0.091	0.091	228.937	13.528	13.528	1.025	0.022	0.022
GALEX_J094712.4+762313	25.087	1.568	1.568	75.232	4.847	4.847	1.915	0.059	0.059
ABELL_2485	74.814	26.486	26.486	123.032	41.709	41.709	0.956	0.190	0.190
ABELL_1204	14.727	1.691	1.691	82.196	4.882	4.882	1.440	0.138	0.138
MACS_J0744.9+3927	53.443	7.508	7.508	86.734	11.754	11.754	1.151	0.086	0.086
ABELL_3094	31.063	66.818	66.818	225.536	83.173	83.173	0.399	0.169	0.169
PLCKESZ_G264.41+19.48	94.347	40.037	40.037	176.575	56.786	56.786	0.783	0.139	0.139
MACS_J1206.2-0847	54.200	11.443	11.443	134.851	20.755	20.755	1.105	0.102	0.102
NGC_4782-3	3.197	0.756	0.756	309.122	63.049	63.049	1.246	0.100	0.100
MCXC_J0437.1+0043	39.939	4.172	4.172	88.447	8.153	8.153	1.301	0.079	0.079
ABELL_0383	10.280	1.047	1.047	117.585	3.732	3.732	1.253	0.041	0.041
ABELL_2069	297.687	41.573	41.573	84.813	46.812	46.812	0.963	0.212	0.212
MCXC_J0338.6+0958	5.111	0.100	0.100	106.901	0.925	0.925	1.395	0.011	0.011
MCXC_J1234.2+0947	194.608	65.368	65.368	87.959	115.821	115.821	0.842	0.419	0.419
UGC_02748	5.953	1.207	1.207	329.791	103.667	103.667	1.659	0.212	0.212
NGC_4325_GROUP	3.284	0.201	0.201	110.659	3.216	3.216	1.289	0.026	0.026
ABELL_2384	25.359	2.675	2.675	139.689	6.597	6.597	1.271	0.056	0.056
MCXC_J0425.8-0833	6.656	1.320	1.320	122.571	3.695	3.695	0.924	0.042	0.042
MCXC_J2211.7-0349	96.790	15.187	15.187	105.826	19.206	19.206	1.343	0.111	0.111
ABELL_0013	130.014	31.300	31.300	156.989	51.950	51.950	0.783	0.219	0.219
MACS_J1427.6-2521	9.474	4.811	4.811	133.733	10.335	10.335	0.922	0.066	0.066
ABELL_1795	15.172	0.779	0.779	118.037	1.460	1.460	1.080	0.018	0.018
CGCG_514-050	0.932	2.217	2.217	547.804	279.588	279.588	0.931	0.163	0.163
NGC_0741_GROUP	1.343	0.211	0.211	595.269	91.607	91.607	1.369	0.065	0.065
Stephans_Quintet	3.065	2.147	2.147	56.500	12.812	12.812	0.728	0.205	0.205

Cluster Name	K_0	σ_{K_0-}	σ_{K_0+}	K_{100}	$\sigma_{K_{100}-}$	$\sigma_{K_{100}+}$	α	$\sigma_{\alpha-}$	$\sigma_{\alpha+}$
		(keV cm^2)			(keV cm^2)				
WHL_J093820.9+520243	92.459	18.089	18.089	60.018	40.973	40.973	1.255	0.546	0.546
ABELL_3528B	15.261	2.683	2.683	218.802	8.800	8.800	1.157	0.061	0.061
ZwCl_0040.8+2404	9.048	1.165	1.165	113.822	3.727	3.727	1.136	0.044	0.044
ABELL_2187	91.556	19.021	19.021	108.736	26.700	26.700	1.194	0.163	0.163
ABELL_3695	307.183	36.618	36.618	41.785	35.309	35.309	1.562	0.278	0.278
MACS_J1931.8-2635	20.746	1.385	1.385	83.339	3.832	3.832	1.474	0.049	0.049
ABELL_0267	148.399	16.487	16.487	54.930	15.020	15.020	1.745	0.148	0.148
MCXC_J0528.2-2942	88.463	18.810	18.810	91.877	37.031	37.031	1.361	0.366	0.366
MCXC_J1750.2+3504	-1.787	2.580	2.580	163.642	7.589	7.589	0.886	0.042	0.042
SPT-CL_J0615-5746	77.522	10.404	10.404	77.435	14.033	14.033	1.314	0.111	0.111
_HB89__1821+643	-27.371	7.264	7.264	182.036	12.223	12.223	0.976	0.051	0.051
MCXC_J0439.0+0715	57.207	11.956	11.956	116.269	17.768	17.768	0.946	0.095	0.095
Cl_0016+16	165.464	19.834	19.834	56.168	16.004	16.004	1.319	0.126	0.126
ABELL_1644	21.222	1.461	1.461	616.093	78.787	78.787	1.815	0.107	0.107
NGC_0777	4.297	0.287	0.287	552.908	227.639	227.639	1.838	0.117	0.117
ABELL_2355	393.293	86.869	86.869	75.518	152.817	152.817	1.183	0.529	0.529
WHL_J135949.5+623047	21.238	6.093	6.093	181.636	13.843	13.843	1.179	0.131	0.131
NGC_2563_GROUP	1.362	0.679	0.679	930.543	51.355	51.355	1.318	0.037	0.037
ABELL_3739	81.936	38.149	38.149	150.954	60.833	60.833	0.824	0.202	0.202
ABELL_2151	6.426	3.102	3.102	150.802	5.699	5.699	0.791	0.056	0.056
NGC_6868	0.698	0.554	0.554	564.773	228.792	228.792	1.219	0.119	0.119
NGC_5129	-0.457	0.659	0.659	212.419	33.879	33.879	0.923	0.075	0.075
ABELL_S0463	117.469	23.573	23.573	100.204	44.890	44.890	1.076	0.411	0.411
ABELL_0193	134.938	9.008	9.008	43.896	16.118	16.118	1.559	0.293	0.293
ABELL_2744	151.716	90.749	90.749	240.949	140.399	140.399	0.480	0.240	0.240
ABELL_3411	194.021	24.317	24.317	76.514	25.816	25.816	1.275	0.179	0.179
PLCKESZ_G304.84-41.42	-48.267	43.675	43.675	356.033	45.563	45.563	0.488	0.083	0.083
SDSS_+137.3+11.0+0.18	88.200	16.425	16.425	99.194	23.788	23.788	1.015	0.165	0.165
ABELL_2204	7.763	0.351	0.351	144.831	3.209	3.209	1.509	0.028	0.028
ABELL_2390	14.260	1.929	1.929	151.843	5.093	5.093	1.070	0.030	0.030

Cluster Name	K_0	$\sigma_{K_0}-$	$\sigma_{K_0}+$	K_{100}	$\sigma_{K_{100}}-$	$\sigma_{K_{100}}+$	α	$\sigma_\alpha-$	$\sigma_\alpha+$
		(keV cm^2)			(keV cm^2)				
ABELL_3126	158.222	13.322	13.322	50.469	14.489	14.489	1.725	0.167	0.167
NGC_4839	-26.397	15.220	15.220	856.067	103.825	103.825	0.777	0.114	0.114
AWM_4	24.474	5.366	5.366	108.464	6.625	6.625	0.655	0.094	0.094
ABELL_2107	10.155	3.138	3.138	327.958	32.782	32.782	0.923	0.086	0.086
ABELL_0644	70.240	6.441	6.441	114.365	8.615	8.615	1.049	0.047	0.047
ABELL_2537	78.806	12.795	12.795	110.222	21.599	21.599	1.101	0.182	0.182
ABELL_1831	77.354	12.848	12.848	100.593	19.688	19.688	1.165	0.154	0.154
ABELL_0209	86.644	24.724	24.724	165.614	30.617	30.617	0.812	0.083	0.083
ABELL_3322	104.613	17.637	17.637	77.060	21.058	21.058	1.196	0.147	0.147
MACS_J0417.5-1154	23.919	8.332	8.332	159.396	14.094	14.094	0.935	0.061	0.061
LCDCS_0829	3.460	2.299	2.299	177.098	6.231	6.231	1.074	0.036	0.036
MCXC_J0340.8-4542	189.419	55.692	55.692	68.974	132.705	132.705	0.633	0.750	0.750
ZwCl_1742.1+3306	12.335	1.209	1.209	120.830	4.566	4.566	1.256	0.064	0.064
ZwCl_0857.9+2107	18.933	2.344	2.344	81.093	5.949	5.949	1.716	0.129	0.129
ABELL_0478	11.580	0.910	0.910	216.321	33.585	33.585	1.549	0.130	0.130
ABELL_0496	4.569	0.330	0.330	146.262	1.605	1.605	0.984	0.014	0.014
MCXC_J1947.3-7623	17.503	8.752	8.752	179.217	16.098	16.098	0.824	0.059	0.059
UGC_05088_GROUP	3.275	3.277	3.277	104.321	8.406	8.406	0.788	0.142	0.142
MACS_J1359.2-1929	19.013	3.628	3.628	92.645	9.761	9.761	1.330	0.106	0.106
ESO3060170-A	2.005	1.515	1.515	441.229	108.030	108.030	1.170	0.126	0.126
SPT-CL_J2023-5535	186.127	83.939	83.939	142.241	160.670	160.670	0.758	0.646	0.646
ABELL_0795	27.927	3.477	3.477	115.745	6.809	6.809	1.085	0.059	0.059
WHL_J150407.5-024816	9.077	0.494	0.494	82.228	2.096	2.096	1.329	0.019	0.019
UGC_12491	6.963	0.491	0.491	206.196	23.395	23.395	1.541	0.084	0.084
ABELL_2445	69.915	11.294	11.294	87.841	15.912	15.912	0.992	0.117	0.117
NGC_6482	0.837	0.243	0.243	75.095	9.968	9.968	0.826	0.057	0.057
ABELL_0545	146.987	21.961	21.961	114.049	28.338	28.338	0.894	0.125	0.125
NSCS_J000619+105206	58.428	11.089	11.089	135.616	17.235	17.235	0.908	0.084	0.084
MACS_J1532.8+3021	13.365	0.901	0.901	82.169	2.761	2.761	1.339	0.030	0.030
SDSS-C4-DR3_3018	130.902	37.892	37.892	103.086	73.251	73.251	1.068	0.657	0.657

Cluster Name	K_0	σ_{K_0-}	σ_{K_0+}	K_{100}	$\sigma_{K_{100}-}$	$\sigma_{K_{100}+}$	α	$\sigma_{\alpha-}$	$\sigma_{\alpha+}$
		(keV cm^2)			(keV cm^2)				
ABELL_1689	61.841	4.922	4.922	126.295	7.801	7.801	1.156	0.048	0.048
MACS_J2140.2-2339	12.928	1.101	1.101	91.533	3.478	3.478	1.350	0.041	0.041
ABELL_2507	198.227	27.121	27.121	36.570	18.949	18.949	1.743	0.176	0.176
ABELL_1942_AND_CLUMP	67.023	74.345	74.345	229.305	101.357	101.357	0.466	0.200	0.200
Abell_223	101.808	21.115	21.115	120.946	31.330	31.330	1.023	0.160	0.160
ABELL_0773	179.097	21.364	21.364	64.053	17.288	17.288	1.388	0.130	0.130
NGC5419-offset1	0.834	0.936	0.936	795.366	128.597	128.597	1.053	0.064	0.064
ABELL_2734_NED01	25.692	17.051	17.051	153.977	24.192	24.192	0.578	0.078	0.078
WHL_J141623.8+444528	18.734	17.583	17.583	104.876	37.534	37.534	0.900	0.233	0.233
GMBCG_J029.95560-08.83299	-10.805	5.842	5.842	217.850	13.766	13.766	0.837	0.049	0.049
ABELL_3088	20.390	9.298	9.298	178.149	18.196	18.196	0.886	0.074	0.074
NGC_0766	1.208	0.676	0.676	294.920	298.944	298.944	1.338	0.299	0.299
ABELL_1758	166.511	49.643	49.643	189.649	105.927	105.927	1.036	0.431	0.431
ABELL_S1063	78.785	19.913	19.913	127.407	31.163	31.163	0.868	0.166	0.166
NGC_4104_GROUP	0.021	0.396	0.396	871.354	94.140	94.140	1.316	0.044	0.044
ABELL_2895	168.687	33.931	33.931	90.111	37.843	37.843	1.130	0.194	0.194
ABELL_3140	91.667	6.967	6.967	194.228	16.033	16.033	1.808	0.124	0.124
ABELL_3827	133.726	15.264	15.264	102.414	22.405	22.405	1.118	0.186	0.186
MACS_J0553.4-3342	106.577	46.574	46.574	220.930	82.059	82.059	0.694	0.179	0.179
ESO_351-_G_021	3.731	0.865	0.865	104.966	6.880	6.880	0.942	0.056	0.056
ABELL_2124	91.073	24.555	24.555	196.375	38.843	38.843	0.814	0.173	0.173
MACS_J2046.0-3430	6.476	2.108	2.108	103.510	6.179	6.179	1.145	0.061	0.061
IC_1633	2.846	0.783	0.783	845.517	95.777	95.777	1.219	0.057	0.057
ABELL_1201	63.600	8.173	8.173	176.604	19.440	19.440	1.575	0.259	0.259
NSCS_J145715+222009	12.779	1.247	1.247	80.992	3.027	3.027	1.135	0.027	0.027
HCG_097	-2.965	2.537	2.537	90.326	5.550	5.550	0.577	0.074	0.074
MACS_J0242.6-2132	9.402	1.573	1.573	85.748	5.660	5.660	1.302	0.059	0.059
ABELL_1736	139.631	39.368	39.368	75.724	80.890	80.890	0.691	0.463	0.463
MCXC_J2011.3-5725	39.441	8.622	8.622	64.575	15.583	15.583	1.194	0.206	0.206
ABELL_3532	150.770	20.305	20.305	83.651	29.757	29.757	1.251	0.249	0.249

Cluster Name	K_0	σ_{K_0-}	σ_{K_0+}	K_{100}	$\sigma_{K_{100}-}$	$\sigma_{K_{100}+}$	α	$\sigma_{\alpha-}$	$\sigma_{\alpha+}$
		(keV cm^2)			(keV cm^2)				
MCXC_J0220.9-3829	18.431	3.386	3.386	110.540	7.654	7.654	1.049	0.059	0.059
SDSS-C4-DR3_3144	3.097	0.714	0.714	393.635	61.006	61.006	1.448	0.104	0.104
ABELL_2667	19.098	2.169	2.169	93.037	5.623	5.623	1.241	0.054	0.054
ABELL_2717	29.928	6.217	6.217	123.474	9.684	9.684	0.933	0.114	0.114
MCXC_J0510.7-0801	122.172	51.636	51.636	150.700	79.443	79.443	0.574	0.180	0.180
ABELL_3292	108.116	10.191	10.191	35.724	10.662	10.662	1.694	0.168	0.168
A1882a	61.304	63.352	63.352	189.657	97.281	97.281	0.529	0.356	0.356
WBL_518	89.363	48.075	48.075	144.171	94.679	94.679	0.405	0.307	0.307
NGC_7618	-2.042	0.974	0.974	54.095	3.680	3.680	0.510	0.057	0.057
2MASX_J13312961+1107566	4.504	1.406	1.406	130.128	37.766	37.766	1.462	0.285	0.285
ABELL_2061	224.737	24.178	24.178	38.185	19.474	19.474	1.434	0.233	0.233
ABELL_3343	163.757	19.794	19.794	46.150	19.915	19.915	1.602	0.225	0.225
MaxBCG_J016.70077+01.05926	11.751	0.707	0.707	68.442	2.757	2.757	1.517	0.047	0.047
MCXC_J0035.4-2015	136.376	16.255	16.255	41.337	12.893	12.893	1.521	0.149	0.149
ABELL_2426	54.818	12.515	12.515	104.600	20.310	20.310	1.307	0.201	0.201
ESO_552-_G_020	-6.756	7.226	7.226	206.197	10.816	10.816	0.609	0.081	0.081
ABELL_0262	3.562	0.138	0.138	484.188	26.609	26.609	1.459	0.026	0.026
ABELL_2556	12.041	1.363	1.363	123.647	4.080	4.080	1.084	0.044	0.044
MCXC_J1053.7+5452	63.300	12.560	12.560	60.464	16.230	16.230	1.189	0.161	0.161
ABELL_2111	189.915	27.115	27.115	88.337	27.655	27.655	1.189	0.156	0.156
ABELL_0400	86.201	20.899	20.899	104.441	45.919	45.919	0.939	0.588	0.588
MACS_J2214-1359	150.198	23.601	23.601	62.246	24.888	24.888	1.286	0.195	0.195
MACS_J0025.4-1222	149.815	20.362	20.362	63.487	19.633	19.633	1.337	0.154	0.154
UGC_00842	-22.632	19.270	19.270	215.221	20.699	20.699	0.430	0.160	0.160
ABELL_2147	163.008	18.556	18.556	78.332	36.313	36.313	1.411	0.378	0.378
ABELL_0697	229.645	22.639	22.639	54.663	16.890	16.890	1.620	0.148	0.148
ZwCl_0823.2+0425	72.063	16.331	16.331	90.869	25.862	25.862	1.267	0.215	0.215
ABELL_1767	136.566	62.655	62.655	147.731	126.407	126.407	0.647	0.585	0.585
NSC_J174715+451155	290.692	35.204	35.204	11.492	16.426	16.426	1.751	0.186	0.186
ABELL_0868	192.942	14.459	14.459	14.989	6.529	6.529	1.866	0.099	0.099

Cluster Name	K_0	$\sigma_{K_0}-$	$\sigma_{K_0}+$	K_{100}	$\sigma_{K_{100}}-$	$\sigma_{K_{100}}+$	α	$\sigma_{\alpha}-$	$\sigma_{\alpha}+$
		(keV cm^2)			(keV cm^2)				
Abell_2276	24.173	11.035	11.035	132.597	18.928	18.928	0.818	0.125	0.125
ABELL_2631	76.914	106.409	106.409	230.751	114.628	114.628	0.412	0.218	0.218
MCXC_J0352.9+1941	7.106	0.380	0.380	56.749	2.013	2.013	1.494	0.061	0.061
PKS_0745-19	8.581	0.315	0.315	118.197	1.029	1.029	1.167	0.012	0.012
CIZA_J0107.7+5408	305.475	45.983	45.983	66.095	52.333	52.333	1.107	0.300	0.300
ABELL_3395_SW	190.118	25.741	25.741	99.607	44.497	44.497	1.376	0.344	0.344
CIZA_J1938.3+5409	82.492	12.545	12.545	63.256	15.557	15.557	1.427	0.155	0.155
ABELL_1569	136.449	21.463	21.463	44.110	65.747	65.747	0.904	0.672	0.672
ABELL_1413	57.420	5.077	5.077	129.718	8.112	8.112	1.047	0.044	0.044
ABELL_0376	61.935	16.644	16.644	178.494	32.288	32.288	0.869	0.157	0.157
RCS_J2327-0204	45.275	7.173	7.173	212.711	14.883	14.883	1.224	0.088	0.088
ABELL_1664	14.131	0.879	0.879	107.446	4.539	4.539	1.690	0.081	0.081
MCXC_J0331.1-2100	11.718	1.574	1.574	114.991	5.396	5.396	1.252	0.053	0.053
ABELL_3560	40.383	61.464	61.464	198.695	85.109	85.109	0.367	0.251	0.251
ABELL_1750N	93.060	22.131	22.131	117.458	37.180	37.180	0.980	0.211	0.211
a1750ss	34.901	69.701	69.701	186.190	91.102	91.102	0.580	0.361	0.361
WEIN_051	84.177	55.153	55.153	196.260	94.348	94.348	0.420	0.258	0.258
ABELL_2302	190.544	77.382	77.382	121.021	139.110	139.110	0.764	0.418	0.418
ABELL_1763	186.619	22.108	22.108	54.570	15.648	15.648	1.348	0.124	0.124
HCG_051	-7.020	2.692	2.692	130.845	10.858	10.858	0.558	0.075	0.075
MACS_J2245.0+2637	38.968	6.768	6.768	90.585	13.342	13.342	1.271	0.145	0.145
ABELL_2092	79.498	62.076	62.076	120.495	105.986	105.986	0.690	0.623	0.623
BLOX_J1023.6+0411.1	8.947	0.960	0.960	106.958	3.162	3.162	1.216	0.026	0.026
MACS_J1108.9+0906	80.249	38.940	38.940	111.019	64.854	64.854	0.789	0.252	0.252
NGC_6269	1.305	1.932	1.932	279.709	47.558	47.558	0.892	0.100	0.100
ABELL_2670	30.012	4.629	4.629	125.808	8.013	8.013	0.817	0.062	0.062
ZwCl_0008.8+5215	170.494	40.772	40.772	114.906	53.516	53.516	0.932	0.198	0.198
WBL_671	-10.889	12.285	12.285	254.081	101.207	101.207	0.702	0.395	0.395
ABELL_1361	18.048	3.005	3.005	134.880	8.970	8.970	1.464	0.144	0.144
ABELL_3558	49.877	14.911	14.911	194.069	20.760	20.760	0.772	0.094	0.094

Cluster Name	K_0	σ_{K_0-}	σ_{K_0+}	K_{100}	$\sigma_{K_{100}-}$	$\sigma_{K_{100}+}$	α	$\sigma_{\alpha-}$	$\sigma_{\alpha+}$
		(keV cm^2)			(keV cm^2)				
NGC_3209	3.265	0.846	0.846	182.701	297.526	297.526	1.217	0.527	0.527
ABELL_2597	9.501	0.288	0.288	99.234	1.035	1.035	1.206	0.015	0.015
NSC_J084254+292723	22.863	2.043	2.043	100.849	6.189	6.189	1.546	0.106	0.106
NGC5419-offset2	-1.973	1.107	1.107	423.685	52.658	52.658	0.861	0.056	0.056
MCXC_J1000.5+4409	16.985	5.367	5.367	111.258	9.943	9.943	0.940	0.083	0.083
ABELL_1068	6.283	0.705	0.705	109.284	3.042	3.042	1.157	0.031	0.031
MACS_J1115.8+0129	22.147	2.422	2.422	124.017	9.386	9.386	1.667	0.183	0.183
ABELL_2409	12.424	34.876	34.876	167.993	57.542	57.542	0.512	0.194	0.194
ABELL_S0592	30.594	7.827	7.827	141.163	13.223	13.223	0.915	0.073	0.073
HCG_042	1.714	0.342	0.342	188.993	23.760	23.760	1.009	0.060	0.060
ABELL_2261	41.818	9.759	9.759	139.288	14.832	14.832	0.899	0.070	0.070
BLOX_J1056.9-0337.3	126.798	36.945	36.945	87.750	78.523	78.523	1.248	0.487	0.487
WHL_J125933.4+600409	327.114	56.118	56.118	36.889	80.081	80.081	1.332	0.418	0.418
MACS_J0358.8-2955	26.151	14.956	14.956	167.420	22.122	22.122	0.687	0.062	0.062
ABELL_2626	13.528	2.257	2.257	123.832	4.379	4.379	0.861	0.051	0.051
ABELL_S0520	320.133	39.838	39.838	30.757	30.494	30.494	1.656	0.233	0.233
SC_1329-313	167.330	16.567	16.567	61.944	24.466	24.466	1.703	0.208	0.208
ABELL_3911	338.381	36.851	36.851	27.578	34.618	34.618	1.607	0.276	0.276
ABELL_3391	203.151	29.569	29.569	122.635	45.810	45.810	0.917	0.228	0.228
SPT-CL_J0232-4421	16.418	17.740	17.740	416.131	384.037	384.037	1.254	0.509	0.509
MCXC_J0819.6+6336	6.464	14.100	14.100	160.309	26.200	26.200	0.695	0.134	0.134
ABELL_3378	8.528	3.136	3.136	120.248	6.808	6.808	0.910	0.060	0.060
NGC_4759_GROUP	2.485	0.104	0.104	168.149	8.097	8.097	1.156	0.025	0.025
ABELL_1446	157.742	17.020	17.020	62.913	31.082	31.082	1.462	0.362	0.362
ZwCl_0735.7+7421	16.140	0.906	0.906	121.650	2.649	2.649	1.155	0.022	0.022
MKW_04	2.617	0.437	0.437	176.954	7.150	7.150	0.863	0.025	0.025
MCXC_J1010.5-1239	22.531	50.166	50.166	227.985	73.456	73.456	0.561	0.187	0.187
MCXC_J0301.6+0155	12.181	1.870	1.870	112.084	4.925	4.925	1.064	0.045	0.045
1RXS_J111039.6+284316	64.272	9.246	9.246	84.537	44.615	44.615	1.464	0.397	0.397
MZ_10451	11.591	10.746	10.746	73.110	20.113	20.113	0.569	0.459	0.459

Cluster Name	K_0	$\sigma_{K_0}-$	$\sigma_{K_0}+$	K_{100}	$\sigma_{K_{100}}-$	$\sigma_{K_{100}}+$	α	$\sigma_\alpha-$	$\sigma_\alpha+$
		(keV cm^2)			(keV cm^2)				
ABELL_1033	122.945	16.451	16.451	116.344	22.449	22.449	1.044	0.126	0.126
MKW_03s	18.044	1.755	1.755	117.220	2.724	2.724	0.910	0.029	0.029
ABELL_3404	95.055	18.879	18.879	119.833	26.794	26.794	1.080	0.141	0.141
NGC_5098_GROUP	4.798	0.944	0.944	129.716	6.625	6.625	1.160	0.060	0.060
ABELL_3854	103.513	18.154	18.154	96.946	24.929	24.929	1.201	0.151	0.151
MACS_J0429.6-0253	12.169	3.110	3.110	109.873	8.616	8.616	1.166	0.071	0.071
MCXC_J1130.0+3637	21.316	2.683	2.683	119.264	8.124	8.124	1.098	0.124	0.124
ABELL_1240	196.271	92.437	92.437	117.624	160.964	160.964	0.672	0.708	0.708
MCXC_J2344.2-0422	108.571	13.251	13.251	66.387	15.739	15.739	1.283	0.157	0.157
WHL_J142716.1+440730	12.595	3.479	3.479	135.389	10.844	10.844	1.267	0.078	0.078
MCXC_J0454.1-0300	193.350	20.561	20.561	49.053	20.322	20.322	1.387	0.197	0.197
MACS_J0329.6-0211	4.991	2.268	2.268	118.081	5.828	5.828	1.095	0.042	0.042
MCXC_J1514.9-1523	356.147	108.545	108.545	137.948	191.290	191.290	0.611	0.399	0.399
ABELL_1991	0.392	0.244	0.244	122.804	2.375	2.375	0.996	0.017	0.017
MACS_J0416.1-2403	76.272	106.522	106.522	245.717	116.894	116.894	0.421	0.225	0.225
MCXC_J1853.9+6822	76.431	14.615	14.615	198.874	33.895	33.895	1.402	0.384	0.384
ABELL_1285	186.247	29.134	29.134	77.426	35.964	35.964	0.997	0.214	0.214
SDSS_J015021.27-100530.5_GROUP	2.481	6.357	6.357	113.785	14.645	14.645	0.895	0.131	0.131
ABELL_1930	-3.707	2.733	2.733	182.246	6.827	6.827	0.823	0.042	0.042
NSC_J092017+303027	128.487	76.673	76.673	206.504	111.689	111.689	0.593	0.193	0.193
ABELL_3120	17.504	5.900	5.900	153.473	12.136	12.136	0.982	0.122	0.122
NGC_1132	-1.648	0.843	0.843	112.294	3.305	3.305	0.663	0.035	0.035
MACS_J0011.7-1523	7.906	6.688	6.688	139.323	14.306	14.306	0.861	0.076	0.076
GMBCG_J215.94948+24.07846	5.560	3.403	3.403	132.581	7.921	7.921	1.167	0.105	0.105
ABELL_1750C	159.868	10.761	10.761	56.099	9.678	9.678	1.886	0.082	0.082
MACS_J1149.6+2223	267.540	25.887	25.887	18.052	9.184	9.184	1.859	0.104	0.104

APPENDIX C

ACCEPT 2.0 RADIAL ENTROPY PROFILES

Deprojected radial entropy profiles and fits for the clusters from ACCEPT 2.0 with deprojected profiles. Included on each plot are the best-fit values for K_0, K_{100}, and α with their 1σ errors as well as the reduced χ^2 for the fit and the radial range of the fit. The RA and DEC of the profile center are given in $hh : mm : ss$ in the title of each plot.

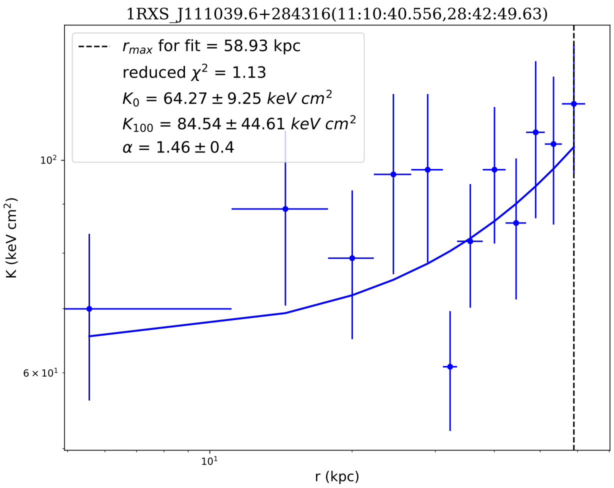
1RXS_J111039.6+284316(11:10:40.556,28:42:49.63)
r_{max} for fit = 58.93 kpc
reduced χ^2 = 1.13
$K_0 = 64.27 \pm 9.25$ $keV\ cm^2$
$K_{100} = 84.54 \pm 44.61$ $keV\ cm^2$
$\alpha = 1.46 \pm 0.4$
K (keV cm^2)
r (kpc)

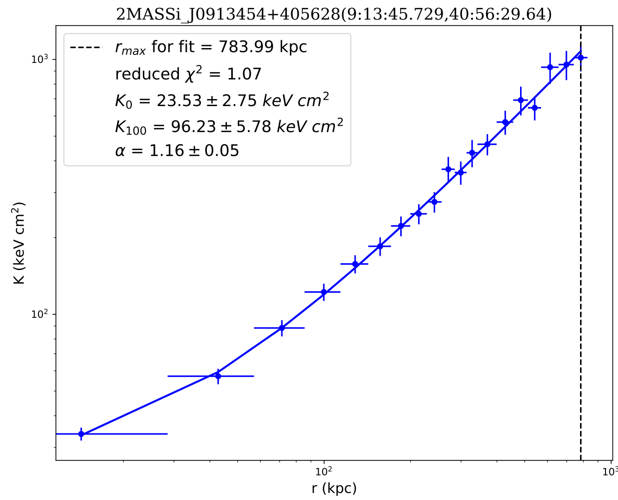
2MASSi_J0913454+405628(9:13:45.729,40:56:29.64)
r_{max} for fit = 783.99 kpc
reduced χ^2 = 1.07
$K_0 = 23.53 \pm 2.75$ $keV\ cm^2$
$K_{100} = 96.23 \pm 5.78$ $keV\ cm^2$
$\alpha = 1.16 \pm 0.05$
K (keV cm^2)
r (kpc)

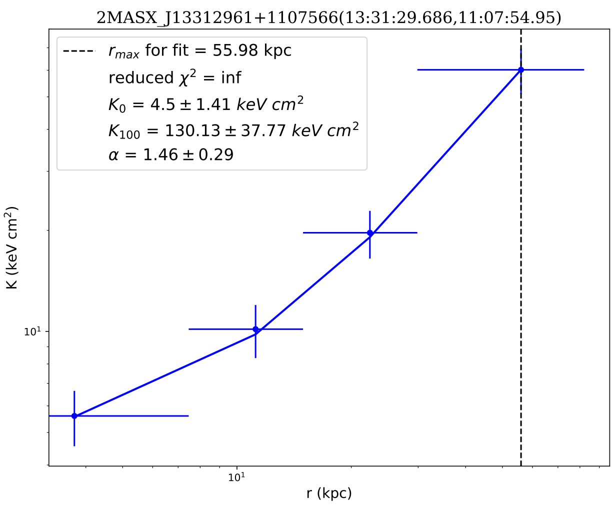
2MASX_J13312961+1107566(13:31:29.686,11:07:54.95)
r_{max} for fit = 55.98 kpc
reduced χ^2 = inf
$K_0 = 4.5 \pm 1.41$ $keV\ cm^2$
$K_{100} = 130.13 \pm 37.77$ $keV\ cm^2$
$\alpha = 1.46 \pm 0.29$
K (keV cm^2)
r (kpc)

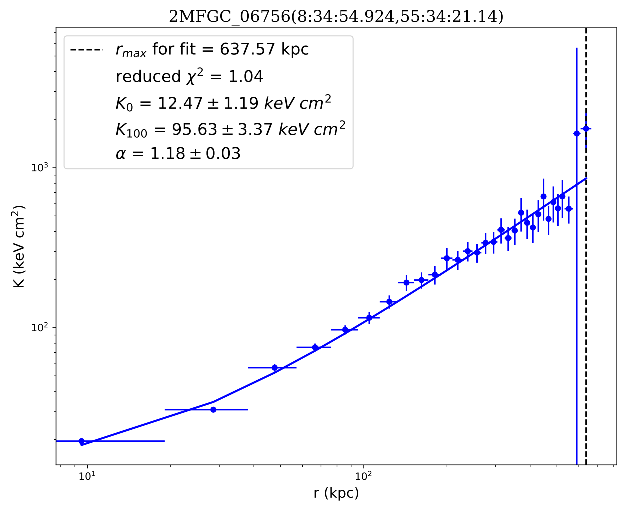
2MFGC_06756(8:34:54.924,55:34:21.14)
r_{max} for fit = 637.57 kpc
reduced χ^2 = 1.04
$K_0 = 12.47 \pm 1.19$ $keV\ cm^2$
$K_{100} = 95.63 \pm 3.37$ $keV\ cm^2$
$\alpha = 1.18 \pm 0.03$
K (keV cm^2)
r (kpc)

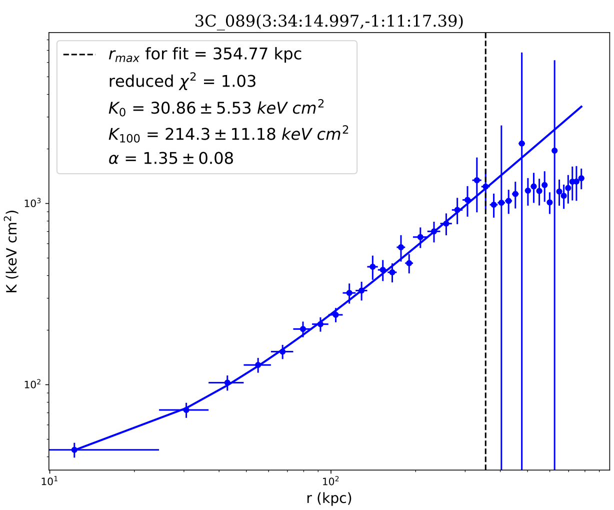
3C_089(3:34:14.997,-1:11:17.39)
r_{max} for fit = 354.77 kpc
reduced χ^2 = 1.03
$K_0 = 30.86 \pm 5.53$ $keV\ cm^2$
$K_{100} = 214.3 \pm 11.18$ $keV\ cm^2$
$\alpha = 1.35 \pm 0.08$
K (keV cm^2)
r (kpc)

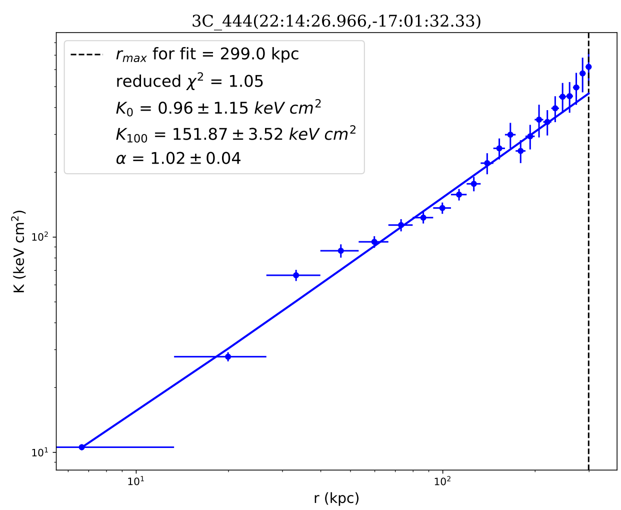
3C_444(22:14:26.966,-17:01:32.33)
r_{max} for fit = 299.0 kpc
reduced χ^2 = 1.05
$K_0 = 0.96 \pm 1.15$ $keV\ cm^2$
$K_{100} = 151.87 \pm 3.52$ $keV\ cm^2$
$\alpha = 1.02 \pm 0.04$
K (keV cm^2)
r (kpc)

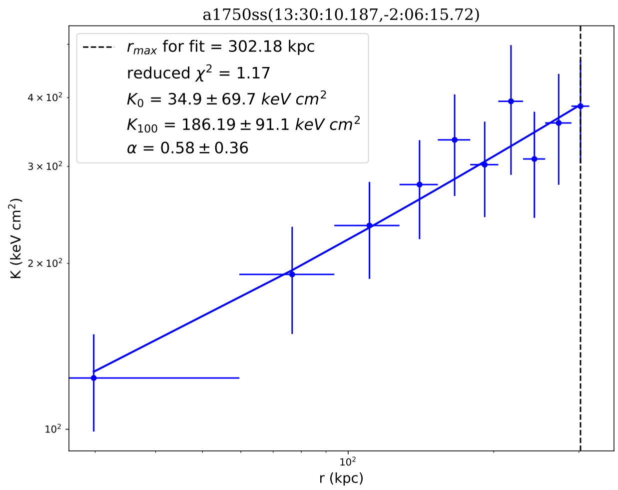
a1750ss(13:30:10.187,-2:06:15.72)
r_{max} for fit = 302.18 kpc
reduced χ^2 = 1.17
K_0 = 34.9 ± 69.7 $keV\ cm^2$
K_{100} = 186.19 ± 91.1 $keV\ cm^2$
α = 0.58 ± 0.36
K (keV cm^2)
r (kpc)

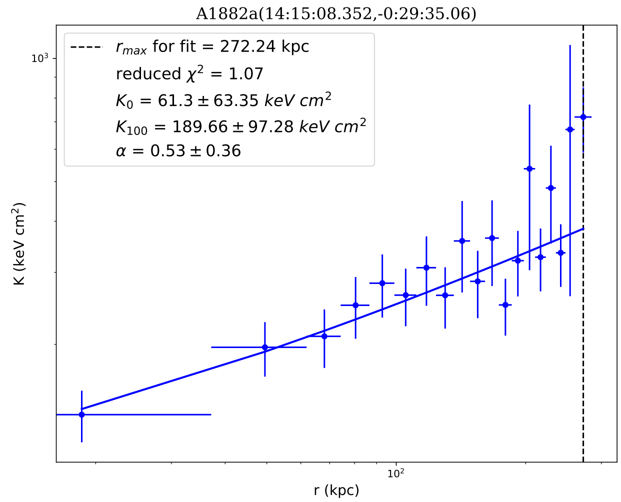
A1882a(14:15:08.352,-0:29:35.06)
r_{max} for fit = 272.24 kpc
reduced χ^2 = 1.07
K_0 = 61.3 ± 63.35 $keV\ cm^2$
K_{100} = 189.66 ± 97.28 $keV\ cm^2$
α = 0.53 ± 0.36
K (keV cm^2)
r (kpc)

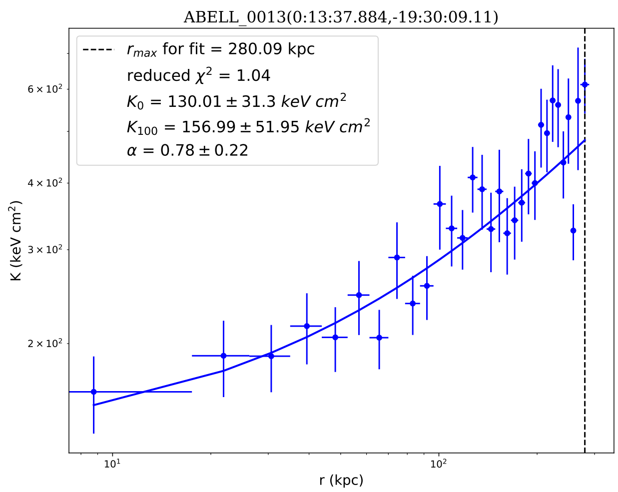
ABELL_0013(0:13:37.884,-19:30:09.11)
r_{max} for fit = 280.09 kpc
reduced χ^2 = 1.04
K_0 = 130.01 ± 31.3 $keV\ cm^2$
K_{100} = 156.99 ± 51.95 $keV\ cm^2$
α = 0.78 ± 0.22
K (keV cm^2)
r (kpc)

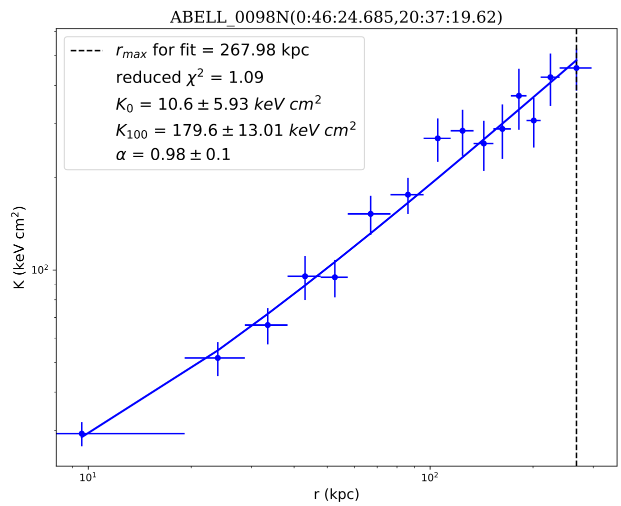
ABELL_0098N(0:46:24.685,20:37:19.62)
r_{max} for fit = 267.98 kpc
reduced χ^2 = 1.09
K_0 = 10.6 ± 5.93 $keV\ cm^2$
K_{100} = 179.6 ± 13.01 $keV\ cm^2$
α = 0.98 ± 0.1
K (keV cm^2)
r (kpc)

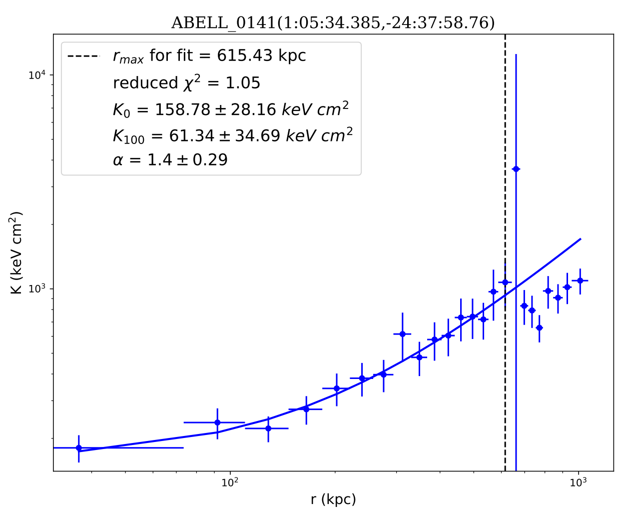
ABELL_0141(1:05:34.385,-24:37:58.76)
r_{max} for fit = 615.43 kpc
reduced χ^2 = 1.05
K_0 = 158.78 ± 28.16 $keV\ cm^2$
K_{100} = 61.34 ± 34.69 $keV\ cm^2$
α = 1.4 ± 0.29
K (keV cm^2)
r (kpc)

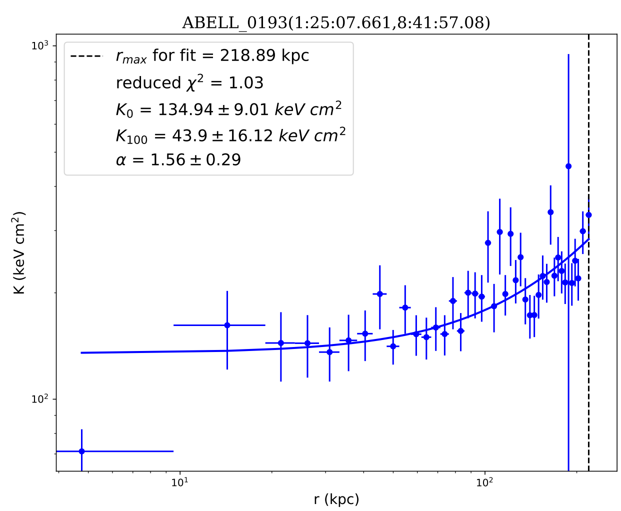
ABELL_0193(1:25:07.661,8:41:57.08)
r_{max} for fit = 218.89 kpc
reduced χ^2 = 1.03
K_0 = 134.94 ± 9.01 $keV\ cm^2$
K_{100} = 43.9 ± 16.12 $keV\ cm^2$
α = 1.56 ± 0.29
K (keV cm^2)
r (kpc)

ABELL_0209(1:31:52.565,-13:36:38.81)

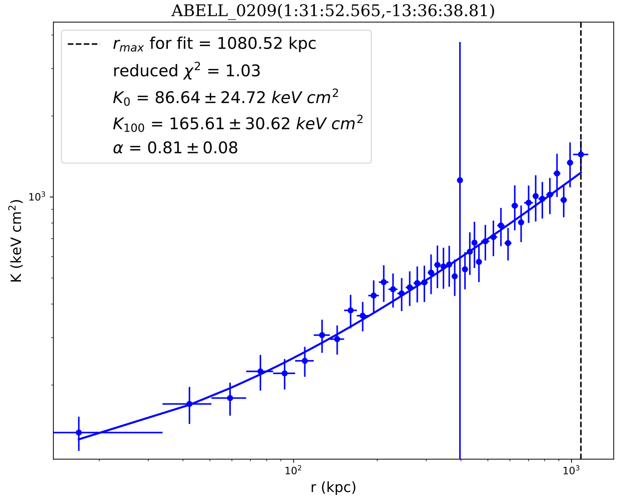

ABELL_0262(1:52:46.298,36:09:11.81)

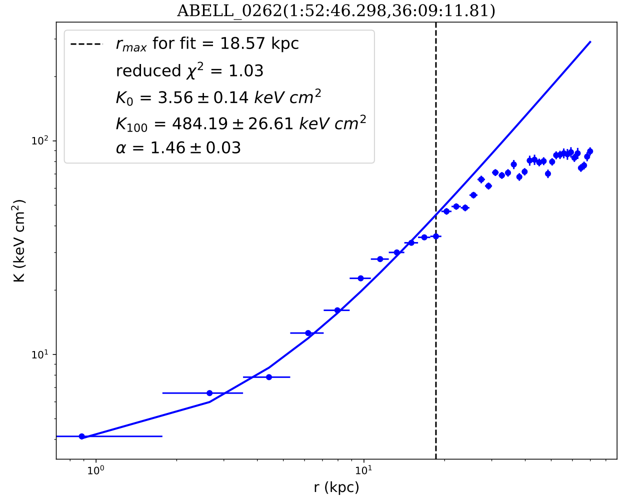

ABELL_0267(1:52:42.269,1:00:45.32)

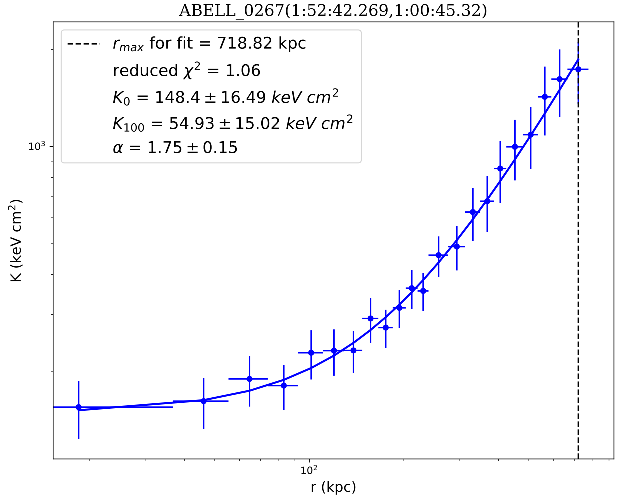

ABELL_0370(2:39:53.170,-1:34:36.95)

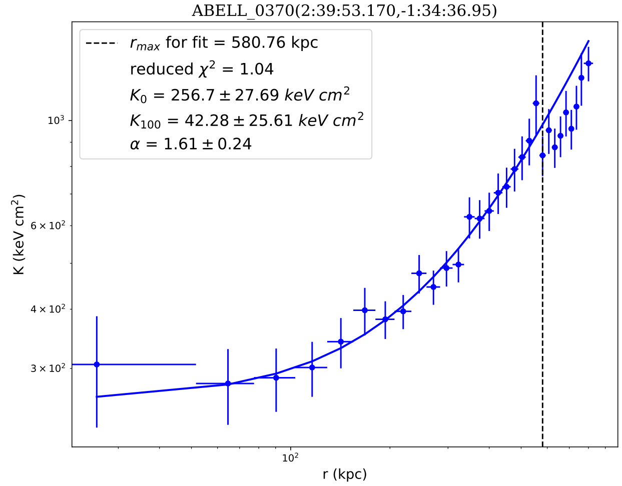

ABELL_0376(2:46:03.946,36:54:19.75)

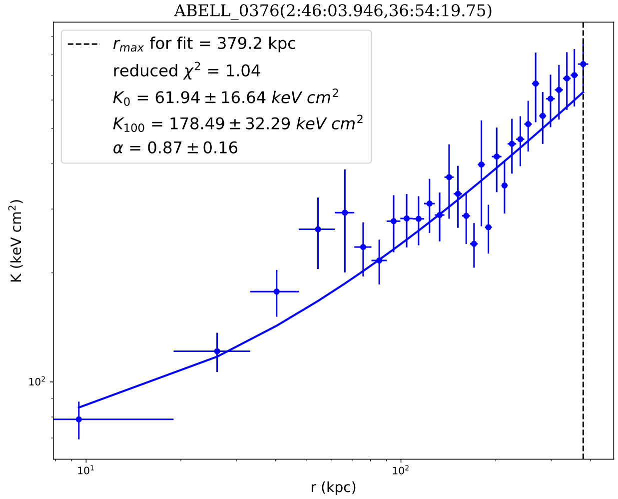

ABELL_0383(2:48:03.365,-3:31:44.69)

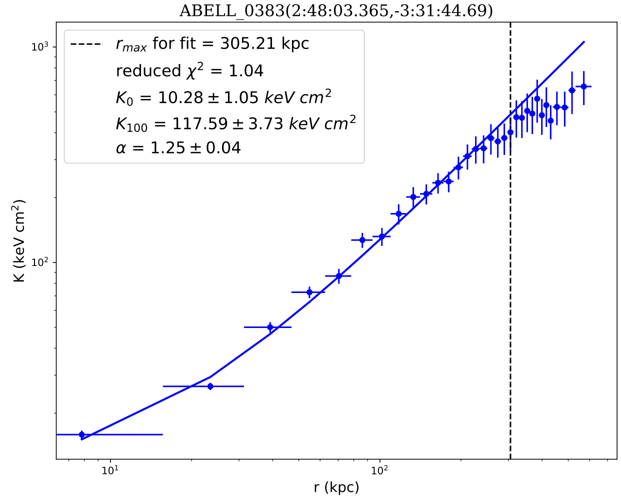

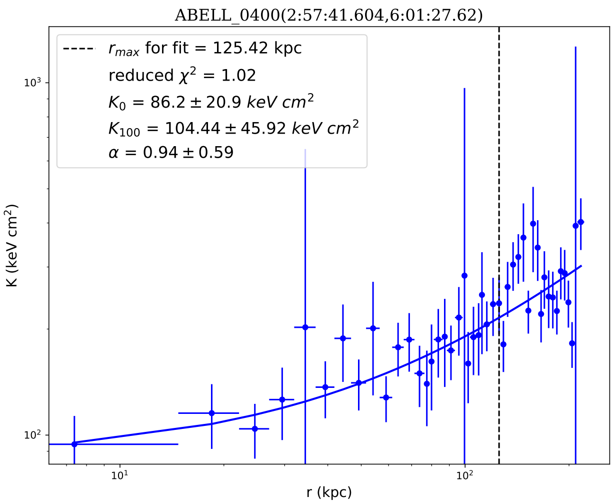
ABELL_0400(2:57:41.604,6:01:27.62)
r_{max} for fit = 125.42 kpc
reduced χ^2 = 1.02
K_0 = 86.2 ± 20.9 $keV\ cm^2$
K_{100} = 104.44 ± 45.92 $keV\ cm^2$
α = 0.94 ± 0.59
K (keV cm^2)
r (kpc)

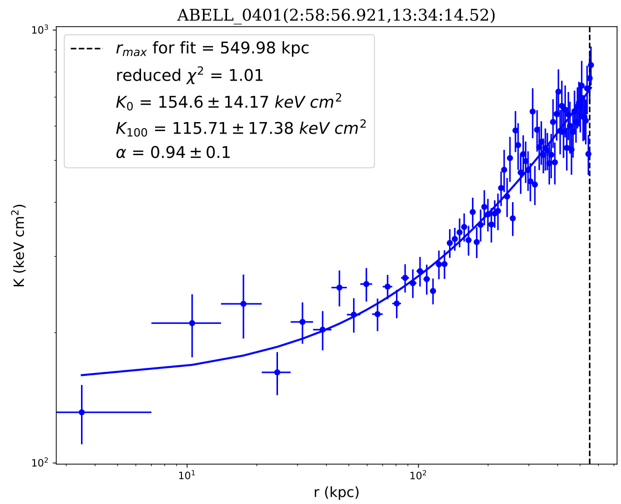
ABELL_0401(2:58:56.921,13:34:14.52)
r_{max} for fit = 549.98 kpc
reduced χ^2 = 1.01
K_0 = 154.6 ± 14.17 $keV\ cm^2$
K_{100} = 115.71 ± 17.38 $keV\ cm^2$
α = 0.94 ± 0.1
K (keV cm^2)
r (kpc)

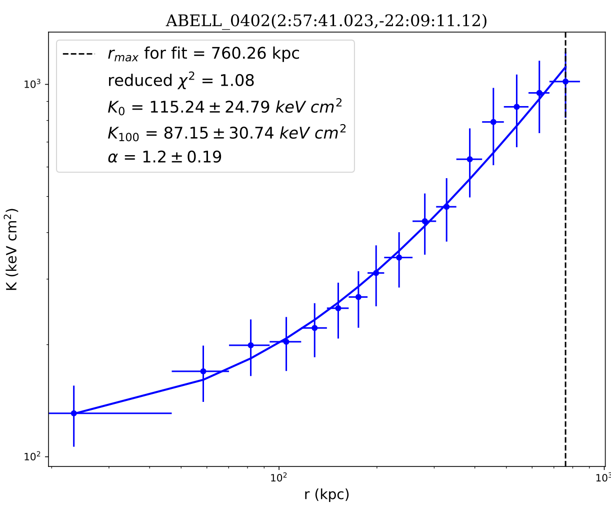
ABELL_0402(2:57:41.023,-22:09:11.12)
r_{max} for fit = 760.26 kpc
reduced χ^2 = 1.08
K_0 = 115.24 ± 24.79 $keV\ cm^2$
K_{100} = 87.15 ± 30.74 $keV\ cm^2$
α = 1.2 ± 0.19
K (keV cm^2)
r (kpc)

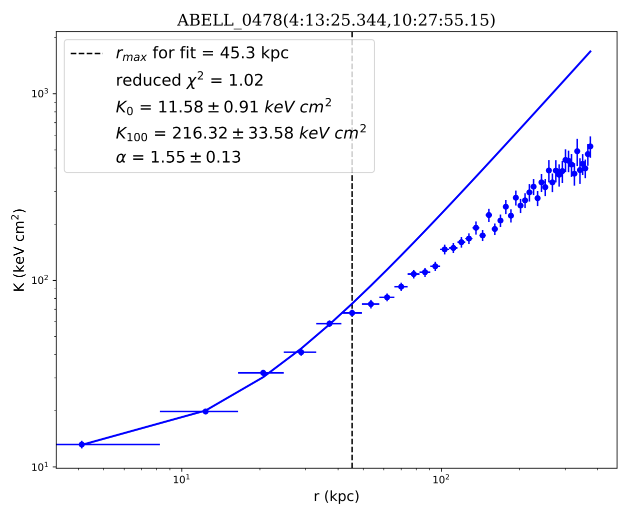
ABELL_0478(4:13:25.344,10:27:55.15)
r_{max} for fit = 45.3 kpc
reduced χ^2 = 1.02
K_0 = 11.58 ± 0.91 $keV\ cm^2$
K_{100} = 216.32 ± 33.58 $keV\ cm^2$
α = 1.55 ± 0.13
K (keV cm^2)
r (kpc)

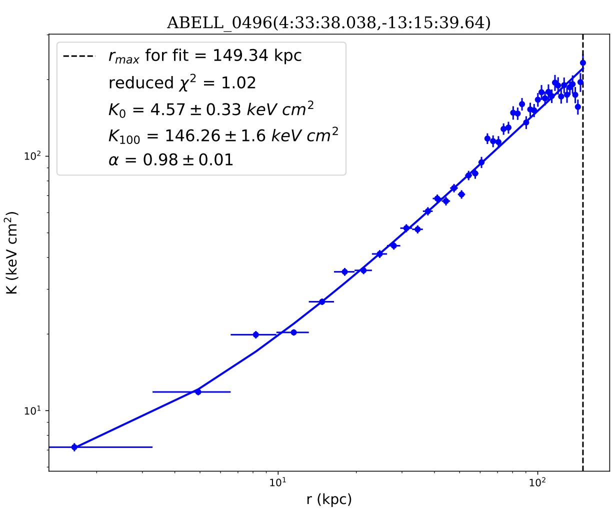
ABELL_0496(4:33:38.038,-13:15:39.64)
r_{max} for fit = 149.34 kpc
reduced χ^2 = 1.02
K_0 = 4.57 ± 0.33 $keV\ cm^2$
K_{100} = 146.26 ± 1.6 $keV\ cm^2$
α = 0.98 ± 0.01
K (keV cm^2)
r (kpc)

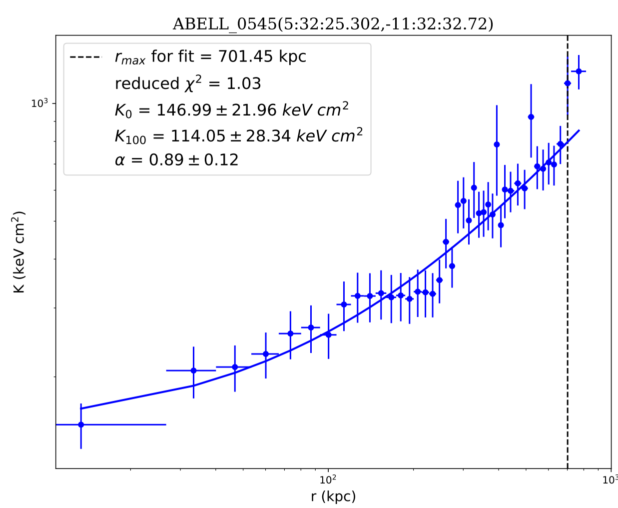
ABELL_0545(5:32:25.302,-11:32:32.72)
r_{max} for fit = 701.45 kpc
reduced χ^2 = 1.03
K_0 = 146.99 ± 21.96 $keV\ cm^2$
K_{100} = 114.05 ± 28.34 $keV\ cm^2$
α = 0.89 ± 0.12
K (keV cm^2)
r (kpc)

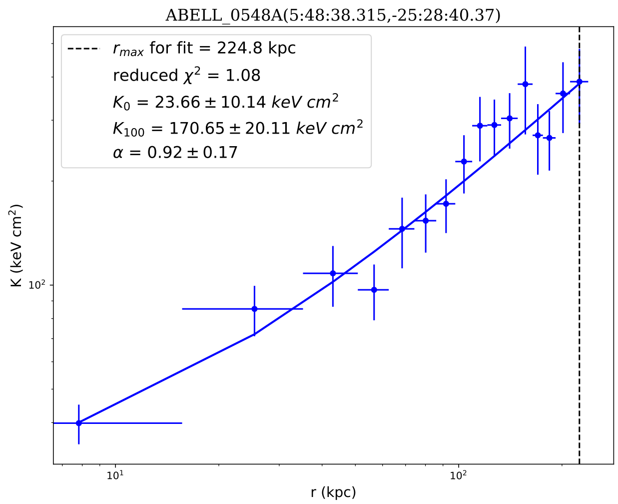
ABELL_0548A(5:48:38.315,-25:28:40.37)
r_{max} for fit = 224.8 kpc
reduced χ^2 = 1.08
K_0 = 23.66 ± 10.14 $keV\ cm^2$
K_{100} = 170.65 ± 20.11 $keV\ cm^2$
α = 0.92 ± 0.17
K (keV cm^2)
r (kpc)

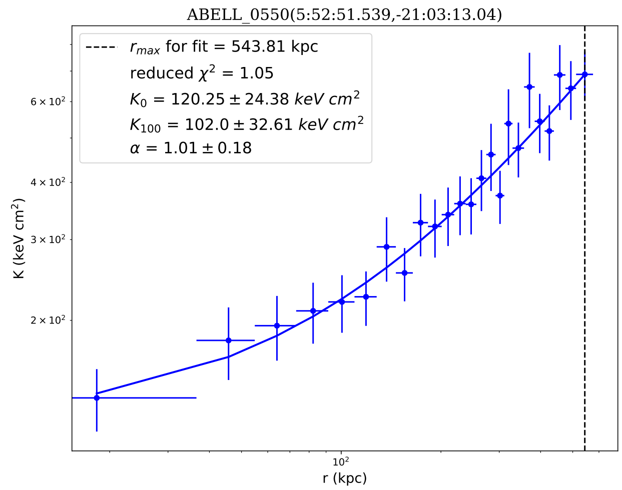
ABELL_0550(5:52:51.539,-21:03:13.04)
r_{max} for fit = 543.81 kpc
reduced χ^2 = 1.05
K_0 = 120.25 ± 24.38 $keV\ cm^2$
K_{100} = 102.0 ± 32.61 $keV\ cm^2$
α = 1.01 ± 0.18
K (keV cm^2)
r (kpc)

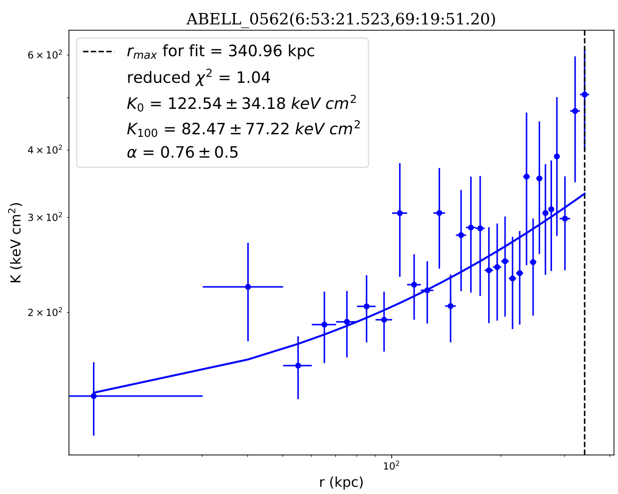
ABELL_0562(6:53:21.523,69:19:51.20)
r_{max} for fit = 340.96 kpc
reduced χ^2 = 1.04
K_0 = 122.54 ± 34.18 $keV\ cm^2$
K_{100} = 82.47 ± 77.22 $keV\ cm^2$
α = 0.76 ± 0.5
K (keV cm^2)
r (kpc)

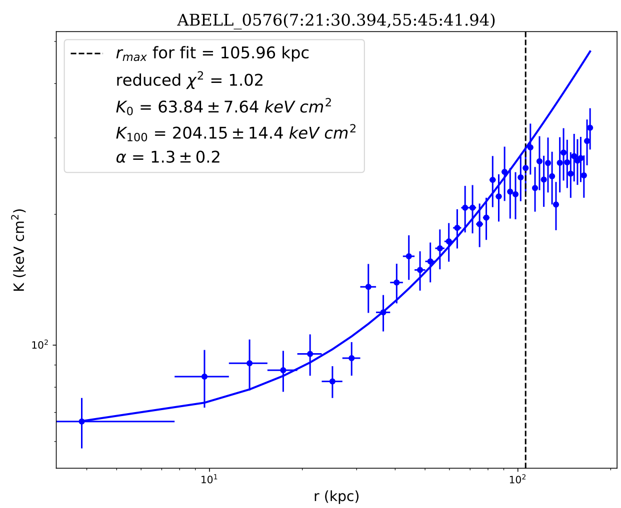
ABELL_0576(7:21:30.394,55:45:41.94)
r_{max} for fit = 105.96 kpc
reduced χ^2 = 1.02
K_0 = 63.84 ± 7.64 $keV\ cm^2$
K_{100} = 204.15 ± 14.4 $keV\ cm^2$
α = 1.3 ± 0.2
K (keV cm^2)
r (kpc)

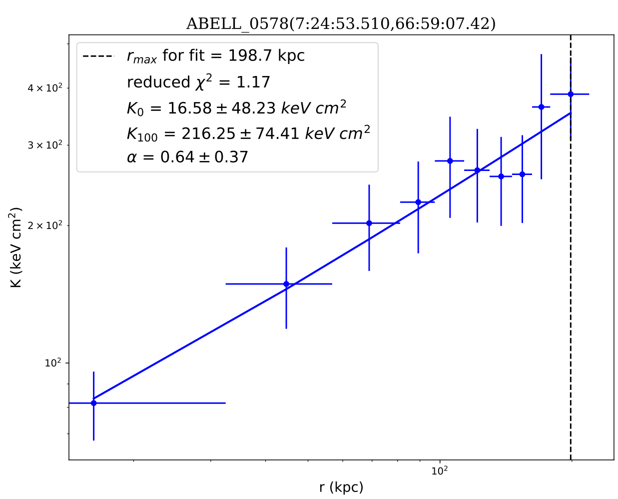
ABELL_0578(7:24:53.510,66:59:07.42)
r_{max} for fit = 198.7 kpc
reduced χ^2 = 1.17
K_0 = 16.58 ± 48.23 $keV\ cm^2$
K_{100} = 216.25 ± 74.41 $keV\ cm^2$
α = 0.64 ± 0.37
K (keV cm^2)
r (kpc)

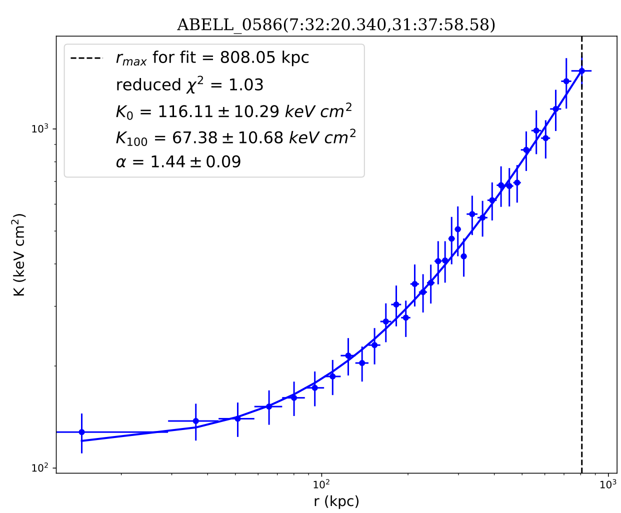
ABELL_0586(7:32:20.340,31:37:58.58)
r_{max} for fit = 808.05 kpc
reduced χ^2 = 1.03
K_0 = 116.11 ± 10.29 $keV\ cm^2$
K_{100} = 67.38 ± 10.68 $keV\ cm^2$
α = 1.44 ± 0.09
K (keV cm^2)
r (kpc)

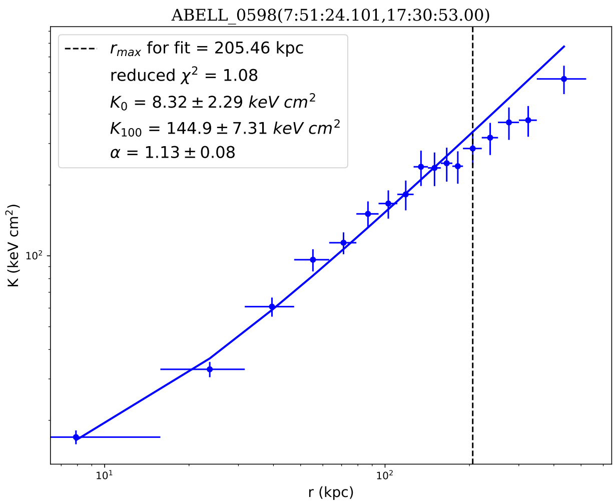
ABELL_0598(7:51:24.101,17:30:53.00)
r_{max} for fit = 205.46 kpc
reduced χ^2 = 1.08
K_0 = 8.32 ± 2.29 $keV\ cm^2$
K_{100} = 144.9 ± 7.31 $keV\ cm^2$
α = 1.13 ± 0.08
K (keV cm^2)
r (kpc)

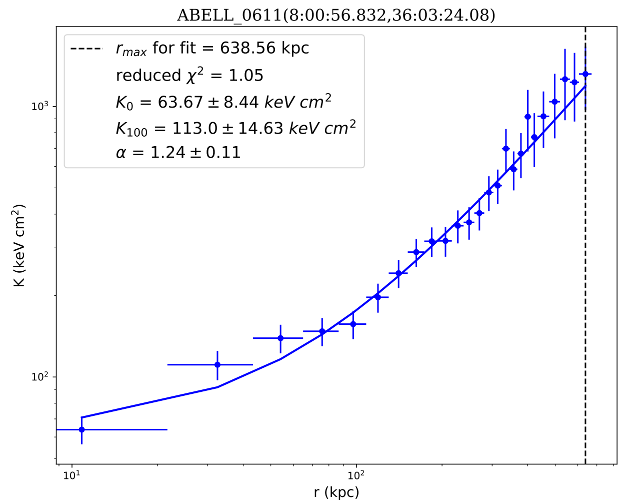
ABELL_0611(8:00:56.832,36:03:24.08)
r_{max} for fit = 638.56 kpc
reduced χ^2 = 1.05
K_0 = 63.67 ± 8.44 $keV\ cm^2$
K_{100} = 113.0 ± 14.63 $keV\ cm^2$
α = 1.24 ± 0.11
K (keV cm^2)
r (kpc)

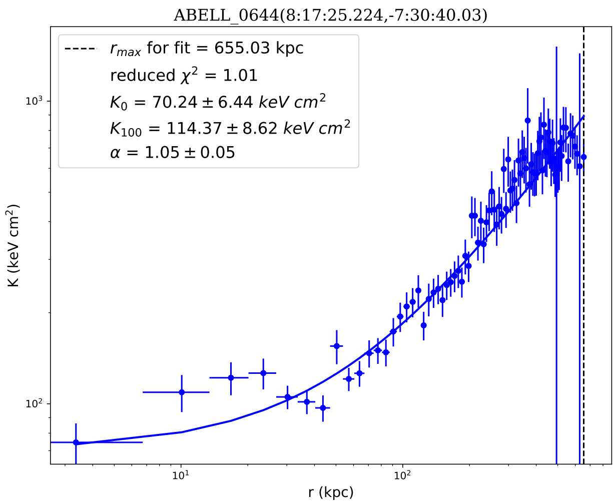
ABELL_0644(8:17:25.224,-7:30:40.03)
r_{max} for fit = 655.03 kpc
reduced χ^2 = 1.01
K_0 = 70.24 ± 6.44 $keV\ cm^2$
K_{100} = 114.37 ± 8.62 $keV\ cm^2$
α = 1.05 ± 0.05
K (keV cm^2)
r (kpc)

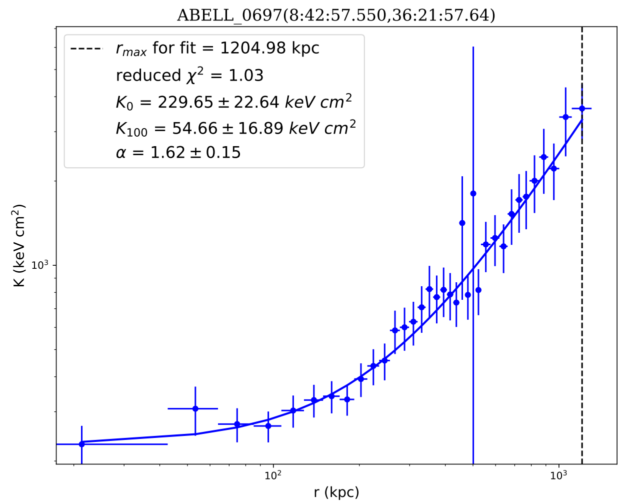
ABELL_0697(8:42:57.550,36:21:57.64)
r_{max} for fit = 1204.98 kpc
reduced χ^2 = 1.03
K_0 = 229.65 ± 22.64 $keV\ cm^2$
K_{100} = 54.66 ± 16.89 $keV\ cm^2$
α = 1.62 ± 0.15
K (keV cm^2)
r (kpc)

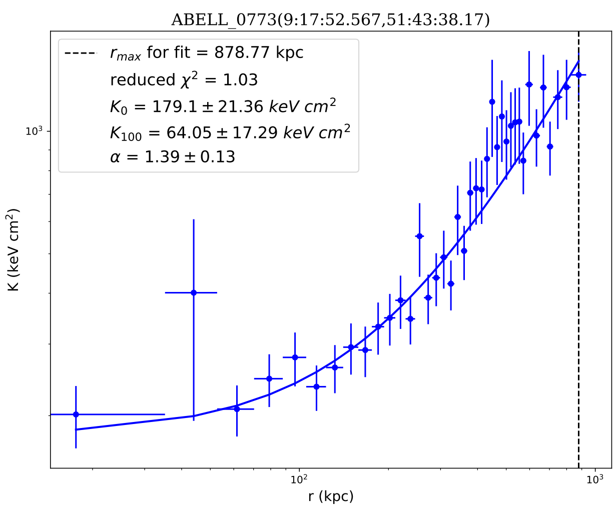
ABELL_0773(9:17:52.567,51:43:38.17)
r_{max} for fit = 878.77 kpc
reduced χ^2 = 1.03
K_0 = 179.1 ± 21.36 $keV\ cm^2$
K_{100} = 64.05 ± 17.29 $keV\ cm^2$
α = 1.39 ± 0.13
K (keV cm^2)
r (kpc)

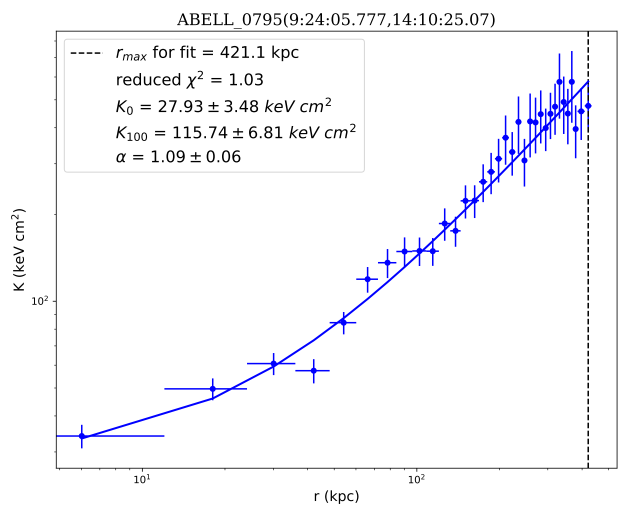
ABELL_0795(9:24:05.777,14:10:25.07)
r_{max} for fit = 421.1 kpc
reduced χ^2 = 1.03
K_0 = 27.93 ± 3.48 $keV\ cm^2$
K_{100} = 115.74 ± 6.81 $keV\ cm^2$
α = 1.09 ± 0.06
K (keV cm^2)
r (kpc)

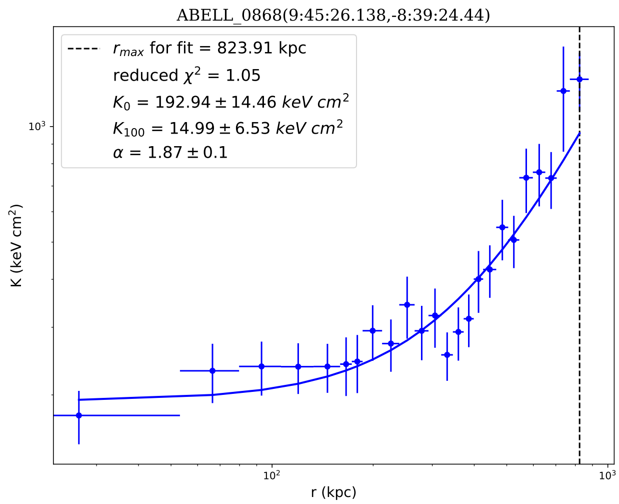

ABELL_0868(9:45:26.138,-8:39:24.44)
r_{max} for fit = 823.91 kpc
reduced χ^2 = 1.05
K_0 = 192.94 ± 14.46 $keV\ cm^2$
K_{100} = 14.99 ± 6.53 $keV\ cm^2$
α = 1.87 ± 0.1
K (keV cm^2)
r (kpc)

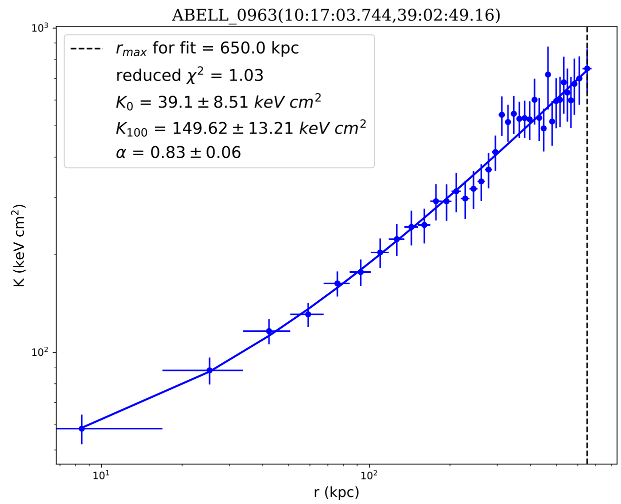

ABELL_0963(10:17:03.744,39:02:49.16)
r_{max} for fit = 650.0 kpc
reduced χ^2 = 1.03
K_0 = 39.1 ± 8.51 $keV\ cm^2$
K_{100} = 149.62 ± 13.21 $keV\ cm^2$
α = 0.83 ± 0.06
K (keV cm^2)
r (kpc)

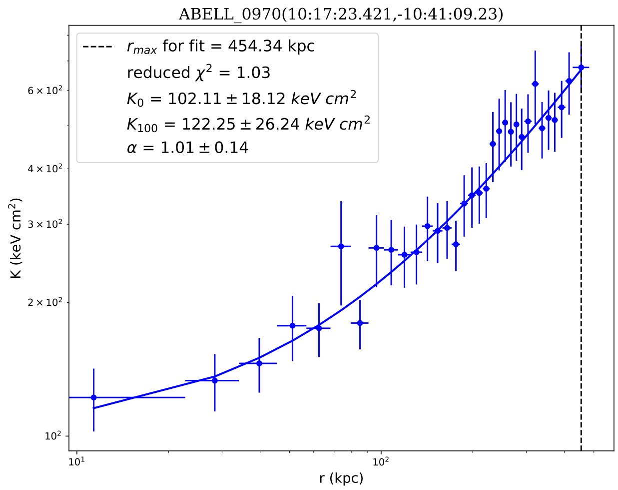

ABELL_0970(10:17:23.421,-10:41:09.23)
r_{max} for fit = 454.34 kpc
reduced χ^2 = 1.03
K_0 = 102.11 ± 18.12 $keV\ cm^2$
K_{100} = 122.25 ± 26.24 $keV\ cm^2$
α = 1.01 ± 0.14
K (keV cm^2)
r (kpc)

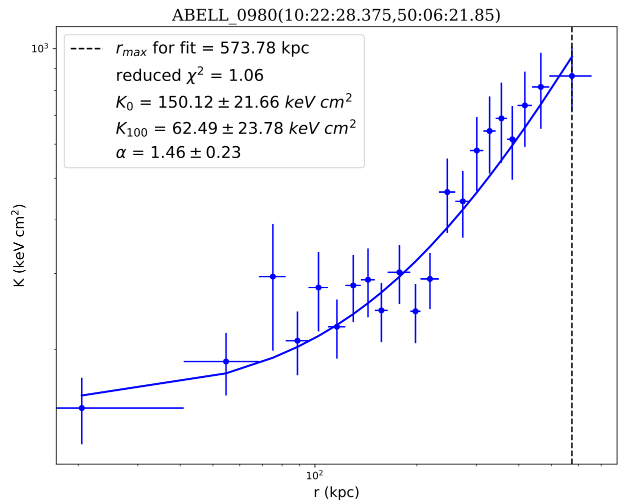

ABELL_0980(10:22:28.375,50:06:21.85)
r_{max} for fit = 573.78 kpc
reduced χ^2 = 1.06
K_0 = 150.12 ± 21.66 $keV\ cm^2$
K_{100} = 62.49 ± 23.78 $keV\ cm^2$
α = 1.46 ± 0.23
K (keV cm^2)
r (kpc)

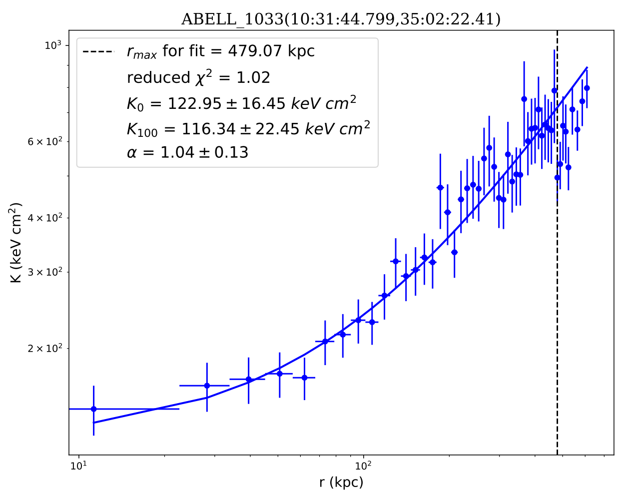

ABELL_1033(10:31:44.799,35:02:22.41)
r_{max} for fit = 479.07 kpc
reduced χ^2 = 1.02
K_0 = 122.95 ± 16.45 $keV\ cm^2$
K_{100} = 116.34 ± 22.45 $keV\ cm^2$
α = 1.04 ± 0.13
K (keV cm^2)
r (kpc)

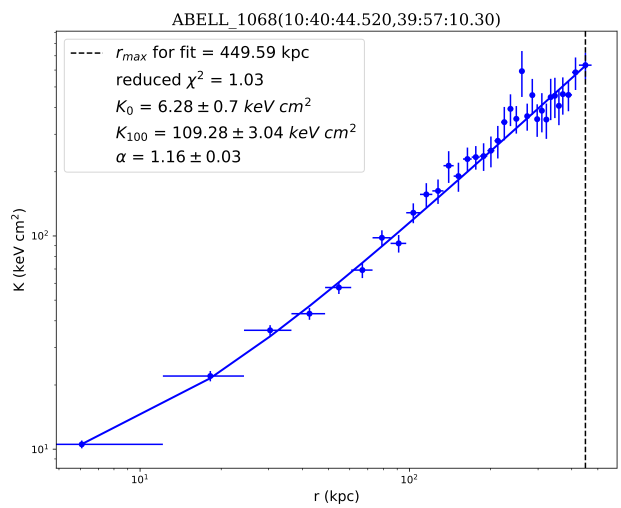

ABELL_1068(10:40:44.520,39:57:10.30)
r_{max} for fit = 449.59 kpc
reduced χ^2 = 1.03
K_0 = 6.28 ± 0.7 $keV\ cm^2$
K_{100} = 109.28 ± 3.04 $keV\ cm^2$
α = 1.16 ± 0.03
K (keV cm^2)
r (kpc)

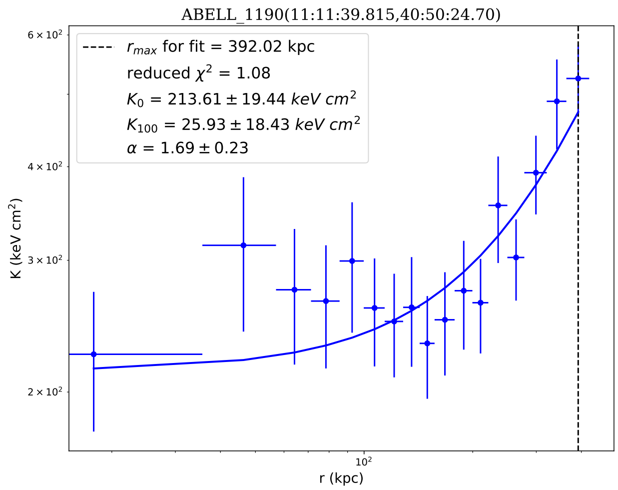
ABELL_1190(11:11:39.815,40:50:24.70)
r_{max} for fit = 392.02 kpc
reduced χ^2 = 1.08
$K_0 = 213.61 \pm 19.44\ keV\ cm^2$
$K_{100} = 25.93 \pm 18.43\ keV\ cm^2$
$\alpha = 1.69 \pm 0.23$
K (keV cm^2)
r (kpc)

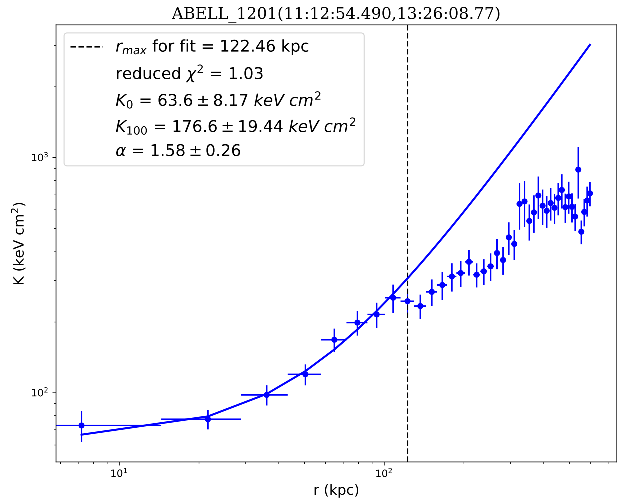
ABELL_1201(11:12:54.490,13:26:08.77)
r_{max} for fit = 122.46 kpc
reduced χ^2 = 1.03
$K_0 = 63.6 \pm 8.17\ keV\ cm^2$
$K_{100} = 176.6 \pm 19.44\ keV\ cm^2$
$\alpha = 1.58 \pm 0.26$
K (keV cm^2)
r (kpc)

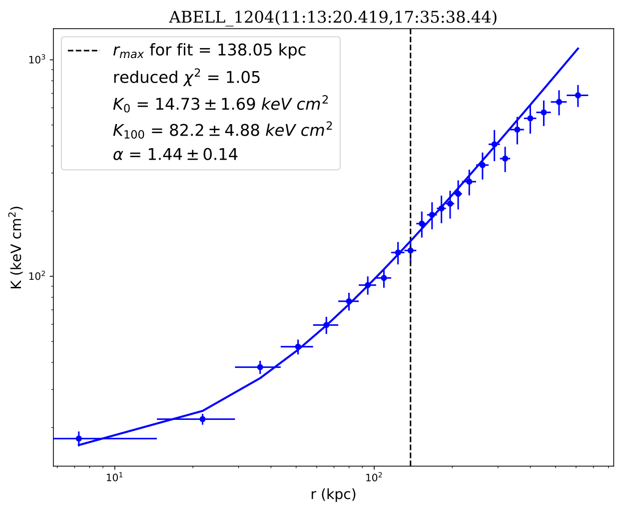
ABELL_1204(11:13:20.419,17:35:38.44)
r_{max} for fit = 138.05 kpc
reduced χ^2 = 1.05
$K_0 = 14.73 \pm 1.69\ keV\ cm^2$
$K_{100} = 82.2 \pm 4.88\ keV\ cm^2$
$\alpha = 1.44 \pm 0.14$
K (keV cm^2)
r (kpc)

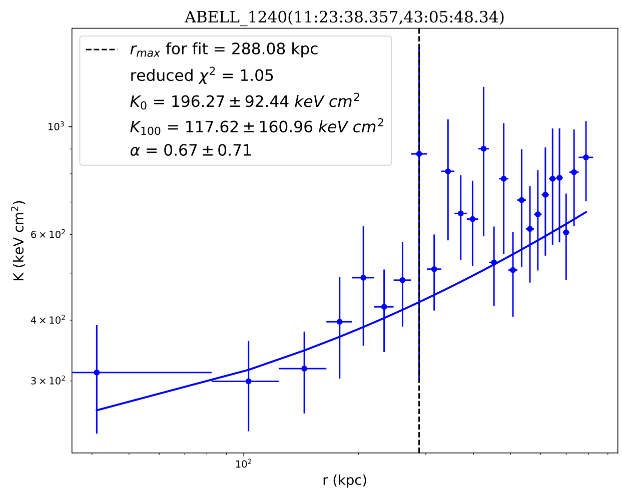
ABELL_1240(11:23:38.357,43:05:48.34)
r_{max} for fit = 288.08 kpc
reduced χ^2 = 1.05
$K_0 = 196.27 \pm 92.44\ keV\ cm^2$
$K_{100} = 117.62 \pm 160.96\ keV\ cm^2$
$\alpha = 0.67 \pm 0.71$
K (keV cm^2)
r (kpc)

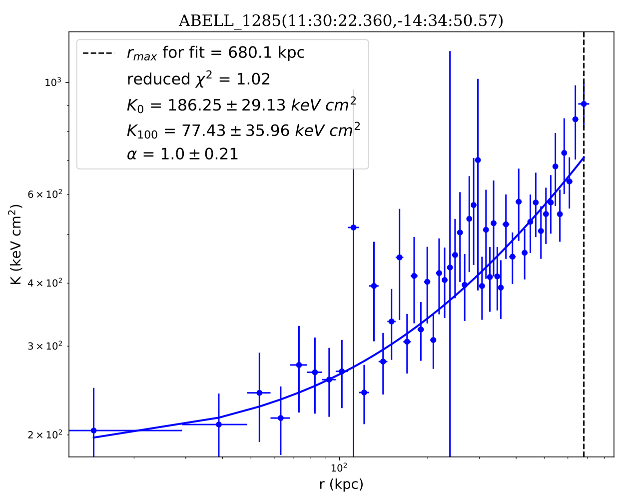
ABELL_1285(11:30:22.360,-14:34:50.57)
r_{max} for fit = 680.1 kpc
reduced χ^2 = 1.02
$K_0 = 186.25 \pm 29.13\ keV\ cm^2$
$K_{100} = 77.43 \pm 35.96\ keV\ cm^2$
$\alpha = 1.0 \pm 0.21$
K (keV cm^2)
r (kpc)

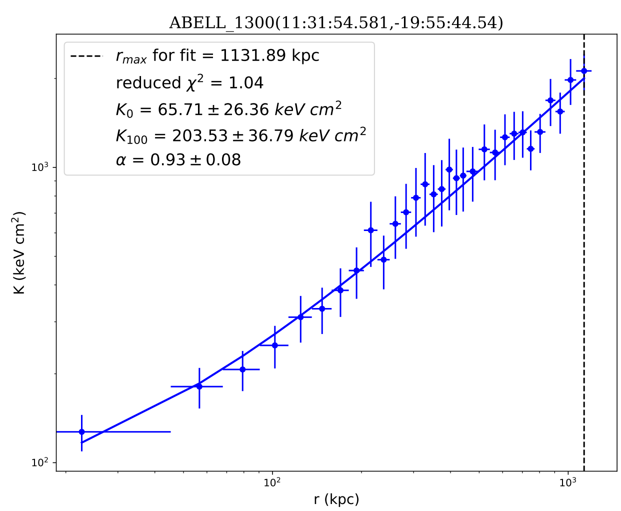
ABELL_1300(11:31:54.581,-19:55:44.54)
r_{max} for fit = 1131.89 kpc
reduced χ^2 = 1.04
$K_0 = 65.71 \pm 26.36\ keV\ cm^2$
$K_{100} = 203.53 \pm 36.79\ keV\ cm^2$
$\alpha = 0.93 \pm 0.08$
K (keV cm^2)
r (kpc)

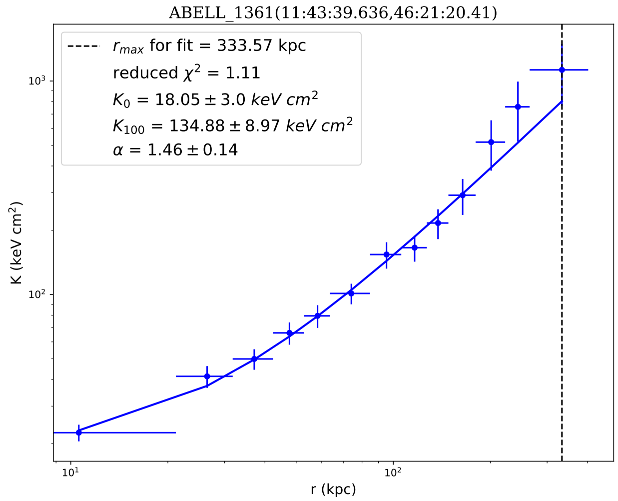
ABELL_1361(11:43:39.636,46:21:20.41)
r_{max} for fit = 333.57 kpc
reduced χ^2 = 1.11
K_0 = 18.05 ± 3.0 $keV\ cm^2$
K_{100} = 134.88 ± 8.97 $keV\ cm^2$
α = 1.46 ± 0.14
K (keV cm^2)
r (kpc)

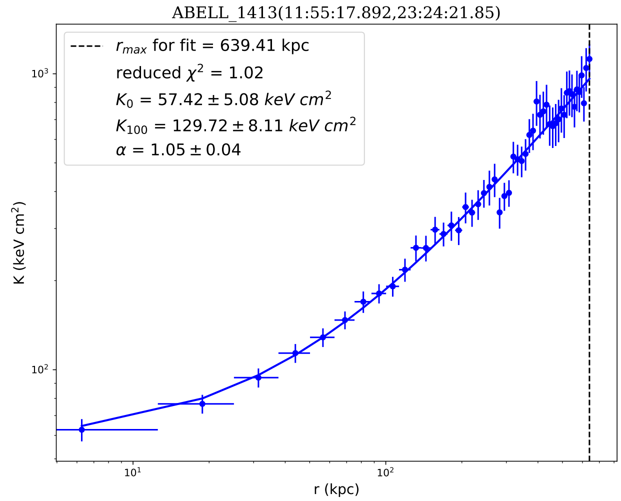
ABELL_1413(11:55:17.892,23:24:21.85)
r_{max} for fit = 639.41 kpc
reduced χ^2 = 1.02
K_0 = 57.42 ± 5.08 $keV\ cm^2$
K_{100} = 129.72 ± 8.11 $keV\ cm^2$
α = 1.05 ± 0.04
K (keV cm^2)
r (kpc)

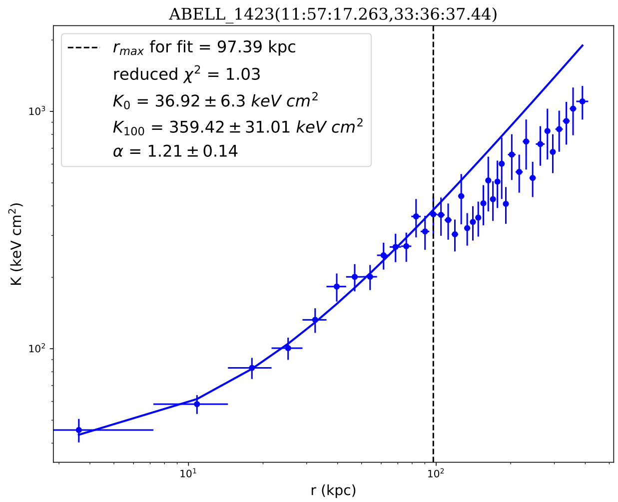
ABELL_1423(11:57:17.263,33:36:37.44)
r_{max} for fit = 97.39 kpc
reduced χ^2 = 1.03
K_0 = 36.92 ± 6.3 $keV\ cm^2$
K_{100} = 359.42 ± 31.01 $keV\ cm^2$
α = 1.21 ± 0.14
K (keV cm^2)
r (kpc)

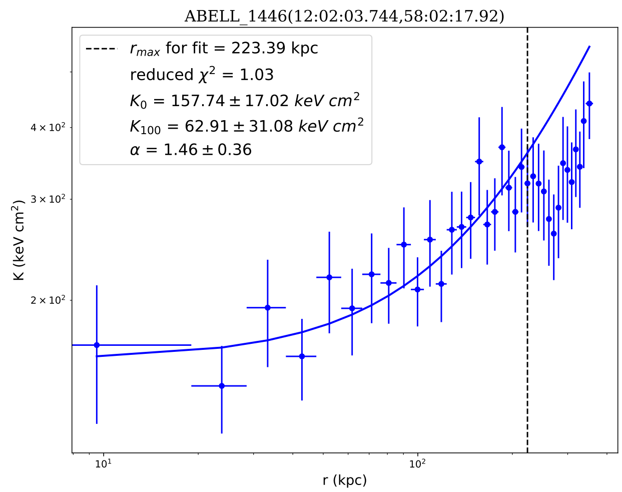
ABELL_1446(12:02:03.744,58:02:17.92)
r_{max} for fit = 223.39 kpc
reduced χ^2 = 1.03
K_0 = 157.74 ± 17.02 $keV\ cm^2$
K_{100} = 62.91 ± 31.08 $keV\ cm^2$
α = 1.46 ± 0.36
K (keV cm^2)
r (kpc)

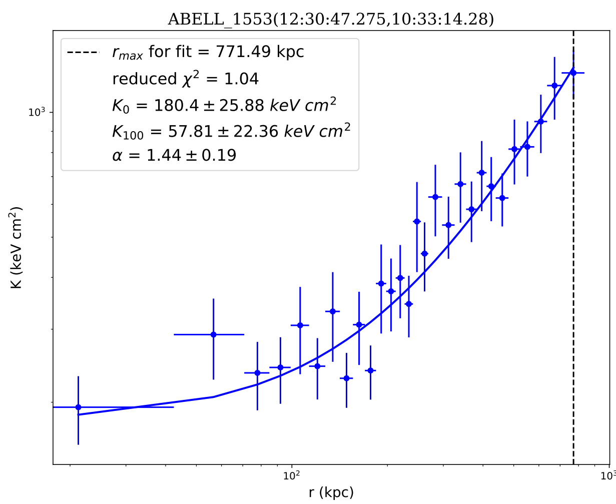
ABELL_1553(12:30:47.275,10:33:14.28)
r_{max} for fit = 771.49 kpc
reduced χ^2 = 1.04
K_0 = 180.4 ± 25.88 $keV\ cm^2$
K_{100} = 57.81 ± 22.36 $keV\ cm^2$
α = 1.44 ± 0.19
K (keV cm^2)
r (kpc)

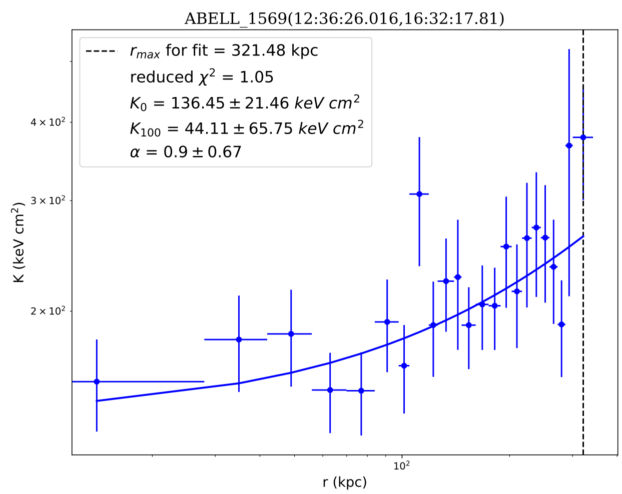
ABELL_1569(12:36:26.016,16:32:17.81)
r_{max} for fit = 321.48 kpc
reduced χ^2 = 1.05
K_0 = 136.45 ± 21.46 $keV\ cm^2$
K_{100} = 44.11 ± 65.75 $keV\ cm^2$
α = 0.9 ± 0.67
K (keV cm^2)
r (kpc)

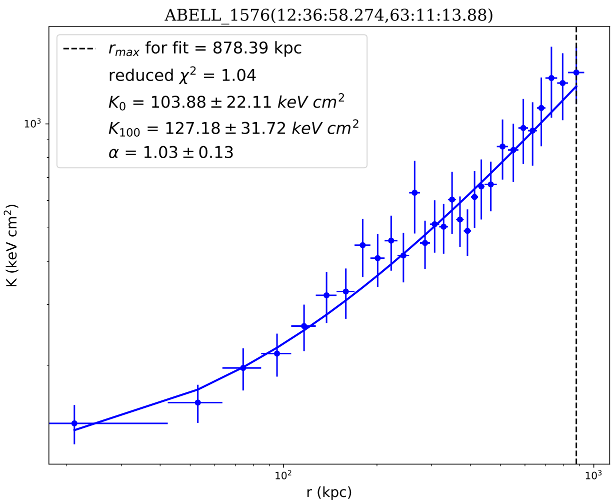
ABELL_1576(12:36:58.274,63:11:13.88)
r_{max} for fit = 878.39 kpc
reduced χ^2 = 1.04
K_0 = 103.88 ± 22.11 $keV\ cm^2$
K_{100} = 127.18 ± 31.72 $keV\ cm^2$
α = 1.03 ± 0.13
K (keV cm^2)
r (kpc)

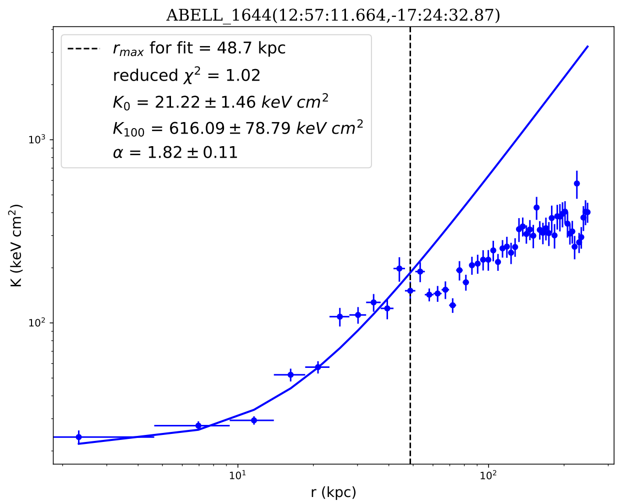
ABELL_1644(12:57:11.664,-17:24:32.87)
r_{max} for fit = 48.7 kpc
reduced χ^2 = 1.02
K_0 = 21.22 ± 1.46 $keV\ cm^2$
K_{100} = 616.09 ± 78.79 $keV\ cm^2$
α = 1.82 ± 0.11
K (keV cm^2)
r (kpc)

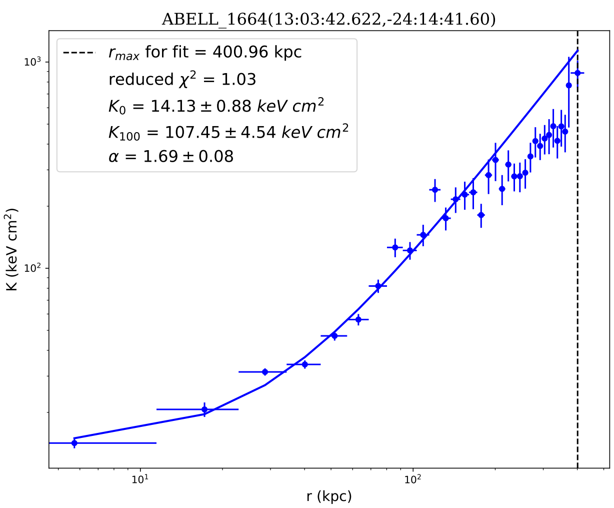
ABELL_1664(13:03:42.622,-24:14:41.60)
r_{max} for fit = 400.96 kpc
reduced χ^2 = 1.03
K_0 = 14.13 ± 0.88 $keV\ cm^2$
K_{100} = 107.45 ± 4.54 $keV\ cm^2$
α = 1.69 ± 0.08
K (keV cm^2)
r (kpc)

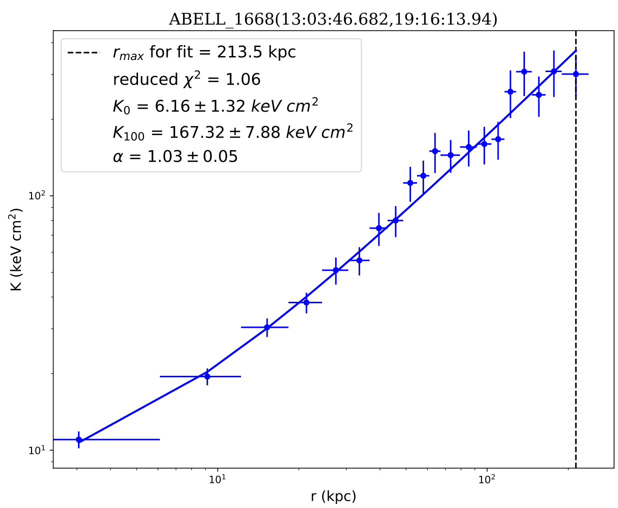
ABELL_1668(13:03:46.682,19:16:13.94)
r_{max} for fit = 213.5 kpc
reduced χ^2 = 1.06
K_0 = 6.16 ± 1.32 $keV\ cm^2$
K_{100} = 167.32 ± 7.88 $keV\ cm^2$
α = 1.03 ± 0.05
K (keV cm^2)
r (kpc)

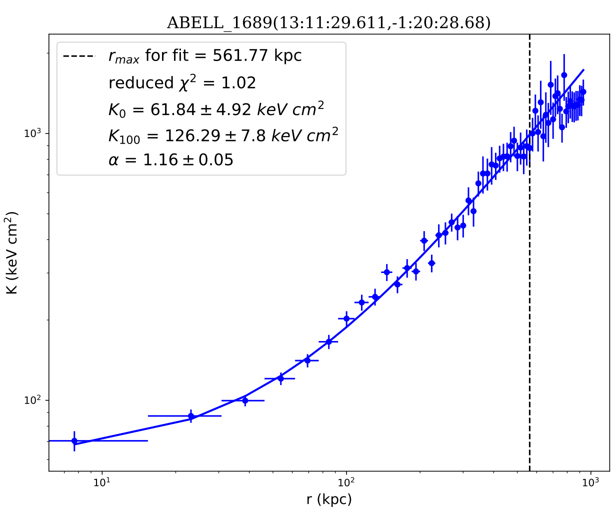
ABELL_1689(13:11:29.611,-1:20:28.68)
r_{max} for fit = 561.77 kpc
reduced χ^2 = 1.02
K_0 = 61.84 ± 4.92 $keV\ cm^2$
K_{100} = 126.29 ± 7.8 $keV\ cm^2$
α = 1.16 ± 0.05
K (keV cm^2)
r (kpc)

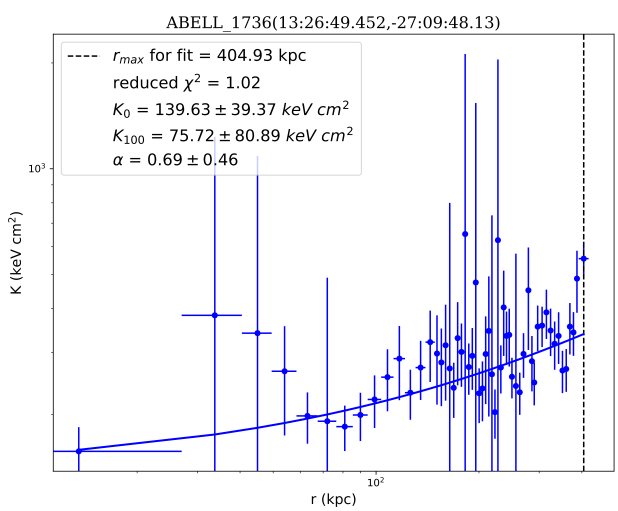
ABELL_1736(13:26:49.452,-27:09:48.13)
r_{max} for fit = 404.93 kpc
reduced χ^2 = 1.02
K_0 = 139.63 ± 39.37 $keV\ cm^2$
K_{100} = 75.72 ± 80.89 $keV\ cm^2$
α = 0.69 ± 0.46
K (keV cm^2)
r (kpc)

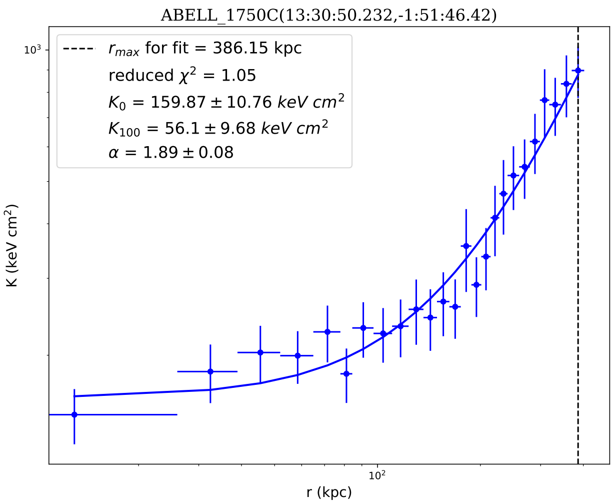
ABELL_1750C(13:30:50.232,-1:51:46.42)
r_{max} for fit = 386.15 kpc
reduced χ^2 = 1.05
K_0 = 159.87 ± 10.76 $keV\ cm^2$
K_{100} = 56.1 ± 9.68 $keV\ cm^2$
α = 1.89 ± 0.08
K (keV cm^2)
r (kpc)

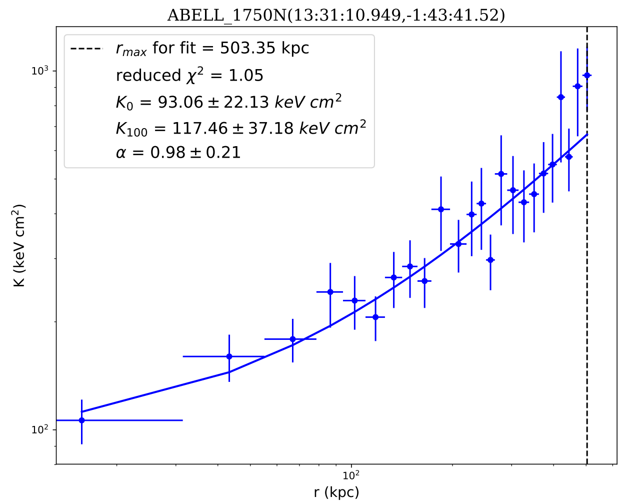
ABELL_1750N(13:31:10.949,-1:43:41.52)
r_{max} for fit = 503.35 kpc
reduced χ^2 = 1.05
K_0 = 93.06 ± 22.13 $keV\ cm^2$
K_{100} = 117.46 ± 37.18 $keV\ cm^2$
α = 0.98 ± 0.21
K (keV cm^2)
r (kpc)

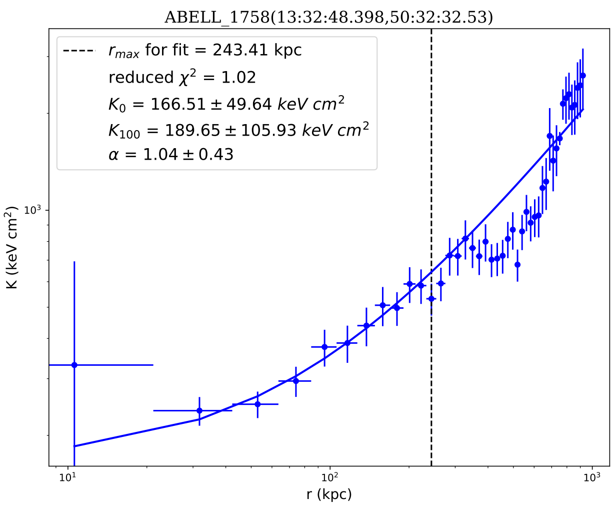
ABELL_1758(13:32:48.398,50:32:32.53)
r_{max} for fit = 243.41 kpc
reduced χ^2 = 1.02
K_0 = 166.51 ± 49.64 $keV\ cm^2$
K_{100} = 189.65 ± 105.93 $keV\ cm^2$
α = 1.04 ± 0.43
K (keV cm^2)
r (kpc)

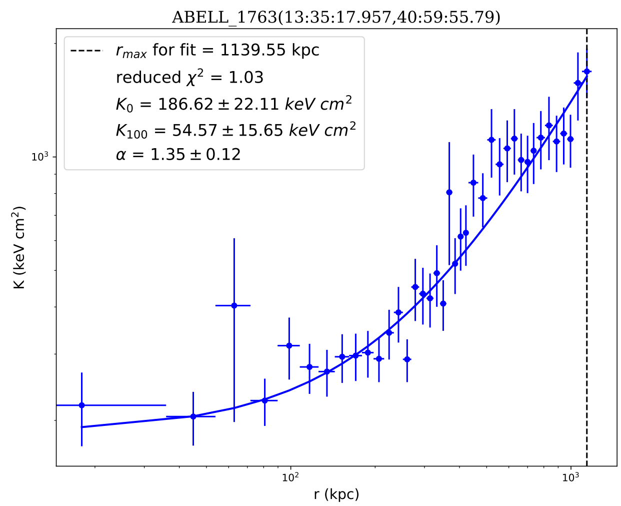
ABELL_1763(13:35:17.957,40:59:55.79)
r_{max} for fit = 1139.55 kpc
reduced χ^2 = 1.03
K_0 = 186.62 ± 22.11 $keV\ cm^2$
K_{100} = 54.57 ± 15.65 $keV\ cm^2$
α = 1.35 ± 0.12
K (keV cm^2)
r (kpc)

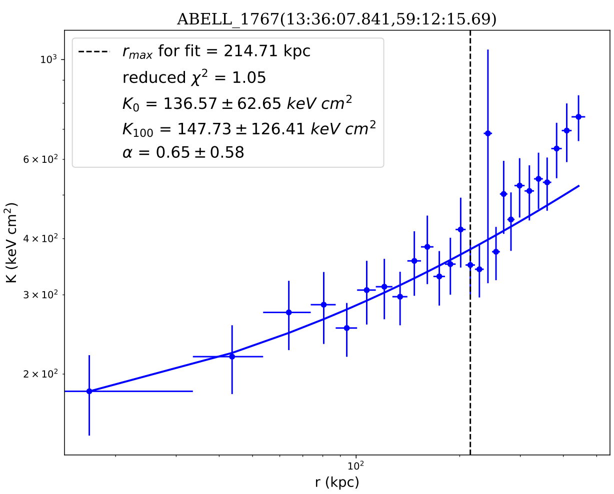
ABELL_1767(13:36:07.841,59:12:15.69)
r_{max} for fit = 214.71 kpc
reduced χ^2 = 1.05
K_0 = 136.57 ± 62.65 $keV\ cm^2$
K_{100} = 147.73 ± 126.41 $keV\ cm^2$
α = 0.65 ± 0.58
K (keV cm^2)
r (kpc)

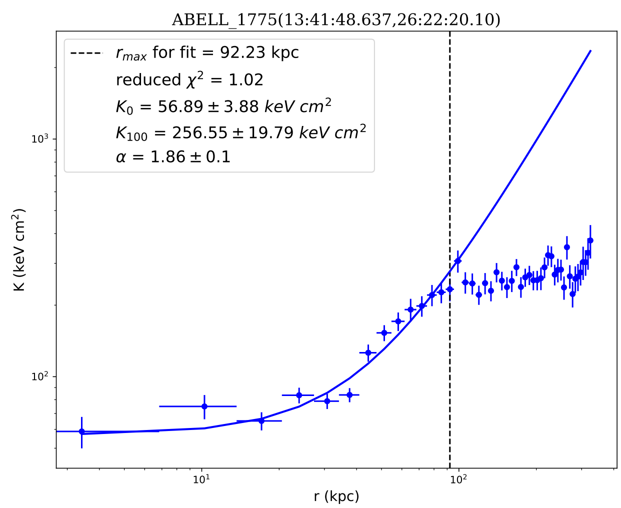
ABELL_1775(13:41:48.637,26:22:20.10)
r_{max} for fit = 92.23 kpc
reduced χ^2 = 1.02
K_0 = 56.89 ± 3.88 $keV\ cm^2$
K_{100} = 256.55 ± 19.79 $keV\ cm^2$
α = 1.86 ± 0.1
K (keV cm^2)
r (kpc)

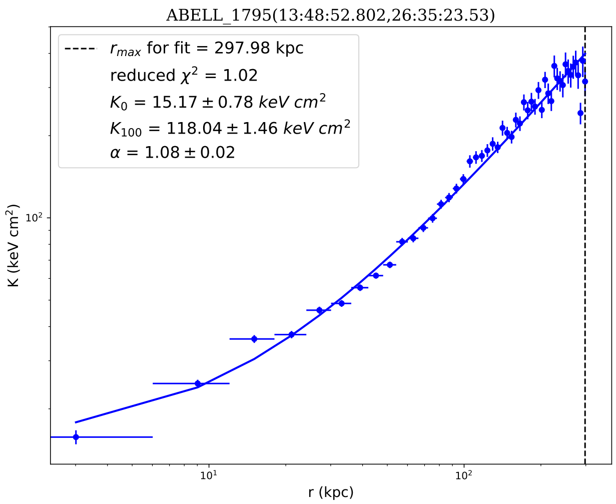
ABELL_1795(13:48:52.802,26:35:23.53)
r_{max} for fit = 297.98 kpc
reduced χ^2 = 1.02
K_0 = 15.17 ± 0.78 $keV\ cm^2$
K_{100} = 118.04 ± 1.46 $keV\ cm^2$
α = 1.08 ± 0.02
K (keV cm^2)
r (kpc)

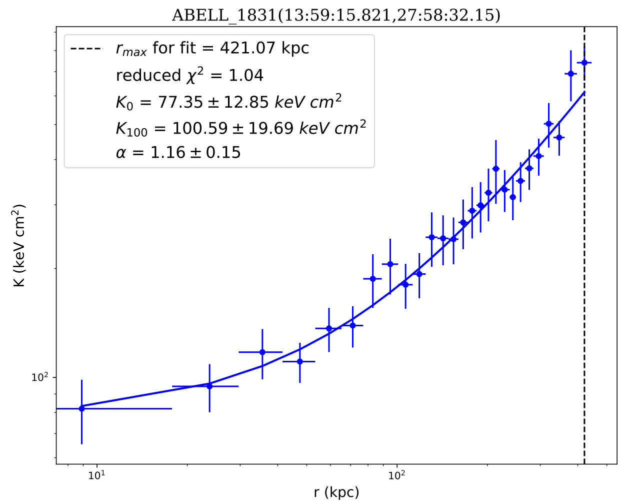
ABELL_1831(13:59:15.821,27:58:32.15)
r_{max} for fit = 421.07 kpc
reduced χ^2 = 1.04
K_0 = 77.35 ± 12.85 $keV\ cm^2$
K_{100} = 100.59 ± 19.69 $keV\ cm^2$
α = 1.16 ± 0.15
K (keV cm^2)
r (kpc)

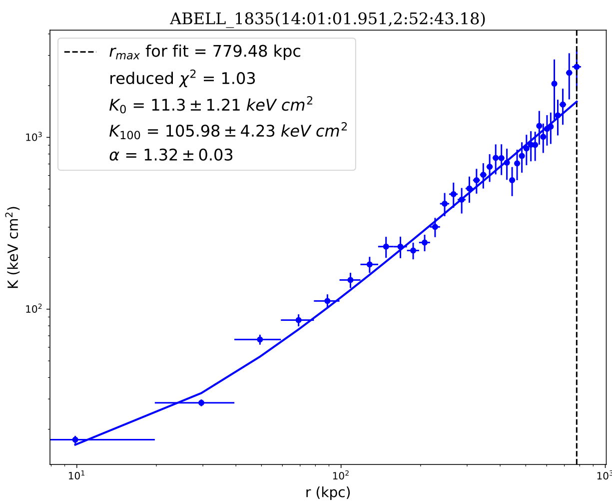
ABELL_1835(14:01:01.951,2:52:43.18)
r_{max} for fit = 779.48 kpc
reduced χ^2 = 1.03
K_0 = 11.3 ± 1.21 $keV\ cm^2$
K_{100} = 105.98 ± 4.23 $keV\ cm^2$
α = 1.32 ± 0.03
K (keV cm^2)
r (kpc)

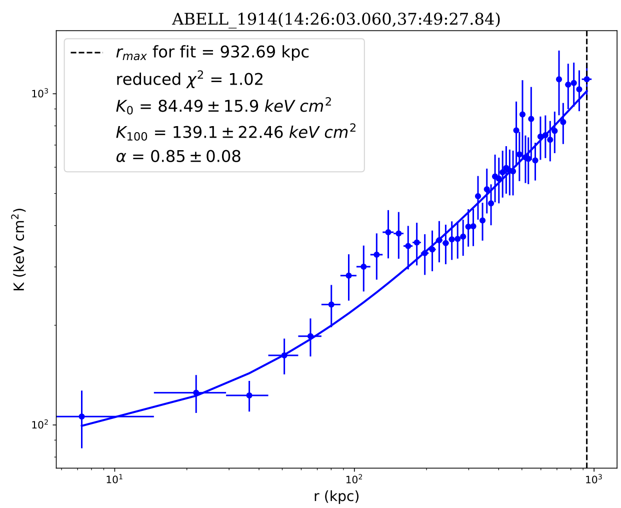
ABELL_1914(14:26:03.060,37:49:27.84)
r_{max} for fit = 932.69 kpc
reduced χ^2 = 1.02
K_0 = 84.49 ± 15.9 $keV\ cm^2$
K_{100} = 139.1 ± 22.46 $keV\ cm^2$
α = 0.85 ± 0.08
K (keV cm^2)
r (kpc)

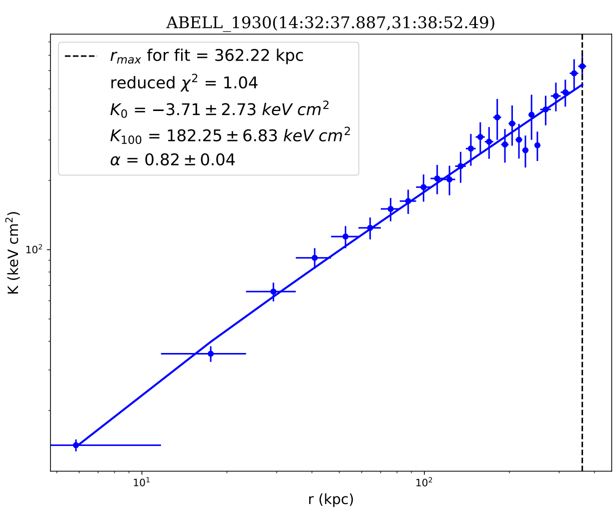
ABELL_1930(14:32:37.887,31:38:52.49)
r_{max} for fit = 362.22 kpc
reduced χ^2 = 1.04
K_0 = −3.71 ± 2.73 $keV\ cm^2$
K_{100} = 182.25 ± 6.83 $keV\ cm^2$
α = 0.82 ± 0.04
K (keV cm^2)
r (kpc)

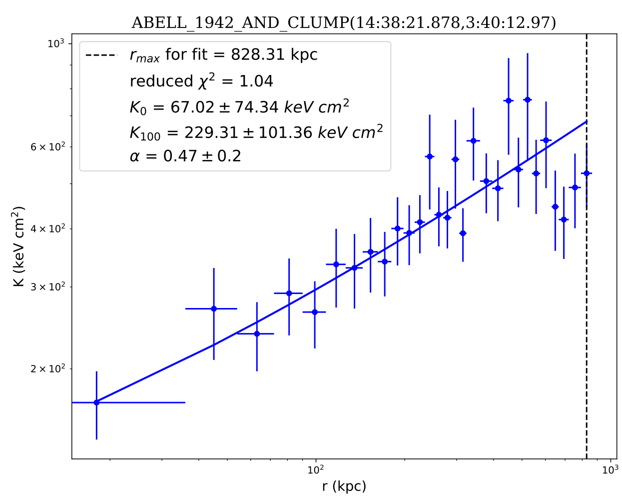
ABELL_1942_AND_CLUMP(14:38:21.878,3:40:12.97)
r_{max} for fit = 828.31 kpc
reduced χ^2 = 1.04
K_0 = 67.02 ± 74.34 $keV\ cm^2$
K_{100} = 229.31 ± 101.36 $keV\ cm^2$
α = 0.47 ± 0.2
K (keV cm^2)
r (kpc)

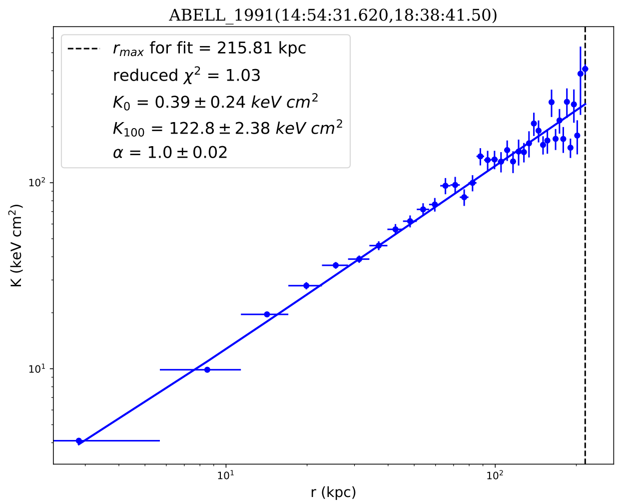
ABELL_1991(14:54:31.620,18:38:41.50)
r_{max} for fit = 215.81 kpc
reduced χ^2 = 1.03
K_0 = 0.39 ± 0.24 $keV\ cm^2$
K_{100} = 122.8 ± 2.38 $keV\ cm^2$
α = 1.0 ± 0.02
K (keV cm^2)
r (kpc)

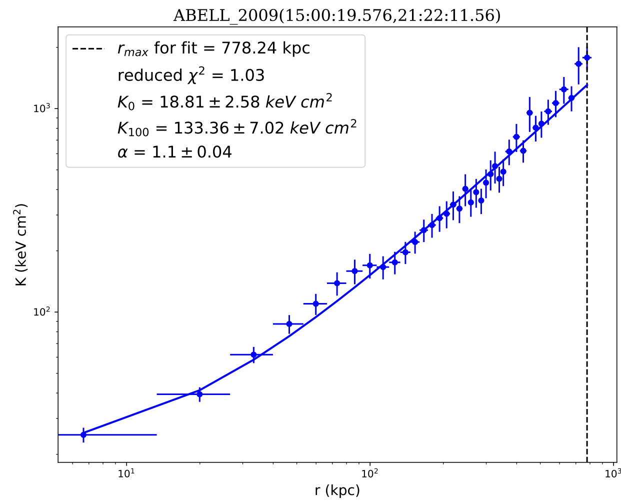
ABELL_2009(15:00:19.576,21:22:11.56)
r_{max} for fit = 778.24 kpc
reduced χ^2 = 1.03
K_0 = 18.81 ± 2.58 $keV\ cm^2$
K_{100} = 133.36 ± 7.02 $keV\ cm^2$
α = 1.1 ± 0.04
K (keV cm^2)
r (kpc)

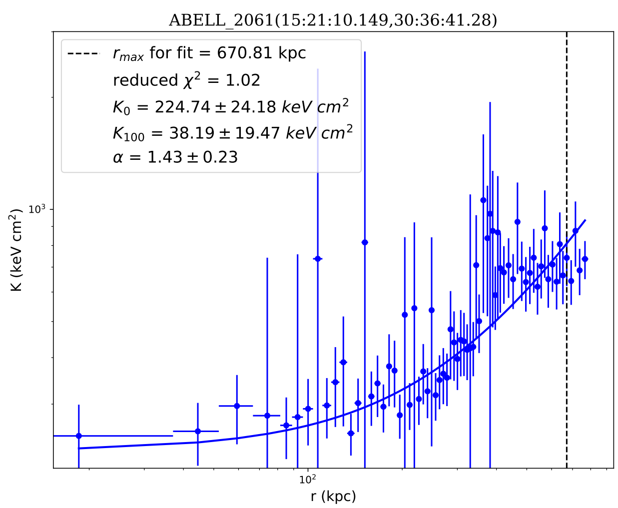
ABELL_2061(15:21:10.149,30:36:41.28)
r_{max} for fit = 670.81 kpc
reduced χ^2 = 1.02
K_0 = 224.74 ± 24.18 $keV\ cm^2$
K_{100} = 38.19 ± 19.47 $keV\ cm^2$
α = 1.43 ± 0.23
K (keV cm^2)
r (kpc)

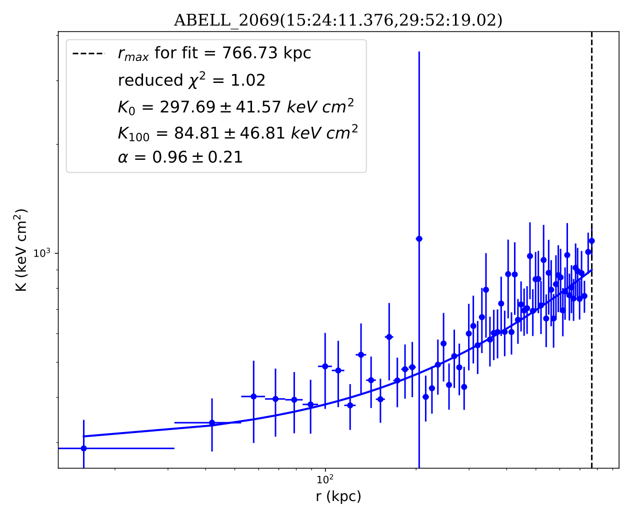
ABELL_2069(15:24:11.376,29:52:19.02)
r_{max} for fit = 766.73 kpc
reduced χ^2 = 1.02
K_0 = 297.69 ± 41.57 $keV\ cm^2$
K_{100} = 84.81 ± 46.81 $keV\ cm^2$
α = 0.96 ± 0.21
K (keV cm^2)
r (kpc)

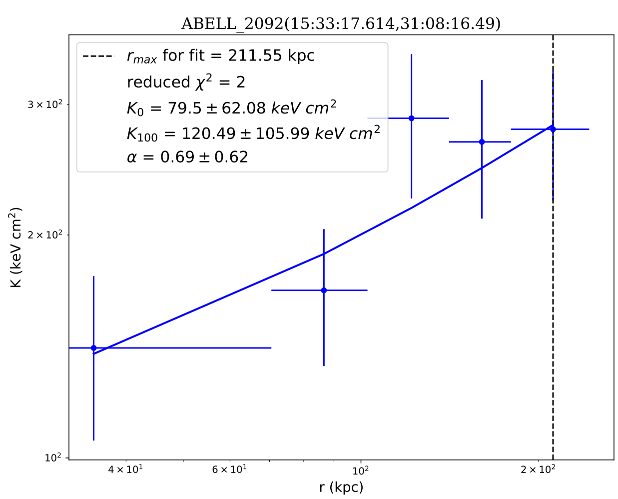
ABELL_2092(15:33:17.614,31:08:16.49)
r_{max} for fit = 211.55 kpc
reduced χ^2 = 2
K_0 = 79.5 ± 62.08 $keV\ cm^2$
K_{100} = 120.49 ± 105.99 $keV\ cm^2$
α = 0.69 ± 0.62
K (keV cm^2)
r (kpc)

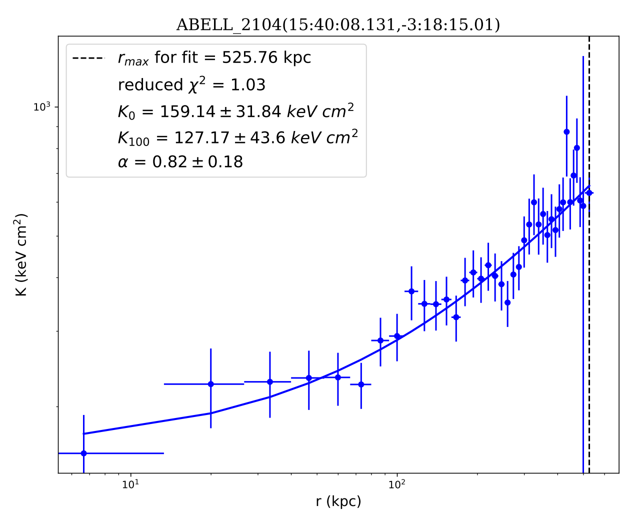
ABELL_2104(15:40:08.131,-3:18:15.01)
r_{max} for fit = 525.76 kpc
reduced χ^2 = 1.03
K_0 = 159.14 ± 31.84 $keV\ cm^2$
K_{100} = 127.17 ± 43.6 $keV\ cm^2$
α = 0.82 ± 0.18
K (keV cm^2)
r (kpc)

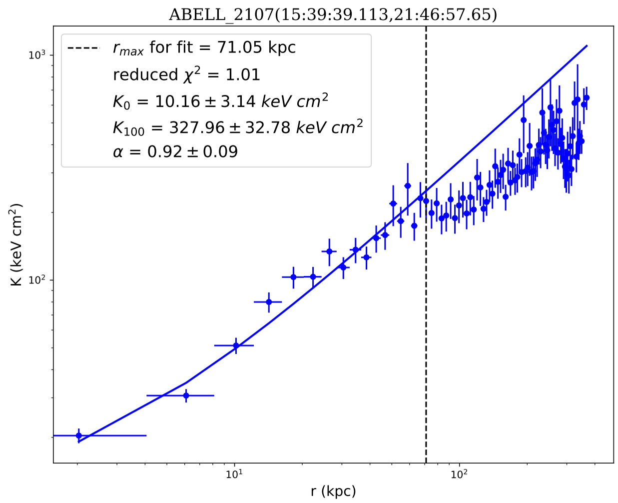

ABELL_2107(15:39:39.113,21:46:57.65)
r_{max} for fit = 71.05 kpc
reduced χ^2 = 1.01
$K_0 = 10.16 \pm 3.14\ keV\ cm^2$
$K_{100} = 327.96 \pm 32.78\ keV\ cm^2$
$\alpha = 0.92 \pm 0.09$
K (keV cm^2)
r (kpc)

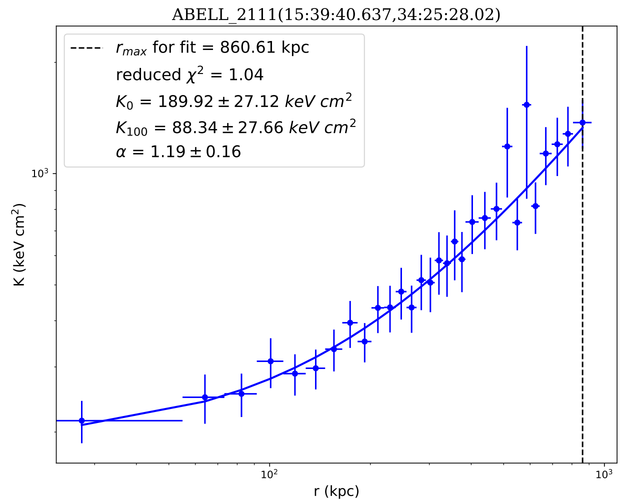

ABELL_2111(15:39:40.637,34:25:28.02)
r_{max} for fit = 860.61 kpc
reduced χ^2 = 1.04
$K_0 = 189.92 \pm 27.12\ keV\ cm^2$
$K_{100} = 88.34 \pm 27.66\ keV\ cm^2$
$\alpha = 1.19 \pm 0.16$
K (keV cm^2)
r (kpc)

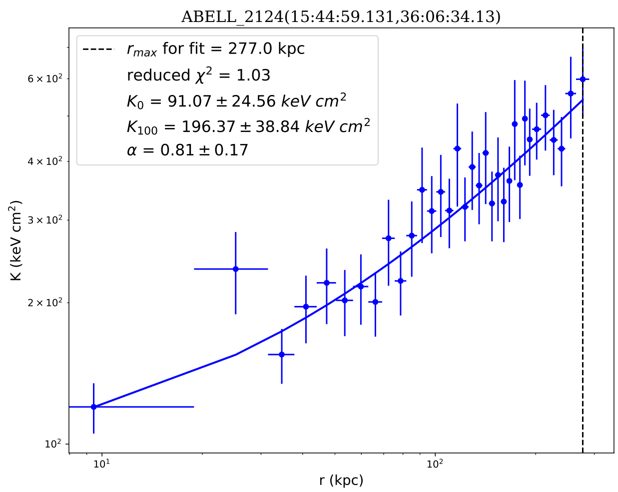

ABELL_2124(15:44:59.131,36:06:34.13)
r_{max} for fit = 277.0 kpc
reduced χ^2 = 1.03
$K_0 = 91.07 \pm 24.56\ keV\ cm^2$
$K_{100} = 196.37 \pm 38.84\ keV\ cm^2$
$\alpha = 0.81 \pm 0.17$
K (keV cm^2)
r (kpc)

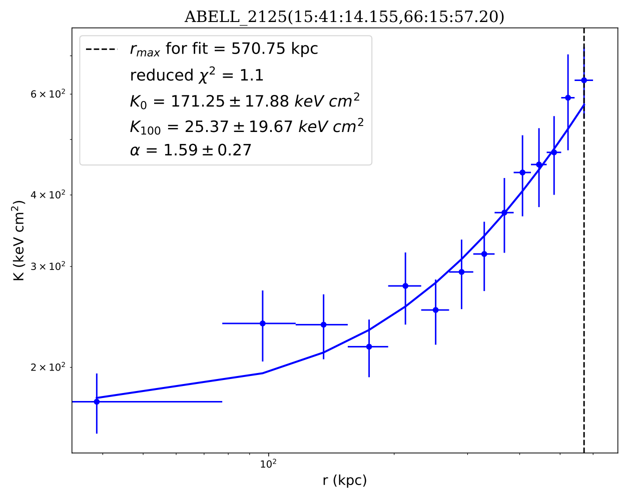

ABELL_2125(15:41:14.155,66:15:57.20)
r_{max} for fit = 570.75 kpc
reduced χ^2 = 1.1
$K_0 = 171.25 \pm 17.88\ keV\ cm^2$
$K_{100} = 25.37 \pm 19.67\ keV\ cm^2$
$\alpha = 1.59 \pm 0.27$
K (keV cm^2)
r (kpc)

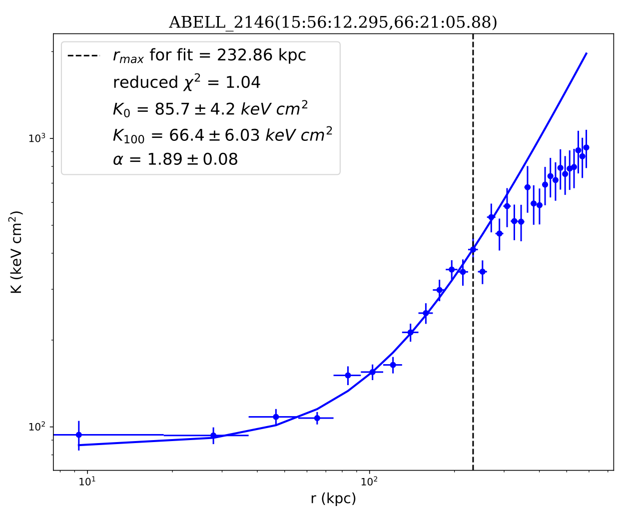

ABELL_2146(15:56:12.295,66:21:05.88)
r_{max} for fit = 232.86 kpc
reduced χ^2 = 1.04
$K_0 = 85.7 \pm 4.2\ keV\ cm^2$
$K_{100} = 66.4 \pm 6.03\ keV\ cm^2$
$\alpha = 1.89 \pm 0.08$
K (keV cm^2)
r (kpc)

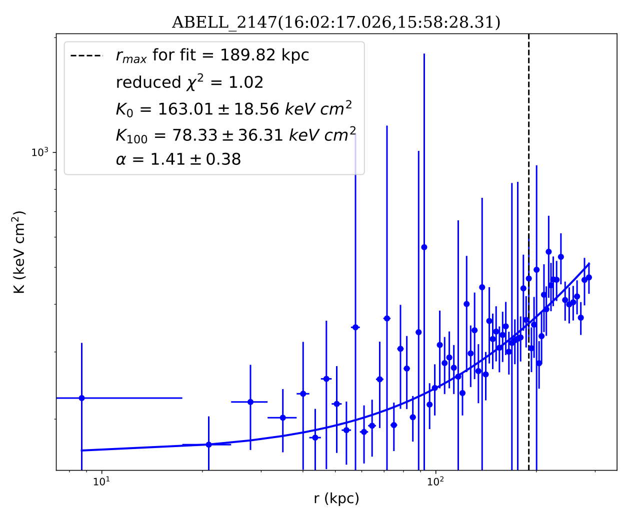

ABELL_2147(16:02:17.026,15:58:28.31)
r_{max} for fit = 189.82 kpc
reduced χ^2 = 1.02
$K_0 = 163.01 \pm 18.56\ keV\ cm^2$
$K_{100} = 78.33 \pm 36.31\ keV\ cm^2$
$\alpha = 1.41 \pm 0.38$
K (keV cm^2)
r (kpc)

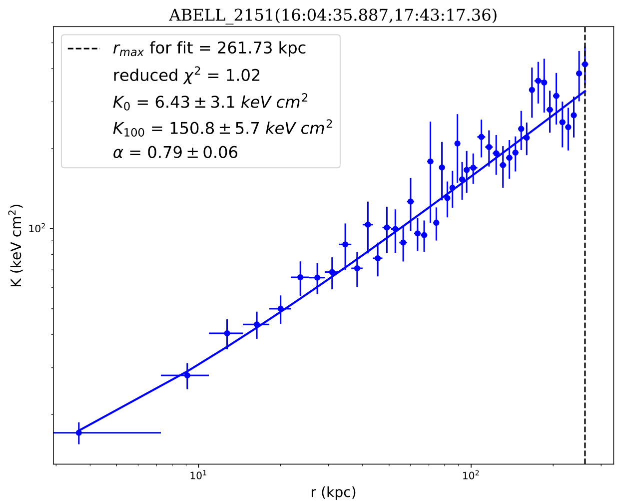
ABELL_2151(16:04:35.887,17:43:17.36)
r_{max} for fit = 261.73 kpc
reduced χ^2 = 1.02
K_0 = 6.43 ± 3.1 $keV\ cm^2$
K_{100} = 150.8 ± 5.7 $keV\ cm^2$
α = 0.79 ± 0.06
K (keV cm^2)
r (kpc)

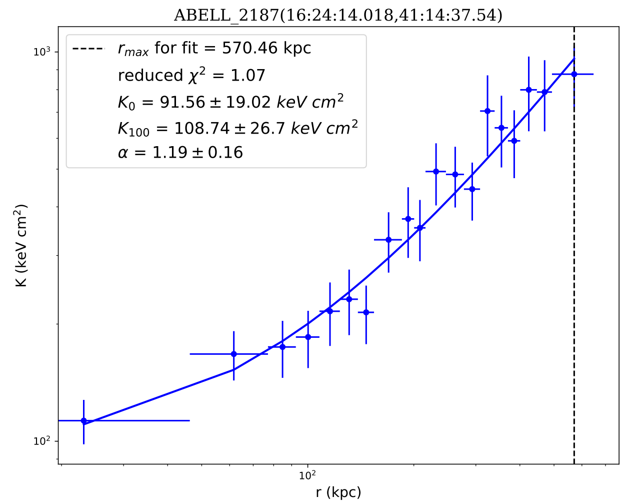
ABELL_2187(16:24:14.018,41:14:37.54)
r_{max} for fit = 570.46 kpc
reduced χ^2 = 1.07
K_0 = 91.56 ± 19.02 $keV\ cm^2$
K_{100} = 108.74 ± 26.7 $keV\ cm^2$
α = 1.19 ± 0.16
K (keV cm^2)
r (kpc)

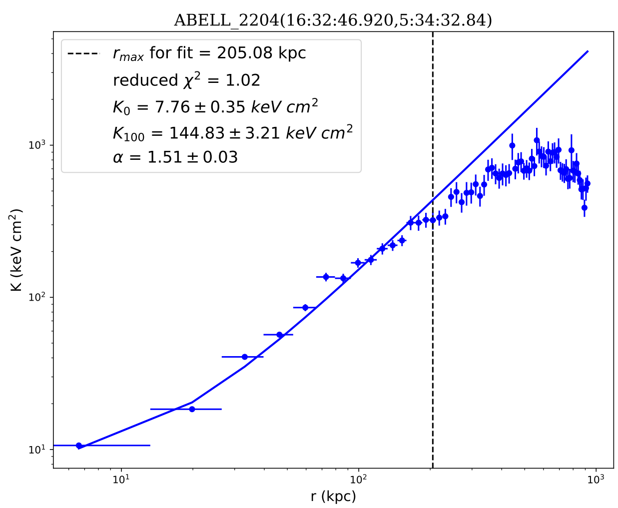
ABELL_2204(16:32:46.920,5:34:32.84)
r_{max} for fit = 205.08 kpc
reduced χ^2 = 1.02
K_0 = 7.76 ± 0.35 $keV\ cm^2$
K_{100} = 144.83 ± 3.21 $keV\ cm^2$
α = 1.51 ± 0.03
K (keV cm^2)
r (kpc)

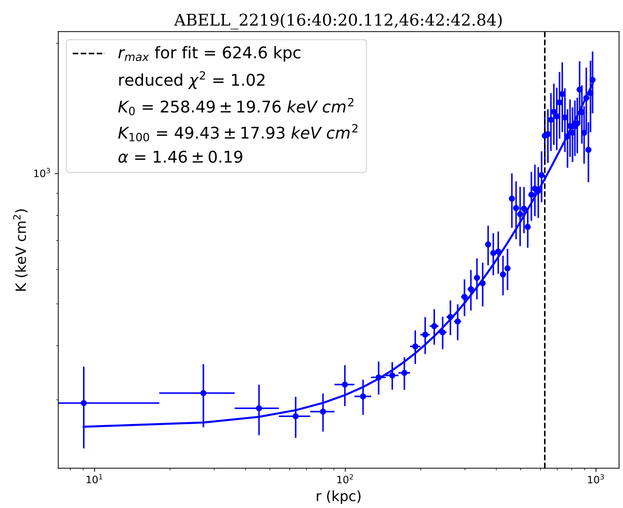
ABELL_2219(16:40:20.112,46:42:42.84)
r_{max} for fit = 624.6 kpc
reduced χ^2 = 1.02
K_0 = 258.49 ± 19.76 $keV\ cm^2$
K_{100} = 49.43 ± 17.93 $keV\ cm^2$
α = 1.46 ± 0.19
K (keV cm^2)
r (kpc)

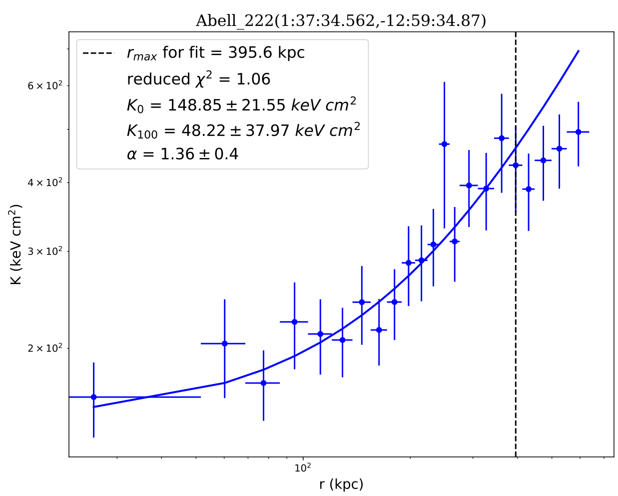
Abell_222(1:37:34.562,-12:59:34.87)
r_{max} for fit = 395.6 kpc
reduced χ^2 = 1.06
K_0 = 148.85 ± 21.55 $keV\ cm^2$
K_{100} = 48.22 ± 37.97 $keV\ cm^2$
α = 1.36 ± 0.4
K (keV cm^2)
r (kpc)

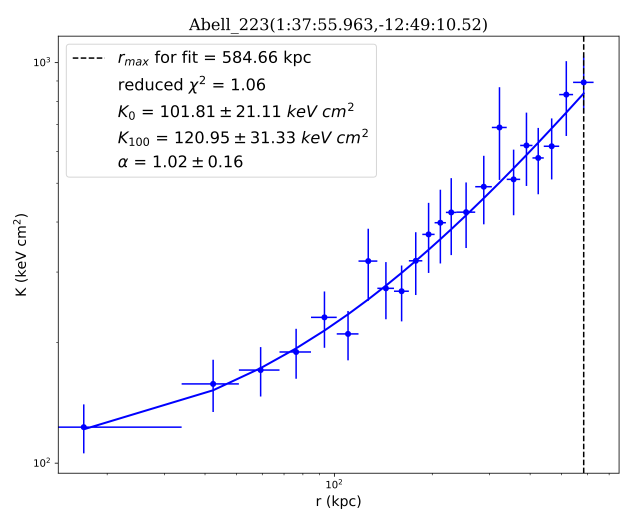
Abell_223(1:37:55.963,-12:49:10.52)
r_{max} for fit = 584.66 kpc
reduced χ^2 = 1.06
K_0 = 101.81 ± 21.11 $keV\ cm^2$
K_{100} = 120.95 ± 31.33 $keV\ cm^2$
α = 1.02 ± 0.16
K (keV cm^2)
r (kpc)

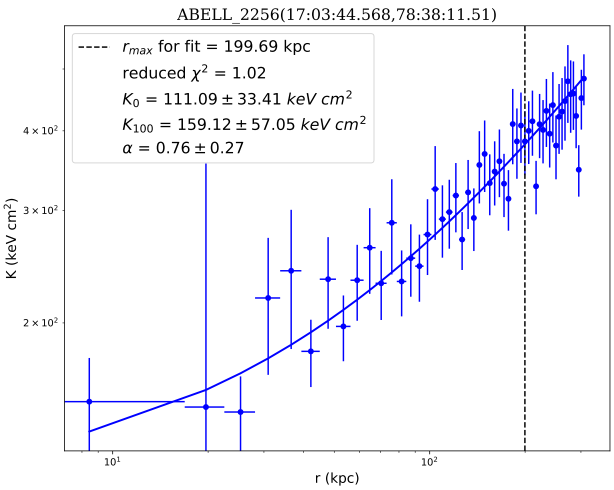
ABELL_2256(17:03:44.568,78:38:11.51)
r_{max} for fit = 199.69 kpc
reduced χ^2 = 1.02
K_0 = 111.09 ± 33.41 $keV\ cm^2$
K_{100} = 159.12 ± 57.05 $keV\ cm^2$
α = 0.76 ± 0.27
K (keV cm^2)
r (kpc)

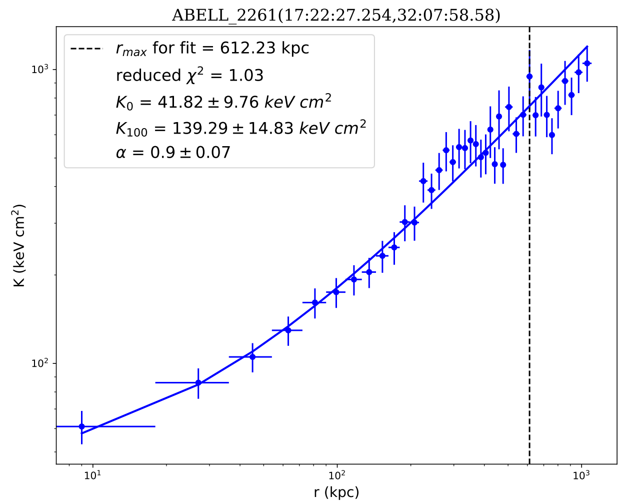
ABELL_2261(17:22:27.254,32:07:58.58)
r_{max} for fit = 612.23 kpc
reduced χ^2 = 1.03
K_0 = 41.82 ± 9.76 $keV\ cm^2$
K_{100} = 139.29 ± 14.83 $keV\ cm^2$
α = 0.9 ± 0.07
K (keV cm^2)
r (kpc)

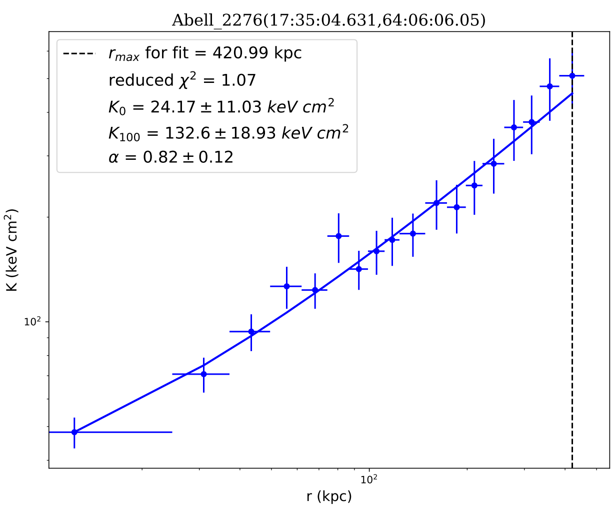
Abell_2276(17:35:04.631,64:06:06.05)
r_{max} for fit = 420.99 kpc
reduced χ^2 = 1.07
K_0 = 24.17 ± 11.03 $keV\ cm^2$
K_{100} = 132.6 ± 18.93 $keV\ cm^2$
α = 0.82 ± 0.12
K (keV cm^2)
r (kpc)

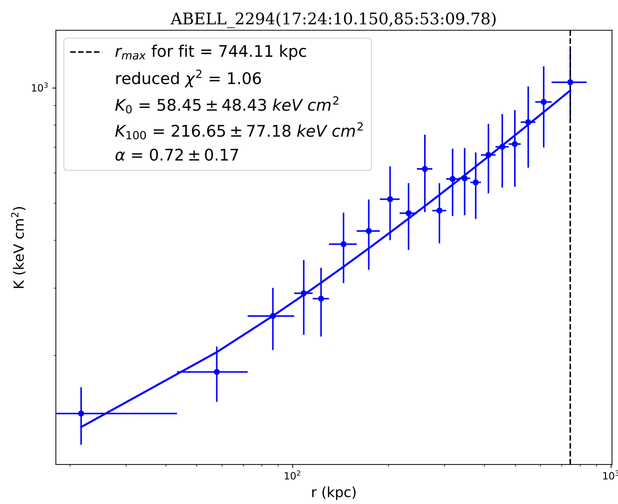
ABELL_2294(17:24:10.150,85:53:09.78)
r_{max} for fit = 744.11 kpc
reduced χ^2 = 1.06
K_0 = 58.45 ± 48.43 $keV\ cm^2$
K_{100} = 216.65 ± 77.18 $keV\ cm^2$
α = 0.72 ± 0.17
K (keV cm^2)
r (kpc)

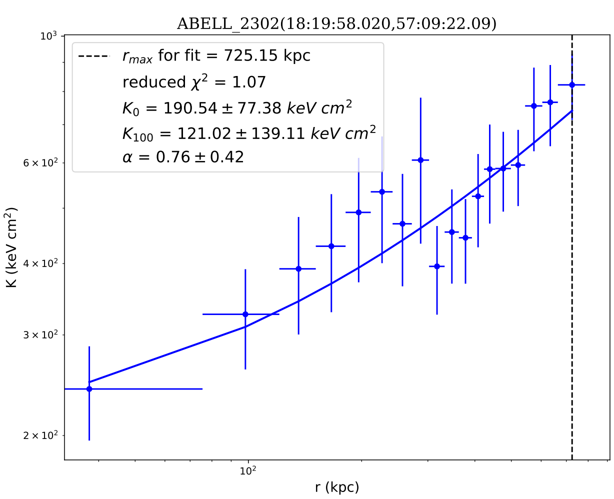
ABELL_2302(18:19:58.020,57:09:22.09)
r_{max} for fit = 725.15 kpc
reduced χ^2 = 1.07
K_0 = 190.54 ± 77.38 $keV\ cm^2$
K_{100} = 121.02 ± 139.11 $keV\ cm^2$
α = 0.76 ± 0.42
K (keV cm^2)
r (kpc)

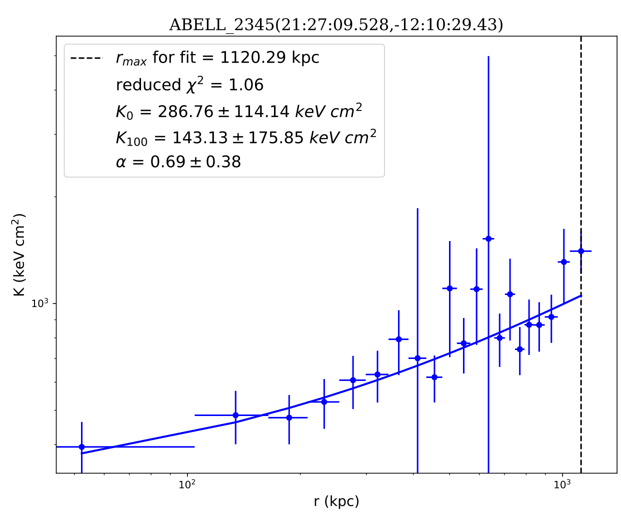
ABELL_2345(21:27:09.528,-12:10:29.43)
r_{max} for fit = 1120.29 kpc
reduced χ^2 = 1.06
K_0 = 286.76 ± 114.14 $keV\ cm^2$
K_{100} = 143.13 ± 175.85 $keV\ cm^2$
α = 0.69 ± 0.38
K (keV cm^2)
r (kpc)

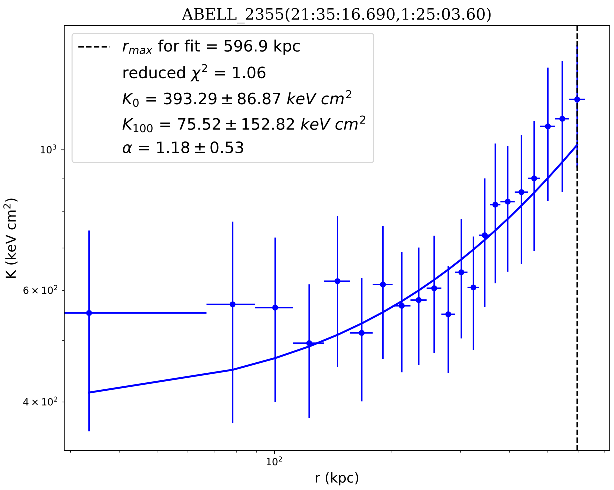
ABELL_2355(21:35:16.690,1:25:03.60)
r_{max} for fit = 596.9 kpc
reduced χ^2 = 1.06
K_0 = 393.29 ± 86.87 $keV\ cm^2$
K_{100} = 75.52 ± 152.82 $keV\ cm^2$
α = 1.18 ± 0.53
K (keV cm^2)
r (kpc)

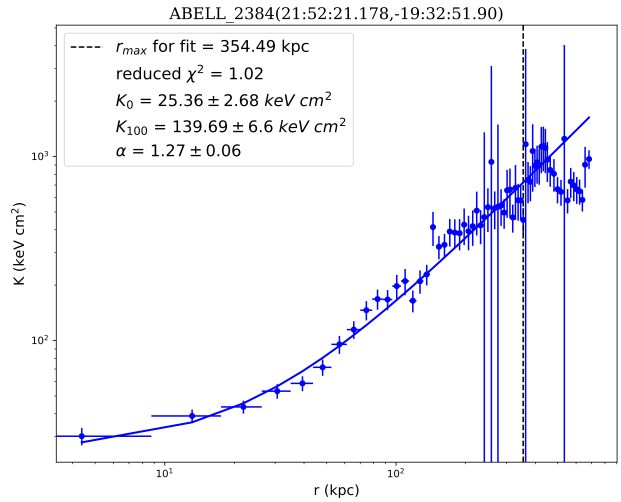
ABELL_2384(21:52:21.178,-19:32:51.90)
r_{max} for fit = 354.49 kpc
reduced χ^2 = 1.02
K_0 = 25.36 ± 2.68 $keV\ cm^2$
K_{100} = 139.69 ± 6.6 $keV\ cm^2$
α = 1.27 ± 0.06
K (keV cm^2)
r (kpc)

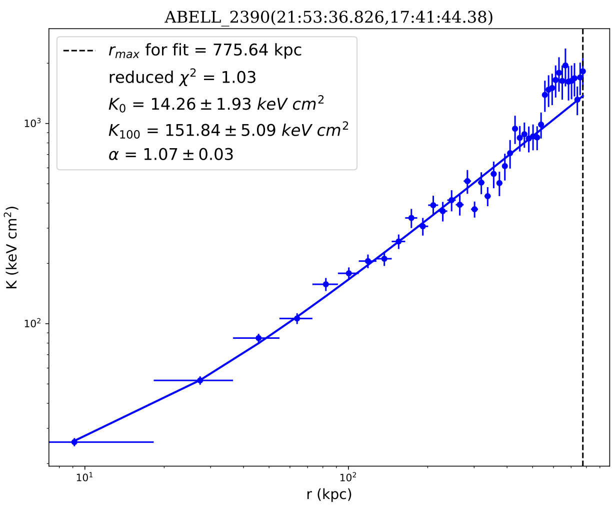
ABELL_2390(21:53:36.826,17:41:44.38)
r_{max} for fit = 775.64 kpc
reduced χ^2 = 1.03
K_0 = 14.26 ± 1.93 $keV\ cm^2$
K_{100} = 151.84 ± 5.09 $keV\ cm^2$
α = 1.07 ± 0.03
K (keV cm^2)
r (kpc)

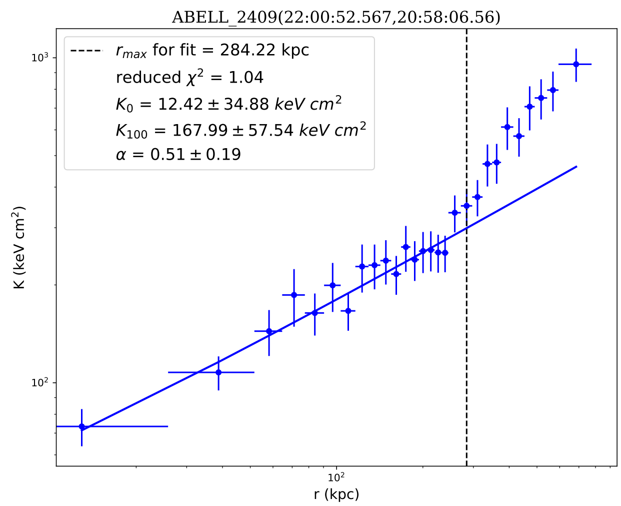
ABELL_2409(22:00:52.567,20:58:06.56)
r_{max} for fit = 284.22 kpc
reduced χ^2 = 1.04
K_0 = 12.42 ± 34.88 $keV\ cm^2$
K_{100} = 167.99 ± 57.54 $keV\ cm^2$
α = 0.51 ± 0.19
K (keV cm^2)
r (kpc)

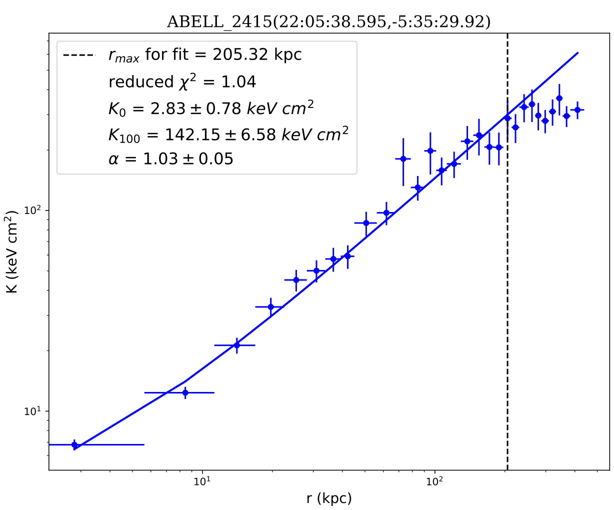
ABELL_2415(22:05:38.595,-5:35:29.92)
r_{max} for fit = 205.32 kpc
reduced χ^2 = 1.04
K_0 = 2.83 ± 0.78 $keV\ cm^2$
K_{100} = 142.15 ± 6.58 $keV\ cm^2$
α = 1.03 ± 0.05
K (keV cm^2)
r (kpc)

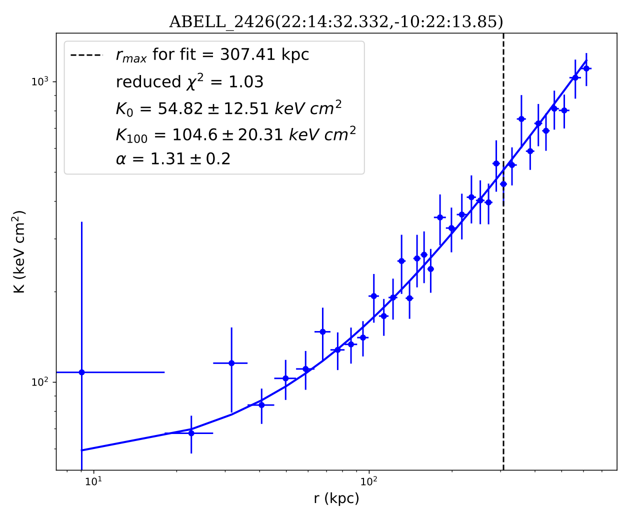
ABELL_2426(22:14:32.332,-10:22:13.85)
r_{max} for fit = 307.41 kpc
reduced χ^2 = 1.03
K_0 = 54.82 ± 12.51 $keV\ cm^2$
K_{100} = 104.6 ± 20.31 $keV\ cm^2$
α = 1.31 ± 0.2
K (keV cm^2)
r (kpc)

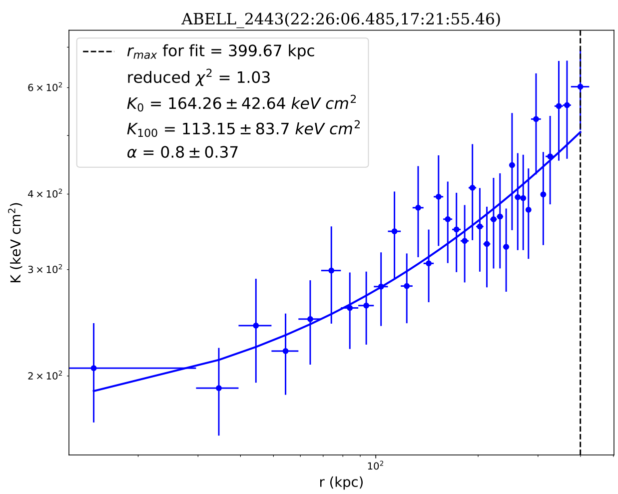
ABELL_2443(22:26:06.485,17:21:55.46)
r_{max} for fit = 399.67 kpc
reduced χ^2 = 1.03
K_0 = 164.26 ± 42.64 $keV\ cm^2$
K_{100} = 113.15 ± 83.7 $keV\ cm^2$
α = 0.8 ± 0.37
K (keV cm^2)
r (kpc)

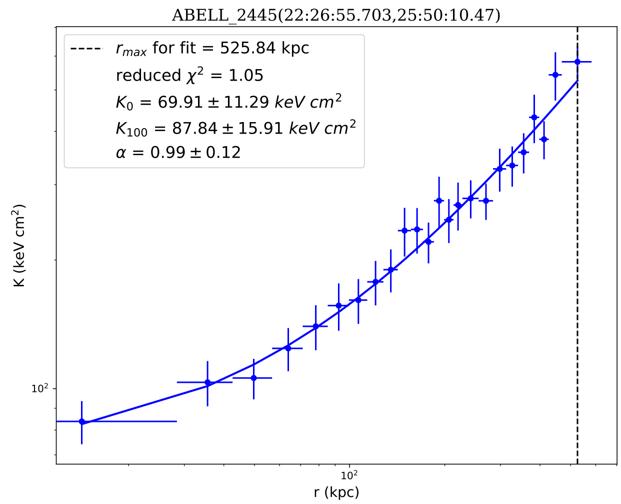
ABELL_2445(22:26:55.703,25:50:10.47)
r_{max} for fit = 525.84 kpc
reduced χ^2 = 1.05
K_0 = 69.91 ± 11.29 $keV\ cm^2$
K_{100} = 87.84 ± 15.91 $keV\ cm^2$
α = 0.99 ± 0.12
K (keV cm^2)
r (kpc)

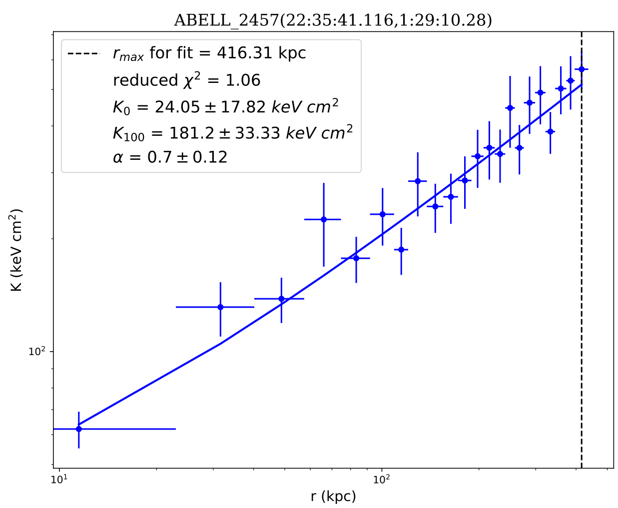
ABELL_2457(22:35:41.116,1:29:10.28)
r_{max} for fit = 416.31 kpc
reduced χ^2 = 1.06
K_0 = 24.05 ± 17.82 $keV\ cm^2$
K_{100} = 181.2 ± 33.33 $keV\ cm^2$
α = 0.7 ± 0.12
K (keV cm^2)
r (kpc)

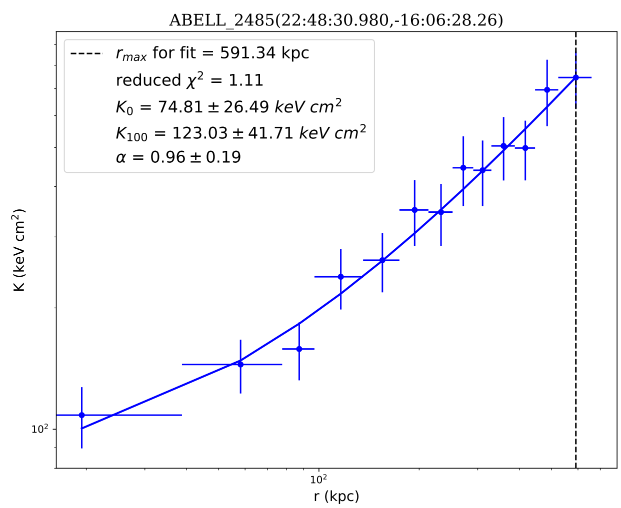
ABELL_2485(22:48:30.980,-16:06:28.26)
r_{max} for fit = 591.34 kpc
reduced χ^2 = 1.11
K_0 = 74.81 ± 26.49 $keV\ cm^2$
K_{100} = 123.03 ± 41.71 $keV\ cm^2$
α = 0.96 ± 0.19
K (keV cm^2)
r (kpc)

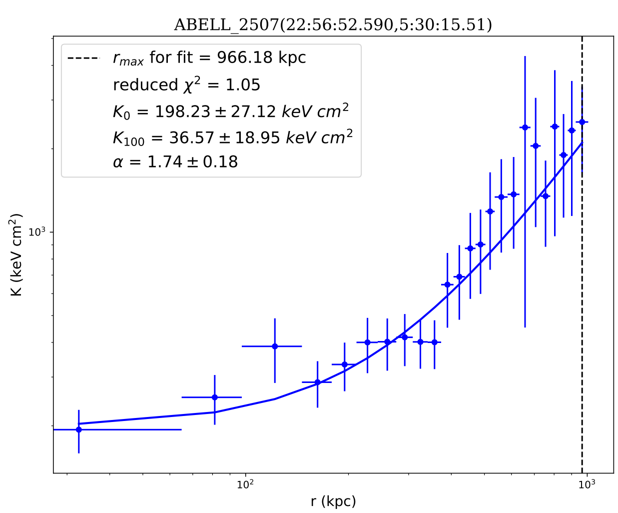
ABELL_2507(22:56:52.590,5:30:15.51)
r_{max} for fit = 966.18 kpc
reduced χ^2 = 1.05
K_0 = 198.23 ± 27.12 $keV\ cm^2$
K_{100} = 36.57 ± 18.95 $keV\ cm^2$
α = 1.74 ± 0.18
K (keV cm^2)
r (kpc)

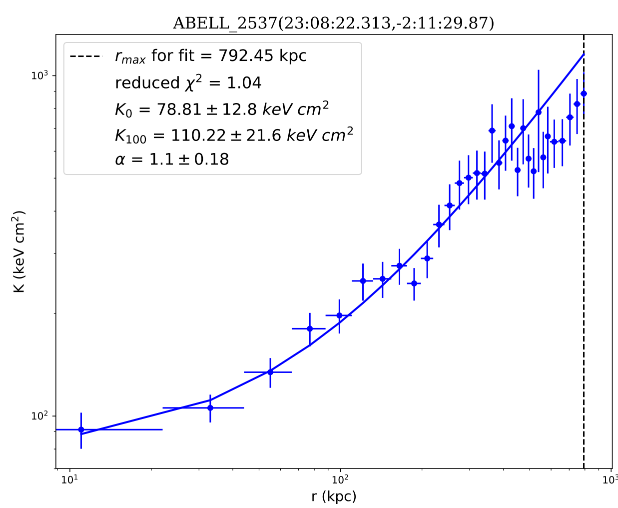
ABELL_2537(23:08:22.313,-2:11:29.87)
r_{max} for fit = 792.45 kpc
reduced χ^2 = 1.04
K_0 = 78.81 ± 12.8 $keV\ cm^2$
K_{100} = 110.22 ± 21.6 $keV\ cm^2$
α = 1.1 ± 0.18
K (keV cm^2)
r (kpc)

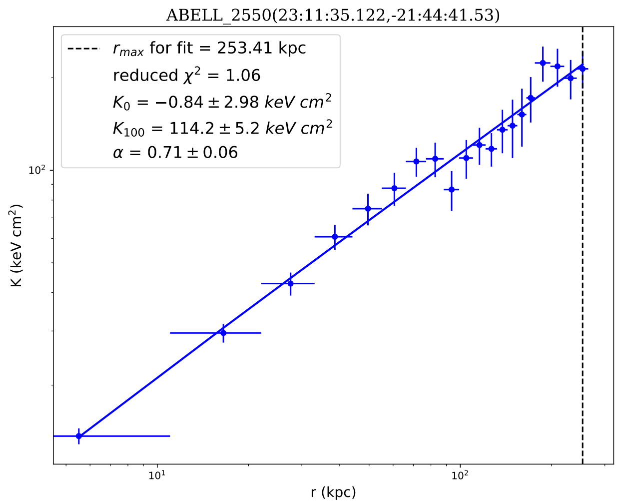
ABELL_2550(23:11:35.122,-21:44:41.53)
r_{max} for fit = 253.41 kpc
reduced χ^2 = 1.06
K_0 = -0.84 ± 2.98 $keV\ cm^2$
K_{100} = 114.2 ± 5.2 $keV\ cm^2$
α = 0.71 ± 0.06
K (keV cm^2)
r (kpc)

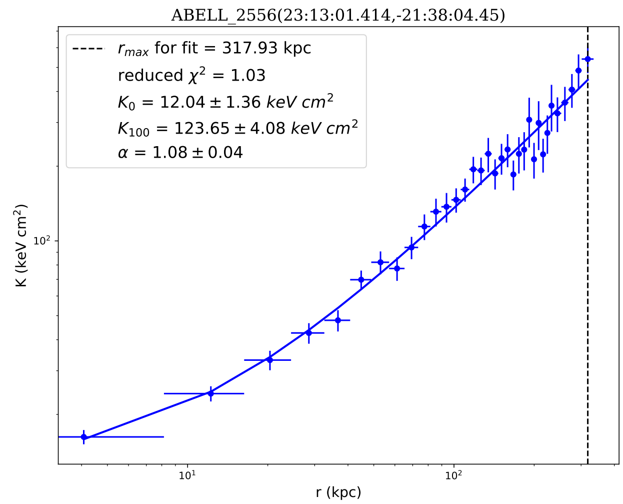
ABELL_2556(23:13:01.414,-21:38:04.45)
r_{max} for fit = 317.93 kpc
reduced χ^2 = 1.03
K_0 = 12.04 ± 1.36 $keV\ cm^2$
K_{100} = 123.65 ± 4.08 $keV\ cm^2$
α = 1.08 ± 0.04
K (keV cm^2)
r (kpc)

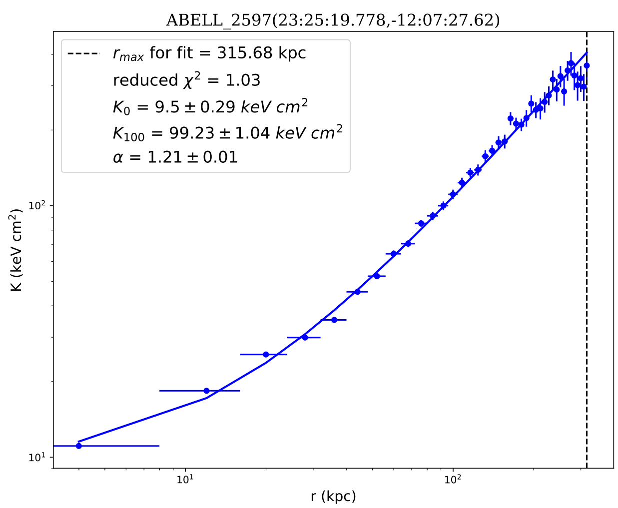
ABELL_2597(23:25:19.778,-12:07:27.62)
r_{max} for fit = 315.68 kpc
reduced χ^2 = 1.03
K_0 = 9.5 ± 0.29 $keV\ cm^2$
K_{100} = 99.23 ± 1.04 $keV\ cm^2$
α = 1.21 ± 0.01
K (keV cm^2)
r (kpc)

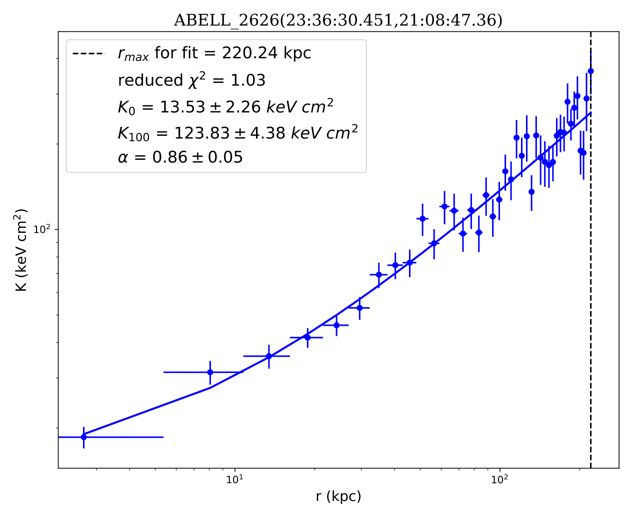
ABELL_2626(23:36:30.451,21:08:47.36)
r_{max} for fit = 220.24 kpc
reduced χ^2 = 1.03
K_0 = 13.53 ± 2.26 $keV\ cm^2$
K_{100} = 123.83 ± 4.38 $keV\ cm^2$
α = 0.86 ± 0.05
K (keV cm^2)
r (kpc)

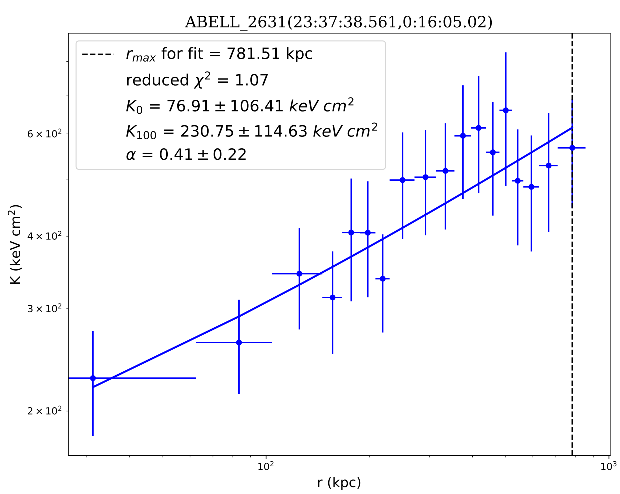
ABELL_2631(23:37:38.561,0:16:05.02)
r_{max} for fit = 781.51 kpc
reduced χ^2 = 1.07
K_0 = 76.91 ± 106.41 $keV\ cm^2$
K_{100} = 230.75 ± 114.63 $keV\ cm^2$
α = 0.41 ± 0.22
K (keV cm^2)
r (kpc)

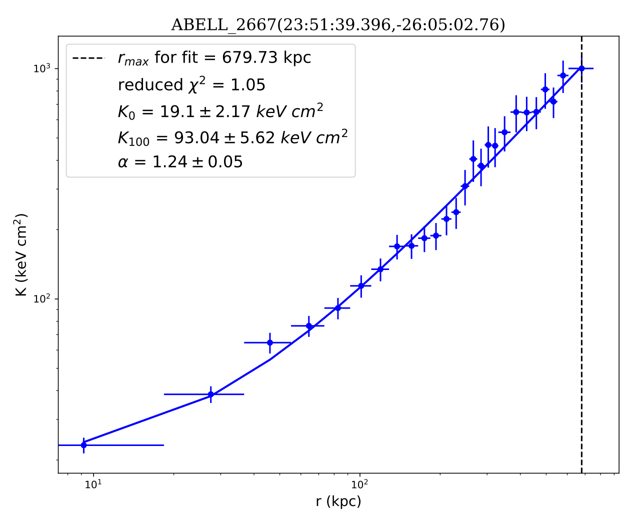
ABELL_2667(23:51:39.396,-26:05:02.76)
r_{max} for fit = 679.73 kpc
reduced χ^2 = 1.05
K_0 = 19.1 ± 2.17 $keV\ cm^2$
K_{100} = 93.04 ± 5.62 $keV\ cm^2$
α = 1.24 ± 0.05
K (keV cm^2)
r (kpc)

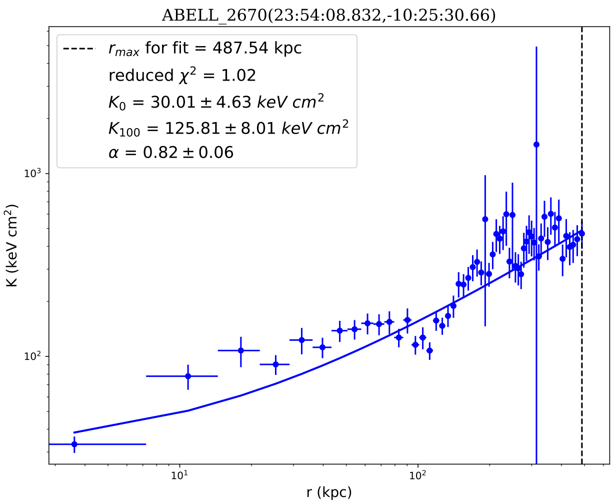
ABELL_2670(23:54:08.832,-10:25:30.66)
r_{max} for fit = 487.54 kpc
reduced χ^2 = 1.02
K_0 = 30.01 ± 4.63 $keV\ cm^2$
K_{100} = 125.81 ± 8.01 $keV\ cm^2$
α = 0.82 ± 0.06
K (keV cm^2)
r (kpc)

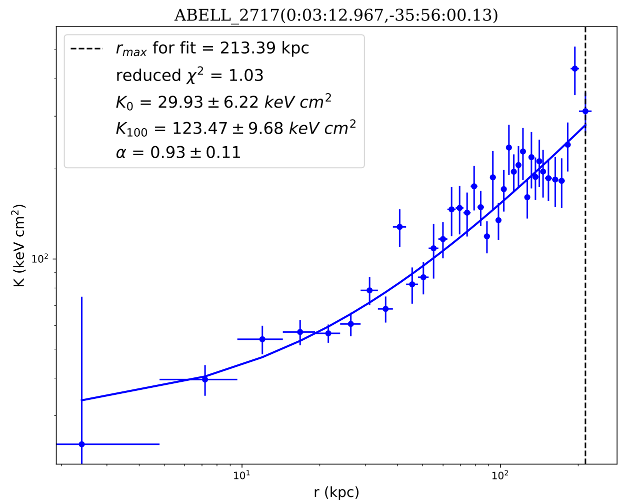
ABELL_2717(0:03:12.967,-35:56:00.13)
r_{max} for fit = 213.39 kpc
reduced χ^2 = 1.03
K_0 = 29.93 ± 6.22 $keV\ cm^2$
K_{100} = 123.47 ± 9.68 $keV\ cm^2$
α = 0.93 ± 0.11
K (keV cm^2)
r (kpc)

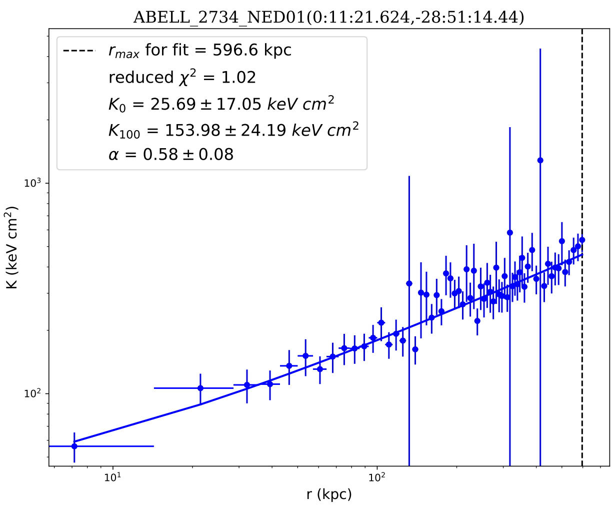
ABELL_2734_NED01(0:11:21.624,-28:51:14.44)
r_{max} for fit = 596.6 kpc
reduced χ^2 = 1.02
K_0 = 25.69 ± 17.05 $keV\ cm^2$
K_{100} = 153.98 ± 24.19 $keV\ cm^2$
α = 0.58 ± 0.08
K (keV cm^2)
r (kpc)

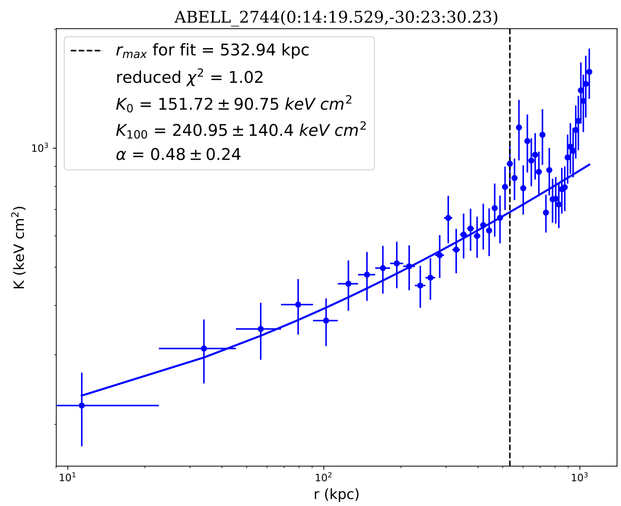
ABELL_2744(0:14:19.529,-30:23:30.23)
r_{max} for fit = 532.94 kpc
reduced χ^2 = 1.02
K_0 = 151.72 ± 90.75 $keV\ cm^2$
K_{100} = 240.95 ± 140.4 $keV\ cm^2$
α = 0.48 ± 0.24
K (keV cm^2)
r (kpc)

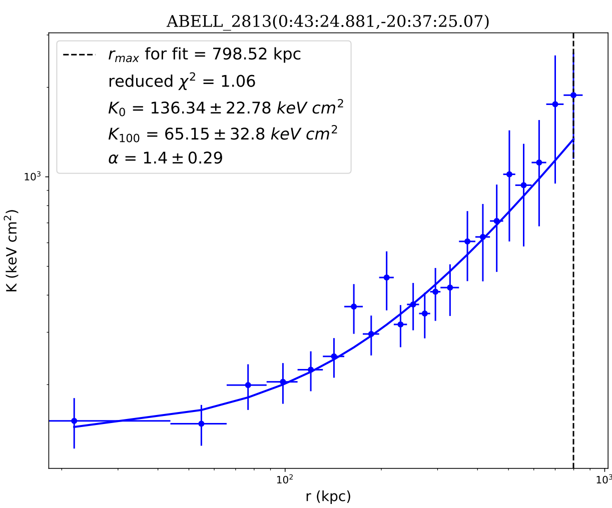
ABELL_2813(0:43:24.881,-20:37:25.07)
r_{max} for fit = 798.52 kpc
reduced χ^2 = 1.06
K_0 = 136.34 ± 22.78 $keV\ cm^2$
K_{100} = 65.15 ± 32.8 $keV\ cm^2$
α = 1.4 ± 0.29
K (keV cm^2)
r (kpc)

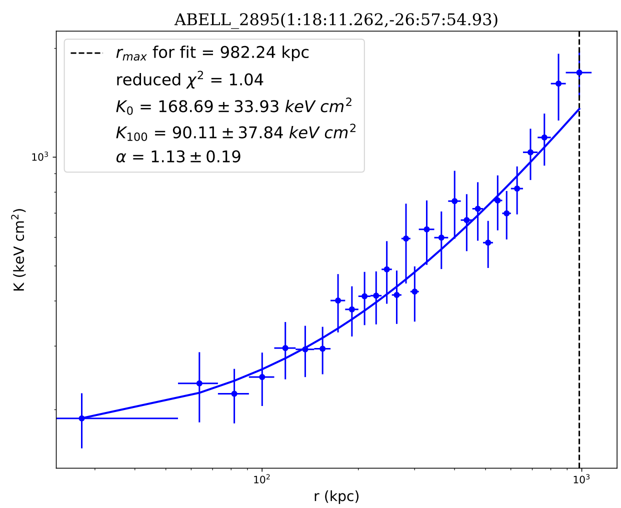
ABELL_2895(1:18:11.262,-26:57:54.93)
r_{max} for fit = 982.24 kpc
reduced χ^2 = 1.04
K_0 = 168.69 ± 33.93 $keV\ cm^2$
K_{100} = 90.11 ± 37.84 $keV\ cm^2$
α = 1.13 ± 0.19
K (keV cm^2)
r (kpc)

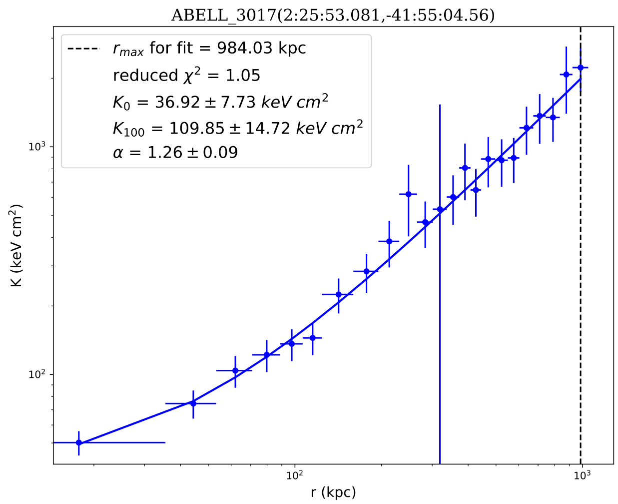
ABELL_3017(2:25:53.081,-41:55:04.56)
r_{max} for fit = 984.03 kpc
reduced χ^2 = 1.05
$K_0 = 36.92 \pm 7.73\ keV\ cm^2$
$K_{100} = 109.85 \pm 14.72\ keV\ cm^2$
$\alpha = 1.26 \pm 0.09$
K (keV cm^2)
r (kpc)

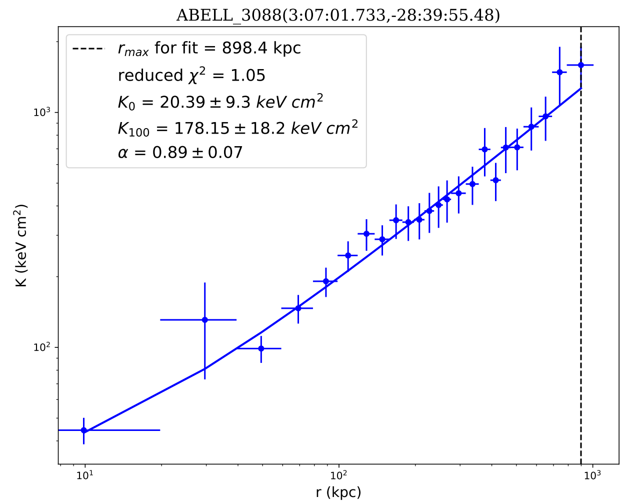
ABELL_3088(3:07:01.733,-28:39:55.48)
r_{max} for fit = 898.4 kpc
reduced χ^2 = 1.05
$K_0 = 20.39 \pm 9.3\ keV\ cm^2$
$K_{100} = 178.15 \pm 18.2\ keV\ cm^2$
$\alpha = 0.89 \pm 0.07$
K (keV cm^2)
r (kpc)

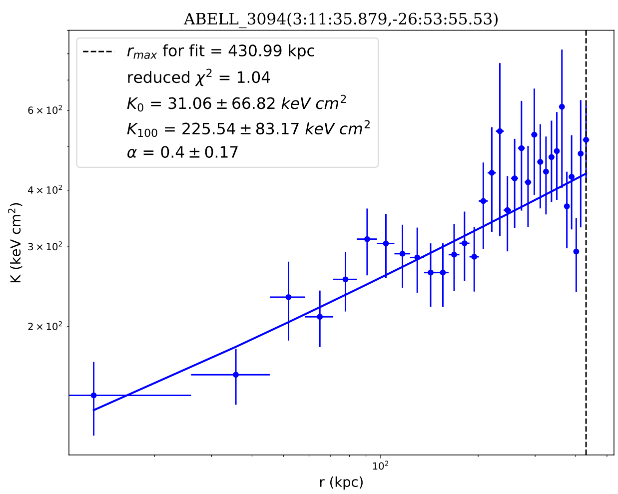
ABELL_3094(3:11:35.879,-26:53:55.53)
r_{max} for fit = 430.99 kpc
reduced χ^2 = 1.04
$K_0 = 31.06 \pm 66.82\ keV\ cm^2$
$K_{100} = 225.54 \pm 83.17\ keV\ cm^2$
$\alpha = 0.4 \pm 0.17$
K (keV cm^2)
r (kpc)

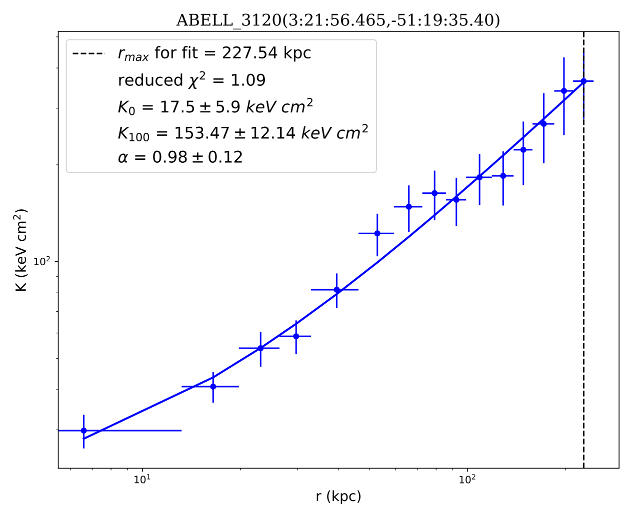
ABELL_3120(3:21:56.465,-51:19:35.40)
r_{max} for fit = 227.54 kpc
reduced χ^2 = 1.09
$K_0 = 17.5 \pm 5.9\ keV\ cm^2$
$K_{100} = 153.47 \pm 12.14\ keV\ cm^2$
$\alpha = 0.98 \pm 0.12$
K (keV cm^2)
r (kpc)

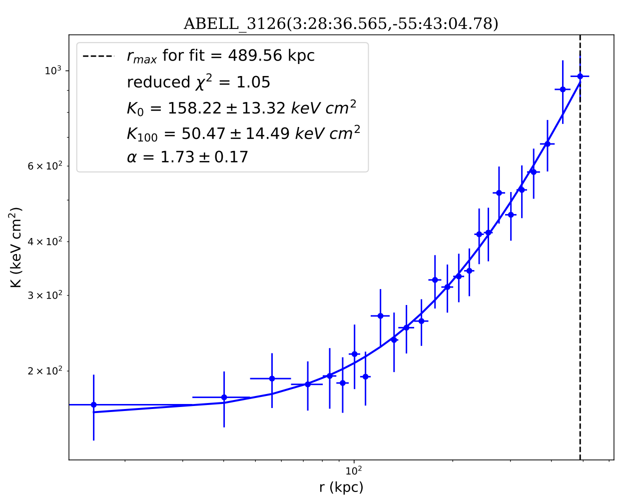
ABELL_3126(3:28:36.565,-55:43:04.78)
r_{max} for fit = 489.56 kpc
reduced χ^2 = 1.05
$K_0 = 158.22 \pm 13.32\ keV\ cm^2$
$K_{100} = 50.47 \pm 14.49\ keV\ cm^2$
$\alpha = 1.73 \pm 0.17$
K (keV cm^2)
r (kpc)

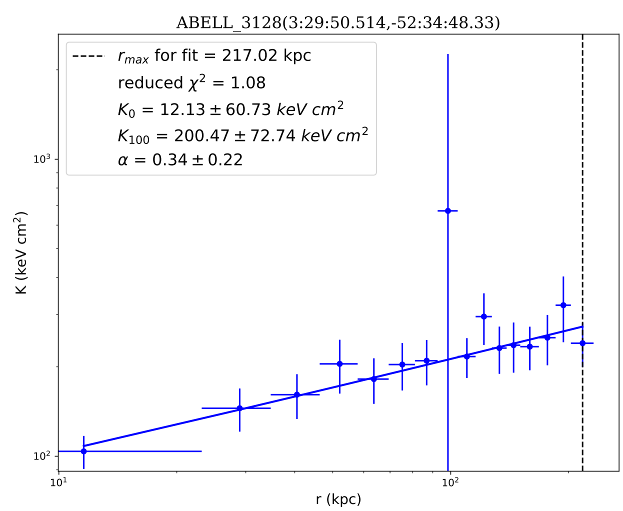
ABELL_3128(3:29:50.514,-52:34:48.33)
r_{max} for fit = 217.02 kpc
reduced χ^2 = 1.08
$K_0 = 12.13 \pm 60.73\ keV\ cm^2$
$K_{100} = 200.47 \pm 72.74\ keV\ cm^2$
$\alpha = 0.34 \pm 0.22$
K (keV cm^2)
r (kpc)

ABELL_3140(3:36:15.636,-40:37:42.68)

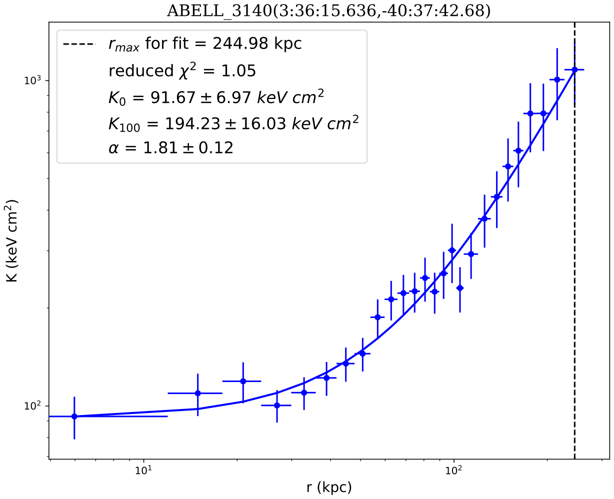

ABELL_3292(4:49:56.189,-44:40:21.16)

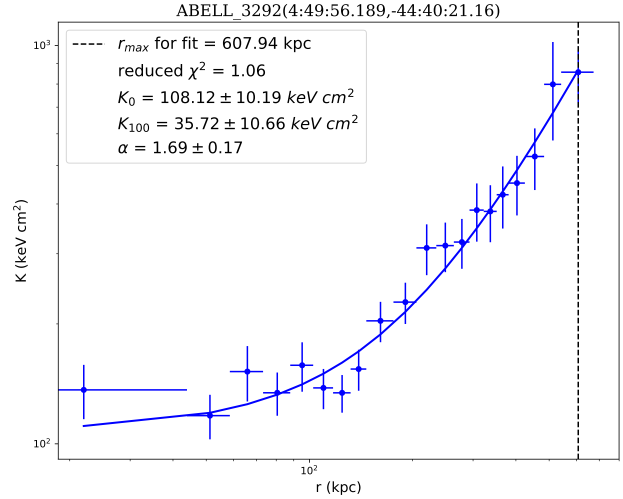

ABELL_3322(5:10:16.916,-45:19:16.24)

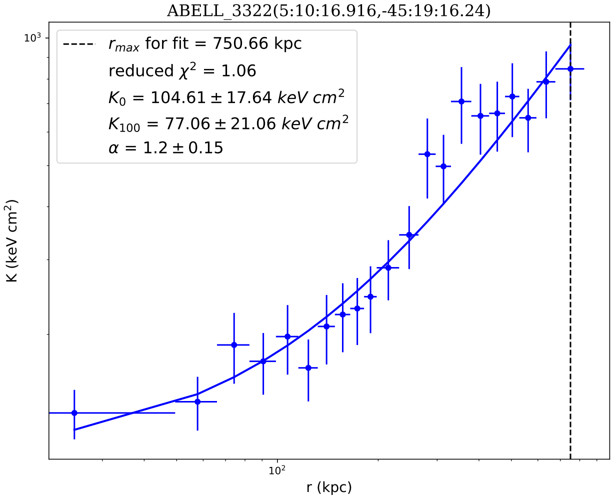

ABELL_3343(5:25:48.712,-47:15:10.19)

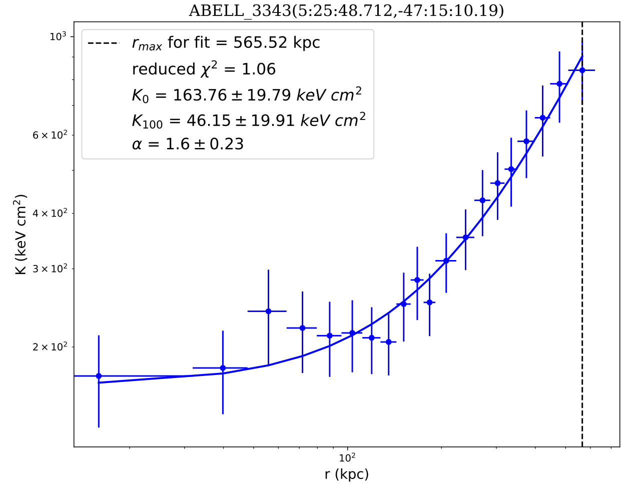

ABELL_3364(5:47:37.697,-31:52:23.63)

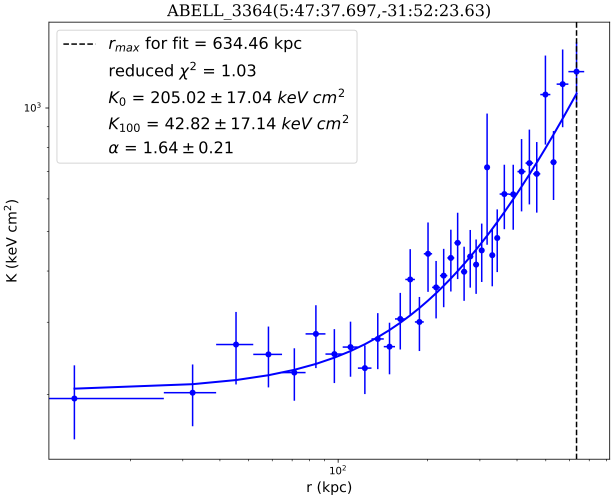

ABELL_3378(6:05:53.987,-35:18:08.09)

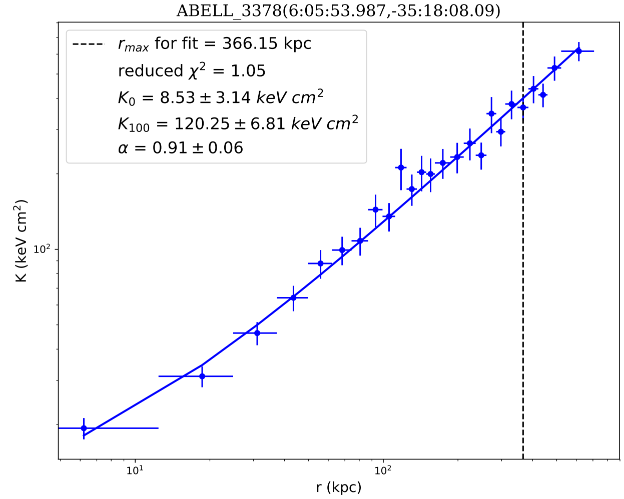

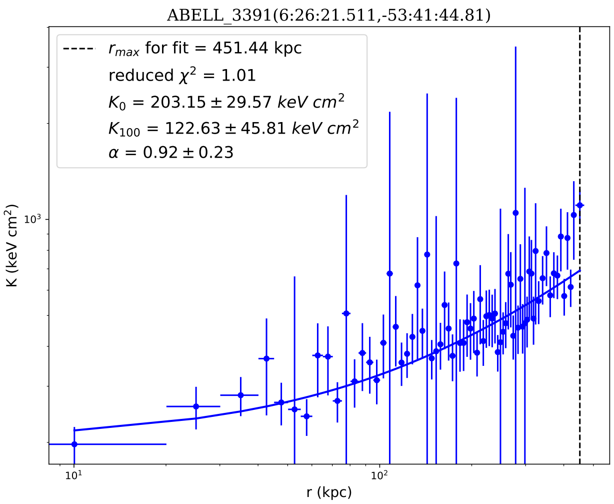
ABELL_3391(6:26:21.511,-53:41:44.81)
r_{max} for fit = 451.44 kpc
reduced χ^2 = 1.01
$K_0 = 203.15 \pm 29.57$ $keV\ cm^2$
$K_{100} = 122.63 \pm 45.81$ $keV\ cm^2$
$\alpha = 0.92 \pm 0.23$
K (keV cm^2)
r (kpc)

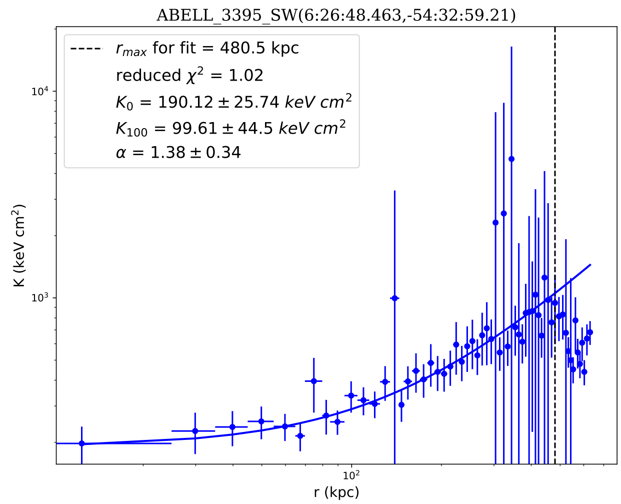
ABELL_3395_SW(6:26:48.463,-54:32:59.21)
r_{max} for fit = 480.5 kpc
reduced χ^2 = 1.02
$K_0 = 190.12 \pm 25.74$ $keV\ cm^2$
$K_{100} = 99.61 \pm 44.5$ $keV\ cm^2$
$\alpha = 1.38 \pm 0.34$
K (keV cm^2)
r (kpc)

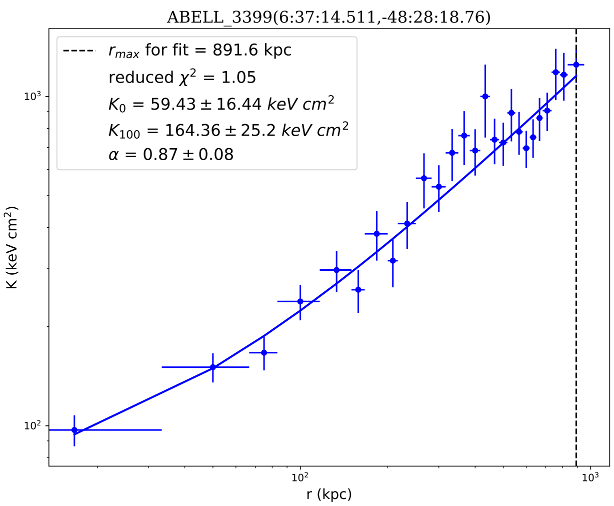
ABELL_3399(6:37:14.511,-48:28:18.76)
r_{max} for fit = 891.6 kpc
reduced χ^2 = 1.05
$K_0 = 59.43 \pm 16.44$ $keV\ cm^2$
$K_{100} = 164.36 \pm 25.2$ $keV\ cm^2$
$\alpha = 0.87 \pm 0.08$
K (keV cm^2)
r (kpc)

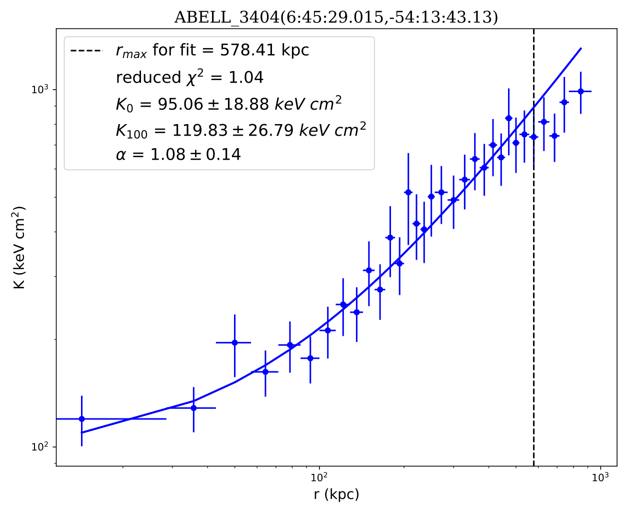
ABELL_3404(6:45:29.015,-54:13:43.13)
r_{max} for fit = 578.41 kpc
reduced χ^2 = 1.04
$K_0 = 95.06 \pm 18.88$ $keV\ cm^2$
$K_{100} = 119.83 \pm 26.79$ $keV\ cm^2$
$\alpha = 1.08 \pm 0.14$
K (keV cm^2)
r (kpc)

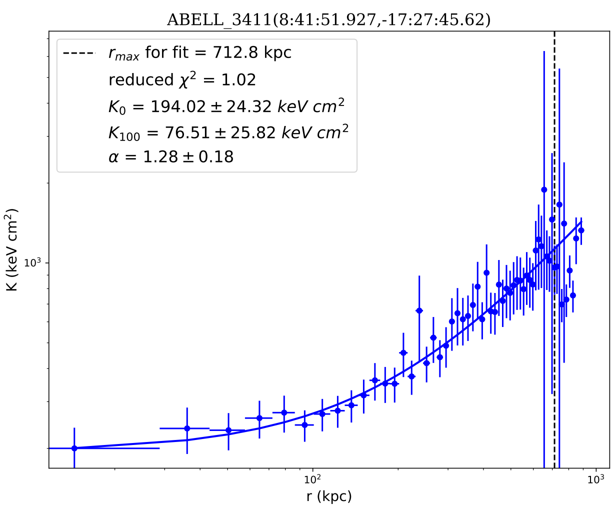
ABELL_3411(8:41:51.927,-17:27:45.62)
r_{max} for fit = 712.8 kpc
reduced χ^2 = 1.02
$K_0 = 194.02 \pm 24.32$ $keV\ cm^2$
$K_{100} = 76.51 \pm 25.82$ $keV\ cm^2$
$\alpha = 1.28 \pm 0.18$
K (keV cm^2)
r (kpc)

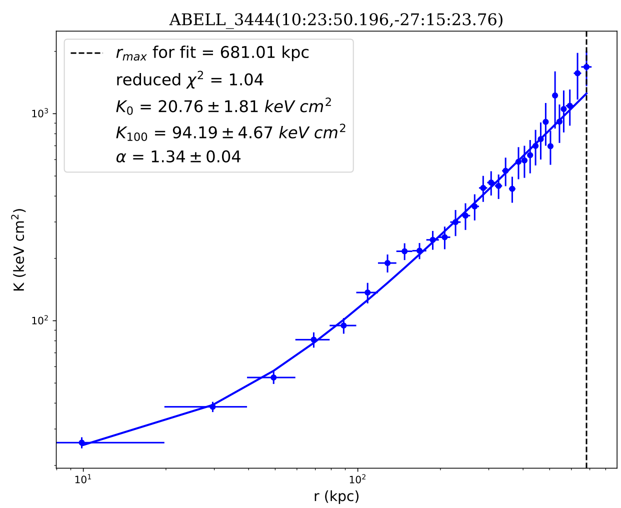
ABELL_3444(10:23:50.196,-27:15:23.76)
r_{max} for fit = 681.01 kpc
reduced χ^2 = 1.04
$K_0 = 20.76 \pm 1.81$ $keV\ cm^2$
$K_{100} = 94.19 \pm 4.67$ $keV\ cm^2$
$\alpha = 1.34 \pm 0.04$
K (keV cm^2)
r (kpc)

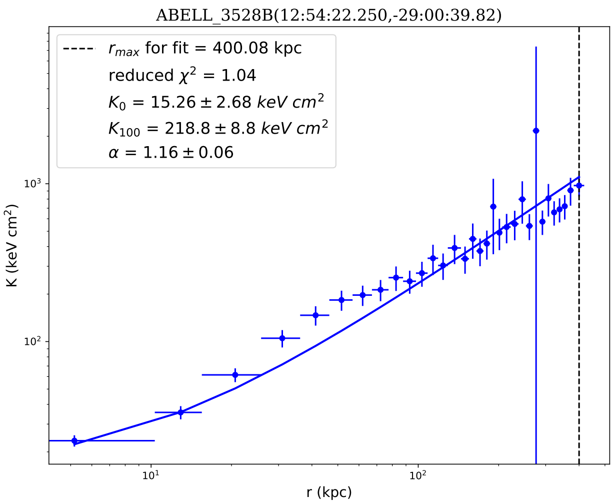
ABELL_3528B(12:54:22.250,-29:00:39.82)
r_{max} for fit = 400.08 kpc
reduced χ^2 = 1.04
K_0 = 15.26 ± 2.68 $keV\ cm^2$
K_{100} = 218.8 ± 8.8 $keV\ cm^2$
α = 1.16 ± 0.06
K (keV cm^2)
r (kpc)

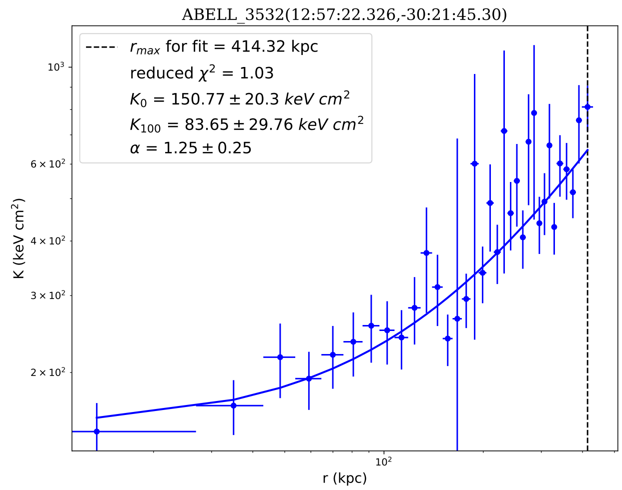
ABELL_3532(12:57:22.326,-30:21:45.30)
r_{max} for fit = 414.32 kpc
reduced χ^2 = 1.03
K_0 = 150.77 ± 20.3 $keV\ cm^2$
K_{100} = 83.65 ± 29.76 $keV\ cm^2$
α = 1.25 ± 0.25
K (keV cm^2)
r (kpc)

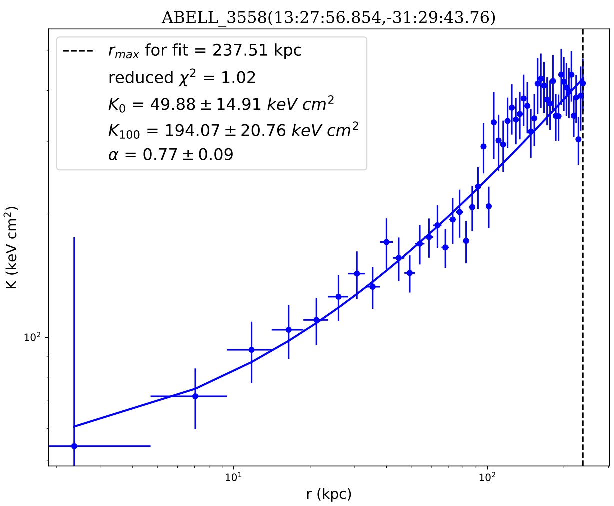
ABELL_3558(13:27:56.854,-31:29:43.76)
r_{max} for fit = 237.51 kpc
reduced χ^2 = 1.02
K_0 = 49.88 ± 14.91 $keV\ cm^2$
K_{100} = 194.07 ± 20.76 $keV\ cm^2$
α = 0.77 ± 0.09
K (keV cm^2)
r (kpc)

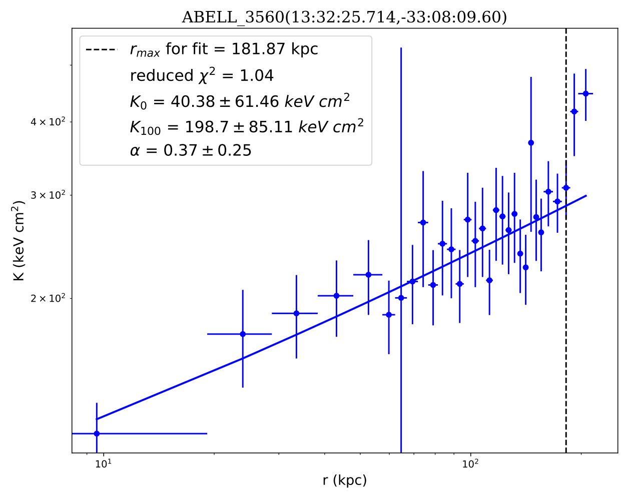
ABELL_3560(13:32:25.714,-33:08:09.60)
r_{max} for fit = 181.87 kpc
reduced χ^2 = 1.04
K_0 = 40.38 ± 61.46 $keV\ cm^2$
K_{100} = 198.7 ± 85.11 $keV\ cm^2$
α = 0.37 ± 0.25
K (keV cm^2)
r (kpc)

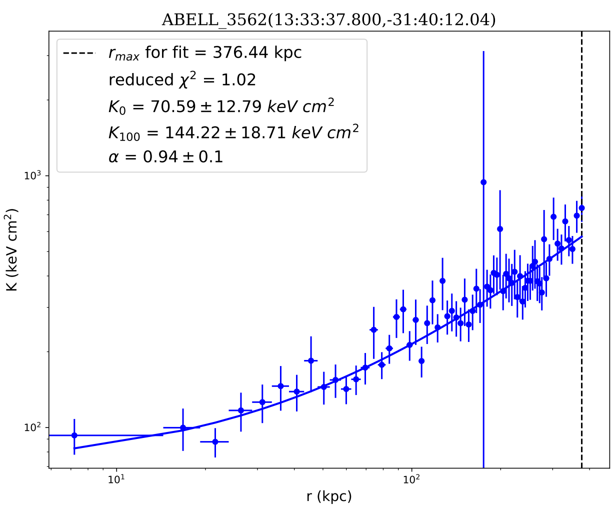
ABELL_3562(13:33:37.800,-31:40:12.04)
r_{max} for fit = 376.44 kpc
reduced χ^2 = 1.02
K_0 = 70.59 ± 12.79 $keV\ cm^2$
K_{100} = 144.22 ± 18.71 $keV\ cm^2$
α = 0.94 ± 0.1
K (keV cm^2)
r (kpc)

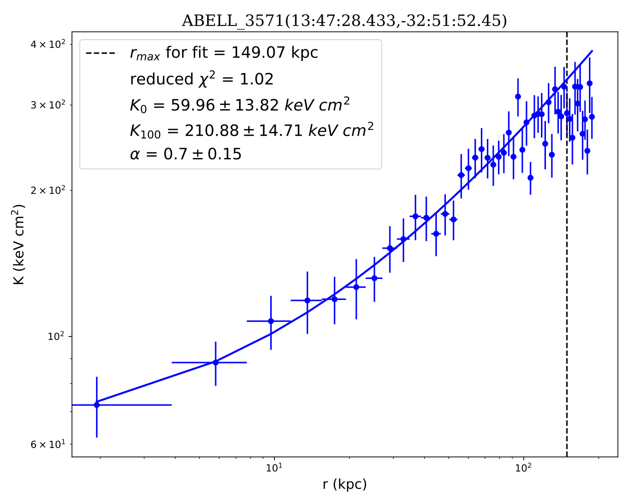
ABELL_3571(13:47:28.433,-32:51:52.45)
r_{max} for fit = 149.07 kpc
reduced χ^2 = 1.02
K_0 = 59.96 ± 13.82 $keV\ cm^2$
K_{100} = 210.88 ± 14.71 $keV\ cm^2$
α = 0.7 ± 0.15
K (keV cm^2)
r (kpc)

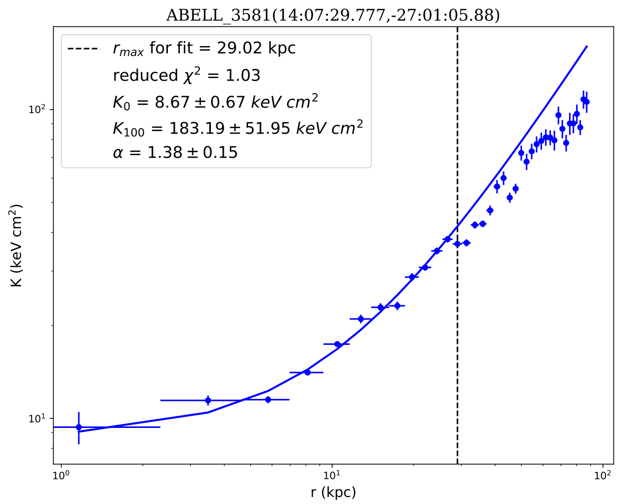
ABELL_3581(14:07:29.777,-27:01:05.88)
r_{max} for fit = 29.02 kpc
reduced χ^2 = 1.03
K_0 = 8.67 ± 0.67 $keV\ cm^2$
K_{100} = 183.19 ± 51.95 $keV\ cm^2$
α = 1.38 ± 0.15
K (keV cm^2)
r (kpc)

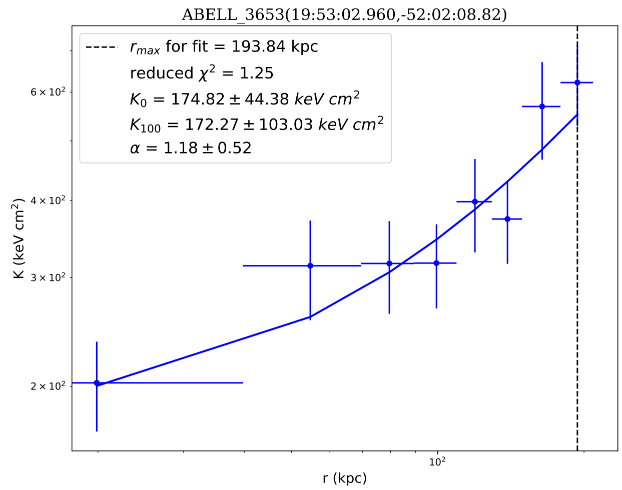
ABELL_3653(19:53:02.960,-52:02:08.82)
r_{max} for fit = 193.84 kpc
reduced χ^2 = 1.25
K_0 = 174.82 ± 44.38 $keV\ cm^2$
K_{100} = 172.27 ± 103.03 $keV\ cm^2$
α = 1.18 ± 0.52
K (keV cm^2)
r (kpc)

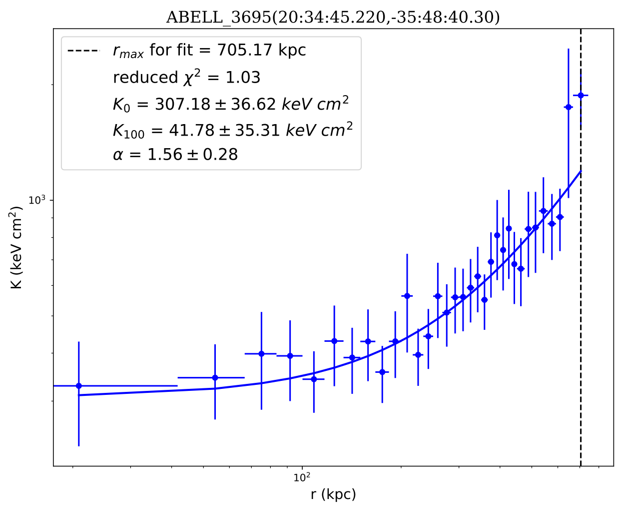
ABELL_3695(20:34:45.220,-35:48:40.30)
r_{max} for fit = 705.17 kpc
reduced χ^2 = 1.03
K_0 = 307.18 ± 36.62 $keV\ cm^2$
K_{100} = 41.78 ± 35.31 $keV\ cm^2$
α = 1.56 ± 0.28
K (keV cm^2)
r (kpc)

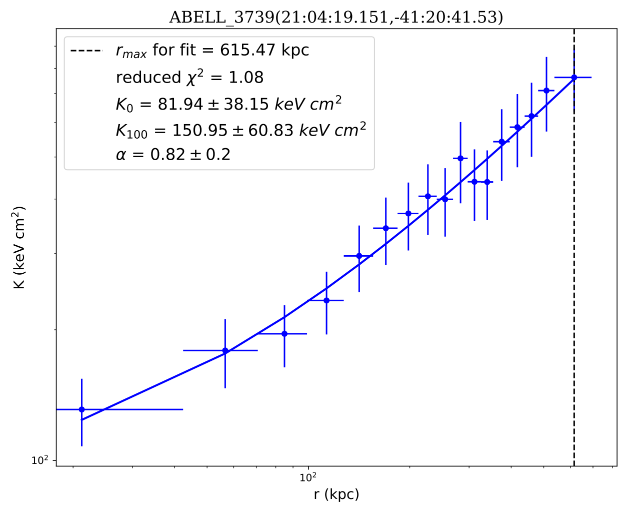
ABELL_3739(21:04:19.151,-41:20:41.53)
r_{max} for fit = 615.47 kpc
reduced χ^2 = 1.08
K_0 = 81.94 ± 38.15 $keV\ cm^2$
K_{100} = 150.95 ± 60.83 $keV\ cm^2$
α = 0.82 ± 0.2
K (keV cm^2)
r (kpc)

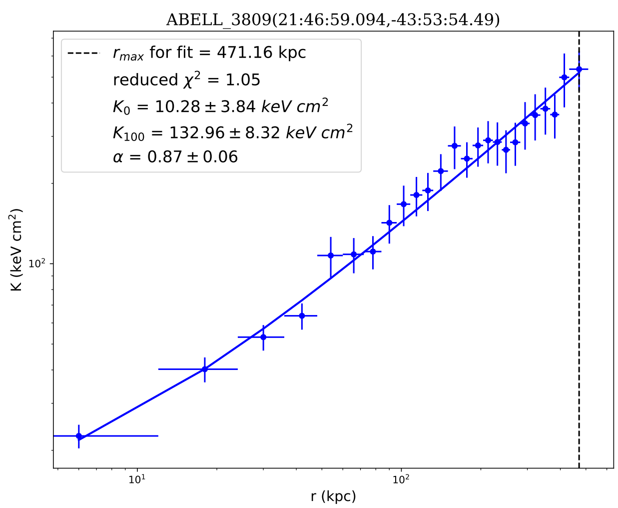
ABELL_3809(21:46:59.094,-43:53:54.49)
r_{max} for fit = 471.16 kpc
reduced χ^2 = 1.05
K_0 = 10.28 ± 3.84 $keV\ cm^2$
K_{100} = 132.96 ± 8.32 $keV\ cm^2$
α = 0.87 ± 0.06
K (keV cm^2)
r (kpc)

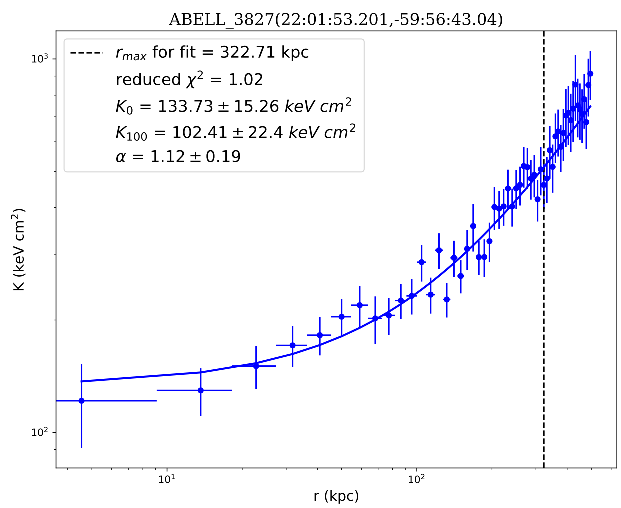
ABELL_3827(22:01:53.201,-59:56:43.04)
r_{max} for fit = 322.71 kpc
reduced χ^2 = 1.02
K_0 = 133.73 ± 15.26 $keV\ cm^2$
K_{100} = 102.41 ± 22.4 $keV\ cm^2$
α = 1.12 ± 0.19
K (keV cm^2)
r (kpc)

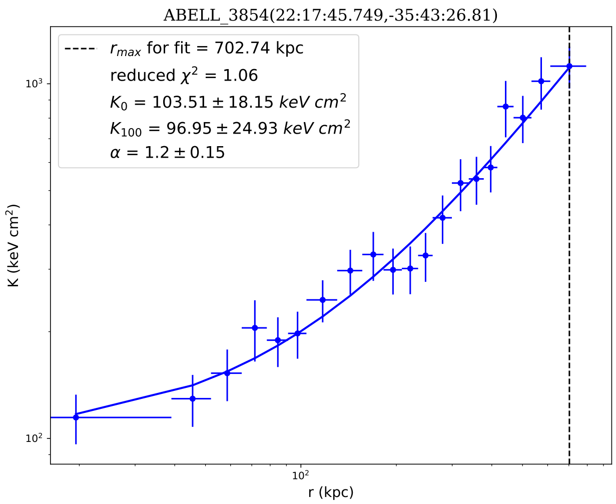
ABELL_3854(22:17:45.749,-35:43:26.81)
r_{max} for fit = 702.74 kpc
reduced χ^2 = 1.06
K_0 = 103.51 ± 18.15 $keV\ cm^2$
K_{100} = 96.95 ± 24.93 $keV\ cm^2$
α = 1.2 ± 0.15
K (keV cm^2)
r (kpc)

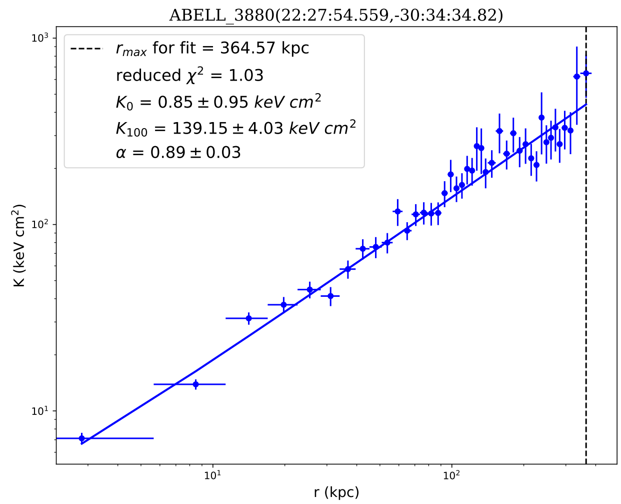
ABELL_3880(22:27:54.559,-30:34:34.82)
r_{max} for fit = 364.57 kpc
reduced χ^2 = 1.03
K_0 = 0.85 ± 0.95 $keV\ cm^2$
K_{100} = 139.15 ± 4.03 $keV\ cm^2$
α = 0.89 ± 0.03
K (keV cm^2)
r (kpc)

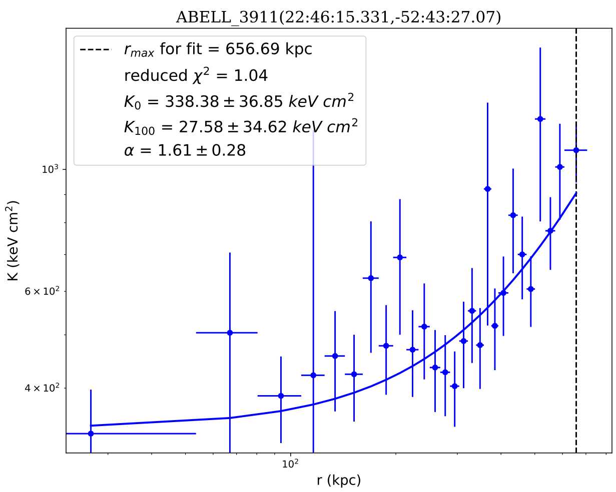
ABELL_3911(22:46:15.331,-52:43:27.07)
r_{max} for fit = 656.69 kpc
reduced χ^2 = 1.04
K_0 = 338.38 ± 36.85 $keV\ cm^2$
K_{100} = 27.58 ± 34.62 $keV\ cm^2$
α = 1.61 ± 0.28
K (keV cm^2)
r (kpc)

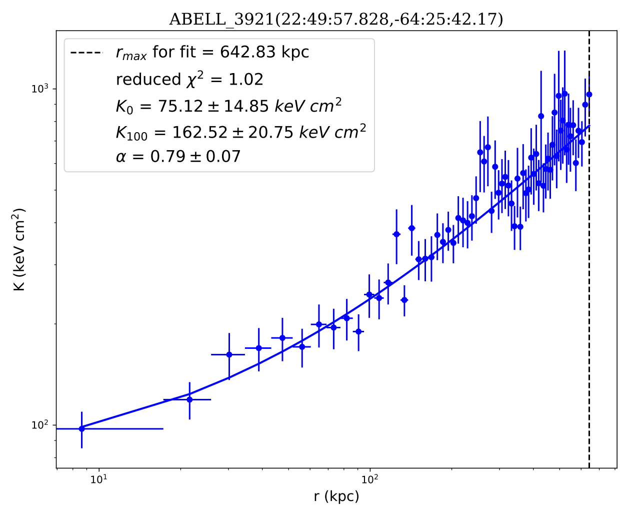
ABELL_3921(22:49:57.828,-64:25:42.17)
r_{max} for fit = 642.83 kpc
reduced χ^2 = 1.02
K_0 = 75.12 ± 14.85 $keV\ cm^2$
K_{100} = 162.52 ± 20.75 $keV\ cm^2$
α = 0.79 ± 0.07
K (keV cm^2)
r (kpc)

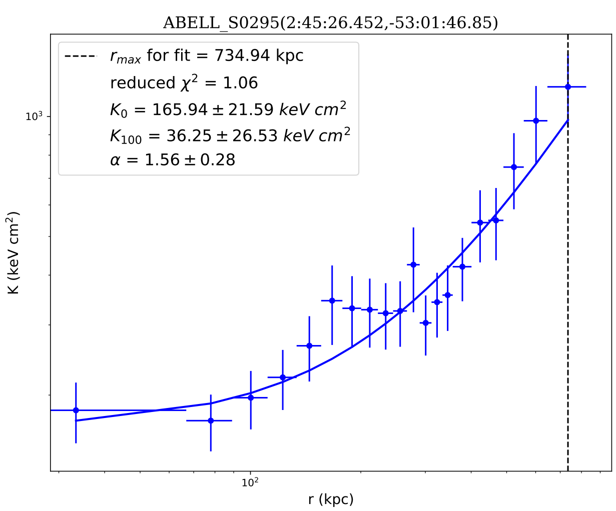
ABELL_S0295(2:45:26.452,-53:01:46.85)
r_{max} for fit = 734.94 kpc
reduced χ^2 = 1.06
K_0 = 165.94 ± 21.59 $keV\ cm^2$
K_{100} = 36.25 ± 26.53 $keV\ cm^2$
α = 1.56 ± 0.28
K (keV cm^2)
r (kpc)

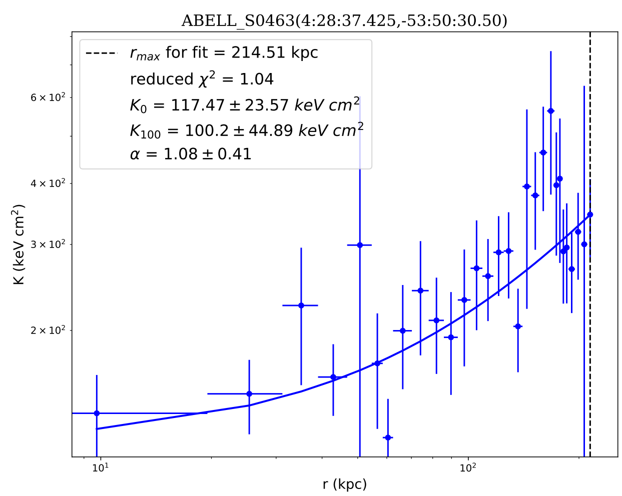
ABELL_S0463(4:28:37.425,-53:50:30.50)
r_{max} for fit = 214.51 kpc
reduced χ^2 = 1.04
K_0 = 117.47 ± 23.57 $keV\ cm^2$
K_{100} = 100.2 ± 44.89 $keV\ cm^2$
α = 1.08 ± 0.41
K (keV cm^2)
r (kpc)

ABELL_S0520(5:16:37.711,-54:30:47.30)

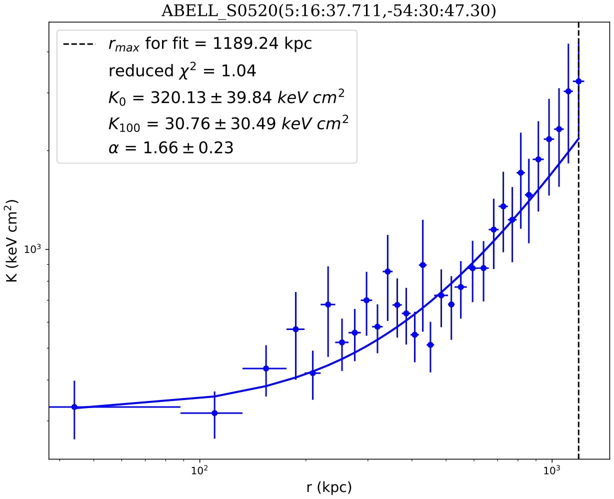

ABELL_S0579(6:16:32.139,-39:47:48.63)

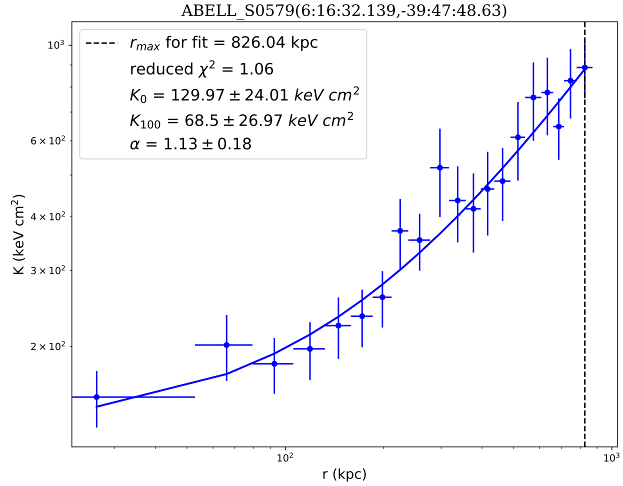

ABELL_S0592(6:38:48.610,-53:58:26.33)

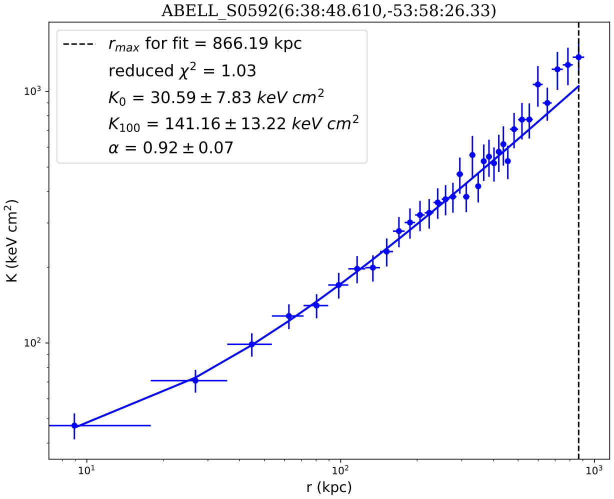

ABELL_S0780(14:59:28.817,-18:10:43.49)

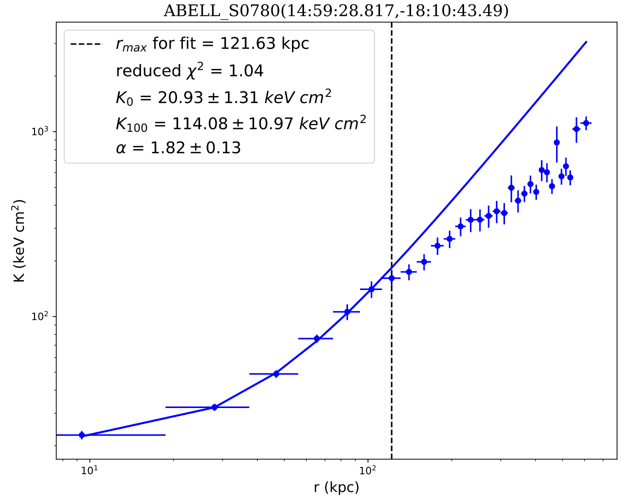

ABELL_S1063(22:48:44.294,-44:31:48.36)

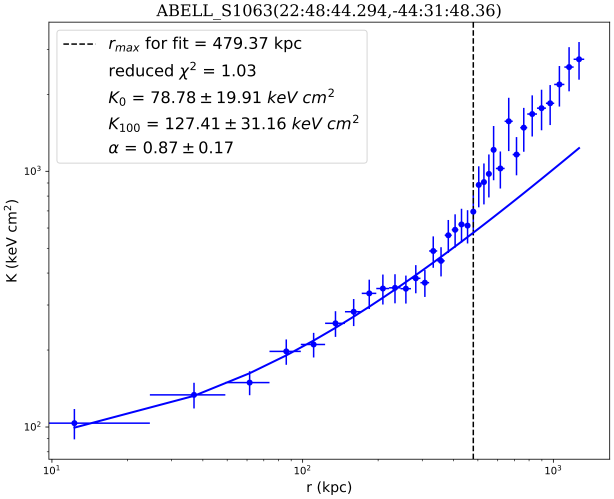

ABELL_S1101(23:13:58.764,-42:43:34.72)

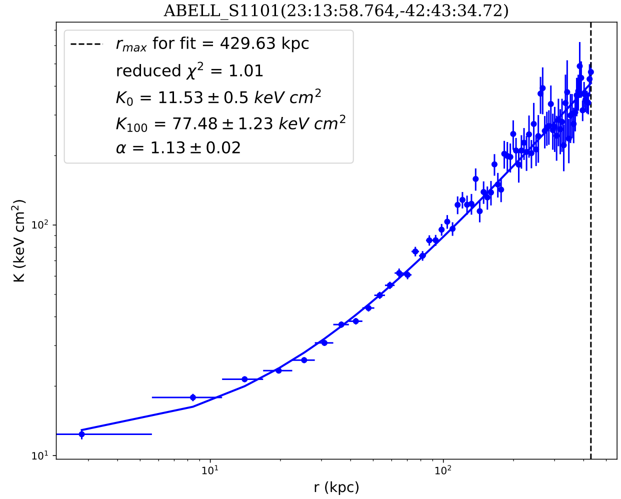

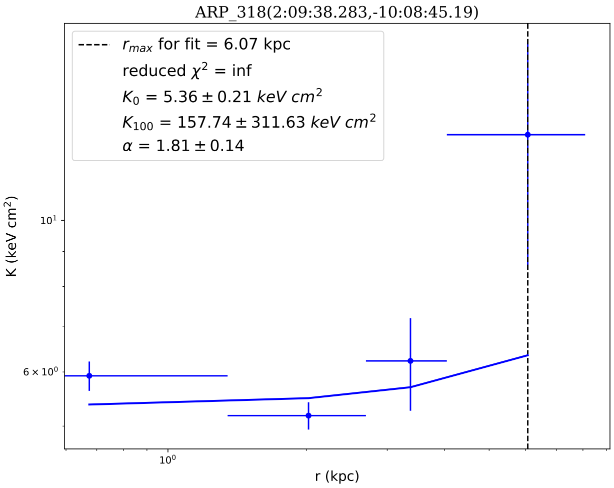
ARP_318(2:09:38.283,-10:08:45.19)
r_{max} for fit = 6.07 kpc
reduced χ^2 = inf
$K_0 = 5.36 \pm 0.21\ keV\ cm^2$
$K_{100} = 157.74 \pm 311.63\ keV\ cm^2$
$\alpha = 1.81 \pm 0.14$
K (keV cm^2)
r (kpc)

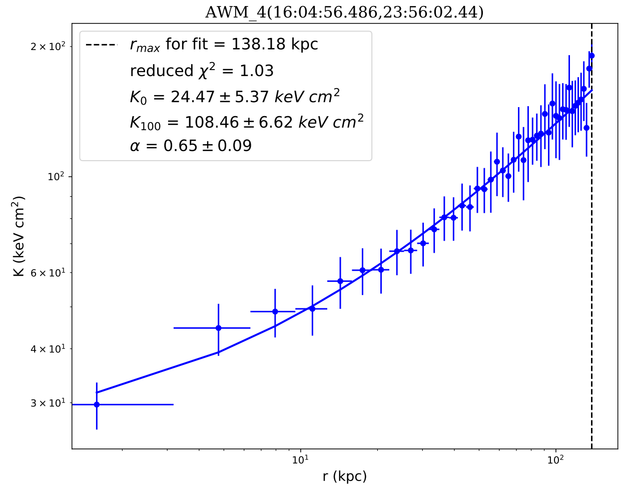
AWM_4(16:04:56.486,23:56:02.44)
r_{max} for fit = 138.18 kpc
reduced χ^2 = 1.03
$K_0 = 24.47 \pm 5.37\ keV\ cm^2$
$K_{100} = 108.46 \pm 6.62\ keV\ cm^2$
$\alpha = 0.65 \pm 0.09$
K (keV cm^2)
r (kpc)

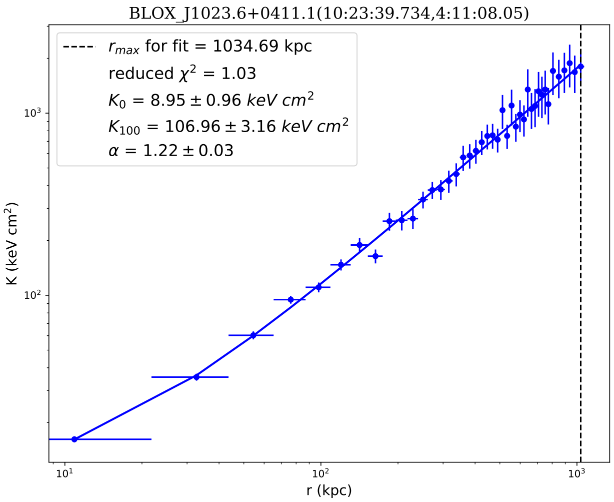
BLOX_J1023.6+0411.1(10:23:39.734,4:11:08.05)
r_{max} for fit = 1034.69 kpc
reduced χ^2 = 1.03
$K_0 = 8.95 \pm 0.96\ keV\ cm^2$
$K_{100} = 106.96 \pm 3.16\ keV\ cm^2$
$\alpha = 1.22 \pm 0.03$
K (keV cm^2)
r (kpc)

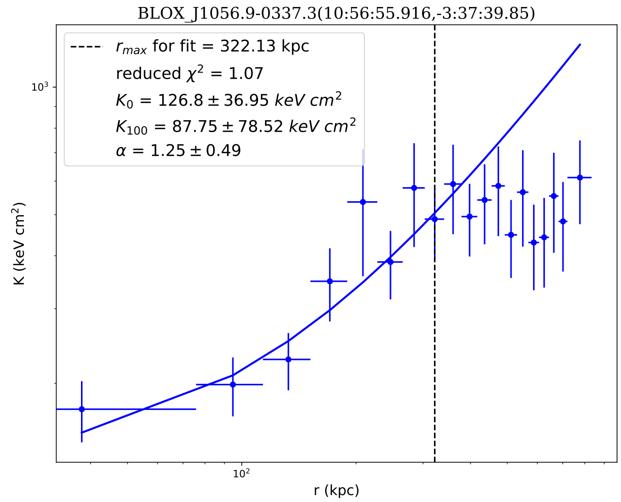
BLOX_J1056.9-0337.3(10:56:55.916,-3:37:39.85)
r_{max} for fit = 322.13 kpc
reduced χ^2 = 1.07
$K_0 = 126.8 \pm 36.95\ keV\ cm^2$
$K_{100} = 87.75 \pm 78.52\ keV\ cm^2$
$\alpha = 1.25 \pm 0.49$
K (keV cm^2)
r (kpc)

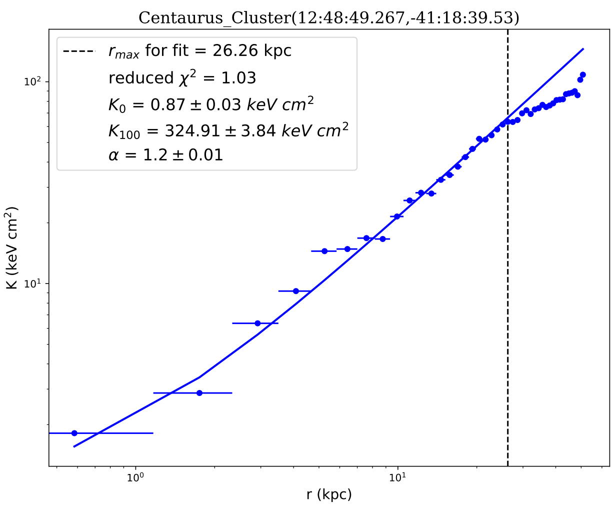
Centaurus_Cluster(12:48:49.267,-41:18:39.53)
r_{max} for fit = 26.26 kpc
reduced χ^2 = 1.03
$K_0 = 0.87 \pm 0.03\ keV\ cm^2$
$K_{100} = 324.91 \pm 3.84\ keV\ cm^2$
$\alpha = 1.2 \pm 0.01$
K (keV cm^2)
r (kpc)

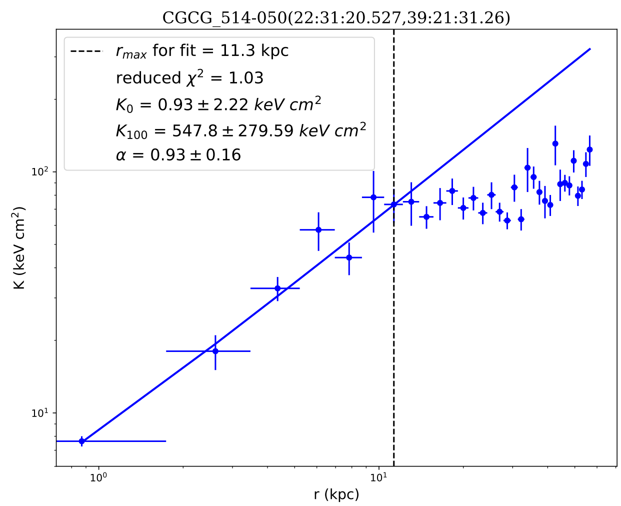
CGCG_514-050(22:31:20.527,39:21:31.26)
r_{max} for fit = 11.3 kpc
reduced χ^2 = 1.03
$K_0 = 0.93 \pm 2.22\ keV\ cm^2$
$K_{100} = 547.8 \pm 279.59\ keV\ cm^2$
$\alpha = 0.93 \pm 0.16$
K (keV cm^2)
r (kpc)

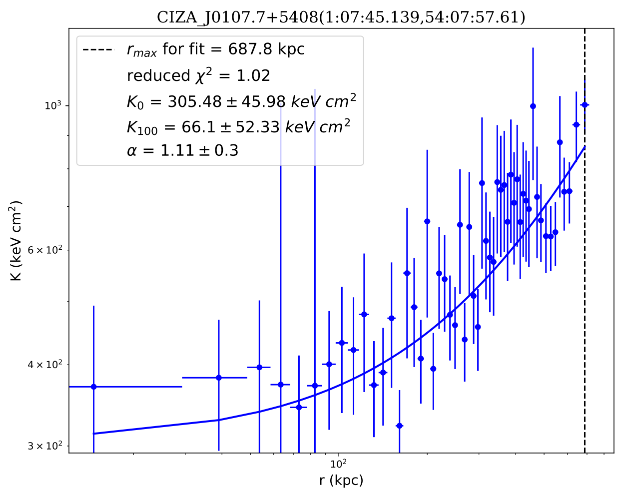
CIZA_J0107.7+5408(1:07:45.139,54:07:57.61)
r_{max} for fit = 687.8 kpc
reduced χ^2 = 1.02
$K_0 = 305.48 \pm 45.98\ keV\ cm^2$
$K_{100} = 66.1 \pm 52.33\ keV\ cm^2$
$\alpha = 1.11 \pm 0.3$
K (keV cm^2)
r (kpc)

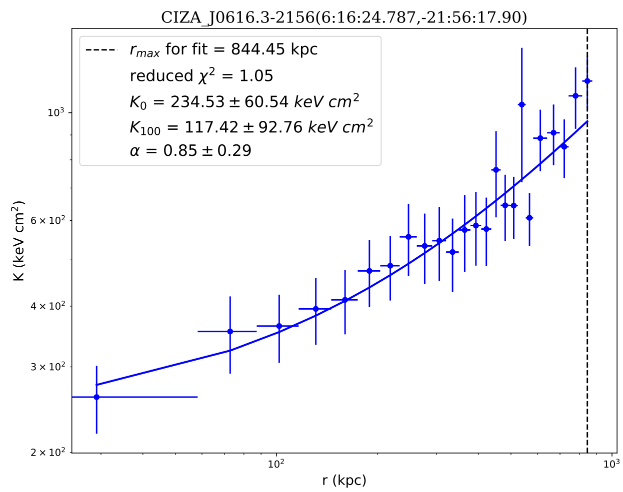
CIZA_J0616.3-2156(6:16:24.787,-21:56:17.90)
r_{max} for fit = 844.45 kpc
reduced χ^2 = 1.05
$K_0 = 234.53 \pm 60.54\ keV\ cm^2$
$K_{100} = 117.42 \pm 92.76\ keV\ cm^2$
$\alpha = 0.85 \pm 0.29$
K (keV cm^2)
r (kpc)

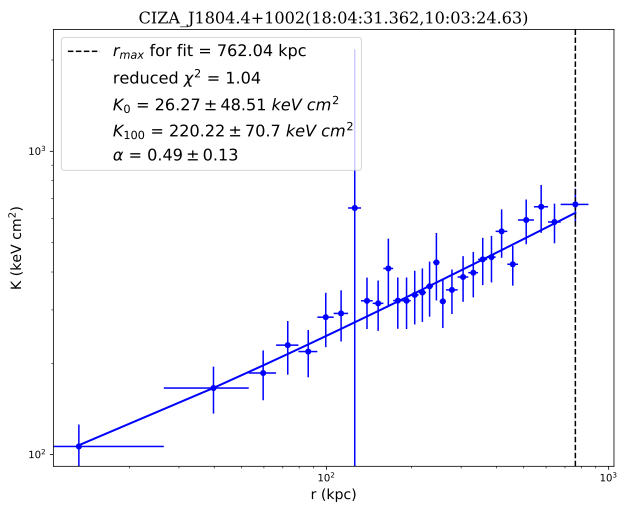
CIZA_J1804.4+1002(18:04:31.362,10:03:24.63)
r_{max} for fit = 762.04 kpc
reduced χ^2 = 1.04
$K_0 = 26.27 \pm 48.51\ keV\ cm^2$
$K_{100} = 220.22 \pm 70.7\ keV\ cm^2$
$\alpha = 0.49 \pm 0.13$
K (keV cm^2)
r (kpc)

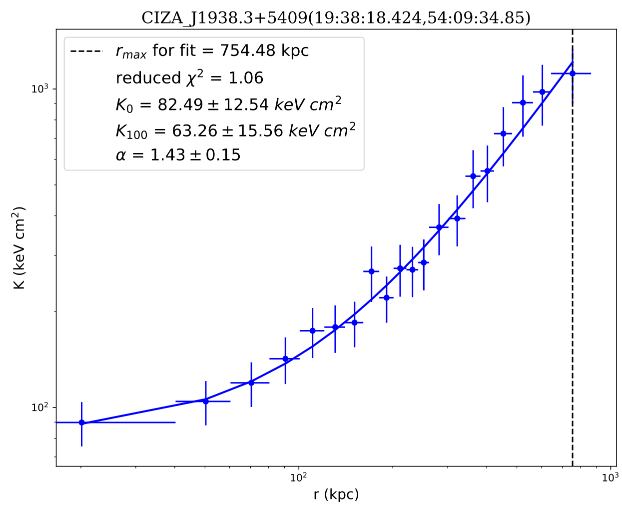
CIZA_J1938.3+5409(19:38:18.424,54:09:34.85)
r_{max} for fit = 754.48 kpc
reduced χ^2 = 1.06
$K_0 = 82.49 \pm 12.54\ keV\ cm^2$
$K_{100} = 63.26 \pm 15.56\ keV\ cm^2$
$\alpha = 1.43 \pm 0.15$
K (keV cm^2)
r (kpc)

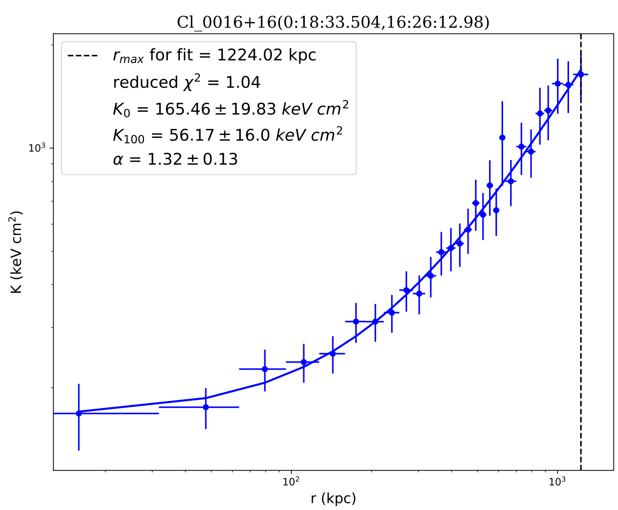
Cl_0016+16(0:18:33.504,16:26:12.98)
r_{max} for fit = 1224.02 kpc
reduced χ^2 = 1.04
$K_0 = 165.46 \pm 19.83\ keV\ cm^2$
$K_{100} = 56.17 \pm 16.0\ keV\ cm^2$
$\alpha = 1.32 \pm 0.13$
K (keV cm^2)
r (kpc)

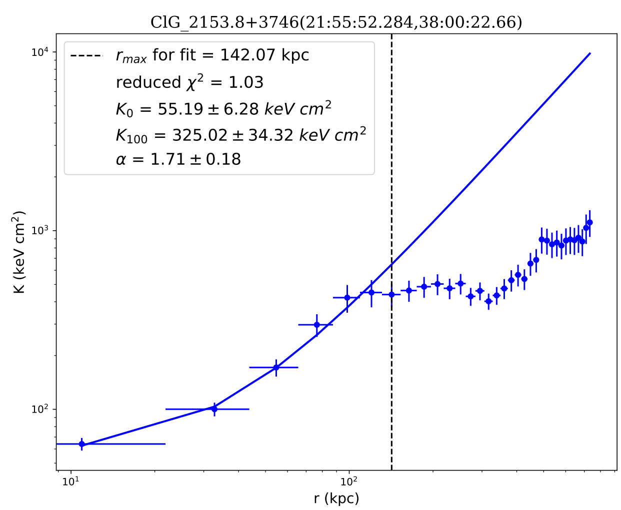
ClG_2153.8+3746(21:55:52.284,38:00:22.66)
r_{max} for fit = 142.07 kpc
reduced χ^2 = 1.03
$K_0 = 55.19 \pm 6.28\ keV\ cm^2$
$K_{100} = 325.02 \pm 34.32\ keV\ cm^2$
$\alpha = 1.71 \pm 0.18$
K (keV cm^2)
r (kpc)

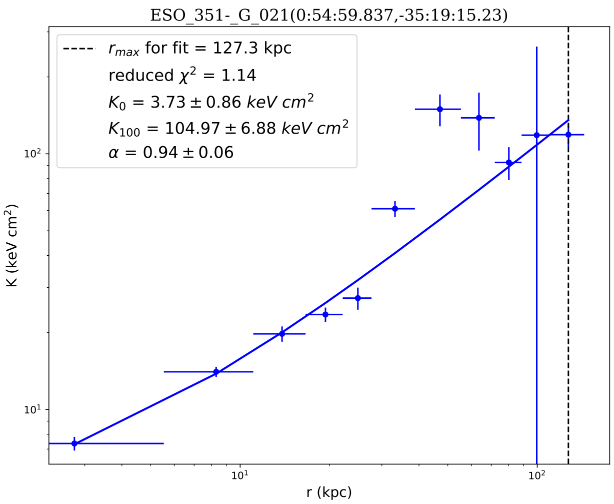
ESO_351-_G_021(0:54:59.837,-35:19:15.23)
r_{max} for fit = 127.3 kpc
reduced χ^2 = 1.14
$K_0 = 3.73 \pm 0.86$ $keV\ cm^2$
$K_{100} = 104.97 \pm 6.88$ $keV\ cm^2$
$\alpha = 0.94 \pm 0.06$
K (keV cm^2)
r (kpc)

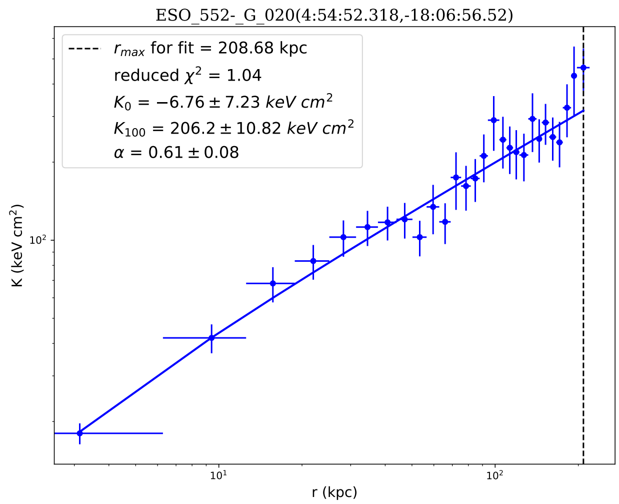
ESO_552-_G_020(4:54:52.318,-18:06:56.52)
r_{max} for fit = 208.68 kpc
reduced χ^2 = 1.04
$K_0 = -6.76 \pm 7.23$ $keV\ cm^2$
$K_{100} = 206.2 \pm 10.82$ $keV\ cm^2$
$\alpha = 0.61 \pm 0.08$
K (keV cm^2)
r (kpc)

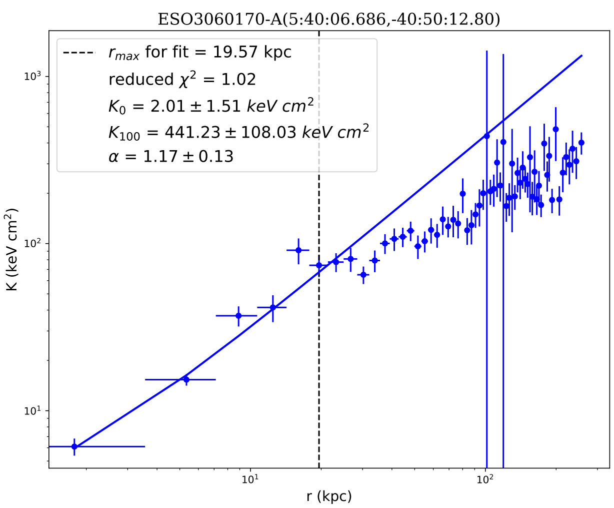
ESO3060170-A(5:40:06.686,-40:50:12.80)
r_{max} for fit = 19.57 kpc
reduced χ^2 = 1.02
$K_0 = 2.01 \pm 1.51$ $keV\ cm^2$
$K_{100} = 441.23 \pm 108.03$ $keV\ cm^2$
$\alpha = 1.17 \pm 0.13$
K (keV cm^2)
r (kpc)

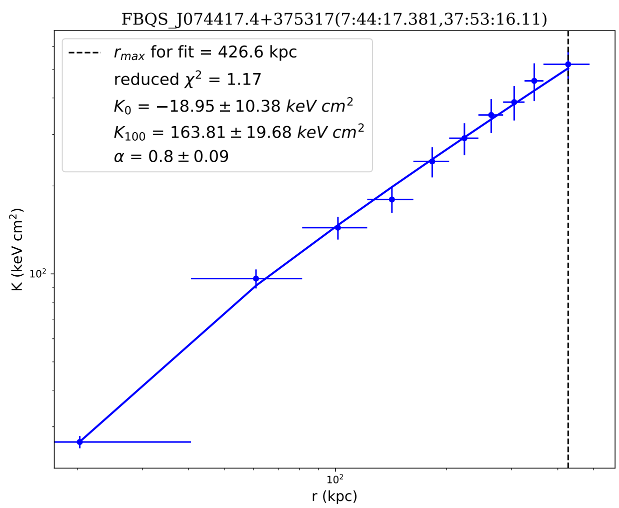
FBQS_J074417.4+375317(7:44:17.381,37:53:16.11)
r_{max} for fit = 426.6 kpc
reduced χ^2 = 1.17
$K_0 = -18.95 \pm 10.38$ $keV\ cm^2$
$K_{100} = 163.81 \pm 19.68$ $keV\ cm^2$
$\alpha = 0.8 \pm 0.09$
K (keV cm^2)
r (kpc)

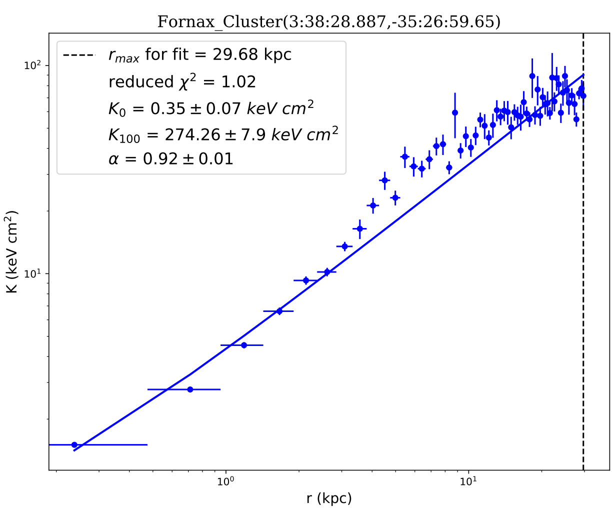
Fornax_Cluster(3:38:28.887,-35:26:59.65)
r_{max} for fit = 29.68 kpc
reduced χ^2 = 1.02
$K_0 = 0.35 \pm 0.07$ $keV\ cm^2$
$K_{100} = 274.26 \pm 7.9$ $keV\ cm^2$
$\alpha = 0.92 \pm 0.01$
K (keV cm^2)
r (kpc)

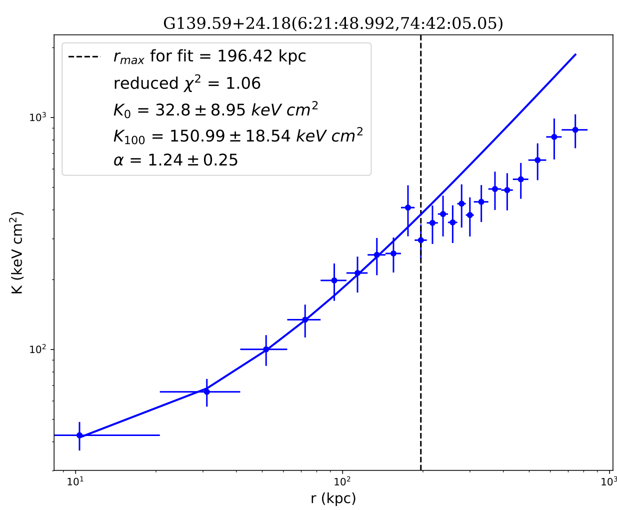
G139.59+24.18(6:21:48.992,74:42:05.05)
r_{max} for fit = 196.42 kpc
reduced χ^2 = 1.06
$K_0 = 32.8 \pm 8.95$ $keV\ cm^2$
$K_{100} = 150.99 \pm 18.54$ $keV\ cm^2$
$\alpha = 1.24 \pm 0.25$
K (keV cm^2)
r (kpc)

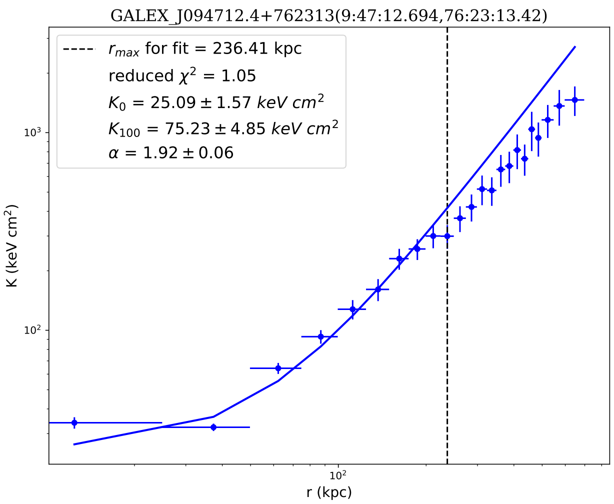
GALEX_J094712.4+762313(9:47:12.694,76:23:13.42)
r_{max} for fit = 236.41 kpc
reduced χ^2 = 1.05
K_0 = 25.09 ± 1.57 $keV\ cm^2$
K_{100} = 75.23 ± 4.85 $keV\ cm^2$
α = 1.92 ± 0.06
K (keV cm^2)
r (kpc)

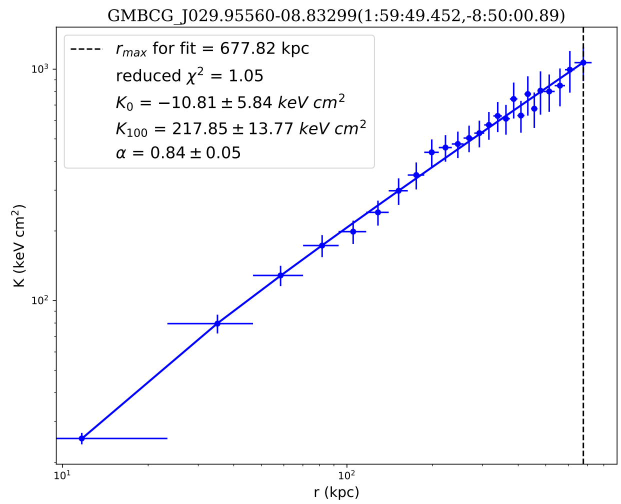
GMBCG_J029.95560-08.83299(1:59:49.452,-8:50:00.89)
r_{max} for fit = 677.82 kpc
reduced χ^2 = 1.05
K_0 = −10.81 ± 5.84 $keV\ cm^2$
K_{100} = 217.85 ± 13.77 $keV\ cm^2$
α = 0.84 ± 0.05
K (keV cm^2)
r (kpc)

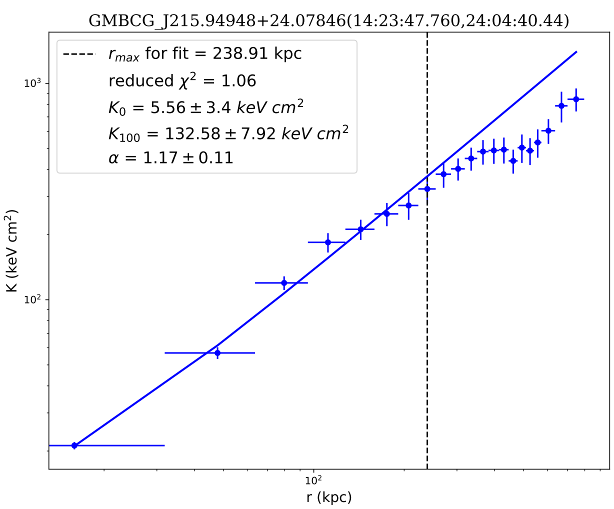
GMBCG_J215.94948+24.07846(14:23:47.760,24:04:40.44)
r_{max} for fit = 238.91 kpc
reduced χ^2 = 1.06
K_0 = 5.56 ± 3.4 $keV\ cm^2$
K_{100} = 132.58 ± 7.92 $keV\ cm^2$
α = 1.17 ± 0.11
K (keV cm^2)
r (kpc)

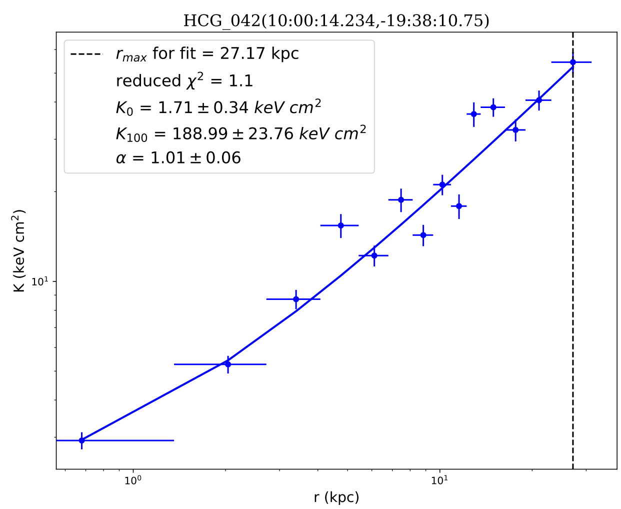
HCG_042(10:00:14.234,-19:38:10.75)
r_{max} for fit = 27.17 kpc
reduced χ^2 = 1.1
K_0 = 1.71 ± 0.34 $keV\ cm^2$
K_{100} = 188.99 ± 23.76 $keV\ cm^2$
α = 1.01 ± 0.06
K (keV cm^2)
r (kpc)

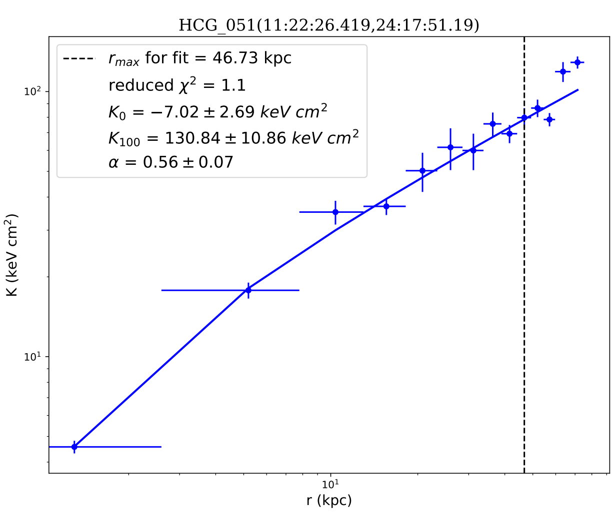
HCG_051(11:22:26.419,24:17:51.19)
r_{max} for fit = 46.73 kpc
reduced χ^2 = 1.1
K_0 = −7.02 ± 2.69 $keV\ cm^2$
K_{100} = 130.84 ± 10.86 $keV\ cm^2$
α = 0.56 ± 0.07
K (keV cm^2)
r (kpc)

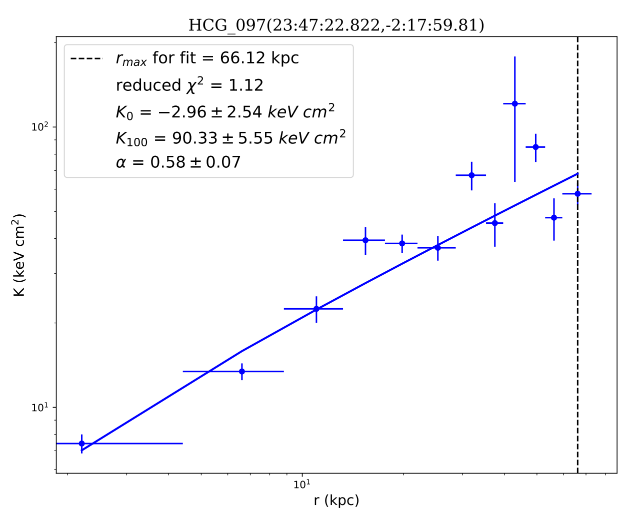
HCG_097(23:47:22.822,-2:17:59.81)
r_{max} for fit = 66.12 kpc
reduced χ^2 = 1.12
K_0 = −2.96 ± 2.54 $keV\ cm^2$
K_{100} = 90.33 ± 5.55 $keV\ cm^2$
α = 0.58 ± 0.07
K (keV cm^2)
r (kpc)

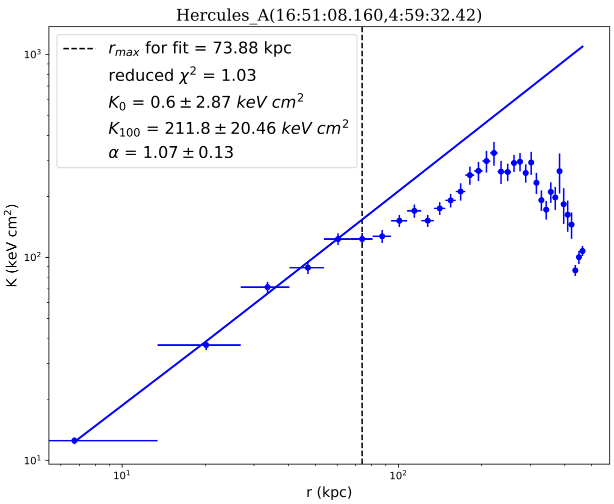
Hercules_A(16:51:08.160,4:59:32.42)
r_{max} for fit = 73.88 kpc
reduced χ^2 = 1.03
K_0 = 0.6 ± 2.87 $keV\ cm^2$
K_{100} = 211.8 ± 20.46 $keV\ cm^2$
α = 1.07 ± 0.13
K (keV cm^2)
r (kpc)

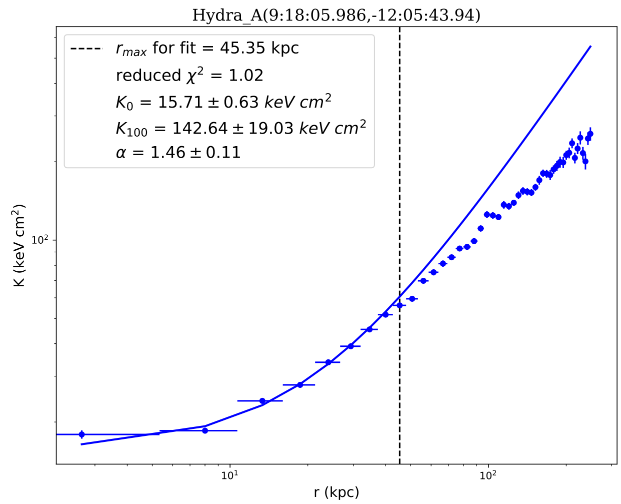
Hydra_A(9:18:05.986,-12:05:43.94)
r_{max} for fit = 45.35 kpc
reduced χ^2 = 1.02
K_0 = 15.71 ± 0.63 $keV\ cm^2$
K_{100} = 142.64 ± 19.03 $keV\ cm^2$
α = 1.46 ± 0.11
K (keV cm^2)
r (kpc)

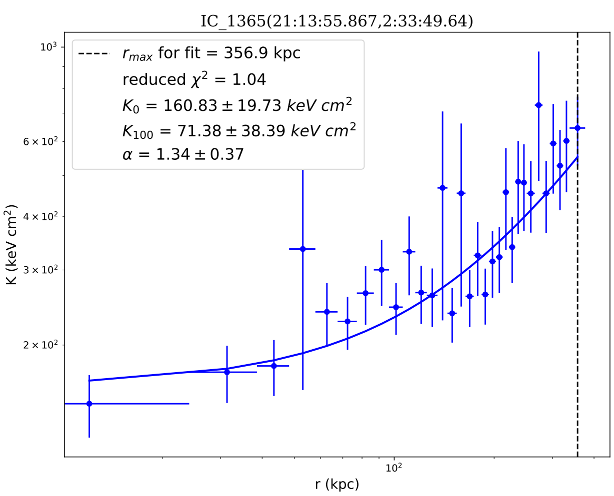
IC_1365(21:13:55.867,2:33:49.64)
r_{max} for fit = 356.9 kpc
reduced χ^2 = 1.04
K_0 = 160.83 ± 19.73 $keV\ cm^2$
K_{100} = 71.38 ± 38.39 $keV\ cm^2$
α = 1.34 ± 0.37
K (keV cm^2)
r (kpc)

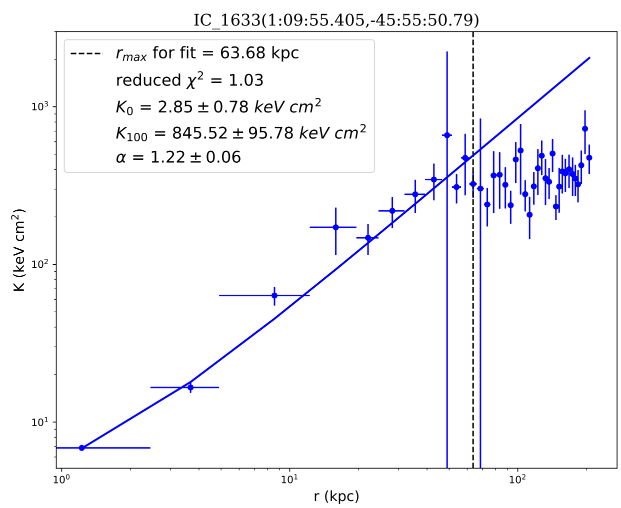
IC_1633(1:09:55.405,-45:55:50.79)
r_{max} for fit = 63.68 kpc
reduced χ^2 = 1.03
K_0 = 2.85 ± 0.78 $keV\ cm^2$
K_{100} = 845.52 ± 95.78 $keV\ cm^2$
α = 1.22 ± 0.06
K (keV cm^2)
r (kpc)

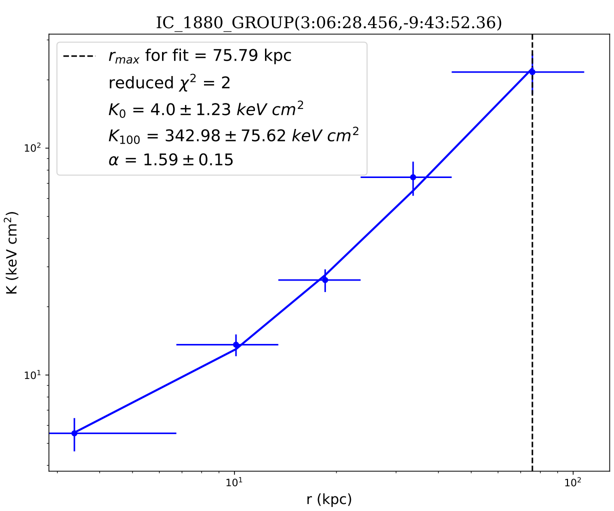
IC_1880_GROUP(3:06:28.456,-9:43:52.36)
r_{max} for fit = 75.79 kpc
reduced χ^2 = 2
K_0 = 4.0 ± 1.23 $keV\ cm^2$
K_{100} = 342.98 ± 75.62 $keV\ cm^2$
α = 1.59 ± 0.15
K (keV cm^2)
r (kpc)

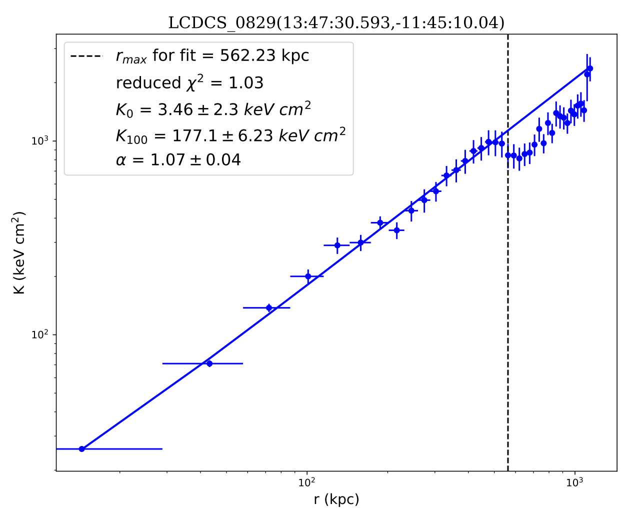
LCDCS_0829(13:47:30.593,-11:45:10.04)
r_{max} for fit = 562.23 kpc
reduced χ^2 = 1.03
K_0 = 3.46 ± 2.3 $keV\ cm^2$
K_{100} = 177.1 ± 6.23 $keV\ cm^2$
α = 1.07 ± 0.04
K (keV cm^2)
r (kpc)

MACS_J0011.7-1523(0:11:42.965,-15:23:20.80)

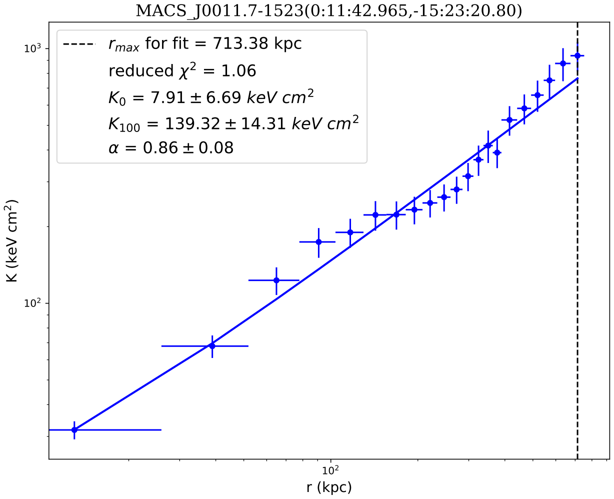

MACS_J0025.4-1222(0:25:29.688,-12:22:33.87)

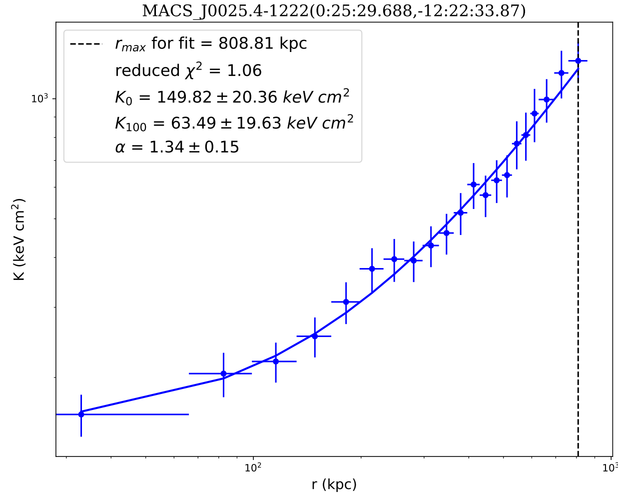

MACS_J0242.6-2132(2:42:35.906,-21:32:26.30)

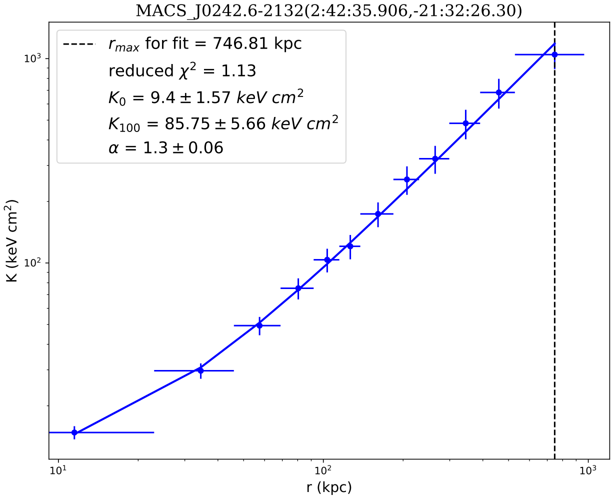

MACS_J0308.9+2645(3:08:55.927,26:45:38.34)

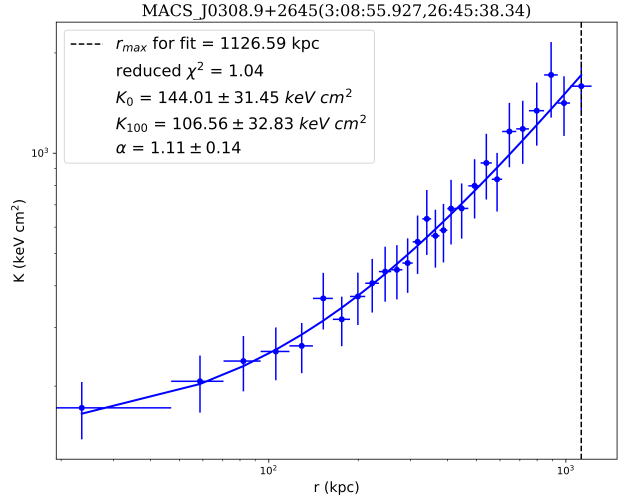

MACS_J0329.6-0211(3:29:41.681,-2:11:47.65)

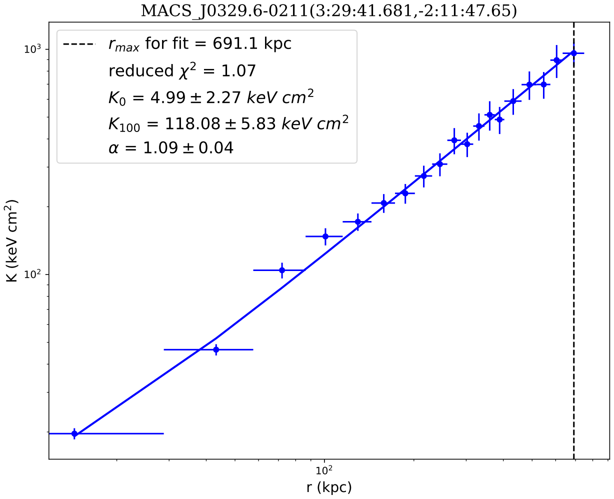

MACS_J0358.8-2955(3:58:52.563,-29:55:49.10)

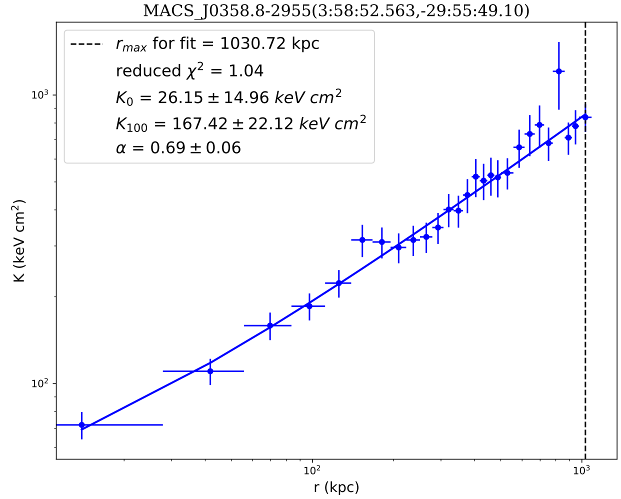

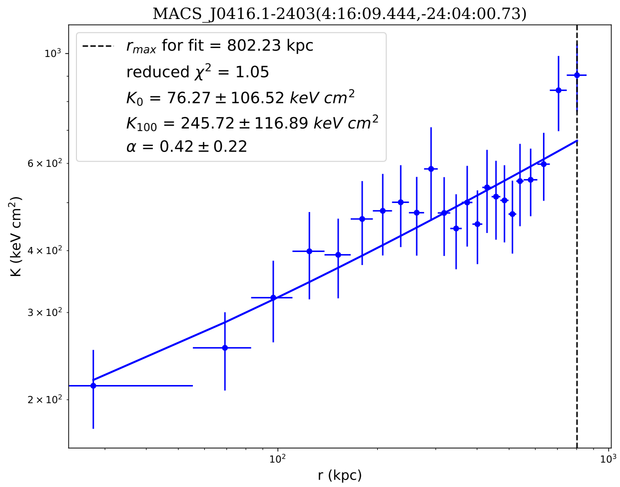
MACS_J0416.1-2403(4:16:09.444,-24:04:00.73)
r_{max} for fit = 802.23 kpc
reduced χ^2 = 1.05
$K_0 = 76.27 \pm 106.52$ $keV\ cm^2$
$K_{100} = 245.72 \pm 116.89$ $keV\ cm^2$
$\alpha = 0.42 \pm 0.22$
K (keV cm^2)
r (kpc)

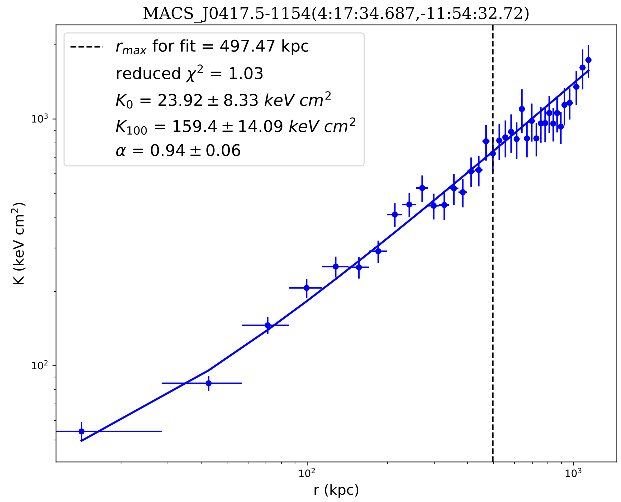
MACS_J0417.5-1154(4:17:34.687,-11:54:32.72)
r_{max} for fit = 497.47 kpc
reduced χ^2 = 1.03
$K_0 = 23.92 \pm 8.33$ $keV\ cm^2$
$K_{100} = 159.4 \pm 14.09$ $keV\ cm^2$
$\alpha = 0.94 \pm 0.06$
K (keV cm^2)
r (kpc)

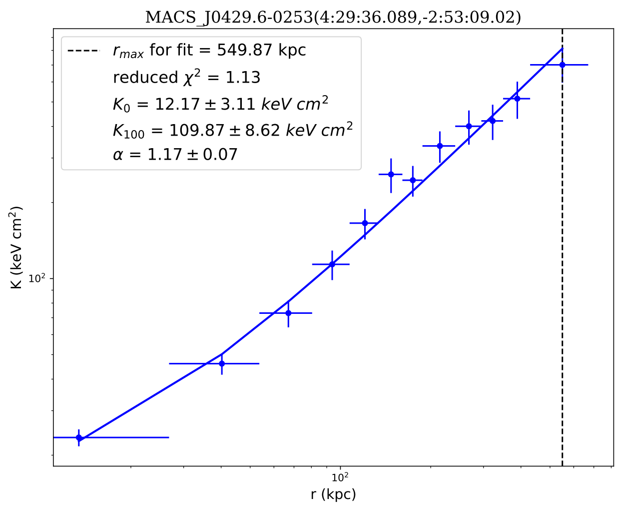
MACS_J0429.6-0253(4:29:36.089,-2:53:09.02)
r_{max} for fit = 549.87 kpc
reduced χ^2 = 1.13
$K_0 = 12.17 \pm 3.11$ $keV\ cm^2$
$K_{100} = 109.87 \pm 8.62$ $keV\ cm^2$
$\alpha = 1.17 \pm 0.07$
K (keV cm^2)
r (kpc)

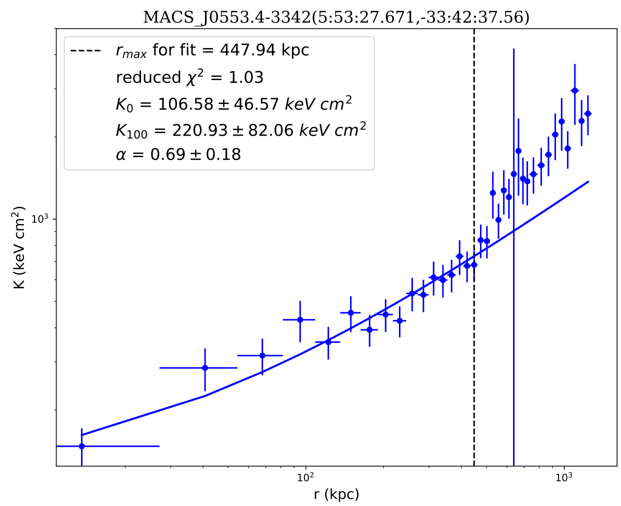
MACS_J0553.4-3342(5:53:27.671,-33:42:37.56)
r_{max} for fit = 447.94 kpc
reduced χ^2 = 1.03
$K_0 = 106.58 \pm 46.57$ $keV\ cm^2$
$K_{100} = 220.93 \pm 82.06$ $keV\ cm^2$
$\alpha = 0.69 \pm 0.18$
K (keV cm^2)
r (kpc)

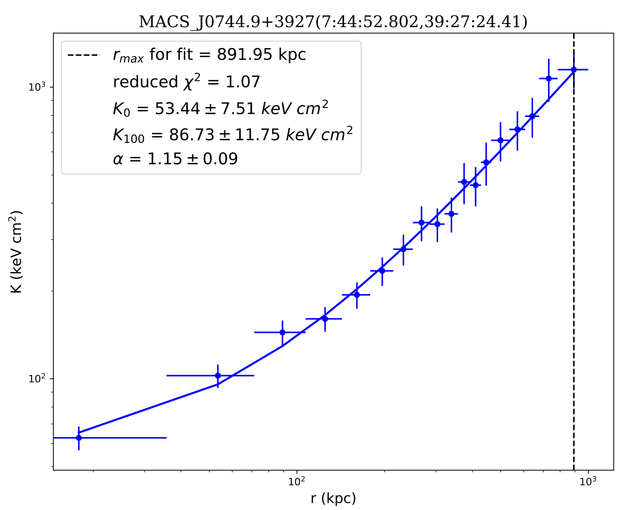
MACS_J0744.9+3927(7:44:52.802,39:27:24.41)
r_{max} for fit = 891.95 kpc
reduced χ^2 = 1.07
$K_0 = 53.44 \pm 7.51$ $keV\ cm^2$
$K_{100} = 86.73 \pm 11.75$ $keV\ cm^2$
$\alpha = 1.15 \pm 0.09$
K (keV cm^2)
r (kpc)

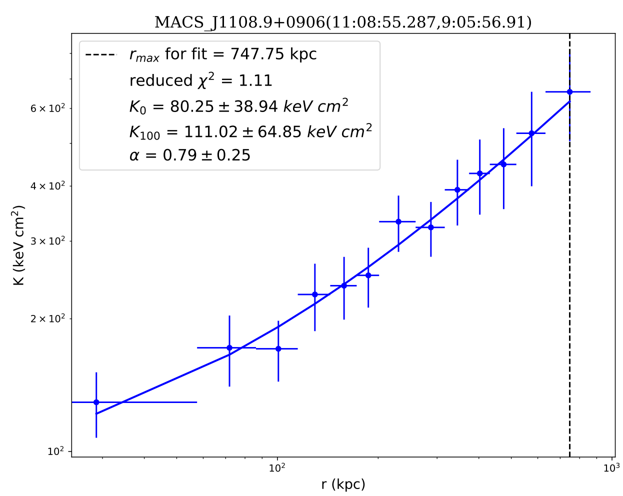
MACS_J1108.9+0906(11:08:55.287,9:05:56.91)
r_{max} for fit = 747.75 kpc
reduced χ^2 = 1.11
$K_0 = 80.25 \pm 38.94$ $keV\ cm^2$
$K_{100} = 111.02 \pm 64.85$ $keV\ cm^2$
$\alpha = 0.79 \pm 0.25$
K (keV cm^2)
r (kpc)

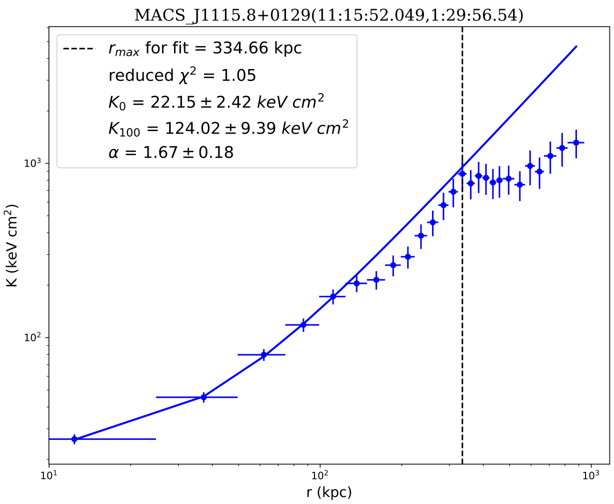
MACS_J1115.8+0129(11:15:52.049,1:29:56.54)
r_{max} for fit = 334.66 kpc
reduced χ^2 = 1.05
K_0 = 22.15 ± 2.42 $keV\ cm^2$
K_{100} = 124.02 ± 9.39 $keV\ cm^2$
α = 1.67 ± 0.18
K (keV cm^2)
r (kpc)

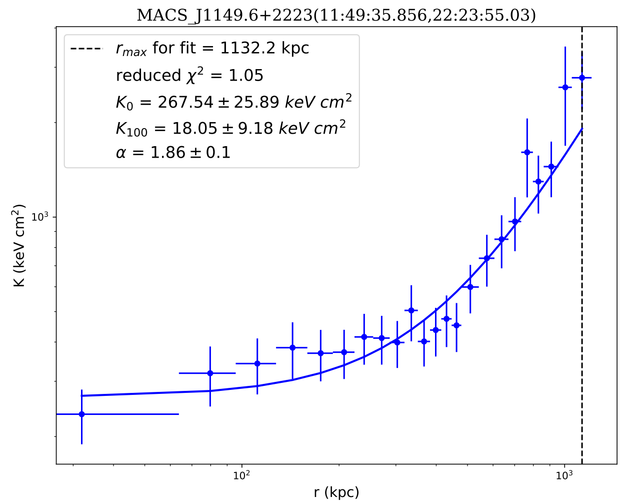
MACS_J1149.6+2223(11:49:35.856,22:23:55.03)
r_{max} for fit = 1132.2 kpc
reduced χ^2 = 1.05
K_0 = 267.54 ± 25.89 $keV\ cm^2$
K_{100} = 18.05 ± 9.18 $keV\ cm^2$
α = 1.86 ± 0.1
K (keV cm^2)
r (kpc)

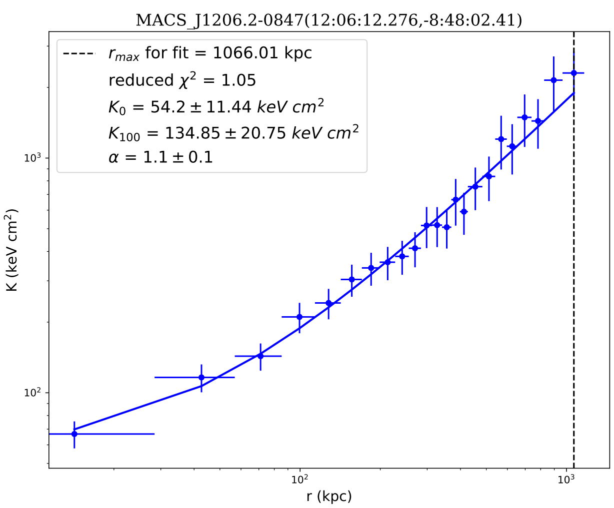
MACS_J1206.2-0847(12:06:12.276,-8:48:02.41)
r_{max} for fit = 1066.01 kpc
reduced χ^2 = 1.05
K_0 = 54.2 ± 11.44 $keV\ cm^2$
K_{100} = 134.85 ± 20.75 $keV\ cm^2$
α = 1.1 ± 0.1
K (keV cm^2)
r (kpc)

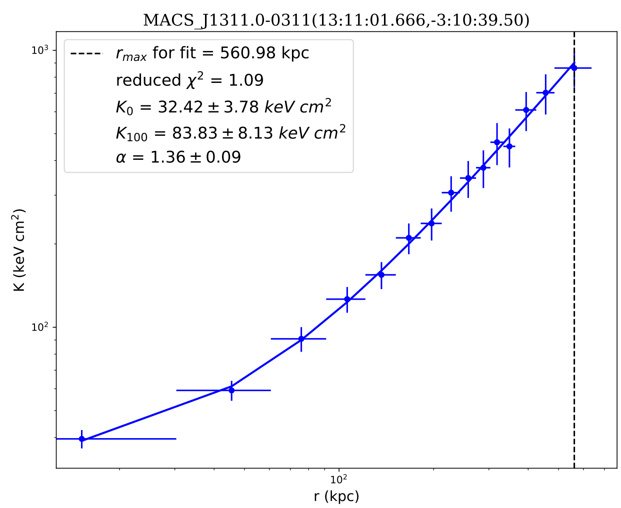
MACS_J1311.0-0311(13:11:01.666,-3:10:39.50)
r_{max} for fit = 560.98 kpc
reduced χ^2 = 1.09
K_0 = 32.42 ± 3.78 $keV\ cm^2$
K_{100} = 83.83 ± 8.13 $keV\ cm^2$
α = 1.36 ± 0.09
K (keV cm^2)
r (kpc)

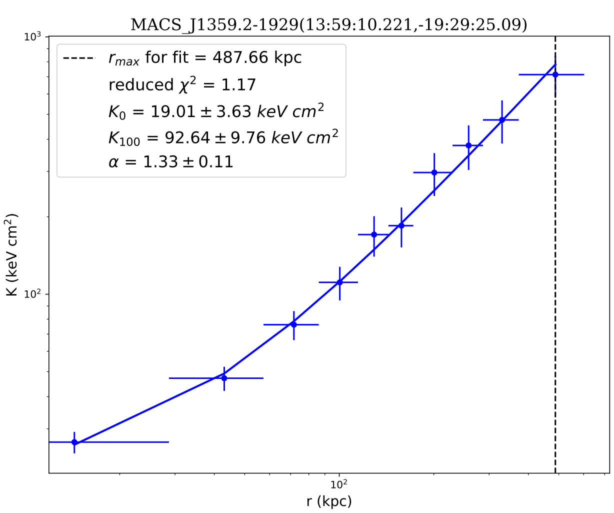
MACS_J1359.2-1929(13:59:10.221,-19:29:25.09)
r_{max} for fit = 487.66 kpc
reduced χ^2 = 1.17
K_0 = 19.01 ± 3.63 $keV\ cm^2$
K_{100} = 92.64 ± 9.76 $keV\ cm^2$
α = 1.33 ± 0.11
K (keV cm^2)
r (kpc)

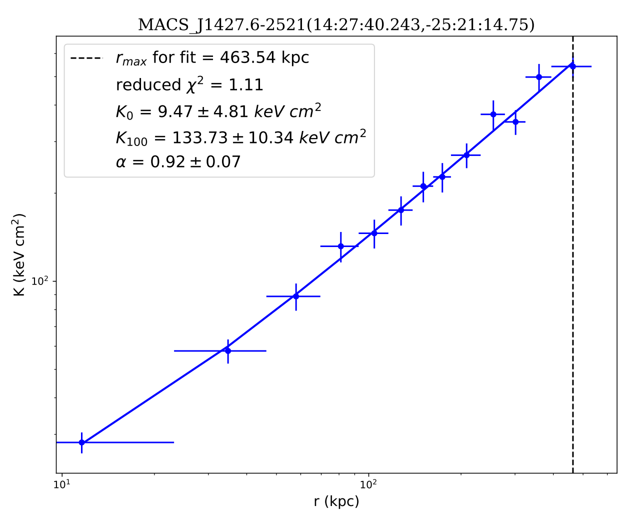
MACS_J1427.6-2521(14:27:40.243,-25:21:14.75)
r_{max} for fit = 463.54 kpc
reduced χ^2 = 1.11
K_0 = 9.47 ± 4.81 $keV\ cm^2$
K_{100} = 133.73 ± 10.34 $keV\ cm^2$
α = 0.92 ± 0.07
K (keV cm^2)
r (kpc)

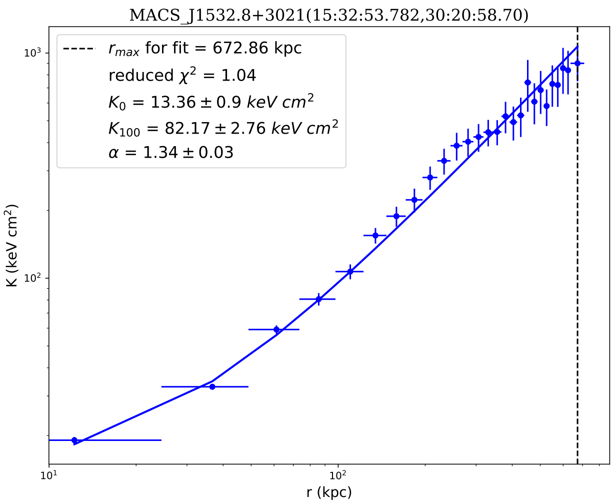
MACS_J1532.8+3021(15:32:53.782,30:20:58.70)
r_{max} for fit = 672.86 kpc
reduced χ^2 = 1.04
K_0 = 13.36 ± 0.9 $keV\ cm^2$
K_{100} = 82.17 ± 2.76 $keV\ cm^2$
α = 1.34 ± 0.03
K (keV cm^2)
r (kpc)

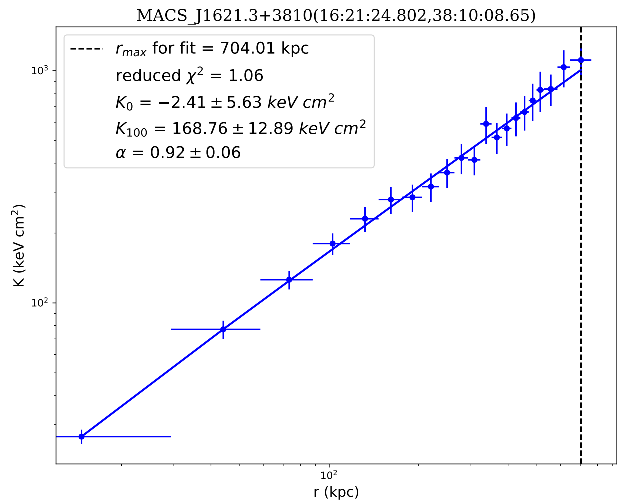
MACS_J1621.3+3810(16:21:24.802,38:10:08.65)
r_{max} for fit = 704.01 kpc
reduced χ^2 = 1.06
K_0 = -2.41 ± 5.63 $keV\ cm^2$
K_{100} = 168.76 ± 12.89 $keV\ cm^2$
α = 0.92 ± 0.06
K (keV cm^2)
r (kpc)

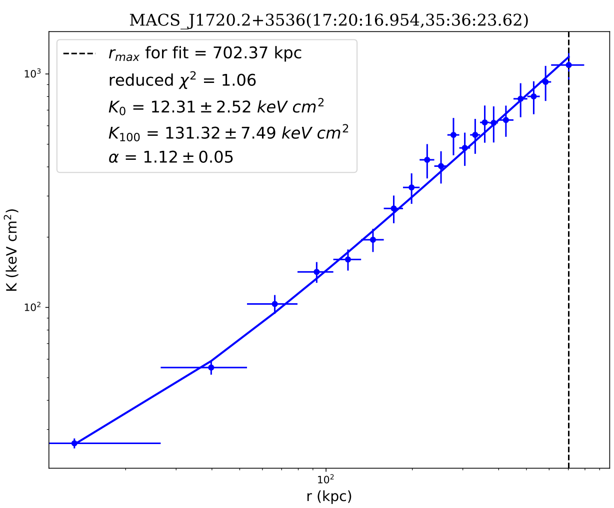
MACS_J1720.2+3536(17:20:16.954,35:36:23.62)
r_{max} for fit = 702.37 kpc
reduced χ^2 = 1.06
K_0 = 12.31 ± 2.52 $keV\ cm^2$
K_{100} = 131.32 ± 7.49 $keV\ cm^2$
α = 1.12 ± 0.05
K (keV cm^2)
r (kpc)

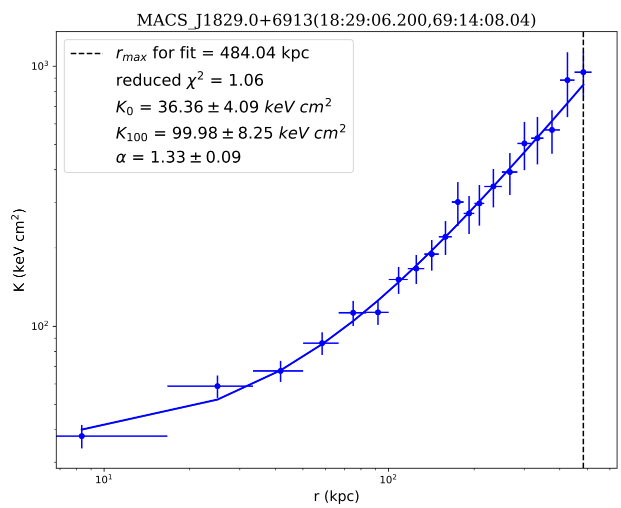
MACS_J1829.0+6913(18:29:06.200,69:14:08.04)
r_{max} for fit = 484.04 kpc
reduced χ^2 = 1.06
K_0 = 36.36 ± 4.09 $keV\ cm^2$
K_{100} = 99.98 ± 8.25 $keV\ cm^2$
α = 1.33 ± 0.09
K (keV cm^2)
r (kpc)

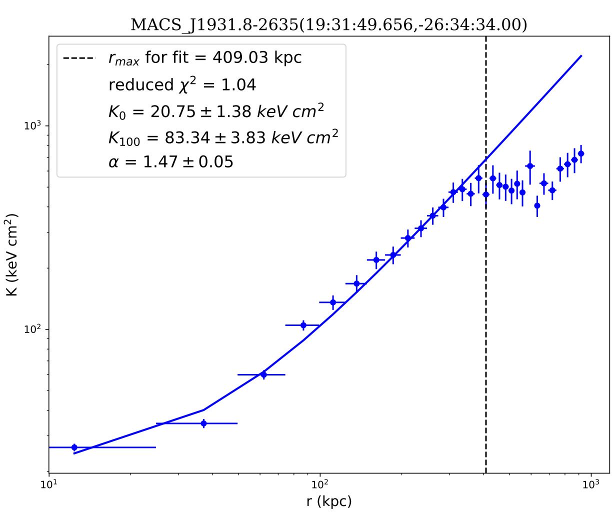
MACS_J1931.8-2635(19:31:49.656,-26:34:34.00)
r_{max} for fit = 409.03 kpc
reduced χ^2 = 1.04
K_0 = 20.75 ± 1.38 $keV\ cm^2$
K_{100} = 83.34 ± 3.83 $keV\ cm^2$
α = 1.47 ± 0.05
K (keV cm^2)
r (kpc)

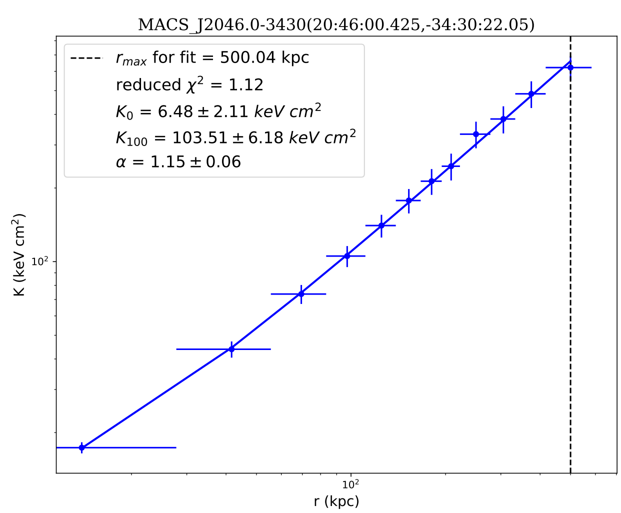
MACS_J2046.0-3430(20:46:00.425,-34:30:22.05)
r_{max} for fit = 500.04 kpc
reduced χ^2 = 1.12
K_0 = 6.48 ± 2.11 $keV\ cm^2$
K_{100} = 103.51 ± 6.18 $keV\ cm^2$
α = 1.15 ± 0.06
K (keV cm^2)
r (kpc)

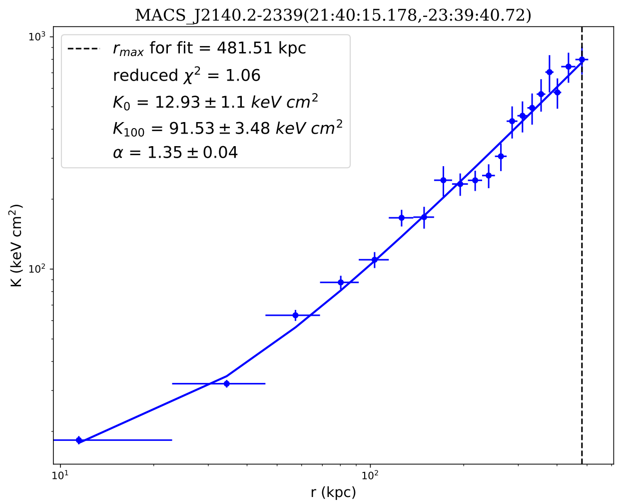
MACS_J2140.2-2339(21:40:15.178,-23:39:40.72)
r_{max} for fit = 481.51 kpc
reduced χ^2 = 1.06
K_0 = 12.93 ± 1.1 $keV\ cm^2$
K_{100} = 91.53 ± 3.48 $keV\ cm^2$
α = 1.35 ± 0.04
K (keV cm^2)
r (kpc)

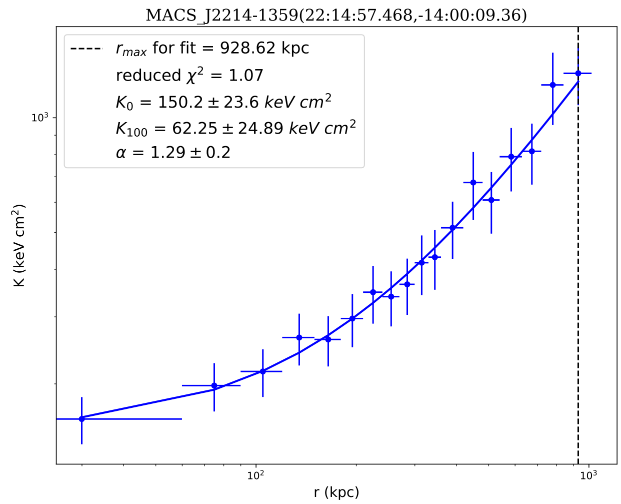
MACS_J2214-1359(22:14:57.468,-14:00:09.36)
r_{max} for fit = 928.62 kpc
reduced χ^2 = 1.07
K_0 = 150.2 ± 23.6 $keV\ cm^2$
K_{100} = 62.25 ± 24.89 $keV\ cm^2$
α = 1.29 ± 0.2
K (keV cm^2)
r (kpc)

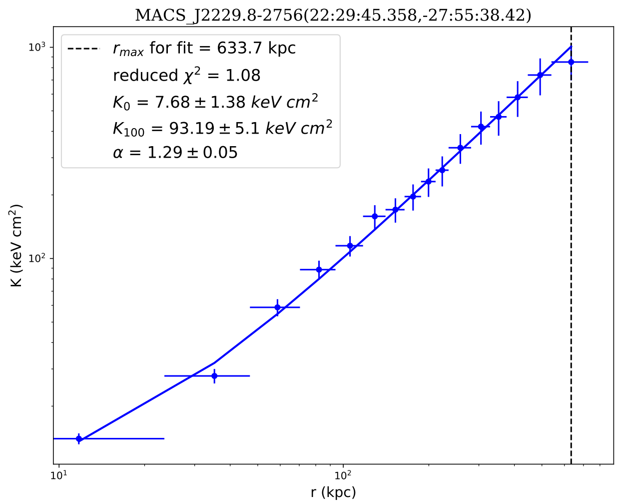
MACS_J2229.8-2756(22:29:45.358,-27:55:38.42)
r_{max} for fit = 633.7 kpc
reduced χ^2 = 1.08
K_0 = 7.68 ± 1.38 $keV\ cm^2$
K_{100} = 93.19 ± 5.1 $keV\ cm^2$
α = 1.29 ± 0.05
K (keV cm^2)
r (kpc)

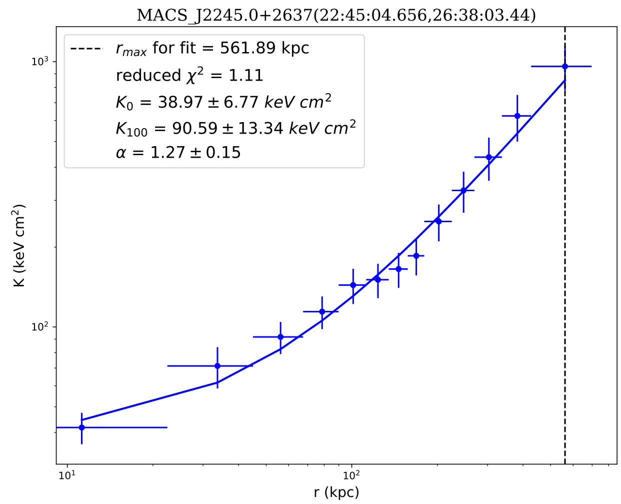
MACS_J2245.0+2637(22:45:04.656,26:38:03.44)
r_{max} for fit = 561.89 kpc
reduced χ^2 = 1.11
K_0 = 38.97 ± 6.77 $keV\ cm^2$
K_{100} = 90.59 ± 13.34 $keV\ cm^2$
α = 1.27 ± 0.15
K (keV cm^2)
r (kpc)

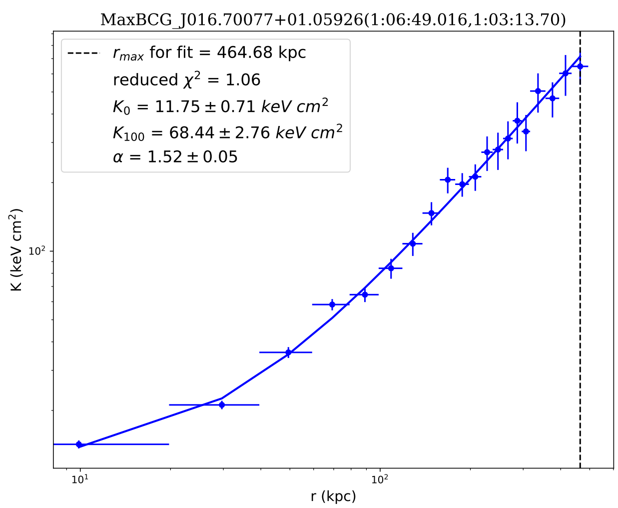
MaxBCG_J016.70077+01.05926(1:06:49.016,1:03:13.70)
r_{max} for fit = 464.68 kpc
reduced χ^2 = 1.06
K_0 = 11.75 ± 0.71 $keV\ cm^2$
K_{100} = 68.44 ± 2.76 $keV\ cm^2$
α = 1.52 ± 0.05
K (keV cm^2)
r (kpc)

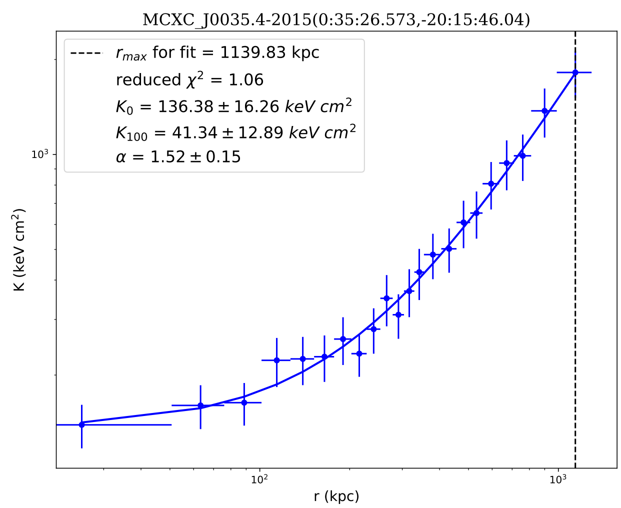
MCXC_J0035.4-2015(0:35:26.573,-20:15:46.04)
r_{max} for fit = 1139.83 kpc
reduced χ^2 = 1.06
K_0 = 136.38 ± 16.26 $keV\ cm^2$
K_{100} = 41.34 ± 12.89 $keV\ cm^2$
α = 1.52 ± 0.15
K (keV cm^2)
r (kpc)

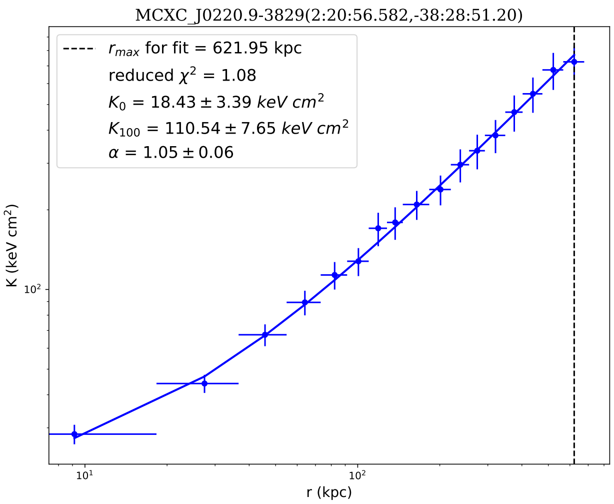
MCXC_J0220.9-3829(2:20:56.582,-38:28:51.20)
r_{max} for fit = 621.95 kpc
reduced χ^2 = 1.08
K_0 = 18.43 ± 3.39 $keV\ cm^2$
K_{100} = 110.54 ± 7.65 $keV\ cm^2$
α = 1.05 ± 0.06
K (keV cm^2)
r (kpc)

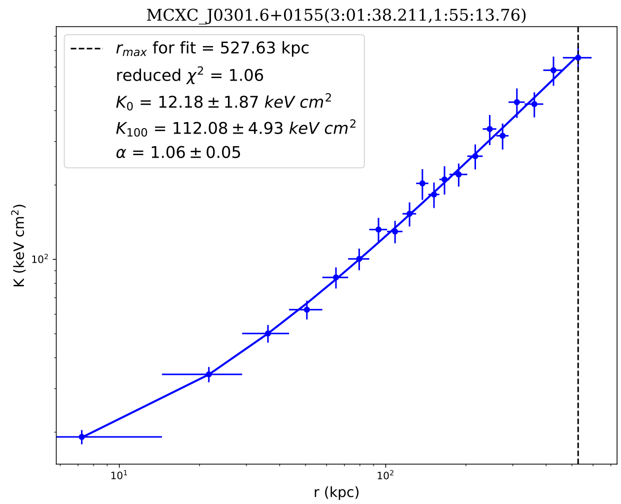
MCXC_J0301.6+0155(3:01:38.211,1:55:13.76)
r_{max} for fit = 527.63 kpc
reduced χ^2 = 1.06
K_0 = 12.18 ± 1.87 $keV\ cm^2$
K_{100} = 112.08 ± 4.93 $keV\ cm^2$
α = 1.06 ± 0.05
K (keV cm^2)
r (kpc)

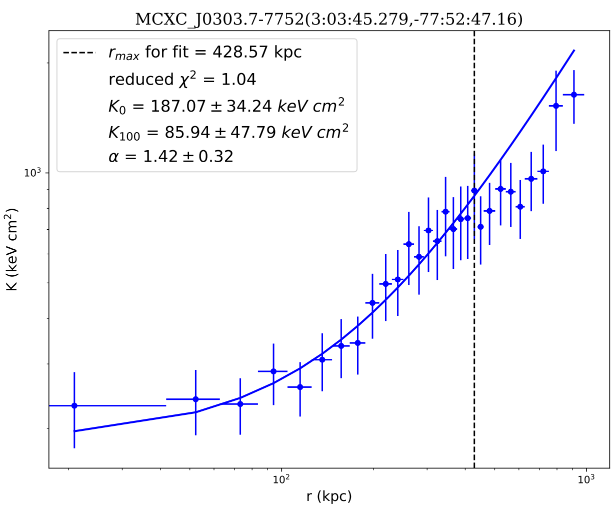
MCXC_J0303.7-7752(3:03:45.279,-77:52:47.16)
r_{max} for fit = 428.57 kpc
reduced χ^2 = 1.04
K_0 = 187.07 ± 34.24 $keV\ cm^2$
K_{100} = 85.94 ± 47.79 $keV\ cm^2$
α = 1.42 ± 0.32
K (keV cm^2)
r (kpc)

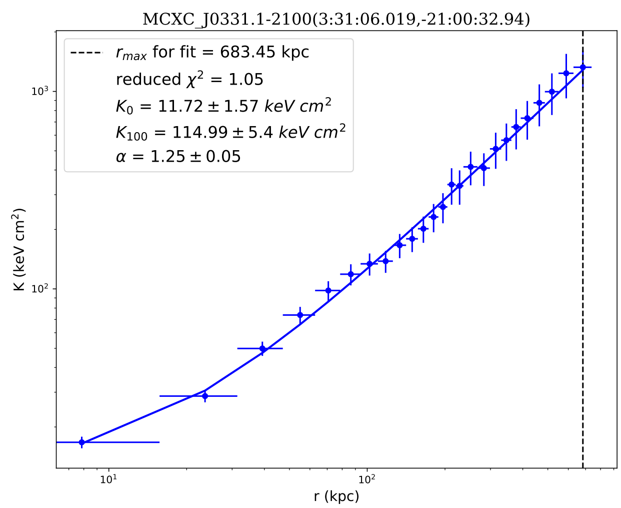
MCXC_J0331.1-2100(3:31:06.019,-21:00:32.94)
r_{max} for fit = 683.45 kpc
reduced χ^2 = 1.05
K_0 = 11.72 ± 1.57 $keV\ cm^2$
K_{100} = 114.99 ± 5.4 $keV\ cm^2$
α = 1.25 ± 0.05
K (keV cm^2)
r (kpc)

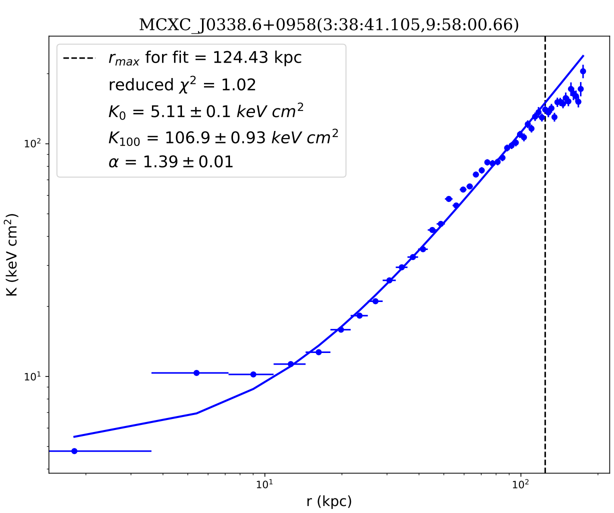
MCXC_J0338.6+0958(3:38:41.105,9:58:00.66)
r_{max} for fit = 124.43 kpc
reduced χ^2 = 1.02
K_0 = 5.11 ± 0.1 $keV\ cm^2$
K_{100} = 106.9 ± 0.93 $keV\ cm^2$
α = 1.39 ± 0.01
K (keV cm^2)
r (kpc)

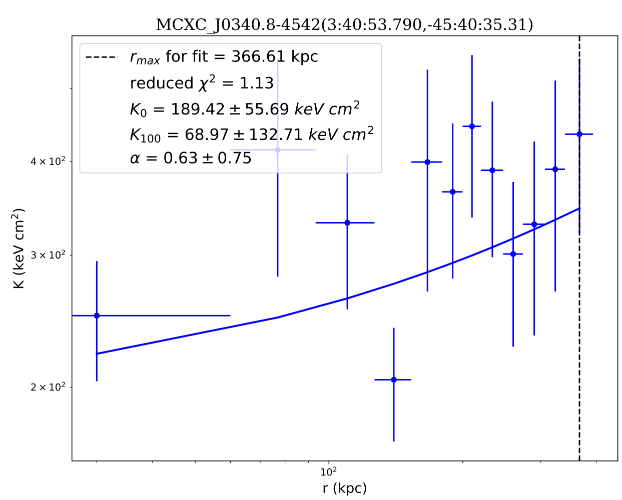
MCXC_J0340.8-4542(3:40:53.790,-45:40:35.31)
r_{max} for fit = 366.61 kpc
reduced χ^2 = 1.13
K_0 = 189.42 ± 55.69 $keV\ cm^2$
K_{100} = 68.97 ± 132.71 $keV\ cm^2$
α = 0.63 ± 0.75
K (keV cm^2)
r (kpc)

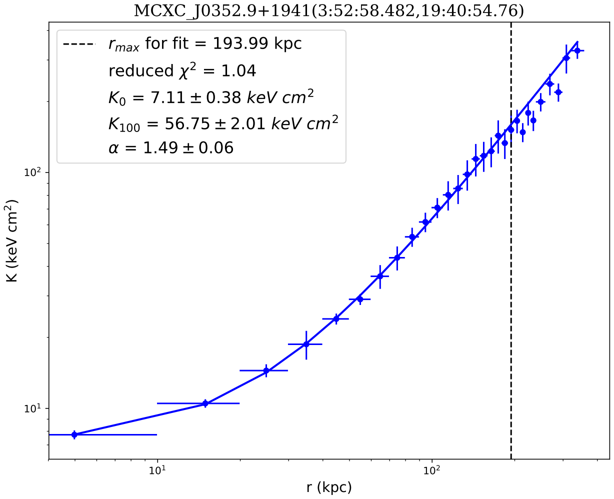

MCXC_J0352.9+1941(3:52:58.482,19:40:54.76)

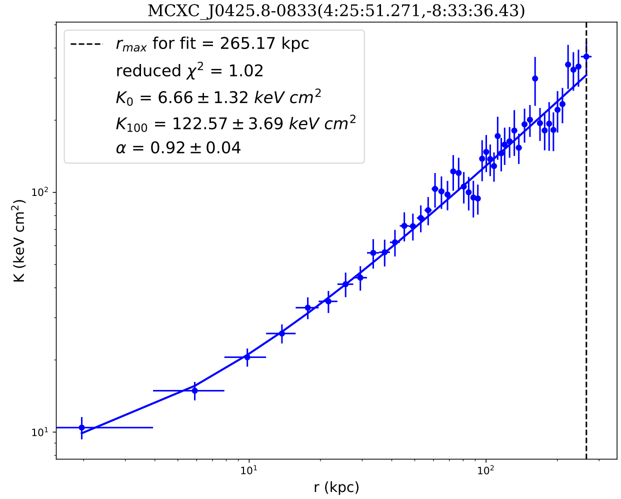

MCXC_J0425.8-0833(4:25:51.271,-8:33:36.43)

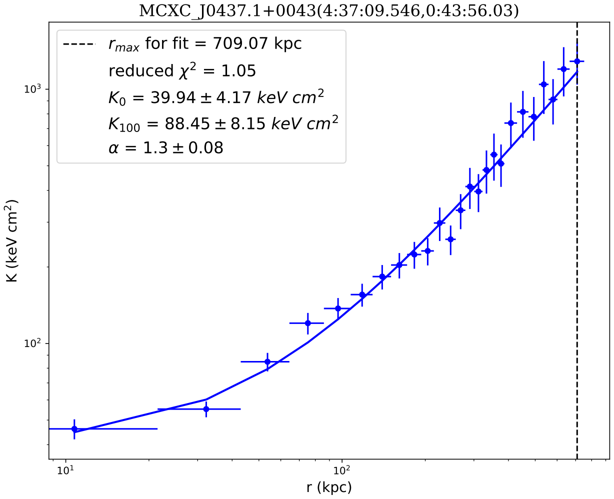

MCXC_J0437.1+0043(4:37:09.546,0:43:56.03)

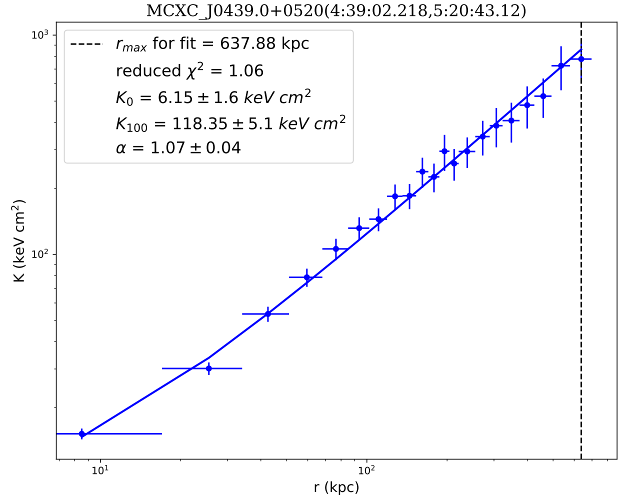

MCXC_J0439.0+0520(4:39:02.218,5:20:43.12)

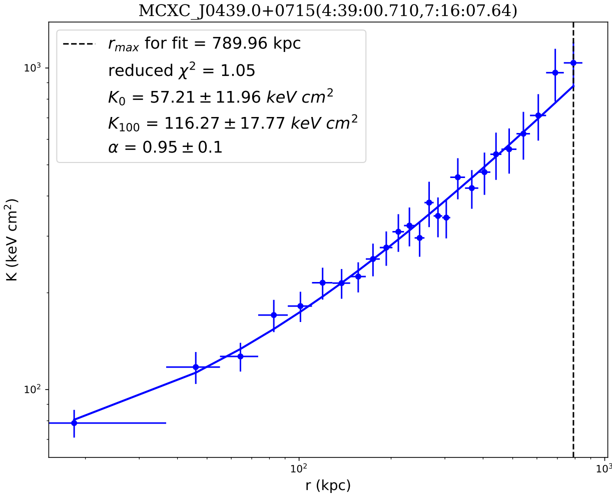

MCXC_J0439.0+0715(4:39:00.710,7:16:07.64)

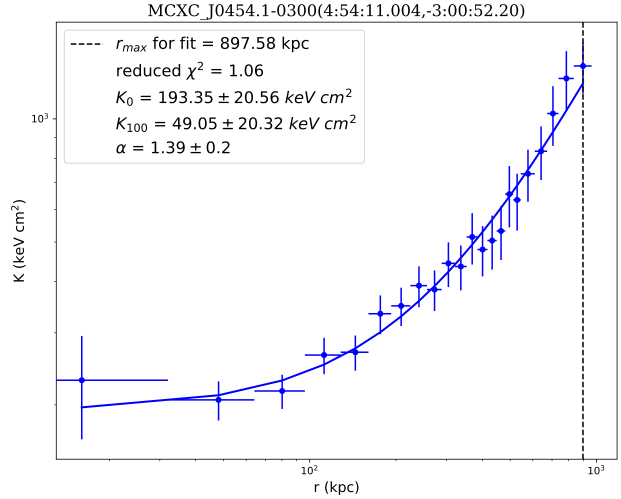

MCXC_J0454.1-0300(4:54:11.004,-3:00:52.20)

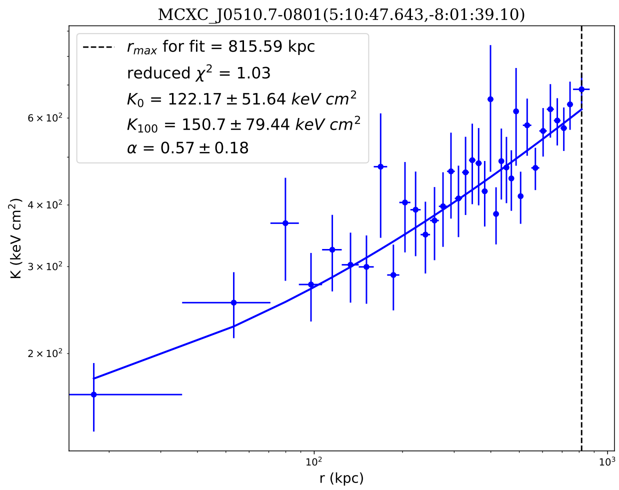
MCXC_J0510.7-0801(5:10:47.643,-8:01:39.10)
r_{max} for fit = 815.59 kpc
reduced χ^2 = 1.03
K_0 = 122.17 ± 51.64 $keV\ cm^2$
K_{100} = 150.7 ± 79.44 $keV\ cm^2$
α = 0.57 ± 0.18
K (keV cm^2)
r (kpc)

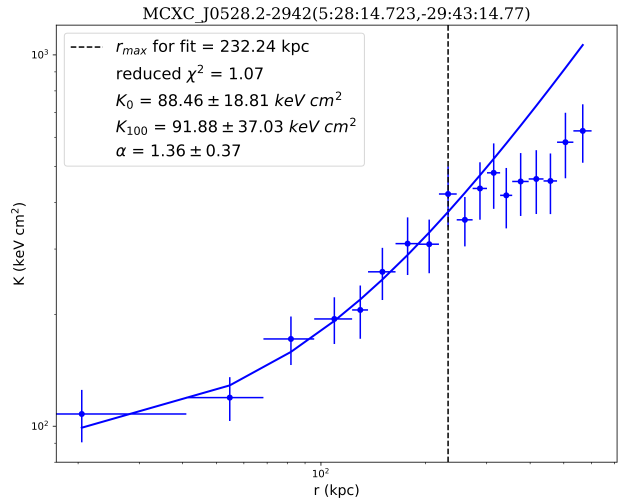
MCXC_J0528.2-2942(5:28:14.723,-29:43:14.77)
r_{max} for fit = 232.24 kpc
reduced χ^2 = 1.07
K_0 = 88.46 ± 18.81 $keV\ cm^2$
K_{100} = 91.88 ± 37.03 $keV\ cm^2$
α = 1.36 ± 0.37
K (keV cm^2)
r (kpc)

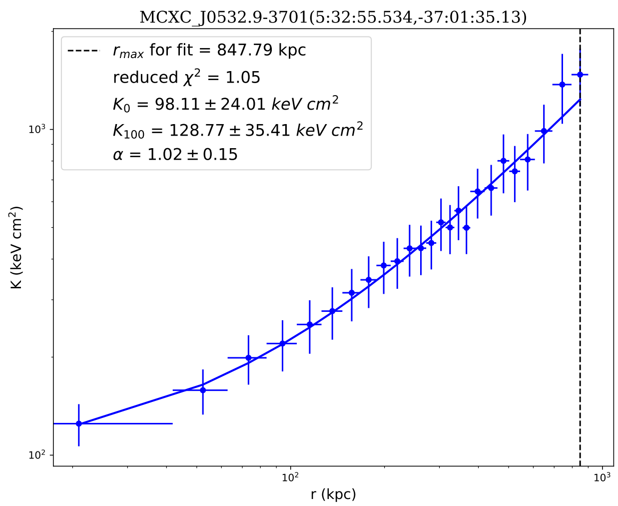
MCXC_J0532.9-3701(5:32:55.534,-37:01:35.13)
r_{max} for fit = 847.79 kpc
reduced χ^2 = 1.05
K_0 = 98.11 ± 24.01 $keV\ cm^2$
K_{100} = 128.77 ± 35.41 $keV\ cm^2$
α = 1.02 ± 0.15
K (keV cm^2)
r (kpc)

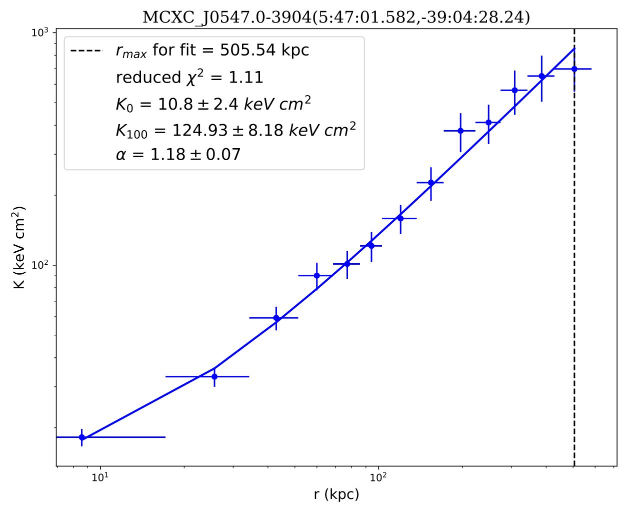
MCXC_J0547.0-3904(5:47:01.582,-39:04:28.24)
r_{max} for fit = 505.54 kpc
reduced χ^2 = 1.11
K_0 = 10.8 ± 2.4 $keV\ cm^2$
K_{100} = 124.93 ± 8.18 $keV\ cm^2$
α = 1.18 ± 0.07
K (keV cm^2)
r (kpc)

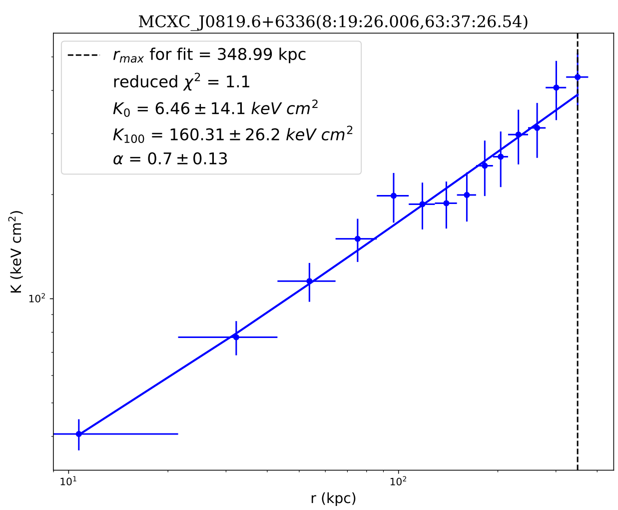
MCXC_J0819.6+6336(8:19:26.006,63:37:26.54)
r_{max} for fit = 348.99 kpc
reduced χ^2 = 1.1
K_0 = 6.46 ± 14.1 $keV\ cm^2$
K_{100} = 160.31 ± 26.2 $keV\ cm^2$
α = 0.7 ± 0.13
K (keV cm^2)
r (kpc)

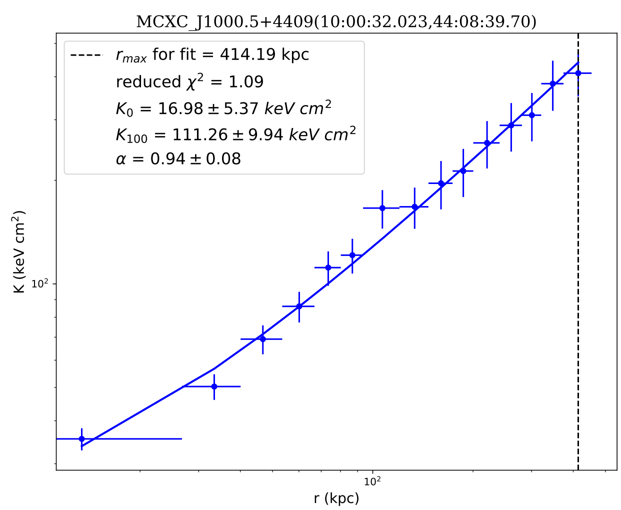
MCXC_J1000.5+4409(10:00:32.023,44:08:39.70)
r_{max} for fit = 414.19 kpc
reduced χ^2 = 1.09
K_0 = 16.98 ± 5.37 $keV\ cm^2$
K_{100} = 111.26 ± 9.94 $keV\ cm^2$
α = 0.94 ± 0.08
K (keV cm^2)
r (kpc)

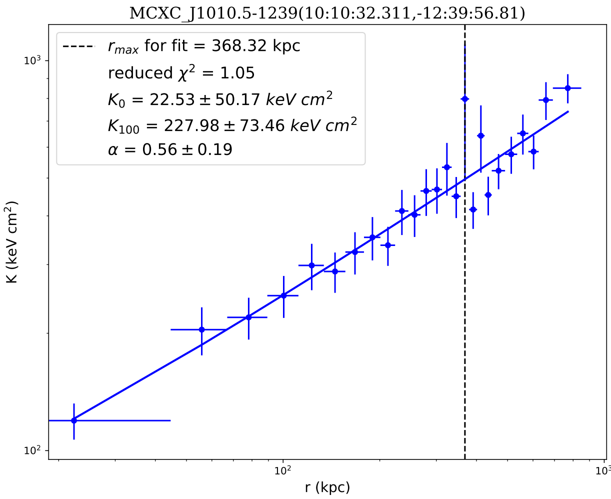
MCXC_J1010.5-1239(10:10:32.311,-12:39:56.81)
r_{max} for fit = 368.32 kpc
reduced χ^2 = 1.05
K_0 = 22.53 ± 50.17 $keV\ cm^2$
K_{100} = 227.98 ± 73.46 $keV\ cm^2$
α = 0.56 ± 0.19
K (keV cm^2)
r (kpc)

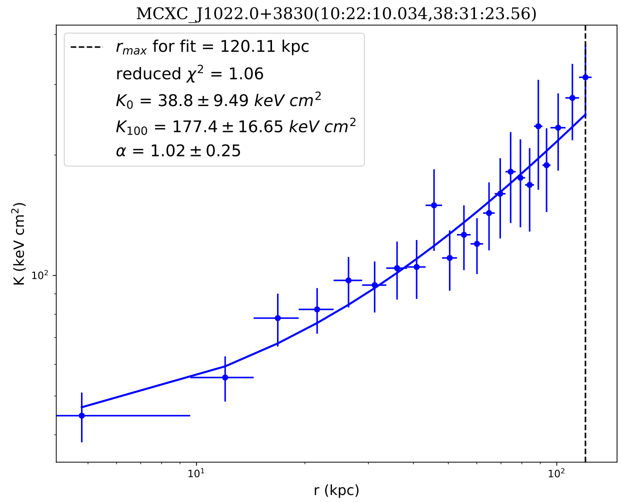
MCXC_J1022.0+3830(10:22:10.034,38:31:23.56)
r_{max} for fit = 120.11 kpc
reduced χ^2 = 1.06
K_0 = 38.8 ± 9.49 $keV\ cm^2$
K_{100} = 177.4 ± 16.65 $keV\ cm^2$
α = 1.02 ± 0.25
K (keV cm^2)
r (kpc)

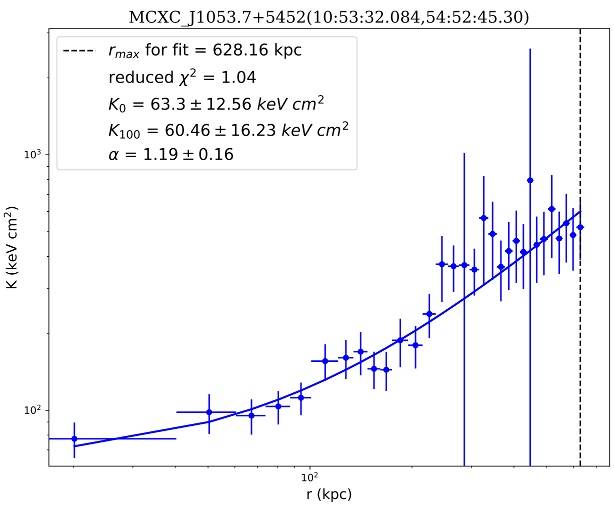
MCXC_J1053.7+5452(10:53:32.084,54:52:45.30)
r_{max} for fit = 628.16 kpc
reduced χ^2 = 1.04
K_0 = 63.3 ± 12.56 $keV\ cm^2$
K_{100} = 60.46 ± 16.23 $keV\ cm^2$
α = 1.19 ± 0.16
K (keV cm^2)
r (kpc)

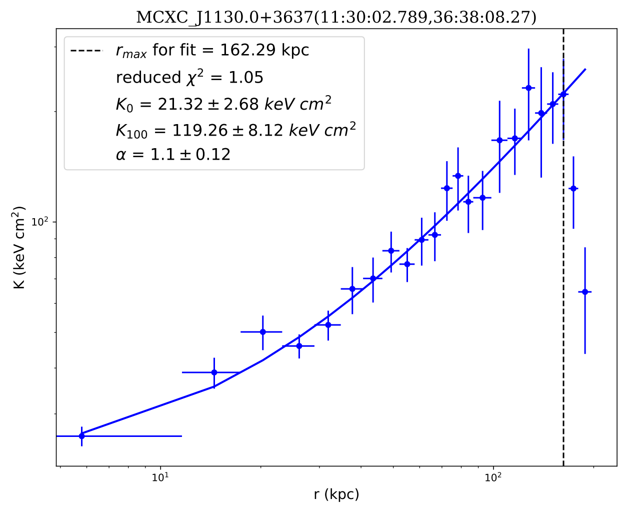
MCXC_J1130.0+3637(11:30:02.789,36:38:08.27)
r_{max} for fit = 162.29 kpc
reduced χ^2 = 1.05
K_0 = 21.32 ± 2.68 $keV\ cm^2$
K_{100} = 119.26 ± 8.12 $keV\ cm^2$
α = 1.1 ± 0.12
K (keV cm^2)
r (kpc)

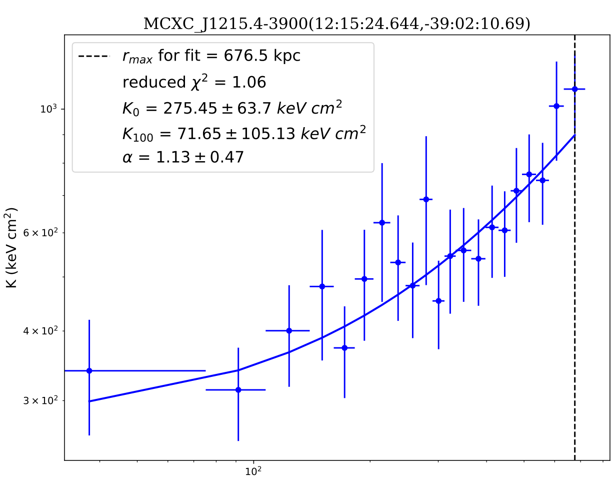
MCXC_J1215.4-3900(12:15:24.644,-39:02:10.69)
r_{max} for fit = 676.5 kpc
reduced χ^2 = 1.06
K_0 = 275.45 ± 63.7 $keV\ cm^2$
K_{100} = 71.65 ± 105.13 $keV\ cm^2$
α = 1.13 ± 0.47
K (keV cm^2)
r (kpc)

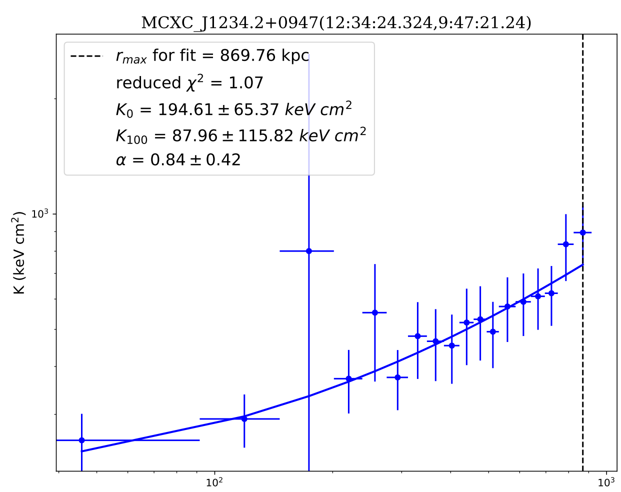
MCXC_J1234.2+0947(12:34:24.324,9:47:21.24)
r_{max} for fit = 869.76 kpc
reduced χ^2 = 1.07
K_0 = 194.61 ± 65.37 $keV\ cm^2$
K_{100} = 87.96 ± 115.82 $keV\ cm^2$
α = 0.84 ± 0.42
K (keV cm^2)
r (kpc)

MCXC_J1514.9-1523(15:15:02.556,-15:23:21.09)

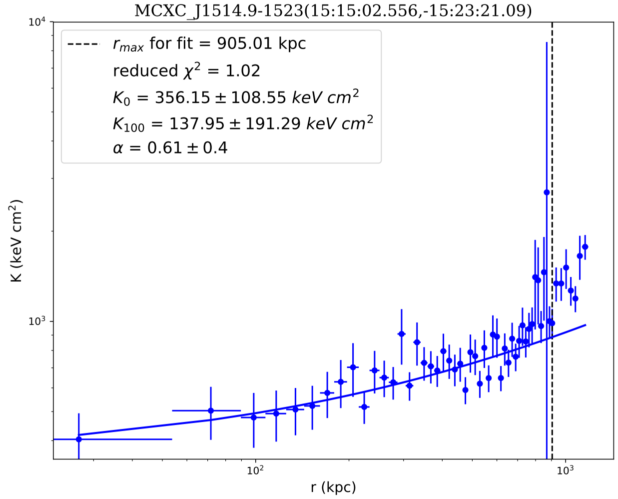

MCXC_J1524.2-3154(15:24:12.831,-31:54:16.15)

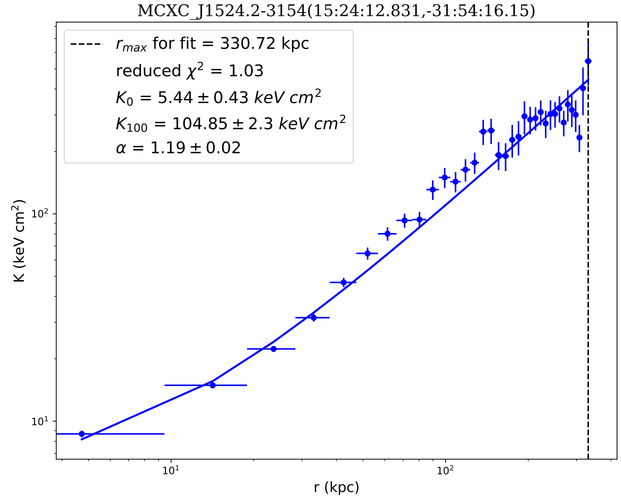

MCXC_J1558.3-1410(15:58:21.847,-14:09:57.86)

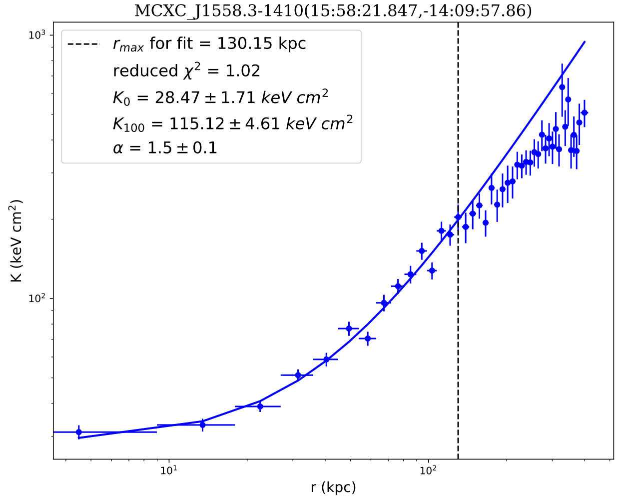

MCXC_J1750.2+3504(17:50:16.577,35:04:58.17)

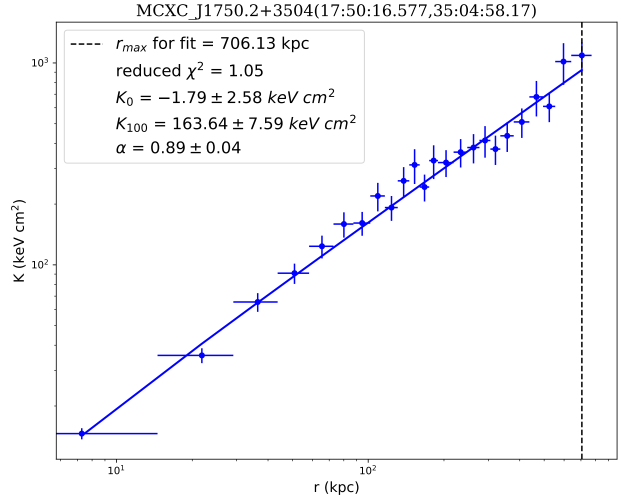

MCXC_J1852.1+5711(18:52:08.815,57:11:42.61)

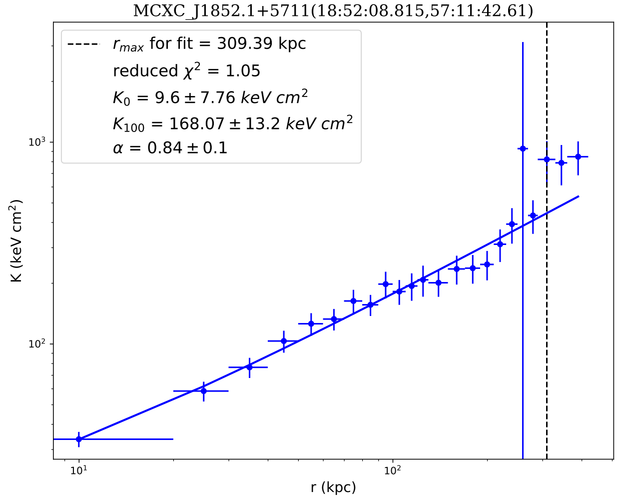

MCXC_J1853.9+6822(18:54:02.258,68:22:57.72)

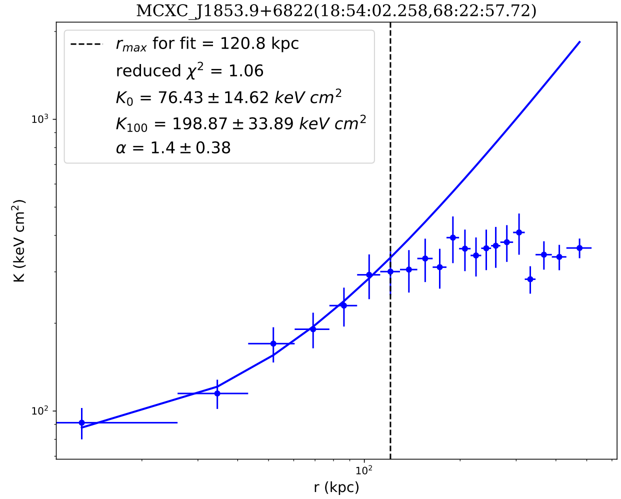

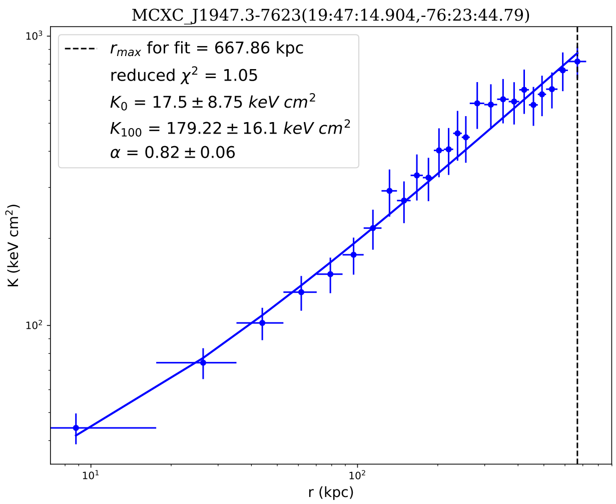
MCXC_J1947.3-7623(19:47:14.904,-76:23:44.79)
r_{max} for fit = 667.86 kpc
reduced χ^2 = 1.05
K_0 = 17.5 ± 8.75 $keV\ cm^2$
K_{100} = 179.22 ± 16.1 $keV\ cm^2$
α = 0.82 ± 0.06
K (keV cm^2)
r (kpc)

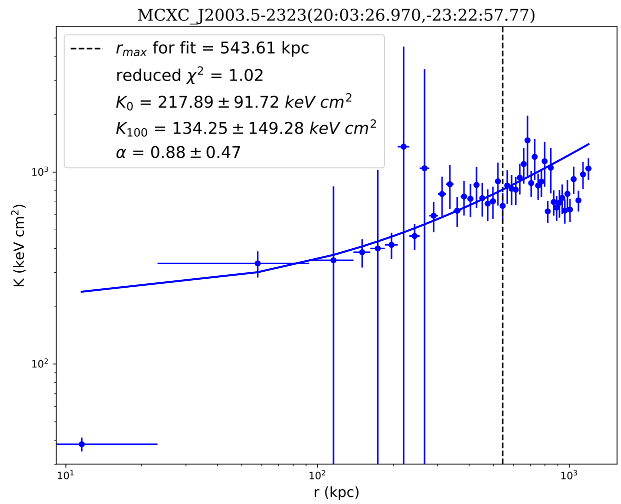
MCXC_J2003.5-2323(20:03:26.970,-23:22:57.77)
r_{max} for fit = 543.61 kpc
reduced χ^2 = 1.02
K_0 = 217.89 ± 91.72 $keV\ cm^2$
K_{100} = 134.25 ± 149.28 $keV\ cm^2$
α = 0.88 ± 0.47
K (keV cm^2)
r (kpc)

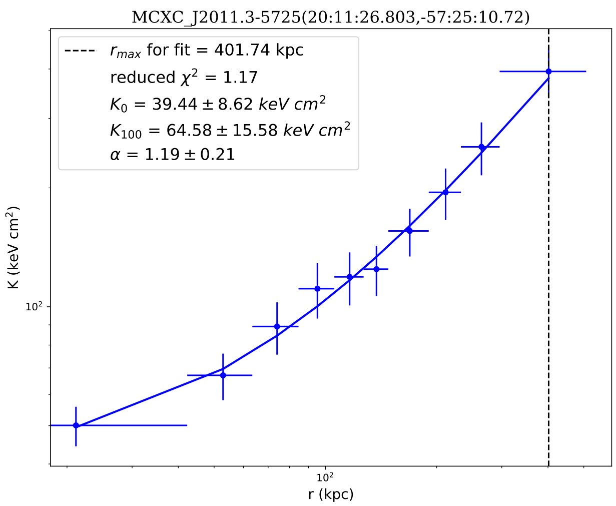
MCXC_J2011.3-5725(20:11:26.803,-57:25:10.72)
r_{max} for fit = 401.74 kpc
reduced χ^2 = 1.17
K_0 = 39.44 ± 8.62 $keV\ cm^2$
K_{100} = 64.58 ± 15.58 $keV\ cm^2$
α = 1.19 ± 0.21
K (keV cm^2)
r (kpc)

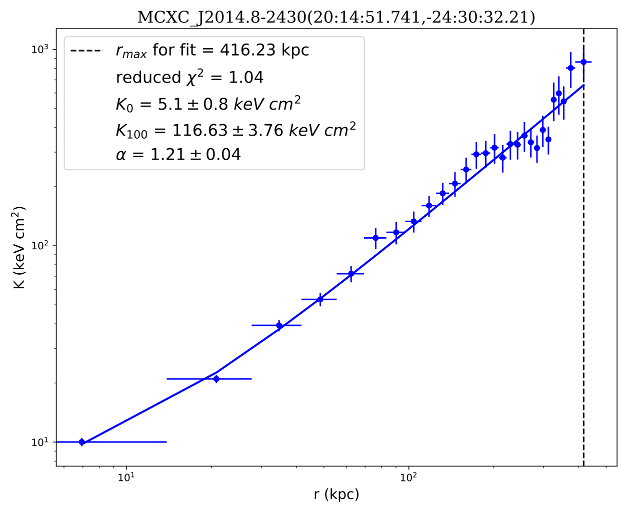
MCXC_J2014.8-2430(20:14:51.741,-24:30:32.21)
r_{max} for fit = 416.23 kpc
reduced χ^2 = 1.04
K_0 = 5.1 ± 0.8 $keV\ cm^2$
K_{100} = 116.63 ± 3.76 $keV\ cm^2$
α = 1.21 ± 0.04
K (keV cm^2)
r (kpc)

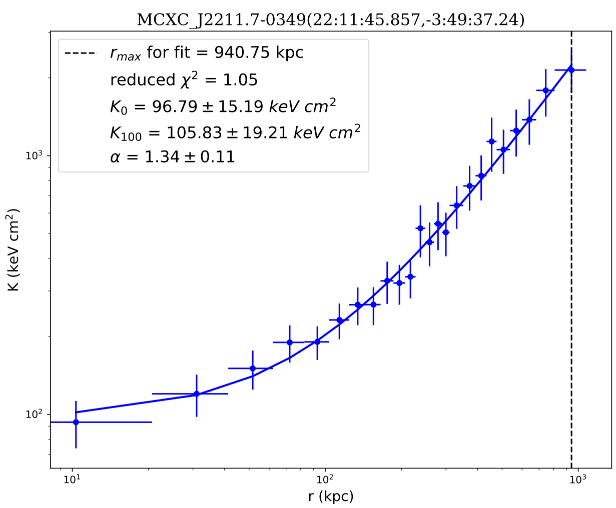
MCXC_J2211.7-0349(22:11:45.857,-3:49:37.24)
r_{max} for fit = 940.75 kpc
reduced χ^2 = 1.05
K_0 = 96.79 ± 15.19 $keV\ cm^2$
K_{100} = 105.83 ± 19.21 $keV\ cm^2$
α = 1.34 ± 0.11
K (keV cm^2)
r (kpc)

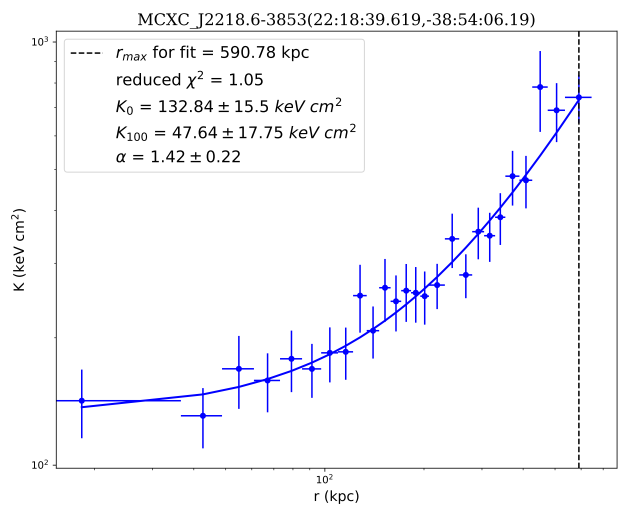
MCXC_J2218.6-3853(22:18:39.619,-38:54:06.19)
r_{max} for fit = 590.78 kpc
reduced χ^2 = 1.05
K_0 = 132.84 ± 15.5 $keV\ cm^2$
K_{100} = 47.64 ± 17.75 $keV\ cm^2$
α = 1.42 ± 0.22
K (keV cm^2)
r (kpc)

MCXC_J2311.5+0338(23:11:33.230,3:38:08.23)

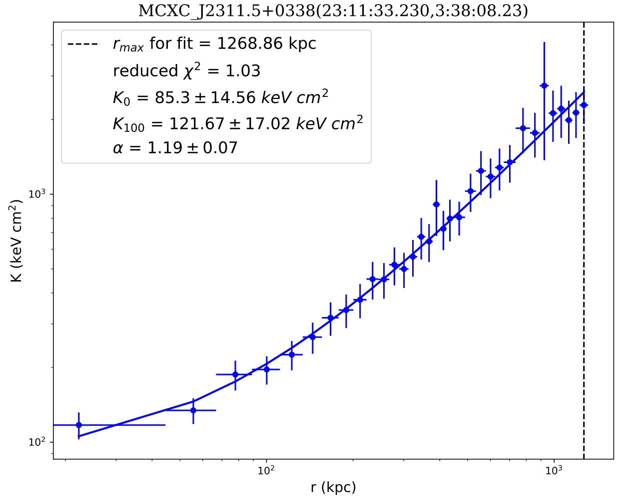

MCXC_J2344.2-0422(23:44:18.524,-4:22:52.79)

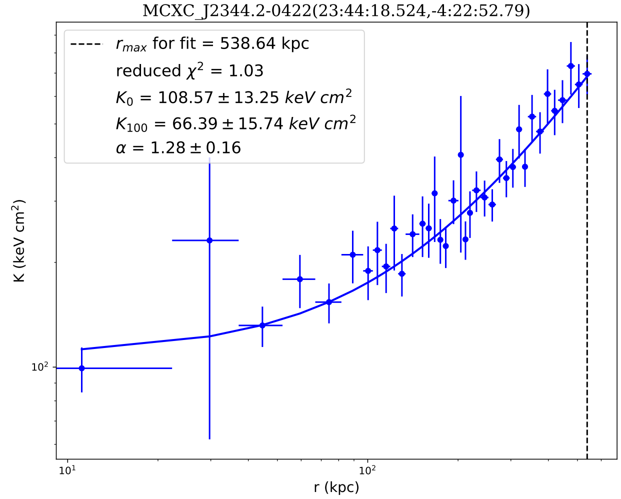

MESSIER_089(12:35:39.773,12:33:23.97)

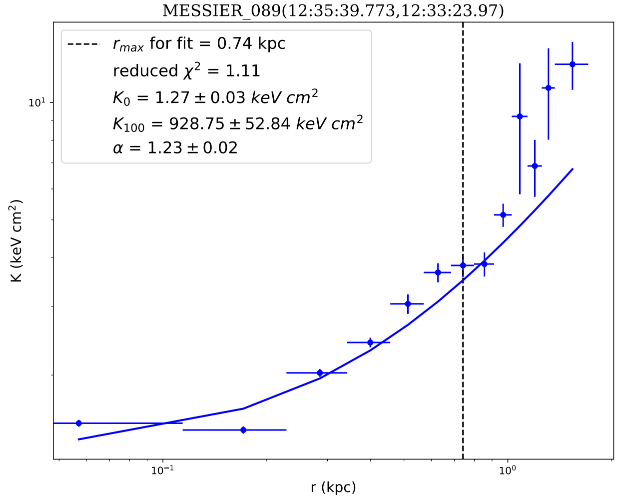

MKW_03s(15:21:51.929,7:42:31.97)

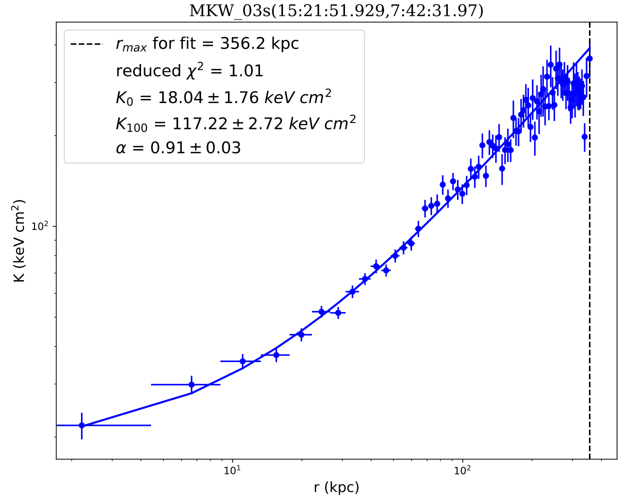

MKW_04(12:04:27.218,1:53:42.79)

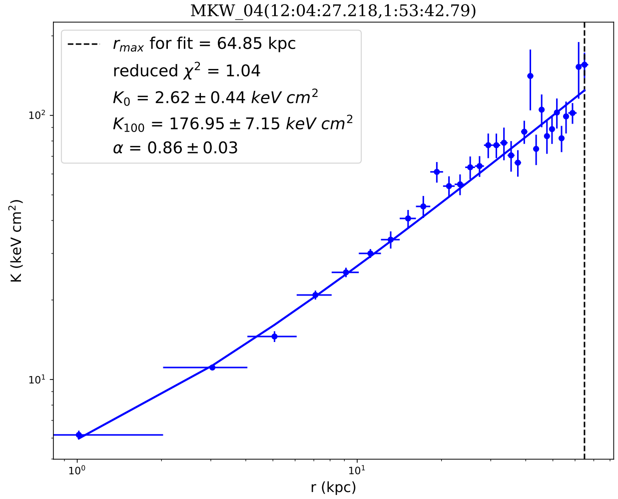

MZ_10451(2:29:45.684,-29:37:48.17)

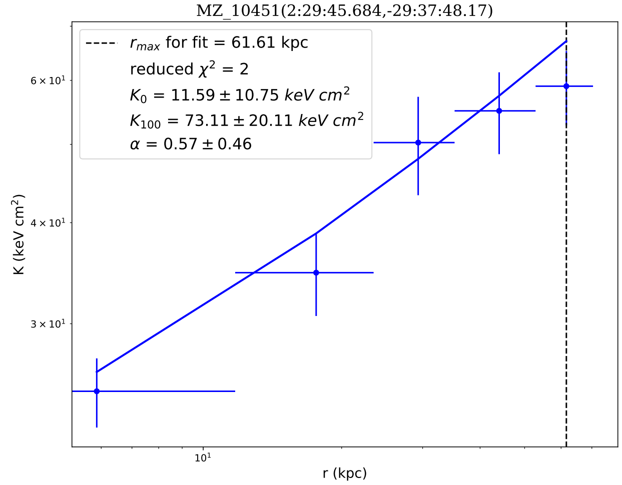

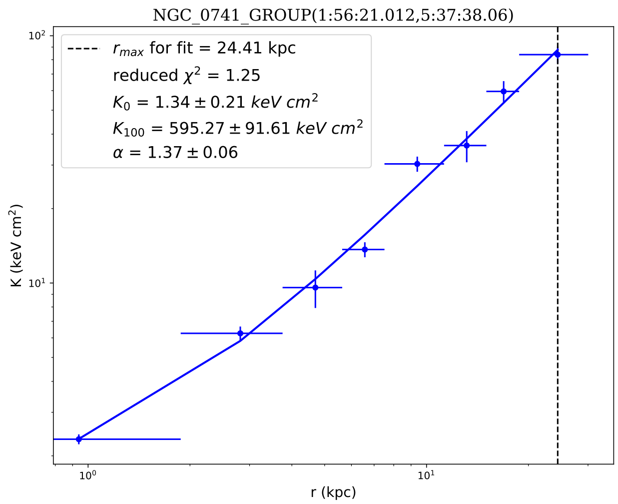
NGC_0741_GROUP(1:56:21.012,5:37:38.06)
r_{max} for fit = 24.41 kpc
reduced χ^2 = 1.25
K_0 = 1.34 ± 0.21 $keV\ cm^2$
K_{100} = 595.27 ± 91.61 $keV\ cm^2$
α = 1.37 ± 0.06
K (keV cm^2)
r (kpc)

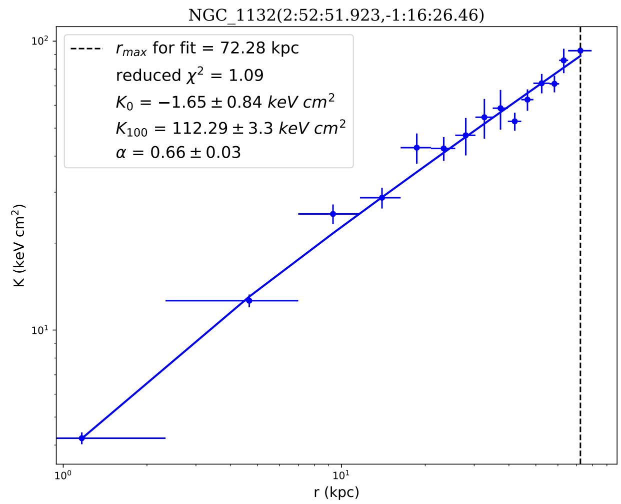
NGC_1132(2:52:51.923,-1:16:26.46)
r_{max} for fit = 72.28 kpc
reduced χ^2 = 1.09
K_0 = -1.65 ± 0.84 $keV\ cm^2$
K_{100} = 112.29 ± 3.3 $keV\ cm^2$
α = 0.66 ± 0.03
K (keV cm^2)
r (kpc)

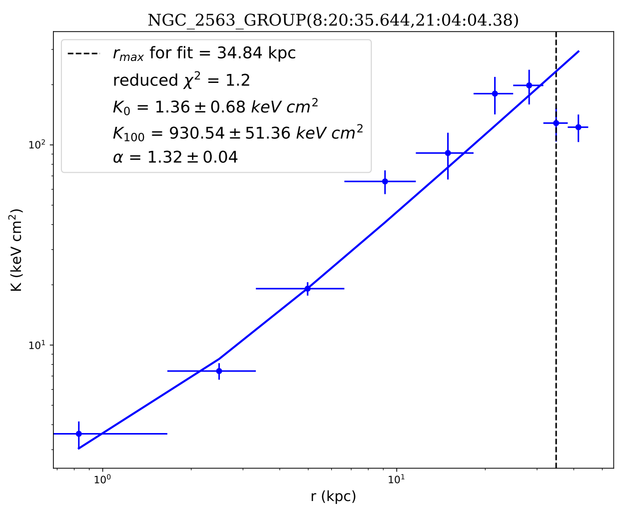
NGC_2563_GROUP(8:20:35.644,21:04:04.38)
r_{max} for fit = 34.84 kpc
reduced χ^2 = 1.2
K_0 = 1.36 ± 0.68 $keV\ cm^2$
K_{100} = 930.54 ± 51.36 $keV\ cm^2$
α = 1.32 ± 0.04
K (keV cm^2)
r (kpc)

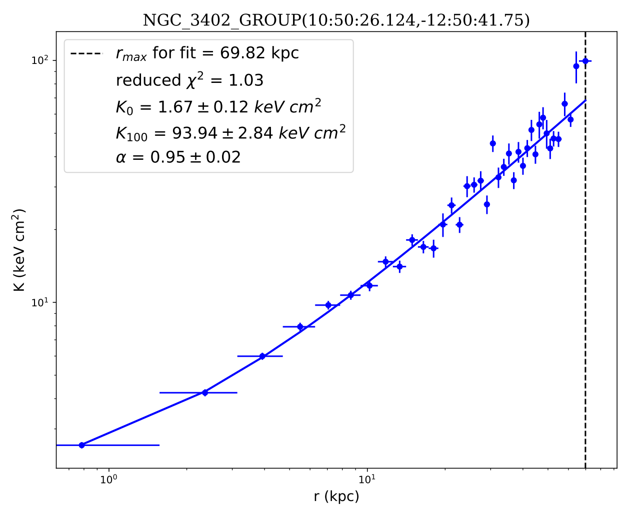
NGC_3402_GROUP(10:50:26.124,-12:50:41.75)
r_{max} for fit = 69.82 kpc
reduced χ^2 = 1.03
K_0 = 1.67 ± 0.12 $keV\ cm^2$
K_{100} = 93.94 ± 2.84 $keV\ cm^2$
α = 0.95 ± 0.02
K (keV cm^2)
r (kpc)

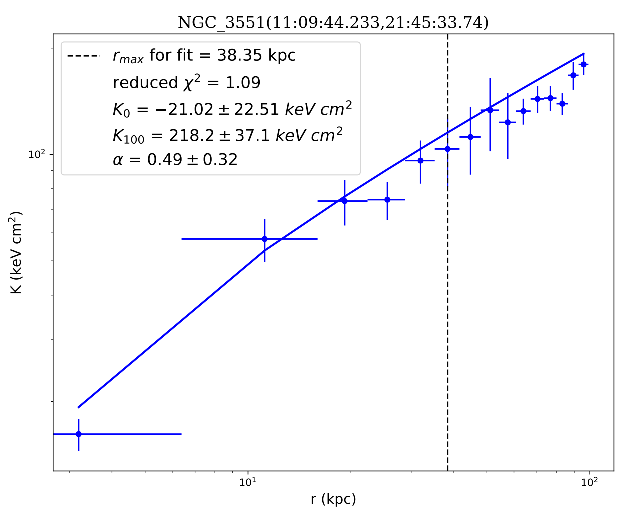
NGC_3551(11:09:44.233,21:45:33.74)
r_{max} for fit = 38.35 kpc
reduced χ^2 = 1.09
K_0 = -21.02 ± 22.51 $keV\ cm^2$
K_{100} = 218.2 ± 37.1 $keV\ cm^2$
α = 0.49 ± 0.32
K (keV cm^2)
r (kpc)

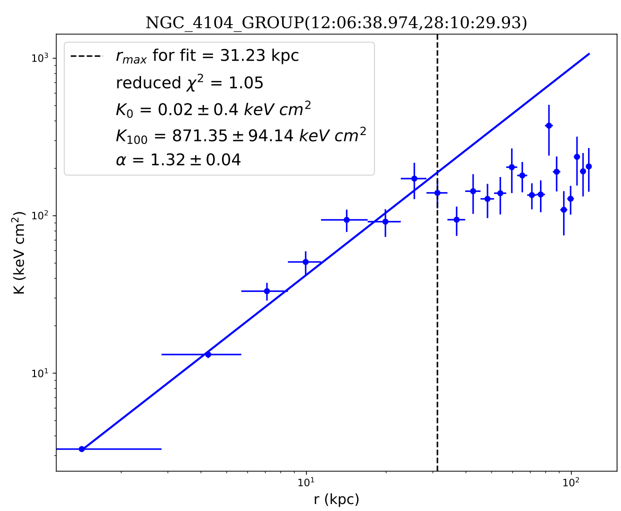
NGC_4104_GROUP(12:06:38.974,28:10:29.93)
r_{max} for fit = 31.23 kpc
reduced χ^2 = 1.05
K_0 = 0.02 ± 0.4 $keV\ cm^2$
K_{100} = 871.35 ± 94.14 $keV\ cm^2$
α = 1.32 ± 0.04
K (keV cm^2)
r (kpc)

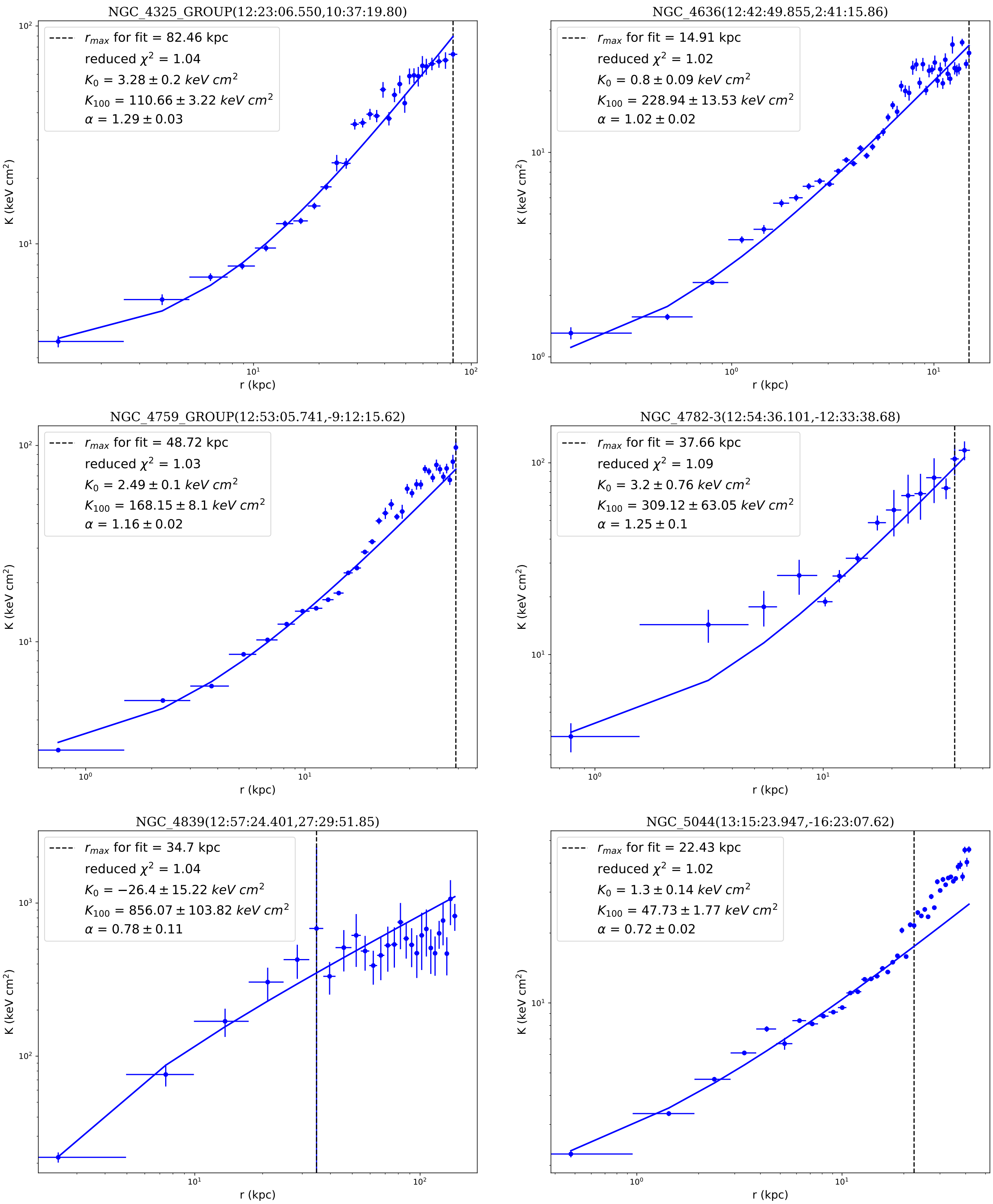
NGC_4325_GROUP(12:23:06.550,10:37:19.80)
r_{max} for fit = 82.46 kpc
reduced χ^2 = 1.04
K_0 = 3.28 ± 0.2 $keV\ cm^2$
K_{100} = 110.66 ± 3.22 $keV\ cm^2$
α = 1.29 ± 0.03
K (keV cm^2)
r (kpc)
NGC_4636(12:42:49.855,2:41:15.86)
r_{max} for fit = 14.91 kpc
reduced χ^2 = 1.02
K_0 = 0.8 ± 0.09 $keV\ cm^2$
K_{100} = 228.94 ± 13.53 $keV\ cm^2$
α = 1.02 ± 0.02
K (keV cm^2)
r (kpc)
NGC_4759_GROUP(12:53:05.741,-9:12:15.62)
r_{max} for fit = 48.72 kpc
reduced χ^2 = 1.03
K_0 = 2.49 ± 0.1 $keV\ cm^2$
K_{100} = 168.15 ± 8.1 $keV\ cm^2$
α = 1.16 ± 0.02
K (keV cm^2)
r (kpc)
NGC_4782-3(12:54:36.101,-12:33:38.68)
r_{max} for fit = 37.66 kpc
reduced χ^2 = 1.09
K_0 = 3.2 ± 0.76 $keV\ cm^2$
K_{100} = 309.12 ± 63.05 $keV\ cm^2$
α = 1.25 ± 0.1
K (keV cm^2)
r (kpc)
NGC_4839(12:57:24.401,27:29:51.85)
r_{max} for fit = 34.7 kpc
reduced χ^2 = 1.04
K_0 = −26.4 ± 15.22 $keV\ cm^2$
K_{100} = 856.07 ± 103.82 $keV\ cm^2$
α = 0.78 ± 0.11
K (keV cm^2)
r (kpc)
NGC_5044(13:15:23.947,-16:23:07.62)
r_{max} for fit = 22.43 kpc
reduced χ^2 = 1.02
K_0 = 1.3 ± 0.14 $keV\ cm^2$
K_{100} = 47.73 ± 1.77 $keV\ cm^2$
α = 0.72 ± 0.02
K (keV cm^2)
r (kpc)

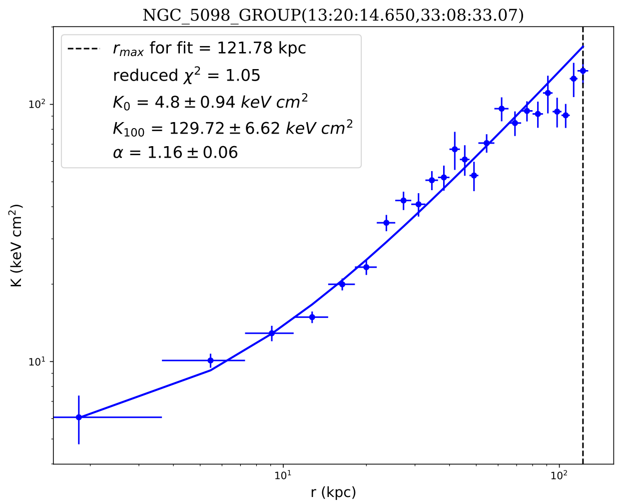
NGC_5098_GROUP(13:20:14.650,33:08:33.07)
r_{max} for fit = 121.78 kpc
reduced χ^2 = 1.05
K_0 = 4.8 ± 0.94 $keV\ cm^2$
K_{100} = 129.72 ± 6.62 $keV\ cm^2$
α = 1.16 ± 0.06
K (keV cm^2)
r (kpc)

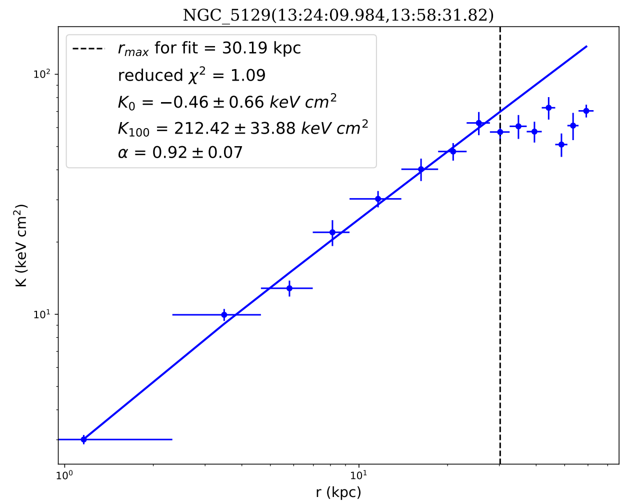
NGC_5129(13:24:09.984,13:58:31.82)
r_{max} for fit = 30.19 kpc
reduced χ^2 = 1.09
K_0 = -0.46 ± 0.66 $keV\ cm^2$
K_{100} = 212.42 ± 33.88 $keV\ cm^2$
α = 0.92 ± 0.07
K (keV cm^2)
r (kpc)

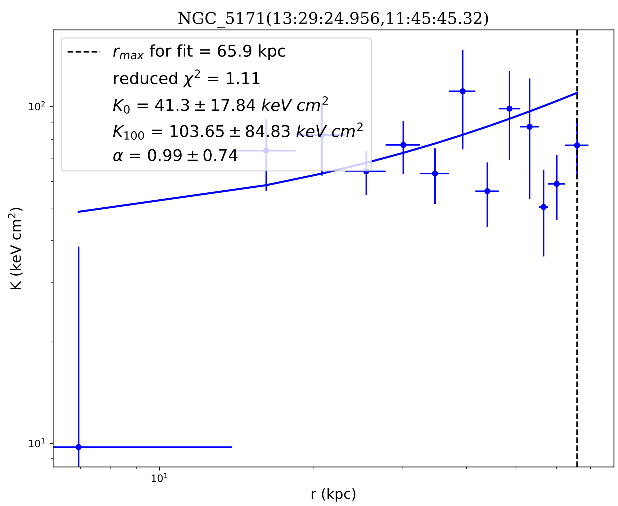
NGC_5171(13:29:24.956,11:45:45.32)
r_{max} for fit = 65.9 kpc
reduced χ^2 = 1.11
K_0 = 41.3 ± 17.84 $keV\ cm^2$
K_{100} = 103.65 ± 84.83 $keV\ cm^2$
α = 0.99 ± 0.74
K (keV cm^2)
r (kpc)

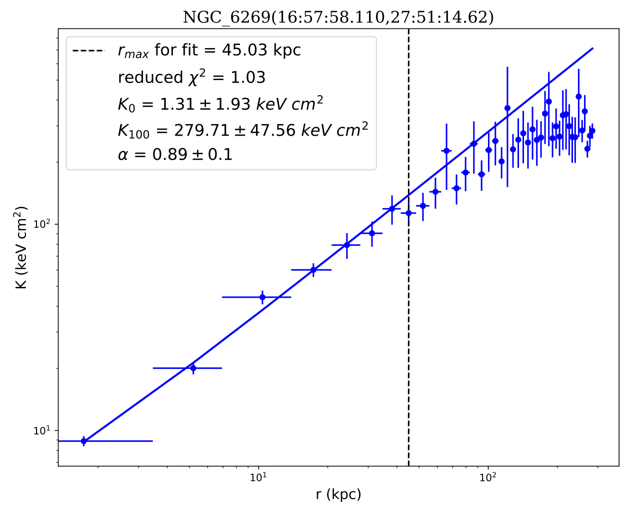
NGC_6269(16:57:58.110,27:51:14.62)
r_{max} for fit = 45.03 kpc
reduced χ^2 = 1.03
K_0 = 1.31 ± 1.93 $keV\ cm^2$
K_{100} = 279.71 ± 47.56 $keV\ cm^2$
α = 0.89 ± 0.1
K (keV cm^2)
r (kpc)

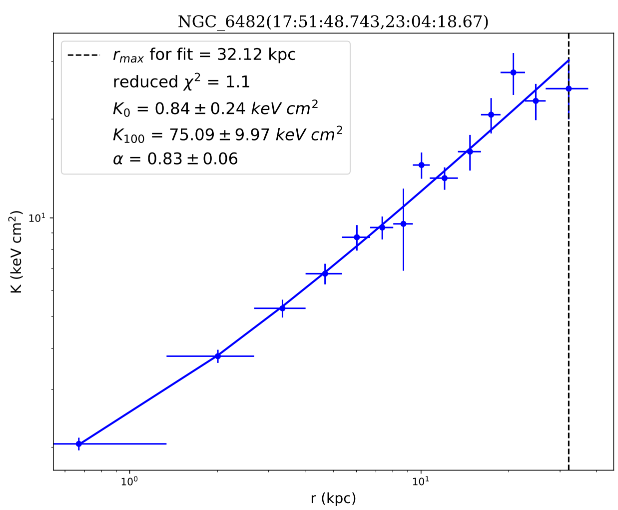
NGC_6482(17:51:48.743,23:04:18.67)
r_{max} for fit = 32.12 kpc
reduced χ^2 = 1.1
K_0 = 0.84 ± 0.24 $keV\ cm^2$
K_{100} = 75.09 ± 9.97 $keV\ cm^2$
α = 0.83 ± 0.06
K (keV cm^2)
r (kpc)

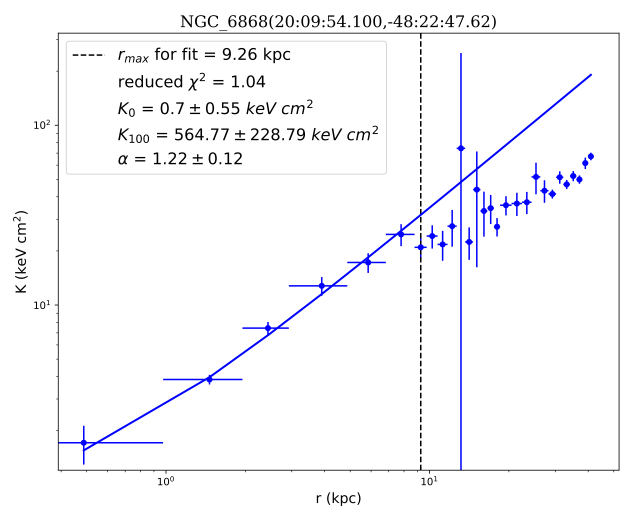
NGC_6868(20:09:54.100,-48:22:47.62)
r_{max} for fit = 9.26 kpc
reduced χ^2 = 1.04
K_0 = 0.7 ± 0.55 $keV\ cm^2$
K_{100} = 564.77 ± 228.79 $keV\ cm^2$
α = 1.22 ± 0.12
K (keV cm^2)
r (kpc)

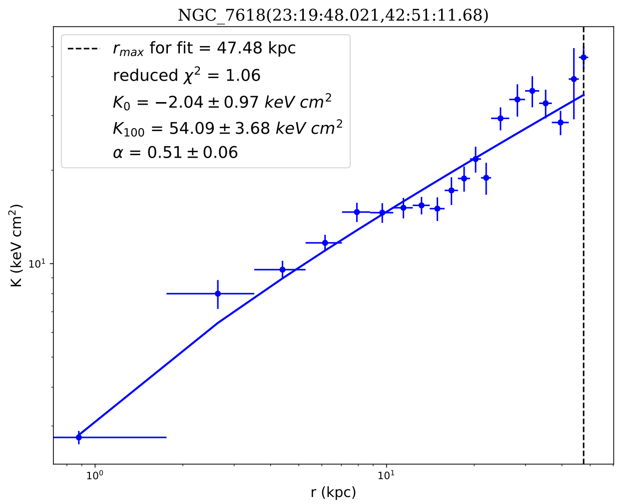
NGC_7618(23:19:48.021,42:51:11.68)
r_{max} for fit = 47.48 kpc
reduced χ^2 = 1.06
$K_0 = -2.04 \pm 0.97$ $keV\ cm^2$
$K_{100} = 54.09 \pm 3.68$ $keV\ cm^2$
$\alpha = 0.51 \pm 0.06$
K (keV cm^2)
r (kpc)

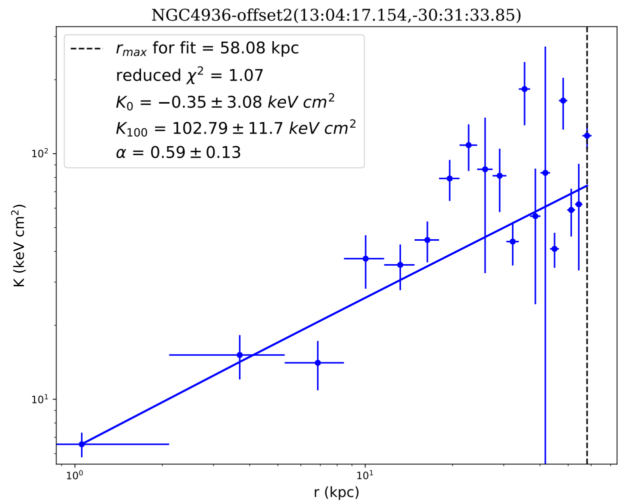
NGC4936-offset2(13:04:17.154,-30:31:33.85)
r_{max} for fit = 58.08 kpc
reduced χ^2 = 1.07
$K_0 = -0.35 \pm 3.08$ $keV\ cm^2$
$K_{100} = 102.79 \pm 11.7$ $keV\ cm^2$
$\alpha = 0.59 \pm 0.13$
K (keV cm^2)
r (kpc)

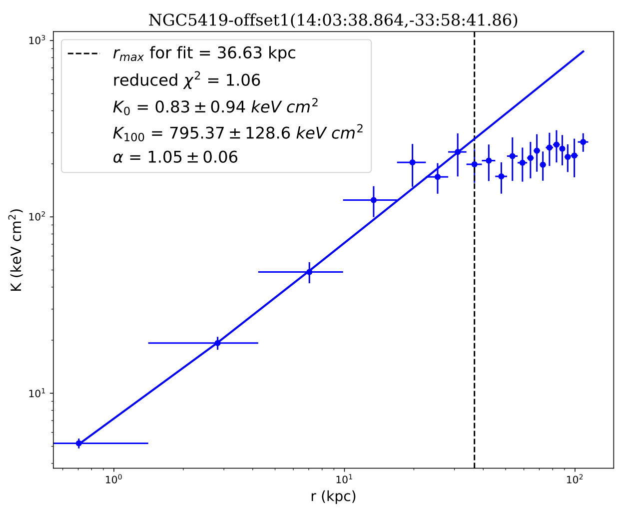
NGC5419-offset1(14:03:38.864,-33:58:41.86)
r_{max} for fit = 36.63 kpc
reduced χ^2 = 1.06
$K_0 = 0.83 \pm 0.94$ $keV\ cm^2$
$K_{100} = 795.37 \pm 128.6$ $keV\ cm^2$
$\alpha = 1.05 \pm 0.06$
K (keV cm^2)
r (kpc)

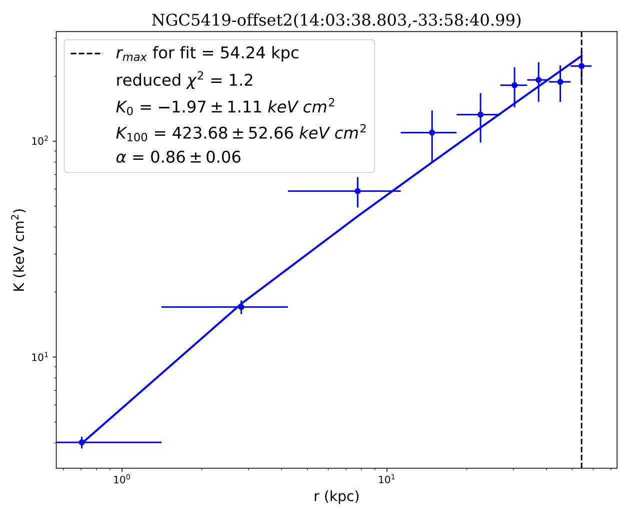
NGC5419-offset2(14:03:38.803,-33:58:40.99)
r_{max} for fit = 54.24 kpc
reduced χ^2 = 1.2
$K_0 = -1.97 \pm 1.11$ $keV\ cm^2$
$K_{100} = 423.68 \pm 52.66$ $keV\ cm^2$
$\alpha = 0.86 \pm 0.06$
K (keV cm^2)
r (kpc)

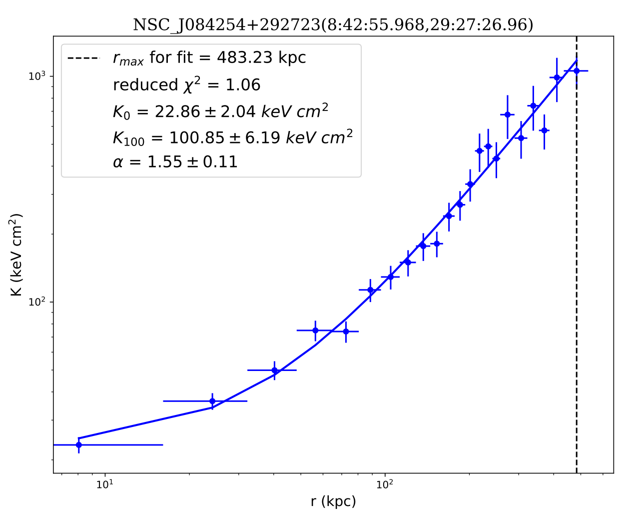
NSC_J084254+292723(8:42:55.968,29:27:26.96)
r_{max} for fit = 483.23 kpc
reduced χ^2 = 1.06
$K_0 = 22.86 \pm 2.04$ $keV\ cm^2$
$K_{100} = 100.85 \pm 6.19$ $keV\ cm^2$
$\alpha = 1.55 \pm 0.11$
K (keV cm^2)
r (kpc)

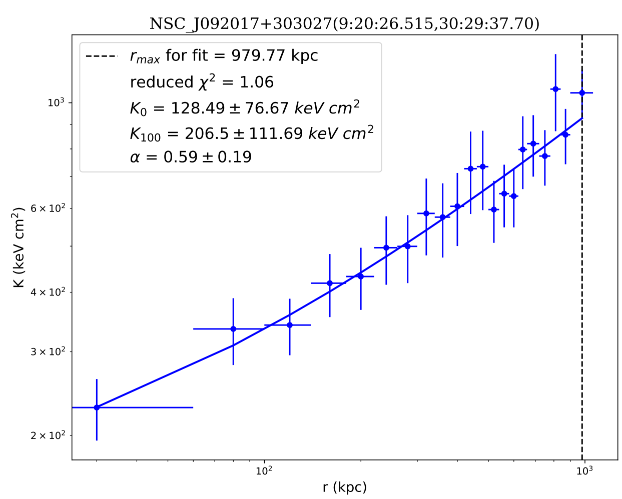
NSC_J092017+303027(9:20:26.515,30:29:37.70)
r_{max} for fit = 979.77 kpc
reduced χ^2 = 1.06
$K_0 = 128.49 \pm 76.67$ $keV\ cm^2$
$K_{100} = 206.5 \pm 111.69$ $keV\ cm^2$
$\alpha = 0.59 \pm 0.19$
K (keV cm^2)
r (kpc)

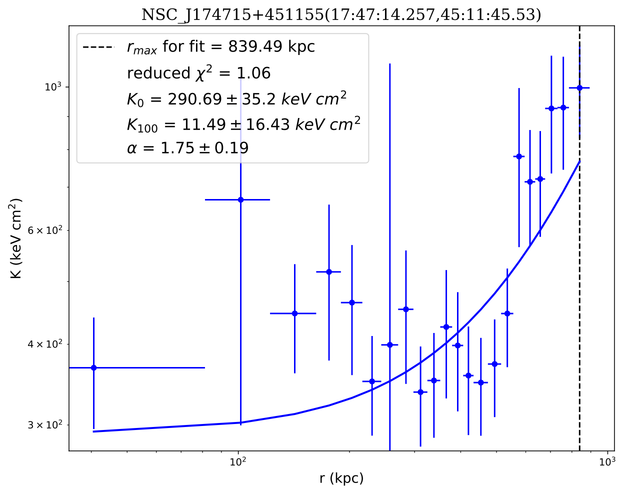
NSC_J174715+451155(17:47:14.257,45:11:45.53)
r_{max} for fit = 839.49 kpc
reduced χ^2 = 1.06
$K_0 = 290.69 \pm 35.2\ keV\ cm^2$
$K_{100} = 11.49 \pm 16.43\ keV\ cm^2$
$\alpha = 1.75 \pm 0.19$
K (keV cm^2)
r (kpc)

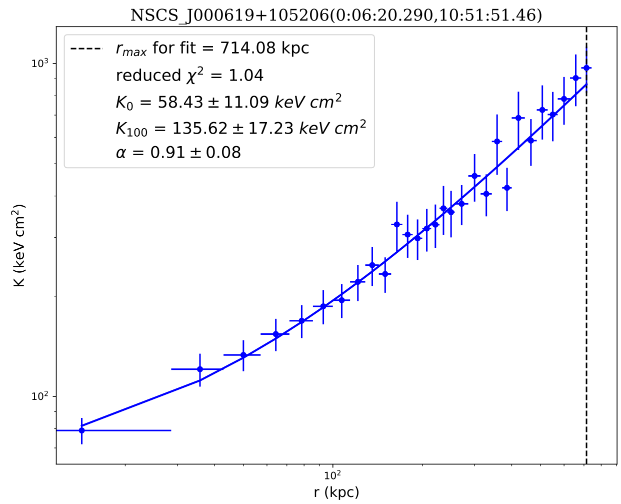
NSCS_J000619+105206(0:06:20.290,10:51:51.46)
r_{max} for fit = 714.08 kpc
reduced χ^2 = 1.04
$K_0 = 58.43 \pm 11.09\ keV\ cm^2$
$K_{100} = 135.62 \pm 17.23\ keV\ cm^2$
$\alpha = 0.91 \pm 0.08$
K (keV cm^2)
r (kpc)

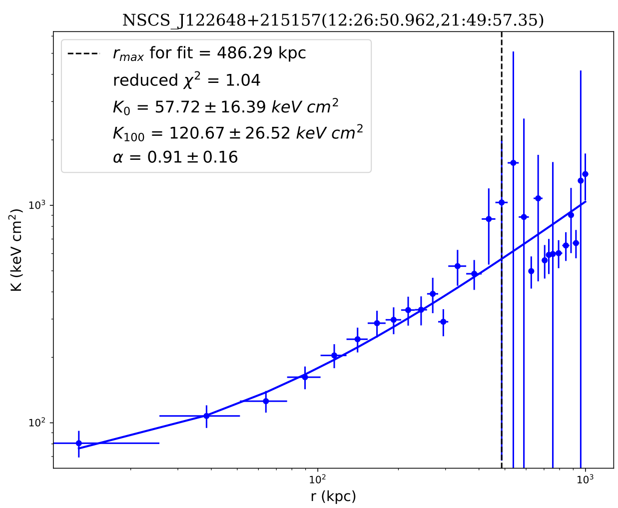
NSCS_J122648+215157(12:26:50.962,21:49:57.35)
r_{max} for fit = 486.29 kpc
reduced χ^2 = 1.04
$K_0 = 57.72 \pm 16.39\ keV\ cm^2$
$K_{100} = 120.67 \pm 26.52\ keV\ cm^2$
$\alpha = 0.91 \pm 0.16$
K (keV cm^2)
r (kpc)

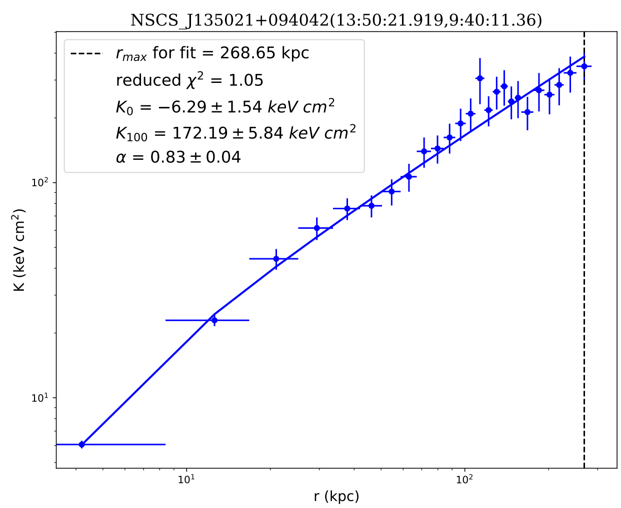
NSCS_J135021+094042(13:50:21.919,9:40:11.36)
r_{max} for fit = 268.65 kpc
reduced χ^2 = 1.05
$K_0 = -6.29 \pm 1.54\ keV\ cm^2$
$K_{100} = 172.19 \pm 5.84\ keV\ cm^2$
$\alpha = 0.83 \pm 0.04$
K (keV cm^2)
r (kpc)

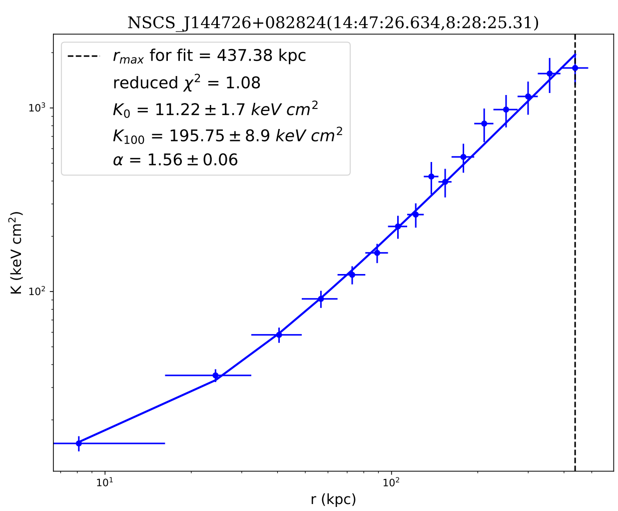
NSCS_J144726+082824(14:47:26.634,8:28:25.31)
r_{max} for fit = 437.38 kpc
reduced χ^2 = 1.08
$K_0 = 11.22 \pm 1.7\ keV\ cm^2$
$K_{100} = 195.75 \pm 8.9\ keV\ cm^2$
$\alpha = 1.56 \pm 0.06$
K (keV cm^2)
r (kpc)

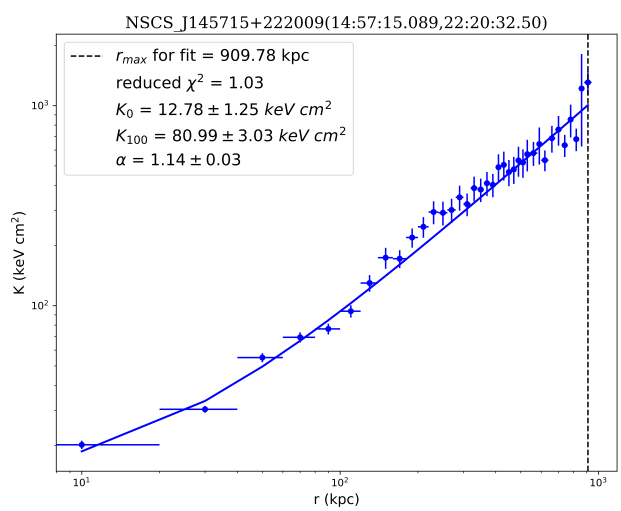
NSCS_J145715+222009(14:57:15.089,22:20:32.50)
r_{max} for fit = 909.78 kpc
reduced χ^2 = 1.03
$K_0 = 12.78 \pm 1.25\ keV\ cm^2$
$K_{100} = 80.99 \pm 3.03\ keV\ cm^2$
$\alpha = 1.14 \pm 0.03$
K (keV cm^2)
r (kpc)

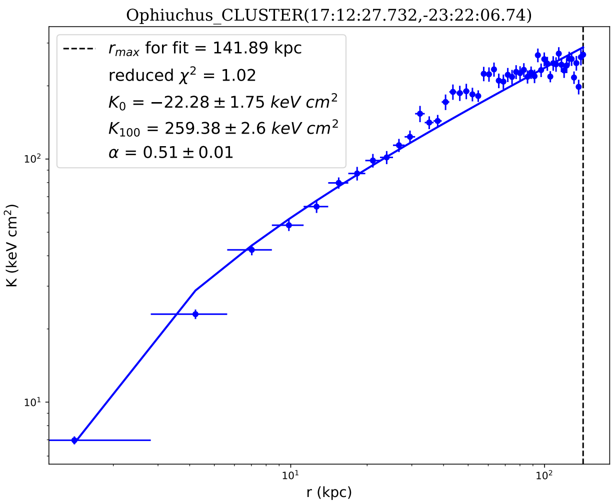
Ophiuchus_CLUSTER(17:12:27.732,-23:22:06.74)
r_{max} for fit = 141.89 kpc
reduced χ^2 = 1.02
K_0 = -22.28 ± 1.75 $keV\ cm^2$
K_{100} = 259.38 ± 2.6 $keV\ cm^2$
α = 0.51 ± 0.01
K (keV cm^2)
r (kpc)

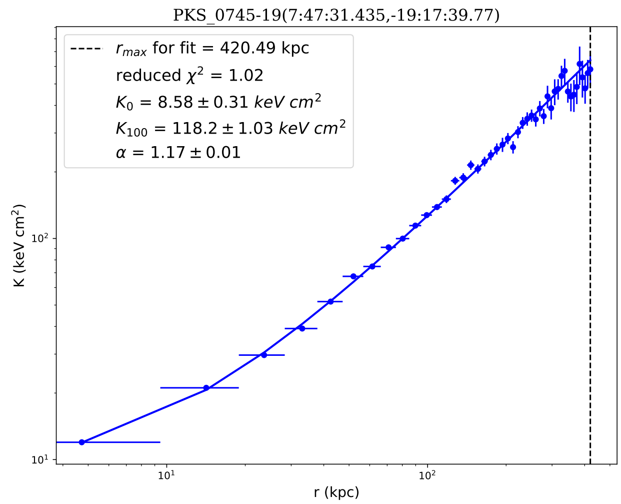
PKS_0745-19(7:47:31.435,-19:17:39.77)
r_{max} for fit = 420.49 kpc
reduced χ^2 = 1.02
K_0 = 8.58 ± 0.31 $keV\ cm^2$
K_{100} = 118.2 ± 1.03 $keV\ cm^2$
α = 1.17 ± 0.01
K (keV cm^2)
r (kpc)

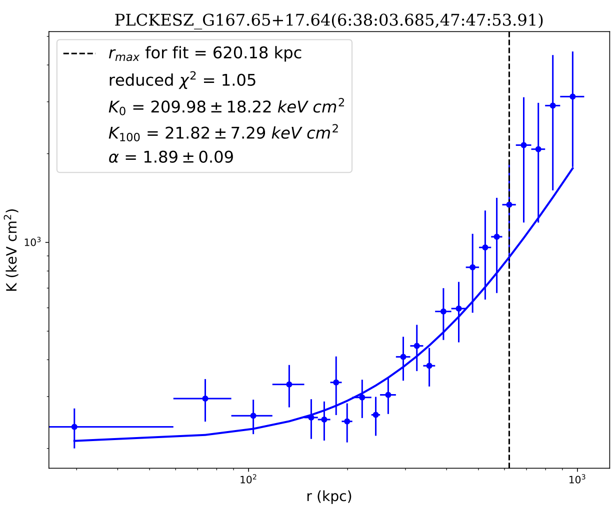
PLCKESZ_G167.65+17.64(6:38:03.685,47:47:53.91)
r_{max} for fit = 620.18 kpc
reduced χ^2 = 1.05
K_0 = 209.98 ± 18.22 $keV\ cm^2$
K_{100} = 21.82 ± 7.29 $keV\ cm^2$
α = 1.89 ± 0.09
K (keV cm^2)
r (kpc)

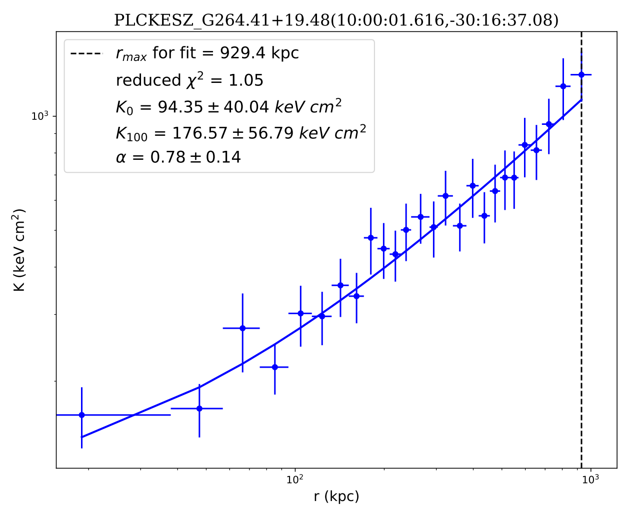
PLCKESZ_G264.41+19.48(10:00:01.616,-30:16:37.08)
r_{max} for fit = 929.4 kpc
reduced χ^2 = 1.05
K_0 = 94.35 ± 40.04 $keV\ cm^2$
K_{100} = 176.57 ± 56.79 $keV\ cm^2$
α = 0.78 ± 0.14
K (keV cm^2)
r (kpc)

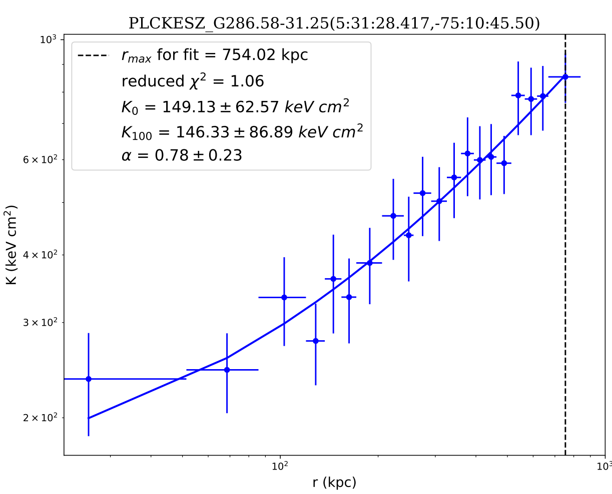
PLCKESZ_G286.58-31.25(5:31:28.417,-75:10:45.50)
r_{max} for fit = 754.02 kpc
reduced χ^2 = 1.06
K_0 = 149.13 ± 62.57 $keV\ cm^2$
K_{100} = 146.33 ± 86.89 $keV\ cm^2$
α = 0.78 ± 0.23
K (keV cm^2)
r (kpc)

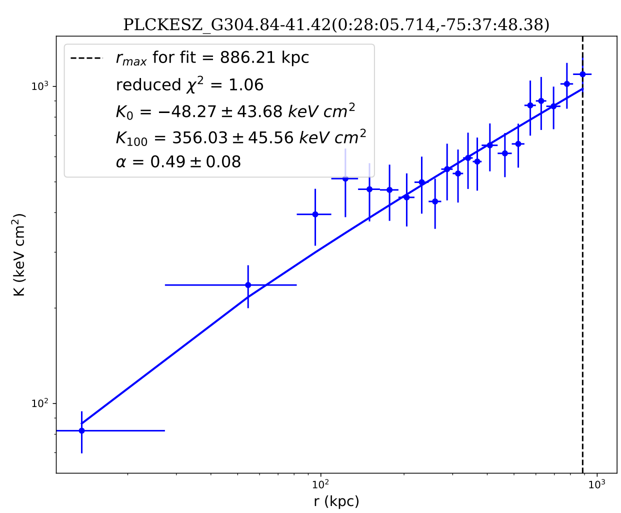
PLCKESZ_G304.84-41.42(0:28:05.714,-75:37:48.38)
r_{max} for fit = 886.21 kpc
reduced χ^2 = 1.06
K_0 = -48.27 ± 43.68 $keV\ cm^2$
K_{100} = 356.03 ± 45.56 $keV\ cm^2$
α = 0.49 ± 0.08
K (keV cm^2)
r (kpc)

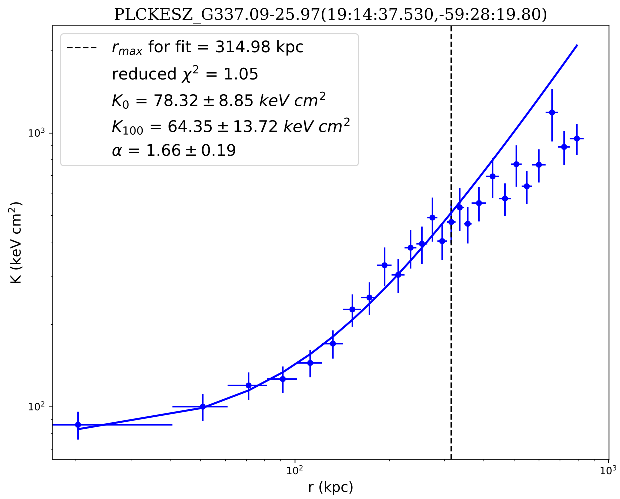
PLCKESZ_G337.09-25.97(19:14:37.530,-59:28:19.80)
r_{max} for fit = 314.98 kpc
reduced χ^2 = 1.05
K_0 = 78.32 ± 8.85 $keV\ cm^2$
K_{100} = 64.35 ± 13.72 $keV\ cm^2$
α = 1.66 ± 0.19
K (keV cm^2)
r (kpc)

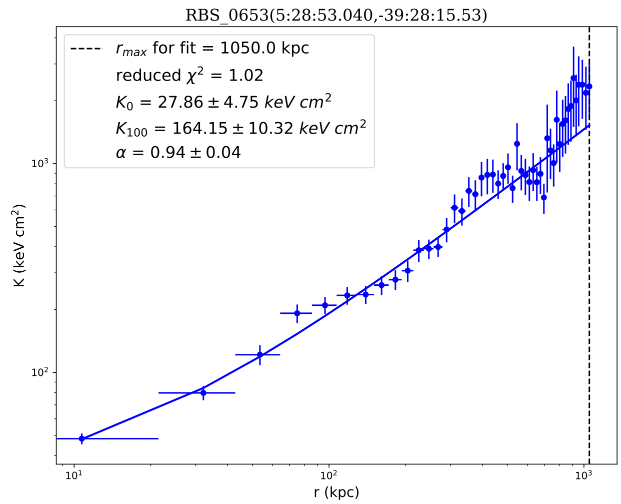
RBS_0653(5:28:53.040,-39:28:15.53)
r_{max} for fit = 1050.0 kpc
reduced χ^2 = 1.02
K_0 = 27.86 ± 4.75 $keV\ cm^2$
K_{100} = 164.15 ± 10.32 $keV\ cm^2$
α = 0.94 ± 0.04
K (keV cm^2)
r (kpc)

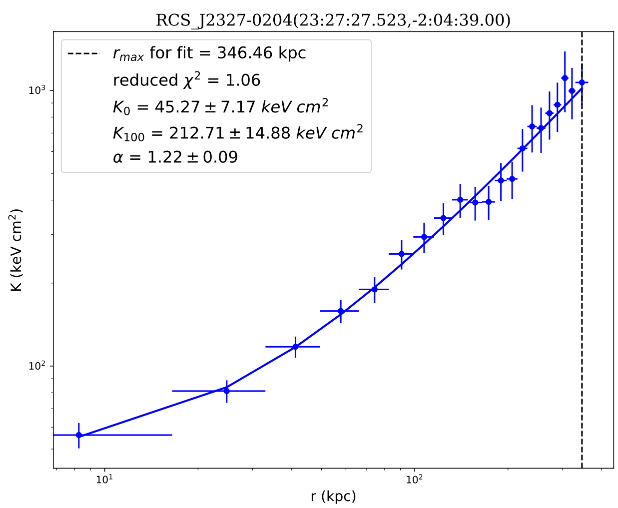
RCS_J2327-0204(23:27:27.523,-2:04:39.00)
r_{max} for fit = 346.46 kpc
reduced χ^2 = 1.06
K_0 = 45.27 ± 7.17 $keV\ cm^2$
K_{100} = 212.71 ± 14.88 $keV\ cm^2$
α = 1.22 ± 0.09
K (keV cm^2)
r (kpc)

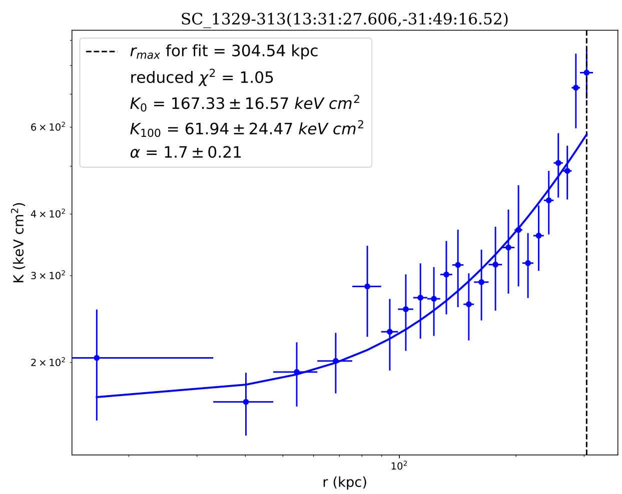
SC_1329-313(13:31:27.606,-31:49:16.52)
r_{max} for fit = 304.54 kpc
reduced χ^2 = 1.05
K_0 = 167.33 ± 16.57 $keV\ cm^2$
K_{100} = 61.94 ± 24.47 $keV\ cm^2$
α = 1.7 ± 0.21
K (keV cm^2)
r (kpc)

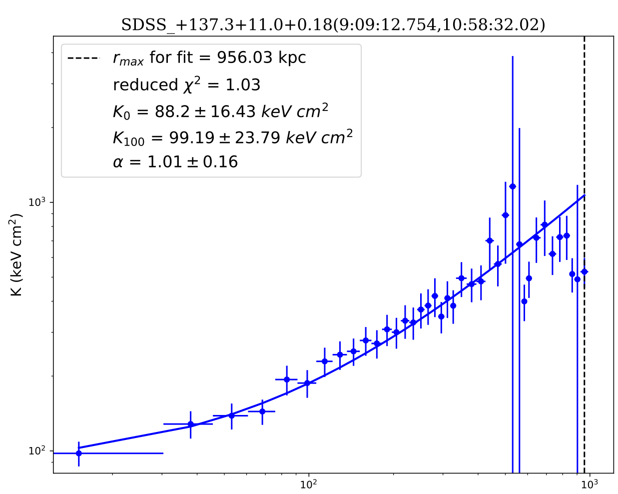
SDSS_+137.3+11.0+0.18(9:09:12.754,10:58:32.02)
r_{max} for fit = 956.03 kpc
reduced χ^2 = 1.03
K_0 = 88.2 ± 16.43 $keV\ cm^2$
K_{100} = 99.19 ± 23.79 $keV\ cm^2$
α = 1.01 ± 0.16
K (keV cm^2)
r (kpc)

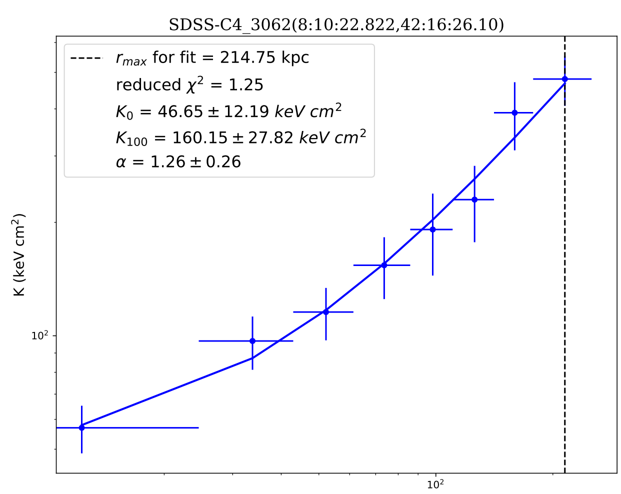
SDSS-C4_3062(8:10:22.822,42:16:26.10)
r_{max} for fit = 214.75 kpc
reduced χ^2 = 1.25
K_0 = 46.65 ± 12.19 $keV\ cm^2$
K_{100} = 160.15 ± 27.82 $keV\ cm^2$
α = 1.26 ± 0.26
K (keV cm^2)
r (kpc)

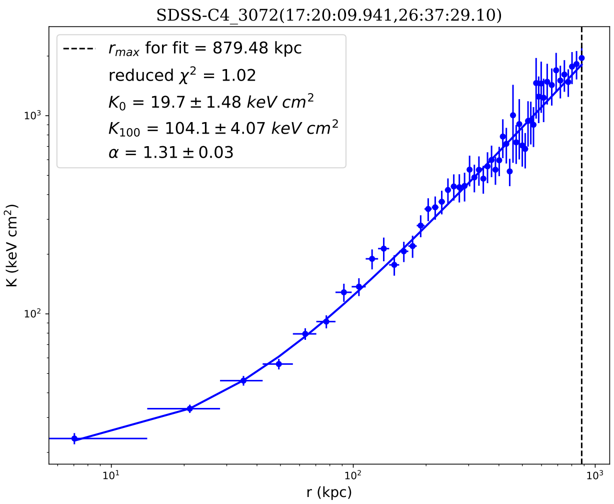
SDSS-C4_3072(17:20:09.941,26:37:29.10)
r_{max} for fit = 879.48 kpc
reduced χ^2 = 1.02
K_0 = 19.7 ± 1.48 $keV\ cm^2$
K_{100} = 104.1 ± 4.07 $keV\ cm^2$
α = 1.31 ± 0.03
K (keV cm^2)
r (kpc)

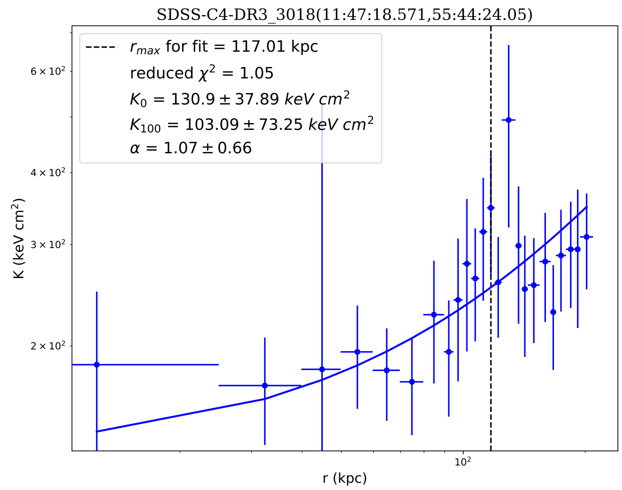
SDSS-C4-DR3_3018(11:47:18.571,55:44:24.05)
r_{max} for fit = 117.01 kpc
reduced χ^2 = 1.05
K_0 = 130.9 ± 37.89 $keV\ cm^2$
K_{100} = 103.09 ± 73.25 $keV\ cm^2$
α = 1.07 ± 0.66
K (keV cm^2)
r (kpc)

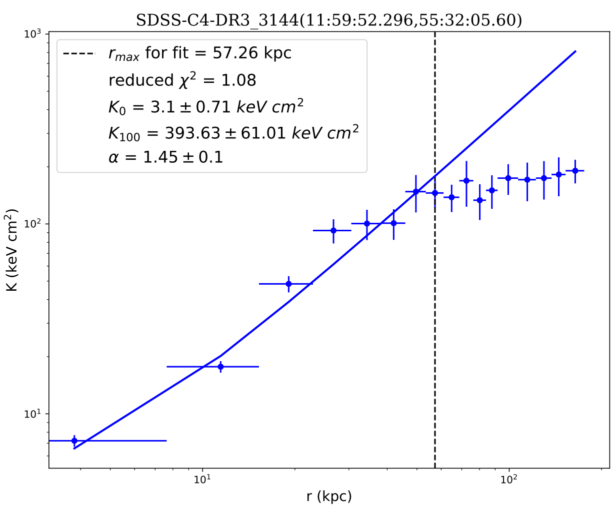
SDSS-C4-DR3_3144(11:59:52.296,55:32:05.60)
r_{max} for fit = 57.26 kpc
reduced χ^2 = 1.08
K_0 = 3.1 ± 0.71 $keV\ cm^2$
K_{100} = 393.63 ± 61.01 $keV\ cm^2$
α = 1.45 ± 0.1
K (keV cm^2)
r (kpc)

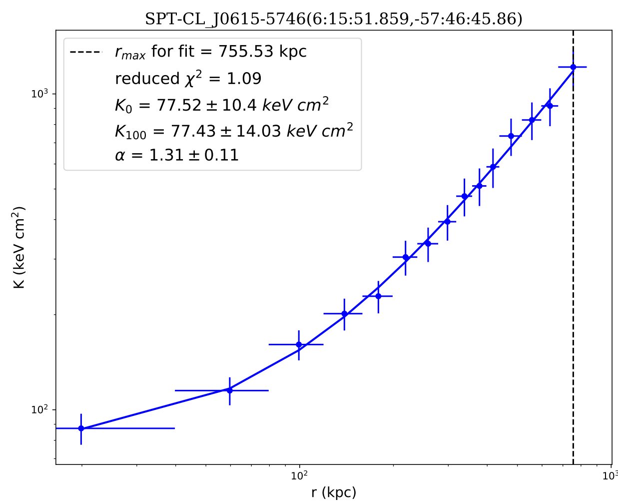
SPT-CL_J0615-5746(6:15:51.859,-57:46:45.86)
r_{max} for fit = 755.53 kpc
reduced χ^2 = 1.09
K_0 = 77.52 ± 10.4 $keV\ cm^2$
K_{100} = 77.43 ± 14.03 $keV\ cm^2$
α = 1.31 ± 0.11
K (keV cm^2)
r (kpc)

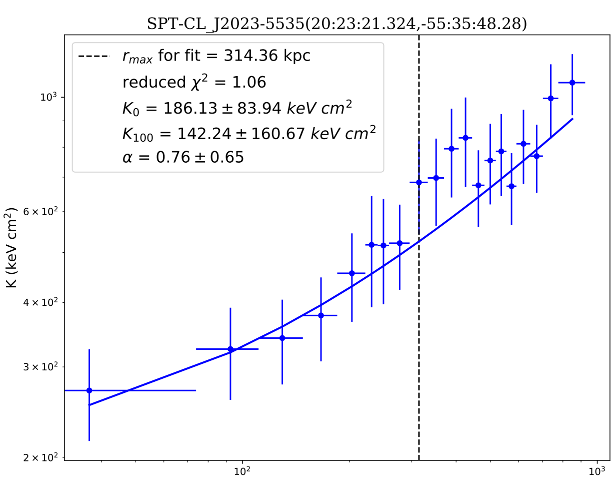
SPT-CL_J2023-5535(20:23:21.324,-55:35:48.28)
r_{max} for fit = 314.36 kpc
reduced χ^2 = 1.06
K_0 = 186.13 ± 83.94 $keV\ cm^2$
K_{100} = 142.24 ± 160.67 $keV\ cm^2$
α = 0.76 ± 0.65
K (keV cm^2)
r (kpc)

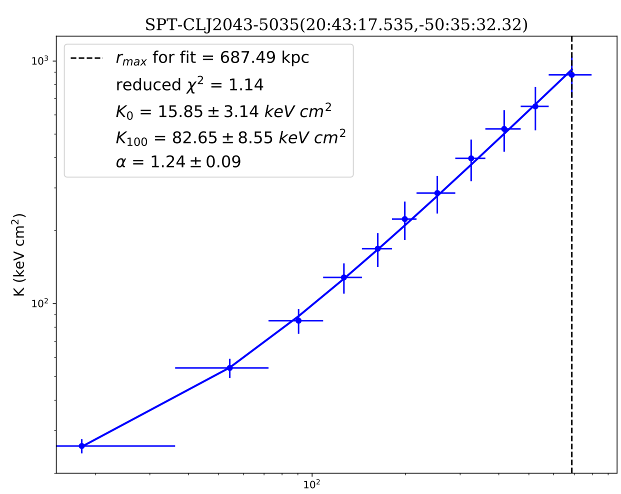
SPT-CLJ2043-5035(20:43:17.535,-50:35:32.32)
r_{max} for fit = 687.49 kpc
reduced χ^2 = 1.14
K_0 = 15.85 ± 3.14 $keV\ cm^2$
K_{100} = 82.65 ± 8.55 $keV\ cm^2$
α = 1.24 ± 0.09
K (keV cm^2)
r (kpc)

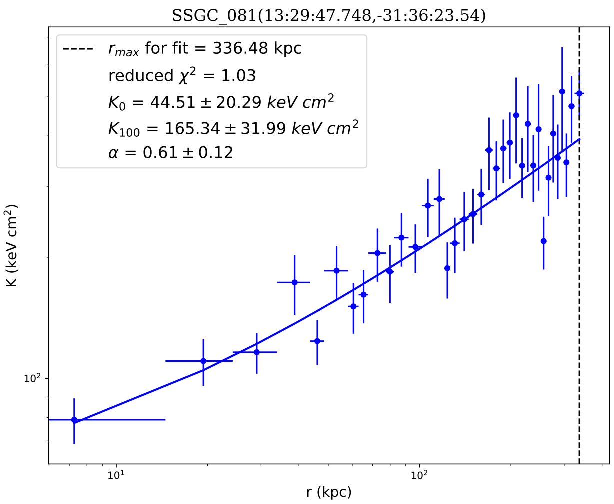
SSGC_081(13:29:47.748,-31:36:23.54)
r_{max} for fit = 336.48 kpc
reduced χ^2 = 1.03
K_0 = 44.51 ± 20.29 $keV\ cm^2$
K_{100} = 165.34 ± 31.99 $keV\ cm^2$
α = 0.61 ± 0.12
K (keV cm^2)
r (kpc)

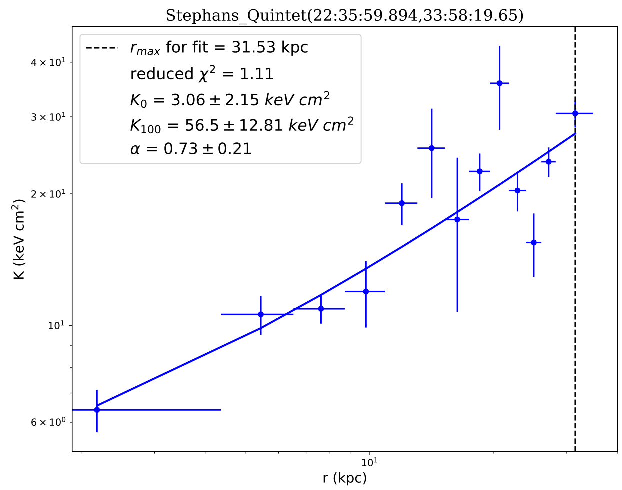
Stephans_Quintet(22:35:59.894,33:58:19.65)
r_{max} for fit = 31.53 kpc
reduced χ^2 = 1.11
K_0 = 3.06 ± 2.15 $keV\ cm^2$
K_{100} = 56.5 ± 12.81 $keV\ cm^2$
α = 0.73 ± 0.21
K (keV cm^2)
r (kpc)

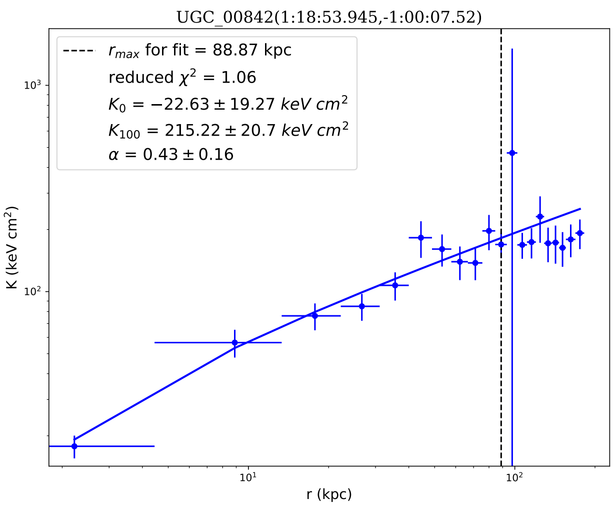
UGC_00842(1:18:53.945,-1:00:07.52)
r_{max} for fit = 88.87 kpc
reduced χ^2 = 1.06
K_0 = −22.63 ± 19.27 $keV\ cm^2$
K_{100} = 215.22 ± 20.7 $keV\ cm^2$
α = 0.43 ± 0.16
K (keV cm^2)
r (kpc)

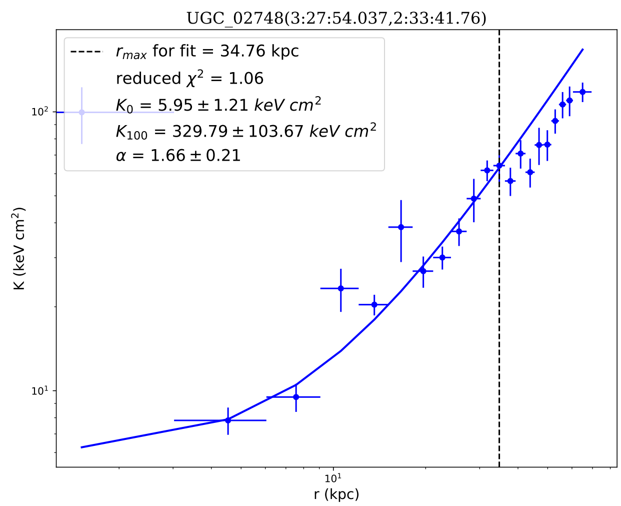
UGC_02748(3:27:54.037,2:33:41.76)
r_{max} for fit = 34.76 kpc
reduced χ^2 = 1.06
K_0 = 5.95 ± 1.21 $keV\ cm^2$
K_{100} = 329.79 ± 103.67 $keV\ cm^2$
α = 1.66 ± 0.21
K (keV cm^2)
r (kpc)

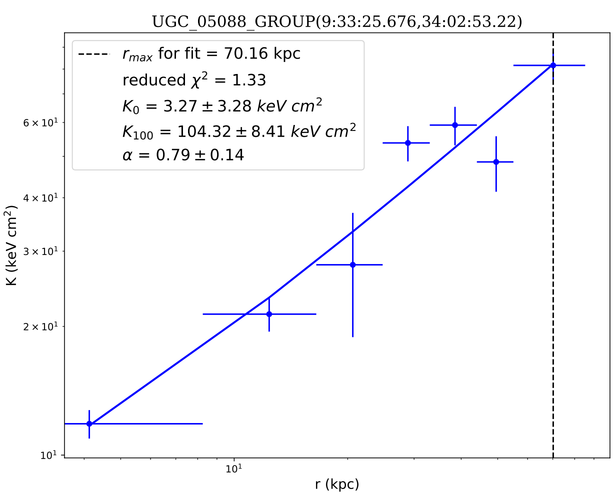
UGC_05088_GROUP(9:33:25.676,34:02:53.22)
r_{max} for fit = 70.16 kpc
reduced χ^2 = 1.33
K_0 = 3.27 ± 3.28 $keV\ cm^2$
K_{100} = 104.32 ± 8.41 $keV\ cm^2$
α = 0.79 ± 0.14
K (keV cm^2)
r (kpc)

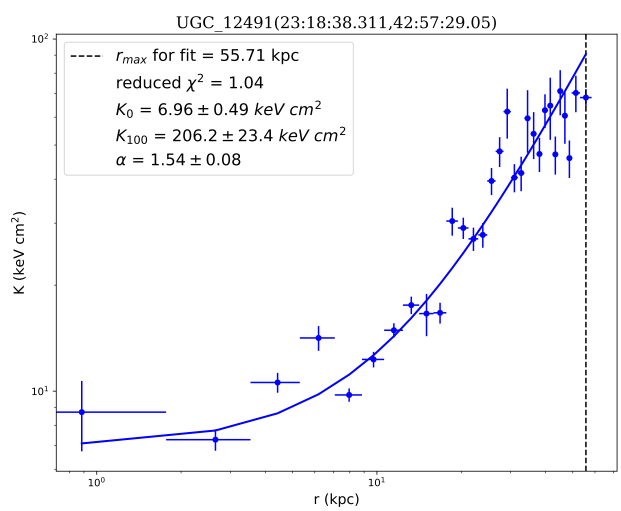
UGC_12491(23:18:38.311,42:57:29.05)
r_{max} for fit = 55.71 kpc
reduced χ^2 = 1.04
K_0 = 6.96 ± 0.49 $keV\ cm^2$
K_{100} = 206.2 ± 23.4 $keV\ cm^2$
α = 1.54 ± 0.08
K (keV cm^2)
r (kpc)

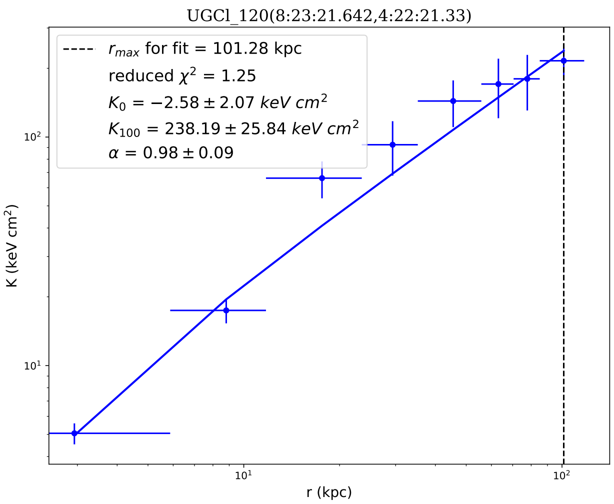
UGCl_120(8:23:21.642,4:22:21.33)
r_{max} for fit = 101.28 kpc
reduced χ^2 = 1.25
$K_0 = -2.58 \pm 2.07$ $keV\ cm^2$
$K_{100} = 238.19 \pm 25.84$ $keV\ cm^2$
$\alpha = 0.98 \pm 0.09$
K (keV cm^2)
r (kpc)

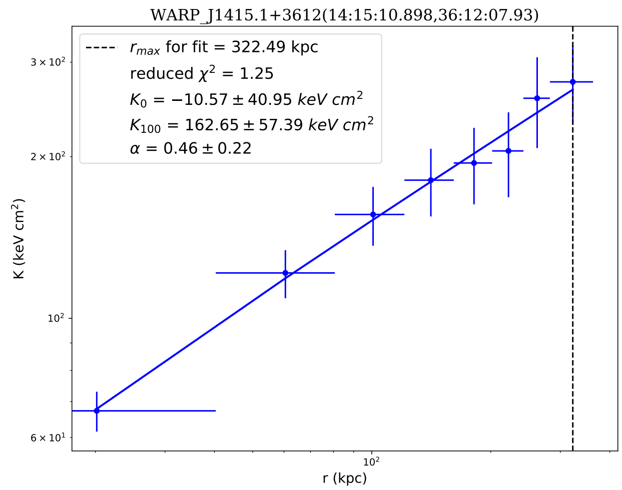
WARP_J1415.1+3612(14:15:10.898,36:12:07.93)
r_{max} for fit = 322.49 kpc
reduced χ^2 = 1.25
$K_0 = -10.57 \pm 40.95$ $keV\ cm^2$
$K_{100} = 162.65 \pm 57.39$ $keV\ cm^2$
$\alpha = 0.46 \pm 0.22$
K (keV cm^2)
r (kpc)

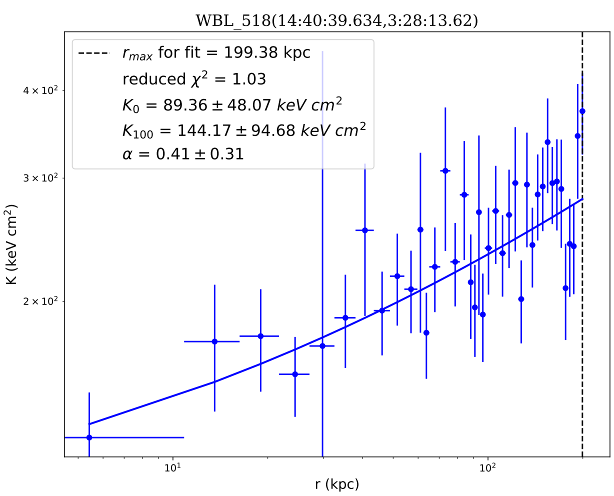
WBL_518(14:40:39.634,3:28:13.62)
r_{max} for fit = 199.38 kpc
reduced χ^2 = 1.03
$K_0 = 89.36 \pm 48.07$ $keV\ cm^2$
$K_{100} = 144.17 \pm 94.68$ $keV\ cm^2$
$\alpha = 0.41 \pm 0.31$
K (keV cm^2)
r (kpc)

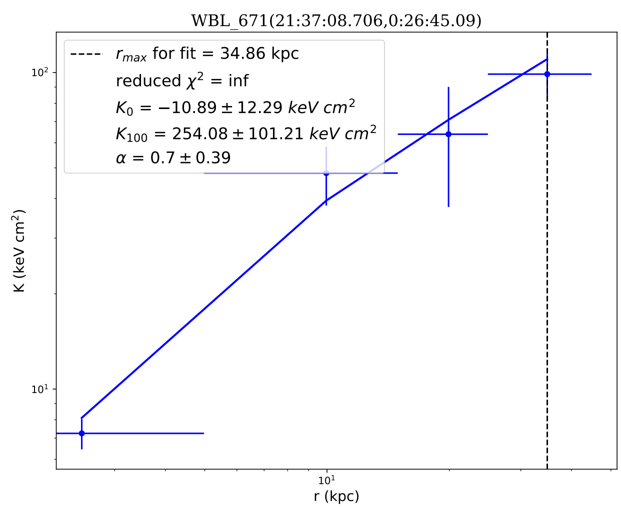
WBL_671(21:37:08.706,0:26:45.09)
r_{max} for fit = 34.86 kpc
reduced χ^2 = inf
$K_0 = -10.89 \pm 12.29$ $keV\ cm^2$
$K_{100} = 254.08 \pm 101.21$ $keV\ cm^2$
$\alpha = 0.7 \pm 0.39$
K (keV cm^2)
r (kpc)

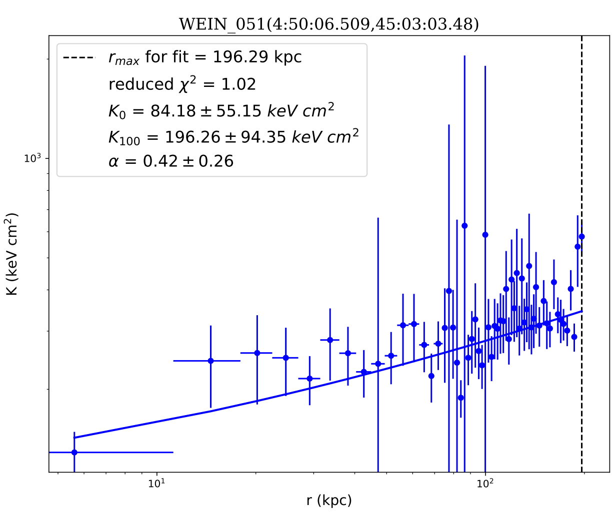
WEIN_051(4:50:06.509,45:03:03.48)
r_{max} for fit = 196.29 kpc
reduced χ^2 = 1.02
$K_0 = 84.18 \pm 55.15$ $keV\ cm^2$
$K_{100} = 196.26 \pm 94.35$ $keV\ cm^2$
$\alpha = 0.42 \pm 0.26$
K (keV cm^2)
r (kpc)

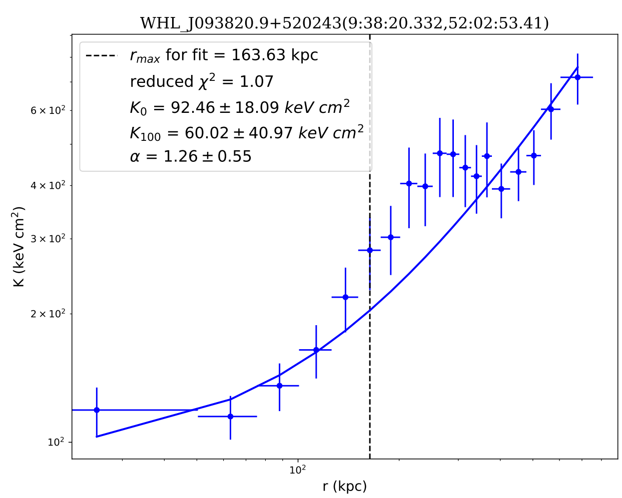
WHL_J093820.9+520243(9:38:20.332,52:02:53.41)
r_{max} for fit = 163.63 kpc
reduced χ^2 = 1.07
$K_0 = 92.46 \pm 18.09$ $keV\ cm^2$
$K_{100} = 60.02 \pm 40.97$ $keV\ cm^2$
$\alpha = 1.26 \pm 0.55$
K (keV cm^2)
r (kpc)

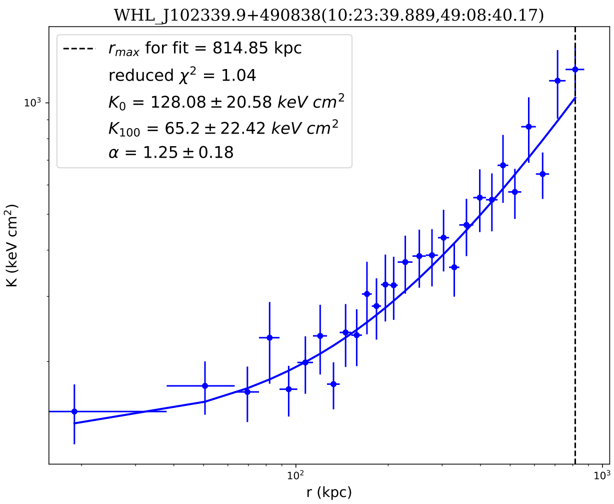
WHL_J102339.9+490838(10:23:39.889,49:08:40.17)
r_{max} for fit = 814.85 kpc
reduced χ^2 = 1.04
K_0 = 128.08 ± 20.58 $keV\ cm^2$
K_{100} = 65.2 ± 22.42 $keV\ cm^2$
α = 1.25 ± 0.18
K (keV cm^2)
r (kpc)

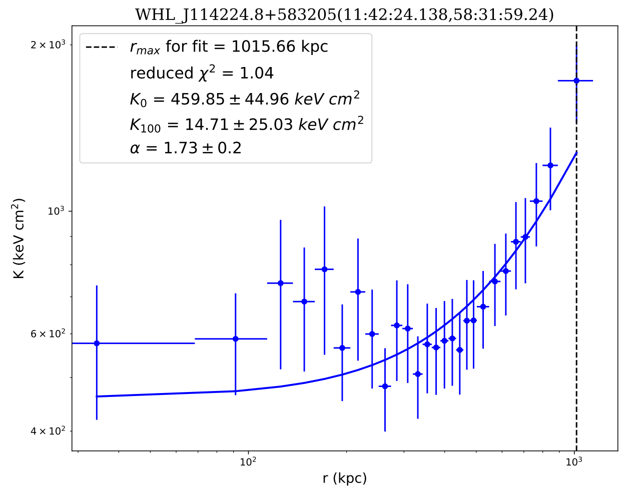
WHL_J114224.8+583205(11:42:24.138,58:31:59.24)
r_{max} for fit = 1015.66 kpc
reduced χ^2 = 1.04
K_0 = 459.85 ± 44.96 $keV\ cm^2$
K_{100} = 14.71 ± 25.03 $keV\ cm^2$
α = 1.73 ± 0.2
K (keV cm^2)
r (kpc)

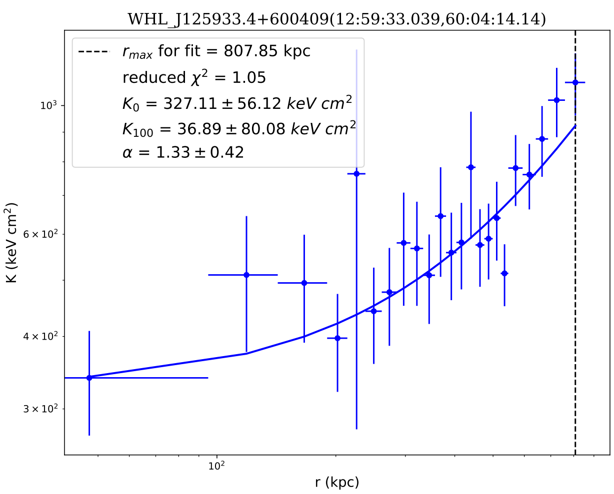
WHL_J125933.4+600409(12:59:33.039,60:04:14.14)
r_{max} for fit = 807.85 kpc
reduced χ^2 = 1.05
K_0 = 327.11 ± 56.12 $keV\ cm^2$
K_{100} = 36.89 ± 80.08 $keV\ cm^2$
α = 1.33 ± 0.42
K (keV cm^2)
r (kpc)

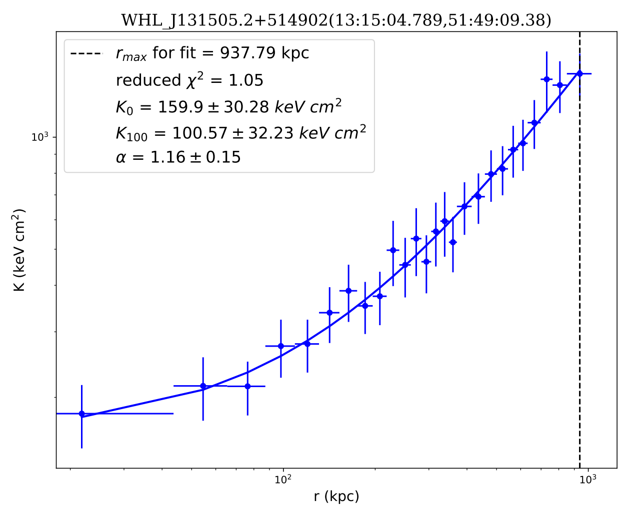
WHL_J131505.2+514902(13:15:04.789,51:49:09.38)
r_{max} for fit = 937.79 kpc
reduced χ^2 = 1.05
K_0 = 159.9 ± 30.28 $keV\ cm^2$
K_{100} = 100.57 ± 32.23 $keV\ cm^2$
α = 1.16 ± 0.15
K (keV cm^2)
r (kpc)

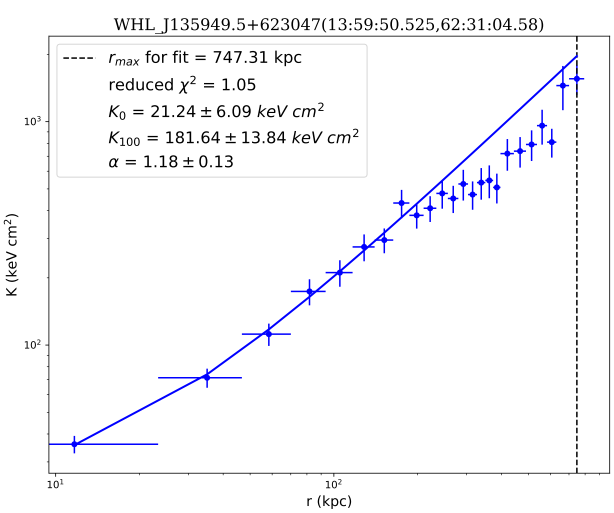
WHL_J135949.5+623047(13:59:50.525,62:31:04.58)
r_{max} for fit = 747.31 kpc
reduced χ^2 = 1.05
K_0 = 21.24 ± 6.09 $keV\ cm^2$
K_{100} = 181.64 ± 13.84 $keV\ cm^2$
α = 1.18 ± 0.13
K (keV cm^2)
r (kpc)

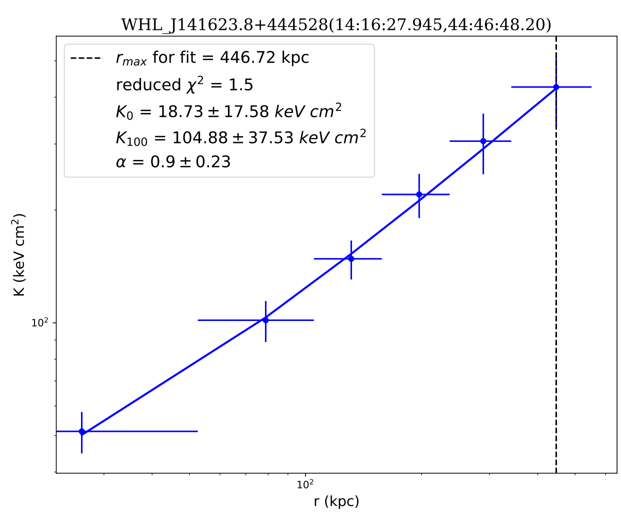
WHL_J141623.8+444528(14:16:27.945,44:46:48.20)
r_{max} for fit = 446.72 kpc
reduced χ^2 = 1.5
K_0 = 18.73 ± 17.58 $keV\ cm^2$
K_{100} = 104.88 ± 37.53 $keV\ cm^2$
α = 0.9 ± 0.23
K (keV cm^2)
r (kpc)

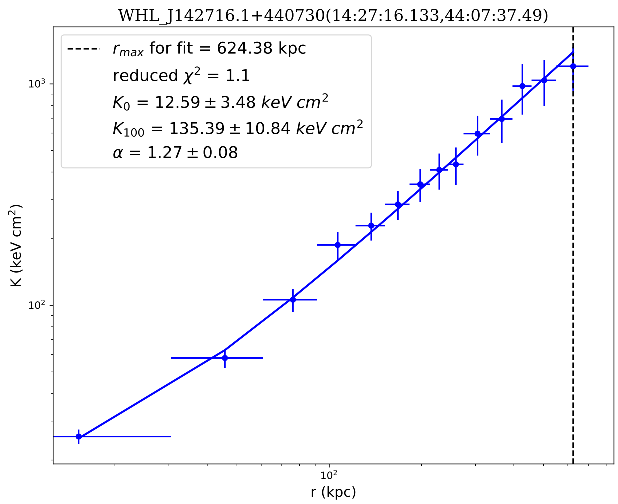
WHL_J142716.1+440730(14:27:16.133,44:07:37.49)
r_{max} for fit = 624.38 kpc
reduced χ^2 = 1.1
K_0 = 12.59 ± 3.48 $keV\ cm^2$
K_{100} = 135.39 ± 10.84 $keV\ cm^2$
α = 1.27 ± 0.08
K (keV cm^2)
r (kpc)

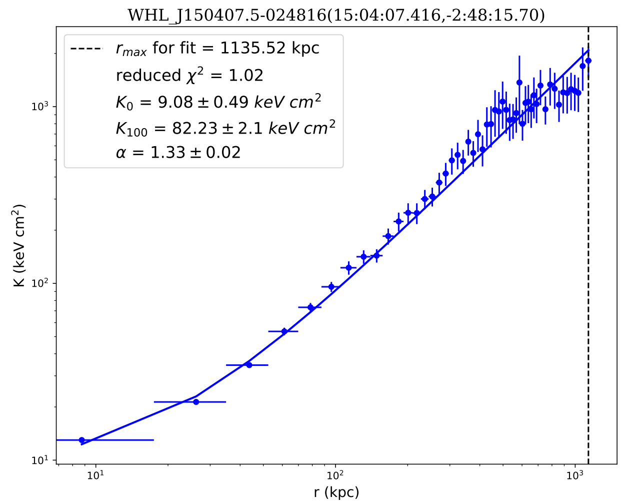
WHL_J150407.5-024816(15:04:07.416,-2:48:15.70)
r_{max} for fit = 1135.52 kpc
reduced χ^2 = 1.02
K_0 = 9.08 ± 0.49 $keV\ cm^2$
K_{100} = 82.23 ± 2.1 $keV\ cm^2$
α = 1.33 ± 0.02
K (keV cm^2)
r (kpc)

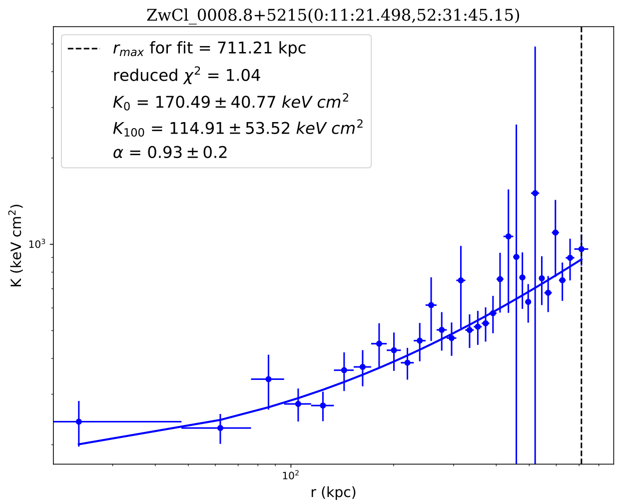
ZwCl_0008.8+5215(0:11:21.498,52:31:45.15)
r_{max} for fit = 711.21 kpc
reduced χ^2 = 1.04
K_0 = 170.49 ± 40.77 $keV\ cm^2$
K_{100} = 114.91 ± 53.52 $keV\ cm^2$
α = 0.93 ± 0.2
K (keV cm^2)
r (kpc)

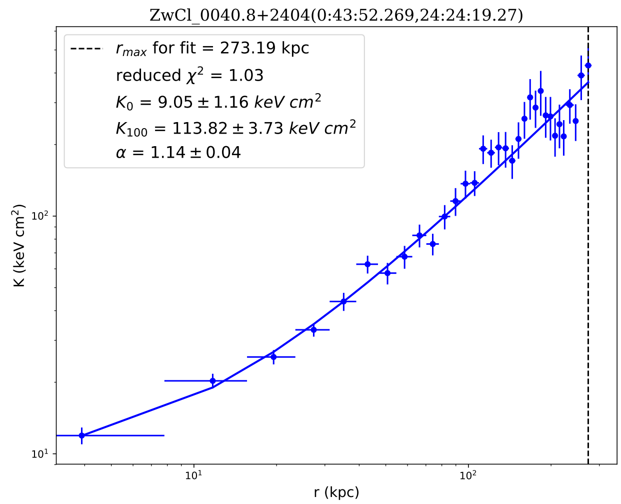
ZwCl_0040.8+2404(0:43:52.269,24:24:19.27)
r_{max} for fit = 273.19 kpc
reduced χ^2 = 1.03
K_0 = 9.05 ± 1.16 $keV\ cm^2$
K_{100} = 113.82 ± 3.73 $keV\ cm^2$
α = 1.14 ± 0.04
K (keV cm^2)
r (kpc)

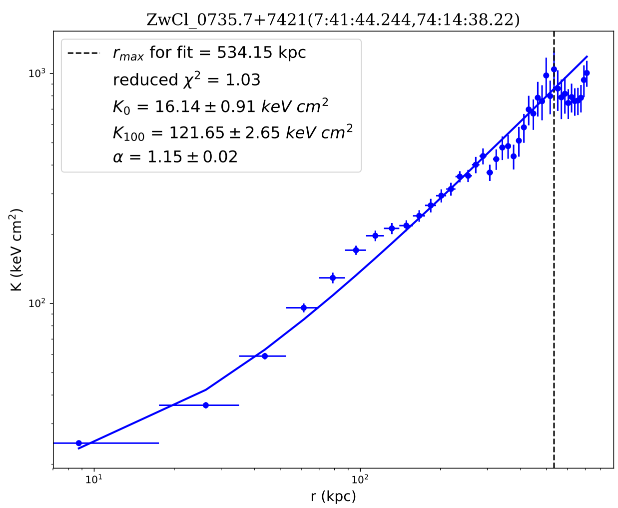
ZwCl_0735.7+7421(7:41:44.244,74:14:38.22)
r_{max} for fit = 534.15 kpc
reduced χ^2 = 1.03
K_0 = 16.14 ± 0.91 $keV\ cm^2$
K_{100} = 121.65 ± 2.65 $keV\ cm^2$
α = 1.15 ± 0.02
K (keV cm^2)
r (kpc)

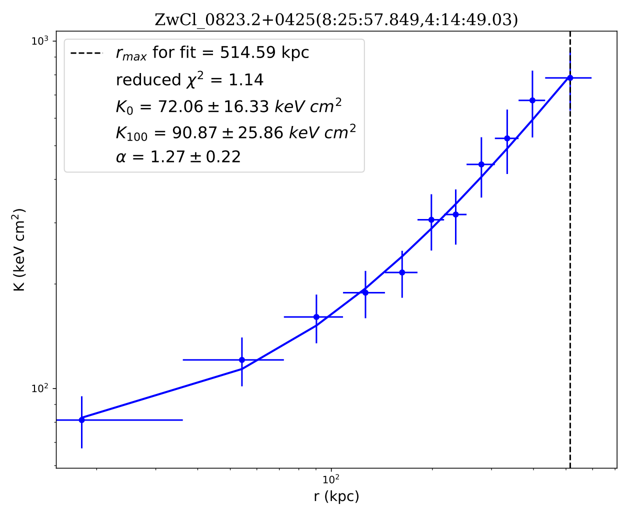
ZwCl_0823.2+0425(8:25:57.849,4:14:49.03)
r_{max} for fit = 514.59 kpc
reduced χ^2 = 1.14
K_0 = 72.06 ± 16.33 $keV\ cm^2$
K_{100} = 90.87 ± 25.86 $keV\ cm^2$
α = 1.27 ± 0.22
K (keV cm^2)
r (kpc)

APPENDIX D

ACCEPT 2.0 MORPHOLOGICAL PROPERTIES

Table D.1: **Morphological properties, profile centers, and BCG locations for ACCEPT 2.0 clusters with deprojected entropy profiles.** Column 1: Cluster Name in ACCEPT 2.0; Column 2: redshift; Column 3-4: concentration and error using R_{500}; Column 5-6: concentration and error with $r = 500$ kpc; Column 7: centroid shift calculated from the data; Column 8: centroid shift from 100 bootstrapped versions of the original data; Column 9: dispersion in the centroid shift from the simulated data; Column 10: power ratio P_3/P_0 calculated from the data; Column 11: power ratio from 100 bootstrapped versions of the original data; Column 12: dispersion in the power ratio from the simulated data; Column 13-14: Best fit global temperatures and errors; Column 15-16: Best fit global luminosity and errors; Column 17-18: profile center RA and DEC in degrees.

Cluster	**z**	c_{500}	δc_{500}	c	δc	w_{data}	w_{sim}	$\delta\, w_{sim}$	p_{data}	p_{sim}	$\delta\, p_{sim}$	kT	δkT	L_X	δL_X	**RA**	**DEC**
									10^7			(keV)		($10^{44} erg\ s^{-1}$)		(deg)	(deg)
ABELL_0141	0.230	0.250	0.025	0.242	0.024	0.053	0.042	0.009	16.600	18.000	3.400	6.58	0.77	3.13	0.13	16.39327	-24.63299
RBS_0653	0.284	0.160	0.008	0.264	0.009	0.071	0.075	0.001	0.583	0.600	0.146	9.15	0.34	8.20	0.12	82.22100	-39.47098
ABELL_0401	0.074	0.046	0.002	0.184	0.001	0.015	0.011	0.003	0.883	0.878	0.060	7.57	0.10	4.40	0.02	44.73717	13.57070
ABELL_S0579	0.152	0.096	0.014	0.337	0.030	0.042	0.040	0.003	1.880	2.420	0.986	4.79	0.35	1.50	0.06	94.13391	-39.79684
NGC_5044	0.009	0.054	0.009	0.206	0.002	0.024	0.024	0.000	0.120	0.122	0.023	1.32	0.03	0.00	0.00	198.84978	-16.38545
ABELL_0980	0.158	0.126	0.011	0.240	0.016	0.019	0.019	0.002	0.216	0.365	0.316	6.54	0.53	3.07	0.09	155.61823	50.10607
ClG_2153.8+3746	0.292	0.180	0.007	0.260	0.007	0.069	0.069	0.001	0.458	0.501	0.177	9.49	0.36	11.90	0.16	328.96785	38.00629
ABELL_3128	0.060	0.111	0.015	0.214	0.016	0.168	0.168	0.003	5.490	5.420	1.560	3.14	0.19	0.31	0.01	52.46048	-52.58009

Cluster	**z**	c_{500}	δc_{500}	c	δc	w_{data}	w_{sim}	$\delta\, w_{sim}$	p_{data}	p_{sim}	$\delta\, p_{sim}$	kT	δkT	L_X	δL_X	**RA**	**DEC**
									10^7			(keV)		($10^{44} erg\ s^{-1}$)		(deg)	(deg)
MACS_J0308.9+2645	0.324	0.239	0.013	0.215	0.012	0.014	0.013	0.003	0.350	0.464	0.302	9.66	1.05	11.60	0.32	47.23303	26.76065
MCXC_J2014.8-2430	0.161	0.332	0.009	0.371	0.009	0.005	0.005	0.000	0.999	1.000	0.153	7.15	0.39	4.26	0.10	303.71559	-24.50895
ABELL_2443	0.108	0.085	0.007	0.348	0.019	0.052	0.051	0.003	4.220	4.290	0.681	9.72	1.44	1.70	0.05	336.52702	17.36541
ABELL_1835	0.253	0.312	0.006	0.352	0.007	0.010	0.010	0.000	0.118	0.132	0.043	10.33	0.62	12.80	0.18	210.25813	2.87866
ABELL_2813	0.292	0.160	0.012	0.213	0.014	0.011	0.015	0.007	0.264	0.494	0.402	7.95	0.74	7.71	0.24	10.85367	-20.62363
ABELL_1300	0.307	0.544	0.037	0.204	0.013	0.066	0.064	0.002	2.060	2.160	0.781	11.26	1.17	10.50	0.26	172.97742	-19.92904
MCXC_J0547.0-3904	0.210	0.421	0.033	0.530	0.047	0.010	0.010	0.002	0.243	0.383	0.295	5.19	0.70	0.98	0.06	86.75659	-39.07451
ABELL_3880	0.058	0.198	0.011	0.644	0.041	0.023	0.022	0.000	0.028	0.055	0.044	5.31	0.23	0.33	0.02	336.97733	-30.57634
ABELL_0586	0.171	0.125	0.008	0.305	0.013	0.005	0.006	0.002	0.733	0.792	0.304	6.24	0.40	3.38	0.09	113.08475	31.63294
NGC_3402_GROUP	0.015	0.122	0.012	0.411	0.013	0.009	0.010	0.001	0.040	0.075	0.056	0.82	0.01	0.01	0.00	162.60885	-12.84493
ABELL_S0780	0.236	0.251	0.009	0.409	0.012	0.015	0.015	0.001	0.321	0.362	0.130	7.33	0.29	5.56	0.08	224.87007	-18.17875
MCXC_J1524.2-3154	0.103	0.175	0.005	0.417	0.008	0.003	0.003	0.000	0.032	0.044	0.027	4.47	0.12	1.34	0.02	231.05346	-31.90449
ABELL_0562	0.110	0.144	0.017	NaN	NaN	0.025	0.025	0.003	0.133	0.214	0.183	2.94	0.19	0.38	0.02	103.33968	69.33089
ABELL_2256	0.058	0.046	0.004	0.073	0.002	0.140	0.136	0.006	4.260	4.220	0.360	3.56	0.23	3.40	0.03	255.93570	78.63653
SDSS-C4_3072	0.164	0.189	0.005	0.333	0.006	0.004	0.004	0.000	0.129	0.139	0.040	7.11	0.27	4.43	0.08	260.04142	26.62475
G139.59+24.18	0.270	0.281	0.017	0.314	0.018	0.036	0.035	0.002	7.790	7.960	1.520	7.19	0.64	8.23	0.30	95.45413	74.70140
NGC_3551	0.032	0.324	0.052	NaN	NaN	0.017	0.018	0.004	0.286	0.424	0.361	1.62	0.06	0.02	0.00	167.43430	21.75937
MCXC_J0303.7-7752	0.274	0.272	0.015	0.193	0.012	0.025	0.025	0.003	0.915	1.160	0.551	9.34	0.89	7.38	0.21	45.93866	-77.87977
NSCS_J144726+082824	0.195	NaN	NaN	0.526	0.027	0.002	0.002	0.001	0.055	0.095	0.072	19.22	7.76	1.71	0.23	221.86098	8.47370
ABELL_2415	0.058	0.194	0.018	NaN	NaN	0.032	0.031	0.002	0.154	0.271	0.200	2.66	0.12	0.39	0.01	331.41081	-5.59164
Hercules_A	0.155	0.184	0.008	0.392	0.008	0.003	0.004	0.000	0.052	0.061	0.031	4.26	0.10	1.81	0.03	252.78400	4.99234

Cluster	**z**	c_{500}	δc_{500}	c	δc	w_{data}	w_{sim}	$\delta\, w_{sim}$	p_{data}	p_{sim}	$\delta\, p_{sim}$	kT	δkT	L_X	δL_X	**RA**	**DEC**
									10^7			(keV)		($10^{44} erg\ s^{-1}$)		(deg)	(deg)
ABELL_1775	0.072	0.045	0.007	0.235	0.004	0.063	0.063	0.001	1.450	1.460	0.140	5.47	1.02	0.90	0.01	205.45265	26.37225
ABELL_2219	0.226	0.059	0.003	0.140	0.002	0.037	0.036	0.001	0.526	0.515	0.074	11.27	0.20	15.70	0.10	250.08380	46.71190
ABELL_0550	0.099	0.080	0.011	0.226	0.014	0.052	0.050	0.004	0.390	0.508	0.304	5.67	0.30	2.15	0.06	88.21475	-21.05362
MCXC_J2311.5+0338	0.300	0.218	0.013	0.241	0.014	0.005	0.006	0.002	0.357	0.469	0.338	9.52	1.00	7.83	0.30	347.88846	3.63562
CIZA_J0616.3-2156	0.171	0.109	0.012	0.220	0.017	0.034	0.033	0.003	0.100	0.352	0.287	7.24	0.51	3.06	0.07	94.10328	-21.93831
CIZA_J1804.4+1002	0.152	0.141	0.011	0.216	0.012	0.079	0.079	0.002	0.082	0.168	0.130	7.10	0.59	5.23	0.15	271.13068	10.05684
MCXC_J1215.4-3900	0.119	0.073	0.014	0.305	0.033	0.033	0.028	0.007	2.610	2.960	1.320	5.50	0.36	1.60	0.04	183.85268	-39.03630
PLCKESZ_G286.58-31.25	0.210	0.104	0.011	0.219	0.018	0.023	0.018	0.006	0.227	0.465	0.423	6.48	0.54	3.85	0.13	82.86840	-75.17931
MCXC_J2218.6-3853	0.138	0.082	0.009	0.252	0.015	0.018	0.018	0.003	0.066	0.158	0.112	5.60	0.33	3.29	0.09	334.66508	-38.90172
ABELL_1576	0.279	0.207	0.013	0.283	0.017	0.016	0.015	0.002	1.530	1.610	0.551	8.00	0.77	3.02	0.11	189.24281	63.18719
ABELL_2550	0.123	0.164	0.015	0.516	0.031	0.004	0.004	0.001	0.058	0.128	0.098	1.93	0.12	0.20	0.01	347.89634	-21.74487
MACS_J1720.2+3536	0.391	0.310	0.014	0.353	0.016	0.016	0.015	0.001	0.070	0.141	0.110	7.87	0.65	7.30	0.22	260.07064	35.60656
Hydra_A	0.055	0.067	0.002	0.272	0.002	0.014	0.014	0.000	4.540	4.540	0.063	4.08	0.03	1.12	0.00	139.52494	-12.09554
MCXC_J0439.0+0520	0.208	0.303	0.017	0.401	0.021	0.004	0.004	0.001	0.045	0.090	0.082	5.02	0.48	1.89	0.10	69.75924	5.34531
ABELL_2457	0.059	0.157	0.025	NaN	NaN	0.015	0.016	0.003	1.080	1.260	0.539	3.81	0.22	0.54	0.02	338.92132	1.48619
2MFGC_06756	0.241	0.193	0.006	0.439	0.011	0.005	0.005	0.000	0.055	0.062	0.033	5.05	0.23	2.71	0.06	128.72885	55.57254
HCG_037	0.022	0.007	0.001	0.585	0.214	0.012	0.015	0.005	0.296	8.070	9.790	0.96	0.24	0.00	0.00	138.41297	29.99522
ZwCl_1006.1+1201	0.221	0.097	0.008	0.301	0.015	0.086	0.079	0.005	0.828	0.914	0.328	5.86	0.33	2.85	0.07	152.19776	11.79342
SPT-CLJ2043-5035	0.723	0.432	0.037	0.583	0.060	0.005	0.006	0.001	0.283	0.498	0.452	5.44	0.68	6.60	0.49	310.82306	-50.59231
ABELL_3921	0.093	0.085	0.006	0.236	0.007	0.012	0.012	0.001	0.490	0.543	0.178	6.92	0.41	1.96	0.04	342.49095	-64.42838
ABELL_3571	0.039	0.069	0.002	0.096	0.001	0.083	0.083	0.001	3.550	3.530	0.172	7.76	0.27	0.55	0.01	206.86847	-32.86457

Cluster	**z**	c_{500}	δc_{500}	c	δc	w_{data}	w_{sim}	$\delta\, w_{sim}$	p_{data}	p_{sim}	$\delta\, p_{sim}$	kT	δkT	L_X	δL_X	**RA**	**DEC**
									10^7			(keV)		($10^{44} erg\ s^{-1}$)		(deg)	(deg)
MESSIER_089	0.001	0.040	0.000	0.503	0.019	0.011	0.011	0.001	1.050	1.080	0.264	3.00	10.00	0.00	0.00	188.91572	12.55666
NSCS_J122648+215157	0.370	0.127	0.013	NaN	NaN	0.214	0.212	0.004	9.120	9.760	3.190	4.78	0.47	1.62	0.08	186.71234	21.83260
MCXC_J2003.5-2323	0.317	0.237	0.017	0.233	0.016	0.133	0.133	0.005	0.975	1.150	0.749	9.18	0.80	8.46	0.20	300.86238	-23.38271
ABELL_0611	0.288	0.264	0.011	0.324	0.013	0.006	0.006	0.001	0.291	0.308	0.181	8.55	0.73	5.00	0.13	120.23680	36.05669
ABELL_2125	0.246	0.092	0.027	NaN	NaN	0.083	0.080	0.006	3.140	3.920	1.500	3.16	0.21	0.61	0.03	235.30898	66.26589
NSCS_J135021+094042	0.090	0.321	0.015	0.508	0.026	0.005	0.005	0.000	0.065	0.108	0.093	6.24	0.40	0.39	0.02	207.59133	9.66982
MCXC_J1022.0+3830	0.049	NaN	NaN	NaN	NaN	0.014	0.013	0.002	4.750	4.580	1.300	2.66	0.24	0.05	0.00	155.54181	38.52321
ABELL_1190	0.075	0.065	0.015	0.816	0.198	0.017	0.017	0.004	0.690	0.951	0.573	3.60	0.19	0.58	0.03	167.91590	40.84019
3C_444	0.153	0.128	0.005	0.326	0.009	0.016	0.016	0.001	2.080	2.050	0.278	5.40	0.21	0.61	0.02	333.61236	-17.02565
ABELL_3399	0.203	0.156	0.016	0.265	0.020	0.075	0.074	0.004	5.720	5.990	1.510	6.76	0.45	3.38	0.07	99.31046	-48.47188
ABELL_1914	0.171	0.115	0.005	0.206	0.006	0.063	0.061	0.003	0.775	0.784	0.190	8.74	0.46	9.73	0.15	216.51275	37.82440
WHL_J114224.8+583205	0.311	0.079	0.008	0.096	0.008	0.080	0.080	0.006	1.800	2.160	1.020	8.86	0.68	8.37	0.20	175.60058	58.53312
ABELL_3444	0.253	0.247	0.007	0.379	0.009	0.006	0.006	0.001	0.223	0.245	0.090	7.92	0.45	7.84	0.13	155.95915	-27.25660
ABELL_S1101	0.058	0.075	0.002	0.542	0.007	0.005	0.005	0.000	0.025	0.028	0.010	7.57	0.10	0.52	0.01	348.49485	-42.72631
PLCKESZ_G167.65+17.64	0.174	0.083	0.010	0.145	0.011	0.020	0.020	0.003	0.983	1.160	0.715	6.18	0.41	4.90	0.11	99.51535	47.79831
ABELL_0370	0.375	0.089	0.006	0.163	0.008	0.048	0.043	0.006	0.580	0.660	0.336	8.75	0.46	7.42	0.12	39.97154	-1.57693
ABELL_2009	0.153	0.227	0.009	0.327	0.011	0.005	0.005	0.001	0.207	0.266	0.108	6.70	0.44	3.58	0.10	225.08157	21.36988
ABELL_2104	0.153	0.065	0.004	0.191	0.005	0.012	0.011	0.001	4.520	4.490	0.414	7.17	0.25	3.79	0.05	235.03388	-3.30417
ABELL_3562	0.049	0.074	0.007	0.251	0.009	0.015	0.015	0.002	6.150	6.190	0.567	4.70	0.26	0.81	0.02	203.40750	-31.67001
ABELL_2294	0.169	0.181	0.014	0.216	0.015	0.028	0.026	0.003	0.296	0.486	0.378	7.30	0.74	4.67	0.17	261.04229	85.88605
ZwCl_0949.6+5207	0.214	0.135	0.005	0.467	0.013	0.029	0.029	0.001	7.640	7.700	0.440	5.64	0.21	2.26	0.05	148.20493	51.88480

Cluster	z	c_{500}	δc_{500}	c	δc	w_{data}	w_{sim}	$\delta\, w_{sim}$	p_{data}	p_{sim}	$\delta\, p_{sim}$	kT	δkT	L_X	δL_X	RA	DEC
									10^7			(keV)		($10^{44} erg\ s^{-1}$)		(deg)	(deg)
ABELL_0963	0.206	0.130	0.005	0.292	0.008	0.015	0.015	0.001	1.180	1.220	0.237	6.49	0.32	4.63	0.08	154.26560	39.04699
WHL_J131505.2+514902	0.291	0.155	0.011	0.196	0.013	0.010	0.011	0.004	0.948	1.060	0.529	8.76	0.77	7.12	0.14	198.76995	51.81927
ABELL_3364	0.148	0.130	0.008	0.211	0.010	0.022	0.019	0.005	0.341	0.416	0.237	7.19	0.55	3.19	0.08	86.90707	-31.87323
3C_089	0.139	0.185	0.013	NaN	NaN	0.040	0.039	0.002	0.161	0.269	0.186	4.53	0.33	0.46	0.02	53.56249	-1.18816
MACS_J1829.0+6913	0.203	0.188	0.014	NaN	NaN	0.004	0.005	0.001	1.080	1.210	0.492	4.06	0.30	0.83	0.04	277.27583	69.23557
ABELL_3653	0.109	NaN	NaN	NaN	NaN	0.053	0.053	0.008	1.550	2.150	1.190	4.78	0.34	0.52	0.01	298.26233	-52.03578
Abell_222	0.211	0.064	0.012	0.265	0.020	0.080	0.073	0.005	2.640	2.940	0.954	4.14	0.27	1.64	0.07	24.39401	-12.99302
ABELL_0598	0.189	0.294	0.019	0.489	0.034	0.029	0.029	0.001	0.482	0.600	0.274	5.05	0.54	1.69	0.08	117.85042	17.51472
ABELL_0576	0.039	0.072	0.005	0.141	0.004	0.037	0.037	0.002	0.638	0.644	0.203	4.40	0.15	0.21	0.00	110.37664	55.76165
SDSS-C4_3062	0.064	NaN	NaN	NaN	NaN	0.026	0.026	0.005	0.007	0.525	0.615	3.76	0.54	0.19	0.04	122.59509	42.27392
UGCl_120	0.029	NaN	NaN	NaN	NaN	0.023	0.023	0.004	1.810	2.410	1.440	1.90	0.12	0.05	0.01	125.84018	4.37259
2MASSi_J0913454+405628	0.442	0.372	0.015	0.492	0.021	0.002	0.002	0.000	0.010	0.038	0.034	6.42	0.59	4.90	0.20	138.44054	40.94157
Centaurus_Cluster	0.011	0.109	0.002	0.204	0.001	0.023	0.023	0.000	0.336	0.339	0.017	3.00	10.00	0.00	0.00	192.20528	-41.31098
MCXC_J0532.9-3701	0.275	0.299	0.016	0.271	0.015	0.011	0.010	0.002	0.112	0.219	0.173	8.64	0.84	7.20	0.21	83.23139	-37.02643
ABELL_0548A	0.040	0.211	0.037	NaN	NaN	0.031	0.031	0.002	0.571	0.697	0.518	3.07	0.16	0.25	0.01	87.15965	-25.47788
ABELL_1423	0.076	0.172	0.012	0.307	0.016	0.015	0.015	0.002	0.445	0.496	0.190	4.33	0.26	0.32	0.01	179.32193	33.61040
ABELL_0578	0.087	NaN	NaN	NaN	NaN	0.083	0.083	0.007	0.632	0.740	0.592	2.55	0.23	0.14	0.01	111.22296	66.98539
ABELL_0402	0.322	0.358	0.026	0.313	0.023	0.012	0.012	0.002	1.970	2.040	0.834	8.23	1.24	4.74	0.20	44.42093	-22.15309
ABELL_3809	0.062	0.142	0.018	NaN	NaN	0.013	0.013	0.002	0.188	0.291	0.216	2.89	0.12	0.41	0.01	326.74622	-43.89847
MACS_J1621.3+3810	0.465	0.309	0.013	0.447	0.020	0.008	0.008	0.001	0.144	0.187	0.109	7.23	0.58	5.35	0.20	245.35334	38.16907
IC_1365	0.049	0.083	0.010	NaN	NaN	0.356	0.356	0.003	11.400	11.700	1.370	4.84	0.13	0.56	0.02	318.48278	2.56379

Cluster	**z**	c_{500}	δc_{500}	c	δc	w_{data}	w_{sim}	$\delta\, w_{sim}$	p_{data}	p_{sim}	$\delta\, p_{sim}$	kT	δkT	L_X	δL_X	**RA**	**DEC**
									10^7			(keV)		($10^{44} erg\ s^{-1}$)		(deg)	(deg)
MACS_J2229.8-2756	0.324	0.364	0.018	0.435	0.022	0.001	0.002	0.001	0.171	0.216	0.135	5.88	0.56	4.20	0.20	337.43899	-27.92734
ABELL_0098N	0.104	0.511	0.053	NaN	NaN	0.010	0.011	0.002	0.364	0.491	0.387	3.78	0.39	0.32	0.02	11.60285	20.62212
SSGC_081	0.050	0.099	0.012	0.296	0.015	0.034	0.034	0.002	9.040	9.130	1.090	8.32	0.22	0.41	0.01	202.44895	-31.60654
ABELL_1668	0.063	0.283	0.016	0.367	0.020	0.033	0.033	0.002	1.190	1.310	0.507	3.33	0.29	0.30	0.02	195.94451	19.27054
PLCKESZ_G337.09-25.97	0.264	0.183	0.011	0.288	0.015	0.032	0.031	0.002	0.510	0.631	0.345	7.66	0.54	6.85	0.14	288.65638	-59.47217
MCXC_J1852.1+5711	0.109	0.243	0.018	NaN	NaN	0.005	0.005	0.001	1.660	1.880	0.685	4.00	0.28	0.45	0.02	283.03673	57.19517
ABELL_S0295	0.300	0.122	0.011	0.189	0.014	0.159	0.158	0.003	0.608	0.788	0.505	7.35	0.71	9.68	0.33	41.36022	-53.02968
MCXC_J1558.3-1410	0.097	0.104	0.004	0.353	0.006	0.007	0.007	0.000	1.250	1.250	0.143	5.18	0.12	1.98	0.02	239.59103	-14.16607
GALEX_J094712.4+762313	0.354	0.351	0.011	0.424	0.013	0.001	0.002	0.000	0.010	0.020	0.015	8.46	0.57	8.35	0.19	146.80289	76.38706
ABELL_2485	0.247	0.292	0.029	0.526	0.063	0.005	0.007	0.002	0.249	0.515	0.415	6.25	0.71	2.77	0.12	342.12908	-16.10785
ABELL_1204	0.171	0.255	0.010	0.422	0.015	0.003	0.003	0.000	0.159	0.171	0.082	4.33	0.28	1.61	0.07	168.33508	17.59401
MACS_J0744.9+3927	0.698	0.285	0.017	0.342	0.020	0.024	0.024	0.002	2.700	2.810	0.775	7.80	0.63	15.00	0.65	116.22001	39.45678
ABELL_3094	0.068	0.073	0.013	NaN	NaN	0.053	0.052	0.004	0.153	0.302	0.210	3.11	0.21	0.23	0.01	47.89950	-26.89876
PLCKESZ_G264.41+19.48	0.240	0.204	0.016	0.263	0.020	0.007	0.008	0.001	0.176	0.354	0.347	7.50	0.70	3.76	0.13	150.00673	-30.27697
MACS_J1206.2-0847	0.440	0.273	0.014	0.228	0.013	0.028	0.028	0.002	2.640	2.660	0.871	11.37	1.42	19.30	0.56	181.55115	-8.80067
NGC_4782-3	0.015	0.450	0.054	NaN	NaN	0.039	0.039	0.002	5.200	5.560	1.710	1.05	0.20	0.00	0.00	193.65042	-12.56074
MCXC_J0437.1+0043	0.285	0.234	0.013	0.366	0.020	0.009	0.009	0.001	0.229	0.251	0.157	6.83	0.48	5.14	0.14	69.28978	0.73223
ABELL_0383	0.187	0.216	0.008	0.409	0.012	0.004	0.004	0.001	0.560	0.575	0.125	5.31	0.23	2.02	0.06	42.01402	-3.52908
ABELL_2069	0.116	0.063	0.007	0.152	0.006	0.201	0.198	0.012	6.500	6.520	1.030	4.46	0.58	1.79	0.03	231.04740	29.87195
MCXC_J0338.6+0958	0.036	0.060	0.002	0.308	0.002	0.024	0.024	0.000	0.037	0.038	0.008	3.62	0.03	0.48	0.00	54.67127	9.96685
MCXC_J1234.2+0947	0.229	0.172	0.038	NaN	NaN	0.101	0.093	0.020	4.680	4.570	2.490	4.55	0.48	1.74	0.11	188.60135	9.78923

Cluster	**z**	c_{500}	δc_{500}	c	δc	w_{data}	w_{sim}	$\delta\, w_{sim}$	p_{data}	p_{sim}	$\delta\, p_{sim}$	kT	δkT	L_X	δL_X	**RA**	**DEC**
									10^7			(keV)		($10^{44} erg\ s^{-1}$)		(deg)	(deg)
UGC_02748	0.030	0.386	0.039	NaN	NaN	0.018	0.019	0.002	0.041	0.161	0.141	11.99	1.11	0.01	0.00	51.97515	2.56160
NGC_4325_GROUP	0.025	0.053	0.010	0.396	0.012	0.010	0.010	0.001	0.355	0.371	0.129	0.98	0.02	0.02	0.00	185.77729	10.62217
ABELL_2384	0.094	0.149	0.008	0.339	0.011	0.056	0.056	0.002	0.955	0.969	0.262	4.77	0.26	1.11	0.02	328.08824	-19.54775
MCXC_J0425.8-0833	0.040	0.186	0.010	0.473	0.023	0.022	0.022	0.001	5.320	5.430	0.619	3.07	0.16	0.37	0.02	66.46363	-8.56012
ABELL_0013	0.094	0.079	0.006	0.199	0.008	0.040	0.039	0.003	6.410	6.650	0.779	4.77	0.26	0.63	0.02	3.40785	-19.50253
MACS_J1427.6-2521	0.318	0.256	0.020	0.557	0.049	0.004	0.005	0.001	0.541	0.678	0.368	4.69	0.34	2.07	0.10	216.91768	-25.35410
ABELL_1795	0.062	0.078	0.002	0.248	0.002	0.009	0.010	0.000	1.120	1.120	0.047	6.13	0.10	1.88	0.01	207.22001	26.58987
CGCG_514-050	0.017	0.391	0.039	NaN	NaN	0.022	0.022	0.002	4.840	4.750	0.778	1.23	0.04	0.00	0.00	337.83553	39.35868
WHL_J093820.9+520243	0.360	0.158	0.015	0.316	0.023	0.098	0.098	0.002	1.360	1.400	0.673	6.42	0.50	5.66	0.19	144.58472	52.04817
ABELL_3528B	0.053	0.344	0.022	NaN	NaN	0.016	0.016	0.002	1.790	1.880	0.562	7.57	0.63	0.57	0.02	193.59271	-29.01106
ZwCl_0040.8+2404	0.083	0.227	0.008	0.383	0.012	0.005	0.005	0.000	0.134	0.161	0.087	4.24	0.23	0.81	0.03	10.96779	24.40535
ABELL_2187	0.184	0.300	0.024	0.357	0.029	0.043	0.043	0.003	0.358	0.525	0.337	6.71	0.76	2.43	0.10	246.05841	41.24376
ABELL_3695	0.089	0.079	0.012	0.304	0.030	0.057	0.057	0.003	0.263	0.442	0.308	6.46	0.43	1.90	0.04	308.68842	-35.81119
MACS_J1931.8-2635	0.352	0.270	0.007	0.393	0.009	0.002	0.002	0.000	0.031	0.039	0.028	7.87	0.33	9.42	0.11	292.95690	-26.57611
ABELL_0267	0.231	0.181	0.013	0.256	0.016	0.031	0.027	0.004	0.202	0.348	0.249	7.57	0.63	4.34	0.11	28.17612	1.01259
MCXC_J0528.2-2942	0.158	0.099	0.014	0.655	0.092	0.027	0.026	0.003	0.262	0.505	0.432	4.49	0.31	1.62	0.09	82.06135	-29.72077
MCXC_J1750.2+3504	0.171	0.261	0.017	0.436	0.025	0.004	0.004	0.001	0.072	0.141	0.123	4.64	0.36	1.67	0.08	267.56907	35.08282
MCXC_J0439.0+0715	0.230	0.181	0.012	0.279	0.015	0.013	0.012	0.002	2.930	3.060	0.648	6.53	0.53	5.46	0.17	69.75296	7.26879
Cl_0016+16	0.541	0.132	0.008	0.151	0.008	0.020	0.018	0.003	0.559	0.735	0.373	9.73	0.74	18.40	0.40	4.63960	16.43694
ABELL_1644	0.047	0.111	0.007	0.157	0.003	0.032	0.032	0.001	5.210	5.190	0.339	4.12	0.87	0.80	0.01	194.29860	-17.40913
ABELL_2355	0.124	0.229	0.030	0.441	0.065	0.031	0.034	0.005	0.888	0.966	0.521	7.24	0.69	1.48	0.05	323.81954	1.41767

Cluster	**z**	c_{500}	δc_{500}	c	δc	w_{data}	w_{sim}	$\delta\, w_{sim}$	p_{data}	p_{sim}	$\delta\, p_{sim}$	kT	δkT	L_X	δL_X	**RA**	**DEC**
									10^7			(keV)		($10^{44} erg\ s^{-1}$)		(deg)	(deg)
WHL_J135949.5+623047	0.322	0.255	0.013	0.358	0.017	0.011	0.011	0.001	0.319	0.452	0.289	6.86	0.59	4.20	0.13	209.96052	62.51794
ABELL_3739	0.165	0.129	0.014	0.274	0.023	0.015	0.014	0.002	0.021	0.272	0.271	6.08	0.53	2.90	0.12	316.07980	-41.34487
ABELL_2151	0.037	0.144	0.013	0.483	0.026	0.011	0.011	0.001	1.990	2.090	0.455	4.48	1.15	0.18	0.02	241.14953	17.72149
NGC_5129	0.023	0.321	0.032	NaN	NaN	0.012	0.012	0.003	0.398	0.681	0.496	0.75	0.02	0.01	0.00	201.04160	13.97551
ABELL_S0463	0.039	0.439	0.136	NaN	NaN	0.195	0.194	0.003	1.080	1.130	0.421	2.83	0.09	0.09	0.00	67.15594	-53.84181
ABELL_0193	0.049	0.067	0.006	0.139	0.005	0.023	0.021	0.002	5.390	5.440	0.655	3.64	0.14	0.39	0.01	21.28192	8.69919
ABELL_2744	0.308	0.062	0.004	0.102	0.003	0.044	0.040	0.003	2.200	2.230	0.394	10.48	0.43	14.30	0.18	3.58137	-30.39173
ABELL_3411	0.169	0.065	0.008	0.241	0.015	0.146	0.143	0.005	0.105	0.197	0.164	6.25	0.31	2.87	0.05	130.46636	-17.46267
PLCKESZ_G304.84-41.42	0.410	0.251	0.018	0.253	0.018	0.047	0.047	0.003	8.750	8.920	1.890	9.80	1.23	8.31	0.30	7.02381	-75.63011
SDSS_+137.3+11.0+0.18	0.180	0.097	0.008	0.298	0.013	0.312	0.310	0.003	141.000	140.000	5.900	5.38	0.31	2.70	0.08	137.30314	10.97556
ABELL_2204	0.152	0.283	0.003	0.340	0.003	0.006	0.006	0.000	0.020	0.023	0.011	4.42	1.07	6.43	0.05	248.19550	5.57579
ABELL_2390	0.228	0.165	0.003	0.258	0.003	0.013	0.013	0.000	0.357	0.354	0.066	11.16	0.31	14.50	0.10	328.40344	17.69566
ABELL_3126	0.086	0.088	0.009	0.360	0.023	0.022	0.020	0.004	0.320	0.362	0.217	4.99	0.31	1.19	0.04	52.15235	-55.71799
AWM_4	0.032	0.094	0.005	0.345	0.008	0.005	0.005	0.001	0.416	0.436	0.110	2.74	0.09	0.06	0.00	241.23536	23.93401
ABELL_2107	0.041	0.135	0.007	0.649	0.032	0.014	0.014	0.001	0.492	0.508	0.124	3.18	0.76	0.42	0.01	234.91297	21.78268
ABELL_0644	0.070	0.065	0.003	0.255	0.004	0.027	0.026	0.001	0.143	0.143	0.037	4.76	0.75	2.86	0.03	124.35510	-7.51112
ABELL_2537	0.295	0.142	0.007	0.333	0.013	0.010	0.009	0.001	0.059	0.115	0.093	6.65	0.37	4.84	0.11	347.09297	-2.19163
ABELL_1831	0.062	0.114	0.018	NaN	NaN	0.012	0.014	0.003	0.655	0.689	0.324	3.54	0.16	0.52	0.02	209.81592	27.97560
ABELL_0209	0.206	0.140	0.008	0.171	0.009	0.027	0.025	0.002	0.386	0.422	0.279	8.55	0.66	6.57	0.17	22.96902	-13.61078
ABELL_3322	0.200	0.217	0.017	0.272	0.019	0.017	0.015	0.002	0.022	0.242	0.221	6.65	0.60	3.87	0.14	77.57048	-45.32118
MACS_J0417.5-1154	0.440	0.219	0.008	0.272	0.009	0.037	0.037	0.001	6.830	7.160	0.714	11.32	0.50	24.50	0.42	64.39453	-11.90909

Cluster	**z**	c_{500}	δc_{500}	c	δc	w_{data}	w_{sim}	$\delta\, w_{sim}$	p_{data}	p_{sim}	$\delta\, p_{sim}$	kT	δkT	L_X	δL_X	**RA**	**DEC**
									10^7			(keV)		($10^{44} erg\ s^{-1}$)		(deg)	(deg)
LCDCS_0829	0.451	0.349	0.005	0.376	0.005	0.017	0.016	0.000	0.434	0.434	0.060	13.75	0.53	23.90	0.29	206.87747	-11.75279
MCXC_J0340.8-4542	0.070	NaN	NaN	0.014	0.001	0.100	0.099	0.005	0.018	0.304	0.277	2.66	0.30	0.18	0.02	55.22412	-45.67648
ZwCl_1742.1+3306	0.076	0.098	0.004	0.319	0.005	0.010	0.010	0.000	0.567	0.589	0.083	5.00	0.30	1.08	0.02	266.06048	32.99158
ZwCl_0857.9+2107	0.230	0.269	0.010	0.531	0.020	0.002	0.002	0.000	0.093	0.111	0.064	4.39	0.26	2.15	0.08	135.15348	20.89454
ABELL_0478	0.088	0.135	0.002	0.268	0.002	0.004	0.004	0.000	0.017	0.017	0.008	7.61	0.17	5.86	0.04	63.35560	10.46532
ABELL_0496	0.033	0.080	0.002	0.218	0.002	0.013	0.013	0.000	0.810	0.805	0.061	4.84	0.13	0.19	0.00	68.40849	-13.26101
MCXC_J1947.3-7623	0.217	0.300	0.017	0.309	0.017	0.027	0.027	0.001	1.320	1.450	0.601	7.34	0.63	5.67	0.18	296.81210	-76.39578
UGC_05088_GROUP	0.027	0.144	0.034	NaN	NaN	0.047	0.047	0.004	0.562	1.070	0.979	2.33	0.23	0.01	0.00	143.35698	34.04812
MACS_J1359.2-1929	0.447	0.802	0.155	0.685	0.091	0.013	0.013	0.002	0.362	0.490	0.419	6.56	1.20	2.74	0.21	209.79259	-19.49030
ESO3060170-A	0.036	0.172	0.011	0.417	0.015	0.022	0.022	0.001	0.021	0.049	0.040	2.67	0.10	0.17	0.01	85.02786	-40.83689
SPT-CL_J2023-5535	0.232	0.137	0.013	0.145	0.013	0.095	0.092	0.005	2.440	2.620	1.040	8.39	0.76	6.12	0.18	305.83885	-55.59674
ABELL_0795	0.136	0.179	0.008	0.453	0.018	0.013	0.013	0.001	0.887	0.927	0.275	5.00	0.30	1.85	0.05	141.02407	14.17363
WHL_J150407.5-024816	0.215	0.265	0.004	0.434	0.008	0.004	0.004	0.000	0.033	0.035	0.013	8.96	0.38	9.96	0.14	226.03090	-2.80436
ABELL_2445	0.166	0.081	0.010	0.488	0.034	0.013	0.013	0.002	1.110	1.140	0.359	4.16	0.22	1.70	0.06	336.73210	25.83624
NGC_6482	0.013	0.279	0.021	0.494	0.034	0.006	0.006	0.001	0.187	0.285	0.258	0.48	0.04	0.00	0.00	267.95310	23.07185
ABELL_0545	0.154	0.092	0.005	0.151	0.005	0.067	0.067	0.001	5.000	4.960	0.457	7.37	0.31	3.50	0.05	83.10542	-11.54242
NSCS_J000619+105206	0.167	0.163	0.013	0.397	0.025	0.009	0.010	0.001	1.000	1.160	0.521	5.18	0.40	1.85	0.07	1.58454	10.86429
MACS_J1532.8+3021	0.345	0.240	0.005	0.430	0.009	0.002	0.002	0.000	0.012	0.019	0.017	7.49	0.41	6.98	0.12	233.22409	30.34964
SDSS-C4-DR3_3018	0.051	0.019	0.002	0.020	0.001	0.036	0.037	0.005	1.470	1.540	0.523	2.64	0.17	0.09	0.00	176.82738	55.74001
ABELL_1689	0.183	0.125	0.002	0.294	0.003	0.004	0.004	0.000	0.030	0.033	0.015	9.95	0.22	8.92	0.11	197.87338	-1.34130
MACS_J2140.2-2339	0.313	0.300	0.009	0.423	0.011	0.001	0.001	0.000	0.137	0.139	0.059	5.92	0.34	4.10	0.11	325.06324	-23.66131

Cluster	**z**	c_{500}	δc_{500}	c	δc	w_{data}	w_{sim}	$\delta\, w_{sim}$	p_{data}	p_{sim}	$\delta\, p_{sim}$	kT	δkT	L_X	δL_X	**RA**	**DEC**
									10^7			(keV)		($10^{44} erg\ s^{-1}$)		(deg)	(deg)
ABELL_2507	0.196	0.253	0.040	NaN	NaN	0.315	0.316	0.008	1.180	1.920	1.330	4.31	0.43	0.99	0.06	344.21912	5.50431
ABELL_1942_AND_CLUMP	0.224	0.120	0.014	0.335	0.025	0.027	0.026	0.003	2.500	2.610	0.998	5.39	0.36	1.42	0.05	219.59116	3.67027
Abell_223	0.207	0.156	0.013	0.444	0.036	0.019	0.019	0.002	1.230	1.410	0.704	5.47	0.50	1.38	0.06	24.48318	-12.81959
ABELL_0773	0.217	0.119	0.007	0.195	0.009	0.024	0.020	0.004	0.326	0.400	0.240	8.10	0.56	6.11	0.14	139.46903	51.72727
ABELL_2734_NED01	0.075	0.146	0.007	0.589	0.034	0.027	0.027	0.001	3.610	3.550	0.448	4.61	0.63	0.07	0.00	2.84010	-28.85401
WHL_J141623.8+444528	0.386	0.200	0.032	0.623	0.112	0.042	0.040	0.005	83.100	80.800	18.400	3.65	0.28	1.61	0.14	214.11644	44.78006
NGC_0766	0.027	0.038	0.001	0.702	0.250	0.005	0.009	0.003	0.616	3.030	3.050	0.17	0.01	0.04	0.06	29.67692	8.34708
ABELL_S1063	0.348	0.181	0.007	0.208	0.007	0.043	0.042	0.002	0.025	0.072	0.066	11.30	0.72	25.00	0.46	342.18456	-44.53010
ABELL_2895	0.227	0.209	0.015	0.209	0.015	0.068	0.065	0.004	2.630	2.500	0.799	8.39	0.86	4.96	0.15	19.54693	-26.96526
ABELL_3140	0.062	NaN	NaN	0.536	0.036	0.010	0.008	0.002	0.466	0.503	0.258	5.46	2.33	0.12	0.02	54.06515	-40.62852
MACS_J0553.4-3342	0.407	0.126	0.006	0.132	0.006	0.042	0.041	0.002	2.960	3.130	0.656	10.46	0.68	15.00	0.24	88.36530	-33.71043
ESO_351-_G_021	0.057	0.307	0.027	NaN	NaN	0.016	0.016	0.002	1.110	1.200	0.790	1.28	0.05	0.03	0.00	13.74932	-35.32090
ABELL_2124	0.066	0.181	0.010	0.245	0.012	0.021	0.020	0.002	1.880	1.920	0.479	5.09	0.40	0.32	0.01	236.24638	36.10948
MACS_J2046.0-3430	0.423	0.343	0.024	0.478	0.036	0.002	0.002	0.000	0.048	0.133	0.122	5.61	0.45	4.33	0.22	311.50177	-34.50612
IC_1633	0.024	0.284	0.022	NaN	NaN	0.073	0.074	0.002	1.780	1.760	0.465	3.26	0.36	0.08	0.00	17.48085	-45.93078
ABELL_1201	0.169	0.111	0.008	0.298	0.010	0.028	0.028	0.001	5.040	4.900	0.622	5.69	0.21	2.54	0.05	168.22704	13.43577
NSCS_J145715+222009	0.258	0.176	0.005	0.419	0.009	0.006	0.006	0.000	0.071	0.081	0.031	5.27	0.22	4.00	0.08	224.31287	22.34236
HCG_097	0.022	NaN	NaN	NaN	NaN	0.020	0.020	0.003	2.790	2.960	1.180	0.81	0.04	0.01	0.00	356.84509	-2.29995
MACS_J0242.6-2132	0.314	0.388	0.025	0.429	0.027	0.002	0.002	0.001	0.285	0.306	0.189	5.75	0.77	4.96	0.31	40.64961	-21.54064
ABELL_1736	0.046	0.059	0.018	0.195	0.010	0.039	0.040	0.008	6.520	6.660	0.812	2.82	0.67	0.62	0.01	201.70605	-27.16337
MCXC_J2011.3-5725	0.279	0.199	0.019	0.459	0.041	0.006	0.006	0.001	1.420	1.570	0.717	3.63	0.37	2.08	0.15	302.86168	-57.41964

Cluster	**z**	c_{500}	δc_{500}	c	δc	w_{data}	w_{sim}	$\delta\, w_{sim}$	p_{data}	p_{sim}	$\delta\, p_{sim}$	kT	δkT	L_X	δL_X	**RA**	**DEC**
									10^7			(keV)		($10^{44} erg\ s^{-1}$)		(deg)	(deg)
ABELL_3532	0.055	0.100	0.009	0.889	0.246	0.045	0.044	0.003	3.160	3.190	0.783	6.08	0.77	0.86	0.03	194.34302	-30.36258
MCXC_J0220.9-3829	0.229	0.234	0.020	0.492	0.043	0.006	0.007	0.002	0.018	0.171	0.161	4.35	0.37	2.34	0.14	35.23576	-38.48089
SDSS-C4-DR3_3144	0.081	0.357	0.023	0.911	0.236	0.003	0.004	0.001	0.056	0.252	0.192	1.77	0.08	0.07	0.01	179.96790	55.53489
ABELL_2667	0.230	0.301	0.012	0.320	0.013	0.011	0.010	0.001	0.672	0.786	0.262	7.60	0.68	8.12	0.22	357.91415	-26.08410
ABELL_2717	0.049	0.103	0.007	0.219	0.007	0.116	0.116	0.001	21.100	21.200	1.170	5.85	0.39	0.20	0.01	0.80403	-35.93337
MCXC_J0510.7-0801	0.220	0.112	0.010	0.166	0.010	0.048	0.047	0.005	0.480	0.661	0.363	7.15	0.43	8.68	0.22	77.69851	-8.02753
ABELL_3292	0.172	0.097	0.012	0.478	0.044	0.022	0.019	0.002	1.090	1.180	0.629	4.20	0.30	1.75	0.08	72.48412	-44.67254
A1882a	0.140	NaN	NaN	NaN	NaN	0.022	0.021	0.003	0.226	0.468	0.411	3.56	0.23	0.31	0.02	213.78480	-0.49307
WBL_518	0.027	0.083	0.009	NaN	NaN	0.059	0.051	0.006	0.888	0.911	0.334	8.14	0.36	0.14	0.00	220.16514	3.47045
NGC_7618	0.017	0.205	0.022	0.743	0.089	0.014	0.014	0.001	0.118	0.218	0.163	0.78	0.02	0.01	0.00	349.95009	42.85324
2MASX_J13312961+1107566	0.079	0.219	0.077	NaN	NaN	0.013	0.016	0.006	14.000	18.400	11.400	0.64	0.04	0.01	0.00	202.87369	11.13193
ABELL_3343	0.191	0.167	0.014	0.301	0.021	0.009	0.008	0.002	0.772	0.926	0.429	6.43	0.53	3.08	0.09	81.45297	-47.25283
MaxBCG_J016.70077+01.05926	0.254	0.252	0.009	0.556	0.021	0.005	0.005	0.000	0.025	0.045	0.037	4.57	0.27	2.12	0.07	16.70423	1.05381
ABELL_2426	0.098	0.163	0.016	0.476	0.039	0.027	0.028	0.002	0.057	0.138	0.105	5.82	0.39	1.66	0.05	333.63472	-10.37051
ESO_552-_G_020	0.031	0.207	0.018	NaN	NaN	0.031	0.031	0.002	0.039	0.148	0.166	8.23	1.24	0.07	0.00	73.71799	-18.11570
ABELL_0262	0.017	0.066	0.004	0.191	0.002	0.047	0.047	0.000	7.330	7.340	0.212	2.26	0.03	0.02	0.00	28.19291	36.15328
ABELL_2556	0.087	0.174	0.008	0.364	0.011	0.008	0.008	0.000	5.430	5.600	0.554	3.86	0.16	0.79	0.02	348.25589	-21.63457
ABELL_2111	0.229	0.128	0.011	0.216	0.015	0.028	0.025	0.004	0.286	0.438	0.348	7.70	0.57	3.90	0.08	234.91932	34.42445
MACS_J2214-1359	0.483	0.224	0.016	0.228	0.016	0.011	0.011	0.003	1.600	2.010	0.942	8.83	0.99	12.10	0.47	333.73945	-14.00260
MACS_J0025.4-1222	0.584	0.102	0.010	0.197	0.014	0.052	0.047	0.005	1.370	1.550	0.743	7.82	0.60	9.83	0.38	6.37370	-12.37608
UGC_00842	0.045	0.303	0.037	NaN	NaN	0.020	0.021	0.002	2.240	2.160	0.803	1.67	0.08	0.04	0.00	19.72477	-1.00209

Cluster	**z**	c_{500}	δc_{500}	c	δc	w_{data}	w_{sim}	$\delta\, w_{sim}$	p_{data}	p_{sim}	$\delta\, p_{sim}$	kT	δkT	L_X	δL_X	**RA**	**DEC**
									10^7			(keV)		($10^{44} erg\ s^{-1}$)		(deg)	(deg)
ABELL_2147	0.035	0.052	0.009	0.153	0.006	0.044	0.043	0.003	2.380	2.410	0.430	7.16	1.08	0.52	0.01	240.57094	15.97453
ABELL_0697	0.282	0.293	0.013	0.155	0.009	0.010	0.009	0.003	0.361	0.534	0.387	11.99	1.11	13.20	0.32	130.73979	36.36601
ZwCl_0823.2+0425	0.225	0.188	0.022	0.943	0.507	0.006	0.007	0.002	1.140	1.400	0.787	4.66	0.51	1.72	0.11	126.49104	4.24695
NSC_J174715+451155	0.156	0.094	0.021	0.203	0.023	0.055	0.048	0.008	3.990	4.640	1.670	4.73	0.38	1.51	0.07	266.80940	45.19598
ABELL_0868	0.153	0.060	0.013	0.218	0.016	0.043	0.035	0.006	0.524	0.640	0.403	4.41	0.22	2.58	0.09	146.35891	-8.65679
Abell_2276	0.141	0.233	0.021	NaN	NaN	0.006	0.007	0.002	1.340	1.640	0.638	2.83	0.28	0.48	0.04	263.76930	64.10168
ABELL_2631	0.273	0.212	0.018	0.185	0.016	0.047	0.038	0.006	1.710	2.020	1.040	8.02	0.96	7.57	0.26	354.41067	0.26806
MCXC_J0352.9+1941	0.109	0.221	0.008	0.505	0.018	0.004	0.004	0.000	0.034	0.062	0.047	3.14	0.16	0.98	0.04	58.24368	19.68188
PKS_0745-19	0.103	0.142	0.001	0.333	0.002	0.009	0.009	0.000	0.438	0.435	0.021	8.55	0.73	5.82	0.03	116.88098	-19.29438
CIZA_J0107.7+5408	0.107	0.065	0.005	0.127	0.006	0.034	0.025	0.009	1.600	1.660	0.406	7.68	0.37	3.90	0.06	16.93808	54.13267
ABELL_3395_SW	0.051	0.076	0.008	NaN	NaN	0.029	0.029	0.001	30.100	30.100	1.490	2.26	0.03	0.61	0.02	96.70193	-54.54978
CIZA_J1938.3+5409	0.260	0.195	0.013	0.271	0.016	0.022	0.021	0.002	3.090	3.030	0.766	7.20	0.73	9.11	0.36	294.57677	54.15968
ABELL_1569	0.074	0.067	0.017	NaN	NaN	0.020	0.021	0.002	1.810	1.770	0.594	6.03	1.00	0.25	0.02	189.10840	16.53828
ABELL_1413	0.143	0.092	0.003	0.239	0.003	0.007	0.007	0.000	0.557	0.565	0.077	7.41	0.17	4.23	0.04	178.82455	23.40607
ABELL_0376	0.048	0.169	0.019	NaN	NaN	0.038	0.038	0.003	0.651	0.781	0.355	4.53	0.33	0.50	0.01	41.51644	36.90549
RCS_J2327-0204	0.200	NaN	NaN	0.569	0.030	0.005	0.004	0.001	0.011	0.057	0.049	9.55	1.43	0.43	0.02	351.86468	-2.07750
ABELL_1664	0.128	0.166	0.006	0.404	0.011	0.009	0.009	0.001	0.568	0.585	0.126	5.02	0.21	1.91	0.04	195.92759	-24.24489
MCXC_J0331.1-2100	0.188	0.334	0.016	0.423	0.020	0.008	0.008	0.001	0.043	0.098	0.077	5.86	0.53	2.63	0.10	52.77508	-21.00915
ABELL_3560	0.049	0.084	0.010	0.300	0.021	0.029	0.028	0.003	8.370	8.410	1.330	8.75	0.46	0.18	0.00	203.10714	-33.13600
ABELL_1750N	0.084	0.182	0.027	NaN	NaN	0.031	0.032	0.003	0.006	0.158	0.155	3.59	0.23	0.44	0.02	202.79562	-1.72820
a1750ss	0.091	NaN	NaN	0.013	0.001	0.049	0.046	0.007	0.659	0.894	0.761	2.40	0.20	0.13	0.02	202.54245	-2.10437

Cluster	**z**	c_{500}	δc_{500}	c	δc	w_{data}	w_{sim}	$\delta\, w_{sim}$	p_{data}	p_{sim}	$\delta\, p_{sim}$	kT	δkT	L_X	δL_X	**RA**	**DEC**
									10^7			(keV)		($10^{44} erg\ s^{-1}$)		(deg)	(deg)
WEIN_051	0.022	0.068	0.005	0.095	0.004	0.050	0.049	0.003	0.596	0.614	0.263	8.10	0.56	0.39	0.01	72.52712	45.05097
ABELL_2302	0.179	0.090	0.020	NaN	NaN	0.092	0.085	0.008	0.703	0.953	0.638	4.82	0.38	1.32	0.05	274.99175	57.15614
ABELL_1763	0.223	0.094	0.008	0.158	0.009	0.040	0.040	0.003	0.701	0.741	0.406	7.67	0.59	7.19	0.19	203.82482	40.99883
HCG_051	0.026	0.312	0.050	NaN	NaN	0.050	0.050	0.004	1.510	1.760	0.860	1.32	0.03	0.01	0.00	170.61008	24.29755
MACS_J2245.0+2637	0.304	0.346	0.025	0.368	0.027	0.008	0.008	0.001	0.414	0.532	0.365	6.71	0.93	4.67	0.25	341.26940	26.63429
ABELL_2092	0.067	0.218	0.074	NaN	NaN	0.059	0.054	0.010	4.740	5.090	2.790	2.86	0.44	0.12	0.02	233.32339	31.13791
BLOX_J1023.6+0411.1	0.291	0.231	0.005	0.338	0.006	0.010	0.011	0.000	0.121	0.122	0.041	8.75	0.37	9.03	0.14	155.91556	4.18557
MACS_J1108.9+0906	0.449	0.164	0.019	0.255	0.027	0.032	0.028	0.004	0.220	0.574	0.567	6.86	0.74	6.09	0.29	167.23036	9.09914
NGC_6269	0.035	0.293	0.025	NaN	NaN	0.014	0.015	0.001	3.750	3.850	0.886	2.94	0.19	0.08	0.00	254.49212	27.85406
ABELL_2670	0.076	0.079	0.006	0.675	0.042	0.021	0.021	0.001	0.040	0.070	0.060	3.78	0.39	0.73	0.02	358.53680	-10.42518
ZwCl_0008.8+5215	0.104	0.098	0.017	NaN	NaN	0.180	0.179	0.004	0.506	0.692	0.421	4.71	0.30	0.74	0.03	2.83958	52.52921
WBL_671	0.051	0.037	0.001	NaN	NaN	0.016	0.023	0.008	0.017	4.940	4.990	1.00	0.12	0.01	0.00	324.28628	0.44586
ABELL_1361	0.117	0.382	0.023	0.396	0.030	0.005	0.006	0.001	0.252	0.363	0.221	17.00	10.00	0.68	0.16	175.91515	46.35567
ABELL_3558	0.048	0.089	0.004	0.122	0.003	0.036	0.036	0.001	8.860	8.950	0.596	7.44	0.30	0.60	0.01	201.98689	-31.49549
ABELL_2597	0.085	0.086	0.002	0.379	0.003	0.003	0.003	0.000	0.238	0.242	0.024	4.36	0.06	0.86	0.01	351.33241	-12.12434
NSC_J084254+292723	0.194	0.300	0.014	0.470	0.022	0.005	0.005	0.001	0.114	0.181	0.115	5.89	0.44	1.51	0.05	130.73320	29.45749
MCXC_J1000.5+4409	0.154	0.206	0.020	0.551	0.052	0.067	0.067	0.003	2.370	2.670	0.948	3.28	0.27	1.03	0.07	150.13343	44.14436
ABELL_1068	0.138	0.243	0.007	0.409	0.010	0.003	0.003	0.000	0.011	0.019	0.014	4.96	0.25	1.87	0.04	160.18550	39.95286
MACS_J1115.8+0129	0.352	0.349	0.014	0.345	0.014	0.008	0.008	0.001	0.042	0.081	0.060	9.18	0.73	8.71	0.25	168.96687	1.49904
ABELL_2409	0.148	0.111	0.010	0.207	0.012	0.032	0.031	0.002	0.161	0.292	0.214	5.96	0.38	4.31	0.14	330.21903	20.96849
ABELL_S0592	0.222	0.203	0.009	0.259	0.011	0.028	0.028	0.001	0.055	0.117	0.087	8.58	0.65	8.34	0.20	99.70254	-53.97398

Cluster	**z**	c_{500}	δc_{500}	c	δc	w_{data}	w_{sim}	$\delta\, w_{sim}$	p_{data}	p_{sim}	$\delta\, p_{sim}$	kT	δkT	L_X	δL_X	**RA**	**DEC**
									10^7			(keV)		($10^{44} erg\ s^{-1}$)		(deg)	(deg)
HCG_042	0.013	0.196	0.020	0.480	0.040	0.017	0.016	0.002	2.810	2.840	0.888	0.82	0.05	0.00	0.00	150.05931	-19.63632
ABELL_2261	0.224	0.223	0.009	0.283	0.010	0.009	0.009	0.001	0.268	0.320	0.137	8.10	0.59	7.49	0.16	260.61356	32.13294
BLOX_J1056.9-0337.3	0.823	0.375	0.045	0.402	0.048	0.280	0.268	0.007	11.000	11.600	2.890	7.49	1.08	8.11	0.43	164.23298	-3.62774
WHL_J125933.4+600409	0.330	0.080	0.014	0.160	0.017	0.094	0.089	0.006	3.430	3.780	1.430	6.89	0.52	4.09	0.15	194.88766	60.07059
MACS_J0358.8-2955	0.425	0.133	0.008	0.242	0.011	0.069	0.069	0.001	1.740	1.890	0.488	8.75	0.49	14.00	0.37	59.71901	-29.93031
ABELL_2626	0.055	0.126	0.006	0.255	0.007	0.012	0.012	0.001	0.730	0.724	0.174	3.26	0.11	0.43	0.01	354.12688	21.14649
ABELL_S0520	0.295	0.099	0.011	0.118	0.012	0.075	0.067	0.008	0.630	1.050	0.777	8.27	0.73	6.96	0.21	79.15713	-54.51314
SC_1329-313	0.048	0.068	0.016	NaN	NaN	0.050	0.047	0.007	1.070	1.160	0.601	6.50	0.43	0.26	0.01	202.86502	-31.82126
ABELL_3911	0.096	0.063	0.009	0.149	0.013	0.600	0.599	0.004	1.840	1.960	0.644	6.11	0.39	2.18	0.06	341.56388	-52.72419
ABELL_3391	0.051	0.079	0.006	0.318	0.014	0.017	0.017	0.001	1.230	1.300	0.323	8.55	0.66	1.01	0.02	96.58963	-53.69578
MCXC_J0819.6+6336	0.119	0.197	0.019	0.462	0.041	0.025	0.025	0.002	0.816	1.060	0.630	3.50	0.32	0.74	0.04	124.85836	63.62404
ABELL_3378	0.141	0.201	0.015	0.377	0.020	0.021	0.021	0.002	0.296	0.366	0.224	4.78	0.27	3.17	0.10	91.47495	-35.30225
NGC_4759_GROUP	0.015	0.082	0.005	0.484	0.010	0.019	0.019	0.001	0.003	0.009	0.009	1.38	0.03	0.00	0.00	193.27392	-9.20434
ABELL_1446	0.104	0.055	0.008	0.692	0.063	0.034	0.034	0.001	0.566	0.603	0.204	3.53	0.12	0.69	0.02	180.51560	58.03831
ZwCl_0735.7+7421	0.216	0.114	0.004	0.328	0.004	0.005	0.005	0.000	0.450	0.449	0.070	6.47	0.11	3.97	0.03	115.43435	74.24395
MCXC_J1010.5-1239	0.301	0.127	0.012	0.236	0.015	0.098	0.098	0.002	0.335	0.524	0.347	6.48	0.40	4.22	0.09	152.63463	-12.66578
MCXC_J0301.6+0155	0.170	0.222	0.014	0.446	0.026	0.008	0.008	0.001	0.166	0.240	0.171	4.45	0.33	1.67	0.08	45.40921	1.92049
1RXS_J111039.6+284316	0.022	NaN	NaN	NaN	NaN	0.071	0.069	0.007	4.840	5.060	1.580	1.29	0.09	0.01	0.00	167.66898	28.71379
MZ_10451	0.061	0.039	0.001	NaN	NaN	0.040	0.037	0.007	0.890	1.960	2.160	0.73	0.04	0.01	0.00	37.44035	-29.63005
ABELL_1033	0.126	0.067	0.005	0.362	0.011	0.056	0.055	0.001	7.930	8.040	0.738	5.61	0.18	1.47	0.03	157.93666	35.03956
MKW_03s	0.045	0.064	0.003	0.307	0.003	0.011	0.011	0.000	1.200	1.200	0.076	5.67	0.30	0.63	0.01	230.46637	7.70888

Cluster	z	c_{500}	δc_{500}	c	δc	w_{data}	w_{sim}	$\delta\, w_{sim}$	p_{data}	p_{sim}	$\delta\, p_{sim}$	kT	δkT	L_X	δL_X	RA	DEC
									10^7			(keV)		($10^{44} erg\ s^{-1}$)		(deg)	(deg)
ABELL_3404	0.167	0.231	0.013	0.247	0.014	0.040	0.039	0.003	1.570	1.850	0.643	7.85	0.64	6.50	0.16	101.37090	-54.22865
NGC_5098_GROUP	0.037	0.187	0.026	NaN	NaN	0.011	0.011	0.001	0.277	0.328	0.213	1.07	0.02	0.02	0.00	200.06104	33.14252
ABELL_3854	0.149	0.152	0.015	0.329	0.024	0.009	0.009	0.002	0.095	0.213	0.196	5.18	0.39	2.27	0.08	334.44062	-35.72411
MACS_J0429.6-0253	0.399	0.383	0.025	0.404	0.027	0.009	0.009	0.001	0.361	0.477	0.262	7.00	0.90	5.72	0.27	67.40037	-2.88584
MCXC_J1130.0+3637	0.060	0.445	0.048	NaN	NaN	0.016	0.016	0.002	1.760	1.950	0.634	1.74	0.08	0.07	0.00	172.51162	36.63563
ABELL_1240	0.159	NaN	NaN	NaN	NaN	0.059	0.060	0.010	10.200	9.950	3.170	4.16	0.42	0.48	0.03	170.90982	43.09676
MCXC_J2344.2-0422	0.079	0.063	0.010	0.591	0.064	0.034	0.033	0.002	0.325	0.405	0.254	4.46	0.18	1.44	0.04	356.07718	-4.38133
WHL_J142716.1+440730	0.498	0.683	0.069	0.425	0.029	0.010	0.010	0.001	1.190	1.240	0.519	10.40	1.42	7.62	0.31	216.81722	44.12708
MCXC_J1514.9-1523	0.223	0.056	0.007	0.087	0.005	0.062	0.052	0.010	0.596	0.816	0.467	8.90	0.48	5.82	0.09	228.76065	-15.38919
ABELL_1991	0.059	0.150	0.006	0.338	0.007	0.011	0.011	0.000	0.307	0.312	0.085	2.77	0.06	0.32	0.01	223.63175	18.64486
MACS_J0416.1-2403	0.420	0.158	0.013	0.193	0.015	0.071	0.070	0.005	1.690	1.980	0.938	8.66	0.73	9.94	0.36	64.03935	-24.06687
MCXC_J1853.9+6822	0.093	0.098	0.015	0.807	0.147	0.046	0.043	0.002	0.101	0.175	0.169	4.13	0.22	1.01	0.02	283.50941	68.38270
ABELL_1285	0.106	0.061	0.009	0.212	0.010	0.035	0.030	0.005	0.723	0.846	0.290	5.52	0.21	2.25	0.04	172.59317	-14.58071
ABELL_1930	0.131	0.225	0.012	0.615	0.041	0.003	0.004	0.001	0.168	0.202	0.123	4.51	0.26	0.94	0.04	218.15786	31.64791
NSC_J092017+303027	0.258	0.142	0.017	0.254	0.026	0.598	0.585	0.020	5.610	5.690	1.810	6.35	0.66	3.13	0.13	140.11048	30.49381
ABELL_3120	0.069	NaN	NaN	NaN	NaN	0.009	0.009	0.002	0.534	0.671	0.446	4.33	0.25	0.10	0.01	50.48527	-51.32650
NGC_1132	0.023	0.223	0.043	0.350	0.029	0.046	0.046	0.003	5.070	5.580	1.790	1.04	0.02	0.01	0.00	43.21635	-1.27402
MACS_J0011.7-1523	0.378	0.192	0.011	0.337	0.016	0.010	0.010	0.001	0.351	0.387	0.202	5.89	0.40	6.23	0.20	2.92902	-15.38911
GMBCG_J215.94948+24.07846	0.543	0.307	0.010	0.445	0.014	0.002	0.002	0.000	0.049	0.080	0.064	7.26	0.36	6.71	0.13	215.94900	24.07790
ABELL_1750C	0.068	0.117	0.013	NaN	NaN	0.028	0.028	0.002	2.760	2.950	0.707	4.43	0.25	0.44	0.02	202.70930	-1.86289

APPENDIX E

RADIAL PROFILES OF EARLY-TYPE GALAXIES WITH POWERFUL RADIO SOURCES

Table E.1: Radial profile properties for each galaxy with sufficient counts for temperature deprojection. A portion of this table is printed here for form and content, Additional profiles can be found in Appendix E. Errors given for radius represent bin widths, all other errors are 1 sigma. Column 1: galaxy name; Column 2: radial bin center; Column 3: half-width of the radial bin; Column 4: grouping of temperature bins; Columns 5-6: best fit temperatures and their errors; Column 7: electron density bin number; Columns 8-9: best fit densities and their errors; in units of 10^{-2} cm^{-3} for compactness; Columns 10-11: calculated entropies and their errors.

Galaxy	**radius**	Δr	kT **bin**	kT	σ_{kT}	n_e **bin**	n_e	σ_{n_e}	K	σ_K
	(kpc)	(kpc)	ID	(keV)	(keV)	ID	(10^{-2} cm^{-3})	(10^{-2} cm^{-3})	(keV cm^2)	(keV cm^2)
NGC 315	1.12	0.56	1	0.70	0.04	1	7.36	0.35	3.99	0.26
NGC 315	1.60	0.24	1	0.70	0.04	2	4.33	0.20	5.69	0.37
NGC 315	2.24	0.32	2	0.77	0.03	3	2.90	0.15	8.17	0.42
NGC 315	3.05	0.40	2	0.77	0.03	4	1.68	0.08	11.77	0.58
NGC 315	4.49	0.72	3	0.75	0.02	5	1.08	0.04	15.35	0.52
NGC 741	2.52	1.26	1	0.82	0.01	6	1.74	0.03	12.23	0.24
NGC 741	5.04	1.26	1	0.82	0.01	7	0.90	0.03	18.98	0.46
NGC 741	8.10	1.53	1	0.82	0.01	8	0.45	0.01	30.07	0.79
NGC 741	11.69	1.80	2	1.24	0.03	9	0.44	0.03	46.21	2.20
NGC 741	16.37	2.34	2	1.24	0.03	10	0.17	0.01	86.63	2.53
NGC 741	26.80	5.22	2	1.24	0.03	11	0.12	0.01	110.53	4.08
NGC 741	37.24	5.22	3	1.74	0.21	12	0.08	0.01	193.51	24.86
NGC 741	46.23	4.50	3	1.74	0.21	13	0.07	0.01	228.92	32.23
NGC 741	54.15	3.96	3	1.74	0.21	14	0.08	0.01	205.20	33.25
NGC 741	61.52	3.69	4	1.64	0.16	15	0.02	0.00	470.97	55.73
NGC 741	68.72	3.60	4	1.64	0.16	16	0.06	0.07	242.57	202.78

Galaxy	radius	Δr	kT bin	kT	σ_{kT}	n_e bin	n_e	σ_{n_e}	K	σ_K
	(kpc)	(kpc)	ID	(keV)	(keV)	ID	(10^{-2} cm^{-3})	(10^{-2} cm^{-3})	(keV cm^2)	(keV cm^2)
NGC 741	75.74	3.51	4	1.64	0.16	17	0.06	0.01	219.04	30.52
NGC 1316	0.24	0.12	1	0.77	0.02	1	15.50	1.14	2.66	0.15
NGC 1316	0.37	0.06	1	0.77	0.02	2	10.30	0.82	3.52	0.21
NGC 1316	0.61	0.12	1	0.77	0.02	3	7.57	0.35	4.30	0.18
NGC 1316	0.85	0.12	2	0.93	0.02	4	4.70	0.23	7.16	0.30
NGC 1316	1.10	0.12	2	0.93	0.02	5	3.54	0.25	8.64	0.46
NGC 1316	1.46	0.18	2	0.93	0.02	6	1.95	0.09	12.87	0.52
NGC 1316	2.07	0.30	3	0.79	0.02	7	1.10	0.05	15.86	0.61
NGC 1316	2.92	0.43	3	0.79	0.02	8	0.57	0.03	24.66	1.01
NGC 1316	3.89	0.49	3	0.79	0.02	9	0.50	0.05	26.87	1.75
NGC 1316	4.99	0.55	4	0.73	0.03	10	0.21	0.01	44.83	2.63
NGC 1316	6.08	0.55	4	0.73	0.03	11	0.46	0.14	26.45	5.46
NGC 1316	6.94	0.43	4	0.73	0.03	12	0.45	0.03	26.82	1.44
NGC 1316	8.15	0.61	5	0.31	0.03	13	0.25	0.01	16.68	1.85
NGC 1316	9.61	0.73	6	0.61	0.07	14	0.26	0.02	32.27	3.85
NGC 4261	0.28	0.14	1	0.72	0.01	1	29.50	0.90	1.62	0.04
NGC 4261	0.43	0.07	1	0.72	0.01	2	19.30	0.40	2.15	0.04
NGC 4261	0.57	0.07	1	0.72	0.01	3	13.80	0.38	2.69	0.06
NGC 4261	0.71	0.07	2	0.74	0.02	4	9.65	0.33	3.54	0.11
NGC 4261	0.85	0.07	2	0.74	0.02	5	6.74	0.31	4.50	0.17
NGC 4261	0.99	0.07	2	0.74	0.02	6	6.21	0.42	4.75	0.24
NGC 4261	1.13	0.07	3	0.76	0.03	7	3.66	0.22	6.87	0.38
NGC 4261	1.28	0.07	3	0.76	0.03	8	4.24	0.57	6.24	0.60
NGC 4261	1.42	0.07	3	0.76	0.03	9	3.28	0.28	7.40	0.50
NGC 4261	1.56	0.07	4	0.73	0.05	10	2.73	0.31	8.07	0.82
NGC 4261	1.70	0.07	4	0.73	0.05	11	2.56	0.35	8.44	0.96
NGC 4261	1.84	0.07	4	0.73	0.05	12	2.38	0.32	8.84	0.99
NGC 4261	1.99	0.07	5	0.78	0.04	13	1.30	0.18	14.14	1.46
NGC 4261	2.27	0.14	5	0.78	0.04	14	2.58	0.44	8.94	1.12
NGC 4261	2.41	0.07	5	0.78	0.04	15	1.54	0.13	12.61	0.95

Galaxy	**radius**	Δr	kT **bin**	kT	σ_{kT}	n_e **bin**	n_e	σ_{n_e}	K	σ_K
	(kpc)	(kpc)	ID	(keV)	(keV)	ID	(10^{-2} cm^{-3})	(10^{-2} cm^{-3})	(keV cm^2)	(keV cm^2)
NGC 4261	2.55	0.07	6	0.72	0.05	16	1.09	0.24	14.58	2.38
NGC 4261	2.84	0.14	6	0.72	0.05	17	1.22	0.21	13.51	1.87
NGC 4261	3.12	0.14	6	0.72	0.05	18	1.14	0.12	14.16	1.42
NGC 4261	3.40	0.14	7	0.85	0.05	19	0.76	0.08	21.79	1.85
NGC 4261	3.69	0.14	7	0.85	0.05	20	0.75	0.13	22.13	2.89
NGC 4261	4.11	0.21	7	0.85	0.05	21	0.53	0.05	27.99	2.42
NGC 4261	4.54	0.21	8	0.94	0.05	22	0.58	0.10	29.05	3.78
NGC 4261	4.96	0.21	8	0.94	0.05	23	0.44	0.06	34.86	3.47
NGC 4261	5.53	0.28	8	0.94	0.05	24	0.48	0.06	32.96	3.32
NGC 4261	6.38	0.43	9	1.29	0.03	25	0.31	0.02	60.35	3.29
NGC 4374	0.14	0.07	1	0.78	0.02	1	16.30	0.63	2.62	0.09
NGC 4374	0.28	0.07	1	0.78	0.02	2	9.75	0.45	3.68	0.14
NGC 4374	0.41	0.07	1	0.78	0.02	3	6.68	0.39	4.74	0.21
NGC 4374	0.55	0.07	1	0.78	0.02	4	4.04	0.30	6.63	0.35
NGC 4374	0.69	0.07	1	0.78	0.02	5	5.24	0.72	5.57	0.53
NGC 4374	0.83	0.07	2	0.61	0.02	6	3.20	0.19	6.09	0.31
NGC 4374	1.03	0.10	2	0.61	0.02	7	1.74	0.14	9.12	0.56
NGC 4374	1.17	0.07	2	0.61	0.02	8	2.61	0.76	6.97	1.36
NGC 4374	1.38	0.10	2	0.61	0.02	9	2.23	0.16	7.74	0.45
NGC 4374	1.59	0.10	2	0.61	0.02	10	1.67	0.12	9.40	0.55
NGC 4374	1.79	0.10	3	0.74	0.02	11	1.33	0.14	13.13	0.97
NGC 4374	2.00	0.10	3	0.74	0.02	12	1.78	0.25	10.84	1.03
NGC 4374	2.21	0.10	3	0.74	0.02	13	0.96	0.06	16.32	0.76
NGC 4374	2.55	0.17	3	0.74	0.02	14	1.02	0.10	15.74	1.07
NGC 4374	2.83	0.14	3	0.74	0.02	15	0.91	0.08	16.92	1.01
NGC 4374	3.17	0.17	4	0.94	0.02	16	0.77	0.06	24.02	1.27
NGC 4374	3.66	0.24	4	0.94	0.02	17	0.62	0.04	27.81	1.20
NGC 4374	4.21	0.28	4	0.94	0.02	18	0.37	0.02	38.95	1.59
NGC 4374	4.97	0.38	4	0.94	0.02	19	0.32	0.02	43.51	2.31
NGC 4374	5.86	0.45	4	0.94	0.02	20	0.48	0.03	33.02	1.47

Galaxy	**radius**	Δr	kT **bin**	kT	σ_{kT}	n_e **bin**	n_e	σ_{n_e}	K	σ_K
	(kpc)	(kpc)	ID	(keV)	(keV)	ID	(10^{-2} cm^{-3})	(10^{-2} cm^{-3})	(keV cm^2)	(keV cm^2)
NGC 4782	7.10	0.62	1	10.89	4.50	1	0.30	0.06	524.03	227.54
NGC 4782	4.81	1.05	1	0.76	0.03	2	0.20	0.03	46.94	4.59
NGC 4782	6.32	0.75	1	0.76	0.03	3	0.28	0.13	38.01	12.19
NGC 4782	7.82	0.75	1	0.76	0.03	4	0.42	0.08	29.27	3.77
NGC 4782	9.03	0.60	2	1.55	0.18	5	0.36	0.07	66.07	11.66
NGC 4782	10.23	0.60	2	1.55	0.18	6	0.52	0.14	51.71	11.05
NGC 4782	11.13	0.45	2	1.55	0.18	7	0.48	0.08	54.52	8.69
NGC 4782	12.04	0.45	2	1.55	0.18	8	0.32	0.04	70.95	10.38
NGC 4782	13.24	0.60	3	0.78	0.03	9	0.25	0.02	42.95	2.72
NGC 4782	14.74	0.75	3	0.78	0.03	10	0.13	0.01	66.32	4.46
NGC 4782	17.45	1.35	3	0.78	0.03	11	0.02	0.00	206.97	17.10
NGC 4782	20.16	1.35	3	0.78	0.03	12	0.19	0.42	50.81	74.84
NGC 4782	22.57	1.20	4	2.13	0.52	13	0.16	0.02	157.71	40.60
NGC 4782	25.28	1.35	4	2.13	0.52	14	0.10	0.02	214.57	56.87
NGC 4782	28.29	1.50	4	2.13	0.52	15	0.15	0.04	159.81	49.71
NGC 4782	30.99	1.35	4	2.13	0.52	16	0.05	0.01	353.88	90.56
NGC 5419	0.28	0.14	1	3.41	0.86	1	22.00	0.57	9.36	2.37
NGC 5419	1.12	0.42	1	3.41	0.86	2	3.48	0.14	31.95	8.11
NGC 5419	3.09	0.98	2	1.13	0.06	3	0.68	0.03	31.53	2.04
NGC 5419	7.59	2.25	2	1.13	0.06	4	0.43	0.04	43.06	3.52
NGC 5419	12.65	2.53	3	2.17	1.98	5	0.25	0.03	116.87	107.10
NGC 5419	17.43	2.39	3	2.17	1.98	6	0.23	0.05	123.06	113.54
NGC 5419	22.50	2.53	4	4.37	1.70	7	0.25	0.09	238.79	110.92
NGC 5419	26.43	1.97	4	4.37	1.70	8	0.34	0.15	194.70	94.62
NGC 7626	0.67	0.33	1	1.01	0.05	1	4.03	0.16	8.62	0.46
NGC 7626	2.00	0.67	2	0.93	0.05	2	1.62	0.06	14.56	0.81
NGC 7626	3.77	0.89	3	0.89	0.05	3	0.66	0.03	25.35	1.65
NGC 7626	6.65	1.44	4	0.86	0.05	4	0.37	0.02	36.08	2.33
NGC 7626	9.98	1.66	5	0.96	0.08	5	0.27	0.02	49.64	4.62
NGC 7626	13.53	1.77	6	0.91	0.08	6	0.18	0.01	62.74	6.20

Galaxy	radius	Δr	kT bin	kT	σ_{kT}	n_e bin	n_e	σ_{n_e}	K	σ_K
	(kpc)	(kpc)	ID	(keV)	(keV)	ID	(10^{-2} cm^{-3})	(10^{-2} cm^{-3})	(keV cm^2)	(keV cm^2)
NGC 7626	17.52	2.00	7	0.87	0.09	7	0.28	0.03	43.40	5.54
IC 1459	0.49	0.24	1	0.94	0.02	1	5.14	0.19	6.78	0.23
IC 1459	0.73	0.12	1	0.94	0.02	2	2.70	0.14	10.41	0.45
IC 1459	0.97	0.12	1	0.94	0.02	3	1.92	0.18	13.08	0.89
IC 1459	1.22	0.12	1	0.94	0.02	4	1.67	0.19	14.34	1.12
IC 1459	1.46	0.12	2	0.38	0.09	5	1.09	0.17	7.81	2.05
IC 1459	1.83	0.18	2	0.38	0.09	6	0.98	0.16	8.38	2.21
IC 1459	2.07	0.12	2	0.38	0.09	7	0.96	0.23	8.53	2.45
IC 1459	2.43	0.18	2	0.38	0.09	8	0.69	0.08	10.59	2.68
IC 1459	2.80	0.18	3	1.53	1.74	9	0.46	0.09	55.32	63.42
IC 1459	3.16	0.18	3	1.53	1.74	10	0.59	0.25	47.01	55.20
IC 1459	3.53	0.18	3	1.53	1.74	11	0.36	0.15	65.09	76.24
IC 1459	3.89	0.18	3	1.53	1.74	12	0.38	0.16	63.09	74.18
IC 1459	4.50	0.30	4	0.59	0.07	13	0.32	0.03	26.94	3.92
IC 1459	4.99	0.24	4	0.59	0.07	14	0.27	0.04	30.16	5.04
IC 1459	5.60	0.30	4	0.59	0.07	15	0.19	0.03	38.20	6.09
IC 1459	6.45	0.43	4	0.59	0.07	16	0.19	0.03	38.17	6.45
IC 1459	7.42	0.49	5	0.74	0.03	17	0.09	0.01	80.01	6.63
IC 1459	8.76	0.67	5	0.74	0.03	18	0.10	0.03	75.13	13.60
IC 1459	10.34	0.79	5	0.74	0.03	19	0.08	0.01	82.70	8.98
IC 1459	12.53	1.10	5	0.74	0.03	20	0.11	0.01	69.92	5.92
IC 4296	0.48	0.24	1	0.75	0.02	1	16.50	0.57	2.48	0.09
IC 4296	0.72	0.12	1	0.75	0.02	2	10.10	0.53	3.44	0.16
IC 4296	0.97	0.12	2	0.78	0.03	3	5.62	0.39	5.29	0.33
IC 4296	1.45	0.24	2	0.78	0.03	4	3.52	0.20	7.23	0.41
IC 4296	1.93	0.24	3	0.84	0.03	5	2.50	0.18	9.82	0.63
IC 4296	2.66	0.36	3	0.84	0.03	6	1.19	0.06	16.08	0.86
IC 4296	3.87	0.60	4	0.89	0.05	7	0.49	0.03	30.82	1.98
IC 4296	6.28	1.21	4	0.89	0.05	8	0.38	0.03	36.60	2.73
IC 4296	9.42	1.57	5	2.10	1.07	9	0.24	0.03	116.60	59.92

Galaxy	**radius**	Δr	kT **bin**	kT	σ_{kT}	n_e **bin**	n_e	σ_{n_e}	K	σ_K
	(kpc)	(kpc)	ID	(keV)	(keV)	ID	(10^{-2} cm^{-3})	(10^{-2} cm^{-3})	(keV cm^2)	(keV cm^2)
IC 4296	12.56	1.57	5	2.10	1.07	10	0.16	0.03	152.23	79.11
IC 4296	15.46	1.45	6	1.29	0.21	11	0.17	0.03	91.31	18.74
IC 4296	17.88	1.21	6	1.29	0.21	12	0.17	0.05	91.62	22.83

APPENDIX F

RADIAL PROFILES FOR THE GALAXIES IN LAKHCHAURA (2018)

Table F.1: Table of all the radial profiles in the HQ sample from (Lakhchaura et al., 2018). Column 1: Galaxy name; Column 2-3: radius and half-bin widths; Column 4-5: entropy and errors; Column 6-7: Ratio between the cooling time and free=fall time, $t_c/t_{\rm ff}$, and errors.

Galaxy	**radius** (kpc)	Δr (kpc)	K (keV cm^2)	σ_K	t_c/t_{ff}	$\delta t_c/t_{ff}$
3C449	2.64	2.64	11.20	0.50	13.46	1.26
3C449	8.79	3.51	61.72	13.87	131.46	48.20
3C449	15.82	3.51	66.22	2.91	105.62	9.78
3C449	22.85	3.51	69.14	2.49	78.87	5.85
3C449	30.21	3.85	72.70	2.79	62.81	5.15
3C449	38.13	4.06	98.98	5.12	81.67	9.70
3C449	46.00	3.80	119.66	9.62	96.02	17.63
3C449	53.26	3.46	110.53	6.61	64.78	9.03
3C449	60.27	3.55	132.54	8.23	116.22	15.84
3C449	67.18	3.37	138.31	9.48	108.28	16.48
3C449	73.76	3.20	118.02	7.78	65.52	9.65
3C449	80.24	3.29	117.18	3.49	56.10	5.22
3C449	86.90	3.37	141.59	10.61	75.67	13.72
3C449	93.73	3.46	96.52	1.91	28.30	2.32
IC1860	2.28	2.28	8.03	0.24	18.42	2.40
IC1860	5.25	0.69	11.85	0.96	19.99	3.30
IC1860	6.62	0.69	16.01	1.50	22.65	4.20
IC1860	7.99	0.69	20.49	2.13	32.70	7.84
IC1860	9.48	0.80	22.30	1.98	32.29	6.80
IC1860	11.31	1.03	25.98	3.07	33.96	7.54
IC1860	13.25	0.91	29.95	3.25	34.22	8.40
IC1860	15.07	0.91	39.68	6.48	57.78	21.71

Galaxy	**radius**	Δr	K	σ_K	t_c/t_{ff}	$\delta t_c/t_{ff}$
	(kpc)	(kpc)	(keV cm^2)			
IC1860	16.90	0.91	34.62	3.60	36.49	9.13
IC1860	19.30	1.48	47.60	5.59	62.63	18.04
IC1860	22.15	1.37	44.83	4.31	45.22	11.31
IC1860	25.47	1.94	47.94	3.09	42.35	9.15
IC1860	29.23	1.83	61.94	6.41	61.89	17.78
IC1860	33.12	2.06	72.42	5.83	58.76	15.18
IC1860	41.34	6.17	62.85	1.59	30.89	6.33
IC4296	0.56	0.23	1.42	0.07	11.63	0.78
IC4296	1.86	1.07	4.89	0.17	21.75	1.01
IC4296	8.29	5.36	38.01	1.83	118.54	9.06
IC4296	18.28	4.63	101.73	12.11	211.85	56.02
IC4296	26.74	3.84	88.88	5.21	81.15	10.19
IC4296	36.22	5.64	95.26	7.23	91.68	14.57
IC4296	48.69	6.83	93.74	4.18	53.10	4.23
IC4765	1.21	1.21	3.03	0.23	11.01	1.20
IC4765	2.77	0.35	5.77	0.63	12.49	2.39
IC4765	3.62	0.50	6.91	0.63	13.18	1.84
IC4765	4.68	0.57	8.76	0.75	13.08	1.82
IC4765	5.89	0.64	13.06	1.73	20.35	4.31
IC4765	7.31	0.78	18.17	3.24	26.30	7.31
IC4765	9.09	0.99	18.21	1.65	20.10	2.99
NGC57	1.50	1.50	6.36	0.34	36.48	3.31
NGC57	4.30	1.31	14.23	1.28	42.44	6.59
NGC57	8.42	2.81	33.17	2.49	81.99	12.68
NGC315	0.73	0.20	3.27	0.32	20.02	4.65
NGC315	1.13	0.20	5.31	0.45	33.71	6.73
NGC315	1.59	0.27	7.94	0.74	53.52	11.93
NGC315	2.19	0.33	9.50	0.63	55.42	13.64
NGC315	3.12	0.60	14.12	0.91	73.57	21.26
NGC315	4.78	1.06	18.25	0.73	57.08	18.90

Galaxy	radius	Δr	K	σ_K	t_c/t_{ff}	$\delta t_c/t_{ff}$
	(kpc)	(kpc)	(keV cm^2)			
NGC410	1.28	1.28	6.57	0.79	42.75	8.62
NGC410	3.52	0.96	9.50	1.11	27.30	5.22
NGC410	7.04	2.56	22.45	1.48	49.70	8.16
NGC499	2.90	2.90	15.11	0.52	45.37	4.27
NGC499	7.82	2.03	33.27	1.99	56.17	7.43
NGC499	11.88	2.03	41.50	2.62	54.75	7.55
NGC499	16.15	2.25	40.00	2.52	35.68	4.35
NGC499	20.79	2.39	46.04	1.53	37.10	3.24
NGC499	25.64	2.46	48.82	1.72	34.18	3.19
NGC499	31.29	3.19	56.55	1.91	39.36	3.64
NGC499	37.96	3.48	74.76	2.88	44.53	4.10
NGC499	44.84	3.40	93.61	4.44	66.19	6.96
NGC499	52.15	3.91	111.35	6.12	107.52	14.76
NGC499	60.05	3.98	115.67	6.23	102.68	15.97
NGC499	67.51	3.48	122.87	6.57	100.94	16.78
NGC499	75.33	4.35	104.18	2.20	58.19	6.79
NGC507	2.78	2.78	13.59	0.42	34.75	3.63
NGC507	7.85	2.28	33.76	3.27	70.77	13.22
NGC507	11.84	1.71	38.59	5.35	63.26	15.56
NGC507	15.05	1.50	35.78	4.36	44.88	9.39
NGC507	17.91	1.36	36.74	3.44	35.32	6.83
NGC507	20.55	1.28	38.55	3.07	30.15	5.61
NGC507	23.19	1.36	42.38	2.21	34.46	5.95
NGC507	25.90	1.36	47.92	4.65	37.88	8.36
NGC507	28.68	1.43	49.56	3.56	34.87	6.78
NGC507	31.61	1.50	60.08	4.98	47.12	10.28
NGC507	34.60	1.50	60.87	3.34	37.26	7.09
NGC507	37.60	1.50	73.96	6.31	51.51	12.48
NGC507	40.60	1.50	69.32	4.61	40.99	8.64
NGC507	43.74	1.64	85.57	7.26	59.38	14.44

Galaxy	**radius**	Δr	K	σ_K	t_c/t_{ff}	$\delta t_c/t_{ff}$
	(kpc)	(kpc)	(keV cm^2)			
NGC507	47.16	1.78	110.05	14.22	77.39	24.47
NGC507	50.73	1.78	92.08	8.08	46.80	10.99
NGC507	54.30	1.78	178.55	68.20	188.69	164.01
NGC507	58.01	1.93	103.39	10.78	63.20	17.44
NGC507	61.79	1.86	109.76	11.44	66.12	18.31
NGC507	65.50	1.86	117.09	12.33	67.22	19.24
NGC507	69.28	1.93	105.18	8.21	48.76	11.66
NGC507	73.28	2.07	109.52	6.80	49.37	11.11
NGC507	77.63	2.28	124.67	9.18	60.86	14.80
NGC507	82.34	2.43	88.44	1.90	25.84	4.80
NGC533	0.29	0.29	1.72	0.24	17.79	5.08
NGC533	0.81	0.22	2.52	0.24	12.28	3.75
NGC533	1.25	0.22	3.76	0.54	17.51	6.24
NGC533	1.69	0.22	4.70	0.44	15.41	5.51
NGC533	2.13	0.22	5.92	0.46	17.49	6.44
NGC533	2.57	0.22	6.01	0.69	17.25	6.76
NGC533	3.01	0.22	6.40	0.73	17.54	7.10
NGC533	3.45	0.22	7.17	0.72	15.30	6.05
NGC533	3.89	0.22	6.90	0.56	14.49	5.76
NGC533	4.33	0.22	9.38	1.47	21.93	9.78
NGC533	4.77	0.22	9.07	0.51	15.05	5.97
NGC533	5.29	0.29	12.48	1.31	26.90	11.60
NGC533	5.88	0.29	13.54	1.14	23.51	9.85
NGC533	6.54	0.37	13.97	0.93	25.56	10.54
NGC533	7.27	0.37	16.07	1.33	25.03	10.42
NGC533	8.08	0.44	20.08	1.68	33.04	13.99
NGC533	9.03	0.51	21.46	1.50	32.27	13.49
NGC533	10.21	0.66	25.37	2.04	38.78	16.52
NGC533	11.82	0.95	33.13	2.54	49.92	21.23
NGC533	14.54	1.76	33.52	0.56	35.54	14.72

Galaxy	**radius**	Δr	K	σ_K	t_c/t_{ff}	$\delta t_c/t_{ff}$
	(kpc)	(kpc)	(keV cm^2)			
NGC708	1.24	1.24	6.72	0.22	27.72	1.34
NGC708	3.73	1.24	7.37	0.07	12.04	0.29
NGC708	6.22	1.24	11.11	0.08	14.95	0.39
NGC708	8.71	1.24	16.59	0.18	19.69	0.66
NGC708	11.51	1.56	19.86	0.10	20.92	0.60
NGC708	14.94	1.87	24.91	0.19	24.78	0.81
NGC708	18.98	2.18	30.63	0.19	28.69	0.93
NGC708	23.65	2.49	41.75	0.76	37.00	1.56
NGC708	28.76	2.62	47.74	0.97	41.60	1.70
NGC708	34.14	2.76	54.91	0.42	37.51	1.34
NGC708	39.65	2.76	66.31	0.63	46.59	1.79
NGC708	45.32	2.91	66.01	0.52	38.26	1.42
NGC708	50.98	2.76	74.20	0.80	42.97	1.70
NGC708	56.57	2.83	73.05	0.71	35.82	1.38
NGC708	62.31	2.91	85.10	1.09	36.49	1.44
NGC708	68.13	2.91	82.00	1.00	29.58	1.15
NGC708	74.18	3.14	89.29	0.75	33.77	1.30
NGC708	81.15	3.83	70.03	0.47	17.20	0.64
NGC741	1.09	1.09	3.63	0.11	19.16	0.73
NGC741	3.28	1.09	8.73	0.31	25.12	1.19
NGC741	5.62	1.25	16.31	0.35	36.04	1.58
NGC741	8.43	1.56	31.80	2.75	77.95	10.45
NGC741	12.02	2.03	34.75	1.33	48.76	3.41
NGC741	18.47	4.42	77.15	3.94	124.13	12.11
NGC741	27.34	4.45	115.53	15.81	174.54	39.26
NGC741	35.63	3.84	173.52	64.03	202.01	92.20
NGC741	42.85	3.38	165.06	25.49	139.44	25.86
NGC741	49.38	3.15	163.43	25.63	123.46	23.88
NGC741	55.60	3.07	195.82	46.47	163.88	63.75
NGC741	61.67	2.99	225.48	50.60	153.69	48.76

Galaxy	**radius**	Δr	K	σ_K	t_c/t_{ff}	$\delta t_c/t_{ff}$
	(kpc)	(kpc)	(keV cm^2)			
NGC741	67.81	3.15	192.79	25.62	108.60	18.33
NGC741	74.18	3.23	242.59	49.36	155.94	39.75
NGC741	80.56	3.15	226.06	25.54	117.48	18.79
NGC741	86.93	3.23	169.45	10.53	74.82	7.02
NGC777	1.73	1.73	6.91	0.25	37.38	2.36
NGC777	4.50	1.04	11.17	1.23	30.25	4.57
NGC777	6.58	1.04	13.70	2.00	29.98	5.81
NGC777	9.07	1.45	19.75	2.02	34.10	5.31
NGC777	12.19	1.66	19.39	1.73	24.11	3.01
NGC777	17.45	3.60	25.56	1.25	26.15	2.17
NGC1132	2.73	2.73	9.68	0.27	33.23	1.47
NGC1132	9.23	3.77	37.08	3.18	80.44	11.76
NGC1132	16.25	3.25	53.59	4.37	64.72	9.54
NGC1132	22.43	2.94	65.36	6.87	80.77	17.85
NGC1132	28.10	2.73	61.24	4.90	50.29	8.02
NGC1132	33.34	2.52	109.38	31.57	146.24	94.86
NGC1132	38.26	2.41	65.53	3.70	37.79	4.66
NGC1132	43.19	2.52	94.64	15.74	70.47	22.89
NGC1132	48.12	2.41	91.03	13.44	56.61	15.87
NGC1132	52.84	2.31	99.82	18.25	59.44	19.51
NGC1132	57.45	2.31	84.29	11.84	40.61	9.67
NGC1132	62.17	2.41	124.78	30.64	84.23	44.69
NGC1132	66.99	2.41	95.26	11.25	41.16	8.90
NGC1132	71.81	2.41	114.65	24.60	55.30	20.21
NGC1132	76.63	2.41	151.87	39.02	83.15	45.79
NGC1132	81.46	2.41	123.46	19.23	47.75	14.48
NGC1132	86.28	2.41	128.80	17.19	51.51	14.66
NGC1132	93.30	4.61	160.85	22.27	75.79	22.47
NGC1132	100.33	2.41	117.01	14.13	34.15	7.60
NGC1132	105.25	2.52	159.05	107.10	87.58	83.60

Galaxy	**radius**	Δr	K	σ_K	t_c/t_{ff}	$\delta t_c/t_{ff}$
	(kpc)	(kpc)	(keV cm^2)			
NGC1132	110.49	2.73	157.93	24.34	56.95	19.72
NGC1132	116.36	3.14	110.23	4.26	23.52	2.00
NGC1316	0.23	0.09	2.56	0.28	32.57	6.72
NGC1316	0.41	0.09	3.26	0.26	38.76	5.82
NGC1316	0.62	0.11	4.42	0.33	51.38	7.43
NGC1316	0.87	0.14	5.97	0.36	68.14	11.05
NGC1316	1.17	0.16	7.03	0.37	61.97	10.22
NGC1316	1.65	0.32	11.26	0.67	94.06	17.26
NGC1316	2.61	0.64	20.57	3.01	169.46	43.63
NGC1316	4.42	1.17	17.17	0.53	55.60	12.24
NGC1399	0.47	0.47	2.48	0.03	26.05	0.40
NGC1399	1.86	0.93	8.26	0.06	43.02	0.60
NGC1399	4.17	1.38	22.11	0.44	90.46	2.99
NGC1399	6.84	1.29	36.16	1.13	110.21	6.62
NGC1399	9.32	1.19	39.80	1.23	84.91	5.04
NGC1399	11.65	1.14	44.08	1.57	76.49	5.10
NGC1399	13.91	1.12	53.32	2.32	89.24	7.77
NGC1399	16.09	1.06	50.90	1.59	59.57	3.76
NGC1399	18.21	1.06	60.99	2.52	73.97	6.47
NGC1399	20.37	1.10	59.74	1.63	56.89	3.44
NGC1399	23.04	1.57	54.88	0.68	38.89	1.02
NGC1404	0.18	0.18	1.28	0.01	20.73	0.42
NGC1404	0.55	0.18	2.21	0.02	20.23	0.51
NGC1404	0.96	0.23	3.25	0.02	21.72	0.58
NGC1404	1.49	0.30	4.45	0.07	23.16	0.75
NGC1404	2.20	0.41	5.70	0.10	24.59	0.86
NGC1404	3.13	0.53	6.86	0.21	24.82	1.14
NGC1404	4.30	0.64	8.27	0.28	23.63	1.17
NGC1404	5.63	0.69	11.61	0.46	30.10	1.71
NGC1404	7.00	0.69	13.38	0.31	26.85	1.13

Galaxy	**radius**	Δr	K	σ_K	t_c/t_{ff}	$\delta t_c/t_{ff}$
	(kpc)	(kpc)	(keV cm^2)			
NGC1404	8.51	0.82	20.09	0.47	41.34	1.74
NGC1404	10.23	0.89	33.96	1.08	83.59	4.67
NGC1404	11.99	0.87	48.40	2.86	124.43	11.56
NGC1404	13.66	0.80	70.55	4.19	171.97	21.36
NGC1404	15.19	0.73	65.86	2.71	122.90	9.66
NGC1404	16.61	0.69	95.69	3.88	143.38	11.46
NGC1404	17.96	0.66	95.67	3.90	125.45	10.10
NGC1404	19.29	0.66	100.91	4.25	125.25	10.52
NGC1404	20.59	0.64	93.39	3.99	98.56	7.76
NGC1404	21.87	0.64	93.53	3.84	89.24	6.62
NGC1404	23.20	0.69	89.64	1.99	75.46	4.15
NGC1404	24.60	0.71	146.84	11.53	207.38	36.95
NGC1404	25.99	0.69	63.66	0.75	28.79	1.01
NGC1407	0.69	0.53	4.67	0.12	47.66	1.71
NGC1407	1.91	0.69	8.57	0.23	44.98	1.79
NGC1407	3.41	0.80	12.78	0.37	41.92	1.67
NGC1407	5.30	1.08	22.75	0.51	63.10	2.41
NGC1407	7.80	1.42	44.32	1.87	128.12	9.47
NGC1407	10.79	1.58	75.03	5.69	221.54	31.42
NGC1407	13.87	1.50	81.63	6.57	182.53	28.17
NGC1407	16.90	1.53	144.82	31.81	478.53	230.97
NGC1407	20.03	1.61	104.88	8.84	178.53	28.08
NGC1407	23.17	1.53	167.67	34.72	410.89	186.47
NGC1407	26.08	1.39	146.99	20.32	260.78	78.22
NGC1407	29.00	1.53	111.38	6.55	118.84	12.30
NGC1521	0.30	0.30	1.79	0.28	20.90	5.21
NGC1521	0.97	0.36	4.57	0.55	23.49	4.05
NGC1521	1.64	0.30	6.36	0.69	23.18	3.77
NGC1521	2.37	0.43	7.38	0.94	25.00	4.33
NGC1521	3.46	0.67	7.76	0.43	18.07	1.47

Galaxy	radius	Δr	K	σ_K	t_c/t_{ff}	$\delta t_c/t_{ff}$
	(kpc)	(kpc)	(keV cm^2)			
NGC1550	3.37	3.37	8.18	0.16	19.89	0.66
NGC1550	9.87	3.13	16.35	0.43	18.39	0.84
NGC1550	16.86	3.85	26.07	0.80	24.77	1.45
NGC1550	24.80	4.09	36.88	0.98	29.18	1.63
NGC1550	32.99	4.09	44.67	1.48	30.09	2.15
NGC1550	41.26	4.17	53.74	1.32	27.22	1.27
NGC1550	50.17	4.74	60.31	1.77	26.80	1.59
NGC1550	60.04	5.14	71.01	2.48	30.89	2.27
NGC1550	71.68	6.50	64.94	1.33	19.70	0.73
NGC1600	0.76	0.76	5.88	0.23	44.88	5.97
NGC1600	2.29	0.76	9.77	0.39	42.60	7.16
NGC1600	4.86	1.80	34.77	3.14	177.36	46.25
NGC1600	8.62	1.97	70.62	11.27	265.42	105.16
NGC1600	12.34	1.75	69.26	8.91	140.35	48.72
NGC1600	15.72	1.64	147.03	74.08	581.47	673.76
NGC1600	18.83	1.47	65.86	5.56	70.44	22.06
NGC2300	1.56	1.56	5.28	0.19	26.09	1.27
NGC2300	5.58	2.45	13.94	0.56	30.76	1.73
NGC2300	11.29	3.26	39.79	2.48	76.58	6.88
NGC2300	17.76	3.21	88.62	9.28	184.36	38.41
NGC2300	23.64	2.66	124.68	17.55	256.24	76.15
NGC2300	28.46	2.16	91.95	8.23	97.13	16.45
NGC2300	32.65	2.03	118.68	9.60	112.37	17.57
NGC2300	36.58	1.90	121.46	11.19	99.41	18.43
NGC2300	40.47	1.99	127.58	9.58	95.08	13.45
NGC2300	44.53	2.07	129.14	14.20	105.19	25.30
NGC2300	48.38	1.78	85.24	3.61	36.37	2.76
NGC2305	0.30	0.30	2.36	0.21	41.58	5.38
NGC2305	0.84	0.25	2.98	0.34	20.22	3.36
NGC2305	1.48	0.40	4.38	0.41	21.28	2.77

Galaxy	**radius**	Δr	K	σ_K	t_c/t_{ff}	$\delta t_c/t_{ff}$
	(kpc)	(kpc)	(keV cm^2)			
NGC2305	2.47	0.59	7.88	0.92	31.43	4.91
NGC2305	3.86	0.79	13.37	1.24	42.83	6.20
NGC2305	5.98	1.33	11.11	0.75	21.51	2.01
NGC3091	1.38	1.38	8.35	0.29	53.15	3.13
NGC3091	3.46	0.69	12.93	1.31	41.98	5.99
NGC3091	4.78	0.63	16.90	2.68	49.59	11.19
NGC3091	5.99	0.58	15.79	1.49	30.74	4.16
NGC3091	7.43	0.86	22.39	1.22	43.43	5.29
NGC3091	9.16	0.86	17.56	0.39	18.47	0.93
NGC3923	0.20	0.20	1.70	0.05	24.64	1.53
NGC3923	0.58	0.18	2.37	0.09	21.98	1.41
NGC3923	1.03	0.28	3.58	0.14	26.99	2.11
NGC3923	1.75	0.45	5.43	0.33	31.16	3.15
NGC3923	2.93	0.73	9.14	0.65	40.15	4.62
NGC3923	4.45	0.80	14.77	1.03	54.93	7.21
NGC3923	6.08	0.83	17.34	1.23	45.51	6.06
NGC3923	7.70	0.80	30.91	3.27	89.41	18.07
NGC3923	9.20	0.70	24.90	2.01	39.50	5.27
NGC4073	1.86	1.86	10.88	0.16	32.22	2.92
NGC4073	4.37	0.64	16.45	0.96	36.79	4.46
NGC4073	5.66	0.64	20.85	1.88	48.00	8.11
NGC4073	7.02	0.72	25.59	4.44	60.18	17.78
NGC4073	8.53	0.79	29.43	3.38	64.60	13.36
NGC4073	10.25	0.93	36.49	4.56	83.06	19.56
NGC4073	12.18	1.00	45.92	5.86	99.94	23.59
NGC4073	14.19	1.00	51.76	7.29	105.51	28.85
NGC4073	16.48	1.29	58.44	6.06	93.81	19.94
NGC4073	19.13	1.36	65.44	6.40	96.61	19.43
NGC4073	21.78	1.29	88.26	16.27	150.39	54.05
NGC4073	24.79	1.72	75.50	10.83	86.32	21.58

Galaxy	**radius**	Δr	K	σ_K	t_c/t_{ff}	$\delta t_c/t_{ff}$
	(kpc)	(kpc)	(keV cm^2)			
NGC4073	28.73	2.22	101.42	7.59	136.11	26.40
NGC4073	34.61	3.65	90.14	3.79	77.10	11.08
NGC4125	0.23	0.08	2.79	0.52	28.22	12.35
NGC4125	0.43	0.13	4.08	0.63	47.29	14.58
NGC4125	0.69	0.13	6.45	0.54	62.15	14.88
NGC4125	0.94	0.13	8.88	0.88	90.95	24.93
NGC4125	1.23	0.15	10.90	1.24	103.67	32.99
NGC4125	1.53	0.15	8.84	0.96	68.73	22.40
NGC4125	1.86	0.18	8.87	0.73	51.68	15.83
NGC4125	2.27	0.23	11.35	0.96	65.98	21.90
NGC4125	2.81	0.31	10.30	0.59	36.36	12.17
NGC4261	0.28	0.14	1.10	0.02	14.17	1.47
NGC4261	0.67	0.25	2.65	0.04	23.73	3.06
NGC4261	1.44	0.53	5.37	0.14	35.27	5.04
NGC4261	3.09	1.12	14.20	0.30	67.99	10.05
NGC4261	5.94	1.72	42.49	1.49	169.87	27.13
NGC4261	12.02	4.36	107.04	12.62	423.98	104.52
NGC4261	18.55	2.18	155.67	21.64	256.21	86.33
NGC4261	24.88	4.15	151.31	11.96	143.39	31.33
NGC4261	31.77	2.74	113.86	3.91	66.51	11.23
NGC4374	0.41	0.24	2.29	0.10	26.32	7.29
NGC4374	0.99	0.34	3.69	0.20	25.04	6.58
NGC4374	1.70	0.38	5.73	0.29	27.13	6.77
NGC4374	2.57	0.49	8.74	0.41	34.74	8.40
NGC4374	3.78	0.71	15.22	0.53	54.98	13.26
NGC4374	5.60	1.11	27.25	1.42	109.44	28.74
NGC4374	7.95	1.25	49.78	6.53	220.69	73.07
NGC4374	10.29	1.09	52.64	6.24	159.97	54.33
NGC4374	12.45	1.07	88.41	15.26	234.34	103.59
NGC4374	14.55	1.03	100.51	20.91	228.15	119.14

Galaxy	radius	Δr	K	σ_K	t_c/t_{ff}	$\delta t_c/t_{ff}$
	(kpc)	(kpc)	(keV cm^2)			
NGC4374	16.52	0.95	139.13	47.12	314.58	260.58
NGC4374	18.37	0.89	80.61	5.49	73.56	27.31
NGC4406	1.61	1.61	10.87	0.43	52.64	2.85
NGC4406	4.37	1.15	26.62	2.02	75.24	8.69
NGC4406	6.41	0.88	22.78	1.43	40.44	3.63
NGC4406	8.09	0.81	23.33	1.41	32.98	2.84
NGC4406	9.68	0.79	31.29	1.60	46.93	5.00
NGC4406	11.24	0.77	26.31	0.87	26.28	1.60
NGC4406	12.85	0.84	36.03	2.79	37.36	4.16
NGC4406	14.56	0.86	41.99	3.04	42.70	4.82
NGC4406	16.22	0.81	48.19	2.20	48.56	5.09
NGC4406	17.80	0.77	45.89	1.69	38.67	3.30
NGC4406	19.33	0.77	53.74	2.78	49.64	5.88
NGC4406	20.85	0.75	35.32	0.48	17.54	0.67
NGC4472	0.32	0.32	2.38	0.02	35.65	0.31
NGC4472	0.96	0.32	4.34	0.03	26.80	0.23
NGC4472	1.74	0.45	7.56	0.05	36.00	0.31
NGC4472	2.79	0.60	13.36	0.10	57.55	0.60
NGC4472	4.02	0.62	18.41	0.14	68.27	1.13
NGC4472	5.24	0.60	23.27	0.27	65.79	1.50
NGC4472	6.47	0.62	28.48	0.32	70.12	1.29
NGC4472	7.71	0.62	30.79	0.32	65.14	1.16
NGC4472	8.98	0.64	35.70	0.44	71.43	1.47
NGC4472	10.28	0.66	36.53	0.49	63.97	1.58
NGC4472	11.62	0.68	41.73	0.42	68.92	1.30
NGC4472	13.00	0.70	42.78	0.64	66.14	1.79
NGC4472	14.41	0.72	47.72	0.59	68.29	1.77
NGC4472	15.86	0.74	52.30	0.85	71.82	2.26
NGC4472	17.39	0.79	56.39	1.07	72.96	2.33
NGC4472	19.09	0.91	65.54	1.31	82.28	2.76

Galaxy	**radius**	Δr	K	σ_K	t_c/t_{ff}	$\delta t_c/t_{ff}$
	(kpc)	(kpc)	(keV cm^2)			
NGC4472	21.13	1.13	57.87	0.41	53.03	0.72
NGC4486	0.79	0.71	5.85	0.02	35.11	0.34
NGC4486	1.93	0.43	8.85	0.03	25.09	0.21
NGC4486	2.78	0.41	9.55	0.07	22.73	0.27
NGC4486	3.64	0.45	11.58	0.06	24.81	0.28
NGC4486	4.61	0.51	15.79	0.04	34.31	0.27
NGC4486	5.65	0.53	17.34	0.07	34.25	0.36
NGC4486	6.76	0.57	20.26	0.08	42.41	0.38
NGC4486	7.88	0.55	22.27	0.11	43.45	0.43
NGC4486	8.96	0.53	23.80	0.11	41.89	0.42
NGC4486	10.01	0.51	25.16	0.09	41.47	0.40
NGC4486	11.03	0.51	29.61	0.10	38.78	0.40
NGC4486	12.08	0.53	32.75	0.12	43.18	0.47
NGC4486	13.14	0.53	34.68	0.13	43.94	0.49
NGC4486	14.22	0.55	35.46	0.17	45.43	0.52
NGC4486	15.33	0.55	35.05	0.14	40.02	0.41
NGC4486	16.45	0.57	37.68	0.17	42.82	0.49
NGC4486	17.61	0.59	40.95	0.21	45.24	0.50
NGC4486	18.81	0.61	42.03	0.21	43.85	0.48
NGC4486	20.09	0.67	45.76	0.20	44.67	0.47
NGC4486	21.47	0.71	49.27	0.21	48.17	0.52
NGC4486	22.93	0.75	52.68	0.36	50.12	0.60
NGC4486	24.49	0.81	57.37	0.16	54.30	0.57
NGC4486	26.12	0.83	56.33	0.14	47.66	0.48
NGC4486	27.80	0.85	74.52	0.30	67.70	0.76
NGC4486	29.51	0.87	47.13	0.16	22.21	0.22
NGC4552	0.21	0.13	2.21	0.07	11.35	0.63
NGC4552	0.49	0.15	3.14	0.07	29.71	1.33
NGC4552	0.76	0.11	3.58	0.08	30.87	1.31
NGC4552	1.02	0.15	3.79	0.04	24.97	0.61

Galaxy	**radius**	Δr	K	σ_K	t_c/t_{ff}	$\delta t_c/t_{ff}$
	(kpc)	(kpc)	(keV cm^2)			
NGC4552	1.44	0.27	5.34	0.13	42.30	1.54
NGC4552	2.12	0.42	7.32	0.33	50.44	3.61
NGC4552	3.04	0.49	8.65	0.45	37.89	2.51
NGC4552	4.21	0.68	12.27	0.92	47.33	4.18
NGC4552	6.22	1.33	25.35	1.72	93.05	9.31
NGC4552	9.71	2.16	42.84	3.29	116.47	15.27
NGC4552	13.66	1.78	66.67	9.14	108.97	18.49
NGC4552	16.92	1.48	110.80	4.91	55.62	4.20
NGC4636	0.38	0.38	1.84	0.06	11.53	0.61
NGC4636	1.01	0.25	2.88	0.05	10.79	0.36
NGC4636	1.56	0.30	4.03	0.07	15.23	0.51
NGC4636	2.21	0.34	5.61	0.15	22.73	0.99
NGC4636	2.87	0.32	6.83	0.09	22.67	0.89
NGC4636	3.50	0.30	7.37	0.09	20.35	0.80
NGC4636	4.09	0.29	9.15	0.15	20.36	0.83
NGC4636	4.68	0.30	10.52	0.07	22.00	0.85
NGC4636	5.31	0.32	11.60	0.10	22.47	0.90
NGC4636	6.01	0.38	13.68	0.18	25.04	1.04
NGC4636	6.85	0.46	16.02	0.22	29.59	1.25
NGC4636	7.86	0.55	20.94	0.23	42.09	1.80
NGC4636	9.00	0.59	23.86	0.26	45.93	2.00
NGC4636	10.22	0.63	30.68	0.57	58.10	2.73
NGC4636	11.51	0.67	30.65	0.54	48.90	2.46
NGC4636	12.90	0.72	35.06	0.63	55.77	2.76
NGC4636	14.41	0.78	40.63	0.80	63.86	3.28
NGC4636	16.00	0.82	41.87	0.65	56.66	2.79
NGC4636	17.70	0.88	43.13	0.63	54.50	2.53
NGC4636	19.54	0.97	51.92	0.42	64.54	2.93
NGC4636	21.67	1.16	44.10	0.24	38.01	1.66
NGC4649	0.16	0.16	1.94	0.01	41.35	0.60

Galaxy	radius	Δr	K	σ_K	t_c/t_{ff}	$\delta t_c/t_{ff}$
	(kpc)	(kpc)	(keV cm^2)			
NGC4649	0.41	0.10	2.15	0.02	22.63	0.35
NGC4649	0.63	0.12	3.27	0.02	34.06	0.59
NGC4649	0.89	0.14	3.78	0.02	28.17	0.47
NGC4649	1.18	0.16	4.80	0.05	31.04	0.61
NGC4649	1.56	0.22	6.30	0.07	37.58	0.77
NGC4649	2.05	0.28	8.44	0.05	44.00	0.81
NGC4649	2.69	0.36	11.88	0.07	60.06	1.20
NGC4649	3.46	0.41	14.62	0.08	61.41	1.22
NGC4649	4.36	0.49	18.30	0.13	67.92	1.43
NGC4649	5.41	0.55	22.61	0.28	75.44	1.78
NGC4649	6.55	0.59	27.24	0.42	80.43	2.09
NGC4649	7.78	0.63	32.78	0.43	82.11	2.02
NGC4649	9.10	0.69	37.71	0.51	85.97	2.15
NGC4649	10.56	0.77	44.71	0.64	96.94	2.53
NGC4649	12.16	0.83	55.05	1.09	124.87	4.00
NGC4649	13.86	0.87	72.12	1.94	177.98	7.48
NGC4649	15.56	0.83	87.41	4.10	232.40	15.59
NGC4649	17.22	0.83	109.43	3.45	295.42	20.67
NGC4649	20.81	2.76	110.16	1.42	216.18	5.71
NGC4696	1.34	1.34	4.60	0.01	4.73	0.03
NGC4696	3.53	0.85	9.31	0.03	9.98	0.06
NGC4696	5.14	0.76	10.25	0.03	10.61	0.06
NGC4696	6.71	0.80	13.92	0.05	14.35	0.07
NGC4696	8.32	0.80	15.46	0.05	15.63	0.09
NGC4696	10.06	0.94	19.34	0.03	20.27	0.08
NGC4696	11.98	0.98	22.60	0.05	24.63	0.10
NGC4696	14.04	1.07	28.72	0.20	30.41	0.40
NGC4696	16.23	1.12	35.10	0.16	37.86	0.23
NGC4696	18.51	1.16	40.86	0.20	44.91	0.29
NGC4696	20.83	1.16	43.92	0.22	46.48	0.31

Galaxy	radius	Δr	K	σ_K	t_c/t_{ff}	$\delta t_c/t_{ff}$
	(kpc)	(kpc)	(keV cm^2)			
NGC4696	23.16	1.16	47.73	0.39	47.27	0.44
NGC4696	25.48	1.16	49.99	0.25	48.21	0.33
NGC4696	27.85	1.21	52.32	0.51	45.66	0.49
NGC4696	30.31	1.25	54.33	0.53	44.14	0.47
NGC4696	32.90	1.34	61.77	0.50	46.99	0.42
NGC4696	35.76	1.52	76.92	0.45	63.02	0.48
NGC4696	38.85	1.56	85.48	0.52	70.96	0.57
NGC4696	42.07	1.65	90.99	0.44	68.23	0.47
NGC4696	45.55	1.83	92.99	0.44	63.64	0.41
NGC4696	49.71	2.32	111.19	0.44	78.21	0.47
NGC4696	54.85	2.82	138.93	0.59	110.93	0.77
NGC4696	61.47	3.80	122.94	0.44	70.47	0.35
NGC4778	1.56	1.56	5.64	0.09	19.99	3.95
NGC4778	4.24	1.13	8.68	0.17	15.02	2.54
NGC4778	6.65	1.27	13.36	0.37	21.79	3.58
NGC4778	9.26	1.34	17.32	0.36	22.67	3.72
NGC4778	12.09	1.49	21.82	0.51	27.70	4.70
NGC4778	15.27	1.70	26.51	0.43	26.28	4.60
NGC4778	19.38	2.40	41.99	1.05	51.95	9.70
NGC4778	24.61	2.83	60.55	2.66	69.48	14.28
NGC4778	30.34	2.90	71.67	3.45	73.01	15.86
NGC4778	36.28	3.04	92.59	3.51	89.51	19.96
NGC4778	42.36	3.04	112.56	5.16	108.76	25.71
NGC4778	48.44	3.04	125.81	7.29	114.13	28.61
NGC4778	54.52	3.04	165.52	16.63	174.48	54.92
NGC4778	60.46	2.90	172.03	17.33	162.30	51.99
NGC4778	66.19	2.83	155.83	10.82	111.77	31.07
NGC4778	71.99	2.97	158.50	9.20	100.89	26.95
NGC4778	78.71	3.75	192.48	12.97	142.79	40.02
NGC4778	86.91	4.46	376.99	119.33	547.61	411.43

Galaxy	**radius**	Δr	K	σ_K	t_c/t_{ff}	$\delta t_c/t_{ff}$
	(kpc)	(kpc)	(keV cm^2)			
NGC4778	96.74	5.37	183.69	6.19	90.45	23.03
NGC4782	0.75	0.41	5.50	1.48	18.94	9.92
NGC4782	2.15	0.99	15.51	4.78	60.42	35.43
NGC4782	4.06	0.93	35.57	7.78	60.68	26.70
NGC4782	5.80	0.81	41.77	9.18	56.43	24.84
NGC4782	7.31	0.70	31.66	3.80	26.26	8.03
NGC4782	10.49	2.48	72.69	12.90	113.93	47.16
NGC4782	15.91	2.95	78.48	11.64	70.41	21.24
NGC4936	2.99	2.99	12.45	1.21	29.89	12.12
NGC4936	8.53	2.54	33.59	2.55	56.79	23.32
NGC4936	13.39	2.32	47.46	5.02	63.84	29.86
NGC4936	17.69	1.98	48.95	4.20	55.72	28.13
NGC4936	21.50	1.83	48.71	5.28	43.94	23.41
NGC4936	25.17	1.83	42.63	2.06	24.12	12.98
NGC5044	1.10	0.93	3.17	0.05	5.75	0.14
NGC5044	2.54	0.51	5.86	0.10	9.39	0.23
NGC5044	3.51	0.47	7.56	0.14	11.54	0.33
NGC5044	4.40	0.42	8.18	0.13	11.29	0.25
NGC5044	5.20	0.38	8.57	0.20	10.83	0.30
NGC5044	5.97	0.38	8.81	0.20	10.65	0.29
NGC5044	6.73	0.38	8.59	0.14	9.26	0.22
NGC5044	7.49	0.38	9.47	0.17	10.03	0.23
NGC5044	8.25	0.38	10.04	0.14	9.71	0.19
NGC5044	9.01	0.38	10.99	0.13	10.10	0.19
NGC5044	9.77	0.38	11.89	0.15	11.14	0.21
NGC5044	10.53	0.38	12.30	0.07	10.66	0.16
NGC5044	11.34	0.42	13.16	0.07	11.39	0.17
NGC5044	12.18	0.42	14.32	0.08	12.60	0.20
NGC5044	13.03	0.42	14.64	0.08	12.19	0.19
NGC5044	13.88	0.42	15.35	0.08	12.54	0.20

Galaxy	**radius**	Δr	K	σ_K	t_c/t_{ff}	$\delta t_c/t_{ff}$
	(kpc)	(kpc)	(keV cm^2)			
NGC5044	14.76	0.47	16.14	0.09	12.79	0.20
NGC5044	15.69	0.47	16.39	0.08	12.23	0.19
NGC5044	16.75	0.59	17.95	0.14	13.70	0.23
NGC5044	18.20	0.87	19.47	0.15	14.40	0.22
NGC5044	20.11	1.04	22.32	0.14	16.03	0.24
NGC5044	22.27	1.13	24.20	0.13	16.24	0.25
NGC5044	24.70	1.30	25.72	0.11	16.01	0.24
NGC5044	27.73	1.73	34.60	0.16	23.80	0.37
NGC5044	31.63	2.17	30.19	0.06	13.64	0.20
NGC5129	2.28	2.28	6.31	0.16	22.58	0.85
NGC5129	9.53	4.97	29.13	1.00	55.41	2.89
NGC5129	19.47	4.97	59.89	4.74	76.66	8.84
NGC5129	28.80	4.35	67.05	3.83	61.04	6.20
NGC5129	36.98	3.83	77.18	5.34	56.21	7.59
NGC5129	44.33	3.52	96.76	12.18	75.95	21.18
NGC5129	51.17	3.31	79.98	4.89	39.75	5.11
NGC5129	57.69	3.21	93.98	7.86	47.58	8.65
NGC5129	64.01	3.11	77.60	6.54	36.60	6.91
NGC5129	70.23	3.11	91.52	8.53	46.06	9.63
NGC5129	76.24	2.90	59.99	1.54	15.71	0.88
NGC5419	0.74	0.25	2.72	0.22	17.30	2.21
NGC5419	1.52	0.54	5.59	0.25	27.59	2.04
NGC5419	6.25	4.19	34.25	3.47	137.55	22.11
NGC5419	14.62	4.19	112.67	42.19	269.90	127.33
NGC5419	22.21	3.40	130.20	29.23	167.59	51.70
NGC5419	28.76	3.15	227.11	83.42	396.10	286.55
NGC5419	34.46	2.55	120.04	21.95	107.06	34.07
NGC5419	39.56	2.55	138.21	20.53	119.27	25.03
NGC5419	44.47	2.37	124.60	19.58	87.61	18.42
NGC5419	49.14	2.31	162.76	44.73	137.41	75.48

Galaxy	**radius**	Δr	K	σ_K	t_c/t_{ff}	$\delta t_c/t_{ff}$
	(kpc)	(kpc)	(keV cm^2)			
NGC5419	53.15	1.70	115.08	14.66	47.57	13.62
NGC5419	56.85	2.00	98.25	3.32	30.10	2.28
NGC5813	1.00	0.59	4.30	0.04	15.90	0.33
NGC5813	2.04	0.45	4.61	0.06	12.20	0.26
NGC5813	2.93	0.45	5.78	0.10	15.01	0.39
NGC5813	3.86	0.48	7.04	0.08	17.24	0.41
NGC5813	4.79	0.45	8.38	0.11	19.33	0.55
NGC5813	5.65	0.41	7.53	0.23	14.27	0.60
NGC5813	6.48	0.41	9.59	0.19	17.10	0.56
NGC5813	7.27	0.38	10.12	0.18	15.61	0.49
NGC5813	8.03	0.38	11.53	0.13	15.48	0.41
NGC5813	8.79	0.38	11.70	0.06	13.87	0.32
NGC5813	9.58	0.41	13.02	0.12	15.15	0.38
NGC5813	10.44	0.45	14.10	0.14	15.28	0.38
NGC5813	11.44	0.55	14.84	0.13	15.42	0.38
NGC5813	12.68	0.69	16.95	0.12	17.99	0.44
NGC5813	14.23	0.86	19.05	0.07	19.77	0.49
NGC5813	16.26	1.17	24.84	0.10	29.16	0.74
NGC5813	18.95	1.52	20.56	0.06	14.12	0.35
NGC5846	0.78	0.78	3.58	0.07	24.27	2.61
NGC5846	2.23	0.68	5.39	0.15	16.49	2.27
NGC5846	3.66	0.74	7.70	0.23	19.06	2.81
NGC5846	5.15	0.74	8.82	0.38	17.71	2.75
NGC5846	6.67	0.78	12.08	0.65	21.72	3.56
NGC5846	8.19	0.74	14.13	0.85	22.07	3.67
NGC5846	9.64	0.71	16.14	0.91	22.33	3.74
NGC5846	11.07	0.71	19.05	0.69	24.36	3.98
NGC5846	12.49	0.71	22.39	0.98	26.67	4.44
NGC5846	13.91	0.71	22.30	1.07	25.24	4.30
NGC5846	15.31	0.68	23.86	0.96	23.23	3.86

Galaxy	**radius**	Δr	K	σ_K	t_c/t_{ff}	$\delta t_c/t_{ff}$
	(kpc)	(kpc)	(keV cm^2)			
NGC5846	16.66	0.68	26.16	1.64	26.31	4.62
NGC5846	18.06	0.71	30.41	1.06	26.03	4.29
NGC5846	19.54	0.78	37.67	2.23	37.80	6.63
NGC5846	21.13	0.81	39.17	1.79	37.19	6.26
NGC5846	22.81	0.87	50.80	2.97	49.44	8.79
NGC5846	24.56	0.87	63.26	4.35	65.45	11.97
NGC5846	26.34	0.91	68.29	5.89	74.94	18.25
NGC5846	28.15	0.91	76.42	4.18	78.23	13.87
NGC5846	29.93	0.87	81.23	8.33	85.34	18.46
NGC5846	31.71	0.91	76.60	4.90	72.61	14.39
NGC5846	33.59	0.97	84.31	5.29	82.49	16.21
NGC5846	35.63	1.07	68.99	1.81	44.99	7.43
NGC6407	3.17	3.17	8.76	0.88	21.33	3.89
NGC6407	8.59	2.25	19.73	3.10	26.60	7.09
NGC6407	12.39	1.55	31.33	9.25	35.81	16.87
NGC6407	17.58	3.64	37.16	4.60	33.46	9.05
NGC6861	0.68	0.47	3.48	0.14	30.62	1.68
NGC6861	2.80	1.65	16.57	1.01	97.89	7.85
NGC6861	6.46	2.01	46.80	6.57	192.75	43.17
NGC6861	10.26	1.79	60.70	6.22	146.87	29.10
NGC6861	13.42	1.36	91.42	23.97	239.61	138.52
NGC6861	16.04	1.26	64.62	6.61	82.39	16.37
NGC6861	18.41	1.11	77.31	18.72	135.92	73.87
NGC6861	20.53	1.00	56.31	5.50	55.90	12.11
NGC6861	22.47	0.93	94.94	37.13	156.62	137.71
NGC6861	24.26	0.86	56.17	5.45	42.49	9.16
NGC6861	25.95	0.83	62.13	7.54	47.84	12.96
NGC6861	27.60	0.83	46.73	2.12	22.82	2.21
NGC6868	1.68	1.45	9.34	0.47	50.39	3.28
NGC6868	5.09	1.96	31.71	2.34	110.13	11.29

Galaxy	**radius**	Δr	K	σ_K	t_c/t_{ff}	$\delta t_c/t_{ff}$
	(kpc)	(kpc)	(keV cm^2)			
NGC6868	9.79	2.74	30.68	1.98	57.11	4.87
NGC6868	15.29	2.75	41.39	1.52	53.53	3.43
NGC6868	20.35	2.31	51.77	2.44	57.78	5.55
NGC6868	24.63	1.97	61.39	4.81	64.21	9.93
NGC6868	28.49	1.89	50.57	2.44	33.77	3.04
NGC6868	33.84	3.47	47.78	1.69	27.55	1.70
NGC7619	1.57	1.57	7.77	0.16	46.50	1.40
NGC7619	6.27	3.13	24.52	0.68	70.33	3.06
NGC7619	13.08	3.68	45.58	1.53	82.17	4.96
NGC7619	20.19	3.43	69.45	4.73	93.46	10.42
NGC7619	27.00	3.37	85.75	7.93	100.42	15.96
NGC7619	33.44	3.07	126.62	13.10	136.13	30.50
NGC7619	39.35	2.83	129.04	12.44	109.57	22.74
NGC7619	45.14	2.95	170.22	24.55	164.14	52.27
NGC7619	50.74	2.65	137.25	13.70	89.14	19.56
NGC7619	55.98	2.59	132.82	10.56	70.76	12.21
NGC7619	61.22	2.65	176.45	26.14	116.21	38.35
NGC7619	66.83	2.95	113.74	4.09	38.42	2.76
NGC7796	1.82	1.82	10.73	0.48	69.46	4.38
NGC7796	5.70	2.06	31.72	3.97	115.70	17.54
NGC7796	11.76	4.00	47.47	2.82	89.39	7.78
NGC7796	22.21	6.45	76.14	9.61	121.91	20.60
NGC7796	33.85	5.19	76.09	11.90	70.50	13.04

BIBLIOGRAPHY

BIBLIOGRAPHY

Aguado, D. S., Ahumada, R., Almeida, A., et al. 2019, The Astrophysical Journal Supplement, 240, 23

Akritas, M. G., & Bershady, M. A. 1996, The Astrophysical Journal, 470, 706

Anders, E., & Grevesse, N. 1989, Geochimica et Cosmochimica Acta, 53, 197

Arnaud, K. A. 1996, in Astronomical Society of the Pacific Conference Series, Vol. 101, Astronomical Data Analysis Software and Systems V, ed. G. H. Jacoby & J. Barnes, 17

Babyk, I. V., McNamara, B. R., Nulsen, P. E. J., et al. 2018, The Astrophysical Journal, 862, 39

Bauer, F. E., Fabian, A. C., Sanders, J. S., Allen, S. W., & Johnstone, R. M. 2005, Monthly Notices of the Royal Astronomical Society, 359, 1481

Bîrzan, L., Rafferty, D. A., McNamara, B. R., Wise, M. W., & Nulsen, P. E. J. 2004, The Astrophysical Journal, 607, 800

Boehringer, H., Voges, W., Fabian, A. C., Edge, A. C., & Neumann, D. M. 1993, Monthly Notices of the Royal Astronomical Society, 264, L25

Böhringer, H., Schuecker, P., Guzzo, L., et al. 2004, Astronomy & Astrophysics, 425, 367

Brandt, W. N., & Hasinger, G. 2005, Annual Reviews of Astronomy and Astrophysics, 43, 827

Bregman, J. N. 2007, Annual Reviews of Astronomy and Astrophysics, 45, 221

Bregman, J. N., Anderson, M. E., Miller, M. J., et al. 2018, The Astrophysical Journal, 862, 3

Brown, M. J. I., Jannuzi, B. T., Floyd, D. J. E., & Mould, J. R. 2011, The Astrophysical Journal Letters, 731, L41

Buote, D. A., & Tsai, J. C. 1995, The Astrophysical Journal, 452, 522

Burnight, T. 1949, Physical Review, 76, 165

Cantiello, M., Blakeslee, J., Raimondo, G., Brocato, E., & Capaccioli, M. 2007, The Astrophysical Journal, 668, 130

Cassano, R., Ettori, S., Giacintucci, S., et al. 2010, The Astrophysical Journal Letters, 721, L82

Cavagnolo, K. W., Donahue, M., Voit, G. M., & Sun, M. 2008, The Astrophysical Journal Letters, 683, L107

Cavagnolo, K. W., Donahue, M., Voit, G. M., & Sun, M. 2009, The Astrophysical Journal Supplement Series, 182, 12

Cen, R., & Ostriker, J. P. 1999, The Astrophysical Journal, 514, 1

Churazov, E., Forman, W., Jones, C., & Böhringer, H. 2000, Astronomy & Astrophysics, 356, 788

Colless, M., Dalton, G., Maddox, S., et al. 2001, Monthly Notices of the Royal Astronomical Society, 328, 1039

Condon, J. J., Cotton, W. D., Greisen, E. W., et al. 1998, The Astronomical Journal, 115, 1693

Connor, T. in preparation

Connor, T., Donahue, M., Sun, M., et al. 2014, The Astrophysical Journal, 794, 48

Dalla Bontà, E., Ferrarese, L., Corsini, E. M., et al. 2009, The Astrophysical Journal, 690, 537

Dekel, A., Birnboim, Y., Engel, G., et al. 2009, Nature, 457, 451

Diehl, S., & Statler, T. S. 2007, The Astrophysical Journal, 668, 150

—. 2008a, The Astrophysical Journal, 687, 986

—. 2008b, The Astrophysical Journal, 680, 897

Donahue, M., Horner, D. J., Cavagnolo, K. W., & Voit, G. M. 2006, The Astrophysical Journal, 643, 730

Donahue, M., Voit, G. M., O'Dea, C. P., Baum, S. A., & Sparks, W. B. 2005, The Astrophysical Journal Letters, 630, L13

Donahue, M., Voit, G. M., Mahdavi, A., et al. 2014, The Astrophysical Journal, 794, 136

Dunn, R. J. H., & Fabian, A. C. 2006, Monthly Notices of the Royal Astronomical Society, 373, 959

—. 2008, Monthly Notices of the Royal Astronomical Society, 385, 757

Dunn, R. J. H., Fabian, A. C., & Taylor, G. B. 2005, Monthly Notices of the Royal Astronomical Society, 364, 1343

Edge, A. C. 2001, Monthly Notices of the Royal Astronomical Society, 328, 762

Ekers, R. D., Goss, W. M., Wellington, K. J., et al. 1983, Astronomy & Astrophysics, 127, 361

Fabian, A. C. 1994, Annual Reviews of Astronomy and Astrophysics, 32, 277

—. 2012, Annual Reviews of Astronomy and Astrophysics, 50, 455

Fabian, A. C., Sanders, J. S., Allen, S. W., et al. 2003, Monthly Notices of the Royal Astronomical Society, 344, L43

Fabian, A. C., Sanders, J. S., Taylor, G. B., et al. 2006, Monthly Notices of the Royal Astronomical Society, 366, 417

Fan, X., Wang, F., Yang, J., et al. 2019, The Astrophysical Journal Letters, 870, L11

Fanaroff, B. L., & Riley, J. M. 1974, Monthly Notices of the Royal Astronomical Society, 167, 31P

Ferrarese, L., Ford, H. C., & Jaffe, W. 1996, The Astrophysical Journal, 470, 444

Ferrarese, L., & Merritt, D. 2000, The Astrophysical Journal Letters, 539, L9

Forman, W., Jones, C., & Tucker, W. 1985, The Astrophysical Journal, 293, 102

Forman, W., Kellogg, E., Gursky, H., Tananbaum, H., & Giacconi, R. 1972, The Astrophysical Journal, 178, 309

Forman, W., Nulsen, P., Heinz, S., et al. 2005, The Astrophysical Journal, 635, 894

Forman, W., Jones, C., Churazov, E., et al. 2007, The Astrophysical Journal, 665, 1057

Freeman, P. E., Kashyap, V., Rosner, R., & Lamb, D. Q. 2002, The Astrophysical Journal Supplement, 138, 185

Frisbie, R. L. S., Donahue, M., Voit, G. M., et al. 2020, The Astrophysical Journal, 899, 159

Fruscione, A., McDowell, J. C., Allen, G. E., et al. 2006, in Society of Photo-Optical Instrumentation Engineers (SPIE) Conference Series, Vol. 6270, Society of Photo-Optical Instrumentation Engineers (SPIE) Conference Series, 62701V

Gaspari, M., Brighenti, F., & Temi, P. 2015, Astronomy & Astrophysics, 579, A62

Gaspari, M., Ruszkowski, M., & Oh, S. P. 2013, Monthly Notices of the Royal Astronomical Society, 432, 3401

Gaspari, M., Ruszkowski, M., & Sharma, P. 2012, The Astrophysical Journal, 746, 94

Gaspari, M., Temi, P., & Brighenti, F. 2017, Monthly Notices of the Royal Astronomical Society, 466, 677

Gebhardt, K., Bender, R., Bower, G., et al. 2000, The Astrophysical Journal Letters, 539, L13

Giacconi, R., Gursky, H., Paolini, F. R., & Rossi, B. B. 1962, Physical Review Letters, 9, 439

Giacconi, R., Kellogg, E., Gorenstein, P., Gursky, H., & Tananbaum, H. 1971, The Astrophysical Journal Letters, 165, L27

Giacconi, R., Bechtold, J., Branduardi, G., et al. 1979a, The Astrophysical Journal Letters, 234, L1

Giacconi, R., Branduardi, G., Briel, U., et al. 1979b, The Astrophysical Journal, 230, 540

Grossová, R., Werner, N., Rajpurohit, K., et al. 2019, Monthly Notices of the Royal Astronomical Society, 488, 1917

Gursky, H., Kellogg, E. M., Leong, C., Tananbaum, H., & Giacconi, R. 1971, The Astrophysical Journal Letters, 165, L43

Haehnelt, M. G., Natarajan, P., & Rees, M. J. 1998, Monthly Notices of the Royal Astronomical Society, 300, 817

Harris, D. E., Finoguenov, A., Bridle, A. H., Hardcastle, M. J., & Laing, R. A. 2002, The Astrophysical Journal, 580, 110

HI4PI Collaboration, Ben Bekhti, N., Flöer, L., et al. 2016, Astronomy & Astrophysics, 594, A116

Hickox, R. C., & Markevitch, M. 2006, The Astrophysical Journal, 645, 95

Ho, L. C., Filippenko, A. V., & Sargent, W. L. W. 1993, The Astrophysical Journal, 417, 63

Ho, L. C., Filippenko, A. V., Sargent, W. L. W., & Peng, C. Y. 1997, The Astrophysical Journal Supplement, 112, 391

Hubble, E. 1929, Proceedings of the National Academy of Science, 15, 168

Hubble, E. P. 1936, Realm of the Nebulae

Jones, C., & Forman, W. 1984, The Astrophysical Journal, 276, 38

Jones, C., Mandel, E., Schwarz, J., et al. 1979, The Astrophysical Journal Letters, 234, L21

Juráňová, A., Werner, N., Gaspari, M., et al. 2019, Monthly Notices of the Royal Astronomical Society, 484, 2886

Kaastra, J. S., Mewe, R., & Nieuwenhuijzen, H. 1996, in UV and X-ray Spectroscopy of Astrophysical and Laboratory Plasmas, 411–414

Kalberla, P. M. W., Burton, W. B., Hartmann, D., et al. 2005, Astronomy & Astrophysics, 440, 775

Kellogg, E., Gursky, H., Leong, C., et al. 1971, The Astrophysical Journal Letters, 165, L49

Kereš, D., Katz, N., Davé, R., Fardal, M., & Weinberg, D. H. 2009, Monthly Notices of the Royal Astronomical Society, 396, 2332

Kereš, D., Katz, N., Weinberg, D. H., & Davé, R. 2005, Monthly Notices of the Royal Astronomical Society, 363, 2

Killeen, N. E. B., Bicknell, G. V., & Carter, D. 1986, The Astrophysical Journal, 309, 45

Kim, D.-W., Anderson, C., Burke, D., et al. 2018, The Astrophysical Journal, 853, 129

Kormendy, J., & Ho, L. C. 2013, Annual Reviews of Astronomy and Astrophysics, 51, 511

Kormendy, J., & Richstone, D. 1995, Annual Reviews of Astronomy and Astrophysics, 33, 581

Lakhchaura, K., Mernier, F., & Werner, N. 2019, Astronomy & Astrophysics, 623, A17

Lakhchaura, K., Werner, N., Sun, M., et al. 2018, Monthly Notices of the Royal Astronomical Society, 481, 4472

Leitner, S. N., & Kravtsov, A. V. 2011, The Astrophysical Journal, 734, 48

Li, Y., & Bryan, G. L. 2014a, The Astrophysical Journal, 789, 54

—. 2014b, The Astrophysical Journal, 789, 153

Liedahl, D. A., Osterheld, A. L., & Goldstein, W. H. 1995, The Astrophysical Journal Letters, 438, L115

Magorrian, J., Tremaine, S., Richstone, D., et al. 1998, The Astronomical Journal, 115, 2285

Makarov, D., Prugniel, P., Terekhova, N., Courtois, H., & Vauglin, I. 2014, Astronomy & Astrophysics, 570, A13

Markevitch, M., Bautz, M. W., Biller, B., et al. 2003, The Astrophysical Journal, 583, 70

Mathews, W. G., & Brighenti, F. 2003, Annual Reviews of Astronomy and Astrophysics, 41, 191

McCourt, M., Sharma, P., Quataert, E., & Parrish, I. J. 2012, Monthly Notices of the Royal Astronomical Society, 419, 3319

McNamara, B. R., & Nulsen, P. E. J. 2007, Annual Reviews of Astronomy and Astrophysics, 45, 117

—. 2012, New Journal of Physics, 14, 055023

Oesch, P. A., Brammer, G., van Dokkum, P. G., et al. 2016, The Astrophysical Journal, 819, 129

Pfeffermann, E., Briel, U. G., Hippmann, H., et al. 1987, in Society of Photo-Optical Instrumentation Engineers (SPIE) Conference Series, Vol. 733, Soft X-ray optics and technology, 519

Pizzolato, F., & Soker, N. 2005, The Astrophysical Journal, 632, 821

—. 2010, Monthly Notices of the Royal Astronomical Society, 408, 961

Planck Collaboration, Adam, R., Ade, P. A. R., et al. 2016, Astronomy & Astrophysics, 594, A1

Planck Collaboration, Aghanim, N., Akrami, Y., et al. 2018, arXiv e-prints, arXiv:1807.06209

Rafferty, D. A., McNamara, B. R., & Nulsen, P. E. J. 2008, The Astrophysical Journal, 687, 899

Rafferty, D. A., McNamara, B. R., Nulsen, P. E. J., & Wise, M. W. 2006, The Astrophysical Journal, 652, 216

Rasia, E., Meneghetti, M., Martino, R., et al. 2012, New Journal of Physics, 14, 055018

Reines, A. E., & Volonteri, M. 2015, The Astrophysical Journal, 813, 82

Ricarte, A., Tremmel, M., Natarajan, P., & Quinn, T. 2019, Monthly Notices of the Royal Astronomical Society, 489, 802

Riess, A. G., Macri, L., Casertano, S., et al. 2011, The Astrophysical Journal, 730, 119

Saglia, R. P., Opitsch, M., Erwin, P., et al. 2016, The Astrophysical Journal, 818, 47

Sarazin, C. L. 1986, Reviews of Modern Physics, 58, 1

Schure, K. M., Kosenko, D., Kaastra, J. S., Keppens, R., & Vink, J. 2009, Astronomy & Astrophysics, 508, 751

Sharma, P., McCourt, M., Quataert, E., & Parrish, I. J. 2012, Monthly Notices of the Royal Astronomical Society, 420, 3174

Snowden, S. L., Freyberg, M. J., Plucinsky, P. P., et al. 1995, The Astrophysical Journal, 454, 643

Soker, N. 2016, New Astronomy Review, 75, 1

Stark, A. A., Gammie, C. F., Wilson, R. W., et al. 1992, The Astrophysical Journal Supplement, 79, 77

Stoughton, C., Lupton, R. H., Bernardi, M., et al. 2002, The Astronomical Journal, 123, 485

Sun, M. 2009, The Astrophysical Journal, 704, 1586

Sun, M. in preparation

Tananbaum, H., Kellogg, E., Gursky, H., et al. 1971, The Astrophysical Journal Letters, 165, L37

Tonry, J. L., Dressler, A., Blakeslee, J. P., et al. 2001, The Astrophysical Journal, 546, 681

Voit, G. M., & Donahue, M. 2005, The Astrophysical Journal, 634, 955

—. 2011, The Astrophysical Journal Letters, 738, L24

—. 2015, The Astrophysical Journal, 799, L1

Voit, G. M., Donahue, M., Bryan, G. L., & McDonald, M. 2015a, Nature, 519, 203

Voit, G. M., Donahue, M., O'Shea, B. W., et al. 2015b, The Astrophysical Journal, 803, L21

Voit, G. M., Meece, G., Li, Y., et al. 2017, The Astrophysical Journal, 845, 80

Voit, G. M., Bryan, G. L., Prasad, D., et al. 2020, arXiv e-prints, arXiv:2006.09381

Wang, C., Li, Y., & Ruszkowski, M. 2019, Monthly Notices of the Royal Astronomical Society, 482, 3576

Weisskopf, M. C., Brinkman, B., Canizares, C., et al. 2002, Publications of the Astronomical Society of the Pacific, 114, 1

Werner, N., Allen, S. W., & Simionescu, A. 2012, Monthly Notices of the Royal Astronomical Society, 425, 2731

Werner, N., McNamara, B. R., Churazov, E., & Scannapieco, E. 2019, Space Science Reviews, 215, 5

Werner, N., Oonk, J. B. R., Sun, M., et al. 2014, Monthly Notices of the Royal Astronomical Society, 439, 2291

White, S. D. M., & Frenk, C. S. 1991, The Astrophysical Journal, 379, 52

Wiklind, T., Combes, F., & Henkel, C. 1995, Astronomy & Astrophysics, 297, 643

Williams, R. E., Blacker, B., Dickinson, M., et al. 1996, The Astronomical Journal, 112, 1335

Zabludoff, A. I., & Mulchaey, J. S. 1998, The Astrophysical Journal, 496, 39